Tuning the Membrane Properties of Functional Polymersomes Developed by Aqueous Polymerization-Induced Self-Assembly (PISA)

by

Spyridon Varlas

A thesis submitted to the University of Birmingham for the degree of
DOCTOR OF PHILOSOPHY

School of Chemistry
College of Engineering and Physical Sciences
University of Birmingham
May 2020

Abstract

Lipid bilayer membranes with precisely programmed properties play a vital role in most biological processes, enabling structural organization, confinement and communication on both a cellular and subcellular level. Self-assembled synthetic analogues, such as liposomes and polymersomes, have been widely investigated as simplified biomimetic models, providing a deeper understanding of fundamental membrane functions. The primary aim of this thesis was to explore novel methodologies for tuning the physicochemical membrane characteristics of functional polymersomes developed *via* aqueous polymerization-induced self-assembly (PISA) and highlight their potential application in biomimicry. In particular, PISA was employed for *in situ* preparation of block copolymer nano-objects at high concentrations throughout this thesis, owing to its robustness, versatility, and high reproducibility. Importantly, highly efficient strategies were established herein that afforded fine control over various properties of the prepared nanostructures, including the thickness, hydrophobicity, permeability, rigidity, and functionality of their membranes. Moreover, polymersomes of controllable size and shape could be also obtained depending on the experimental procedure followed. The outlined findings and identified trends were used for studying different communication and transport mechanisms within or between these nanocompartments, mediated either *via* passive diffusion of small molecules across selectively permeable membranes of catalytic nanoreactors or *via* intervesicular fusion events, and are expected to set the groundwork for future studies in biocatalysis and therapeutic delivery.

This thesis is dedicated to my partner Danai and my mother Eirini

for their unconditional love and invaluable support throughout the years.

Acknowledgements

The Acknowledgements section is personally my favorite part to read in other students' theses, since it gives credit and recognition to all the people who have directly or indirectly contributed to the production of such a significant piece of work in someone's career. Thus, now that it's time to write my own thesis acknowledgements, I will try my best to appropriately thank everyone who supported me throughout my Ph.D. studies.

First of all, I would like to sincerely thank my supervisor Professor Rachel O'Reilly for giving me the opportunity to work in her group, initially at the University of Warwick and then at the University of Birmingham, on such a fruitful research topic. I am truly grateful for her continuous support, mentorship and advice on both a scientific and personal level. I cannot thank her enough for allowing me to get involved in multiple projects, network and collaborate with many of my literature heroes and participate in numerous conferences around the world. I knew from the very beginning (even before starting my Ph.D.) we will have an excellent and constructive collaboration and that I will get the best out of me by working under her supervision. Finally, I would like to thank her for supporting my applications for various awards and scholarships and for providing helpful advice about my future academic steps. I am sure that we will maintain our excellent relationship and scientific collaboration in the years to come.

I would like to thank all the senior academics, as well as their group members, that I had the pleasure to collaborate with over the past four years for their contributions to the research projects that are part (or not) of this thesis. In particular, I would like to give my sincere thanks to Professor Matthew Gibson (University of Warwick, UK), Professor Robert Mathers (Penn State University, USA), Professor Nikos Hadjichristidis (KAUST,

Saudi Arabia), Professor Paula Booth (King's College London, UK), Professor Andrew Dove (University of Birmingham, UK), Professor Kris Thurecht (University of Queensland, Australia) and Dr. David Williams (Swansea University, UK) for their guidance and invaluable help toward putting together the missing pieces for some of my projects and converting them into more complete stories by sharing their knowledge and expertise and/or providing access to their facilities and instrumentation.

I would also like to especially thank my PISA partners and really good friends Dr. Jeffrey Foster, Dr. Robert Keogh and Dr. Lewis Blackman. I am grateful for your mentorship, scientific discussions and exchange of ideas, problem solving, and constructive criticism over the numerous projects that we have worked together. You have helped me greatly in order to develop a more in-depth understanding about ROMP, RAFT polymerization, block copolymer self-assembly, enzyme-mediated catalysis, light scattering, electron microscopy, … (the list can go on forever). You are three of the most talented, ethical and hard-working researchers that I've met in my academic career thus far! You have inspired me in so many ways and I have adopted many of your skills and practices toward becoming a better scientist and person overall. Apart from that, Jeff is the reason why the Polymers GRC has been the best week of my Ph.D. (you know why!), Rob has also been my cryo-TEM buddy (I will miss the cryo-cat and our cryo-related songs) and the person I would always chat about sports, and Lewis made me realize that I had to build a stronger character and learn how to overcome the academia-related failures in order to survive. A Ph.D. is a marathon consisted of multiple 100 meter sprints and without your help and contributions this thesis would not have been written by now!

Next, I would like to thank all my close friends from the O'Reilly and Dove groups who have made my everyday life in the lab a fun and memorable experience and supported

me in good and more challenging times over the past four years. I will truly miss all of you for a million different reasons (mostly our gossiping at the back end of the corridors and our fish ‘n’ chips/basketball Fridays), but I will make sure to stay in touch with everyone. In particular, I would like to personally thank Mr. Matthieu Miclotte (Manneken Pis), Dr. Stefan Lawrenson (loudest keyboard in the world), Miss Marjolaine Thomas (Where are you flying to next weekend?), Dr. Chiara Arno (bio-everything expert), Dr. Turgay Yildirim (Waaaaarrrr!), Dr. Joseph Jones (scattering Guru), the members of Chinese gang – Mr. Bo Li (King of Shanghai), Miss Yujie Xie (Queen of fluorescence and figure making), Dr. Wei You (better than Steph Curry), and Mr. Tianlai Xia (kindest person in the world), as well as the members of the SUSPOL team – Mr. Sètuhn Jimaja (Dr. Helix), Dr. Panagiotis Bexis (Greek lab buddy), Dr. Sofiem Garmendia (What a time to be alive!), and Dr. Noé Fanjul-Mosteirín (Real Oviedo is the only true Real) for all the support you’ve given me throughout the years.

I would also like to express my gratitude to all the Ph.D. (Miss Marjolaine Thomas, Miss Siriporn Chaimueangchuen, and Miss Alisha Miller) and Master’s (Mr. Panagiotis Georgiou, Mr. Robert McNally, Mr. Adam Smith, and Mr. Marcus Grocott) students that I had the pleasure to co-supervise and provide my knowledge and guidance on their research projects. I hope my assistance in your projects was beneficial and constructive, and always remember that if something doesn’t work, you should try PISA! I wish you all the success in your future endeavors.

I would like to thank all the researchers, technicians and assistants at both the University of Warwick and the University of Birmingham for sharing their expertise and knowledge and spending many hours training me in various characterization techniques. Additionally, I would like to thank the Research Administrators Miss Tessa Kintail and

Mrs. Annie Morton for providing their invaluable assistance to me and the rest of the O'Reilly group members and making our lives much easier by sorting out the numerous admin issues that have appeared over the years.

Moreover, I would like to thank the journal editors and reviewers who handled all my published work for their time and positive input. Your fairness, helpful suggestions and comments have been truly constructive and have improved every single one of my projects to a great degree.

Importantly, I would like to thank the European Research Council (ERC) for funding my Ph.D. studies, contributing to the publication of all my papers in open-access form and supporting my participation in many national and international conferences. Without their financial support, I wouldn't be able to pursue my dream and undertake my Ph.D. abroad! Special thanks also go to Macro Group UK for awarding me the DH Richards Memorial Travel Bursary and 2020 Ottewill International Travel Scholarship.

On a more personal level, I would like to thank my Greek/Cypriot best friends Panagiotis Georgiou (Brigitte), Spyridon Efstathiou (Tsitsipas 2.0), Despoina Coursari (Κόρη) and Georgios Patias (Έντεκα), that I was honored to meet during my postgraduate studies. Thank you all for sharing the same passion for polymer science as me, for supporting me every single day and spending countless hours discussing scientific and not-so-scientific matters with me and for making my spare time truly enjoyable. We have proven that a member of the O'Reilly group, a member of the Gibson group and three members of the Haddleton group can hang out together almost every weekend in pure harmony, despite all of us working in similar and highly competitive research fields. You are all AWESOME and I will always be there for you!

Lastly but most importantly, there are no words to describe my gratitude to the most wonderful person I've ever met, my partner Danai Plevria, who has been next to me for more than 10 (!!) years in both really amazing and really difficult times, for the unconditional love she has given me, her kindness, and the tremendous patience and constant support she has shown in every decision that I make (no matter how crazy they might often be!). We have taken countless leaps of faith over the years and we have proven that we can fight every difficulty that appears in our lives when we are together. Without you, I wouldn't be the person that I am today and I wouldn't have fulfilled many of my dreams and ambitions. I promise you that the best in our lives are about to come! Equally, I would like to thank my family back in Greece from the bottom of my heart for all their love and support throughout the years. Thank you all for always being there for me and making it seem like there hadn't been a single day that passed since I left home to pursue my Ph.D. studies. I love you all and I will keep trying my hardest to make you proud every single day!

Table of Contents

Table of Contents I
List of Figures III
List of Schemes VI
List of Symbols and Abbreviations VIII
List of Publications XVII
Declaration of Authorship XX
Chapter 1. Introduction 1
1.1. Introduction to Synthetic Polymers 2
1.2. Polymerization Techniques 4
1.2.1. Free Radical Polymerization (FRP) 8
1.2.2. Reversible-Deactivation Radical Polymerization (RDRP) Techniques 10
1.2.3. Reversible Addition−Fragmentation Chain Transfer (RAFT) Polymerization 13
1.2.3.1. Photoinitiated RAFT Polymerization (Photo-RAFT) 19
1.2.4. Ring-Opening Metathesis Polymerization (ROMP) 22
1.2.4.1. ROMP in Aqueous Media 27
1.3. Block Copolymer Self-Assembly in Solution 31
1.4. Polymerization-Induced Self-Assembly (PISA) 34
1.4.1. RAFT-mediated Photo-PISA 38
1.4.2. ROMP-mediated PISA (ROMPISA) 43
1.5. Block Copolymer Vesicles (Polymersomes) as Cell-Mimicking Bioreactors 46
1.6. Summary 55
1.7. References 56
Chapter 2. Photoinitiated Polymerization-Induced Self-Assembly in the Presence of Surfactants Enables Membrane Protein Incorporation into Vesicles 72
2.1. Publication Details and Overview 73
2.2. Appendix – Supporting Information Material 77
Chapter 3. Tuning the Membrane Permeability of Polymersome Nanoreactors Developed by Aqueous Emulsion Polymerization-Induced Self-Assembly 78
3.1. Publication Details and Overview 79

3.2. Appendix – Supporting Information Material.....83
Chapter 4. Predicting Monomers for Use in Aqueous Ring-Opening Metathesis Polymerization-Induced Self-Assembly 84
4.1. Publication Details and Overview.....85
4.2. Appendix – Supporting Information Material.....89
Chapter 5. Polymerization-Induced Polymersome Fusion.....92
5.1. Publication Details and Overview.....93
5.2. Appendix – Supporting Information Material.....98
Chapter 6. Conclusions and Outlook 100

List of Figures

Figure 1.1. The composition, topology and functionality of polymer-based materials are among the main features that determine their properties and, as a consequence, their potential applications. 4

Figure 1.2. Evolution of polymer molecular weight with increasing monomer conversion for (A) step-growth polymerization, (B) conventional chain-growth polymerization, and (C) living polymerization. 5

Figure 1.3. Electron microscopy images of typical and more "exotic" nanostructures arising from amphiphilic block copolymer self-assembly in solution. Images reproduced with permission from the following ref.: spherical micelles,[123] worm-like micelles,[124] spherical vesicles,[125] tubular vesicles,[126] "jellyfish"-like particles,[127] "sea urchin"-like particles,[128] lacunal spheres,[129] and porous vesicles.[130] 32

Figure 1.4. The adapted morphology for amphiphilic block copolymer nano-objects under thermodynamic equilibrium is dictated by the interfacial curvature between the incompatible blocks and packing of the individual chains within the structure, which can be estimated by calculating its packing parameter, *p*. 33

Figure 1.5. Schematic illustration of morphological evolution of diblock copolymer nano-objects developed during RAFT-mediated polymerization-induced self-assembly (PISA) under dispersion polymerization conditions. Reproduced from ref. 145 with permission from the Royal Society of Chemistry. 35

Figure 1.6. Phase diagram and representative TEM images of $PGMA_{78}$-*b*-$PHPMA_n$ diblock copolymer nano-objects developed *via* aqueous RAFT-mediated PISA upon varying the total solids content and DP_{PHPMA}. Reproduced from ref. 152 with permission from the American Chemical Society. 37

Figure 1.7. (A) Schematic of the synthetic procedure followed for preparation of PEG_{113}-*b*-$PHPMA_n$ diblock copolymer nano-objects *via* photo-PISA along with representative TEM images. (B) Encapsulation of BSA into the polymersomes developed under photo-PISA conditions and activity determination for native (1), post-PISA isolated (2) and denatured (3) BSA. Reproduced from ref. 180 with permission from the American Chemical Society. 40

Figure 1.8. Schematic illustration of the synthesis of BSA-based star macro-CTA and *in-situ* photo-PISA for preparation of BSA-*g*-PHPMA$_n$ spherical nano-objects. Reproduced from ref. 187 with permission from the American Chemical Society. 41
Figure 1.9. (A) Enzymatic cascade reaction between GOx- and HRP-loaded PEG$_{113}$-*b*-PHPMA$_{400}$ polymersome nanoreactors monitored by kinetic colorimetric analysis. Reproduced from ref. 172 with permission from the American Chemical Society. (B) Comparison of proteolytic susceptibility and antibody recognition for ASNS-loaded PEG$_{113}$-*b*-PHPMA$_{400}$ polymersomes, free ASNS and a PEGylated ASNS conjugate. Reproduced from ref. 125 with permission from the American Chemical Society..... 43
Figure 1.10. Representative TEM images of PNB-(tertiary amine)$_{10}$-*b*-PNB-(carboxylic acid)$_n$ diblock copolymer nano-objects developed *via* aqueous dispersion ROMPISA, and corresponding particle counting analysis in each case. Reproduced from ref. 88 with permission from Wiley-VCH Verlag GmbH & Co. 45
Figure 1.11. Schematic representation of the responsiveness of cargo-loaded polymersomes toward various externally applied stimuli and their potential utilization in biotechnological and biomedical applications. Reproduced from ref. 197 with permission from the American Chemical Society. 46
Figure 1.12. Schematic illustration of lipid (left) and block copolymer (right) vesicles, also referred to as liposomes and polymersomes, respectively. The main properties in each case are shown, signifying the higher physical stability and enhanced chemical versatility of polymersomes over liposomes. Reproduced from ref. 200 with permission from Elsevier. 47
Figure 1.13. Existing methodologies for development of tubular block copolymer polymersomes *via* (A) osmotic pressure-induced shape transformation of spherical polymersomes. Reproduced from ref. 220 with permission from the American Chemical Society, (B) cross-linking-induced shape transformation of spherical polymersomes. Reproduced from ref. 209 with permission from the American Chemical Society, and (C) block copolymer self-assembly in the presence of external additives, such as cholesterol. Reproduced from ref. 210 with permission from the American Chemical Society..... 50
Figure 1.14. Commonly employed methodologies for controllable regulation of small molecule transport across the membrane of enzyme-loaded polymersome nanoreactors: (A) Permeabilization through utilization of core-forming polymers that yield intrinsically

permeable membranes. Reproduced from ref. 227 with permission from Wiley-VCH Verlag GmbH & Co. (B) Incorporation of hydrophobic biopores, such as membrane proteins and ion channels, into the polymersome membranes. Reproduced from ref. 228 with permission from the Royal Society of Chemistry. (C) Permeabilization through utilization of stimuli-responsive membrane-forming polymers. Reproduced from ref. 229 with permission from the Royal Society of Chemistry. (D) Permeabilization through utilization of post-assembly approaches for membrane modification. Reproduced from ref. 230 with permission from the American Chemical Society. 51

List of Schemes

Scheme 1.1. Principal mechanistic steps along with their associated rate constants involved in free radical polymerization (FRP).....9
Scheme 1.2. Principal mechanistic steps along with their associated rate constants involved in atom transfer radical polymerization (ATRP). 12
Scheme 1.3. Principal mechanistic steps along with their associated rate constants involved in nitroxide-mediated radical polymerization (NMP).....13
Scheme 1.4. Principal mechanistic steps along with their associated rate constants involved in reversible addition–fragmentation chain transfer (RAFT) polymerization. 15
Scheme 1.5. (A) Classification of CTAs based on the functionality of the Z– group. (B) General guidelines for selection of R– and Z– groups of CTAs expressed in terms of RAFT polymerization control of various monomers (the dashed lines represent limited or poor polymerization control). Abbreviations: MMA - methylmethacrylate, HPAM - 2-hydroxypropyl methacrylamide, St - styrene, MA - methyl acrylate, AM - acrylamide, AN - acrylonitrile, VAc - vinyl acetate, NVP - *N*-vinylpyrrolidone, NVC - *N*-vinylcarbazole. Reproduced from ref. 34 with permission from the American Chemical Society.....17
Scheme 1.6. Utilization of either R- or Z-functionalized macro-CTAs for the synthesis of diblock copolymers *via* RAFT polymerization dictates the localization of the thiocarbonylthio moiety within the polymer chain. Reproduced from ref. 44 with permission from the Royal Society of Chemistry. 18
Scheme 1.7. Different mechanisms of photo-RAFT: (A) photoinitiator-mediated RAFT polymerization, (B) PET-RAFT polymerization *via* electron (top) and energy (bottom) transfer, (C) oxygen-tolerant PET-RAFT polymerization, and (D) photoiniferter-mediated RAFT polymerization. Reproduced from ref. 54 and 55 with permission from Wiley-VCH Verlag GmbH & Co and the Royal Society of Chemistry, respectively. ...20
Scheme 1.8. Accepted mechanism of ring-opening metathesis polymerization (ROMP). 24
Scheme 1.9. Chemical structures of common, commercially available metathesis catalysts. 25

Scheme 1.10. Chemical structures of water-soluble Ru-based catalysts based on either (A) **HG2** or (B) **G3** scaffolds recently reported for aqueous ROMP. 29
Scheme 1.11. Two-step methodology for controlled aqueous ROMP mediated by a water-soluble macroinitiator, reported by O'Reilly and coworkers.[88] 30

List of Symbols and Abbreviations

[M]	Monomer concentration
$[M]_0$	Initial monomer concentration
°C	Degrees Celsius
1D	One-dimensional
a	Area
Å	Angstrom(s)
ACM	Aminochloromaleimide
ACVA	Azobis(4-cyanovaleric acid)
ADMET	Acyclic diene metathesis
$AgC_{22}H_{43}O_2$	Silver behenate
AMA	1-Adamantanemethylamine
AqpZ	Aquaporin Z
ASNS	*L*-Asparaginase
ATRP	Atom-transfer radical polymerization
BA	Benzylamine
BSA	Bovine serum albumin
C	Local membrane curvature
c	Concentration
C	Circularity
C_2DA	Ethylenediamine
C_3DA	1,3-Diaminopropane
C_4DA	1,4-Diaminobutane
C_6DA	Hexamethylenediamine
ca.	Circa
C_{ave}	Average circularity
CD	Circular dichroism
C_D	Dissociation constant
CD_3OD	Methanol-d_4
$CDCl_3$	Chloroform-*d*
CEPA	4-Cyano-4-[(ethylsulfanylthiocarbonyl)sulfanyl]pentanoic acid

CHAPS	3-[(3-Cholamidopropyl)dimethylammonio]-1-propanesulfonate
CM	Cross metathesis
cm^{-1}	Wavenumber(s)
CMC	Critical micelle concentration
cryo-TEM	Cryogenic transmission electron microscopy
C_{surf}	Surfactant concentration
CTA	Chain transfer agent
CTAB	Cetyltrimethylammonium bromide
Cu	Copper
Cy5-NHS	Cyanine5 succinimidyl ester
d	Deuterium labelled
D	Diameter
D	Diffusion coefficient
D_{ave}	Average diameter
DCC	*N,N′*-Dicyclohexylcarbodiimide
DCM	Dichloromethane
DDM	*n*-Dodecyl *β*-D-maltoside
D_h	Hydrodynamic diameter
DI water	Deionized water
DIAD	Diisopropyl azodicarboxylate
$Đ_L$	Length dispersity
DLS	Dynamic light scattering
$Đ_M$	Dispersity
DMAEMA	2-(Dimethylamino)ethyl methacrylate
DMAP	4-(Dimethylamino)pyridine
DMB	3,3′-Dimethoxybenzidine
DMF	*N,N*-Dimethyl formamide
DMPA	2,2-Dimethoxy-2-phenylacetophenone
DMSO	Dimethyl sulfoxide
d*n*/dc	Refractive index increment
DNA	Deoxyribonucleic acid
DP	Degree of polymerization

DPC	*n*-Dodecylphosphocholine
DPD	Dissipative particle dynamics
DSC	Differential scanning calorimetry
E(t')	Measured instrumental response function
E_b	Membrane bending energy
EDC.HCl	*N*-(3-Dimethylaminopropyl)-*N*′-ethylcarbodiimide hydrochloride
eq	Equivalent(s)
EtOAc	Ethyl acetate
EVE	Ethyl vinyl ether
FAM-NHS	5/6-Carboxyfluorescein succinimidyl ester
F_C	Fraction of cylindrical tubesomes over spherical particles
FL	Fluorescence lifetime
FRET	Förster resonance energy transfer
FRP	Free radical polymerization
FT-IR	Fourier Transform-Infrared
g	Gram(s)
G1	First-generation Grubbs catalyst
G2	Second-generation Grubbs catalyst
G3	Third-generation Grubbs catalyst
gA	Gramicidin
GFP	Green fluorescent protein
GlpF	Glycerol facilitator
GlyMA	Glycidyl methacrylate
GO	Graphene oxide
GOx	Glucose oxidase
GTP	Group transfer polymerization
GULVs	Giant unilamellar vesicles
h	Hour(s)
H_2O	Water
H_2O_2	Hydrogen peroxide
HG1	First-generation Hoveyda-Grubbs catalyst

HG2	Second-generation Hoveyda-Grubbs catalyst
HPLC	High-performance liquid chromatography
HPMA	2-Hydroxypropyl methacrylate
HRMS	High resolution mass spectrometry
HRP	Horseradish peroxidase
IRF	Instrument response functions
I_{sample}	Intensity of the scattered light
$I_{x/y\ ppm}$	Integral ratio corresponding to proton signals at x and y ppm
K	Degrees Kelvin
k	Membrane bending rigidity
k_{app}	Kinetic constant
kcps	Counting rate
kDa	Kilodaltons
kg	Kilogram(s)
K_m	Equilibrium substrate dissociation constant
K_m^*	Apparent substrate dissociation constant
kV	Kilovolts
l	Length
LAMs	Less activated monomers
L_{ave}	Average particle length
LED	Light emitting diode
L_n	Number-average length
LogP_{oct}	Octanol−water partition coefficient
L_w	Weight-average length
m/z	Mass to charge ratio
mA	Milliamp(s)
macro-CTA	Macromolecular chain transfer agent
MALDI-ToF MS	Matrix-assisted laser desorption/ionization time-of-flight mass spectrometry
MAMs	More activated monomers
M_{ave}	Average membrane thickness
MD	Molecular dynamics

MeCN	Acetonitrile
MEG	Monoethylene glycol
MeOH	Methanol
mg	Milligram(s)
$MgSO_4$	Magnesium sulfate
MHz	Megahertz
min	Minute(s)
mL	Milliliter(s)
MLVs	Multilamellar vesicles
mM	Millimolar
mm	Millimeter(s)
mmol	Millimole(s)
M_n	Number average molecular weight
mol	Mole(s)
mV	Millivolt(s)
MVVs	Multivesicular vesicles
M_w	Weight average molecular weight
mW	Milliwatts
MW	Molecular weight
MWCO	Molecular weight cut-off
MΩ	Megaohm(s)
n	Refractive index
$N_2(g)$	Nitrogen gas
N_A	Avogadro's number
Na_2SO_4	Sodium sulfate
NaCl	Sodium chloride
N_{agg}	Aggregation number
$NaHCO_3$	Sodium bicarbonate
NaPhos	Sodium phosphate
NB	Norbornene
NEt_3	Triethylamine
N_F	Average number of fused particles

NH_4BF_4	Ammonium tetrafluoroborate
NH_4Cl	Ammonium chloride
NH_4OH	Ammonium hydroxide
NHC	*N*-Heterocyclic carbene
nm	Nanometer(s)
NMA	1-Naphthylmethylamine
NMP	Nitroxide-mediated polymerization
NMR	Nuclear magnetic resonance
N_S	Number of spherical polymersomes
ns	Nanoseconds
N_T	Number of tubular polymersomes
OG	Octyl β-D-glucopyranoside
OmpF	Outer membrane protein F
ONB	Oxanorbornene
p	Monomer conversion
p	Perimeter
p	Packing parameter
PB	Phosphate buffer
PB-*b*-P2VP-*b*-PEO	Poly(butadiene)-*b*-poly(2-vinylpyridine)-*b*-poly(ethylene oxide)
PB-*b*-PEO	Poly(butadiene)-*b*-poly(ethylene oxide)
PC	Photoredox catalyst
PD	Polydispersity
PDMAEMA	Poly(2-(dimethylamino)ethyl methacrylate)
PEG	Poly(ethylene glycol)
PEG-*b*-PHPMA	Poly(ethylene glycol)-*b*-poly(2-hydroxypropyl methacrylate)
PEG_nDA	Poly(ethylene glycol)$_n$ diamine
PET	Photo-induced electron/energy transfer
PGlyMA	Poly(glycidyl methacrylate)
PGMA-*b*-PHPMA	Poly(glycerol monomethacrylate)-*b*-poly(2-hydroxypropyl methacrylate)
Photo-PISA	Photoinitiated polymerization-induced self-assembly

Photo-RAFT	Photoinitiated reversible addition−fragmentation chain-transfer
PISA	Polymerization-induced self-assembly
PMMA	Poly(methyl methacrylate)
PMOXA-*b*-PDMS-*b*-PMOXA	Poly(2-methyl-2-oxazoline)-*b*-poly(dimethylsiloxane)-*b*-poly(2-methyl-2-oxazoline)
PMPC-*b*-PDPA	Poly(2-methacryloyloxyethyl phosphorylcholine)-*b*-poly(2-(diisopropylamine)ethyl methacrylate)
PNB	Polynorbornene
PNIPAAm-*b*-PNBOCA	Poly(*N*-isopropylacrylamide)-*b*-poly(2-((((2-nitrobenzyl)-oxy)carbonyl)amino)ethyl acrylate)
PPh_3	Triphenylphosphine
ppm	Parts per million
PP-OH	2-Hydroxy-4′-2-(hydroxyethoxy)-2-methylpropiophenone
PRE	Persistent radical effect
PS	Polystyrene
PS-*b*-PIAT	Polystyrene-*b*-poly(L-isocyanoalanine(2-thiophen-3-yl-ethyl)amide)
PXDA	*p*-Xylylenediamine
q	Scattering vector
R	Radius
R(t - t')	Theoretical sample decay model function
RAFT	Reversible addition−fragmentation chain-transfer
RCM	Ring-closing metathesis
RDRP	Reversible-deactivation radical polymerization
R_g	Radius of gyration
R_h	Hydrodynamic radius
RhB	Rhodamine B
RI	Refractive index
ROMP	Ring-opening metathesis polymerization
ROMPISA	Ring-opening metathesis polymerization-induced self-assembly
ROP	Ring-opening polymerization
RP-HPLC	Reverse phase high-pressure liquid chromatography

rpm	Rounds per minute
Ru	Ruthenium
R_Z	External radius
R_θ	Rayleigh ratio
S	Spherical micelles
s	Second(s)
S	Maximum dimension
S(t)	Measured fluorescence decay
SA	Solvent-accessible surface area
S_{ave}	Average maximum dimension
SAXS	Small-angle X-ray scattering
SDS	Sodium dodecyl sulfate
SDS-PAGE	Sodium dodecyl sulfate–polyacrylamide gel electrophoresis
SEC	Size exclusion chromatography
SLS	Static light scattering
SNARE	SNAP receptor
SPTP	Sodium phenyl-2,4,6-trimethylbenzoylphosphinate
t	Time
T	Tubesomes
$t_{1/2}$	Half-life
TEM	Transmission electron microscopy
TFA	Trifluoroacetic acid
T_g	Glass transition temperature
THF	Tetrahydrofuran
TLC	Thin-layer chromatography
TMS	Tetramethylsilane
Triton X-100	4-(1,1,3,3-Tetramethylbutyl)phenyl-polyethylene glycol
U	Units
UA	Uranyl acetate
ULVs	Unilamellar vesicles
UV	Ultraviolet
UV-Vis	Ultraviolet–visible

V	Vesicles
V	Volts
V_0	Reaction velocity
V_{max}	Maximal velocity
vs	Versus
W	Worm-like micelles
W	Watts
W_k	Weighting factor
Xe	Xeon
X_n	Average degree of polymerization
δ	Chemical shift
ΔA	Membrane surface area
$\Delta Abs_{x\ nm}$	Difference in absorbance at a wavelength of x nm
η	Viscosity
λ	Wavelength
$\lambda_{em.}$	Emission wavelength
$\lambda_{ex.}$	Excitation wavelength
μ_E	Electrophoretic mobility
µg	Microgram(s)
µL	Microliter(s)
µM	Micromolar
µm	Micrometer(s)
µmol	Micromole(s)
ν	Wavenumbers
σ	Membrane tension
T	Temperature
$\tau_{Av,A}$	Amplitute-average fluorescence lifetime
$\tau_{Av,I}$	Intensity-average fluorescence lifetime
θ	Angle

List of Publications

16. Foster, J. C.; Grocott, M. C.; Arkinstall, L. A.; **Varlas, S.**; Redding, M. J.; Grayson, S. M.; O'Reilly, R. K. It's Better with Salt: Aqueous Ring-Opening Metathesis Polymerization at Neutral pH. *J. Am. Chem. Soc*. **2020**, DOI: 10.1021/jacs.0c05499.

15. **Varlas, S.**; Lawrenson, S. B.; Arkinstall, L. A.; O'Reilly, R. K.; Foster, J. C. Self-assembled nanostructures from amphiphilic block copolymers prepared *via* ring-opening metathesis polymerization (ROMP). *Prog. Polym. Sci*. **2020**, *107*, 101278.

14. Jimaja, S.; **Varlas, S.**; Xie, Y.; Foster, J. C.; Taton, D.; Dove, A. P.; O'Reilly, R. K. Nickel-Catalyzed Coordination Polymerization-Induced Self-Assembly of Helical Poly(Arylisocyanide)s. *ACS Macro Lett*. **2020**, *9*, 226-232.

13. Keogh, R.; Blackman, L. D.; Foster, J. C.; **Varlas, S.**; O'Reilly, R. K. The Importance of Cooperativity in Polymer Blending: Toward Controlling the Thermoresponsive Behavior of Blended Block Copolymer Micelles. *Macromol. Rapid Commun*. **2020**, *41*, 1900599.

12. **Varlas, S.**; Keogh, R.; Xie, Y.; Horswell, S. L.; Foster, J. C.; O'Reilly, R. K. Polymerization-Induced Polymersome Fusion. *J. Am. Chem. Soc*. **2019**, *141*, 20234-20248.

11. **Varlas, S.**; Foster, J. C.; O'Reilly, R. K. Ring-opening metathesis polymerization-induced self-assembly (ROMPISA). *Chem. Commun*. **2019**, *55*, 9066-9071.

10. **Varlas, S.**; Foster, J. C.; Georgiou, P. G.; Keogh, R.; Husband, J. T.; Williams, D. S.; O'Reilly, R. K. Tuning the membrane permeability of polymersome nanoreactors

developed by aqueous emulsion polymerization-induced self-assembly. *Nanoscale* **2019**, *11*, 12643-12654.

9. **Varlas, S.**; Foster, J. C.; Arkinstall, L. A.; Jones, J. R.; Keogh, R.; Mathers, R. T.; O'Reilly, R. K. Predicting Monomers for Use in Aqueous Ring-Opening Metathesis Polymerization-Induced Self-Assembly. *ACS Macro Lett*. **2019**, *8*, 466-472.

8. Foster, J. C.; **Varlas, S.**; Couturaud, B.; Coe, Z.; O'Reilly, R. K. Getting into Shape: Reflections on a New Generation of Cylindrical Nanostructures' Self-Assembly using Polymer Building Blocks. *J. Am. Chem. Soc.* **2019**, *141*, 2742-2753.

7. †Couturaud, B.; †Georgiou, P. G.; **Varlas, S.**; Jones, J. R.; Arno, M. C.; Foster, J. C.; O'Reilly, R. K. Poly(Pentafluorophenyl Methacrylate)-Based Nano-Objects Developed by Photo-PISA as Scaffolds for Post-Polymerization Functionalization. *Macromol. Rapid Commun*. **2019**, *40*, 1800460.

6. **Varlas, S.**; Georgiou, P. G.; Bilalis, P.; Jones, J. R.; Hadjichristidis, N.; O'Reilly, R. K. Poly(Sarcosine)-Based Nano-Objects with Multi-Protease Resistance by Aqueous Photoinitiated Polymerization-Induced Self-Assembly (Photo-PISA). *Biomacromolecules* **2018**, *19*, 4453-4462.

5. Foster, J. C.; †**Varlas, S.**; †Couturaud, B.; Jones, J. R.; Keogh, R.; Mathers, R. T.; O'Reilly, R. K. Predicting Monomers for use in Polymerization-Induced Self-Assembly. *Angew. Chem. Int. Ed*. **2018**, *57*, 15733-15737.

4. **Varlas, S.**; Blackman, L. D.; Findlay, H. E.; Reading, E.; Booth, P. J.; Gibson, M. I.; O'Reilly, R. K. Photoinitiated Polymerization-Induced Self-Assembly in the Presence of Surfactants Enables Membrane Protein Incorporation into Vesicles. *Macromolecules* **2018**, *51*, 6190-6201.

3. Foster, J. C.; **Varlas, S.**; Blackman, L. D.; Arkinstall, L. A.; O'Reilly, R. K. Ring-Opening Metathesis Polymerization in Aqueous Media using a Macroinitiator Approach. *Angew. Chem. Int. Ed*. **2018**, *57*, 10672-10676.

2. †Blackman, L. D.; †**Varlas, S.**; Arno, M. C.; Houston, Z. H.; Fletcher, N. L.; Thurecht, K. J.; Hasan, M.; Gibson, M. I.; O'Reilly, R. K. Confinement of Therapeutic Enzymes in Selectively Permeable Polymer Vesicles by Polymerization-Induced Self-Assembly (PISA) Reduces Antibody Binding and Proteolytic Susceptibility. *ACS Cent. Sci*. **2018**, *4*, 718-723.

1. Blackman, L. D.; **Varlas, S.**; Arno, M. C.; Fayter, A.; Gibson, M. I.; O'Reilly, R. K. Permeable Protein-Loaded Polymersome Cascade Nanoreactors by Polymerization-Induced Self-Assembly. *ACS Macro Lett*. **2017**, *6*, 1263-1267.

† Denotes equal author contribution

Declaration of Authorship

This thesis is submitted to the University of Birmingham in support of my application for the degree of Doctor of Philosophy. This thesis was composed by myself and has not been submitted previously for the award of any degree.

Parts of this thesis have been published by the author in the form of open-access articles in peer-reviewed scientific journals as stated below. The work presented herein, including project design and performance of experiments, materials characterization, data collection and analysis, figure and manuscript preparation, was carried out by myself except for contributions from other colleagues which are outlined below in further detail.

Chapter 1 – Sections 1.2.4 and 1.2.4.1 of this Chapter have been adapted from a review article published by the author after the submission process of this thesis with permission from: Varlas, S.; Lawrenson, S. B.; Arkinstall, L. A.; O'Reilly, R. K.; Foster, J. C. Self-assembled nanostructures from amphiphilic block copolymers prepared *via* ring-opening metathesis polymerization (ROMP). *Prog. Polym. Sci*. **2020**, *107*, 101278. Copyright 2020 Elsevier. (link)

Chapter 2 – "Reprinted with permission from: Varlas, S.; Blackman, L. D.; Findlay, H. E.; Reading, E.; Booth, P. J.; Gibson, M. I.; O'Reilly, R. K. Photoinitiated Polymerization-Induced Self-Assembly in the Presence of Surfactants Enables Membrane Protein Incorporation into Vesicles. *Macromolecules* **2018**, *51*, 6190-6201. Copyright 2018 American Chemical Society." (link)

Dry-state TEM imaging of PISA nano-objects in the presence of various surfactants was performed with assistance from Dr. Lewis D. Blackman. OmpF porin purification and characterization by SDS-PAGE and protease resistance assay were performed by Dr. Heather E. Findlay at King's College London. Native mass spectroscopic analysis of purified OmpF porin was performed by Dr. Eamonn Reading at King's College London. Cryo-TEM imaging of block copolymer nano-objects was performed with assistance from Dr. Lewis D. Blackman, Dr. Robert Keogh and Dr. Saskia Bakker at the University of Warwick. Circular dichroism measurements were carried out with assistance from Dr. Muhammad Hasan at the University of Warwick. The design and construction of the photoreactor used for the photoinitiated polymerizations was carried out by Mr. Rod Wesson at the University of Warwick. Prof. Paula J. Booth (King's College London) and Prof. Matthew I. Gibson (University of Warwick) provided guidance and editing of this manuscript. Prof. Rachel K. O'Reilly (University of Birmingham) supervised the research project, provided guidance and editing of this manuscript.

Chapter 3 – "Reprinted with permission from: Varlas, S.; Foster, J. C.; Georgiou, P. G.; Keogh, R.; Husband, J. T.; Williams, D. S.; O'Reilly, R. K. Tuning the membrane permeability of polymersome nanoreactors developed by aqueous emulsion polymerization-induced self-assembly. *Nanoscale* **2019**, *11*, 12643-12654. Copyright 2019 The Royal Society of Chemistry." (link)

Part of the modification reactions of epoxy-functionalized polymersome nanoreactors using hydrophobic primary amines were performed with assistance from Mr. Panagiotis G. Georgiou at the University of Birmingham. Cryo-TEM imaging of polymersome

nanoreactors was performed with assistance from Dr. Robert Keogh and Dr. Saskia Bakker at the University of Warwick. HPLC traces and MALDI-ToF mass spectra of HRP before and after reaction with glycidol were acquired by Mr. Jonathan T. Husband at the University of Birmingham. The design of Michaelis-Menten kinetics determination experiments and discussion of obtained kinetic data were carried out with assistance from Dr. Jeffrey C. Foster and Dr. David S. Williams at the University of Birmingham. Optical microscopy imaging of the initial monomer-in-water emulsion solution was performed with assistance from Dr. Maria C. Arno at the University of Birmingham. The design and construction of the photoreactor used for the photoinitiated polymerizations was carried out by Mr. Rod Wesson at the University of Warwick. Dr. Jeffrey C. Foster (University of Birmingham) and Dr. David S. Williams (Swansea University) provided guidance and editing of this manuscript. Prof. Rachel K. O'Reilly (University of Birmingham) supervised the research project, provided guidance and editing of this manuscript.

Chapter 4 – "Reprinted with permission from: Varlas, S.; Foster, J. C.; Arkinstall, L. A.; Jones, J. R.; Keogh, R.; Mathers, R. T.; O'Reilly, R. K. Predicting Monomers for Use in Aqueous Ring-Opening Metathesis Polymerization-Induced Self-Assembly. *ACS Macro Lett*. **2019**, *8*, 466-472. Copyright 2019 American Chemical Society." (link)

Synthesis of norbornene-based monomers used in this study was performed with assistance from Dr. Jeffrey C. Foster and Ms. Lucy A. Arkinstall at the University of Birmingham. SAXS measurements were performed by Dr. Steven Huband at the University of Warwick, while SAXS data analysis and discussion were performed by Dr. Joseph R. Jones at the University of Birmingham. Cryo-TEM imaging of polymersomes

was performed with assistance from Dr. Robert Keogh and Dr. Saskia Bakker at the University of Warwick. LogP_{oct}/SA calculations for reported and predicted monomers, as well as for their corresponding oligomers were performed by Prof. Robert T. Mathers at the Pennsylvania State University. MicroDSC analysis was performed with assistance from Mr. Zachary Coe at the University of Birmingham. Dr. Jeffrey C. Foster (University of Birmingham) and Prof. Robert T. Mathers (Pennsylvania State University) provided guidance and editing of this manuscript. Prof. Rachel K. O'Reilly (University of Birmingham) supervised the research project, provided guidance and editing of this chapter.

Chapter 5 – "Reprinted with permission from: Varlas, S.; Keogh, R.; Xie, Y.; Horswell, S. L.; Foster, J. C.; O'Reilly, R. K. Polymerization-Induced Polymersome Fusion. *J. Am. Chem. Soc*. **2019**, *141*, 20234-20248. Copyright 2019 American Chemical Society." (link)

ROMPISA kinetic experiments, *in situ* turbidimetric analysis and characterization of obtained kinetic samples by DLS was carried out with assistance from Dr. Robert Keogh at the University of Birmingham. Dry-state TEM image analysis was performed with assistance from Dr. Jeffrey C. Foster at the University of Birmingham. Cryo-TEM imaging of spherical and tubular polymersomes was performed with assistance from Dr. Robert Keogh and Dr. Saskia Bakker at the University of Warwick. Synthesis of ACM- and RhB-functionalized norbornene monomers was carried out with assistance from Ms. Yujie Xie and synthesis of ACM- and RhB-containing triblock copolymer nano-objects was performed with assistance from Dr. Robert Keogh at the University of Birmingham.

Steady-state fluorescence spectroscopy and fluorescence lifetime measurements were performed by Ms. Yujie Xie at the University of Birmingham. Confocal microscopy imaging of dye-loaded samples was carried out with assistance from Ms. Yujie Xie at the University of Birmingham. SLS analysis was carried out by Dr. Robert Keogh at the University of Birmingham. SAXS measurements were performed by Dr. Steven Huband at the University of Warwick, while SAXS data analysis was performed by Dr. Sarah L. Horswell at the University of Birmingham. DSC analysis was performed with assistance from Ms. Irem Akar at the University of Birmingham. Dr. Jeffrey C. Foster (University of Birmingham) and Prof. Rachel K. O'Reilly (University of Birmingham) supervised the research project, provided guidance and editing of this manuscript.

Chapter 1. Introduction

1.1. Introduction to Synthetic Polymers

The term *polymer*, first introduced in 1833 by Swedish chemist Jöns Jakob Berzelius and established with its modern etymology in 1920 by German chemist Hermann Staudinger, derives from the Greek words *πολύς* (*polys*, meaning "many") and *μέρος* (*meros*, meaning "part").[1, 2] Polymers are complex, high molar mass molecules (also referred to as macromolecules) composed of a sequence of smaller repeated subunits, called monomers, that are linked to one another through covalent or non-covalent intermolecular interactions to form long chains or networks. Naturally occurring polymers such as deoxyribonucleic acid (DNA), proteins and polysaccharides, play vital roles in sustaining all forms of life, as they are essential components in the vast majority of biological processes. Not surprisingly, tremendous research effort has been devoted over the past century toward the development of synthetic polymers that mimic certain characteristics and functions of their natural counterparts, and their utilization in a wide range of industrial and biomedical applications. However, such synthetic species have yet to achieve the high complexity and sequence-defined uniformity of natural polymers.[3, 4]

Polymers are synthesized *via* a chemical process termed *polymerization*, during which the overall number of repeated monomeric units within a single polymer chain, also defined as degree of polymerization (DP), and the distribution of molecular mass across all polymer chains, also known as dispersity ($Đ_M$) – the ratio between weight-average molar mass (M_w) to number-average molar mass (M_n), should be precisely controlled.[5] Typically, these values are two of the main parameters that determine the physicochemical properties of polymers, which are distinctly different and often superior with respect to their constituent small molecules. Due to their high molecular mass, polymers present increased viscosity, mechanical strength, and chemical resistance,

amongst other properties.[6] Uniquely, polymers also display glass transition temperatures (T_g) – defined as the temperature at which polymers undergo a glassy-to-amorphous state transition.[6]

Importantly, there are a number of other factors that can affect the final properties and ultimately the application of polymer-based materials. In particular, the composition, topology and functionality of synthetic polymers are parameters that can be externally controlled for the design and preparation of well-defined materials with certain application-oriented characteristics (Figure 1.1).[7-9] Polymer composition can be programmed by precisely tuning the sequence (e.g., homopolymer, block copolymer, alternating copolymer, statistical/random copolymer, *etc*), and tacticity (e.g., isotactic, syndiotactic, or atactic polymer) of monomeric units across the polymer chain, as well as the total polymer molecular weight. In addition, polymers with varying topologies (e.g., linear, cyclic, star, bottlebrush, *etc*), also expressed in terms of their macromolecular architecture, present markedly different macroscopic features. Finally, polymers that bear reactive or polymerizable moieties within their structure are able to undergo subsequent post-polymerization modification for the introduction of a broad range of functionalities and the development of materials with uniquely distinct properties compared to their parent polymers.[7-9]

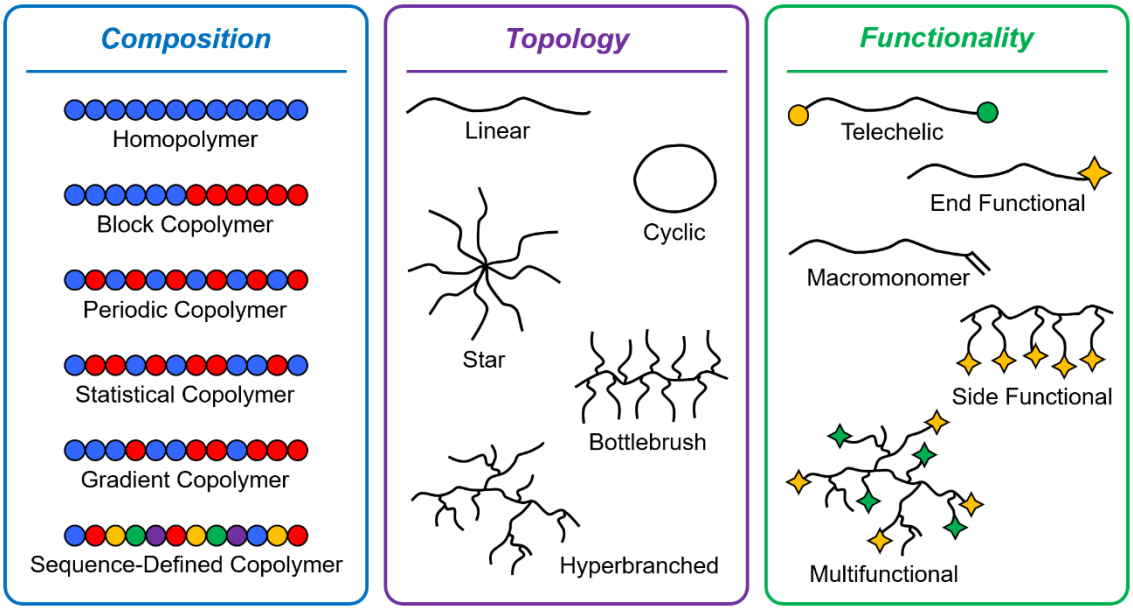

Figure 1.1. The composition, topology and functionality of polymer-based materials are among the main features that determine their properties and, as a consequence, their potential applications.

1.2. Polymerization Techniques

Over the last century, numerous polymerization methodologies have been developed and can be primarily divided into two main categories – step-growth polymerization[10, 11] and chain-growth polymerization[12] – depending on the mechanism under which polymer growth proceeds. The basic principles of each polymerization type will be briefly introduced herein, and particular focus will be given to polymerization techniques utilized within the experimental Chapters of this thesis.

To date, step-growth polymerization, such as polycondensation or polyaddition reactions, remains one of the most widely utilized and economically viable approaches for polymer synthesis at industrial scale.[13] Typical examples of polymers prepared *via* step-growth polymerization processes include polyesters, polyamides, polyurethanes, and polyureas. During the initial stages of step-growth polymerization, two homo-bifunctional or hetero-

bifunctional monomers react to form dimer products. Then, these dimers can react with another monomer to produce a trimer or combine with other dimers to form tetramers. This series of events continues in a step-wise manner until short oligomeric chains are formed. In principle, polymers of high molecular weight are only attained at the late stages of the process, whereby near-quantitative monomer conversions are achieved and oligomers can further react with each other (Figure 1.2A). This also coincides with a broadening in the molecular weight distribution of the resulting polymers. Step-growth polymerizations typically proceed until the limiting reagent/monomer is fully consumed.[11, 14]

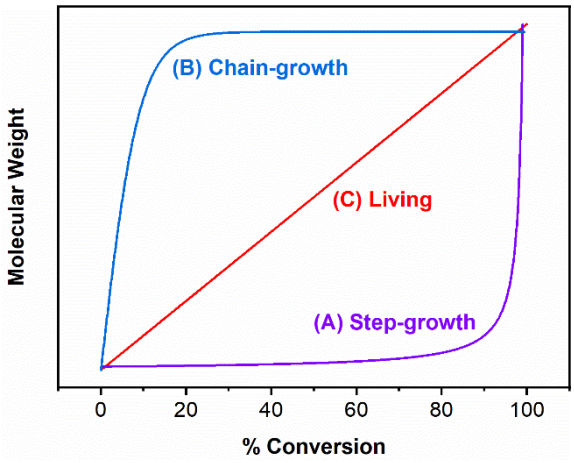

Figure 1.2. Evolution of polymer molecular weight with increasing monomer conversion for (A) step-growth polymerization, (B) conventional chain-growth polymerization, and (C) living polymerization.

It is also important to note that low molecular weight species exist throughout the whole duration of a step-growth polymerization process, highlighting the requirement of additional post-polymerization purification steps to yield highly pure polymers. Additionally, precise control over the stoichiometric ratio of the monomeric species coupled with high monomer purity, strictly monitored reaction conditions and long reaction times are usually required for the synthesis of high molar mass polymers.[11]

Ultimately, step-growth polymerization is prone to terminating side reactions and is considered a less versatile and robust methodology compared to its chain-growth counterpart.

In opposition to the sole chemical reaction occurring between monomers throughout step-growth polymerization, chain-growth polymerization processes involve multiple types of reactions that occur simultaneously at different rates and *via* distinct mechanisms. Generally, these reactions can be classified in initiation, propagation and termination reactions.[15] During the initiation stage, activated polymerization mediators, such as radicals and ions, are generated by the external supply of energy (e.g., heat, light, electromagnetic radiation), which act as intermediate species in propagation and termination steps.[16, 17] Subsequent reaction of these active species with monomers results in the formation of growing polymer chains, which can then repeatedly react with additional monomeric units through their reactive chain ends in a process termed propagation. The propagation step proceeds until full monomer consumption is achieved or the reactive sites of the growing chains are deactivated by reaction with each other, or with other terminating species. Other side-reactions such as (ir)reversible chain transfer often occur during chain-growth polymerization, reducing the average molecular weight of the final polymer.[15]

Contrary to step-growth polymerization, monomer concentration decreases constantly with time during chain-growth polymerization, while high molar mass polymers can form throughout the polymerization process. Moreover, for conventional, poorly controlled chain-growth polymerization methodologies, polymers of high molecular weight can form at the very early reaction stages and at low monomer conversions, since the small amount of initiated polymer chains react with monomer and grow rapidly owing to their

high propagation rate (Figure 1.2B).[16] Importantly, polymerization techniques that proceed *via* a chain-growth mechanism can be categorized as radical, ionic, coordination or ring-opening polymerizations.

In the case that chain transfer and chain termination reactions are completely absent from a chain-growth polymerization process, then this type of polymerization is classified as "living".[18] The term *living polymerization* was first coined by polymer chemist Michael Szwarc in 1956 and describes the polymerization process during which specific prerequisites are satisfied: (a) a linear relationship exists between polymer molecular weight and monomer conversion (Figure 1.2C), (b) the growing polymer chains remain active after full conversion is reached allowing for further chain-extension upon sequential monomer additions, (c) the obtained polymers possess narrow molecular weight distributions (i.e., low dispersity values), and (d) the final polymer DP can be controlled by tuning the stoichiometric ratio of monomer to initiator.[18] Representative examples of living polymerization techniques include anionic[19] and cationic[20] polymerization, group transfer polymerization (GTP)[21] and ring-opening metathesis polymerization (ROMP).[22]

Another important aspect of living polymerizations is that the initiation rate is significantly faster than the propagation rate, leading to a uniform distribution of initiated chains before propagation occurs and ensuring that all polymer chains will grow evenly at similar rates.[23] Selective termination can be achieved by the addition of appropriate reagents, since growing polymer chains do not present reactivity toward each other. However, in the majority of cases, living polymerization methodologies require strictly controlled reaction conditions (e.g., complete removal of oxygen and water from the system) and the use of expensive specialty equipment, drastically limiting their scope.[24]

In summary, a high degree of control over polymer synthesis with regards to the composition, topology and functionality of resulting polymers can be achieved in most cases of conventional and living chain-growth polymerizations. The wide range and high complexity of available monomers, initiators and catalysts, as well as the development of orthogonal polymerization techniques and establishment of adaptable reaction conditions have allowed for the facile preparation of (multi)functional copolymers with well-defined compositions and architectures.

1.2.1. Free Radical Polymerization (FRP)

Free radical polymerization (FRP) currently remains one of the most commonly utilized polymerization methodologies for the production of high molar mass polymers at industrially-relevant scales. This is primarily attributed to the relatively simple and inexpensive nature of FRP compared to other chain-growth polymerization techniques, as well as its robustness, high functional group-tolerance and mild, metal-free reaction conditions.[25, 26] As with all conventional chain-growth polymerizations, FRP proceeds through a mechanism that involves distinct initiation, propagation and termination steps, while the process is also susceptible to chain transfer reactions.

Initially, free radicals ($I^{\cdot}$) are generated by decomposition of an initiator molecule (I–I) by, for instance, thermo- or photolysis. The radical initiator fragments then react with monomer (M) to form propagating radicals ($I–M^{\cdot}$), followed by successive monomer additions during the propagation step for formation of growing polymer chains ($P_n^{\cdot}$). Termination is indicated by the removal of the active radical species from the polymerization mixture through irreversible reactions, typically involving the

recombination (P_{n+m}) or the disproportionation (P_n= and P_m–H) between two growing polymer chains, and the formation of so-called "dead" polymers.[25] Importantly, chain transfer events, where the reactive radicals can be transferred from a growing polymer chain to another chain, a monomer, the solvent or an added chain transfer agent (CTA), are also occurring to a great extent in FRP and often lead to the formation of polymers with lower molecular weight values than the theoretically expected ones, broad molecular weight distributions or branched architectures (i.e., *via* intramolecular chain transfer).[27] The described principal mechanistic steps of FRP are outlined in Scheme 1.1.

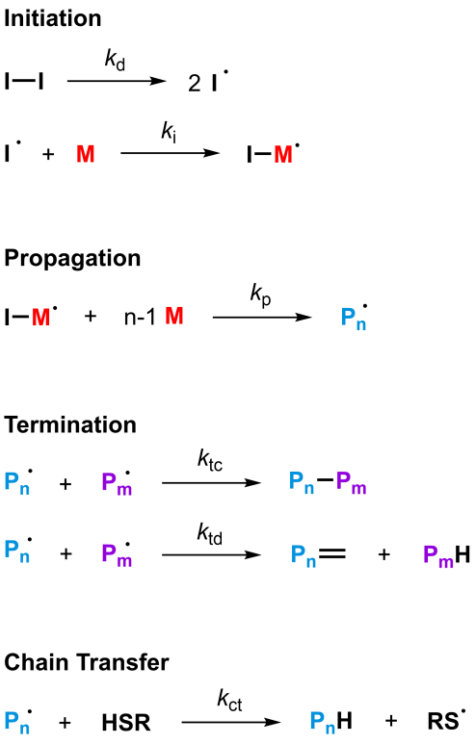

Scheme 1.1. Principal mechanistic steps along with their associated rate constants involved in free radical polymerization (FRP).

Prominently, the radical species generated in FRP are highly reactive with short lifetimes that promote the occurrence of chain transfer and termination events over propagation or initiation reactions.[27] This phenomenon can be more clearly understood upon comparison of the initiation (k_i), propagation (k_p) and termination (k_t) rate constants; a relationship of

$k_t > k_p >> k_i$ is typically true for most FRP reactions. As a consequence, the greater termination and propagation rate constants over the initiation rate constant suggest that the small number of initiated polymer chains grow, reach their final length and terminate rapidly in an uncontrolled manner, while others are still initiating. The dominance of chain transfer and termination phenomena in FRP result in poor control of the polymer composition and topology, prevent the synthesis of block copolymers and limit the potential application of this polymerization methodology for the design of precision polymers with tunable properties.[26, 28]

1.2.2. Reversible-Deactivation Radical Polymerization (RDRP) Techniques

Reversible-deactivation radical polymerizations (RDRP), also known as controlled radical polymerizations, are a family of polymerization techniques that combine many of the advantages of conventional FRP and living polymerization. Over the past 30 years, research involving RDRP techniques has dramatically expanded owing to their high versatility and functional group-tolerance, the requirement of less stringent conditions (i.e., oxygen and water can be tolerated under certain circumstances) and reduced need for highly pure reagents, enabling the preparation of well-defined, functional polymers with controlled molecular weights and compositions, low dispersity values (typically, $Đ_M$ < 1.5), high end-group fidelity, and a wide range of macromolecular architectures.[29, 30]

In RDRP, a dynamic equilibrium between active propagating radicals and deactivated dormant species is achieved by using appropriate capping or chain transfer agents (CTAs), resulting in reduction in the overall concentration and simultaneous increasing

of the lifetime of effective radicals and, thus, in a drastic limitation of undesired chain transfer and termination reactions.[30] This equilibrium can be achieved *via* approaches exploiting either the persistent radical effect (PRE) or degenerative chain transfer processes.[31] The three main examples of RDRP techniques are atom transfer radical polymerization (ATRP),[7] nitroxide-mediated radical polymerization (NMP),[32] and reversible addition–fragmentation chain transfer (RAFT) polymerization.[33, 34] ATRP and NMP are principal examples of polymerizations relying upon the PRE to mediate the reversible activation/deactivation equilibrium between propagating and dormant radicals and will be briefly outlined below. Furthermore, RAFT polymerization – the polymerization technique utilized in Chapters 2 and 3 of this thesis – will be discussed in further detail in Section 1.2.3.

ATRP was independently developed by polymer chemists Mitsuo Sawamoto and Krzysztof Matyjaszewski in 1995.[35, 36] In ATRP, a secondary or tertiary alkyl halide (R–X) is commonly employed as the initiator, which first undergoes a reversible redox reaction using a transition metal complex (M^xL_n, e.g., Cu^ICl) as the catalyst (or activator) to produce the initiating alkyl radicals ($R^{\cdot}$) and an oxidized version of the catalytic species ($X–M^{x+1}L_n$). The produced radicals can then initiate polymerization of vinyl-type monomers for formation of growing polymer chains ($P_n^{\cdot}$). During the main equilibrium/propagation step, the active polymer chain radicals can either continue to propagate by reacting with additional monomer or reversibly react with the oxidized metal complex to produce dormant polymer chains that bear stable halo end-groups (P_n–X) and regenerate the initial catalytic species in its lower oxidation state (Scheme 1.2). This rapid transfer of the halide moieties between the metal activator and the propagating chains drives the equilibrium toward the deactivated species ($k_{act} << k_{deact}$), ensuring

limited termination reactions and excellent control throughout the whole polymerization duration by maintaining a low concentration of reactive radicals.[7, 37] Growing chains can be terminated by procedures such as bimolecular coupling between radicals, although such reactions have been proven to be beneficial for the overall control of ATRP as they further increase the ratio of the oxidized metal halides relevant to $P_n^{\cdot}$ and as a consequence that of dormant species. This phenomenon is known as the PRE, which increases the probability of deactivation over termination reactions.[38, 39]

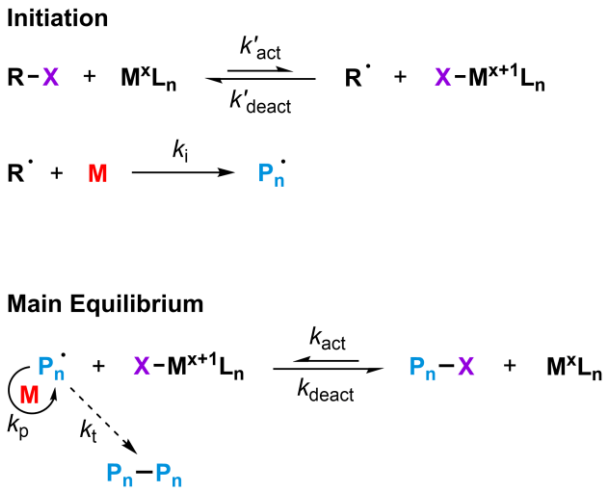

Scheme 1.2. Principal mechanistic steps along with their associated rate constants involved in atom transfer radical polymerization (ATRP).

NMP was discovered by scientists based at the Australian research institute CSIRO in 1985.[40] In NMP, polymerization control is achieved by using sufficiently stable nitroxide radicals that act as capping agents of the growing polymer chains to reversibly afford the deactivated species, in a similar manner to the halide atoms in ATRP. Contrary to ATRP, NMP is a catalyst-free polymerization technique, where alkoxyamines (R–N–O–R_2') are typically utilized as initiators to form nitroxide radicals (R_2'–N–O$^{\cdot}$) and the initiating radical species ($R^{\cdot}$) upon homolysis at elevated temperatures (usually > 100 °C). The main equilibrium step proceeds *via* reaction of the activated propagating radicals ($P_n^{\cdot}$)

with either monomeric units or the stable nitroxide radicals to yield the dormant nitroxide end-capped polymer chains (P_n–N–O–R_2') in a reversible activation/deactivation process (Scheme 1.3).[32, 41, 42] As in all PRE-mediated polymerizations, occurrence of termination reactions result in a simultaneous excess of the stable nitroxide radicals, driving the main equilibrium toward the dormant species and allowing for good polymerization control for certain monomer categories (e.g., styrenics).

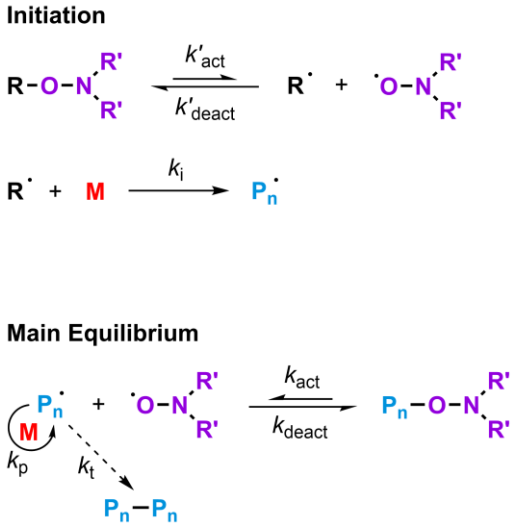

Scheme 1.3. Principal mechanistic steps along with their associated rate constants involved in nitroxide-mediated radical polymerization (NMP).

1.2.3. Reversible Addition−Fragmentation Chain Transfer (RAFT) Polymerization

Reversible addition–fragmentation chain transfer (RAFT) polymerization is a controlled RDRP technique that was also discovered by researchers based at the Australian research institute CSIRO in 1998, although, contrary to ATRP and NMP techniques, RAFT polymerization utilizes a degenerative chain transfer mechanism to achieve the equilibrium between active and dormant species.[43] During a degenerative chain transfer

mechanism, the overall number of radicals remains constant throughout the activation-deactivation process and inherent radical creation or destruction reactions are suppressed, hence an external radical source is typically required to initiate RAFT polymerization.[34] Moreover, the use of thiocarbonylthio compounds (such as dithioesters and trithiocarbonates) that act as chain transfer agents (CTAs) ensures a rapid exchange of radicals between the active propagating polymer chains and the dormant species, minimizing radical-radical coupling termination events and imparting excellent control over RAFT polymerization.[43, 44]

From a mechanistic point of view, the initiation stage mimics that of FRP, whereby initiator (I–I) decomposition *via* thermolysis, photolysis or other initiation procedures results in the generation of free radicals (I$^{\cdot}$) that can react with a few vinyl monomer units (M) for the formation of growing polymer chains ($P_n^{\cdot}$). In the pre-equilibrium step, these active polymer chains can then react with the C=S bond of a small molecule CTA (generally denoted as Z–(C=S)–S–R) in a reversible manner to form intermediate radical species, which can subsequently fragment to produce a growing polymeric CTA (macro-CTA) and a CTA-derived reinitiating radical (R$^{\cdot}$). Radical R$^{\cdot}$ can then reinitiate the polymerization of new polymer chains ($P_m^{\cdot}$) upon reaction with more monomer. Growing polymer chains $P_n^{\cdot}$ and $P_m^{\cdot}$ subsequently enter the main equilibrium stage, whereby either chain can rapidly add onto the C=S bond of the CTA or fragment to mediate further propagation through a series of reversible reactions with $k_{add}/k_{-add} >> k_p$. This preference of addition over fragmentation and propagation reactions results in a low concentration of active growing polymer radicals, which in turn leads to reduction of termination events (e.g., *via* bimolecular coupling of $P_n^{\cdot}$ and $P_m^{\cdot}$) and overall control over the average DP and dispersity of the developed polymer chains, as each propagating polymer radical has

also equal possibility of fragmenting due to the symmetrical nature of the P_n-CTA-P_m intermediate species (Scheme 1.4).[34, 45]

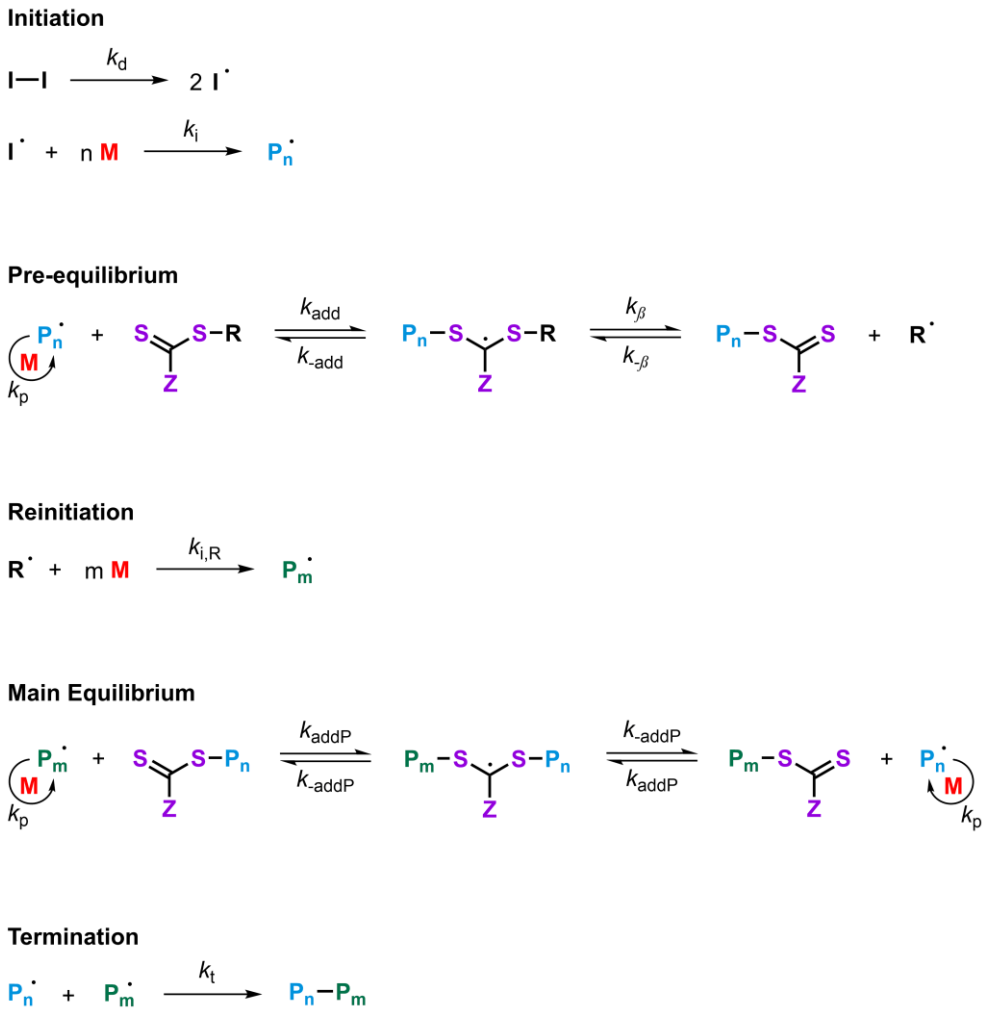

Scheme 1.4. Principal mechanistic steps along with their associated rate constants involved in reversible addition–fragmentation chain transfer (RAFT) polymerization.

In order to achieve well-controlled RAFT polymerization, the pre-equilibrium and reinitiation steps must be completed early in the process to allow for the system to rapidly reach the main equilibrium stage (i.e., $k_\beta > k_{-add}$).[46] Importantly, this is primarily dictated by the nature of the R– and Z– groups of the utilized CTA, hence the CTA must be carefully selected (also depending on the monomer type – more activated monomers

(MAMs) *vs* less activated monomers (LAMs)) for determination of the addition–fragmentation stages. More specifically, the R– group must be a good homolytic leaving group from the intermediate CTA-derived radical species relative to the growing polymer chain to ensure $k_{\beta} > k_{\text{-add}}$ and also the produced R˙ must be an efficient, yet stable, radical to reinitiate polymerization. In contrast, the leaving ability of the growing P_n is directly related to the nature of the monomer utilized and is found to decrease in the order methacrylates, methacrylamides >> styrenics, acrylamides, acrylates > *N*-vinyl amides, vinyl esters.[46, 47]

On the other hand, variation in the Z– group chemistry directly influences the stability of the CTA-derived radical intermediates and their susceptibility to fragmentation during the pre-equilibrium and main equilibrium stages. Thus, the Z– group must be appropriately chosen such that the intermediate radical species are stable enough to ensure $k_{\text{add}} > k_{\text{-add}}$, but should simultaneously be unstable enough allowing for fragmentation events to occur to a certain degree to promote propagation. In addition, the Z– group nature and electron density regulates the reactivity of the C=S bond toward radical addition and the extent of side-reaction occurrence during a RAFT polymerization process (e.g., hydrolysis, irreversible chain transfer, *etc*). Electron withdrawing Z– groups were found to generally favor the formation of the intermediate radicals due to their enhanced stabilization over the propagating polymer chain radicals, and thus increase the rate of chain transfer over propagation events. The opposite trend has been observed for electron donating Z– groups.[44, 46] Four main categories of CTAs have been reported to date based on the atom of the Z– group that is adjacent to the thiocarbonylthio moiety, namely dithioesters (for C), trithiocarbonates (for S), dithiocarbamates (for N), and

xanthates (for O) (Scheme 1.5A),[46] while a generic guide for selection of CTA R– and Z– groups based on each monomer type is shown in Scheme 1.5B.[34]

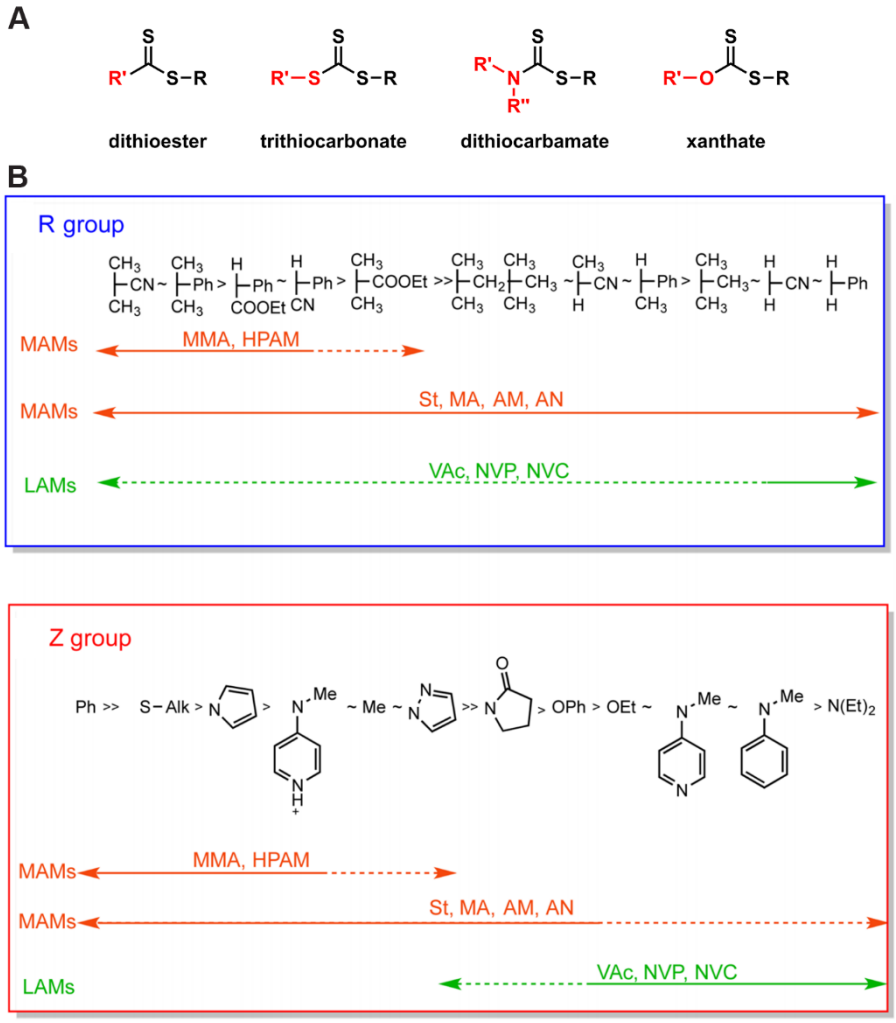

Scheme 1.5. (A) Classification of CTAs based on the functionality of the Z– group. (B) General guidelines for selection of R– and Z– groups of CTAs expressed in terms of RAFT polymerization control of various monomers (the dashed lines represent limited or poor polymerization control). Abbreviations: MMA - methylmethacrylate, HPAM - 2-hydroxypropyl methacrylamide, St - styrene, MA - methyl acrylate, AM - acrylamide, AN - acrylonitrile, VAc - vinyl acetate, NVP - *N*-vinylpyrrolidone, NVC - *N*-vinylcarbazole. Reproduced from ref. 34 with permission from the American Chemical Society.

Typically, RAFT-derived polymers are characterized by high end-group fidelity, while the presence of a CTA moiety at the end of each polymer chain can be further utilized for

the synthesis of block copolymers upon sequential monomer additions or for pre-/post-polymerization modification methodologies through introduction of functionalities on either R– or Z– groups of the CTA (Scheme 1.6).[44] In Chapters 2 and 3 of this thesis, an R-functionalized PEG-based macro-CTA is utilized for the chain-extension of methacrylate monomers and the synthesis of diblock copolymer nano-objects *via* RAFT-mediated polymerization-induced self-assembly, suggesting that the CTA groups are located at the ω-end of the prepared diblock copolymers.

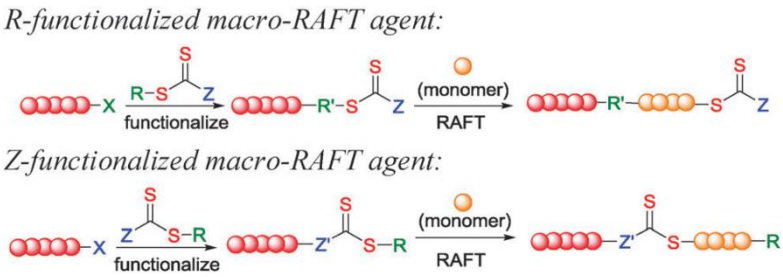

Scheme 1.6. Utilization of either R- or Z-functionalized macro-CTAs for the synthesis of diblock copolymers *via* RAFT polymerization dictates the localization of the thiocarbonylthio moiety within the polymer chain. Reproduced from ref. 44 with permission from the Royal Society of Chemistry.

Ultimately, there exists a plethora of advantages that make RAFT polymerization the most widely established RDRP technique, including its compatibility with a wide range of monomers and solvents (allowing even for pseudo-living polymerizations in aqueous and other protic media), robustness and versatility, high functional group-tolerance, requirement of relatively mild, metal-free conditions, commercial availability of small molecule and polymeric CTAs, facile synthesis and post-polymerization functionalization of polymers with complex macromolecular architectures, quantitative end-group removal for certain industrial and biomedical applications, and its orthogonality with other non-radical polymerization methodologies, amongst other

features.[34, 44] Furthermore, there are also an increasing number of reports focusing on oxygen-tolerant and initiator-free RAFT polymerization methodologies that allow for synthesis of polymers with quantitative monomer conversions and high degree of livingness with potential aim toward the development of (multi)block or sequence-controlled copolymers of particular biotechnological interest.[48-50]

1.2.3.1. Photoinitiated RAFT Polymerization (Photo-RAFT)

Conventional RAFT polymerization typically employs thermal initiators as the source of radical generation. Recently, research efforts have been devoted toward the development of milder alternative methodologies for the formation of initiating radicals (e.g., light, enzymes, microwaves, redox species) for controlled RAFT polymerization with bio-relevant scope.[51, 52] In particular, photoinitiated RAFT polymerization (photo-RAFT) has attracted significant interest over the past 20 years, mainly owing to the ambient reaction temperatures required and the spatiotemporal control over photo-RAFT offered by simple "ON/OFF" switching of the light source (i.e., radical formation and polymerization progresses when the light source is switched "ON" and energy is supplied to the system, while they instantly stop when the source is switched "OFF"). Additionally, the ability to regulate externally-controlled parameters such as the intensity and wavelength of incident light drastically affects polymerization control and kinetics, with photo-RAFT processes being found to possess faster kinetics compared to thermally initiated ones in certain cases.[53-55]

Photo-RAFT can be mediated by the use of classical photoinitiators and special organo-photoredox catalysts or *via* the initiator-free "iniferter" mechanism of CTAs depending

primarily on the irradiation wavelength selected for the reaction.[34, 51] Similar to radical generation *via* thermolysis of temperature-sensitive molecules, photoinitiators are radical-generating compounds that contain labile bonds susceptible to photolysis and they typically operate in the UV-Vis area of low wavelengths (λ = 360 – 485 nm). Mechanistically, the only difference between thermally initiated RAFT polymerization and photoinitiator-mediated RAFT lies in the homolytic initiator decomposition step (Scheme 1.7A).[51, 53] Representative examples of photoinitiators commonly utilized in photo-RAFT are 2,2-dimethoxy-2-phenylacetophenone (DMPA), sodium phenyl-2,4,6-trimethylbenzoylphosphinate (SPTP) and 2-hydroxy-4′-2-(hydroxyethoxy)-2-methylpropiophenone (PP-OH).

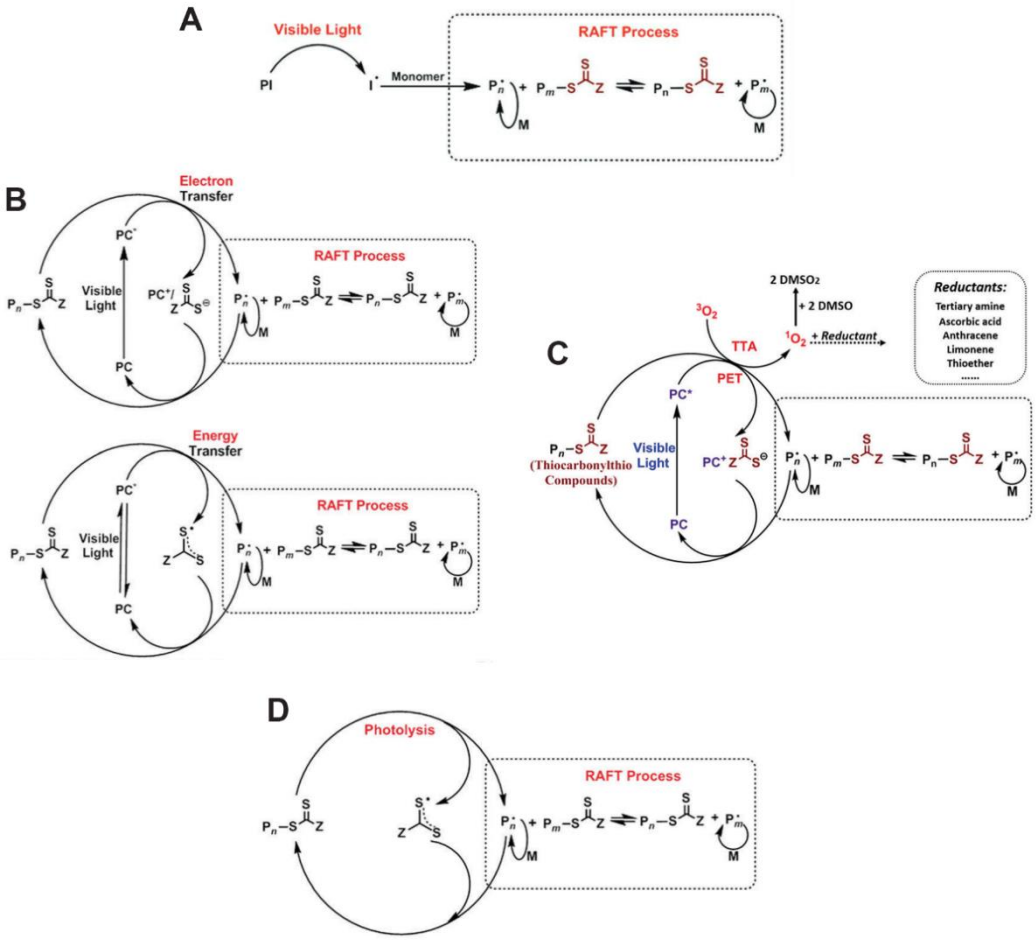

Scheme 1.7. Different mechanisms of photo-RAFT: (A) photoinitiator-mediated RAFT polymerization, (B) PET-RAFT polymerization *via* electron (top) and energy (bottom) transfer,

(C) oxygen-tolerant PET-RAFT polymerization, and (D) photoiniferter-mediated RAFT polymerization. Reproduced from ref. 54 and 55 with permission from Wiley-VCH Verlag GmbH & Co and the Royal Society of Chemistry, respectively.

Furthermore, the use of organic dyes (e.g., Eosin Y, fluorescein) and metal complexes with long-lived excited states as photoredox catalysts (PC) for activating photo-RAFT *via* a mechanism that involves photo-induced electron/energy transfer (PET) has been comprehensively investigated by the Boyer group and others over recent years.[55-57] Given the electron accepting nature of CTAs, the visible light-mediated excitation of specific photoredox catalysts can promote electron transfer to the thiocarbonylthio group and its subsequent reduction for formation of radicals ($R^{\cdot}$ or $P_n^{\cdot}$) (the CTA itself forms a stable anion). The produced radicals can then either take part in polymerization initiation, pre- and main-equilibrium processes in a similar manner to conventional RAFT polymerization or react with the oxidized version of the catalyst to reform the original species and complete the catalytic cycle. In the case that energy transfer is expected to occur rather than transfer of electrons, active propagating and CTA radicals are formed through energy transferred from the excited photoredox catalyst toward the thiocarbonylthio moieties, which can rapidly recombine to form the dormant species (Scheme 1.7B). It should be highlighted that PET-RAFT can also proceed under atmospheric conditions, as molecular oxygen (O_2) can act as the potential electron/energy acceptor for formation of an oxygen radical anion ($O_2^{\cdot -}$), thereby reducing its overall concentration in the system (Scheme 1.7C).[58, 59]

Moreover, the use of CTAs as "iniferter" ("*ini*tiator – trans*fer* agent – *ter*minator") molecules and their inherent susceptibility to photolysis by various UV and visible light irradiation sources has been extensively studied as a simple, yet efficient, radical

generation approach in controlled photo-RAFT without the necessity of external photoinitiators or photocatalysts.[60] In photo-iniferter RAFT, photolytic cleavage of CTA–R and CTA–P_n bonds leads to the formation of propagating and CTA-derived radicals. The active radicals can then be inserted in the RAFT mechanism and mediate polymerization as previously discussed (Scheme 1.7D). Importantly, control over photo-iniferter RAFT polymerization has been shown to strongly rely on the type of CTA utilized and also on the intensity and wavelength of incident light. In particular, it was found that UV irradiation generally results in limited polymerization control, especially at high conversions, due to rapid degradation of the CTA end-group, while visible light leads to well-controlled polymerization processes.[54] Additionally, low light intensity generates a low concentration of active radical species, which in turn ensures good polymerization control.[34] Owing to the procedural simplicity of photo-iniferter RAFT polymerization and its compatibility with sensitive biomacromolecules, such as enzymes, peptides and DNA, this methodology has been utilized for the studies described in Chapters 2 and 3 of this thesis.

1.2.4. Ring-Opening Metathesis Polymerization (ROMP)

Ring-opening metathesis polymerization (ROMP) is one of the most recently developed, but also among the most widely established and versatile living chain-growth polymerization techniques. ROMP belongs to the Nobel Prize-awarded family of olefin metathesis reactions, along with cross metathesis (CM), ring-closing metathesis (RCM) and acyclic diene metathesis (ADMET), involving primarily the rearrangement of carbon-carbon double bonds.[61-63]

In 1971, Hérrison and Chauvin were the first to propose that all metathesis reactions proceed through a metallocyclobutane intermediate, which led to the now well-accepted ROMP mechanism (Scheme 1.8).[64-66] Based on these early investigations, it was demonstrated that the initiation step in ROMP encompasses coordination of an organometallic alkylidene (pre)catalyst ($L_nM=CH_2R$, M = Mo, W, Ru) with a cyclic olefin monomer, followed by [2+2] cycloaddition between the alkylidene and the incoming olefin, leading to the formation of an intermediate metallocyclobutane species. This metallocyclobutane then undergoes cycloreversion to yield a product olefin and a new alkylidene moiety. To date, it has been shown that there are three plausible, catalyst-dependent mechanisms of initiation: (a) an "associative" mechanism, whereby the monomer first coordinates to the metal alkylidene precatalyst prior to ligand displacement; (b) a "dissociative" mechanism that assumes a ligand is lost prior to olefin binding; or (c) an "interchange" mechanism, whereby the loss of a ligand and olefin binding occur simultaneously through a common transition state.[67] During the propagation step, a highly reactive 14-electron metal alkylidene complex continues to react with monomeric cyclic olefins to grow the polymer from the metal center (i.e., monomer insertion at the ω-chain end). It is worth noting that both initiation and propagation reactions are theoretically reversible, therefore the thermodynamics of ROMP should be considered when selecting the monomers to drive the reaction toward polymer formation. Typically, chain propagation continues until either (1) all monomer has been consumed; (2) an equilibrium has been reached due to thermodynamic considerations; or (3) the reaction has been terminated by catalyst deactivation.[22] In contrast to other living polymerization techniques, termination of ROMP most commonly occurs by intentional catalyst deactivation through a CM process using appropriate

quenching reagents (e.g., vinyl ethers)[68] or by uncontrolled catalyst decomposition,[69, 70] whilst chain termination *via* bimolecular coupling has yet to be observed to occur.

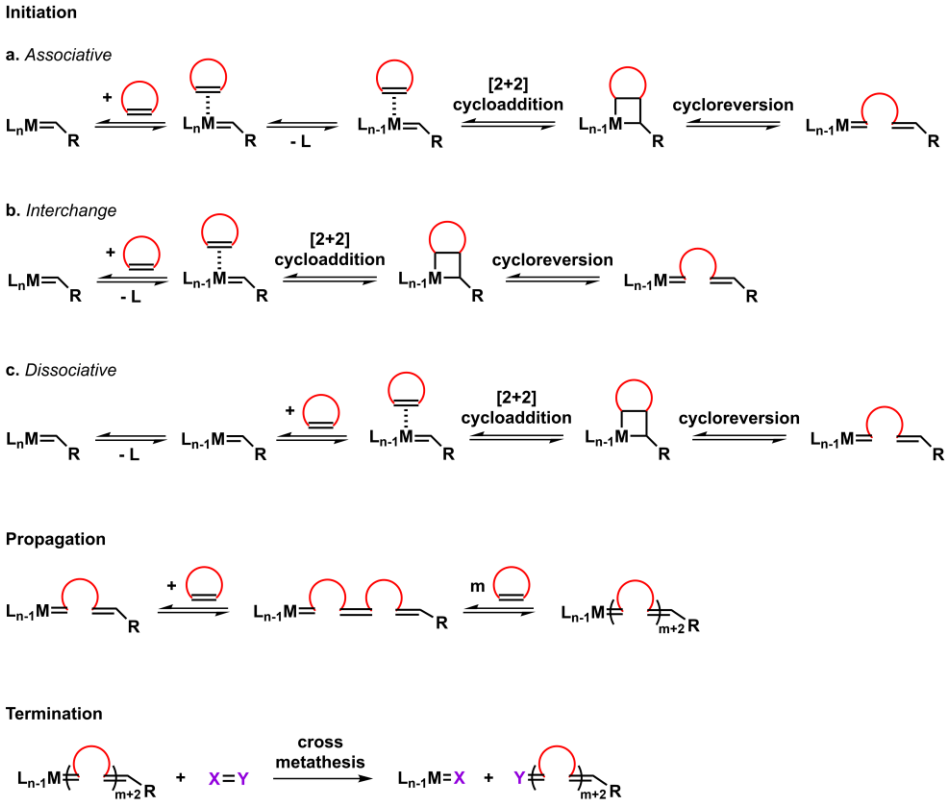

Scheme 1.8. Accepted mechanism of ring-opening metathesis polymerization (ROMP).

One of the principal reasons that led to the widespread utilization of ROMP for synthesis of precision (co)polymers over the past 20 years is the development of highly active and tolerant transition metal complexes and their use as efficient catalysts/initiators in ROMP. Initial metathesis catalysts were based on early transition metal salts; however, use of these ill-defined, heterogeneous systems resulted in uncontrolled metathesis reactions that were poorly understood from a mechanistic point of view.[71] The subsequent rapid development of homogeneous Mo and Ru alkylidene catalysts allowed for controlled polymerizations, greater mechanistic understanding of olefin metathesis chemistry, and as a consequence to the commercialization of such catalytic species (Scheme 1.9).[71-73]

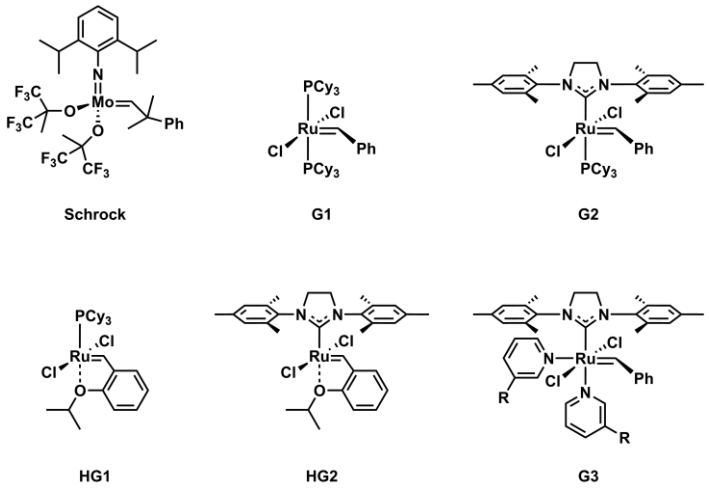

Scheme 1.9. Chemical structures of common, commercially available metathesis catalysts.

In 1990, the first commercially available ROMP catalyst was developed in the form of "Schrock's catalyst".[74] Grubbs and coworkers were the first to report a metathesis catalyst based on a Ru center – namely Grubbs 1st generation catalyst (**G1**) – in the late 1990s, which became the first of several commercially available Ru-based catalysts (i.e., **G2**, **G3**, **HG1**, and **HG2**) developed in the Grubbs lab and elsewhere in later years.[75-78] In particular, **G1**-mediated ROMP was found to afford polymers with relatively moderate control, whilst **G2** showed high activity but also very limited control over ROMP reactions due to slow phosphine ligand dissociation for formation of the active catalytic species and, thus, slower initiation relative to propagation rate.[79-81] This led to the development of a new catalyst – namely Grubbs 3rd generation catalyst (**G3**) – in 2002, that contains more labile pyridine ligands compared to **G1** and **G2**, promotes rapid ligand dissociation in solution and presents extremely fast initiation rates.[82] Unsurprisingly, **G3** has been established as the main commercially available catalyst utilized for living ROMP of norbornene-based monomers and preparation of well-defined polymers with narrow molecular weight distributions, under mild reaction conditions. However, the lability of the pyridine ligands of **G3** also results in a simultaneous reduction in its

catalytic stability, with the active catalytic species reported to typically deactivate in solution after 1 hour, even under stringent reaction conditions.[83] Ultimately, the inherent advantages of Ru-based catalysts, especially those of **G3**, over those based on Mo or W centers, such as greater functional group-tolerance, fast polymerization kinetics, quantitative monomer conversions, and enhanced stability toward oxygen and moisture, along with the in-depth mechanistic understanding of such species has allowed for the application of ROMP as a powerful tool for synthesis of (multi)block copolymers[84, 85] and for even more challenging polymerizations such as those of macromonomers,[86, 87] and those carried out in aqueous or protic media.[88]

Typically, cyclic olefins, such as cycloalkenes and bicycloalkenes, are utilized as monomers for ROMP for the formation of unsaturated polymers with unique characteristics, including rigid rod-like backbones, high T_g values and improved mechanical and thermal properties relative to their (meth)acrylate/acrylamide-based counterparts.[22] Additionally, polymers with degradable or responsive backbones can be developed in certain cases by using functional cyclic monomers.[89-91] However, it should be noted that not all cyclic olefins can be effectively polymerized *via* ROMP. The driving force for ROMP is primarily based on alleviation of the ring strain of the monomer, but also on a number of other factors including sterics surrounding the cyclic olefin, the electronic nature of the olefin itself, and the relative reactivity of the formed olefins within the polymer backbone (as they can be involved in back-biting reactions).[22] In order to favor ROMP and drive the polymerization equilibrium toward the polymer product, reactions are typically conducted at room temperature or below using monomers which possess a large ring strain (i.e., > 7 kcal mol^{-1}).[92] To date, a wide range of highly-strained monomers have been utilized for ROMP with the most common examples being

norbornene (NB), oxanorbornene (ONB), cyclopentene, cyclooctene and their derivatives.

In particular, NB and its derivatives have attracted immense research interest across the ROMP community owing to their facile synthesis and modification with a wide range of functionalities, exceedingly high ring strain (27.2 kcal mol^{-1} for NB) and rapid polymerization kinetics.[93] Additionally, the steric hindrance provided by the polynorbornene backbone suppresses the occurrence of secondary metathesis reactions between the catalyst and polymer olefins, allowing for living ROMP and preparation of polymers with controllable molecular weight and low $Đ_M$.[94] However, stereopure monomers are usually required for controlled ROMP as there is a significant difference in polymerization rates between *exo*- and *endo*-norbornenes (i.e., *exo*-NB possesses considerably faster initiation rate over the *endo*- product).[95, 96]

1.2.4.1. ROMP in Aqueous Media

Recently, there has been significant research interest in carrying out controlled ROMP and other metathesis reactions in aqueous media or in heterogeneous mixtures containing organic solvent and water for certain biological applications, such as DNA or protein modification.[97, 98] Modern Ru-based metathesis catalysts have demonstrated remarkable tolerance toward both oxygen and water, expanding the scope of metathesis transformations and opening up the possibility for carrying out ROMP in aqueous solutions. In order to successfully conduct living ROMP in water, three main criteria must be satisfied: (1) the utilized catalyst must be water-soluble, (2) the utilized catalyst must present enhanced stability in water over the timescale of ROMP, and (3) the utilized

catalyst must exhibit increased activity in aqueous media, ideally similar to its activity in organic solvent.

Initial attempts for aqueous ROMP have focused on utilization of emulsion polymerization conditions, enabled by the addition of small molecule surfactants for sequestration of the monomer and catalytic species.[99, 100] While relatively simple to perform, emulsion ROMP cannot be exploited to directly prepare hydrophilic polymers or to carry out metathesis in aqueous media in the presence of biomacromolecules, among other limitations. Early reports on homogenous ROMP in water involved polymerization of ONB-based monomers using water-soluble metal salts, such as $RuCl_3$.[101, 102] Although low dispersity polymers could be obtained, the active catalytic species were ill-defined and intolerant to oxygen. Moreover, these Ru salts lack a pre-formed alkylidene moiety, hence their practical usefulness was rather limited.

In the past 20 years, the development of well-defined Ru-alkylidene complexes has dramatically expanded the scope of metathesis chemistry in both organic solvents and aqueous media.[103] In particular, synthetic efforts have been primarily devoted on the preparation of novel water-soluble ROMP catalysts through their functionalization with hydrophilic ligands. **G1** derivatives bearing charged phosphine ligands were among the first catalysts to be used in aqueous ROMP of water-soluble ONB monomers.[104] Since these preliminary studies, numerous water-soluble catalysts based on the Grubbs and Hoveyda-Grubbs (HG) catalysts' scaffolds have been reported upon modification of *N*-heterocyclic carbene (NHC),[105, 106] phosphine,[107] pyridine,[108, 109] or benzylidene[110, 111] ligands with solubilizing moieties such as ammonium, pyridinium, and sulfonate groups, or hydrophilic polymers. However, it is often observed that water-soluble **G1**-**G3** derivatives are typically limited by poor activity for mediating ROMP in aqueous milieu.

This phenomenon was generally attributed to slow phosphine and pyridine ligand dissociation, driving the equilibrium away from the active catalytic species, while it was found that addition of specific additives (i.e., acid or metal salts) to the polymerization mixture showed significant improvement toward ROMP control and polymerization kinetics.[108, 112, 113] On the contrary, HG catalysts have been more extensively studied for aqueous metathesis, as they do not possess phosphine or pyridine ligands and, hence, ligand dissociation is not required prior to formation of the active species and monomer coordination.[107] As a result, the often biologically incompatible acid or metal salt additives are not required to perform aqueous metathesis reactions using HG-type catalysts. However, it is important to note that water-soluble **HG2** catalysts are generally unsuitable for aqueous ROMP – especially for NB-based monomers – owing to slow initiation kinetics affected by strong chelation interactions between the metal center and benzylidene ligand,[114] although a recent study showed that an NHC-modified **HG2** catalyst can effectively mediate ROMP-induced self-assembly (ROMPISA) in water with excellent polymerization control.[115] Typical examples of water-soluble ROMP catalysts based on **HG2** and **G3** scaffolds are shown in Scheme 1.10.

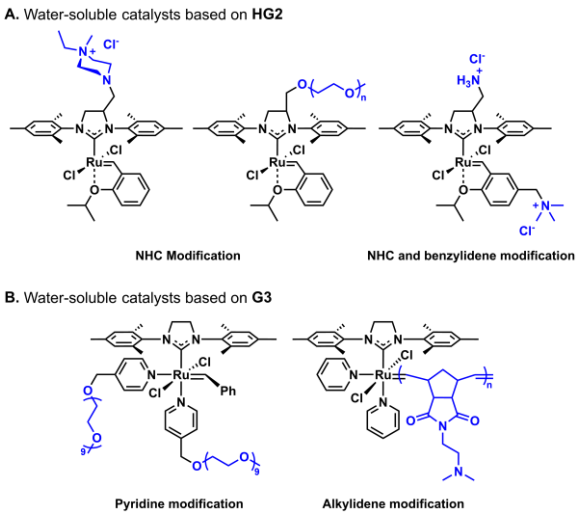

Scheme 1.10. Chemical structures of water-soluble Ru-based catalysts based on either (A) **HG2** or (B) **G3** scaffolds recently reported for aqueous ROMP.

Recently, our group has developed a facile alternative strategy to existing catalyst solubilization methodologies that allowed for living open-to-air ROMP in aqueous media.[88] This approach involves the synthesis of a short, water-soluble macroinitiator block in a water-miscible organic solvent (i.e., THF) using commercially available **G3**. Transfer of the prepared macroinitiator from organic to acidic aqueous media containing a wide range of water-miscible NB-based monomers promoted chain-extension of the macroinitiator block in a living manner for the synthesis of well-defined diblock copolymers (Scheme 1.11).

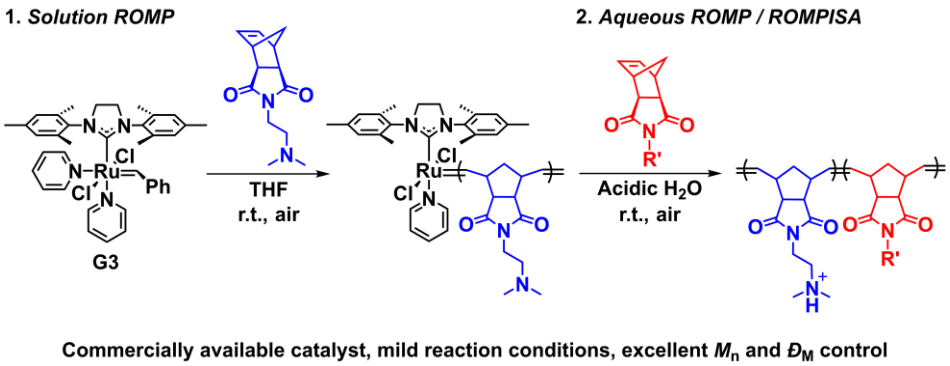

Scheme 1.11. Two-step methodology for controlled aqueous ROMP mediated by a water-soluble macroinitiator, reported by O'Reilly and coworkers.[88]

In Chapters 4 and 5 of this thesis, the described methodology developed within our group is utilized and further expanded to aqueous dispersion ROMPISA, revealing a unique block copolymer self-assembly behavior for polynorbornene-based copolymers. Overall, the development of catalysts that exhibit excellent ROMP control in water at neutral or basic pH currently remains an ongoing challenge and further research on this field could dramatically expand the scope of aqueous ROMP.

1.3. Block Copolymer Self-Assembly in Solution

As previously discussed, controlled/living polymerization techniques, such as RAFT polymerization and ROMP, represent excellent methodologies for precision synthesis of well-defined block copolymers. Similar to small molecule surfactants composed of a solvophilic head group and a solvophobic tail, preparation of copolymers comprised of discrete blocks that differ significantly in their solvophilicity leads to microphase separation between the incompatible blocks either in bulk or in solution.[116] In particular, spontaneous aggregation of such amphiphilic block copolymers occurs in an appropriately chosen solvent that is selective for one (or more) of the blocks in an attempt for the system to minimize unfavorable polymer-polymer and polymer-solvent interactions. This process, known as solution self-assembly of block copolymer amphiphiles, results in the formation of ordered nanostructures with distinct domains owing to strong attraction forces developed between the associating blocks.[117, 118] Such polymer-based assemblies typically exhibit superior physicochemical characteristics compared to their small molecule surfactant analogues, including increased chemical versatility, improved colloidal stability, slower chain rearrangement and easier functionalization.[119]

Importantly, there is a wide range of factors – many of which have been thoroughly explored in the present thesis – that affect the amphiphilic block copolymer self-assembly pathway followed and thus the obtained nanoparticle morphology. Amongst the most important parameters are the extent of core-block stretching and its solvophobicity, corona-forming chain repulsion, overall copolymer molecular weight, rigidity of each constituent block (e.g., coil-coil, rod-coil, or rod-rod copolymers), copolymer architecture, and solvent composition.[116, 120] Upon systematically varying at least two of

these parameters, phase diagrams can be constructed to facilitate reproducible preparation of nanostructures with predictable morphologies. Typical morphologies arising from block copolymer self-assembly in solution include core-shell spherical and worm-like micelles, bilayer lamellae and vesicles, and other more complex nanostructures (Figure 1.3).[121, 122]

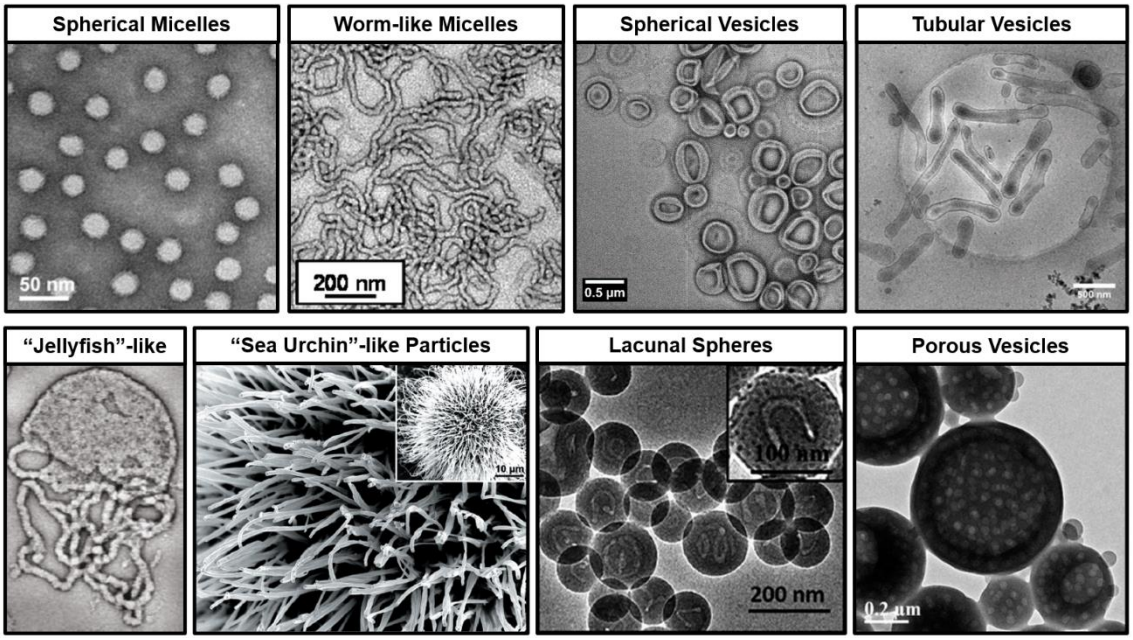

Figure 1.3. Electron microscopy images of typical and more "exotic" nanostructures arising from amphiphilic block copolymer self-assembly in solution. Images reproduced with permission from the following ref.: spherical micelles,[123] worm-like micelles,[124] spherical vesicles,[125] tubular vesicles,[126] "jellyfish"-like particles,[127] "sea urchin"-like particles,[128] lacunal spheres,[129] and porous vesicles.[130]

For self-assembled block copolymer aggregates with fast unimer exchange dynamics (i.e., assemblies under thermodynamic equilibrium), the adapted nanostructure morphology is primarily dictated by the "dimensionless" packing parameter, $p = v/a_0 l_c$, where v is the volume of the solvophobic segment, a_0 is the contact area of the solvophilic domain at the particle-solvent interface, and l_c is the length of the solvophobic segment. As a generic guide, formation of spherical micelles is favored when $p \leq ⅓$, cylindrical

micelles are favored when ⅓ < p ≤ ½, whilst bilayer lamellae and hollow vesicles are favored when ½ < p ≤ 1 (Figure 1.4).[117, 131] However, it should be noted that p-determining values are difficult to be precisely calculated, hence the relative solvophilic/solvophobic volume fractions of the constituent block copolymers are used instead to describe a given formulation.[132]

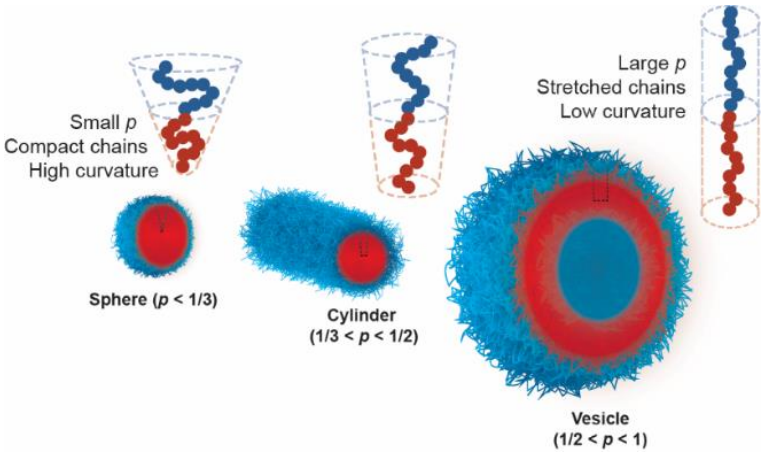

Figure 1.4. The adapted morphology for amphiphilic block copolymer nano-objects under thermodynamic equilibrium is dictated by the interfacial curvature between the incompatible blocks and packing of the individual chains within the structure, which can be estimated by calculating its packing parameter, p.

In certain cases, unimer rearrangement and exchange between particles can be energetically unfavorable processes or can occur over prohibitively long timescales, leading to formation of out-of-equilibrium "kinetically trapped" morphologies.[133, 134] A number of factors can be responsible for low chain mobility within a self-assembled polymeric system, although the main ones include high molecular weight and/or solvophobicity of the core-forming block,[135] the "glassy" nature of copolymers with high T_g values,[136] and increased copolymer rigidity or crystallinity.[137, 138] Such formulations are often susceptible to interparticle fusion phenomena for formation of higher-order nanostructures in order to minimize the overall energy of the system.

Importantly, the self-assembly methodology applied frequently determines whether the developed nanostructure will be under thermodynamic or kinetic control.[116] The most widely utilized methodologies for the development of polymeric nano-objects involve either conventional self-assembly approaches, such as direct dissolution, solvent-switch and thin-film rehydration, or alternative techniques, such as dispersion/emulsion polymerization, nanoprecipitation, crystallization-driven self-assembly (CDSA), and polymerization-induced self-assembly (PISA). Ultimately, owing to the unique properties of self-assembled nanostructures comprised of block copolymer amphiphiles, such constructs have been successfully utilized in a wide range of applications including drug delivery, diagnostic imaging and sensing, catalysis, and cell-mimicry, amongst others.[116, 117, 139]

1.4. Polymerization-Induced Self-Assembly (PISA)

Until recently, preparation of block copolymer nano-objects has primarily relied upon multi-step procedures involving synthesis, post-polymerization purification and self-assembly of constituent amphiphilic block copolymers in dilute solutions (i.e., [solids] ≤ 1% w/w).[140] Over the past decade, polymerization-induced self-assembly (PISA) of block copolymer amphiphiles has emerged as a widely utilized, powerful alternative to conventional self-assembly methodologies that allows for polymerization and *in situ* development of nano-objects with predictable characteristics (e.g., size, morphology, surface chemistry, *etc*) in a single synthetic step at high polymer concentrations (i.e., [solids] = 10–50% w/w) and quantitative monomer conversions.[141, 142] The already highlighted advantages of this technique in addition to its facile scalability and the rather

limited post-PISA processing required, make PISA a highly viable process for implementation at industrial scale.

Fundamental mechanistic investigations during PISA have revealed that formation of block copolymer nanostructures is driven *via* the chain-extension of a solvophilic steric stabilizer block using either solvent-miscible (dispersion polymerization conditions) or solvent-immiscible (emulsion polymerization conditions) core-forming monomers that, upon a critical DP, form solvent-insoluble polymers which in turn aggregate to exclude solvent molecules (Figure 1.5). Typically, this onset of nano-object micellization is accompanied with a marked increase in polymerization rate due to a high local monomer concentration within the developed nanoparticle cores.[142-144]

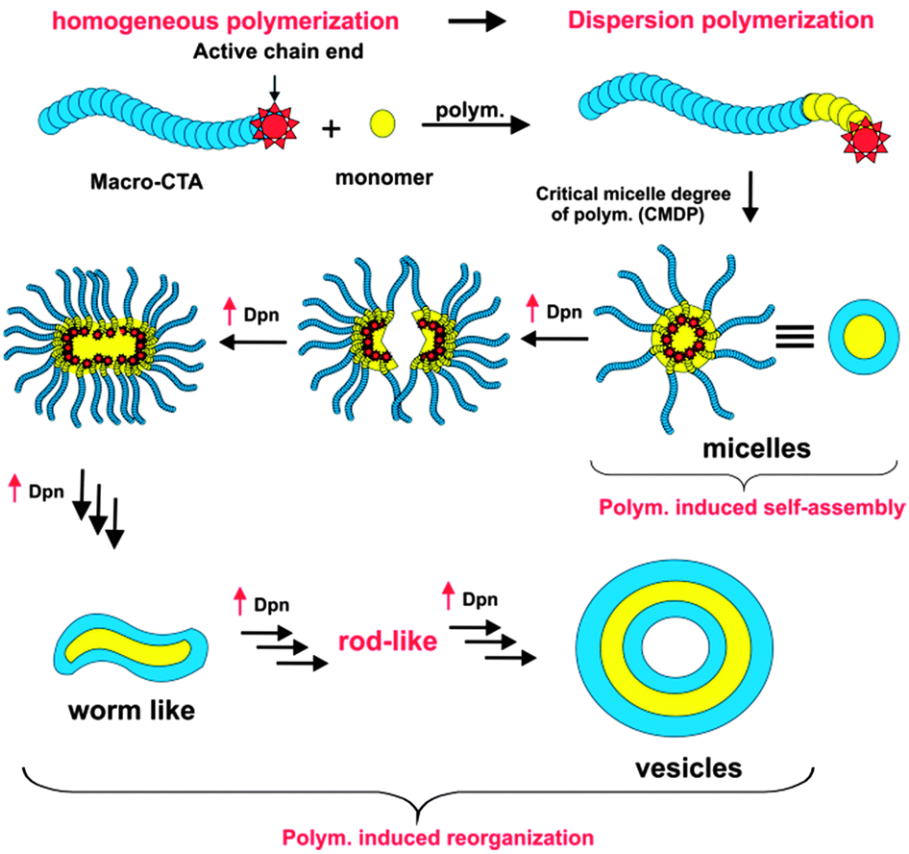

Figure 1.5. Schematic illustration of morphological evolution of diblock copolymer nano-objects developed during RAFT-mediated polymerization-induced self-assembly (PISA) under

dispersion polymerization conditions. Reproduced from ref. 145 with permission from the Royal Society of Chemistry.

Similar to conventional block copolymer self-assembly methodologies, the final morphology obtained through PISA under thermodynamic control is primarily dictated by the relative volume fractions of the stabilizer and core-forming blocks (i.e., packing parameter).[117, 142] This is true for the majority of dispersion PISA formulations, whereby the simultaneous chain-extension and self-assembly of amphiphilic block copolymers drive a continuous alternation of the packing parameter of the assemblies, leading to occurrence of sphere-to-worm-to-vesicle morphological transitions with intermediate morphologies, such as jellyfish- and octopi-like assemblies, also being accessible.[127] On the contrary, morphological evolution is restricted in the vast majority of PISA reactions under emulsion polymerization conditions owing to the limited unimer exchange dynamics between the growing nano-objects, resulting in formation of "kinetically trapped" spherical nano-objects of increasing size as the core-block DP increases.[146-148] However, there exists a limited number of studies demonstrating that higher-order morphologies can arise during emulsion PISA, although the reasoning behind these intriguing findings remains currently unclear.[149-151] Overall, by tuning externally controlled parameters such as the length of both corona- and core-forming blocks, the total solids content, the core-block solvophobicity and the reaction conditions, assemblies of pure morphology can be reproducibly obtained *via* PISA through construction of phase diagrams (Figure 1.6).[152, 153]

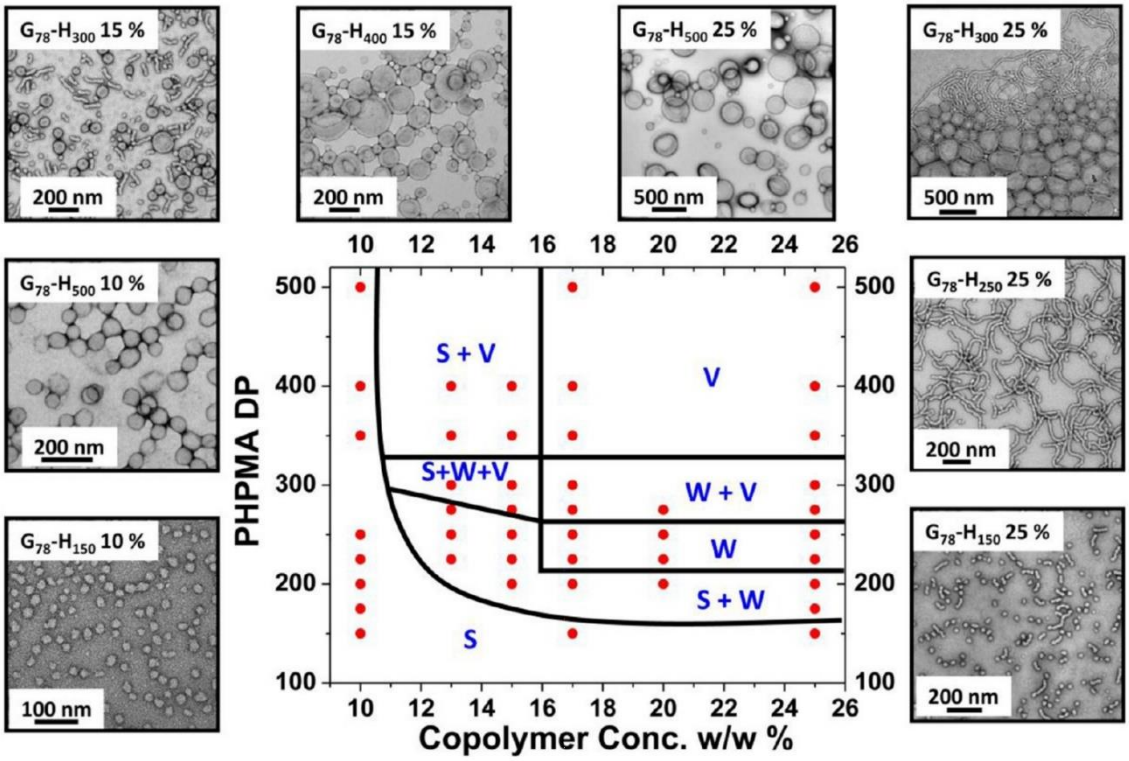

Figure 1.6. Phase diagram and representative TEM images of $PGMA_{78}$-*b*-$PHPMA_n$ diblock copolymer nano-objects developed *via* aqueous RAFT-mediated PISA upon varying the total solids content and DP_{PHPMA}. Reproduced from ref. 152 with permission from the American Chemical Society.

To date, a wide range of PISA methodologies have been developed in both organic and aqueous media, utilizing principally reversible-deactivation radical polymerization (RDRP) techniques (e.g., ATRP,[154, 155] NMP,[156, 157] and RAFT polymerization[140, 158, 159]), but also non-radical approaches including ring-opening polymerization (ROP)[160, 161] and coordination−insertion polymerization mechanisms (e.g., ROMP,[88, 115, 162] and Ni-catalyzed coordination polymerization[163]). Additionally, a vast array of functional and stimuli-responsive monomers that fulfill the necessary solubility requirements have been reported thus far as suitable core-forming PISA monomers based mainly on empirical observations. Moreover, our group has recently reported an *in silico* methodology that allows for prediction of new corona- or core-forming PISA monomers based on

calculation of surface area-normalized octanol-water partition coefficients (LogP_{oct}/SA) for a series of monomers and their oligomeric models.[164] Our computational approach has also provided valuable insight into the obtained nano-object morphology for a certain core-block length with polymers of higher LogP_{oct}/SA values leading to the formation of higher-order morphologies. This methodology has been successfully applied to both aqueous RAFT- and ROMP-mediated PISA and is the subject of discussion in Chapter 4 of this thesis.

Overall, PISA-derived nano-objects of different morphologies have been successfully used in a wide range of industrial, biotechnological and biomedical applications including their utilization as oil modifiers,[165] Pickering emulsifiers,[166, 167] drug delivery vehicles,[145, 168-170] catalytic nanoreactors,[125, 171-173] imaging agents,[174] cryoprotectants,[175] and cell-mimicking models,[176] amongst others.

1.4.1. RAFT-mediated Photo-PISA

Owing to the requirement of polymeric nano-objects to be dispersed in aqueous media for certain bio-related applications, aqueous PISA – primarily mediated *via* RDRP techniques – has attracted significant research interest over the past five years. In particular, the vast majority of studies that have been reported in the literature thus far are based on aqueous RAFT-mediated PISA methodologies, owing to the high versatility and tolerance of RAFT polymerization toward a broad range of functional groups and reaction conditions, as well as its compatibility with water.[142, 147, 176, 177]

Despite the fact that numerous aqueous PISA reports have been relying upon thermally initiated RAFT polymerization,[140, 153, 178, 179] a steadily increasing number of studies have

focused on photoinitiated PISA (photo-PISA) approaches mediated by visible light-active photoinitiators and photoredox catalysts or *via* the "photoiniferter" mechanism of CTAs, following the above described initiation mechanisms for conventional photo-RAFT polymerization. This is attributed to the many advantages of photo-PISA over thermally initiated PISA procedures, including faster polymerization kinetics, milder initiation conditions, ambient reaction temperatures, and compatibility with temperature-sensitive biomacromolecules, allowing for efficient fabrication of cargo-loaded nano-objects directly in water with further biologically relevant scope.[59, 180-183] Since photo-PISA studies have been recently reviewed by Boyer and coworkers,[54] a few key examples of such formulations are presented herein with special emphasis given to the preparation of enzyme-loaded polymersomes and their applications.

In particular, an initial approach was introduced by Tan, Sumerlin and coworkers in 2015, whereby an aqueous visible light-initiated (λ = 405 nm) photo-PISA process was reported for the preparation of various diblock copolymer nano-object morphologies (e.g., micelles, worms, and vesicles) based on poly(ethylene glycol)$_{113}$-*b*-poly(2-hydroxypropyl methacrylate)$_n$ (PEG$_{113}$-*b*-PHPMA$_n$) at room temperature, using SPTP as the photoinitiator (Figure 1.7A).[180] Near quantitative monomer conversions were achieved within 15 min of irradiation, while the ability of the polymersomes to *in situ* encapsulate silica nanoparticles and fluorescein-labeled bovine serum albumin (BSA) protein during PISA was also demonstrated (Figure 1.7B). Importantly, BSA maintained > 95% of its biological activity after photo-PISA, while free BSA could be quantitatively removed from the polymersome solution *via* successive centrifugation/resuspension cycles.

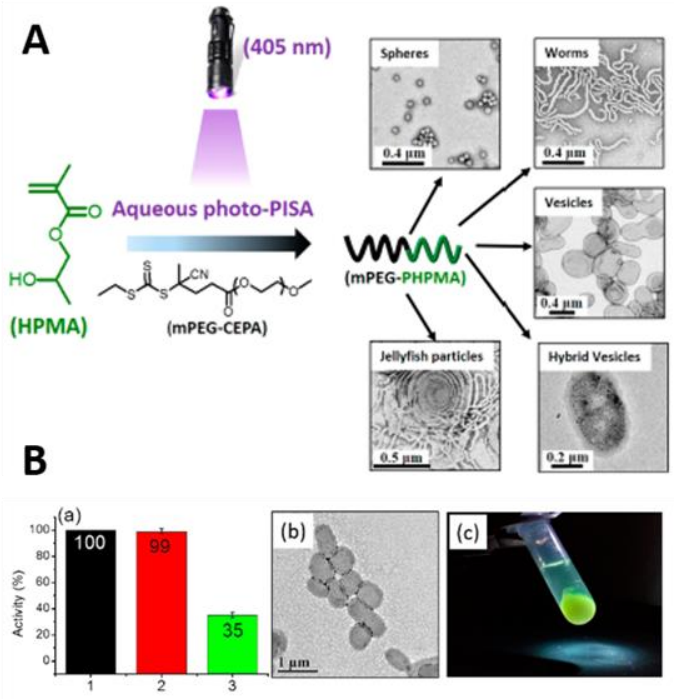

Figure 1.7. (A) Schematic of the synthetic procedure followed for preparation of PEG_{113}-*b*-$PHPMA_n$ diblock copolymer nano-objects *via* photo-PISA along with representative TEM images. (B) Encapsulation of BSA into the polymersomes developed under photo-PISA conditions and activity determination for native (1), post-PISA isolated (2) and denatured (3) BSA. Reproduced from ref. 180 with permission from the American Chemical Society.

In a later study, Tan *et al*. reported the preparation of CO_2-responsive nano-objects *via* aqueous photo-PISA (λ = 405 nm, SPTP as photoinitiator) of $PPEGMA_n$-*b*-P(HPMA-*co*-$DMAEMA)_m$ diblock copolymers at room temperature.[184] Pure higher-order morphologies could be accessed by this approach, while the CO_2-responsive character of the obtained polymersomes was further investigated. It was shown that the presence of DMAEMA units within the membrane of the polymersomes was critical for their disassembly upon treatment with CO_2. Finally, *in situ* encapsulation of BSA into the aqueous lumen of the polymersomes and their CO_2-triggered release behavior was also evaluated by fluorescence measurements. Moreover, the same authors have also developed an enzyme-assisted photo-PISA methodology that can be utilized under both

dispersion and emulsion polymerization conditions based on glucose oxidase (GOx)-mediated degassing to allow for development of block copolymer nano-objects in open-to-air vessels and at low volumes, enabling high-throughput screening.[151, 185, 186]

In a more recent study by Ma *et al*., a protein surface-initiated aqueous RAFT-mediated photo-PISA process was reported.[187] In this example, BSA was modified with trithiocarbonate groups to give a BSA-based star macro-CTA. Chain-extension using HPMA as the core-forming monomer was achieved upon 460 nm irradiation using a water-soluble ruthenium complex as the photoredox catalyst. The authors showed that spherical nanoparticles of various sizes could be obtained upon varying the polymerization parameters (Figure 1.8). The BSA-based nanostructures were loaded with both hydrophobic (doxorubicin) and hydrophilic (DNA) compounds that were released upon treatment of the particles with a model protease. However, it should be noted that the authors failed to report the formation of higher-order structures, such as worm-like micelles and vesicles, being limited to only spherical micelle-like formulations due to the high molecular weight of the BSA steric stabilizer block.

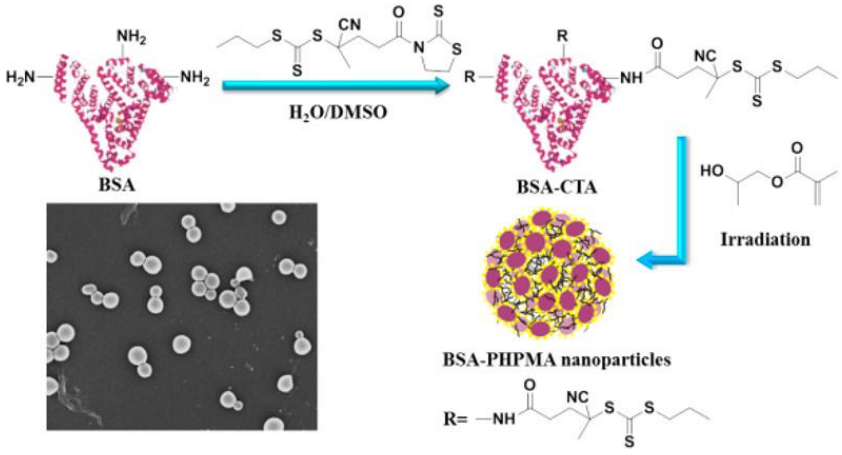

Figure 1.8. Schematic illustration of the synthesis of BSA-based star macro-CTA and *in-situ* photo-PISA for preparation of BSA-*g*-PHPMA$_n$ spherical nano-objects. Reproduced from ref. 187 with permission from the American Chemical Society.

Our group has also carried out pioneering work on this field prior to the projects discussed in Chapters 2 and 3 of this thesis, developing a series of PEG_{113}-*b*-$PHPMA_{400}$ polymersome nanoreactors loaded with various hydrophilic enzymes and exploring their potential applications as artificial cell-mimicking models. In an initial study, the total solids content and core-block DP at which a pure population of PEG-*b*-PHPMA polymersomes could be reproducibly obtained *via* aqueous photo-PISA (λ = 405 nm) at 37 °C were mapped out upon construction of detailed morphology diagrams.[183] In a subsequent report, the inherent permeability of the PHPMA polymersome membranes toward small organic molecules and their ability to efficiently retain larger biomacromolecules such as green fluorescent protein (GFP), horseradish peroxidase (HRP) and GOx within the polymersomes was demonstrated, allowing for the encapsulated proteins to communicate through enzymatic cascades from within the inner aqueous compartment of the nanostructures (Figure 1.9A).[172] Furthermore, the same polymersome system was used for encapsulation of a therapeutic enzyme used for leukemia treatment, *L*-asparaginase (ASNS), showing a great reduction of antibody binding and proteolytic susceptibility in this case as compared to the native enzyme (Figure 1.9B).[125] The efficacy of the polymeric formulation against a cancer line was also demonstrated, whilst its *in vivo* biodistribution was also assessed. Finally, the effect of alternative corona chemistries on the resistance of polymersome nanoreactors toward protease degradation and protein-induced aggregation was investigated upon fabrication of HRP-loaded polysarcosine-based polymersomes and comparison with their PEG-based counterparts.[173] This studies are further extended in Chapters 2 and 3 by exploring ways to incorporate hydrophobic biomolecules into the membrane of such constructs

during photo-PISA and facile methodologies to either enhance or block their membrane permeability toward substrate molecules and reaction products.

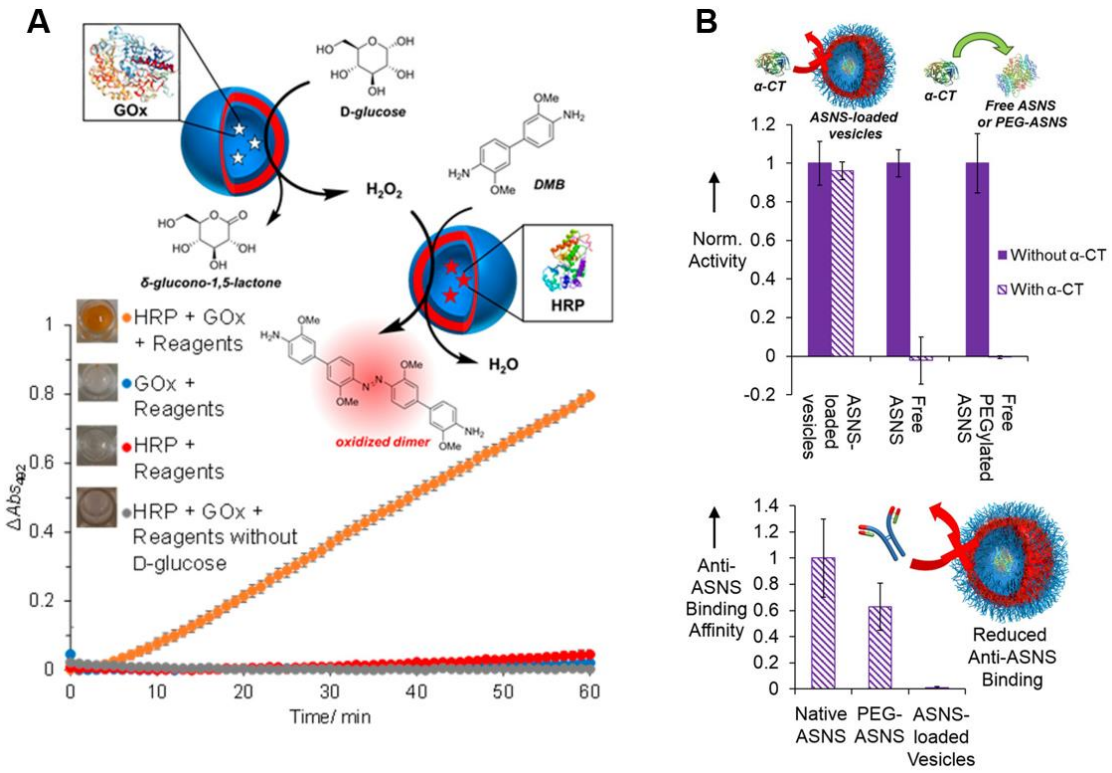

Figure 1.9. (A) Enzymatic cascade reaction between GOx- and HRP-loaded PEG_{113}-*b*-$PHPMA_{400}$ polymersome nanoreactors monitored by kinetic colorimetric analysis. Reproduced from ref. 172 with permission from the American Chemical Society. (B) Comparison of proteolytic susceptibility and antibody recognition for ASNS-loaded PEG_{113}-*b*-$PHPMA_{400}$ polymersomes, free ASNS and a PEGylated ASNS conjugate. Reproduced from ref. 125 with permission from the American Chemical Society.

1.4.2. ROMP-mediated PISA (ROMPISA)

Recently, ROMP-mediated PISA (ROMPISA) has emerged as a highly promising non-radical procedure for the *in situ* fabrication of polynorbornene (PNB)-based nano-objects with common morphologies owing to the previously described advantages of living ROMP.[188] In particular, numerous studies focused on ROMPISA in organic milieu (usually mixtures of organic solvents) have been reported thus far,[115, 189-191] whilst the

potential of aqueous ROMPISA has only very recently been explored by our group and others as a consequence of the significant progress made toward the development of novel approaches to effectively conduct well-controlled aqueous ROMP.[88, 162, 192]

Interestingly, ROMPISA studies realized in both organic and aqueous media have revealed that the prepared nanostructures typically possess uniquely distinct properties compared to RDRP-based PISA and conventional self-assembly formulations. The rapid kinetics of ROMP coupled with the high T_g and rigidity of PNBs have resulted in a high degree of chain stretching (i.e., lower interfacial curvature) within the nanostructures and slow unimer exchange dynamics, allowing for easier access to higher-order morphologies (e.g., worm-like micelles and polymersomes) and unique "kinetically trapped" nano-objects.[88, 188, 193, 194] However, other externally-controlled parameters such as the total solids concentration or the ratio between the corona- and core-forming blocks can be also tuned to access these morphologies.

These observations are typified in a recent study by our group, whereby the developed macroinitiator methodology for conducting living ROMP in acidic media introduced in Section 1.2.4.1 was adapted in aqueous dispersion ROMPISA.[88] In this report, chain-extension of a hydrophilic PNB-(tertiary amine)$_{10}$ macroinitiator using appropriately selected water-miscible monomers (e.g., *exo*-5-norbornenecarboxylic acid and a di(oligo(ethylene glycol))-based norbornene) that gradually become water-insoluble upon polymerization in phosphate buffer (pH = 2) promoted the formation of diblock copolymer nano-objects *via* open-to-air dispersion ROMPISA ([solids] = 1 wt%). Quantitative monomer conversions (> 99%) were achieved within ~2 min, whilst the dimensions of the obtained assemblies were found to be uniquely small, as judged by the acquired transmission electron microscopy (TEM) images (Figure 1.10). Moreover, the

onset of nanoparticle micellization was found to occur very early in the polymerization process with assemblies of core-block DP = 14 and 22 already forming spherical and worm-like micelles, respectively. A higher asymmetry between the corona- and core-forming blocks was found to yield higher-order spherical polymersomes with average diameter of ~30 nm and membrane thickness of ~ 4-5 nm. This initial demonstration has been expanded in Chapters 4 and 5 of this thesis in an attempt to tune the chemistry and physical characteristics of ROMPISA assemblies with overall aim the development of functional polymeric nanoreactors and artificial cell-mimics in future studies. Current advances in ROMPISA have been extensively discussed in a recent Highlight article by our group, where interested readers are redirected for detailed descriptions on individual approaches.[188]

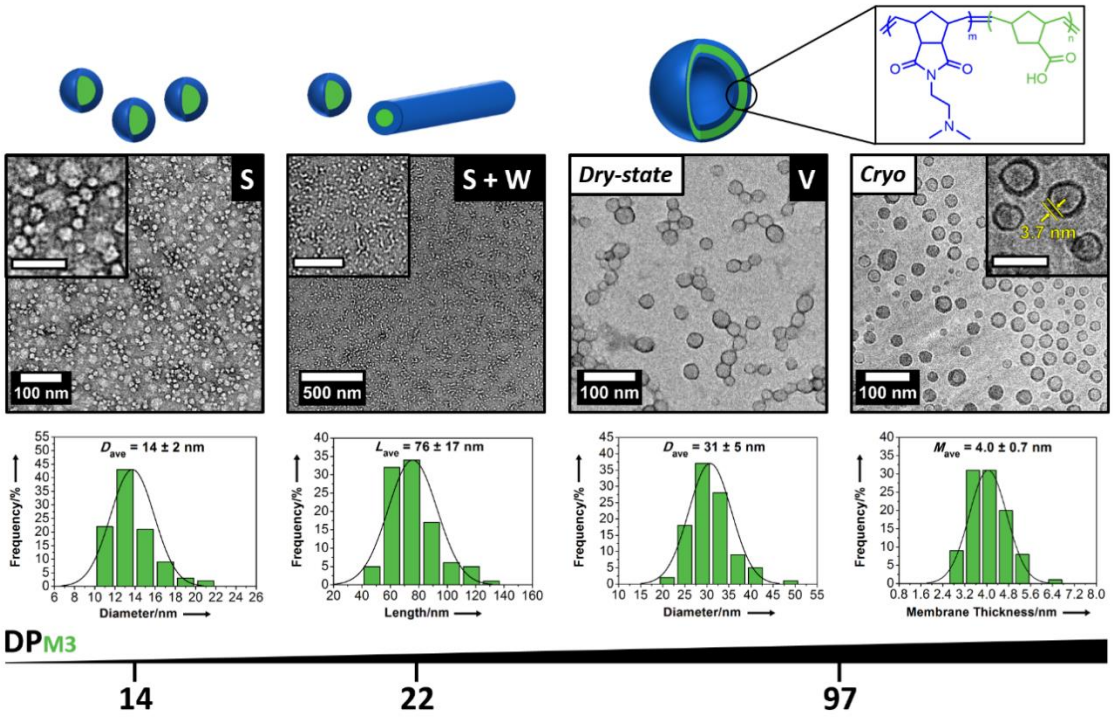

Figure 1.10. Representative TEM images of PNB-(tertiary amine)$_{10}$-*b*-PNB-(carboxylic acid)$_n$ diblock copolymer nano-objects developed *via* aqueous dispersion ROMPISA, and corresponding particle counting analysis in each case. Reproduced from ref. 88 with permission from Wiley-VCH Verlag GmbH & Co.

1.5. Block Copolymer Vesicles (Polymersomes) as Cell-Mimicking Bioreactors

As discussed, existing self-assembly methodologies of block copolymer amphiphiles (i.e., solvent-switch, thin-film rehydration, PISA, *etc*) represent a powerful tool towards generating nanostructured aggregates of various morphologies. Among these, artificial polymeric vesicles (also referred to as polymersomes) have attracted particular research interest owing to their unique properties, their ability to mimic certain functions of cellular membranes and their broad spectrum of biotechnological and biomedical applications in aqueous media, ranging from drug delivery and catalysis to biosensing and cell/organelle mimicry (Figure 1.11).[195-198]

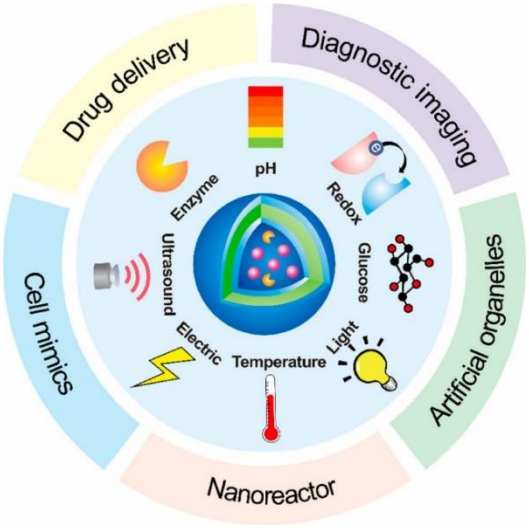

Figure 1.11. Schematic representation of the responsiveness of cargo-loaded polymersomes toward various externally applied stimuli and their potential utilization in biotechnological and biomedical applications. Reproduced from ref. 197 with permission from the American Chemical Society.

Similar to liposomes that are prepared from phospholipids and other types of amphiphilic surfactants, polymersomes are nano- or micro-sized block copolymer vesicles consisted of a hydrophobic bilayer membrane and an inner hydrophilic cavity that are capable of

encapsulating hydrophilic, hydrophobic and/or amphiphilic cargo (e.g., drugs, enzymes, membrane proteins, DNA, *etc*) (Figure 1.12).[119, 199, 200] Notably, the wide range of chemical composition, topology and functionality of synthetic polymers have allowed for formation of a wide range of polymersome nanoconstructs with tailored properties, offering a new dimension of bioinspired polymer-based compartments. To date, numerous research groups have primarily directed their studies toward programming the physicochemical characteristics of self-assembled polymersomes (i.e., size,[201] shape,[202] membrane thickness,[203] composition,[204] surface functionalization,[205] stimuli-responsiveness,[206] *etc*) and exploring their potential biomedical scope. To this extent, the general concept of discovering novel methods for tuning of the characteristics of polymersomes developed *via* aqueous PISA, especially those of their membranes, for *in situ* development of cargo-loaded nanoreactors and minimal cell-mimics has been the main focus of this thesis.

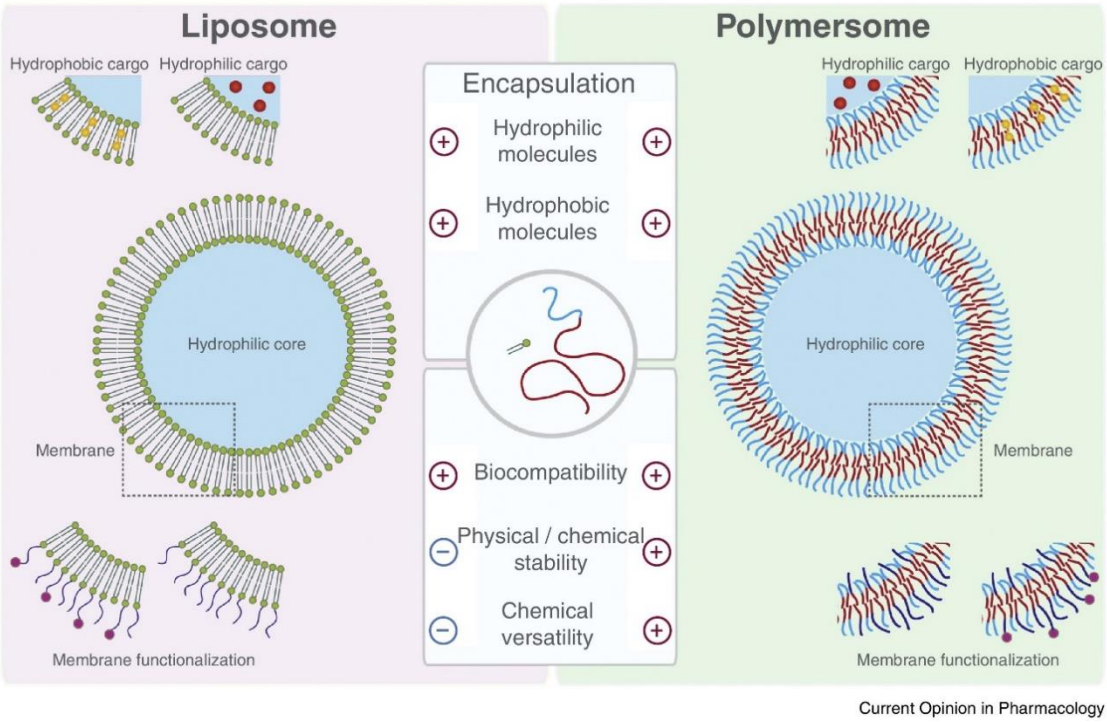

Figure 1.12. Schematic illustration of lipid (left) and block copolymer (right) vesicles, also referred to as liposomes and polymersomes, respectively. The main properties in each case are

shown, signifying the higher physical stability and enhanced chemical versatility of polymersomes over liposomes. Reproduced from ref. 200 with permission from Elsevier.

In terms of their size, both liposomes and polymersomes can self-assemble into small (20 – 100 nm), large (100 – 1000 nm) and giant (> 1 μm) vesicular nanostructures, while such assemblies can also be classified based on their lamellar properties in unilamellar (ULVs), multilamellar (MLVs) and multivesicular (MVVs) (also known as vesosomes).[119, 207] In the vast majority of cases, polymersomes adapt a spherical shape in solution, as this morphology represents the most thermodynamically favoured chain-packing conformation due to minimization of interfacial tension.[202, 208] However, inspired by the high complexity and anisotropy of naturally-occurring systems and their vital role in certain biochemical processes, researchers have developed novel polymerization and self-assembly methodologies to either promote the direct construction of non-spherical polymersomes or to induce shape transformation of spherical polymersomes into tubular,[208-211] ellipsoidal,[212, 213] stomatocyte[214-216] or other non-spherical[202] vesicular morphologies. Importantly, it has been demonstrated that anisotropic assemblies, such as tubular polymersomes, often exhibit superior biophysical properties as compared to their spherical counterparts, showing improved biodistribution, prolonged circulation times *in vivo* and enhanced cellular uptake.[217-219]

Such investigations on the preparation of polymersomes with programmable shape have been primarily pioneered by the van Hest, Wilson and Battaglia groups. The first two groups have developed an osmotic pressure-induced strategy to transform spherical polymersomes into stomatocytes, oblate, prolate and tubular polymersomes.[220-223] First, spherical polymersomes are constructed upon block copolymer self-assembly in an organic solvent/water mixture, whereas subsequent shape transformation is mediated

through a conventional solvent-switch/dialysis approach in salt-containing aqueous media, inducing osmotic deformation and kinetic trapping of the structures (Figure 1.13A). In addition, van Hest and coworkers have also reported the rapid shape transformation of spherical poly(ethylene glycol)-*b*-poly(styrene-*co*-4-vinylbenzyl azide) polymersomes into tubular ones upon covalent cross-linking of their membranes and further increase of their asymmetry (Figure 1.13B).[209] In a different study, the Battaglia group reported the preparation of tubular polymersomes as the major product upon thin-film hydration of a poly(2-methacryloyloxyethyl phosphorylcholine)-*b*-poly(2-(diisopropylamine)ethyl methacrylate) (PMPC-*b*-PDPA) diblock copolymer in aqueous media containing 5% w/w cholesterol (Figure 1.13C).[210] The presence of cholesterol was found to improve the mechanical stability of the intermediate tubular morphology, preventing the occurrence of pearling and budding processes toward the formation spherical polymersomes. However, it should be noted that the described existing strategies for preparation of non-spherical polymersomes are typically rather laborious and require either strategic design of the block copolymer system or use of specific additives that are not always compatible with bio-relevant applications. As such, in Chapter 5 of this thesis, a facile, one-step strategy for controllable preparation of anisotropic tubular polymersomes *via* fusion of spherical precursors during aqueous ROMPISA is explored, which is based on the inherent rigidity (high T_g values) of polynorbornenes and build-up of membrane tension upon polymerization.

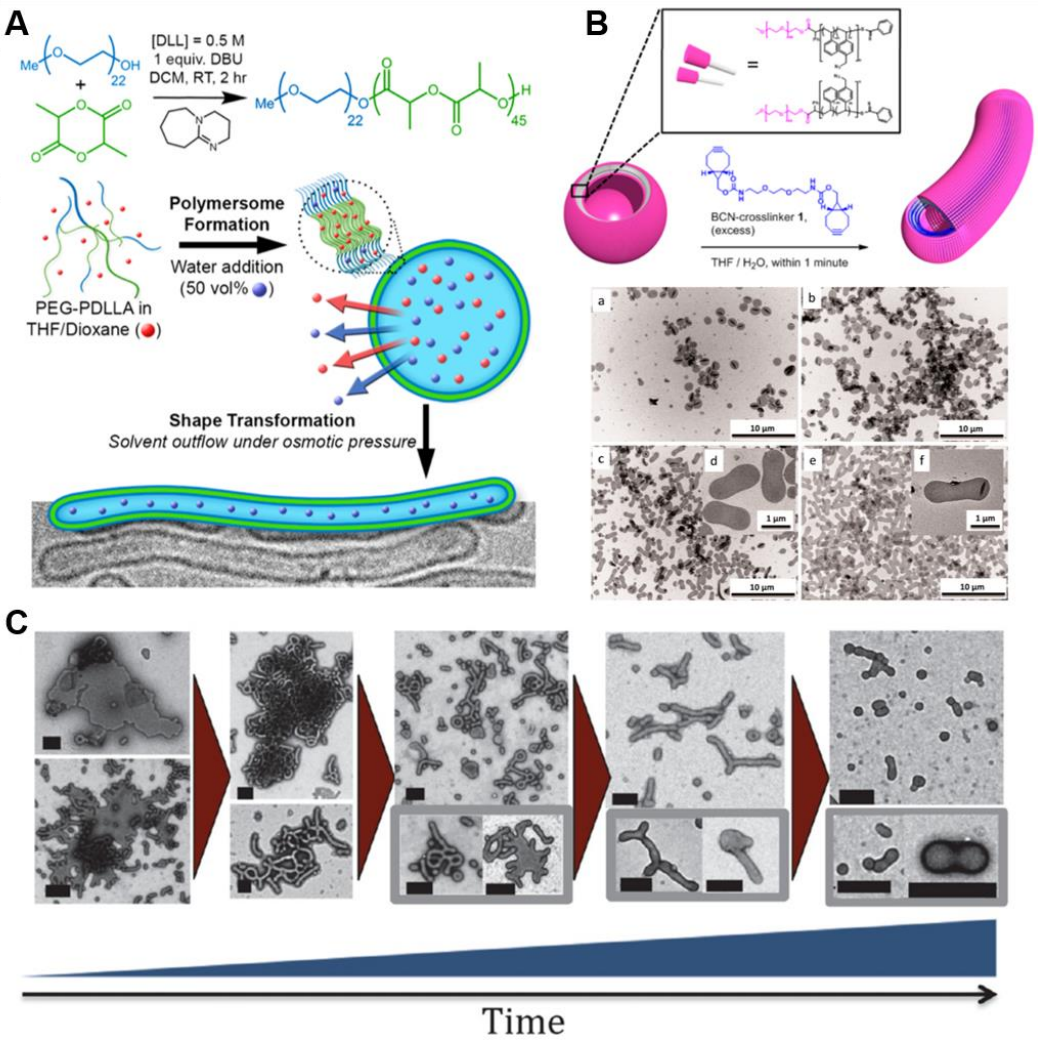

Figure 1.13. Existing methodologies for development of tubular block copolymer polymersomes *via* (A) osmotic pressure-induced shape transformation of spherical polymersomes. Reproduced from ref. 220 with permission from the American Chemical Society, (B) cross-linking-induced shape transformation of spherical polymersomes. Reproduced from ref. 209 with permission from the American Chemical Society, and (C) block copolymer self-assembly in the presence of external additives, such as cholesterol. Reproduced from ref. 210 with permission from the American Chemical Society.

Furthermore, whilst both lipid- and polymer-based vesicular analogues present similar self-assembly behavior, it has been shown that polymersomes form membranes that are not only much thicker (liposome membranes are around 3-5 nm, whereas polymeric membranes range from 5 to 50 nm), but also show greater chemical and mechanical

stability both *in vitro* and *in vivo*.[119, 224, 225] As a consequence of this feature, the properties of these synthetic polymeric membranes, such as their fluidity and permeability, as well as their interactions with other natural or synthetic bilayered systems, are vastly different compared to liposomes. Although by themselves, polymersome membranes generally exhibit lower permeability than liposome membranes, it is possible to regulate the transport of molecules through them by following various reported approaches that offer control over their size-selective permeability (Figure 1.14).[204, 207, 226]

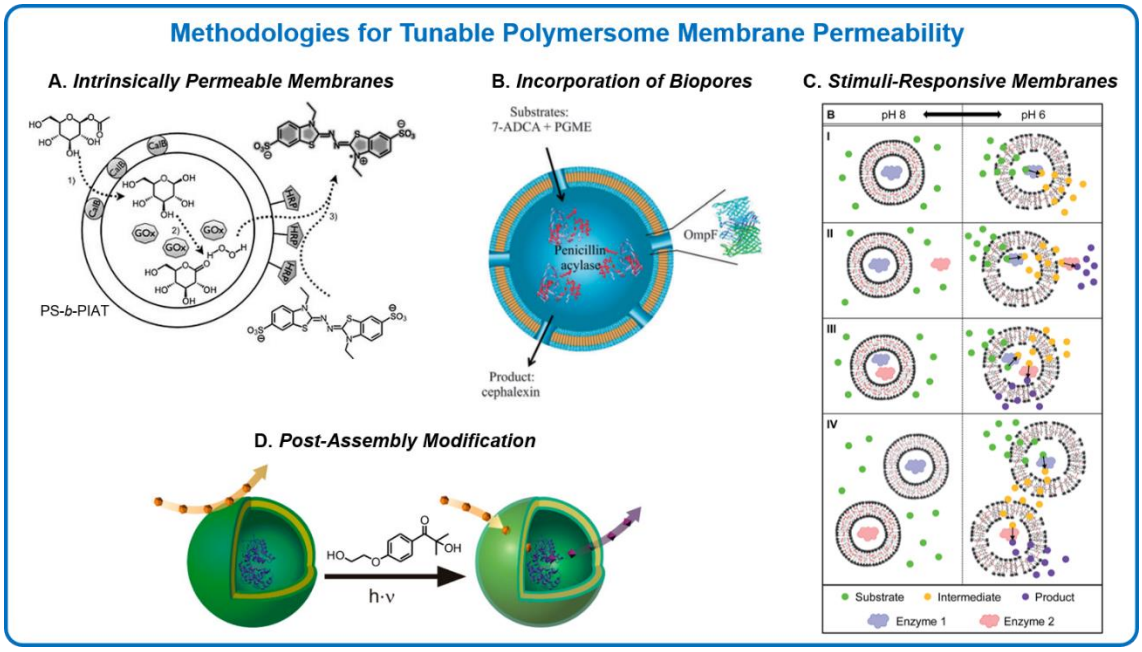

Figure 1.14. Commonly employed methodologies for controllable regulation of small molecule transport across the membrane of enzyme-loaded polymersome nanoreactors: (A) Permeabilization through utilization of core-forming polymers that yield intrinsically permeable membranes. Reproduced from ref. 227 with permission from Wiley-VCH Verlag GmbH & Co. (B) Incorporation of hydrophobic biopores, such as membrane proteins and ion channels, into the polymersome membranes. Reproduced from ref. 228 with permission from the Royal Society of Chemistry. (C) Permeabilization through utilization of stimuli-responsive membrane-forming polymers. Reproduced from ref. 229 with permission from the Royal Society of Chemistry. (D) Permeabilization through utilization of post-assembly approaches for membrane modification. Reproduced from ref. 230 with permission from the American Chemical Society.

One principal approach involves appropriate selection of core-forming polymers that favor the formation of inherently porous membranes.[172, 226, 227, 231-233] In general, these membranes allow for selective diffusion and exchange of small organic molecules located in the inner or outer aqueous polymersome microenvironment, whilst they prevent leakage of larger hydrophilic encapsulates such as proteins, enzymes and DNA, rendering additional protection toward such sensitive cargo against protease degradation and antibody binding. For instance, van Hest and coworkers reported the preparation of multi-enzyme-loaded polystyrene-*b*-poly(L-isocyanoalanine(2-thiophen-3-yl-ethyl)amide) (PS-*b*-PIAT) polymersomes and demonstrated their ability to mediate multi-enzyme cascade or polymerization reactions based on the intrinsic permeability of their PS-based membranes (Figure 1.14A).[227, 234] Moreover, the Lecommandoux and van Hest groups were able to encapsulate such enzyme-loaded PS-*b*-PIAT polymersomes within larger poly(butadiene)-*b*-poly(ethylene oxide) (PB-*b*-PEO) polymersomes for the fabrication of a multi-compartmentalized polymeric formulation that structurally resembled a simplistic cell and its containing organelles.[235] Our group has also reported that enzyme-loaded PEG-*b*-PHPMA polymersome nanoreactors with inherent size-selective membrane permeability could be prepared *via* aqueous photo-PISA under mild reaction conditions and further demonstrated the ability of the confined domains to communicate through enzymatic cascades.[125, 172]

More significantly, insertion of transporters, ion-channels and membrane proteins into polymersome membranes for the introduction of biopores presents a biomimetic strategy for selective membrane permeabilization (Figure 1.14B).[228, 236-239] This methodology allows for control of the flux of electrolytes and the specific or non-specific transport of reactants (e.g., substrates and products of enzyme-catalyzed reactions) across vesicular

membranes. Polymersomes equipped with biopores/membrane proteins, acting as "gates" for the diffusion of molecules across their membranes, constitute nanoscale reaction spaces and are served for the design of complex cell-mimicking nanoreactors.[195, 237, 240] In an early publication by Meier's group, enhanced permeability of polymersomes formed *via* the self-assembly of poly(2-methyl-2-oxazoline)-*b*-poly(dimethylsiloxane)-*b*-poly(2-methyl-2-oxazoline) (PMOXA-*b*-PDMS-*b*-PMOXA) triblock copolymers in aqueous media, was achieved upon incorporation of the hydrophobic outer membrane protein F (OmpF) within their membrane.[241] Additional studies based on further modifications of this type of polymersomes revealed an ever wider range of applications for these nanostructures.[242-244] By inserting other membrane proteins, such as maltoporin LamB, aquaporin Z (AqpZ) or glycerol facilitator (GlpF), into the hydrophobic domain of similar polymersomes, selective permeability towards specific molecules or ions could be also achieved depending on the protein utilized. In a more recent study, Palivan and coworkers introduced gramicidin (gA) channels within the membrane of PMOXA-*b*-PDMS-*b*-PMOXA polymersomes for their selective permeability toward ions.[245] Inserted gA exhibited efficient time response to pH and ions, showing that the nanoreactors are promising candidates for designing sophisticated biosensors for a variety of applications in which stimuli-responsiveness, such as pH or ionic strength variations, is required. In a similar approach, Battaglia and coworkers have also demonstrated that incorporation of DNA-based nanopores into the hydrophobic membrane of block copolymer polymersomes facilitates the diffusion of small molecule reactants, whilst retaining encapsulated macromolecules within their inner aqueous lumen.[246] Importantly, a novel one-step approach for surfactant-mediated incorporation of a porin membrane protein,

OmpF, into enzyme-loaded polymersome nanoreactors prepared *via* aqueous RAFT-mediated photo-PISA is introduced in Chapter 2 of this thesis.

Another commonly employed strategy for controlled membrane permeability of polymersomes involves the utilization of stimuli-responsive core-forming blocks (Figure 1.14C).[229, 247-251] In a seminal study, Yao *et al*. prepared GOx-loaded poly(*N*-isopropylacrylamide)-*b*-poly(2-((((2-nitrobenzyl)-oxy)carbonyl)amino)ethyl acrylate) (PNIPAAm-*b*-PNBOCA) polymersomes with photo-sensitive membranes.[249] Cross-linking of the membrane upon UV irradiation led to a hydrophobic-to-hydrophilic transition of the originally impermeable membrane owing to cleavage of the nitrobenzyl units. This resulted in a significant increase of the membrane permeability of the cross-linked polymersomes toward the corresponding small molecule substrates. In a different example, Voit, Battaglia and coworkers developed GOx-, HRP- and myoglobin-loaded polymersomes with pH-responsive cross-linked membranes based on poly(*N*,*N*-diethylaminoethyl methacrylate) (PDEAEMA).[248] On-demand substrate diffusivity and enzymatic activity were observed upon protonation of the PDEAEMA core-forming block when lowering the solution pH from 8 to 6.

Ultimately, a less explored approach to modulate the exchange of small molecules across polymersome bioreactors encompasses post-assembly membrane modification methodologies (Figure 1.14D). In one of the few reports, Bruns, Meier and coworkers constructed various HRP-loaded polymersome nanoreactors that underwent an impermeable-to-permeable transition upon reaction with externally added PP-OH under UV-irradiation and subsequent radical oxidation of their membrane.[230] The permeability of the PP-OH-treated polymersomes was assessed using a range of different organic molecules of varying hydrophobicity, indicating that more hydrophobic compounds

exhibited increased diffusivity across their membrane. In Chapter 3, an alternative post-PISA membrane modification methodology was developed for diffusivity regulation of semi-permeable polymersome nanoreactors by employing epoxide–amine “click” reactions using various primary amines, providing valuable insight into the effect of the hydrophobicity of the modifier onto the polymersome membrane thickness and their resulting permeability.

1.6. Summary

In Chapter 1, the fundamental methodologies and key concepts investigated within the experimental Chapters of this thesis have been introduced. A general introduction to synthetic polymers and the common polymerization techniques utilized for their preparation have been presented. Particular focus has been given to mechanistic insights of RAFT/photo-RAFT polymerization and ROMP, followed by a detailed description on amphiphilic block copolymer self-assembly, as well as the basic principles that determine the obtained nanoparticle morphology. Moreover, polymerization-induced self-assembly (PISA), which is the general topic area of this thesis, has been highlighted as a rapidly growing one-pot procedure for the synthesis of block copolymer nano-objects with predictable morphologies, whilst relevant aqueous RAFT-mediated photo-PISA and ROMPISA reports of particular significance for the projects explored herein have been discussed. Finally, the main properties of block copolymer vesicles (polymersomes) and specific application-oriented examples have been also presented with special emphasis given to compartmentalization and preparation of tunable biomembrane-mimicking polymersome nanoreactors.

1.7. References

1. Jensen, W. B., The Origin of the Polymer Concept. *J. Chem. Educ.* **2008,** *85*, 624.
2. Staudinger, H., Über Polymerisation. *Ber. dtsch. Chem. Ges. A/B* **1920,** *53*, 1073-1085.
3. Badi, N.; Lutz, J.-F., Sequence control in polymer synthesis. *Chem. Soc. Rev.* **2009,** *38*, 3383-3390.
4. Lutz, J.-F.; Ouchi, M.; Liu, D. R.; Sawamoto, M., Sequence-Controlled Polymers. *Science* **2013,** *341*, 1238149.
5. Robert, F. T. S., Dispersity in polymer science (IUPAC Recommendations 2009). *Pure Appl. Chem.* **2009,** *81*, 351-353.
6. *Physical Properties of Polymers Handbook*. Springer: New York, **2007**.
7. Matyjaszewski, K.; Xia, J., Atom Transfer Radical Polymerization. *Chem. Rev.* **2001,** *101*, 2921-2990.
8. Matyjaszewski, K., Architecturally Complex Polymers with Controlled Heterogeneity. *Science* **2011,** *333*, 1104-1105.
9. Hadjichristidis, N.; Iatrou, H.; Pitsikalis, M.; Mays, J., Macromolecular architectures by living and controlled/living polymerizations. *Prog. Polym. Sci.* **2006,** *31*, 1068-1132.
10. Flory, P. J., Fundamental Principles of Condensation Polymerization. *Chem. Rev.* **1946,** *39*, 137-197.
11. Stille, J. K., Step-growth polymerization. *J. Chem. Educ.* **1981,** *58*, 862.
12. *Polymer Chemistry*. 2nd ed.; CRC Press: New York, **2007**.
13. Korshak, V. V.; Vasnev, V. A., 11 - Interfacial and Dispersion Polymerization. In *Comprehensive Polymer Science and Supplements*, Allen, G.; Bevington, J. C., Eds. Pergamon: Amsterdam, **1989**; pp 167-196.
14. Billiet, L.; Fournier, D.; Du Prez, F., Step-growth polymerization and 'click' chemistry: The oldest polymers rejuvenated. *Polymer* **2009,** *50*, 3877-3886.
15. Odian, G., *Principles of Polymerization*. 4th ed.; John Wiley & Sons, Inc.: **2007**.
16. Odian, G., Chain-Reaction Polymerization. In *Encyclopedia of Polymer Science and Technology*, John Wiley & Sons, Inc.: **2011**.
17. Rudin, A.; Choi, P., Chapter 11 - Ionic and Coordinated Polymerizations. In *The Elements of Polymer Science & Engineering (Third Edition)*, Rudin, A.; Choi, P., Eds. Academic Press: Boston, **2013**; pp 449-493.
18. Szwarc, M., 'Living' Polymers. *Nature* **1956,** *178*, 1168-1169.
19. Hirao, A.; Goseki, R.; Ishizone, T., Advances in Living Anionic Polymerization: From Functional Monomers, Polymerization Systems, to Macromolecular Architectures. *Macromolecules* **2014,** *47*, 1883-1905.
20. Aoshima, S.; Kanaoka, S., A Renaissance in Living Cationic Polymerization. *Chem. Rev.* **2009,** *109*, 5245-5287.
21. Fuchise, K.; Chen, Y.; Satoh, T.; Kakuchi, T., Recent progress in organocatalytic group transfer polymerization. *Polym. Chem.* **2013,** *4*, 4278-4291.
22. Bielawski, C. W.; Grubbs, R. H., Living ring-opening metathesis polymerization. *Prog. Polym. Sci.* **2007,** *32*, 1-29.
23. Szwarc, M., *Living Polymers and Mechanisms of Anionic Polymerization. Advances in Polymer Science*. Springer: **1983**.

24. Hadjichristidis, N.; Iatrou, H.; Pispas, S.; Pitsikalis, M., Anionic polymerization: High vacuum techniques. *J. Polym. Sci. A Polym. Chem.* **2000,** *38*, 3211-3234.
25. Colombani, D., Chain-growth control in free radical polymerization. *Prog. Polym. Sci.* **1997,** *22*, 1649-1720.
26. Bisht, H. S.; Chatterjee, A. K., LIVING FREE-RADICAL POLYMERIZATION—A REVIEW. *J. Macromol. Sci., Part C* **2001,** *41*, 139-173.
27. Soroush, M.; Rappe, A. M., Chapter 5 - Theoretical Insights Into Chain Transfer Reactions of Acrylates. In *Computational Quantum Chemistry*, Soroush, M., Ed. Elsevier: **2019**; pp 135-193.
28. Webster, O. W., Living Polymerization Methods. *Science* **1991,** *251*, 887-893.
29. Shanmugam, S.; Matyjaszewski, K., Reversible Deactivation Radical Polymerization: State-of-the-Art in 2017. In *Reversible Deactivation Radical Polymerization: Mechanisms and Synthetic Methodologies*, American Chemical Society: **2018**; Vol. 1284, pp 1-39.
30. Braunecker, W. A.; Matyjaszewski, K., Controlled/living radical polymerization: Features, developments, and perspectives. *Prog. Polym. Sci.* **2007,** *32*, 93-146.
31. Matyjaszewski, K.; Spanswick, J., Controlled/living radical polymerization. *Mater. Today* **2005,** *8*, 26-33.
32. Hawker, C. J.; Bosman, A. W.; Harth, E., New Polymer Synthesis by Nitroxide Mediated Living Radical Polymerizations. *Chem. Rev.* **2001,** *101*, 3661-3688.
33. Moad, G.; Rizzardo, E.; Thang, S. H., Radical addition–fragmentation chemistry in polymer synthesis. *Polymer* **2008,** *49*, 1079-1131.
34. Perrier, S., 50th Anniversary Perspective: RAFT Polymerization—A User Guide. *Macromolecules* **2017,** *50*, 7433-7447.
35. Kato, M.; Kamigaito, M.; Sawamoto, M.; Higashimura, T., Polymerization of Methyl Methacrylate with the Carbon Tetrachloride/Dichlorotris-(triphenylphosphine)ruthenium(II)/Methylaluminum Bis(2,6-di-tert-butylphenoxide) Initiating System: Possibility of Living Radical Polymerization. *Macromolecules* **1995,** *28*, 1721-1723.
36. Wang, J.-S.; Matyjaszewski, K., Controlled/"living" radical polymerization. atom transfer radical polymerization in the presence of transition-metal complexes. *J. Am. Chem. Soc.* **1995,** *117*, 5614-5615.
37. Matyjaszewski, K., Atom Transfer Radical Polymerization (ATRP): Current Status and Future Perspectives. *Macromolecules* **2012,** *45*, 4015-4039.
38. Fischer, H., The Persistent Radical Effect In “Living” Radical Polymerization. *Macromolecules* **1997,** *30*, 5666-5672.
39. Fischer, H., The Persistent Radical Effect: A Principle for Selective Radical Reactions and Living Radical Polymerizations. *Chem. Rev.* **2001,** *101*, 3581-3610.
40. Moad, G.; Rizzardo, E., Chapter 1 The History of Nitroxide-mediated Polymerization. In *Nitroxide Mediated Polymerization: From Fundamentals to Applications in Materials Science*, The Royal Society of Chemistry: **2016**; pp 1-44.
41. Grubbs, R. B., Nitroxide-Mediated Radical Polymerization: Limitations and Versatility. *Polym. Rev.* **2011,** *51*, 104-137.
42. Nicolas, J.; Guillaneuf, Y.; Lefay, C.; Bertin, D.; Gigmes, D.; Charleux, B., Nitroxide-mediated polymerization. *Prog. Polym. Sci.* **2013,** *38*, 63-235.
43. Chiefari, J.; Chong, Y. K.; Ercole, F.; Krstina, J.; Jeffery, J.; Le, T. P. T.; Mayadunne, R. T. A.; Meijs, G. F.; Moad, C. L.; Moad, G.; Rizzardo, E.; Thang, S. H.,

Living Free-Radical Polymerization by Reversible Addition−Fragmentation Chain Transfer: The RAFT Process. *Macromolecules* **1998,** *31*, 5559-5562.
44. Keddie, D. J., A guide to the synthesis of block copolymers using reversible-addition fragmentation chain transfer (RAFT) polymerization. *Chem. Soc. Rev.* **2014,** *43*, 496-505.
45. Moad, G.; Rizzardo, E.; Thang, S. H., Living Radical Polymerization by the RAFT Process – A Third Update. *Aust. J. Chem.* **2012,** *65*, 985-1076.
46. Keddie, D. J.; Moad, G.; Rizzardo, E.; Thang, S. H., RAFT Agent Design and Synthesis. *Macromolecules* **2012,** *45*, 5321-5342.
47. Destarac, M., On the Critical Role of RAFT Agent Design in Reversible Addition-Fragmentation Chain Transfer (RAFT) Polymerization. *Polym. Rev.* **2011,** *51*, 163-187.
48. Gody, G.; Barbey, R.; Danial, M.; Perrier, S., Ultrafast RAFT polymerization: multiblock copolymers within minutes. *Polym. Chem.* **2015,** *6*, 1502-1511.
49. Zaquen, N.; Kadir, A. M. N. B. P. H. A.; Iasa, A.; Corrigan, N.; Junkers, T.; Zetterlund, P. B.; Boyer, C., Rapid Oxygen Tolerant Aqueous RAFT Photopolymerization in Continuous Flow Reactors. *Macromolecules* **2019,** *52*, 1609-1619.
50. Yeow, J.; Chapman, R.; Gormley, A. J.; Boyer, C., Up in the air: oxygen tolerance in controlled/living radical polymerisation. *Chem. Soc. Rev.* **2018,** *47*, 4357-4387.
51. McKenzie, T. G.; Fu, Q.; Uchiyama, M.; Satoh, K.; Xu, J.; Boyer, C.; Kamigaito, M.; Qiao, G. G., Beyond Traditional RAFT: Alternative Activation of Thiocarbonylthio Compounds for Controlled Polymerization. *Adv. Sci.* **2016,** *3*, 1500394.
52. Tian, X.; Ding, J.; Zhang, B.; Qiu, F.; Zhuang, X.; Chen, Y., Recent Advances in RAFT Polymerization: Novel Initiation Mechanisms and Optoelectronic Applications. *Polymers* **2018,** *10*, 318.
53. Chen, M.; Zhong, M.; Johnson, J. A., Light-Controlled Radical Polymerization: Mechanisms, Methods, and Applications. *Chem. Rev.* **2016,** *116*, 10167-10211.
54. Yeow, J.; Boyer, C., Photoinitiated Polymerization-Induced Self-Assembly (Photo-PISA): New Insights and Opportunities. *Adv. Sci.* **2017,** *4*, 1700137.
55. Phommalysack-Lovan, J.; Chu, Y.; Boyer, C.; Xu, J., PET-RAFT polymerisation: towards green and precision polymer manufacturing. *Chem. Commun.* **2018,** *54*, 6591-6606.
56. Xu, J.; Jung, K.; Atme, A.; Shanmugam, S.; Boyer, C., A Robust and Versatile Photoinduced Living Polymerization of Conjugated and Unconjugated Monomers and Its Oxygen Tolerance. *J. Am. Chem. Soc.* **2014,** *136*, 5508-5519.
57. Xu, J.; Shanmugam, S.; Duong, H. T.; Boyer, C., Organo-photocatalysts for photoinduced electron transfer-reversible addition–fragmentation chain transfer (PET-RAFT) polymerization. *Polym. Chem.* **2015,** *6*, 5615-5624.
58. Shanmugam, S.; Xu, J.; Boyer, C., Photoinduced Electron Transfer–Reversible Addition–Fragmentation Chain Transfer (PET-RAFT) Polymerization of Vinyl Acetate and N-Vinylpyrrolidinone: Kinetic and Oxygen Tolerance Study. *Macromolecules* **2014,** *47*, 4930-4942.
59. Ng, G.; Yeow, J.; Xu, J.; Boyer, C., Application of oxygen tolerant PET-RAFT to polymerization-induced self-assembly. *Polym. Chem.* **2017,** *8*, 2841-2851.
60. Otsu, T., Iniferter concept and living radical polymerization. *J. Polym. Sci. A Polym. Chem.* **2000,** *38*, 2121-2136.
61. Casey, C. P., 2005 Nobel Prize in Chemistry. Development of the Olefin Metathesis Method in Organic Synthesis. *J. Chem. Educ.* **2006,** *83*, 192-195.

62. Randall, M. L.; Snapper, M. L., Selective olefin metatheses—new tools for the organic chemist: A review. *J. Mol. Catal. A Chem.* **1998,** *133*, 29-40.
63. Mutlu, H.; de Espinosa, L. M.; Meier, M. A. R., Acyclic diene metathesis: a versatile tool for the construction of defined polymer architectures. *Chem. Soc. Rev.* **2011,** *40*, 1404-1445.
64. Jean-Louis Hérisson, P.; Chauvin, Y., Catalyse de transformation des oléfines par les complexes du tungstène. II. Télomérisation des oléfines cycliques en présence d'oléfines acycliques. *Makromol. Chem.* **1971,** *141*, 161-176.
65. Grubbs, R. H.; Burk, P. L.; Carr, D. D., Mechanism of the olefin metathesis reaction. *J. Am. Chem. Soc.* **1975,** *97*, 3265-3267.
66. Grubbs, R. H.; Carr, D. D.; Hoppin, C.; Burk, P. L., Consideration of the mechanism of the metal catalyzed olefin metathesis reaction. *J. Am. Chem. Soc.* **1976,** *98*, 3478-3483.
67. Dias, E. L.; Nguyen, S. T.; Grubbs, R. H., Well-Defined Ruthenium Olefin Metathesis Catalysts: Mechanism and Activity. *J. Am. Chem. Soc.* **1997,** *119*, 3887-3897.
68. Liu, W.; Nichols, P. J.; Smith, N., Di(ethylene glycol) vinyl ether: a highly efficient deactivating reagent for olefin metathesis catalysts. *Tetrahedron Lett.* **2009,** *50*, 6103-6105.
69. Hong, S. H.; Wenzel, A. G.; Salguero, T. T.; Day, M. W.; Grubbs, R. H., Decomposition of Ruthenium Olefin Metathesis Catalysts. *J. Am. Chem. Soc.* **2007,** *129*, 7961-7968.
70. Ireland, B. J.; Dobigny, B. T.; Fogg, D. E., Decomposition of a Phosphine-Free Metathesis Catalyst by Amines and Other Bronsted Bases: Metallacyclobutane Deprotonation as a Major Deactivation Pathway. *ACS Catal.* **2015,** *5*, 4690-4698.
71. Deshmukh, P. H.; Blechert, S., Alkene metathesis: the search for better catalysts. *Dalton Trans.* **2007**, 2479-2491.
72. Schrock, R. R., First isolable transition metal methylene complex and analogs. Characterization, mode of decomposition, and some simple reactions. *J. Am. Chem. Soc.* **1975,** *97*, 6577-6578.
73. Kress, J.; Wesolek, M.; Osborn, J. A., Tungsten (IV) carbenes for the metathesis of olefins. Direct observation and identification of the chain carrying carbene complexes in a highly active catalyst system. *J. Chem. Soc., Chem. Commun.* **1982**, 514-516.
74. Schrock, R. R.; Murdzek, J. S.; Bazan, G. C.; Robbins, J.; DiMare, M.; O'Regan, M., Synthesis of molybdenum imido alkylidene complexes and some reactions involving acyclic olefins. *J. Am. Chem. Soc.* **1990,** *112*, 3875-3886.
75. Schwab, P.; France, M. B.; Ziller, J. W.; Grubbs, R. H., A Series of Well-Defined Metathesis Catalysts–Synthesis of [RuCl2(CHR′)(PR3)2] and Its Reactions. *Angew. Chem. Int. Ed.* **1995,** *34*, 2039-2041.
76. Schwab, P.; Grubbs, R. H.; Ziller, J. W., Synthesis and Applications of RuCl2(CHR‘)(PR3)2: The Influence of the Alkylidene Moiety on Metathesis Activity. *J. Am. Chem. Soc.* **1996,** *118*, 100-110.
77. Kingsbury, J. S.; Harrity, J. P. A.; Bonitatebus, P. J.; Hoveyda, A. H., A Recyclable Ru-Based Metathesis Catalyst. *J. Am. Chem. Soc.* **1999,** *121*, 791-799.
78. Garber, S. B.; Kingsbury, J. S.; Gray, B. L.; Hoveyda, A. H., Efficient and Recyclable Monomeric and Dendritic Ru-Based Metathesis Catalysts. *J. Am. Chem. Soc.* **2000,** *122*, 8168-8179.

79. Scholl, M.; Ding, S.; Lee, C. W.; Grubbs, R. H., Synthesis and Activity of a New Generation of Ruthenium-Based Olefin Metathesis Catalysts Coordinated with 1,3-Dimesityl-4,5-dihydroimidazol-2-ylidene Ligands. *Org. Lett.* **1999,** *1*, 953-956.
80. Scholl, M.; Trnka, T. M.; Morgan, J. P.; Grubbs, R. H., Increased ring closing metathesis activity of ruthenium-based olefin metathesis catalysts coordinated with imidazolin-2-ylidene ligands. *Tetrahedron Lett.* **1999,** *40*, 2247-2250.
81. Huang, J.; Stevens, E. D.; Nolan, S. P.; Petersen, J. L., Olefin Metathesis-Active Ruthenium Complexes Bearing a Nucleophilic Carbene Ligand. *J. Am. Chem. Soc.* **1999,** *121*, 2674-2678.
82. Love, J. A.; Morgan, J. P.; Trnka, T. M.; Grubbs, R. H., A Practical and Highly Active Ruthenium-Based Catalyst that Effects the Cross Metathesis of Acrylonitrile. *Angew. Chem. Int. Ed.* **2002,** *41*, 4035-4037.
83. Zhang, K.; Cui, J.; Lackey, M.; Tew, G. N., Hydrogels Based on Living Ring-Opening Metathesis Polymerization. *Macromolecules* **2010,** *43*, 10246-10252.
84. Moatsou, D.; Hansell, C. F.; O'Reilly, R. K., Precision polymers: a kinetic approach for functional poly(norbornenes). *Chem. Sci.* **2014,** *5*, 2246-2250.
85. Gringolts, M. L.; Denisova, Y. I.; Finkelshtein, E. S.; Kudryavtsev, Y. V., Olefin metathesis in multiblock copolymer synthesis. *Beilstein J. Org. Chem.* **2019,** *15*, 218-235.
86. Lin, T.-P.; Chang, A. B.; Chen, H.-Y.; Liberman-Martin, A. L.; Bates, C. M.; Voegtle, M. J.; Bauer, C. A.; Grubbs, R. H., Control of Grafting Density and Distribution in Graft Polymers by Living Ring-Opening Metathesis Copolymerization. *J. Am. Chem. Soc.* **2017,** *139*, 3896-3903.
87. Radzinski, S. C.; Foster, J. C.; Scannelli, S. J.; Weaver, J. R.; Arrington, K. J.; Matson, J. B., Tapered Bottlebrush Polymers: Cone-Shaped Nanostructures by Sequential Addition of Macromonomers. *ACS Macro Lett.* **2017,** *6*, 1175-1179.
88. Foster, J. C.; Varlas, S.; Blackman, L. D.; Arkinstall, L. A.; O'Reilly, R. K., Ring-Opening Metathesis Polymerization in Aqueous Media Using a Macroinitiator Approach. *Angew. Chem. Int. Ed.* **2018,** *57*, 10672-10676.
89. Fishman, J. M.; Kiessling, L. L., Synthesis of Functionalizable and Degradable Polymers by Ring-Opening Metathesis Polymerization. *Angew. Chem. Int. Ed.* **2013,** *52*, 5061-5064.
90. Mallick, A.; Xu, Y.; Lin, Y.; He, J.; Chan-Park, M. B.; Liu, X.-W., Oxadiazabicyclooctenone as a versatile monomer for the construction of pH sensitive functional polymers via ROMP. *Polym. Chem.* **2018,** *9*, 372-377.
91. Shieh, P.; Nguyen, H. V. T.; Johnson, J. A., Tailored silyl ether monomers enable backbone-degradable polynorbornene-based linear, bottlebrush and star copolymers through ROMP. *Nat. Chem.* **2019,** *11*, 1124-1132.
92. Sutthasupa, S.; Shiotsuki, M.; Sanda, F., Recent advances in ring-opening metathesis polymerization, and application to synthesis of functional materials. *Polym. J.* **2010,** *42*, 905-915.
93. Slugovc, C., The Ring Opening Metathesis Polymerisation Toolbox. *Macromol. Rapid Commun.* **2004,** *25*, 1283-1297.
94. Choi, T.-L.; Grubbs, R. H., Controlled Living Ring-Opening-Metathesis Polymerization by a Fast-Initiating Ruthenium Catalyst. *Angew. Chem. Int. Ed.* **2003,** *42*, 1743-1746.
95. Seehof, N.; Grutke, S.; Risse, W., Selective reaction with exo-isomers in ring-opening olefin metathesis polymerization (ROMP) of fluoroalkyl-substituted norbornene derivatives. *Macromolecules* **1993,** *26*, 695-700.

96. Rule, J. D.; Moore, J. S., ROMP Reactivity of endo- and exo-Dicyclopentadiene. *Macromolecules* **2002,** *35*, 7878-7882.
97. Isarov, S. A.; Pokorski, J. K., Protein ROMP: Aqueous Graft-from Ring-Opening Metathesis Polymerization. *ACS Macro Lett.* **2015,** *4*, 969-973.
98. Lu, X.; Fan, L.; Phelps, C. B.; Davie, C. P.; Donahue, C. P., Ruthenium Promoted On-DNA Ring-Closing Metathesis and Cross-Metathesis. *Bioconjugate Chem.* **2017,** *28*, 1625-1629.
99. Claverie, J. P.; Viala, S.; Maurel, V.; Novat, C., Ring-Opening Metathesis Polymerization in Emulsion. *Macromolecules* **2001,** *34*, 382-388.
100. Öztürk, B. Ö.; Kolberg, A.; Karabulut Şehitoğlu, S., Nonaqueous and Aqueous Emulsion ROMP Reactions Induced by Environment-Friendly Latent Ruthenium Indenylidene Catalyst Bearing Morpholine Substituted Bidentate (N, O) Schiff Bases. *Macromol. Chem. Phys.* **2017,** *218*, 1600594/1-11.
101. Novak, B. M.; Grubbs, R. H., The ring opening metathesis polymerization of 7-oxabicyclo[2.2.1]hept-5-ene derivatives: a new acyclic polymeric ionophore. *J. Am. Chem. Soc.* **1988,** *110*, 960-961.
102. Novak, B. M.; Grubbs, R. H., Catalytic organometallic chemistry in water: the aqueous ring-opening metathesis polymerization of 7-oxanorbornene derivatives. *J. Am. Chem. Soc.* **1988,** *110*, 7542-7543.
103. Trnka, T. M.; Grubbs, R. H., The Development of L2X2RuCHR Olefin Metathesis Catalysts: An Organometallic Success Story. *Acc. Chem. Res.* **2000,** *34*, 18-29.
104. Mohr, B.; Lynn, D. M.; Grubbs, R. H., Synthesis of Water-Soluble, Aliphatic Phosphines and Their Application to Well-Defined Ruthenium Olefin Metathesis Catalysts. *Organometallics* **1996,** *15*, 4317-4325.
105. Jordan, J. P.; Grubbs, R. H., Small-Molecule N-Heterocyclic-Carbene-Containing Olefin-Metathesis Catalysts for Use in Water. *Angew. Chem. Int. Ed.* **2007,** *46*, 5152-5155.
106. Hong, S. H.; Grubbs, R. H., Highly Active Water-Soluble Olefin Metathesis Catalyst. *J. Am. Chem. Soc.* **2006,** *128*, 3508-3509.
107. Sabatino, V.; Ward, T. R., Aqueous olefin metathesis: recent developments and applications. *Beilstein J. Org. Chem.* **2019,** *15*, 445-468.
108. Samanta, D.; Kratz, K.; Zhang, X.; Emrick, T., A Synthesis of PEG- and Phosphorylcholine-Substituted Pyridines To Afford Water-Soluble Ruthenium Benzylidene Metathesis Catalysts. *Macromolecules* **2008,** *41*, 530-532.
109. Dunbar, M. A.; Balof, S. L.; Roberts, A. N.; Valente, E. J.; Schanz, H.-J., pH-Responsive Ruthenium-Based Olefin Metathesis Catalysts: Controlled Ring-Opening Metathesis Polymerization in Alcoholic and Aqueous Media upon Acid Addition. *Organometallics* **2011,** *30*, 199-203.
110. Michrowska, A.; Gułajski, Ł.; Kaczmarska, Z.; Mennecke, K.; Kirschning, A.; Grela, K., A green catalyst for green chemistry: Synthesis and application of an olefin metathesis catalyst bearing a quaternary ammonium group. *Green Chem.* **2006,** *8*, 685-688.
111. Binder, J. B.; Guzei, I. A.; Raines, R. T., Salicylaldimine Ruthenium Alkylidene Complexes: Metathesis Catalysts Tuned for Protic Solvents. *Adv. Synth. Catal.* **2007,** *349*, 395-404.

112. Lynn, D. M.; Kanaoka, S.; Grubbs, R. H., Living Ring-Opening Metathesis Polymerization in Aqueous Media Catalyzed by Well-Defined Ruthenium Carbene Complexes. *J. Am. Chem. Soc.* **1996,** *118*, 784-790.
113. Lynn, D. M.; Mohr, B.; Grubbs, R. H., Living Ring-Opening Metathesis Polymerization in Water. *J. Am. Chem. Soc.* **1998,** *120*, 1627-1628.
114. Engle, K. M.; Lu, G.; Luo, S.-X.; Henling, L. M.; Takase, M. K.; Liu, P.; Houk, K. N.; Grubbs, R. H., Origins of Initiation Rate Differences in Ruthenium Olefin Metathesis Catalysts Containing Chelating Benzylidenes. *J. Am. Chem. Soc.* **2015,** *137*, 5782-5792.
115. Wright, D. B.; Touve, M. A.; Adamiak, L.; Gianneschi, N. C., ROMPISA: Ring-Opening Metathesis Polymerization-Induced Self-Assembly. *ACS Macro Lett.* **2017,** *6*, 925-929.
116. Mai, Y.; Eisenberg, A., Self-assembly of block copolymers. *Chem. Soc. Rev.* **2012,** *41*, 5969-5985.
117. Blanazs, A.; Armes, S. P.; Ryan, A. J., Self-Assembled Block Copolymer Aggregates: From Micelles to Vesicles and their Biological Applications. *Macromol. Rapid Commun.* **2009,** *30*, 267-277.
118. Brendel, J. C.; Schacher, F. H., Block Copolymer Self-Assembly in Solution—Quo Vadis? *Chem. Asian J.* **2018,** *13*, 230-239.
119. Rideau, E.; Dimova, R.; Schwille, P.; Wurm, F. R.; Landfester, K., Liposomes and polymersomes: a comparative review towards cell mimicking. *Chem. Soc. Rev.* **2018,** *47*, 8572-8610.
120. Doncom, K. E. B.; Blackman, L. D.; Wright, D. B.; Gibson, M. I.; O'Reilly, R. K., Dispersity effects in polymer self-assemblies: a matter of hierarchical control. *Chem. Soc. Rev.* **2017,** *46*, 4119-4134.
121. Cameron, N. S.; Corbierre, M. K.; Eisenberg, A., 1998 E.W.R. Steacie Award Lecture Asymmetric amphiphilic block copolymers in solution: a morphological wonderland. *Can. J. Chem.* **1999,** *77*, 1311-1326.
122. Antonietti, M.; Förster, S., Vesicles and Liposomes: A Self-Assembly Principle Beyond Lipids. *Adv. Mater.* **2003,** *15*, 1323-1333.
123. Baranello, M. P.; Bauer, L.; Jordan, C. T.; Benoit, D. S. W., Micelle Delivery of Parthenolide to Acute Myeloid Leukemia Cells. *Cel. Mol. Bioeng.* **2015,** *8*, 455-470.
124. Lovett, J. R.; Ratcliffe, L. P. D.; Warren, N. J.; Armes, S. P.; Smallridge, M. J.; Cracknell, R. B.; Saunders, B. R., A Robust Cross-Linking Strategy for Block Copolymer Worms Prepared via Polymerization-Induced Self-Assembly. *Macromolecules* **2016,** *49*, 2928-2941.
125. Blackman, L. D.; Varlas, S.; Arno, M. C.; Houston, Z. H.; Fletcher, N. L.; Thurecht, K. J.; Hasan, M.; Gibson, M. I.; O'Reilly, R. K., Confinement of Therapeutic Enzymes in Selectively Permeable Polymer Vesicles by Polymerization-Induced Self-Assembly (PISA) Reduces Antibody Binding and Proteolytic Susceptibility. *ACS Cent. Sci.* **2018,** *4*, 718-723.
126. Toebes, B. J.; Abdelmohsen, L. K. E. A.; Wilson, D. A., Enzyme-driven biodegradable nanomotor based on tubular-shaped polymeric vesicles. *Polym. Chem.* **2018,** *9*, 3190-3194.
127. Blanazs, A.; Madsen, J.; Battaglia, G.; Ryan, A. J.; Armes, S. P., Mechanistic Insights for Block Copolymer Morphologies: How Do Worms Form Vesicles? *J. Am. Chem. Soc.* **2011,** *133*, 16581-16587.

128. Xu, Q.; Huang, T.; Li, S.; Li, K.; Li, C.; Liu, Y.; Wang, Y.; Yu, C.; Zhou, Y., Emulsion-Assisted Polymerization-Induced Hierarchical Self-Assembly of Giant Sea Urchin-like Aggregates on a Large Scale. *Angew. Chem. Int. Ed.* **2018,** *57*, 8043-8047.
129. Zhang, Y.; Cao, M.; Han, G.; Guo, T.; Ying, T.; Zhang, W., Topology Affecting Block Copolymer Nanoassemblies: Linear Block Copolymers versus Star Block Copolymers under PISA Conditions. *Macromolecules* **2018,** *51*, 5440-5449.
130. Tan, J.; Huang, C.; Liu, D.; Li, X.; He, J.; Xu, Q.; Zhang, L., Polymerization-Induced Self-Assembly of Homopolymer and Diblock Copolymer: A Facile Approach for Preparing Polymer Nano-Objects with Higher-Order Morphologies. *ACS Macro Lett.* **2017,** *6*, 298-303.
131. Israelachvili, J. N.; Mitchell, D. J.; Ninham, B. W., Theory of self-assembly of hydrocarbon amphiphiles into micelles and bilayers. *J. Chem. Soc., Faraday Trans. 2* **1976,** *72*, 1525-1568.
132. Discher, D. E.; Ahmed, F., Polymersomes. *Annu. Rev. Biomed. Eng.* **2006,** *8*, 323-341.
133. Hayward, R. C.; Pochan, D. J., Tailored Assemblies of Block Copolymers in Solution: It Is All about the Process. *Macromolecules* **2010,** *43*, 3577-3584.
134. Nicolai, T.; Colombani, O.; Chassenieux, C., Dynamic polymeric micelles versus frozen nanoparticles formed by block copolymers. *Soft Matter* **2010,** *6*, 3111-3118.
135. Cunningham, V. J.; Alswieleh, A. M.; Thompson, K. L.; Williams, M.; Leggett, G. J.; Armes, S. P.; Musa, O. M., Poly(glycerol monomethacrylate)–Poly(benzyl methacrylate) Diblock Copolymer Nanoparticles via RAFT Emulsion Polymerization: Synthesis, Characterization, and Interfacial Activity. *Macromolecules* **2014,** *47*, 5613-5623.
136. Wright, D. B.; Patterson, J. P.; Gianneschi, N. C.; Chassenieux, C.; Colombani, O.; O'Reilly, R. K., Blending block copolymer micelles in solution; obstacles of blending. *Polym. Chem.* **2016,** *7*, 1577-1583.
137. Barnhill, S. A.; Bell, N. C.; Patterson, J. P.; Olds, D. P.; Gianneschi, N. C., Phase Diagrams of Polynorbornene Amphiphilic Block Copolymers in Solution. *Macromolecules* **2015,** *48*, 1152-1161.
138. Wang, H.; Wu, C.; Xia, G.; Ma, Z.; Mo, G.; Song, R., Semi-crystalline polymethylene-b-poly(acrylic acid) diblock copolymers: aggregation behavior, confined crystallization and controlled growth of semicrystalline micelles from dilute DMF solution. *Soft Matter* **2015,** *11*, 1778-1787.
139. Agrahari, V.; Agrahari, V., Advances and applications of block-copolymer-based nanoformulations. *Drug Discov. Today* **2018,** *23*, 1139-1151.
140. Warren, N. J.; Mykhaylyk, O. O.; Mahmood, D.; Ryan, A. J.; Armes, S. P., RAFT Aqueous Dispersion Polymerization Yields Poly(ethylene glycol)-Based Diblock Copolymer Nano-Objects with Predictable Single Phase Morphologies. *J. Am. Chem. Soc.* **2014,** *136*, 1023-1033.
141. Charleux, B.; Delaittre, G.; Rieger, J.; D'Agosto, F., Polymerization-Induced Self-Assembly: From Soluble Macromolecules to Block Copolymer Nano-Objects in One Step. *Macromolecules* **2012,** *45*, 6753-6765.
142. Canning, S. L.; Smith, G. N.; Armes, S. P., A Critical Appraisal of RAFT-Mediated Polymerization-Induced Self-Assembly. *Macromolecules* **2016,** *49*, 1985-2001.

143. Derry, M. J.; Fielding, L. A.; Armes, S. P., Polymerization-induced self-assembly of block copolymer nanoparticles via RAFT non-aqueous dispersion polymerization. *Prog. Polym. Sci.* **2016,** *52*, 1-18.
144. Foster, J. C.; Varlas, S.; Couturaud, B.; Coe, Z.; O'Reilly, R. K., Getting into Shape: Reflections on a New Generation of Cylindrical Nanostructures' Self-Assembly Using Polymer Building Blocks. *J. Am. Chem. Soc.* **2019,** *141*, 2742-2753.
145. Karagoz, B.; Esser, L.; Duong, H. T.; Basuki, J. S.; Boyer, C.; Davis, T. P., Polymerization-Induced Self-Assembly (PISA) – control over the morphology of nanoparticles for drug delivery applications. *Polym. Chem.* **2014,** *5*, 350-355.
146. Li, D.; Huo, M.; Liu, L.; Zeng, M.; Chen, X.; Wang, X.; Yuan, J., Overcoming Kinetic Trapping for Morphology Evolution during Polymerization-Induced Self-Assembly. *Macromol. Rapid Commun.* **2019,** *40*, 1900202.
147. Penfold, N. J. W.; Yeow, J.; Boyer, C.; Armes, S. P., Emerging Trends in Polymerization-Induced Self-Assembly. *ACS Macro Lett.* **2019,** *8*, 1029-1054.
148. Wang, X.; An, Z., New Insights into RAFT Dispersion Polymerization-Induced Self-Assembly: From Monomer Library, Morphological Control, and Stability to Driving Forces. *Macromol. Rapid Commun.* **2019,** *40*, 1800325.
149. Zhang, W.; D'Agosto, F.; Boyron, O.; Rieger, J.; Charleux, B., Toward a Better Understanding of the Parameters that Lead to the Formation of Nonspherical Polystyrene Particles via RAFT-Mediated One-Pot Aqueous Emulsion Polymerization. *Macromolecules* **2012,** *45*, 4075-4084.
150. Khor, S. Y.; Truong, N. P.; Quinn, J. F.; Whittaker, M. R.; Davis, T. P., Polymerization-Induced Self-Assembly: The Effect of End Group and Initiator Concentration on Morphology of Nanoparticles Prepared via RAFT Aqueous Emulsion Polymerization. *ACS Macro Lett.* **2017,** *6*, 1013-1019.
151. Tan, J.; Dai, X.; Zhang, Y.; Yu, L.; Sun, H.; Zhang, L., Photoinitiated Polymerization-Induced Self-Assembly via Visible Light-Induced RAFT-Mediated Emulsion Polymerization. *ACS Macro Lett.* **2019,** *8*, 205-212.
152. Blanazs, A.; Ryan, A. J.; Armes, S. P., Predictive Phase Diagrams for RAFT Aqueous Dispersion Polymerization: Effect of Block Copolymer Composition, Molecular Weight, and Copolymer Concentration. *Macromolecules* **2012,** *45*, 5099-5107.
153. Figg, C. A.; Carmean, R. N.; Bentz, K. C.; Mukherjee, S.; Savin, D. A.; Sumerlin, B. S., Tuning Hydrophobicity To Program Block Copolymer Assemblies from the Inside Out. *Macromolecules* **2017,** *50*, 935-943.
154. Wang, G.; Schmitt, M.; Wang, Z.; Lee, B.; Pan, X.; Fu, L.; Yan, J.; Li, S.; Xie, G.; Bockstaller, M. R.; Matyjaszewski, K., Polymerization-Induced Self-Assembly (PISA) Using ICAR ATRP at Low Catalyst Concentration. *Macromolecules* **2016,** *49*, 8605-8615.
155. Wang, G.; Wang, Z.; Lee, B.; Yuan, R.; Lu, Z.; Yan, J.; Pan, X.; Song, Y.; Bockstaller, M. R.; Matyjaszewski, K., Polymerization-induced self-assembly of acrylonitrile via ICAR ATRP. *Polymer* **2017,** *129*, 57-67.
156. Qiao, X. G.; Lansalot, M.; Bourgeat-Lami, E.; Charleux, B., Nitroxide-Mediated Polymerization-Induced Self-Assembly of Poly(poly(ethylene oxide) methyl ether methacrylate-co-styrene)-b-poly(n-butyl methacrylate-co-styrene) Amphiphilic Block Copolymers. *Macromolecules* **2013,** *46*, 4285-4295.
157. Qiao, X. G.; Dugas, P. Y.; Charleux, B.; Lansalot, M.; Bourgeat-Lami, E., Nitroxide-mediated polymerization-induced self-assembly of amphiphilic block

copolymers with a pH/temperature dual sensitive stabilizer block. *Polym. Chem.* **2017,** *8*, 4014-4029.
158. Guégain, E.; Zhu, C.; Giovanardi, E.; Nicolas, J., Radical Ring-Opening Copolymerization-Induced Self-Assembly (rROPISA). *Macromolecules* **2019,** *52*, 3612-3624.
159. D'Agosto, F.; Rieger, J.; Lansalot, M., RAFT-Mediated Polymerization-Induced Self-Assembly. *Angew. Chem. Int. Ed.* **2019**, DOI: 10.1002/anie.201911758.
160. Jiang, J.; Zhang, X.; Fan, Z.; Du, J., Ring-Opening Polymerization of N-Carboxyanhydride-Induced Self-Assembly for Fabricating Biodegradable Polymer Vesicles. *ACS Macro Lett.* **2019,** *8*, 1216-1221.
161. Grazon, C.; Salas-Ambrosio, P.; Ibarboure, E.; Buol, A.; Garanger, E.; Grinstaff, M. W.; Lecommandoux, S.; Bonduelle, C., Aqueous Ring-Opening Polymerization-Induced Self-Assembly (ROPISA) of N-Carboxyanhydrides. *Angew. Chem. Int. Ed.* **2020,** *59*, 622-626.
162. Wright, D. B.; Touve, M. A.; Thompson, M. P.; Gianneschi, N. C., Aqueous-Phase Ring-Opening Metathesis Polymerization-Induced Self-Assembly. *ACS Macro Lett.* **2018,** *7*, 401-405.
163. Jimaja, S.; Varlas, S.; Xie, Y.; Foster, J. C.; Taton, D.; Dove, A. P.; O'Reilly, R. K., Nickel-Catalyzed Coordination Polymerization-Induced Self-Assembly of Helical Poly(aryl isocyanide)s. *ACS Macro Lett.* **2020,** *9*, 226-232.
164. Foster, J. C.; Varlas, S.; Couturaud, B.; Jones, J. R.; Keogh, R.; Mathers, R. T.; O'Reilly, R. K., Predicting Monomers for Use in Polymerization-Induced Self-Assembly. *Angew. Chem. Int. Ed.* **2018,** *57*, 15733-15737.
165. Derry, M. J.; Smith, T.; O'Hora, P. S.; Armes, S. P., Block Copolymer Nanoparticles Prepared via Polymerization-Induced Self-Assembly Provide Excellent Boundary Lubrication Performance for Next-Generation Ultralow-Viscosity Automotive Engine Oils. *ACS Appl. Mater. Interfaces* **2019,** *11*, 33364-33369.
166. Thompson, K. L.; Mable, C. J.; Cockram, A.; Warren, N. J.; Cunningham, V. J.; Jones, E. R.; Verber, R.; Armes, S. P., Are block copolymer worms more effective Pickering emulsifiers than block copolymer spheres? *Soft Matter* **2014,** *10*, 8615-8626.
167. Mable, C. J.; Warren, N. J.; Thompson, K. L.; Mykhaylyk, O. O.; Armes, S. P., Framboidal ABC triblock copolymer vesicles: a new class of efficient Pickering emulsifier. *Chem. Sci.* **2015,** *6*, 6179-6188.
168. Zhang, W.-J.; Hong, C.-Y.; Pan, C.-Y., Fabrication of Reductive-Responsive Prodrug Nanoparticles with Superior Structural Stability by Polymerization-Induced Self-Assembly and Functional Nanoscopic Platform for Drug Delivery. *Biomacromolecules* **2016,** *17*, 2992-2999.
169. Zhang, W.-J.; Hong, C.-Y.; Pan, C.-Y., Artificially Smart Vesicles with Superior Structural Stability: Fabrication, Characterizations, and Transmembrane Traffic. *ACS Appl. Mater. Interfaces* **2017,** *9*, 15086-15095.
170. Zhang, W.-J.; Hong, C.-Y.; Pan, C.-Y., Polymerization-Induced Self-Assembly of Functionalized Block Copolymer Nanoparticles and Their Application in Drug Delivery. *Macromol. Rapid Commun.* **2019,** *40*, 1800279.
171. Zhang, X.; Cardozo , A. F.; Chen , S.; Zhang, W.; Julcour , C.; Lansalot, M.; Blanco , J.-F.; Gayet , F.; Delmas , H.; Charleux , B.; Manoury , E.; D'Agosto, F.; Poli , R., Core–Shell Nanoreactors for Efficient Aqueous Biphasic Catalysis. *Chem. Eur. J.* **2014,** *20*, 15505-15517.

172. Blackman, L. D.; Varlas, S.; Arno, M. C.; Fayter, A.; Gibson, M. I.; O'Reilly, R. K., Permeable Protein-Loaded Polymersome Cascade Nanoreactors by Polymerization-Induced Self-Assembly. *ACS Macro Lett.* **2017,** *6*, 1263-1267.
173. Varlas, S.; Georgiou, P. G.; Bilalis, P.; Jones, J. R.; Hadjichristidis, N.; O'Reilly, R. K., Poly(sarcosine)-Based Nano-Objects with Multi-Protease Resistance by Aqueous Photoinitiated Polymerization-Induced Self-Assembly (Photo-PISA). *Biomacromolecules* **2018,** *19*, 4453-4462.
174. Zhao, W.; Ta, H. T.; Zhang, C.; Whittaker, A. K., Polymerization-Induced Self-Assembly (PISA) - Control over the Morphology of 19F-Containing Polymeric Nano-objects for Cell Uptake and Tracking. *Biomacromolecules* **2017,** *18*, 1145-1156.
175. Mitchell, D. E.; Lovett, J. R.; Armes, S. P.; Gibson, M. I., Combining Biomimetic Block Copolymer Worms with an Ice-Inhibiting Polymer for the Solvent-Free Cryopreservation of Red Blood Cells. *Angew. Chem. Int. Ed.* **2016,** *55*, 2801-2804.
176. Cheng, G.; Pérez-Mercader, J., Polymerization-Induced Self-Assembly for Artificial Biology: Opportunities and Challenges. *Macromol. Rapid Commun.* **2019,** *40*, 1800513.
177. Warren, N. J.; Armes, S. P., Polymerization-Induced Self-Assembly of Block Copolymer Nano-objects via RAFT Aqueous Dispersion Polymerization. *J. Am. Chem. Soc.* **2014,** *136*, 10174-10185.
178. Warren, N. J.; Mykhaylyk, O. O.; Ryan, A. J.; Williams, M.; Doussineau, T.; Dugourd, P.; Antoine, R.; Portale, G.; Armes, S. P., Testing the Vesicular Morphology to Destruction: Birth and Death of Diblock Copolymer Vesicles Prepared via Polymerization-Induced Self-Assembly. *J. Am. Chem. Soc.* **2015,** *137*, 1929-1937.
179. Figg, C. A.; Simula, A.; Gebre, K. A.; Tucker, B. S.; Haddleton, D. M.; Sumerlin, B. S., Polymerization-induced thermal self-assembly (PITSA). *Chem. Sci.* **2015,** *6*, 1230-1236.
180. Tan, J.; Sun, H.; Yu, M.; Sumerlin, B. S.; Zhang, L., Photo-PISA: Shedding Light on Polymerization-Induced Self-Assembly. *ACS Macro Lett.* **2015,** *4*, 1249-1253.
181. Tan, J.; Bai, Y.; Zhang, X.; Huang, C.; Liu, D.; Zhang, L., Low-Temperature Synthesis of Thermoresponsive Diblock Copolymer Nano-Objects via Aqueous Photoinitiated Polymerization-Induced Self-Assembly (Photo-PISA) using Thermoresponsive Macro-RAFT Agents. *Macromol. Rapid Commun.* **2016,** *37*, 1434-1440.
182. Tan, J.; Liu, D.; Bai, Y.; Huang, C.; Li, X.; He, J.; Xu, Q.; Zhang, X.; Zhang, L., An insight into aqueous photoinitiated polymerization-induced self-assembly (photo-PISA) for the preparation of diblock copolymer nano-objects. *Polym. Chem.* **2017,** *8*, 1315-1327.
183. Blackman, L. D.; Doncom, K. E. B.; Gibson, M. I.; O'Reilly, R. K., Comparison of photo- and thermally initiated polymerization-induced self-assembly: a lack of end group fidelity drives the formation of higher order morphologies. *Polym. Chem.* **2017,** *8*, 2860-2871.
184. Tan, J.; Zhang, X.; Liu, D.; Bai, Y.; Huang, C.; Li, X.; Zhang, L., Facile Preparation of CO2-Responsive Polymer Nano-Objects via Aqueous Photoinitiated Polymerization-Induced Self-Assembly (Photo-PISA). *Macromol. Rapid Commun.* **2017,** *38*, 1600508.
185. Tan, J.; Liu, D.; Bai, Y.; Huang, C.; Li, X.; He, J.; Xu, Q.; Zhang, L., Enzyme-Assisted Photoinitiated Polymerization-Induced Self-Assembly: An Oxygen-Tolerant

Method for Preparing Block Copolymer Nano-Objects in Open Vessels and Multiwell Plates. *Macromolecules* **2017,** *50*, 5798-5806.
186. Tan, J.; Xu, Q.; Li, X.; He, J.; Zhang, Y.; Dai, X.; Yu, L.; Zeng, R.; Zhang, L., Enzyme-PISA: An Efficient Method for Preparing Well-Defined Polymer Nano-Objects under Mild Conditions. *Macromol. Rapid Commun.* **2018,** *39*, 1700871.
187. Ma, C.; Liu, X.; Wu, G.; Zhou, P.; Zhou, Y.; Wang, L.; Huang, X., Efficient Way to Generate Protein-Based Nanoparticles by in-Situ Photoinitiated Polymerization-Induced Self-Assembly. *ACS Macro Lett.* **2017,** *6*, 689-694.
188. Varlas, S.; Foster, J. C.; O'Reilly, R. K., Ring-opening metathesis polymerization-induced self-assembly (ROMPISA). *Chem. Commun.* **2019,** *55*, 9066-9071.
189. Zhang, L.; Song, C.; Yu, J.; Yang, D.; Xie, M., One-pot synthesis of polymeric nanoparticle by ring-opening metathesis polymerization. *J. Polym. Sci. A Polym. Chem.* **2010,** *48*, 5231-5238.
190. Liu, J.; Liao, Y.; He, X.; Yu, J.; Ding, L.; Xie, M., Facile One-Pot Approach for Preparing Functionalized Polymeric Nanoparticles via ROMP. *Macromol. Chem. Phys.* **2011,** *212*, 55-63.
191. Le, D.; Dilger, M.; Pertici, V.; Diabaté, S.; Gigmes, D.; Weiss, C.; Delaittre, G., Ultra-Fast Synthesis of Multivalent Radical Nanoparticles by Ring-Opening Metathesis Polymerization-Induced Self-Assembly. *Angew. Chem. Int. Ed.* **2019,** *58*, 4725-4731.
192. Torres-Rocha, O. L.; Wu, X.; Zhu, C.; Crudden, C. M.; Cunningham, M. F., Polymerization-Induced Self-Assembly (PISA) of 1,5-Cyclooctadiene Using Ring Opening Metathesis Polymerization. *Macromol. Rapid Commun.* **2019,** *40*, 1800326.
193. Yoon, K. Y.; Lee, I. H.; Kim, K. O.; Jang, J.; Lee, E.; Choi, T. L., One-pot in situ fabrication of stable nanocaterpillars directly from polyacetylene diblock copolymers synthesized by mild ring-opening metathesis polymerization. *J. Am. Chem. Soc.* **2012,** *134*, 14291-14294.
194. Yoon, K. Y.; Shin, S.; Kim, Y. J.; Kim, I.; Lee, E.; Choi, T. L., One-pot preparation of 3D nano- and microaggregates via in situ nanoparticlization of polyacetylene diblock copolymers produced by ROMP. *Macromol. Rapid Commun.* **2015,** *36*, 1069-1074.
195. Tanner, P.; Baumann, P.; Enea, R.; Onaca, O.; Palivan, C.; Meier, W., Polymeric Vesicles: From Drug Carriers to Nanoreactors and Artificial Organelles. *Acc. Chem. Res.* **2011,** *44*, 1039-1049.
196. Balasubramanian, V.; Herranz-Blanco, B.; Almeida, P. V.; Hirvonen, J.; Santos, H. A., Multifaceted polymersome platforms: Spanning from self-assembly to drug delivery and protocells. *Prog. Polym. Sci.* **2016,** *60*, 51-85.
197. Hu, X.; Zhang, Y.; Xie, Z.; Jing, X.; Bellotti, A.; Gu, Z., Stimuli-Responsive Polymersomes for Biomedical Applications. *Biomacromolecules* **2017,** *18*, 649-673.
198. Godoy-Gallardo, M.; York-Duran, M. J.; Hosta-Rigau, L., Recent Progress in Micro/Nanoreactors toward the Creation of Artificial Organelles. *Adv. Healthcare Mater.* **2018,** *7*, 1700917.
199. Onaca, O.; Enea, R.; Hughes, D. W.; Meier, W., Stimuli-Responsive Polymersomes as Nanocarriers for Drug and Gene Delivery. *Macromol. Biosci.* **2009,** *9*, 129-139.
200. Messager, L.; Gaitzsch, J.; Chierico, L.; Battaglia, G., Novel aspects of encapsulation and delivery using polymersomes. *Curr. Opin. Pharmacol.* **2014,** *18*, 104-111.

201. Bleul, R.; Thiermann, R.; Maskos, M., Techniques To Control Polymersome Size. *Macromolecules* **2015,** *48*, 7396-7409.
202. Wong, C. K.; Stenzel, M. H.; Thordarson, P., Non-spherical polymersomes: formation and characterization. *Chem. Soc. Rev.* **2019,** *48*, 4019-4035.
203. Yu, S.; Azzam, T.; Rouiller, I.; Eisenberg, A., "Breathing" Vesicles. *J. Am. Chem. Soc.* **2009,** *131*, 10557-10566.
204. Le Meins, J. F.; Sandre, O.; Lecommandoux, S., Recent trends in the tuning of polymersomes' membrane properties. *Eur. Phys. J. E* **2011,** *34*, 14.
205. Egli, S.; Schlaad, H.; Bruns, N.; Meier, W., Functionalization of Block Copolymer Vesicle Surfaces. *Polymers* **2011,** *3*, 252-280.
206. Thambi, T.; Park, J. H.; Lee, D. S., Stimuli-responsive polymersomes for cancer therapy. *Biomater. Sci.* **2016,** *4*, 55-69.
207. Schmitt, C.; Lippert, A. H.; Bonakdar, N.; Sandoghdar, V.; Voll, L. M., Compartmentalization and Transport in Synthetic Vesicles. *Front. Bioeng. Biotechnol.* **2016,** *4*, 19.
208. Men, Y.; Li, W.; Tu, Y.; Peng, F.; Janssen, G.-J. A.; Nolte, R. J. M.; Wilson, D. A., Nonequilibrium Reshaping of Polymersomes via Polymer Addition. *ACS Nano* **2019,** *13*, 12767-12773.
209. van Oers, M. C. M.; Rutjes, F. P. J. T.; van Hest, J. C. M., Tubular Polymersomes: A Cross-Linker-Induced Shape Transformation. *J. Am. Chem. Soc.* **2013,** *135*, 16308-16311.
210. Robertson, J. D.; Yealland, G.; Avila-Olias, M.; Chierico, L.; Bandmann, O.; Renshaw, S. A.; Battaglia, G., pH-Sensitive Tubular Polymersomes: Formation and Applications in Cellular Delivery. *ACS Nano* **2014,** *8*, 4650-4661.
211. Lv, F.; An, Z.; Wu, P., What Determines the Formation of Block Copolymer Nanotubes? *Macromolecules* **2020,** *53*, 367-373.
212. Lai, M.-H.; Jeong, J. H.; DeVolder, R. J.; Brockman, C.; Schroeder, C.; Kong, H., Ellipsoidal Polyaspartamide Polymersomes with Enhanced Cell-Targeting Ability. *Adv. Funct. Mater.* **2012,** *22*, 3239-3246.
213. L'Amoreaux, N.; Ali, A.; Iqbal, S.; Larsen, J., Persistent prolate polymersomes for enhanced co-delivery of hydrophilic and hydrophobic drugs. *Nanotechnology* **2020,** *31*, 175103.
214. Kim, K. T.; Zhu, J.; Meeuwissen, S. A.; Cornelissen, J. J. L. M.; Pochan, D. J.; Nolte, R. J. M.; van Hest, J. C. M., Polymersome Stomatocytes: Controlled Shape Transformation in Polymer Vesicles. *J. Am. Chem. Soc.* **2010,** *132*, 12522-12524.
215. Rikken, R. S. M.; Engelkamp, H.; Nolte, R. J. M.; Maan, J. C.; van Hest, J. C. M.; Wilson, D. A.; Christianen, P. C. M., Shaping polymersomes into predictable morphologies via out-of-equilibrium self-assembly. *Nat. Commun.* **2016,** *7*, 12606.
216. Shao, J.; Pijpers, I. A. B.; Cao, S.; Williams, D. S.; Yan, X.; Li, J.; Abdelmohsen, L. K. E. A.; van Hest, J. C. M., Biomorphic Engineering of Multifunctional Polylactide Stomatocytes toward Therapeutic Nano-Red Blood Cells. *Adv. Sci.* **2019,** *6*, 1801678.
217. Geng, Y.; Dalhaimer, P.; Cai, S.; Tsai, R.; Tewari, M.; Minko, T.; Discher, D. E., Shape effects of filaments versus spherical particles in flow and drug delivery. *Nat. Nanotech.* **2007,** *2*, 249-255.
218. Truong, N. P.; Quinn, J. F.; Whittaker, M. R.; Davis, T. P., Polymeric filomicelles and nanoworms: two decades of synthesis and application. *Polym. Chem.* **2016,** *7*, 4295-4312.

219. Williams, D. S.; Pijpers, I. A. B.; Ridolfo, R.; van Hest, J. C. M., Controlling the morphology of copolymeric vectors for next generation nanomedicine. *J. Control. Release* **2017,** *259*, 29-39.
220. Abdelmohsen, L. K. E. A.; Williams, D. S.; Pille, J.; Ozel, S. G.; Rikken, R. S. M.; Wilson, D. A.; van Hest, J. C. M., Formation of Well-Defined, Functional Nanotubes via Osmotically Induced Shape Transformation of Biodegradable Polymersomes. *J. Am. Chem. Soc.* **2016,** *138*, 9353-9356.
221. Wauters, A. C.; Pijpers, I. A. B.; Mason, A. F.; Williams, D. S.; Tel, J.; Abdelmohsen, L. K. E. A.; van Hest, J. C. M., Development of Morphologically Discrete PEG–PDLLA Nanotubes for Precision Nanomedicine. *Biomacromolecules* **2019,** *20*, 177-183.
222. Pijpers, I. A. B.; Meng, F.; van Hest, J. C. M.; Abdelmohsen, L. K. E. A., Investigating the self-assembly and shape transformation of poly(ethylene glycol)-b-poly(d,l-lactide) (PEG-PDLLA) polymersomes by tailoring solvent-polymer interactions. *Polym. Chem.* **2020,** *11*, 275-280.
223. Men, Y.; Li, W.; Lebleu, C.; Sun, J.; Wilson, D. A., Tailoring Polymersome Shape Using the Hofmeister Effect. *Biomacromolecules* **2020,** *21*, 89-94.
224. Chandrawati, R.; Caruso, F., Biomimetic Liposome- and Polymersome-Based Multicompartmentalized Assemblies. *Langmuir* **2012,** *28*, 13798-13807.
225. Le Meins, J. F.; Schatz, C.; Lecommandoux, S.; Sandre, O., Hybrid polymer/lipid vesicles: state of the art and future perspectives. *Mater. Today* **2013,** *16*, 397-402.
226. Che, H.; van Hest, J. C. M., Adaptive Polymersome Nanoreactors. *ChemNanoMat* **2019,** *5*, 1092-1109.
227. van Dongen, S. F. M.; Nallani, M.; Cornelissen, J. J. L. M.; Nolte, R. J. M.; van Hest, J. C. M., A Three-Enzyme Cascade Reaction through Positional Assembly of Enzymes in a Polymersome Nanoreactor. *Chem. Eur. J.* **2009,** *15*, 1107-1114.
228. Langowska, K.; Palivan, C. G.; Meier, W., Polymer nanoreactors shown to produce and release antibiotics locally. *Chem. Commun.* **2013,** *49*, 128-130.
229. Gräfe, D.; Gaitzsch, J.; Appelhans, D.; Voit, B., Cross-linked polymersomes as nanoreactors for controlled and stabilized single and cascade enzymatic reactions. *Nanoscale* **2014,** *6*, 10752-10761.
230. Spulber, M.; Najer, A.; Winkelbach, K.; Glaied, O.; Waser, M.; Pieles, U.; Meier, W.; Bruns, N., Photoreaction of a Hydroxyalkyphenone with the Membrane of Polymersomes: A Versatile Method To Generate Semipermeable Nanoreactors. *J. Am. Chem. Soc.* **2013,** *135*, 9204-9212.
231. Axthelm, F.; Casse, O.; Koppenol, W. H.; Nauser, T.; Meier, W.; Palivan, C. G., Antioxidant Nanoreactor Based on Superoxide Dismutase Encapsulated in Superoxide-Permeable Vesicles. *J. Phys. Chem. B* **2008,** *112*, 8211-8217.
232. van Dongen, S. F. M.; Verdurmen, W. P. R.; Peters, R. J. R. W.; Nolte, R. J. M.; Brock, R.; van Hest, J. C. M., Cellular Integration of an Enzyme-Loaded Polymersome Nanoreactor. *Angew. Chem. Int. Ed.* **2010,** *49*, 7213-7216.
233. Louzao, I.; van Hest, J. C. M., Permeability Effects on the Efficiency of Antioxidant Nanoreactors. *Biomacromolecules* **2013,** *14*, 2364-2372.
234. Nallani, M.; de Hoog, H.-P. M.; Cornelissen, J. J. L. M.; Palmans, A. R. A.; van Hest, J. C. M.; Nolte, R. J. M., Polymersome Nanoreactors for Enzymatic Ring-Opening Polymerization. *Biomacromolecules* **2007,** *8*, 3723-3728.

235. Peters, R. J. R. W.; Marguet, M.; Marais, S.; Fraaije, M. W.; van Hest, J. C. M.; Lecommandoux, S., Cascade Reactions in Multicompartmentalized Polymersomes. *Angew. Chem. Int. Ed.* **2014,** *53*, 146-150.
236. Nallani, M.; Andreasson-Ochsner, M.; Tan, C.-W. D.; Sinner, E.-K.; Wisantoso, Y.; Geifman-Shochat, S.; Hunziker, W., Proteopolymersomes: In vitro production of a membrane protein in polymersome membranes. *Biointerphases* **2011,** *6*, 153-157.
237. Einfalt, T.; Goers, R.; Dinu, I. A.; Najer, A.; Spulber, M.; Onaca-Fischer, O.; Palivan, C. G., Stimuli-Triggered Activity of Nanoreactors by Biomimetic Engineering Polymer Membranes. *Nano Lett.* **2015,** *15*, 7596-7603.
238. Einfalt, T.; Witzigmann, D.; Edlinger, C.; Sieber, S.; Goers, R.; Najer, A.; Spulber, M.; Onaca-Fischer, O.; Huwyler, J.; Palivan, C. G., Biomimetic artificial organelles with in vitro and in vivo activity triggered by reduction in microenvironment. *Nat. Commun.* **2018,** *9*, 1127.
239. Garni, M.; Thamboo, S.; Schoenenberger, C.-A.; Palivan, C. G., Biopores/membrane proteins in synthetic polymer membranes. *Biochim. Biophys. Acta Biomembranes* **2017,** *1859*, 619-638.
240. Dobrunz, D.; Toma, A. C.; Tanner, P.; Pfohl, T.; Palivan, C. G., Polymer Nanoreactors with Dual Functionality: Simultaneous Detoxification of Peroxynitrite and Oxygen Transport. *Langmuir* **2012,** *28*, 15889-15899.
241. Ranquin, A.; Versées, W.; Meier, W.; Steyaert, J.; Van Gelder, P., Therapeutic Nanoreactors: Combining Chemistry and Biology in a Novel Triblock Copolymer Drug Delivery System. *Nano Lett.* **2005,** *5*, 2220-2224.
242. Kumar, M.; Grzelakowski, M.; Zilles, J.; Clark, M.; Meier, W., Highly permeable polymeric membranes based on the incorporation of the functional water channel protein Aquaporin Z. *Proc. Natl. Acad. Sci. U.S.A.* **2007,** *104*, 20719-20724.
243. Graff, A.; Sauer, M.; Van Gelder, P.; Meier, W., Virus-assisted loading of polymer nanocontainer. *Proc. Natl. Acad. Sci. U.S.A.* **2002,** *99*, 5064-5068.
244. Zhang, X.; Lomora, M.; Einfalt, T.; Meier, W.; Klein, N.; Schneider, D.; Palivan, C. G., Active surfaces engineered by immobilizing protein-polymer nanoreactors for selectively detecting sugar alcohols. *Biomaterials* **2016,** *89*, 79-88.
245. Lomora, M.; Garni, M.; Itel, F.; Tanner, P.; Spulber, M.; Palivan, C. G., Polymersomes with engineered ion selective permeability as stimuli-responsive nanocompartments with preserved architecture. *Biomaterials* **2015,** *53*, 406-414.
246. Messager, L.; Burns, J. R.; Kim, J.; Cecchin, D.; Hindley, J.; Pyne, A. L. B.; Gaitzsch, J.; Battaglia, G.; Howorka, S., Biomimetic Hybrid Nanocontainers with Selective Permeability. *Angew. Chem. Int. Ed.* **2016,** *55*, 11106-11109.
247. Kim, K. T.; Cornelissen, J. J. L. M.; Nolte, R. J. M.; van Hest, J. C. M., A Polymersome Nanoreactor with Controllable Permeability Induced by Stimuli-Responsive Block Copolymers. *Adv. Mater.* **2009,** *21*, 2787-2791.
248. Gaitzsch, J.; Appelhans, D.; Wang, L.; Battaglia, G.; Voit, B., Synthetic Bio-nanoreactor: Mechanical and Chemical Control of Polymersome Membrane Permeability. *Angew. Chem. Int. Ed.* **2012,** *51*, 4448-4451.
249. Yao, C.; Wang, X.; Liu, G.; Hu, J.; Liu, S., Distinct Morphological Transitions of Photoreactive and Thermoresponsive Vesicles for Controlled Release and Nanoreactors. *Macromolecules* **2016,** *49*, 8282-8295.
250. Che, H.; Cao, S.; van Hest, J. C. M., Feedback-Induced Temporal Control of "Breathing" Polymersomes To Create Self-Adaptive Nanoreactors. *J. Am. Chem. Soc.* **2018,** *140*, 5356-5359.

251. Wang, X.; Yao, C.; Zhang, G.; Liu, S., Regulating vesicle bilayer permeability and selectivity via stimuli-triggered polymersome-to-PICsome transition. *Nat. Commun.* **2020,** *11*, 1524.

Chapter 2. Photoinitiated Polymerization-Induced Self-Assembly in the Presence of Surfactants Enables Membrane Protein Incorporation into Vesicles

2.1. Publication Details and Overview

Title: Photoinitiated Polymerization-Induced Self-Assembly in the Presence of Surfactants Enables Membrane Protein Incorporation into Vesicles

Authors: **Spyridon Varlas**,[†,§] Lewis D. Blackman,[†] Heather E. Findlay,[‖] Eamonn Reading,[‖] Paula J. Booth,[‖] Matthew I. Gibson,[†,‡] and Rachel K. O'Reilly*[,§]

Affiliations: [†]Department of Chemistry and [‡]Warwick Medical School, University of Warwick, Gibbet Hill Road, Coventry CV4 7AL, United Kingdom

[§]School of Chemistry, University of Birmingham, Edgbaston, Birmingham B15 2TT, United Kingdom

[‖]Department of Chemistry, King's College London, Britannia House, 7 Trinity Street, London SE1 1DB, United Kingdom

Journal: Macromolecules

Year: 2018

Volume: 51

Page Numbers: 6190-6201

DOI: 10.1021/acs.macromol.8b00994

Submitted: 9th May 2018, **Published:** 6th August 2018

Coauthor Contributions: Dry-state TEM imaging of PISA nano-objects in the presence of various surfactants was performed with assistance from Dr. Lewis D. Blackman. OmpF porin purification and characterization by SDS-PAGE and protease resistance assay were performed by Dr. Heather E. Findlay at King's College London. Native mass spectroscopic analysis of purified OmpF porin was performed by Dr. Eamonn Reading at King's College London. Cryo-TEM imaging of block copolymer nano-objects was performed with assistance from Dr. Lewis D. Blackman, Dr. Robert Keogh and Dr. Saskia Bakker at the University of Warwick. Circular dichroism measurements were carried out with assistance from Dr. Muhammad Hasan at the University of Warwick. The design and construction of the photoreactor used for the photoinitiated polymerizations was carried out by Mr. Rod Wesson at the University of Warwick. Prof. Paula J. Booth (King's College London) and Prof. Matthew I. Gibson (University of Warwick) provided guidance and editing of this manuscript. Prof. Rachel K. O'Reilly (University of Birmingham) supervised the research project, provided guidance and editing of this manuscript.

Overview: The main objective of this Chapter was to investigate the extent of interaction between an amphiphilic block copolymer formulation and a series of commonly utilized small molecule surfactants of varying nature (i.e., non-ionic, ionic and zwitterionic) in order to provide a guide for future studies on mixed polymer/surfactant systems with industrial or biotechnological scope. Contrary to previous literature reports on systems whereby surfactants are typically introduced into pre-synthesized/assembled block copolymer nanostructures leading to disruption of the assemblies due to solubilization of the polymer chains by the surfactant micelles, in this study polymerization and self-assembly were carried out simultaneously in the presence of different surfactants to allow for polymer/surfactant co-assembly and formation of equilibrium structures.

On the basis of previous studies from our group, aqueous RAFT-mediated photo-PISA was used as a direct and mild methodology for the synthesis of PEG-*b*-PHPMA diblock copolymer nano-objects in the presence of various surfactants, whilst targeting the formation of spherical, unilamellar vesicles as the final morphology (DP_{PHPMA} = 400, [solids] = 11 wt%). In particular, photo-PISA was employed in order to exclude variations in the behavior of each surfactant at high reaction temperatures and further associate these findings with the directed one-pot incorporation of temperature-sensitive and hydrophobic biomacromolecules (e.g., membrane proteins), that require surfactants for their stabilization in aqueous media, within the membrane of the prepared assemblies.

Of all surfactants investigated, only the non-ionic and low-CMC zwitterionic ones presented minimal interactions with the developed block copolymer amphiphiles and were found to promote the formation of polymersomes similar to those obtained in pure water, whereas surfactants of ionic character (including high-CMC zwitterionic

surfactants) were found to drastically affect the final nano-object morphology toward the development of lower-order structures. Moreover, it was possible to regulate the size and membrane thickness of the prepared polymersomes upon appropriately varying the type and concentration of each surfactant utilized.

As a practical demonstration of this study, a non-ionic surfactant was used for stabilization of a model channel-forming membrane protein, OmpF, and photo-PISA was subsequently carried out under the same conditions in an aqueous solution containing the hydrophilic enzyme HRP and surfactant-solubilized OmpF in an attempt to *in situ* construct OmpF-decorated polymersome nanoreactors with enhanced membrane permeability toward reactants and catalysis products. Building upon existing PISA studies primarily focused on encapsulation of hydrophilic enzymes within polymersomes, the results presented in Chapter 2 are expected to pave the way for the facile and reproducible development of biomembrane-mimicking polymersomes decorated with hydrophobic (macro)molecules, that would exhibit higher complexity, specificity and functionality.

Macromolecules

Article

Cite This: Macromolecules 2018, 51, 6190−6201

pubs.acs.org/Macromolecules

Photoinitiated Polymerization-Induced Self-Assembly in the Presence of Surfactants Enables Membrane Protein Incorporation into Vesicles

Spyridon Varlas,[†,§] Lewis D. Blackman,[†] Heather E. Findlay,[∥] Eamonn Reading,[∥] Paula J. Booth,[∥] Matthew I. Gibson,[†,‡] and Rachel K. O'Reilly*[,§]

[†]Department of Chemistry and [‡]Warwick Medical School, University of Warwick, Gibbet Hill Road, CV4 7AL Coventry, U.K.
[§]School of Chemistry, University of Birmingham, B15 2TT Birmingham, U.K.
[∥]Department of Chemistry, King's College London, Britannia House, 7 Trinity Street, SE1 1DB London, U.K.

Supporting Information

ABSTRACT: Photoinitiated polymerization-induced self-assembly (photo-PISA) is an efficient approach to predictably prepare polymeric nanostructures with a wide range of morphologies. Given that this process can be performed at high concentrations and under mild reaction conditions, it has the potential to have significant industrial scope. However, given that the majority of industrial (and more specifically biotechnological) formulations contain mixtures of polymers and surfactants, the effect of such surfactants on the PISA process is an important consideration. Thus, to expand the scope of the methodology, the effect of small molecule surfactants on the PISA process, specifically for the preparation of unilamellar vesicles, was investigated. Similar to aqueous photo-PISA findings in the absence of surfactant molecules, the originally targeted vesicular morphology was retained in the presence of varying concentrations of non-ionic surfactants, while a diverse set of lower-order morphologies was observed for ionic surfactants. Interestingly, a critical micelle concentration (CMC)-dependent behavior was detected in the case of zwitterionic detergents. Additionally, tunable size and membrane thickness of vesicles were observed by using different types and concentration of surfactants. Based on these findings, a functional channel-forming membrane protein (OmpF porin), stabilized in aqueous media by surfactant molecules, was able to be directly inserted into the membrane of vesicles during photo-PISA. Our study demonstrates the potential of photo-PISA for the direct formation of protein−polymer complexes and highlights how this method could be used to design biomimicking polymer/surfactant nanoreactors.

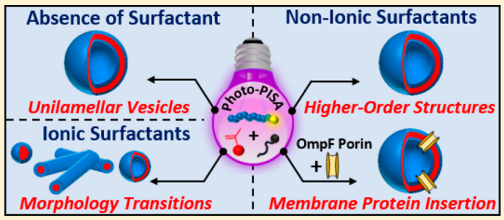

INTRODUCTION

Small molecule surfactants, also known as surface-active agents, have been extensively utilized as wetting agents, emulsifiers, plasticizers, etc., in cleaning, food, oil, and textile industry.[1,2] Self-assembled amphiphilic polymer aggregates (macromolecular counterparts of surfactants) have also accumulated significant interest as they exhibit greater stability compared to surfactant assemblies due to their superior mechanical and physical properties.[3,4] Today, mixed polymer−surfactant formulations that coassemble at a certain critical aggregation concentration are also used in various household, personal care, and other industrial and biotechnological applications.[5,6] Hence, the need to understand the effect of small molecule surfactants on polymeric assemblies and the interaction of such complex systems is increasingly required.

In an early report by Wesley et al., the interaction of anionic surfactant sodium dodecyl sulfate (SDS) with poly(2-(dimethylamino)ethyl methacrylate) (PDMAEMA) homopolymer chains was investigated.[7] Small-angle neutron scattering revealed that the presence of polymer induced the micellization of the surfactant at concentrations below its CMC value, an observation also shown in a different study by Diamant and Andelman.[8] Pata et al. investigated the effect of non-ionic surfactant Triton X-100 on poly(ethylene oxide)-*b*-poly(ethyl ethylene) and poly(ethylene oxide)-*b*-poly(butadiene) diblock copolymer vesicles.[9] Higher resistance to membrane dissolution was achieved upon increasing the bilayer thickness of such vesicles. Armes and co-workers prepared epoxy-functional diblock copolymer vesicles by aqueous RAFT dispersion polymerization.[10] Cross-linking of the membrane of the vesicles was achieved, and the stability of vesicles toward externally added amounts of small molecule surfactants of different nature (i.e., ionic and neutral) was then studied. The non-cross-linked vesicles could tolerate the presence of non-ionic surfactants, while they were easily disrupted upon exposure to ionic species (surfactant-induced dissociation). On the contrary, the cross-linked vesicles remained stable in the presence of both non-ionic and ionic surfactants. More recently, Atanase et al. studied the micellization behavior of poly(butadiene)-*b*-poly(2-vinylpyridine)-*b*-poly(ethylene

Received: May 9, 2018
Revised: July 7, 2018
Published: August 6, 2018

DOI: 10.1021/acs.macromol.8b00994
Macromolecules 2018, 51, 6190−6201

oxide) (PB-*b*-P2VP-*b*-PEO) triblock copolymers as a function of pH and SDS concentration.[11] SDS addition led to a noticeable decrease of particles' size, indicating the development of strong hydrophobic interactions between SDS and P2VP and the formation of surfactant−polymer complexes. Importantly, phospholipid/block copolymer hybrid vesicles (lipo-polymersomes) have been also studied in depth because of their similarity, in terms of thickness and hydrophobicity, to cell membranes and their advantages of combining the best features of both species.[12−15]

Over recent years, polymerization-induced self-assembly (PISA) has become a widely utilized and efficient synthetic methodology to produce block copolymer nano-objects of controlled size, morphology, and tunable properties.[16,17] Owing to the fact that traditional block copolymer self-assembly methods are mostly conducted at low polymer concentrations (≤1% w/w) and in almost all cases require further postpolymerization processing, which makes it difficult to implement on a large scale, PISA has become an alternative one-pot route to reproducibly prepare nano-objects at high concentrations (10−50% w/w).[18,19] Controlled radical polymerization techniques such as nitroxide-mediated polymerization (NMP),[20] atom-transfer radical polymerization (ATRP),[21] and reversible addition−fragmentation chain-transfer (RAFT) polymerization[22−25] have been mainly applied in this process, although RAFT polymerization is still the most popular method owing to its high versatility and broad applicability. Typically, in RAFT-mediated dispersion PISA, a solvophilic macromolecular chain transfer agent (macro-CTA) is chain-extended using miscible monomers such that the growing second block gradually becomes insoluble, which drives *in situ* self-assembly to form amphiphilic diblock copolymers. These generate a set of higher-order polymeric nanostructures with morphologies that evolve by varying the degree of polymerization (DP) and solids concentration.[26]

Nevertheless, research toward bio-related or stimuli-responsive nanomaterials produced by aqueous PISA is currently limited. This is mainly attributed to the elevated reaction temperatures required for most thermally initiated aqueous PISA formulations that can lead to denaturation of delicate biomolecules such as proteins, enzymes, or antibodies.[27] Recently, an increasing number of studies based on aqueous visible-light-initiated PISA (photo-PISA) at ambient temperatures have been reported, showing great promise in the design and preparation of novel materials of particular biotechnological and biomedical interest.[28−34]

The design of facile and mild routes for the preparation of well-defined single-phase vesicles by photo-PISA is of great interest as it allows for the development of cargo-loaded nanocarriers in a single step, which is especially important for the encapsulation of delicate biomolecules. To date, several studies on the encapsulation of hydrophilic proteins and enzymes inside polymeric vesicles via one-pot aqueous photo-PISA under mild reaction conditions (i.e., low temperature, visible light, and aqueous media) have been reported.[27,28,35−38] On the contrary, conventional methods[39,40] used for the insertion of hydrophobic and/or amphiphilic (macro)-molecules (e.g., drugs, enzymes, receptors, and membrane proteins) into vesicles are not often appropriate for delicate and very hydrophobic biomolecules. Indeed, for very hydrophobic biomolecules (e.g., membrane proteins), such uptake into vesicles cannot be achieved without the presence of solubilizing agents such as surfactants.[41−44] The incorporation of membrane proteins (specifically channel proteins, such as OmpF) into vesicles has been pioneered by Meier, Palivan, and co-workers, who have demonstrated such nanoconstructs as synthetic cell mimics (organelles).[40,45,46] To further broaden the scope of the synthesis of such membrane protein−vesicle complexes, we were interested in exploring photo-PISA to allow for uptake into the hydrophobic domain formed during polymerization (given its mild, tolerant, and scalable conditions).

To achieve this, we first explored the interaction and effect of small molecule surfactants of different critical micelle concentration (CMC) values and nature (i.e., neutral, ionic, and zwitterionic), commonly used in various biotechnological applications, on the self-assembly process of a poly(ethylene glycol)-*b*-poly(2-hydroxypropyl methacrylate) (PEG-*b*-PHPMA) block copolymer system developed by aqueous photo-PISA, while always targeting unilamellar vesicles (ULVs) as the desired final morphology. We were able to demonstrate that mixed block copolymer/surfactant vesicles with tunable size and membrane thickness could be obtained upon appropriate usage of different types and concentrations of surfactants. On the basis of these findings, we then moved toward using these conditions for incorporation of the pore-forming outer membrane protein F (OmpF), which is insoluble in water, requires the addition of surfactants for solubilization, and hence is challenging to incorporate directly into polymeric self-assemblies. This was achieved by conducting photo-PISA in the presence of OmpF, which was first stabilized by a non-ionic surfactant to allow for direct reconstitution into the membrane of the vesicles, as demonstrated by their enhanced permeability. We propose that this demonstration highlights the potential application of photo-PISA methodology, in the presence of surfactants, for insertion of challenging hydrophobes and hence could contribute significantly to the further development of biomembrane-mimicking nanoreactors.

RESULTS AND DISCUSSION

Based on findings from other related literature reports by Armes',[47] and Zhang's groups,[28] and more recently by our group[24,36] for similar PISA systems, a poly(ethylene glycol) macro-chain-transfer agent with same molecular weight (5.0×10^3 g mol^{-1}, DP = 113) as the one used in these studies was first synthesized. This was achieved through esterification of an acid functionalized chain-transfer agent (CEPA CTA) with a poly(ethylene glycol) monomethyl ether homopolymer (PEG_{113}-OH) by DCC coupling chemistry (esterification efficiency = 93%; see the Supporting Information for experimental details).

This water-soluble macro-CTA was then chain-extended under dispersion polymerization conditions using a water-miscible monomer, 2-hydroxypropyl methacrylate (HPMA), as the core-forming block. It should be noted that the monomer was a mixture of two isomers: 2-hydroxypropyl methacrylate (major, 75 mol %) and 2-hydroxyisopropyl methacrylate (minor, 25 mol %). Aqueous RAFT-mediated photo-PISA of HPMA occurred upon 405 nm visible-light irradiation of the solution at 37 °C under a N_2 atmosphere for the synthesis of PEG-*b*-PHPMA nano-objects (Scheme S1), and complete monomer conversion (>99%) was achieved after 2 h of reaction, as determined by ^{1}H NMR spectroscopy (Figure S1). It should be mentioned that the polymerization process was

DOI: 10.1021/acs.macromol.8b00994
Macromolecules 2018, 51, 6190−6201

Scheme 1. (A) Schematic Illustration Showing the Obtained PEG_{113}-*b*-$PHPMA_{400}$ Nano-Object Morphologies after Photo-PISA in Deionized Water and in Different Type Surfactant Solutions at Concentrations Equal to or Higher than the Critical Micelle Concentration (CMC) of Each Surfactant; (B) Summary of Chemical Structures and Main Characteristics of the Surfactants Used in the Present Study (CMC Values in Water As Reported in the Literature)

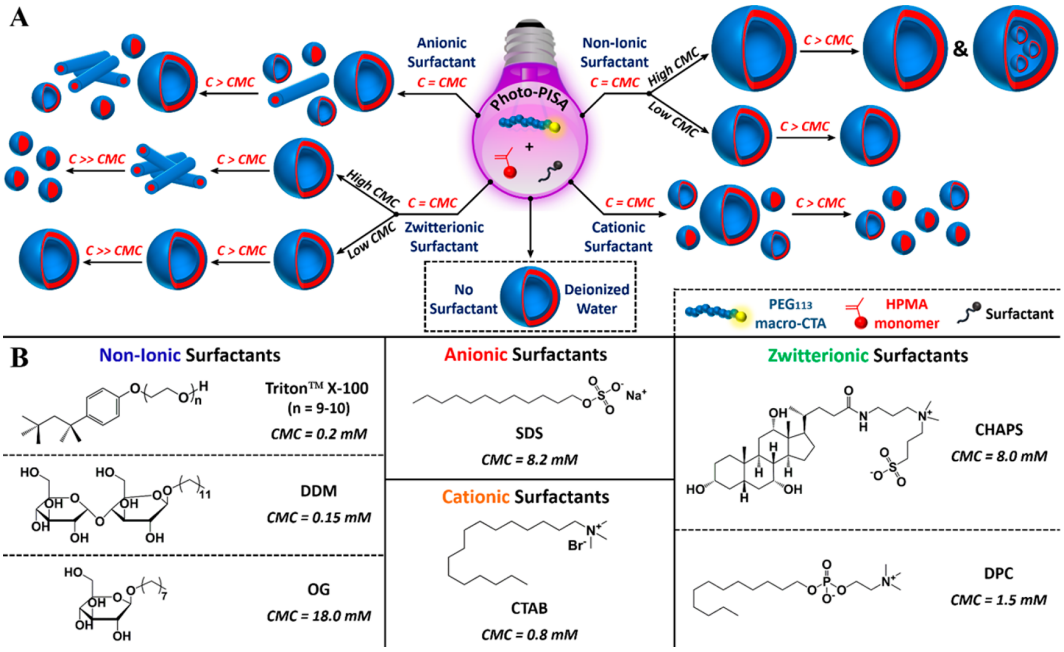

promoted in the absence of an initiator or catalyst, following the well-documented "photoiniferter" mechanism.[48]

Based on the morphologies diagram for photo-PISA of PEG_{113}-*b*-$PHPMA_x$ in deionized (DI) water recently reported by our group,[24] well-defined unilamellar vesicles (ULVs) were formed when targeting DP_{PHPMA} = 400 at 10 wt % HPMA (11 wt % solids content) (Scheme 1A). SEC analysis in DMF of a lyophilized PEG_{113}-*b*-$PHPMA_{400}$ sample confirmed the successful chain extension of HPMA and revealed the controlled character of the photo-PISA process as indicated by the relatively narrow molecular weight distribution determined ($M_{n,SEC\ RI}$ = 80.1 × 10^3 g mol^{-1}, $Đ_{M\ RI}$ = 1.25) (Table S1).

Dry-state stained TEM imaging revealed the successful formation of ULVs of uniform size, while DLS analysis also confirmed a unimodal particle size distribution with hydrodynamic diameter (D_h) in the range 350−400 nm (Figure S2). The shape, size, and unilamellar character of the developed PEG_{113}-*b*-$PHPMA_{400}$ vesicles in solution were confirmed by cryo-TEM imaging, while their average membrane thickness was also determined as 26.8 ± 3.4 nm (Figure S3). These findings were in good agreement with our previously reported characterization results for the same system, suggesting the facile reproducibility of the photo-PISA process.[24,36] Zeta potential measurements of the prepared vesicles after purification in DI water showed a negative value of −30.5 ± 0.4 mV, mainly attributed to the free −OH groups of the relatively hydrated PHPMA membrane that are not entirely screened by the PEG 5 kDa chains.[49−51] It is also important to mention that the purification process of the particles by centrifugation/resuspension cycles in DI water did not significantly affect any of their characteristics (i.e., shape, size, and zeta potential).

The key aim of this research was to evaluate the impact of small molecule surfactants (detergents) used in various industrial and biotechnological applications, such as solubilizing agents of hydrophobic membrane proteins, on the formulations obtained by photo-PISA. Aqueous photo-PISA reactions for the development of PEG_{113}-*b*-$PHPMA_{400}$ nano-objects were performed in the presence of various surfactants (non-ionic, anionic, cationic, and zwitterionic) with differing CMC values, under the same polymerization conditions described above (Scheme 1). A low-CMC non-ionic surfactant with a hydrophilic oligo(ethylene glycol) head, Triton X-100 (n = 9−10), and two non-ionic pyranoside surfactants, *n*-dodecyl β-D-maltoside (DDM, low CMC) and octyl β-D-glucopyranoside (OG, high CMC), were first studied. Additionally, a model anionic surfactant, sodium dodecyl sulfate (SDS), and a cationic surfactant, cetyltrimethylammonium bromide (CTAB), were also investigated. Notably, the effect of two zwitterionic surfactants, 3-[(3-cholamidopropyl)dimethylammonio]-1-propanesulfonate (CHAPS, high CMC) and *n*-dodecylphosphocholine (DPC, low CMC), on photo-PISA nano-object morphologies was finally assessed. It is worth mentioning that the presence of 10 wt % HPMA in PISA solutions did not significantly alter the CMC value of surfactants, as determined by surface tension analysis (Figure S4). The developed polymer−surfactant hybrid formulations could potentially be utilized for *in situ* incorporation of unstable in aqueous media functional (macro)molecules, such as receptors, peptides, enzymes, membrane proteins, and DNA, and fabrication of biomimetic nanoreactors. The observed PEG_{113}-*b*-$PHPMA_{400}$ diblock copolymer/surfactant morphologies formed by aqueous photo-PISA are schematically summarized in Scheme 1A, while the chemical structures along with the main characteristics of the surfactants used in this study are shown in Scheme 1B.

DOI: 10.1021/acs.macromol.8b00994
Macromolecules 2018, 51, 6190−6201

In all cases, photo-PISA reactions were carried out at three different concentrations of each individual surfactant (i.e., at concentrations equal to each detergent's CMC and also at 10 times lower and 10 times higher concentration levels) for the synthesis of nano-objects for the same block copolymer. Moreover, in cases of non-ionic surfactants Triton X-100 and DDM and zwitterionic CHAPS and DPC additional surfactant concentrations were also investigated due to the wide use of these particular surfactants in numerous biotechnologically relevant applications. Purification of samples was achieved by consecutive centrifugation/resuspension cycles in DI water for the removal of unreacted monomer and excess of non-incorporated surfactant molecules. ^{1}H NMR spectroscopy was used for determination of surfactant incorporation in purified OG and CHAPS samples at 10 × CMC (high-CMC surfactants with visible peaks) (Figure S5). For OG, a surfactant incorporation of 6% was calculated, while a higher surfactant incorporation of 14.5% was calculated in the case of CHAPS.

Molecular Characteristics of Polymer–Surfactant Photo-PISA Formulations. The final monomer conversion after photo-PISA in different surfactant solutions for the synthesis of PEG_{113}-*b*-$PHPMA_{400}$ nano-objects was first determined by ^{1}H NMR spectroscopy. It was found that the reaction times of photo-PISA processes were not significantly affected by the presence of surfactants in the system, with almost quantitative monomer conversions (≥96%) achieved after 2 h of irradiation time in almost all cases (Table S2). The only exception was noticed at [CHAPS] = 160.0 mM (= 20 × CMC), where monomer conversion of 70% was calculated (polymerization repeated in duplicate). This rate retardation could be explained by the inability of monomer to reach the gradually growing copolymer chains due to their high solubilization inside the core of the surfactant micelles at high CHAPS concentration. Repeating the polymerization procedure in the same CHAPS solution for 18 h resulted in >99% conversion. SEC analyses in DMF of purified and lyophilized PEG_{113}-*b*-$PHPMA_{400}$ samples at surfactant concentrations (C_{surf}) equal to CMC proved the relatively controlled character of polymerization in each case (Figure 1). In particular, a minimal M_n increase was observed in almost every polymer/surfactant sample as compared to PEG_{113}-*b*-$PHPMA_{400}$ diblock copolymers formed in DI water, accompanied by a minor $Đ_M$ increase from 1.25 (DI water) to 1.29–1.33 (surfactant solutions). Notably, no major M_n and $Đ_M$ differences were detected between diblock copolymer samples in surfactant species of different nature. SEC eluograms of selected diblock copolymer samples prepared at C_{surf} > CMC revealed that a 10-fold surfactant concentration increase did not result in a further increase of molecular weight and $Đ_M$ values (Figure S6). These findings indicate that the presence of surfactants during photo-PISA did not markedly affect the molecular characteristics of the developed PEG_{113}-*b*-$PHPMA_{400}$ diblock copolymers and reveal the high tolerance of dispersion polymerization process toward different types of surfactants.

On the basis of the SEC results, it can be assumed that all nano-objects' size variations and morphology transitions observed are attributed to the nature and CMC value (i.e., amount) of the surfactant used in each case and not to loss of polymerization control during photo-PISA in different surfactant solutions. Exhaustive DLS analysis of the received PEG_{113}-*b*-$PHPMA_{400}$ photo-PISA formulations before and after purification process was performed to monitor the hydrodynamic diameter (D_h) and polydispersity (PD) changes upon increasing concentration of surfactants. Dry-state stained TEM imaging was used for the observation of the prepared

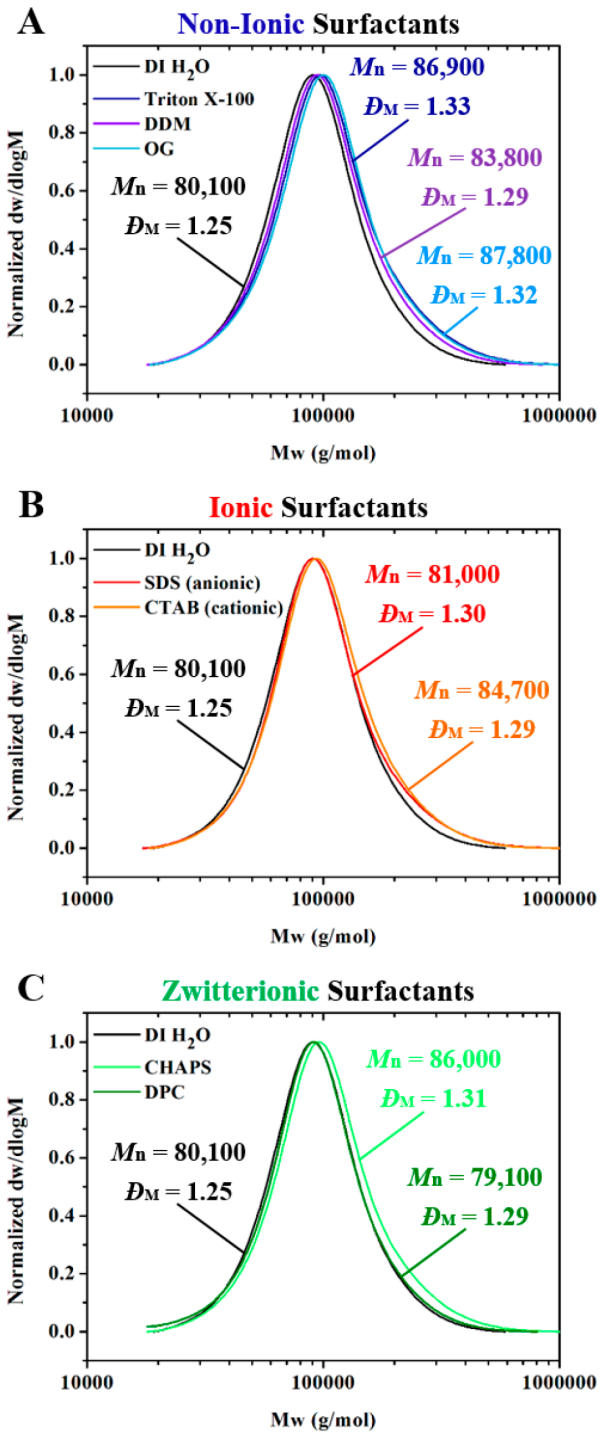

Figure 1. SEC RI molecular weight distributions for PEG_{113}-*b*-$PHPMA_{400}$ diblock copolymers synthesized in the presence of (A) non-ionic, (B) ionic, and (C) zwitterionic surfactants at C_{surf} = CMC in each case along with their corresponding M_n (g mol^{-1}) and $Đ_M$ values calculated from PMMA standards, using 5 mM NH_4BF_4 in DMF as the eluent.

DOI: 10.1021/acs.macromol.8b00994
Macromolecules 2018, 51, 6190–6201

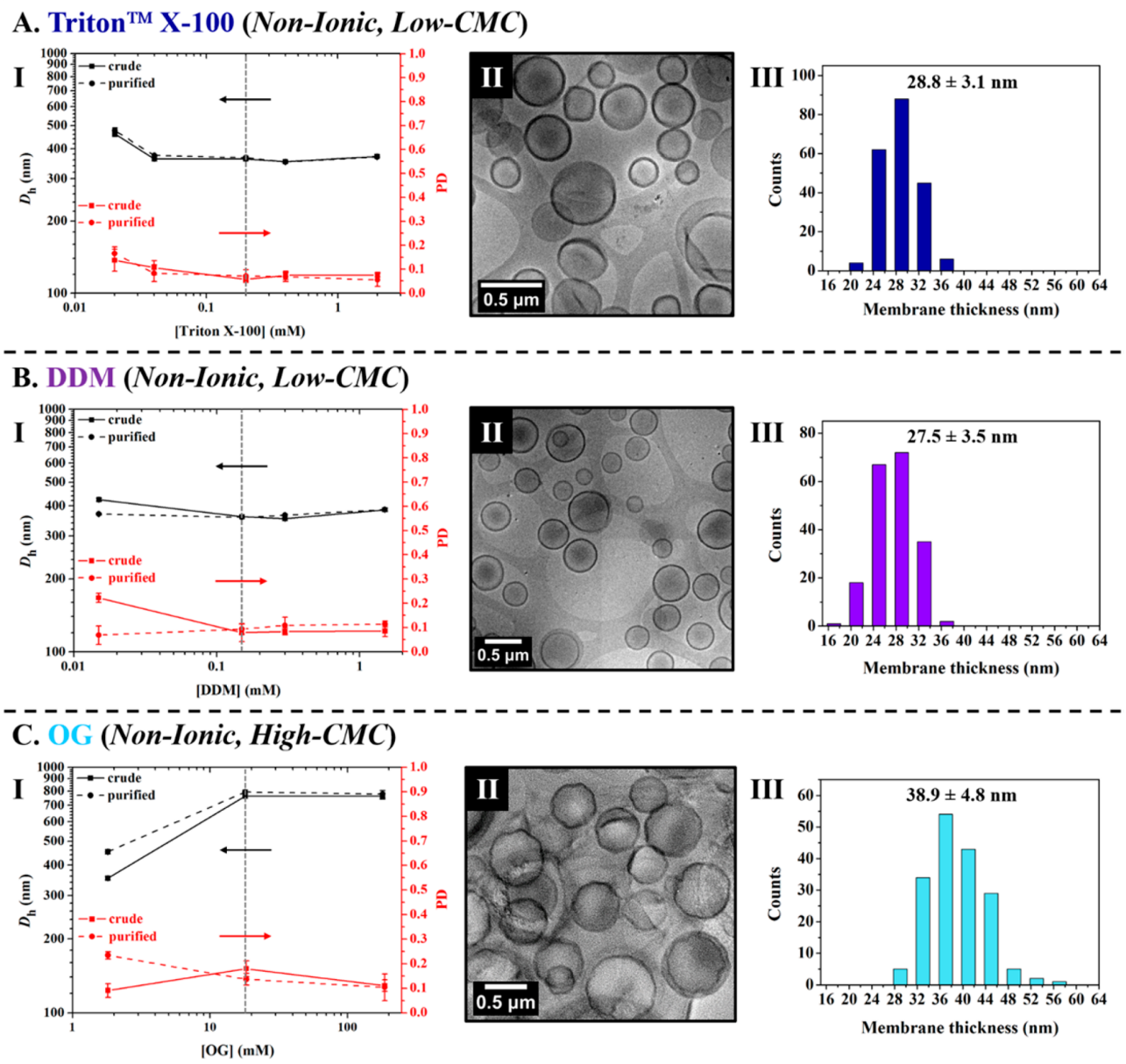

Figure 2. Summary of DLS and cryo-TEM analyses results for PEG_{113}-*b*-$PHPMA_{400}$ diblock copolymer nano-objects developed by aqueous photo-PISA in the presence of non-ionic surfactants Triton X-100 (A), DDM (B), and OG (C). For each individual surfactant: (I) DLS of crude and purified formulations for the monitoring of D_h and PD changes upon increasing surfactant concentration (the error shows the standard deviation from five repeat measurements, while the vertical dashed line indicates the CMC value of each detergent). (II) Representative cryo-TEM images of purified PEG_{113}-*b*-$PHPMA_{400}$ nano-objects formed at C_{surf} = CMC. (III) Distribution of vesicles' membrane thicknesses measured from statistical analysis and calculated average membrane thickness (the error shows the standard deviation from at least 150 particle membranes).

polymer−surfactant nano-object morphologies in each case, while the received purified hybrid nano-objects in solution, formed by photo-PISA at C_{surf} = CMC, were also characterized by cryogenic transmission electron microscopy (cryo-TEM). Additionally, in the case of vesicles, the average membrane thickness was calculated from statistical analysis by measuring at least 150 particle membranes in each sample.

Photo-PISA Nano-Objects Developed in the Presence of Non-Ionic Surfactants. In the case of non-ionic and low-CMC surfactant Triton X-100, it is evident that D_h and PD values were found to be similar to those of original PEG_{113}-*b*-$PHPMA_{400}$ vesicles in DI water, remaining constant for a wide range of surfactant concentrations (Figure 2A-I). Near-identical behavior was noticed for DDM, which is also another low-CMC non-ionic detergent with almost equal CMC value to Triton X-100 (Figure 2B-I). It should also be noted that in these cases the purification process did not affect the D_h or PD values, showing that the nanostructures remain intact after centrifugation/resuspension in DI water. From dry-state TEM imaging, it was observed that spherical unilamellar vesicles (ULVs) of uniform size (350−400 nm) were developed in both cases, analogous to those formed in DI water (Figures S7−S10). Results from cryo-TEM analysis were in good agreement with those received from other characterization

DOI: 10.1021/acs.macromol.8b00994
Macromolecules 2018, 51, 6190−6201

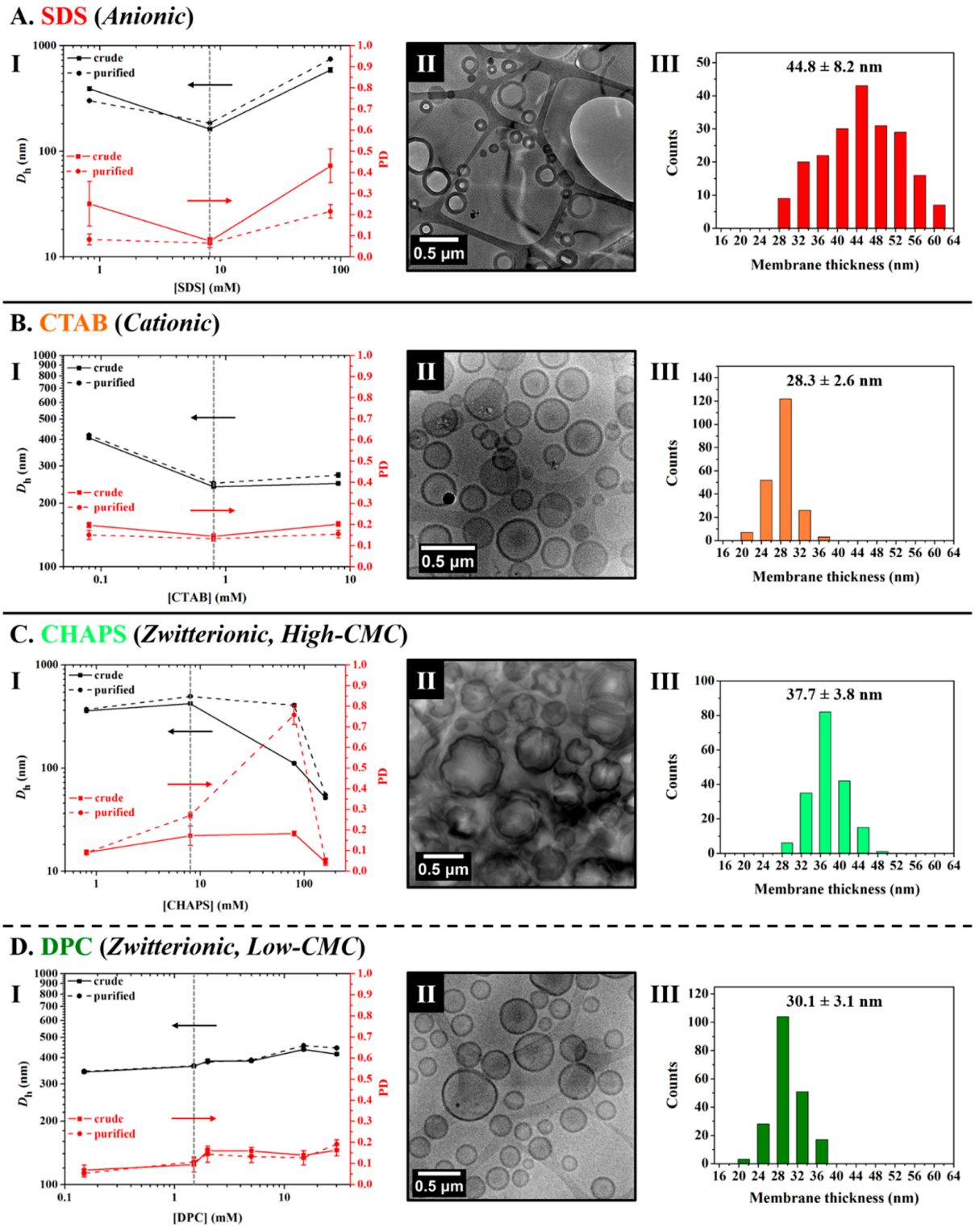

Figure 3. Summary of DLS and cryo-TEM analyses results for PEG_{113}-*b*-$PHPMA_{400}$ diblock copolymer nano-objects prepared by aqueous photo-PISA in the presence of ionic surfactants SDS (anionic) (A) and CTAB (cationic) (B) and zwitterionic surfactants CHAPS (C) and DPC (D). For each individual surfactant: (I) DLS of crude and purified formulations for the monitoring of D_h and PD changes upon increasing surfactant concentration (the error shows the standard deviation from five repeat measurements, while the vertical dashed line indicates the CMC value of each detergent). (II) Representative cryo-TEM images of purified PEG_{113}-*b*-$PHPMA_{400}$ nano-objects formed at C_{surf} = CMC. (III) Distribution of vesicles' membrane thicknesses measured from statistical analysis and calculated average membrane thickness (the error shows the standard deviation from at least 150 particle membranes).

DOI: 10.1021/acs.macromol.8b00994
Macromolecules 2018, 51, 6190−6201

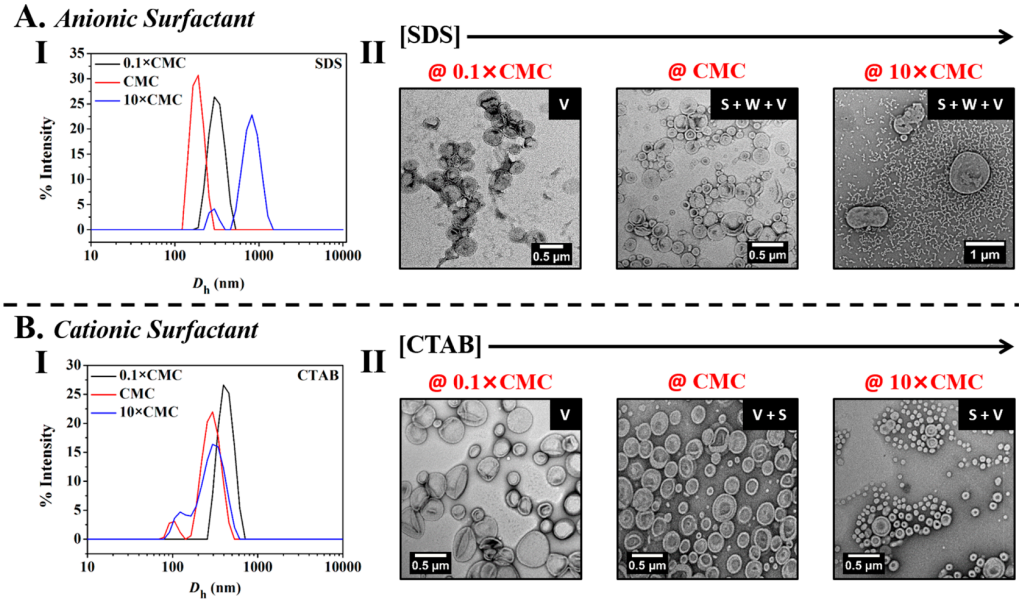

Figure 4. DLS analyses and dry-state TEM imaging results for PEG_{113}-*b*-$PHPMA_{400}$ diblock copolymer nano-objects developed by photo-PISA in aqueous solutions of anionic surfactant SDS (A) and cationic surfactant CTAB (B), upon gradually increasing C_{surf}. For each individual surfactant: (I) Intensity-weighted size distributions of purified PEG_{113}-*b*-$PHPMA_{400}$ nano-objects developed in detergent solutions of different concentrations, as determined by DLS. (II) Representative dry-state TEM micrographs of purified PEG_{113}-*b*-$PHPMA_{400}$ nano-objects formed in the presence of ionic surfactants, stained with 1 wt % UA, revealing a transition from vesicles (V) to mixed morphologies (S + W + V) upon increasing [SDS] and a direct vesicle-to-sphere morphology transition upon increasing [CTAB].

methods. It is apparent that ULVs of comparable size and membrane thickness to PEG_{113}-*b*-$PHPMA_{400}$ vesicles in DI water were formed in cases of non-ionic Triton X-100 and DDM at C_{surf} = CMC (Figures 2A-II, 2A-III, 2B-II, and 2B-III). As a matter of fact, membranes were found to be slightly thicker in both samples (average membrane thickness = 27−29 nm) compared to those in DI water, suggesting the limited insertion of surfactant molecules in the particles' hydrophobic bilayer leading to a negligible increase of average membrane thickness. On the contrary, in the case of high-CMC non-ionic surfactant OG, a significant particles' size increase from 350 to 760 nm was noticed at surfactant concentrations equal to or 10 times higher than its CMC value. In this case, the measured PD values were also found to be higher than those in the other non-ionic surfactants, ranging from 0.1 to 0.2, indicating the formation of particles with broader size distribution (Figure 2C-I). Dry-state TEM imaging at [OG] = 18.0 mM (= CMC) confirmed the formation of giant unilamellar vesicles (GULVs) of varying sizes, while TEM images at [OG] = 180.0 mM (= 10 × CMC) revealed the coexistence of GULVs along with a population of large multilamellar vesicles (MLVs) (Figures S11 and S12). As determined by cryo-TEM imaging, exceptionally large ULVs with rough outline, significantly thicker membranes (average membrane thickness ≈40 nm), and broad bilayer thickness distribution were formed in the case of exceedingly high-CMC OG at C_{surf} = CMC (Figures 2C-II and 2C-III). These findings suggest that the higher surfactant weight fraction required for the preparation of OG solutions leads to the formation of larger hybrid polymer−surfactant vesicular structures due to stronger interaction between OG molecules and vesicle membranes that aids chain mobility and exchange, thereby allowing larger vesicles to form. However, the significantly lower relative amount of surfactant needed for the preparation of Triton X-100 and DDM solutions is not able to strongly affect the size or the interfacial curvature of PEG_{113}-*b*-$PHPMA_{400}$ vesicles. The evidently high tolerance of photo-PISA toward non-ionic surfactant species is also in agreement with relevant literature reports on polymer/surfactant assemblies, supporting that there is no or limited interaction between non-ionic small molecule surfactants and neutral polymer structures.[8,10]

Photo-PISA Nano-Objects Developed in the Presence of Ionic Surfactants. In the case of commonly used high-CMC anionic surfactant SDS, DLS measurements showed significant size and PD differences and coexistence of mixed populations for the developed nano-objects upon increasing detergent concentration (Figures 3A-I and 4A-I). The corresponding hydrodynamic diameter of particles was similar to that of vesicles in DI water only at [SDS] = 0.82 mM (= 0.1 × CMC), while the observed variations of D_h and PD values at [SDS] ≥ CMC indicate strong surfactant interaction with the copolymer chains and the occurrence of morphological transitions. In particular, dry-state TEM imaging verified the development of spherical ULVs around 350−420 nm at low SDS concentration (Figure 4A-II and Figure S13). In contrast, photo-PISA at [SDS] = 8.2 mM (= CMC) resulted in the formation of mixed morphologies of spherical micelles, short worms, and ULVs of various sizes, as judged by dry-state and cryo-TEM imaging, due to greater interaction of surfactant molecules with the block copolymer chains leading to interfacial curvature changes (Figures 3A-II and 4A-II, Figure S14). In this case, the average membrane thickness of vesicles was calculated to be around 45 nm and was remarkably higher compared to that of vesicles in DI water (Figure 3A-III). A 10-fold surfactant concentration increase to [SDS] = 82.0 mM further promoted the surfactant-induced dissociation of polymer/surfactant assemblies toward lower-order structures. Dry-state TEM imaging showed a significant increase in the

DOI: 10.1021/acs.macromol.8b00994
Macromolecules 2018, 51, 6190−6201

worm-like and spherical micelles' population against ULVs (Figure 4A-II and Figure S15). In addition to the described results, the well-known ability of SDS to denature enzymes and other proteins makes it unsuitable candidate for enzyme-loaded nanoreactor development and amphiphile incorporation applications. On the other hand, for cationic surfactant CTAB, a direct vesicle-to-sphere morphology transition was observed at [CTAB] ≥ CMC, as judged by DLS and dry-state TEM analyses. DLS measurements of crude and purified samples for removal of unbound detergent revealed a significant D_h decrease from 400 to 250 nm upon increasing CTAB concentration, while PD values were constantly in the range 0.15−0.2 (Figure 3B-I). DLS size distributions showed the presence of two particle populations for small spherical micelles and vesicles at [CTAB] ≥ 0.8 mM, while a single population of vesicles was detected at low CTAB concentration (Figure 4B-I). DLS results were also verified by dry-state TEM imaging of purified samples at different surfactant concentrations. Unilamellar vesicles identical to those formed in DI water were solely observed at [CTAB] = 0.08 mM (= 0.1 × CMC) (Figure 4B-II and Figure S16), while the formation of spheres as well as small and large ULVs was revealed at [CTAB] = CMC (Figure 4B-II and Figure S17). Cryo-TEM imaging at this CTAB concentration also confirmed the coexistence of a mixture of very small and larger ULVs, while an average bilayer thickness of around 28 nm, similar to that of low-CMC non-ionic surfactant samples, was measured from digital image analysis (Figures 3B-II and 3B-III). A further increase of [CTAB] from 0.8 to 8.0 mM (= 10 × CMC) favored the formation of spherical micelles; hence, the population of spheres was notably larger than that of vesicles in this case (Figure 4B-II and Figure S18). This could be explained by the gradual introduction of positive charges, caused by the increasing [CTAB], that blend into the diblock copolymer chains developing strong repulsive forces and leading to dissociation of vesicles in favor of spheres (i.e., significant increase of interfacial curvature). It should also be mentioned that complete charge screening occurred at [CTAB] = 8.0 mM (measured zeta potential = −1.25 ± 0.32 mV), owing to neutralization of the negative vesicles' charge by the positively charged surfactant molecules. For both ionic surfactants, comparable findings were also discussed by Armes' group in a different study and are mainly attributed to the high sensitivity of RAFT-mediated PISA to the presence of ionic molecules, which makes it more difficult to obtain higher-order morphologies in contrast to the less-disruptive non-ionic surfactants.[10,52] The greater disruptive power of anionic surfactant SDS as compared to that of cationic CTAB is mainly attributed to the greater molar concentration for a given mass concentration of the former (i.e., CMC_{SDS} > CMC_{CTAB}).[10]

Photo-PISA Nano-Objects Developed in the Presence of Zwitterionic Surfactants. Importantly, the effect of two model zwitterionic (ampholytic) surfactants on PEG_{113}-*b*-$PHPMA_{400}$ photo-PISA nano-object formulations was thoroughly investigated. In the case of high-CMC steroid surfactant CHAPS, slight size differences were observed at low surfactant concentrations (i.e., [CHAPS] ≤ CMC), as judged by DLS (Figure 3C-I). However, a dramatic D_h decrease from 420 to 110 nm was observed at [CHAPS] = 80.0 mM (= 10 × CMC) (PD = 0.18, zeta potential = −15.6 ± 0.3 mV), while further [CHAPS] increase to 160.0 mM (= 20 × CMC) resulted in a notable D_h decrease to almost 50 nm (PD = 0.04, zeta potential = −10.4 ± 1.9 mV), indicating the occurrence of morphological transitions from ULVs to lower-order structures upon increasing detergent concentration. Interestingly, dry-state TEM imaging revealed a morphologically distinct vesicle-to-worm-to-sphere transition upon increasing [CHAPS] from CMC to 10 × CMC and subsequently to 20 × CMC (Figure 5A and Figures S19−S21). ULVs of uniform shape and size with significantly thicker hydrophobic membranes (average membrane thickness ≈38 nm) and rough outline were formed at [CHAPS] = 8.0 mM (= CMC), as shown by cryo-TEM (Figures 3C-II and 3C-III), whereas a pure network of branched worms was apparently observed after photo-PISA in 80.0 mM CHAPS solution. This was initially indicated on a macroscopic level by the formation a free-standing gel in the reaction vial after the polymerization process. The increase of both D_h and PD noticed in this sample after purification is mainly attributed to further entanglement of the worm-like micelles during the centrifugation/resuspension process.[24] Additional dry-state TEM imaging at [CHAPS] = 160.0 mM clearly showed the development of small spherical micelles, confirming the results received from DLS analysis. As ^{1}H NMR spectroscopy suggested that only 70% monomer consumption occurred after 2 h of reaction in this sample, an overnight photo-PISA reaction was repeated to ensure full monomer conversion. In this case, dry-state TEM imaging showed the formation of mostly small spherical micelles along with some short worms, derived from the integration of adjacent spheres (Figure S22). Similar to the studied ionic surfactants, it is evident that the presence of high amounts of charged zwitterionic surfactant molecules promotes their ionic-like behavior and markedly affects the photo-

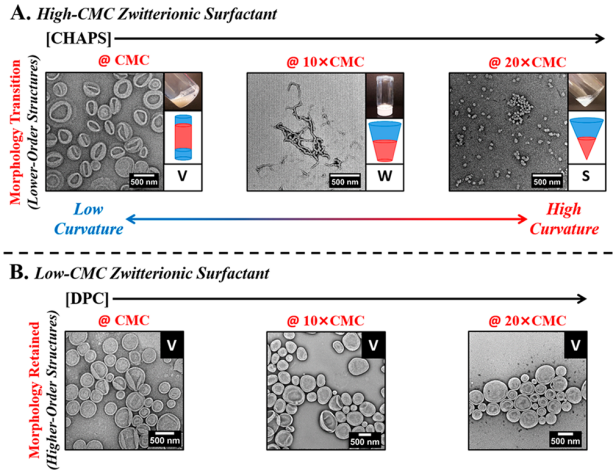

Figure 5. (A) Representative dry-state TEM micrographs, stained with 1 wt % UA, reaction vial images, and illustrations of the interfacial curvature of PEG_{113}-*b*-$PHPMA_{400}$ nano-objects developed by aqueous photo-PISA upon increasing concentration of high-CMC zwitterionic surfactant CHAPS. A vesicle-to-worm morphology transition is observed at [CHAPS] = 10 × CMC, while a subsequent worm-to-sphere transition is noticed at [CHAPS] = 20 × CMC. (B) Representative dry-state TEM micrographs, stained with 1 wt % UA, of PEG_{113}-*b*-$PHPMA_{400}$ nano-objects developed by aqueous photo-PISA upon increasing concentration of low-CMC zwitterionic surfactant DPC. No morphology transitions were observed; hence, ULVs of comparable sizes were achieved at concentrations ranging from [DPC] = CMC to 20 × CMC.

DOI: 10.1021/acs.macromol.8b00994
Macromolecules 2018, 51, 6190−6201

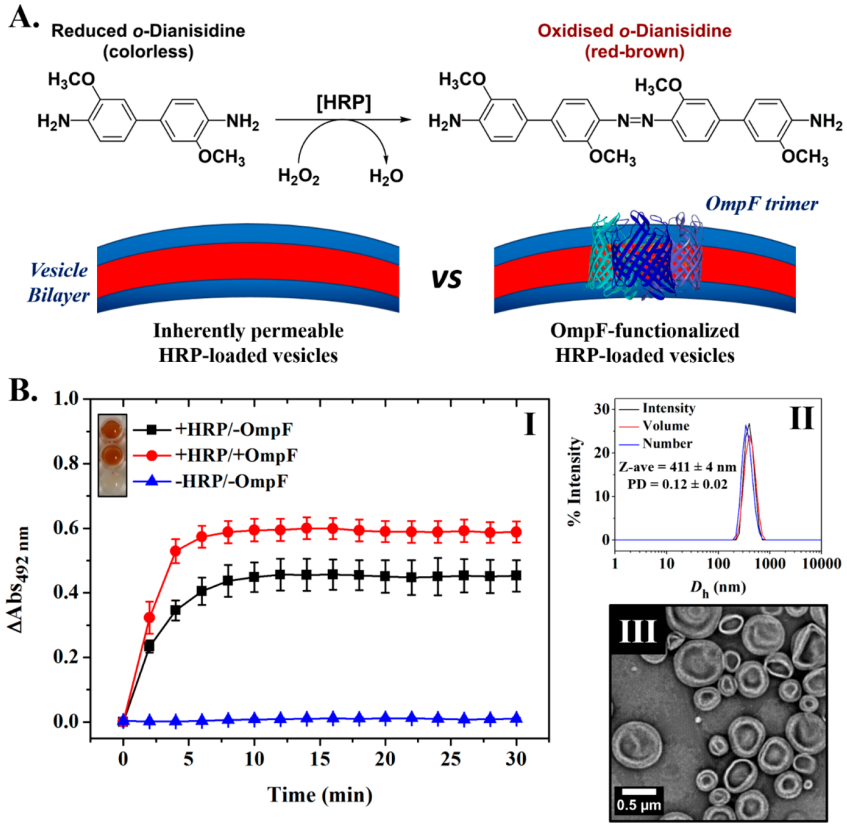

Figure 6. (A) HRP-catalyzed oxidation reaction of *o*-dianisidine to a red-brown dimer product, detected by colorimetric assay, taking place inside inherently permeable HRP-loaded PEG_{113}-*b*-$PHPMA_{400}$ vesicles and OmpF-functionalized + HRP-loaded PEG_{113}-*b*-$PHPMA_{400}$ vesicles. (B) Enzymatic activity of the purified empty (−HRP/−OmpF, blue line), HRP-loaded (+HRP/−OmpF, black line), and OmpF-functionalized + HRP-loaded (+HRP/+OmpF, red line) PEG_{113}-*b*-$PHPMA_{400}$ vesicles at 0.5 wt % (the inset shows the end-point microwells in each case) (I), intensity-weighted size distributions of purified OmpF-functionalized + HRP-loaded PEG_{113}-*b*-$PHPMA_{400}$ vesicles obtained by DLS, along with the average D_h and PD values (the error shows the standard deviation from five repeat measurements) (II), and representative dry-state TEM image, stained with 1 wt % UA (III).

PISA process, preventing the formation of higher-order structures. The incorporation of zwitterionic detergent molecules into the bilayer of the assemblies combined with the introduction of charges in the hydrophilic corona of the nano-objects drives the development of mixed polymer−surfactant formulations with higher interfacial curvature (i.e., transitions to worm-like or spherical micelles). Above all, pure phases of ULVs, worms, and spherical micelles were isolated by careful control of CHAPS concentration during aqueous photo-PISA of the same block copolymer. Surprisingly, in the case of the other studied zwitterionic phospholipid surfactant DPC, completely opposite behavior compared to high-CMC CHAPS and analogous to that of non-ionic and low-CMC detergents Triton X-100 and DDM was observed. In particular, minor size and PD variations were recorded for a wide range of DPC concentrations, in comparison to original PEG_{113}-*b*-$PHPMA_{400}$ ULVs in DI water, suggesting that no dissociation to lower-order constructs occurred in this case, even at extreme detergent concentrations (Figure 3D-I). The hydrodynamic diameter of photo-PISA samples in DPC solutions ranged between 340 nm for low [DPC] and 440 nm for higher [DPC], while low PD values of 0.07−0.15 were also measured. It should also be noted that in the case of DPC the purification process did not affect the D_h or PD values. Dry-state and cryo-TEM imaging at [DPC] = 1.5 mM (= CMC) revealed the successful development of pure spherical ULVs of uniform size (Figures 3D-II and 5B, Figure S23). Based on cryo-TEM analysis, the average membrane thickness of vesicles formed at [DPC] = CMC was determined to be around 30 nm (Figure 3D-III). This indicates negligible interaction between DPC molecules and polymeric chains, following the same trend as low-CMC non-ionic surfactants. Additionally, the vesicular morphology and unilamellar character were retained upon increasing DPC concentration up to 20 times above its CMC value, showing the high tolerance of photo-PISA toward this particular surfactant (Figure 5B, Figures S24 and S25). The marked differences observed between the two zwitterionic detergents are attributed to the higher weight percent of surfactant required in the case of CHAPS ($CMC_{CHAPS} > CMC_{DPC}$), revealing the dual nature of such species that are possible to behave like non-ionic or ionic surfactants depending on the conditions. Finally, these findings are of paramount importance as it was demonstrated that besides neutral detergents, an ampholytic small molecule surfactant could also be used for applications of biorelevant interest without drastically affecting the desired final morphologies prepared by aqueous PISA. The observed morphologies of all formulations developed by RAFT-mediated photo-PISA in aqueous surfactant solutions, as

DOI: 10.1021/acs.macromol.8b00994
Macromolecules 2018, 51, 6190−6201

judged by dry-state and cryo-TEM, are summarized in Table S3.

Outer Membrane Protein F (OmpF) Reconstitution into PEG_{113}-*b*-$PHPMA_{400}$ Vesicles. Guided by the results on the tolerance of PISA to surfactants, a challenging functional membrane protein, which is not soluble in aqueous media in the absence of surfactants, was selected for incorporation during the photo-PISA process. The channel-forming membrane protein OmpF trimer was extracted from *Escherichia coli* (see the Supporting Information), purified, and stabilized in an aqueous surfactant solution mixture of 0.39 mM DDM + 20 mM sodium phosphate (NaPhos) at pH = 6.0 (Figures S27 and S28). Initial photo-PISA reactions for the synthesis of PEG_{113}-*b*-$PHPMA_{400}$ block copolymers in 20 mM NaPHos and 0.39 mM DDM + 20 mM NaPHos solutions (pH = 6.0) in the absence of OmpF protein revealed that the controlled polymerization character ($Đ_M$ ca. = 1.3, monomer conversion >98%) and original vesicular morphology were retained in both cases, with negligible D_h and membrane thickness increases being observed (Figures S29 and S30). Importantly, 405 nm irradiation of DDM-stabilized OmpF for 2 h did not affect the secondary structure and hence functionality of the protein, as judged by circular dichroism (CD) measurements before and after light exposure (Figure S31). These findings suggest that by using this particular surfactant solution, OmpF could be directly reconstituted into the inherently permeable PHPMA membrane of vesicles by photo-PISA. Horseradish peroxidase (HRP) was chosen to be encapsulated into the lumen of both −OmpF and +OmpF-containing ULVs to provide a read-out of function of OmpF (permeability) by kinetic colorimetric assays, following a recently reported procedure by our group.[36] HRP catalyzes the oxidation reaction of the colorless substrate *o*-dianisidine to the colored (red-brown) dimer product, which can be detected by measuring the absorbance at λ = 492 nm over time (Figure 6A). The surfactant-stabilized OmpF protein was reconstituted into HRP-loaded ULVs by a one-pot photo-PISA reaction to introduce nonselective channels that would allow easier exchange of small molecules between the aqueous compartments of particles. From kinetic colorimetric analyses, a noticeable absorbance increase of 24 ± 3% was measured in the case of purified +OmpF-containing ULVs compared to −OmpF ones, demonstrating the permeability enhancement of the former toward *o*-dianisidine and hydrogen peroxide and OmpF retention of function (Figure 6B-I). A similar permeability enhancement was also monitored upon ranging the particles' concentration from 0.5 to 0.1 wt % during kinetic colorimetric analyses. Dry-state TEM imaging confirmed the formation of OmpF-functionalized + HRP-loaded ULVs, while additional DLS analysis showed a negligible D_h increase to 411 ± 4 nm, similar to that observed in DDM + NaPhos mixture without OmpF (Figures 6B-II and 6B-III and Figure S32).

■ CONCLUSIONS

In this study, an insight into the effect of different types of small molecule surfactants on aqueous photoinitiated PISA processes for the formation of polymer/surfactant complex nano-objects was explored. Investigation revealed the high tolerance of photo-PISA toward non-ionic surfactants with varying CMC values, as the originally targeted vesicular morphology was consistently retained in these cases. On the contrary, the high sensitivity of photo-PISA to the presence of ionic species was verified by the occurrence of morphological transitions toward lower-order structures upon increasing concentration of ionic surfactants. The introduction of charged molecules into the polymeric chains markedly affected the self-assembly process, leading to the development of formulations with larger interfacial curvatures. Moreover, the presence of zwitterionic surfactants of high or low CMC values was also studied. An interesting vesicle-to-worm-to-sphere morphology transition was observed upon increasing concentration of high-CMC zwitterionic surfactant, while in the case of low-CMC detergent vesicular structures similar to those developed in non-ionic surfactant solutions were formed at a wide range of concentrations. By using these results as a guide, a low-CMC non-ionic surfactant was selected for the stabilization/solublization of the hydrophobic channel-forming membrane protein OmpF, which was then able to be reconstituted into the membrane of the vesicles by a one-pot photo-PISA process. This highlights the robustness of photo-PISA for the *in situ* insertion of delicate non-stable hydrophobic species to allow for the facile synthesis of biomimetic nanoreactors.

■ METHODS

Materials and Methods. Materials and characterization techniques used are included in the Supporting Information. The syntheses of 4-cyano-4-[(ethylsulfanylthiocarbonyl)sulfanyl]pentanoic acid chain transfer agent (CEPA CTA) and poly(ethylene glycol)$_{113}$−CEPA macro-CTA (PEG_{113}−CEPA mCTA) by *N*,*N*′-dicyclohexylcarbodiimide (DCC) coupling between PEG_{113} monomethyl ether and CEPA CTA were performed according to previously described processes with slight modification.[24,53] The synthetic procedures followed are given in detail in the Supporting Information. All photo-PISA reactions were performed in a custom-built photoreactor setup. This ensured the reaction mixture was only exposed to the light from the 400−410 nm LED source placed underneath the sample.

Synthesis of PEG_{113}-*b*-$PHPMA_{400}$ Diblock Copolymer Nano-Objects by Aqueous Photoinitiated Polymerization-Induced Self-Assembly (Photo-PISA) in Surfactant Solutions. A typical synthetic procedure to achieve PEG_{113}-*b*-$PHPMA_{400}$ diblock copolymer nano-objects at 10 wt % HPMA (or 11% solids content) by aqueous RAFT-mediated photo-PISA is described (Scheme S1).[24] PEG_{113}−CEPA mCTA (9.1 mg, 1.7 μmol, 1 equiv) and HPMA (100 mg, 0.69 mmol, 400 equiv) were dissolved in a freshly prepared aqueous surfactant solution of desired concentration (0.9 mL) in a sealed 20 mL scintillation vial bearing a magnetic stirrer bar. The resulting polymerization solution was degassed by purging with N_2(g) for 15 min. The sealed vial was incubated at 37 °C with magnetic stirring under 405 nm light irradiation for 2 h to ensure full monomer conversion. After this period, the reaction mixture was exposed to air and allowed to cool to room temperature before conversion ^{1}H NMR and SEC analyses. The resulting solution of particles was then diluted 10-fold in DI water and purified by three centrifugation/resuspension cycles in DI water at 14000 rpm for the removal of unreacted monomer and/or excess of non-incorporated surfactant molecules (Figure S1). ^{1}H NMR in methanol-d_4 and DMF SEC traces of the pure polymer were obtained after lyophilization of an aliquot of particles. TEM, DLS, and zeta potential analyses were performed on samples after dilution to an appropriate analysis concentration.

HRP Loading and OmpF Reconstitution into PEG_{113}-*b*-$PHPMA_{400}$ Vesicles by Aqueous Photo-PISA. For the synthesis of permeable non-OmpF-containing HRP-loaded PEG_{113}-*b*-$PHPMA_{400}$ vesicles at 10 wt % HPMA by aqueous photo-PISA, a previously reported procedure was followed.[36] For the reconstitution of OmpF porin, PEG_{113}−CEPA mCTA (9.1 mg, 1.7 μmol, 1 equiv) and HPMA (100 mg, 0.69 mmol, 400 equiv) were first dissolved in DI water (0.53 mL) in a sealed 20 mL scintillation vial bearing a magnetic stirrer bar. Once homogeneous, 0.1 mL of a 200 U mL^{-1} HRP solution in DI water and 0.27 mL of a 750 μg mL^{-1} OmpF solution in 0.39 mM DDM + 20 mM NaPhos (pH = 6.0) were added. The resulting polymerization solution was degassed by purging with N_2(g) for 15

DOI: 10.1021/acs.macromol.8b00994
Macromolecules 2018, 51, 6190−6201

min. The sealed vial was incubated at 37 °C with magnetic stirring under 405 nm light irradiation for 2 h to ensure full monomer conversion. After this period, the reaction mixture was exposed to air and allowed to cool to room temperature before conversion ^{1}H NMR, kinetic colorimetric, and microscopic analyses. The resulting solutions of non-OmpF and OmpF-containing particles were then diluted 10-fold in 100 mM PB (pH = 5.5) and purified by three centrifugation/resuspension cycles in 100 mM PB (pH = 5.5) at 14000 rpm for the removal of unreacted monomer, free HRP enzyme, and/or non-incorporated OmpF molecules.

■ ASSOCIATED CONTENT

Supporting Information

The Supporting Information is available free of charge on the ACS Publications website at DOI: 10.1021/acs.macromol.8b00994.

Materials and characterization techniques, experimental details, additional SEC eluograms of PEG_{113}-*b*-$PHPMA_{400}$ diblock copolymers synthesized in DI water and various surfactant solutions, additional dry-state TEM and cryo-TEM images of nano-objects, OmpF reconstitution supplementary data (PDF)

■ AUTHOR INFORMATION

Corresponding Author

*E-mail: r.oreilly@bham.ac.uk.

ORCID

Eamonn Reading: 0000-0001-8219-0052

Matthew I. Gibson: 0000-0002-8297-1278

Rachel K. O'Reilly: 0000-0002-1043-7172

Notes

The authors declare no competing financial interest.

■ ACKNOWLEDGMENTS

This work was supported by the ERC (638661, 294342, and 615142), EPSRC, and University of Warwick. Dr. E. Reading is funded by BBSRC Future Leader Fellowship BB/N011201/1. Dr. S. Bakker and Mr. R. Keogh (University of Warwick) are thanked for cryo-TEM assistance, and Advanced BioImaging Research Technology Platform, BBSRC ALERT14 award BB/M01228X/1, is thanked for supporting cryo-TEM characterization. Dr. M. Hasan (University of Warwick) is thanked for CD assistance.

■ REFERENCES

(1) Karsa, D. R. *Industrial Applications of Surfactants IV*; The Royal Society of Chemistry: Cambridge, 1999.

(2) Schramm, L. L. *Surfactants: Fundamentals and Applications in the Petroleum Industry*; Cambridge University Press: Cambridge, 2000.

(3) Blanazs, A.; Armes, S. P.; Ryan, A. J. Self-Assembled Block Copolymer Aggregates: From Micelles to Vesicles and their Biological Applications. Macromol. *Macromol. Rapid Commun.* **2009**, *30*, 267–277.

(4) Chang, H.-Y.; Sheng, Y.-H.; Tsao, H.-K. Structural and Mechanical Characteristics of Polymersomes. *Soft Matter* **2014**, *10*, 6373–6381.

(5) Banerjee, S.; Cazeneuve, C.; Baghdadli, N.; Ringeissen, S.; Leermakers, F. A. M.; Luengo, G. S. Surfactant-Polymer Interactions: Molecular Architecture Does Matter. *Soft Matter* **2015**, *11*, 2504–2511.

(6) Holmberg, K.; Jönsson, B.; Kronberg, B.; Lindman, B. *Surfactants and Polymers in Aqueous Solution*, 2nd ed.; John Wiley & Sons, Ltd.: West Sussex, 2003.

(7) Wesley, R.; Cosgrove, T.; Thompson, L.; Armes, S. P.; Baines, F. L. Structure of Polymer/Surfactant Complexes Formed by Poly(2-(dimethylamino)ethyl methacrylate) and Sodium Dodecyl Sulfate. *Langmuir* **2002**, *18*, 5704–5707.

(8) Diamant, H.; Andelman, D. Onset of Self-Assembly in Polymer-Surfactant Systems. *Europhys. Lett.* **1999**, *48*, 170–176.

(9) Pata, V.; Ahmed, F.; Discher, D. E.; Dan, N. Membrane Solubilization by Detergent: Resistance Conferred by Thickness. *Langmuir* **2004**, *20*, 3888–3893.

(10) Chambon, P.; Blanazs, A.; Battaglia, G.; Armes, S. P. How Does Cross-Linking Affect the Stability of Block Copolymer Vesicles in the Presence of Surfactant? *Langmuir* **2012**, *28*, 1196–1205.

(11) Atanase, L. I.; Lerch, J.-P.; Caprarescu, S.; Iurciuc, C. E.; Riess, G. Micellization of pH-Sensitive Poly(butadiene)-*block*-poly(2 vinylpyridine)-*block*-poly(ethylene oxide) Triblock Copolymers: Complex Formation with Anionic Surfactants. *J. Appl. Polym. Sci.* **2017**, *134*, 45313.

(12) Nam, J.; Beales, P. A.; Vanderlick, T. K. Giant Phospholipid/Block Copolymer Hybrid Vesicles: Mixing Behavior and Domain Formation. *Langmuir* **2011**, *27*, 1–6.

(13) Nam, J.; Vanderlick, T. K.; Beales, P. A. Formation and Dissolution of Phospholipid Domains with Varying Textures in Hybrid Lipo-Polymersomes. *Soft Matter* **2012**, *8*, 7982–7988.

(14) Le Meins, J.-F.; Schatz, C.; Lecommandoux, S.; Sandre, O. Hybrid Polymer/Lipid Vesicles: State of the Art and Future Perspectives. Mater. *Mater. Today* **2013**, *16*, 397–402.

(15) Schulz, M.; Binder, W. H. Mixed Hybrid Lipid/Polymer Vesicles as a Novel Membrane Platform. Macromol. *Macromol. Rapid Commun.* **2015**, *36*, 2031–2041.

(16) Warren, N. J.; Armes, S. P. Polymerization-Induced Self-Assembly of Block Copolymer Nano-objects via RAFT Aqueous Dispersion Polymerization. *J. Am. Chem. Soc.* **2014**, *136*, 10174–10185.

(17) Canning, S. L.; Smith, G. N.; Armes, S. P. A Critical Appraisal of RAFT-Mediated Polymerization-Induced Self-Assembly. *Macromolecules* **2016**, *49*, 1985–2001.

(18) Karagoz, B.; Boyer, C.; Davis, T. P. Simultaneous Polymerization-Induced Self-Assembly (PISA) and Guest Molecule Encapsulation. *Macromol. Rapid Commun.* **2014**, *35*, 417–421.

(19) Zhou, W.; Qu, Q.; Xu, Y.; An, Z. Aqueous Polymerization-Induced Self-Assembly for the Synthesis of Ketone-Functionalized Nano-Objects with Low Polydispersity. *ACS Macro Lett.* **2015**, *4*, 495–499.

(20) Qiao, X. G.; Dugas, P.-Y.; Charleux, B.; Lansalot, M.; Bourgeat-Lami, E. Nitroxide-Mediated Polymerization-Induced Self-Assembly of Amphiphilic Block Copolymers with a pH/Temperature Dual Sensitive Stabilizer Block. *Polym. Chem.* **2017**, *8*, 4014–4029.

(21) Wang, G.; Schmitt, M.; Wang, Z.; Lee, B.; Pan, X.; Fu, L.; Yan, J.; Li, S.; Xie, G.; Bockstaller, M. R.; Matyjaszewski, K. Polymerization-Induced Self-Assembly (PISA) Using ICAR ATRP at Low Catalyst Concentration. *Macromolecules* **2016**, *49*, 8605–8615.

(22) Blanazs, A.; Madsen, J.; Battaglia, G.; Ryan, A. J.; Armes, S. P. Mechanistic Insights for Block Copolymer Morphologies: How Do Worms Form Vesicles? *J. Am. Chem. Soc.* **2011**, *133*, 16581–16587.

(23) Williams, M.; Penfold, N. J. W.; Lovett, J. R.; Warren, N. J.; Douglas, C. W. I.; Doroshenko, N.; Verstraete, P.; Smets, J.; Armes, S. P. Bespoke Cationic Nano-Objects via RAFT Aqueous Dispersion Polymerization. *Polym. Chem.* **2016**, *7*, 3864–3873.

(24) Blackman, L. D.; Doncom, K. E. B.; Gibson, M. I.; O'Reilly, R. K. Comparison of Photo- and Thermally Initiated Polymerization-Induced Self-Assembly: A Lack of End Group Fidelity Drives the Formation of Higher Order Morphologies. *Polym. Chem.* **2017**, *8*, 2860–2871.

(25) Figg, C. A.; Carmean, R. N.; Bentz, K. C.; Mukherjee, S.; Savin, D. A.; Sumerlin, B. S. Tuning Hydrophobicity To Program Block Copolymer Assemblies from the Inside Out. *Macromolecules* **2017**, *50*, 935–943.

(26) Derry, M. J.; Fielding, L. A.; Armes, S. P. Polymerization-Induced Self-Assembly of Block Copolymer Nanoparticles via RAFT

DOI: 10.1021/acs.macromol.8b00994
Macromolecules 2018, 51, 6190–6201

Non-Aqueous Dispersion Polymerization. *Prog. Polym. Sci.* **2016**, *52*, 1−18.
(27) Yeow, J.; Boyer, C. Photoinitiated Polymerization-Induced Self-Assembly (Photo-PISA): New Insights and Opportunities. *Adv. Sci.* **2017**, *4*, 1700137.
(28) Tan, J.; Sun, H.; Yu, M.; Sumerlin, B. S.; Zhang, L. Photo-PISA: Shedding Light on Polymerization-Induced Self-Assembly. *ACS Macro Lett.* **2015**, *4*, 1249−1253.
(29) Yeow, J.; Xu, J.; Boyer, C. Polymerization-Induced Self-Assembly Using Visible Light Mediated Photoinduced Electron Transfer−Reversible Addition−Fragmentation Chain Transfer Polymerization. *ACS Macro Lett.* **2015**, *4*, 984−990.
(30) Tan, J.; Bai, Y.; Zhang, X.; Zhang, L. Room Temperature Synthesis of Poly(poly(ethylene glycol) methyl ether methacrylate)-Based Diblock Copolymer Nano-Objects via Photoinitiated Polymerization-Induced Self-Assembly (Photo-PISA). *Polym. Chem.* **2016**, *7*, 2372−2380.
(31) Tan, J.; Liu, D.; Bai, Y.; Huang, C.; Li, X.; He, J.; Xu, Q.; Zhang, X.; Zhang, L. An Insight into Aqueous Photoinitiated Polymerization-Induced Self-Assembly (photo-PISA) for the Preparation of Diblock Copolymer Nano-Objects. *Polym. Chem.* **2017**, *8*, 1315−1327.
(32) Sadrearhami, Z.; Yeow, J.; Nguyen, T.-K.; Ho, K. K. K.; Kumar, N.; Boyer, C. Biofilm Dispersal Using Nitric Oxide Loaded Nanoparticles Fabricated by Photo-PISA: Influence of Morphology. *Chem. Commun.* **2017**, *53*, 12894−12897.
(33) Tan, J.; Li, X.; Zeng, R.; Liu, D.; Xu, Q.; He, J.; Zhang, Y.; Dai, X.; Yu, L.; Zeng, Z.; Zhang, L. Expanding the Scope of Polymerization-Induced Self-Assembly: Z-RAFT-Mediated Photoinitiated Dispersion Polymerization. *ACS Macro Lett.* **2018**, *7*, 255−262.
(34) Tan, J.; Liu, D.; Huang, C.; Li, X.; He, J.; Xu, Q.; Zhang, L. Photoinitiated Polymerization-Induced Self-Assembly of Glycidyl Methacrylate for the Synthesis of Epoxy-Functionalized Block Copolymer Nano-Objects. Macromol. *Macromol. Rapid Commun.* **2017**, *38*, 1700195.
(35) Tan, J.; Liu, D.; Bai, Y.; Huang, C.; Li, X.; He, J.; Xu, Q.; Zhang, L. Enzyme-Assisted Photoinitiated Polymerization-Induced Self-Assembly: An Oxygen-Tolerant Method for Preparing Block Copolymer Nano-Objects in Open Vessels and Multiwell Plates. *Macromolecules* **2017**, *50*, 5798−5806.
(36) Blackman, L. D.; Varlas, S.; Arno, M. C.; Fayter, A.; Gibson, M. I.; O'Reilly, R. K. Permeable Protein-Loaded Polymersome Cascade Nanoreactors by Polymerization-Induced Self-Assembly. *ACS Macro Lett.* **2017**, *6*, 1263−1267.
(37) Tan, J.; Zhang, X.; Liu, D.; Bai, Y.; Huang, C.; Li, X.; Zhang, L. Facile Preparation of CO_2-Responsive Polymer Nano-Objects via Aqueous Photoinitiated Polymerization-Induced Self-Assembly (Photo-PISA). *Macromol. Rapid Commun.* **2017**, *38*, 1600508.
(38) Blackman, L. D.; Varlas, S.; Arno, M. C.; Houston, Z. H.; Fletcher, N. L.; Thurecht, K. J.; Hasan, M.; Gibson, M. I.; O'Reilly, R. K. Confinement of Therapeutic Enzymes in Selectively Permeable Polymer Vesicles by Polymerization-Induced Self-Assembly (PISA) Reduces Antibody Binding and Proteolytic Susceptibility. *ACS Cent. Sci.* **2018**, *4*, 718−723.
(39) Mastrotto, F.; Breen, A. F.; Sicilia, G.; Murdan, S.; Johnstone, A. D.; Marsh, G. E.; Grainger-Boultby, C.; Russell, N. A.; Alexander, C.; Mantovani, G. One-pot RAFT and Fast Polymersomes Assembly: A 'Beeline' from Monomers to Drug-Loaded Nanovectors. *Polym. Chem.* **2016**, *7*, 6714−6724.
(40) Edlinger, C.; Einfalt, T.; Spulber, M.; Car, A.; Meier, W.; Palivan, C. G. Biomimetic Strategy to Reversibly Trigger Functionality of Catalytic Nanocompartments by the Insertion of pH-Responsive Biovalves. *Nano Lett.* **2017**, *17*, 5790−5798.
(41) Iimura, N.; Sawada, K.; Ohashi, Y.; Hirata, H. Complex Formation Between Cationic Surfactants and Insoluble Drugs. *Bull. Chem. Soc. Jpn.* **1999**, *72*, 2417−2422.
(42) Seddon, A. M.; Curnow, P.; Booth, P. J. Membrane Proteins, Lipids and Detergents: Not Just a Soap Opera. *Biochim. Biophys. Acta, Biomembr.* **2004**, *1666*, 105−117.
(43) Privé, G. G. Detergents for the Stabilization and Crystallization of Membrane Proteins. *Methods* **2007**, *41*, 388−397.
(44) Tehrani-Bagha, A. R.; Holmberg, K. Solubilization of Hydrophobic Dyes in Surfactant Solutions. *Materials* **2013**, *6*, 580−608.
(45) Tanner, P.; Onaca, O.; Balasubramanian, V.; Meier, W.; Palivan, C. G. Enzymatic Cascade Reactions Inside Polymeric Nanocontainers: A Means to Combat Oxidative Stress. *Chem. - Eur. J.* **2011**, *17*, 4552−4560.
(46) Einfalt, T.; Goers, R.; Dinu, I. A.; Najer, A.; Spulber, M.; Onaca-Fischer, O.; Palivan, C. G. Stimuli-Triggered Activity of Nanoreactors by Biomimetic Engineering Polymer Membranes. *Nano Lett.* **2015**, *15*, 7596−7603.
(47) Warren, N. J.; Mykhaylyk, O. O.; Mahmood, D.; Ryan, A. J.; Armes, S. P. RAFT Aqueous Dispersion Polymerization Yields Poly(ethylene glycol)-Based Diblock Copolymer Nano-Objects with Predictable Single Phase Morphologies. *J. Am. Chem. Soc.* **2014**, *136*, 1023−1033.
(48) Otsu, T. Iniferter Concept and Living Radical Polymerization. *J. Polym. Sci., Part A: Polym. Chem.* **2000**, *38*, 2121−2136.
(49) Lovett, J. R.; Warren, N. J.; Armes, S. P.; Smallridge, M. J.; Cracknell, R. B. Order-Order Morphological Transitions for Dual Stimulus Responsive Diblock Copolymer Vesicles. *Macromolecules* **2016**, *49*, 1016−1025.
(50) Stiufiuc, R.; Iacovita, C.; Nicoara, R.; Stiufiuc, G.; Florea, A.; Achim, M.; Lucaciu, C. M. One-Step Synthesis of PEGylated Gold Nanoparticles with Tunable Surface Charge. *J. Nanomater.* **2013**, *2013*, 1−7.
(51) Knecht, V.; Risselada, H. J.; Mark, A. E.; Marrink, S. J. Electrophoretic Mobility Does Not Always Reflect the Charge on an Oil Droplet. *J. Colloid Interface Sci.* **2008**, *318*, 477−486.
(52) Semsarilar, M.; Ladmiral, V.; Blanazs, A.; Armes, S. P. Anionic Polyelectrolyte-Stabilized Nanoparticles via RAFT Aqueous Dispersion Polymerization. *Langmuir* **2012**, *28*, 914−922.
(53) Johnson, R. N.; Burke, R. S.; Convertine, A. J.; Hoffman, A. S.; Stayton, P. S.; Pun, S. H. Synthesis of Statistical Copolymers Containing Multiple Functional Peptides for Nucleic Acid Delivery. *Biomacromolecules* **2010**, *11*, 3007−3013.

DOI: 10.1021/acs.macromol.8b00994
Macromolecules 2018, 51, 6190−6201

2.2. Appendix – Supporting Information Material

Electronic Supplementary Information

Photoinitiated Polymerization-Induced Self-Assembly in the Presence of Surfactants Enables Membrane Protein Incorporation into Vesicles

Spyridon Varlas,[a,b] *Lewis D. Blackman,*[a] *Heather E. Findlay,*[c] *Eamonn Reading,*[c] *Paula J. Booth,*[c] *Matthew I. Gibson*[a,d] *and Rachel K. O'Reilly*[b]*

[a] Department of Chemistry, University of Warwick, Gibbet Hill Road, CV4 7AL, Coventry, UK

[b] School of Chemistry, University of Birmingham, B15 2TT, Birmingham, UK

[c] Department of Chemistry, King's College London, Britannia House, 7 Trinity Street, SE1 1DB, London, UK

[d] Warwick Medical School, University of Warwick, Gibbet Hill Road, CV4 7AL, Coventry, UK

*Corresponding Author: r.oreilly@bham.ac.uk (R.K.O.)

Contents

Experimental Section S2
Materials and Methods S2
Materials S2
Characterization Techniques S2
Synthetic Methods S5
Supplementary Data for PEG_{113}-*b*-$PHPMA_{400}$ Vesicles Formed in DI Water S8
Supplementary Data for PEG_{113}-*b*-$PHPMA_{400}$ Nano-Objects Formed in Surfactant Solutions S10
Supplementary Data for OmpF Porin Reconstitution into PEG_{113}-*b*-$PHPMA_{400}$ Vesicles S20
References S23

Experimental Section

Materials and Methods

Materials

Poly(ethylene glycol) methyl ether (average M_n = 5,000 g mol^{-1}, PEG-OH), carbon disulfide (anhydrous, ≥99%), sodium ethanethiolate, *N,N′*-dicyclohexylcarbodiimide (99%, DCC), 4-(dimethylamino)pyridine (≥98%, DMAP), sodium dodecyl sulfate (≥99%, SDS), Triton™ X-100, octyl β-*D*-glucopyranoside (OG) and *o*-dianisidine were purchased from Sigma Aldrich and were used without further purification. Hexadecyl-trimethyl-ammonium bromide (99+%, CTAB) was received from Acros Organics. Iodine, diethyl ether and dichloromethane (DCM) were purchased from Fisher Scientific. Ethyl acetate and *n*-dodecyl β-*D*-maltoside (DDM) were purchased from VWR Chemicals. *n*-Dodecylphosphocholine (DPC) was obtained from Anatrace. 4,4'-Azobis(4-cyanovaleric acid) (98%, ACVA) and 3-[(3-cholamidopropyl) dimethylammonio]-1-propanesulfonate (98+%, CHAPS) were obtained from Alfa Aesar. 2-Hydroxypropyl methacrylate (mixture of isomers, 98%, HPMA) was also purchased from Alfa Aesar and was passed through a column of basic alumina to remove inhibitor prior to use. Hydrogen peroxide (35%) was purchased from Lancaster Synthesis. The enzyme peroxidase from *Amoracia rusticana* (type VI, essentially salt free) (HRP) was purchased from Sigma Aldrich, divided into aliquots at 200 U mL^{-1} in deionized water and stored at -20 °C. Dry solvents used in the experiments were obtained by passing over a column of activated alumina using an Innovative Technologies solvent purification system. Formvar and QUANTIFOIL® lacey-carbon coated copper grids were purchased from EM Resolutions. The light source for the photo-initiated PISA reactions (TruOpto OSV5X3CAC1E) was purchased from Rapid Electronics and had an output power of 800 mW at 12V DC operating at a wavelength of 400–410 nm. This was fitted to a custom-built setup fitted with a dimmer switch for controlling the output light intensity.

Characterization Techniques

NMR Spectroscopy. ^{1}H-NMR and ^{13}C-NMR spectra were recorded at 300 MHz or 400 MHz on a Bruker DPX-300 or DPX-400 spectrometer respectively, with chloroform-*d* ($CDCl_3$) or methanol-d_4 (CD_3OD) as the solvent. Chemical shifts of protons are reported as δ in parts per million (ppm) and are relative to

tetramethylsilane (TMS) at δ = 0 ppm when using $CDCl_3$ or solvent residual peak (CH_3OH, δ = 3.31 ppm).

FT-IR Spectroscopy. Fourier Transform-Infrared (FT-IR) spectroscopy measurements were carried out using a Perkin Elmer Spectrum 100 spectrometer, in the range of 600 to 4000 cm^{-1}.

Size Exclusion Chromatography. Size exclusion chromatography (SEC) analysis was performed on a system composed of a Varian 390-LC-Multi detector suite equipped with a Varian Polymer Laboratories guard column (PLGel 5 μM, 50 × 7.5 mm), two Mixed-C Varian Polymer Laboratories columns (PLGel 5 μM, 300 × 7.5 mm) and a PLAST RT auto-sampler. Detection was conducted using a differential refractive index (RI) and an ultraviolet (UV) detector set to λ = 309 nm. The mobile phase used was DMF (HPLC grade) containing 5 mM NH_4BF_4 at 50 ^oC at flow rate of 1.0 mL min^{-1}. Poly(methyl methacrylate) (PMMA) standards were used for calibration. Number average molecular weights (M_n), weight average molecular weights (M_w) and dispersities ($Đ_M = M_w/M_n$) were determined using Cirrus v3.3 SEC software.

Surface Tension Analysis. Pendant drop surface tension measurements for the determination of CMC of surfactant solutions in pure DI water and 10% v/v HPMA in water were performed using a Krüss DSA25 Drop Shape Analyzer. Droplets of 10 μL were produced in each case and air-water surface tension was measured using ADVANCE software and Young-Laplace fit.

Dynamic Light Scattering. Hydrodynamic diameters (D_h) and size distributions of particles were determined by dynamic light scattering (DLS) using a Malvern Zetasizer Nano ZS with a 4 mW He-Ne 633 nm laser module operating at 25 ^oC. Measurements were carried out at an angle of 173° (back scattering), and results were analyzed using Malvern DTS 7.03 software. All determinations were repeated 5 times with at least 10 measurements recorded for each run. D_h values were calculated using the Stokes-Einstein equation where particles are assumed to be spherical, while for cylindrical particles DLS was used to detect multiple populations and obtain dispersity information.

Zeta Potential Analysis. Zeta potential was measured by the technique of microelectrophoresis, using a Malvern Zetasizer Nano ZS instrument, at room temperature at 633 nm. All reported measurements were the average of at least five runs. Zeta potential was calculated from the corresponding

electrophoretic mobilities (μ_E) by using the Henry's correction of the Smoluchowski equation ($\mu_E = 4\pi\ \varepsilon_0\ \varepsilon_r\ \zeta\ (1+\kappa r)/6\pi\ \mu$).

Transmission Electron Microscopy. Dry-state stained TEM imaging was performed on either a JEOL 2000 FX, a JEOL 2011 or a JEOL 2100 microscope operating at an acceleration voltage of 200 kV. All dry-state samples were diluted with deionized water and then deposited onto formvar-coated copper grids. After roughly 1 min, excess sample was blotted from the grid and the grid was stained with an aqueous 1 wt% uranyl acetate (UA) solution for 1 min prior to blotting, drying and microscopic analysis. Samples for cryo-TEM imaging were prepared at 0.5 wt% solids content in deionized water by depositing 8 μL sample onto a lacey-carbon grid followed by blotting for approximately 4 s and plunging into a pool of liquid ethane, cooled using liquid nitrogen, to vitrify the sample. Transfer into a pre-cooled cryo-TEM holder was performed under liquid nitrogen temperatures prior to microscopic analysis. For the determination of the membrane thickness of the vesicles at least 100 particles were analyzed in each case.

Native mass spectrometry. Native mass spectrometry was acquired on a Synapt G2-Si mass spectrometer with a nESI source. Typical instrument settings were 1.6 kV capillary voltage, source temperature of 30 °C, argon for trap collision gas, and $4.2e^{-2}$ mbar for trap collision gas pressure. OmpF was diluted to a concentration of 5 μM in 50 mM Tris (pH = 8.0), 1% (w/v) OG then buffer exchanged into MS buffer (1 % (w/v) OG, 200 mM ammonium acetate (pH = 8.0)) using a centrifugal buffer exchange device (Micro Bio-Spin 6, Bio-Rad). Moderate activation settings are required to remove OG detergent bound to membrane proteins whilst maintaining the intact native membrane protein complex;[1] a 150 V trap collision voltage, 150 V cone voltage and 60 V source offset were therefore used. Mass spectra were calibrated externally using a 100 mg/mL CsI solution and deconvoluted using the UniDec software program. The deconvoluted spectra indicated that the OmpF protein was trimeric in structure.

Circular Dichroism. Circular dichroism (CD) analysis of OmpF was performed on a Jasco J-815 CD spectropolarimeter, featuring a 150 W air-cooled Xe lamp and a Jasco Peltier PTC-423S/15 temperature controlling system. The samples were contained in a 1 mm Quartz Suprasil cuvette. 0.39 mM DDM + 20 mM NaPhos background spectrum was subtracted from acquired OmpF spectra.

Kinetic Colorimetric Analysis. Kinetic colorimetric analysis was performed in 96-well Nunclon™ plates and measured on a BMG Labtech FLUOstar OPTIMA plate reader running in absorbance mode with a

filter of λ = 492 nm. Absorbance values at this wavelength were measured every two minutes. All measurements were performed in quadruplicate.

Synthetic Methods

Synthesis of 4-cyano-4-[(ethylsulfanylthiocarbonyl)sulfanyl] pentanoic acid (CEPA)

4-Cyano-4-[(ethylsulfanylthiocarbonyl)sulfanyl] pentanoic acid chain transfer agent (CEPA CTA) was synthesized according to a previously described process.[2] In particular, sodium ethanethiolate (10.0 g, 0.119 mol, 1eq) was suspended in 500 mL of dry diethyl ether at 0 °C. Carbon disulfide (7.74 mL, 0.131 mol, 1.1 eq) was subsequently added dropwise over 10 min, resulting to the formation of a thick yellow precipitate of sodium *S*-ethyl trithiocarbonate. After 2 h of stirring at room temperature, solid iodine (15.1 g, 0.059 mol, 0.5 eq) was added to the reaction medium. After 2 h, the solution was washed three times with aqueous sodium thiosulfate (1 M), water and finally saturated NaCl solution. The organic layer was thoroughly dried over $MgSO_4$ and the crude bis-(ethylsulfanylthiocarbonyl) disulfide was then isolated by rotary evaporation (16.2 g, 0.059 mol).

A solution of bis-(ethylsulfanylthiocarbonyl) disulfide (16.2 g, 0.059 mol, 1 eq) and 4,4′-azobis(4-cyanopentanoic acid) (ACVA) (24.8 g, 0.0885 mol, 1.5 eq) in 500 mL of ethyl acetate was heated at reflux for 18 h under N_2(g) atmosphere. Following rotary evaporation of the solvent, the crude CEPA CTA was isolated by column chromatography using silica gel as the stationary phase and 75:25 DCM-petroleum ether as the eluent. The isolated product was precipitated out of solution by using hexane, leaving a yellow-light orange solid. The final product was collected and dried under reduced pressure to afford pure CEPA CTA (21.36 g, 0.081 mol, 69%). ^{1}H-NMR (400 MHz, $CDCl_3$): δ (ppm) 3.35 (q, 2H, S-C***H₂***-CH_3), 2.38-2.71 (m, 4H, C***H₂***-C***H₂***), 1.89 (s, 3H, C(CN)-C***H₃***), 1.36 (t, 3H, S-CH_2-C***H₃***). ^{13}C-NMR (100 MHz, CDCl3): δ (ppm) 217.0, 177.2, 119.2, 46.5, 33.5, 31.7, 29.5, 25.0, 12.9. FT-IR (neat): ν (cm^{-1}) 2235 (C≡N), 1709 (C=O), 1073 (C=S). HRMS: m/z $[C_9H_{13}NO_2S_3+Na]^+$ calc. 286.0001 g mol^{-1}, exp 286.0001 g mol^{-1}.

Synthesis of poly(ethylene glycol)$_{113}$-CEPA macro-CTA (PEG$_{113}$-CEPA mCTA)

PEG_{113}-CEPA macro-CTA was synthesized according to previously reported methods with slight modification.[3,4] Poly(ethylene glycol) methyl ether (average M_n = 5,000 g mol^{-1}, PEG_{113}-OH) (4.75 g, 0.95 mmol, 1 eq) was dissolved in 150 mL of dry DCM. The resulting solution was then purged with N_2(g) for 30 min. After complete dissolution, CEPA CTA (1g, 3.8 mmol, 4 eq), DCC (392 mg, 1.9 mmol, 2 eq) and DMAP (23 mg, 0.19 mmol, 0.2 eq) were added to the reaction mixture. The esterification reaction proceeded with stirring at room temperature for 18 h under continuous N_2(g) flow. After this period, DCC (392 mg, 1.9 mmol, 2 eq) and DMAP (23 mg, 0.19 mmol, 0.2 eq) were added again to the reaction mixture and then stirred at room temperature for an additional period of 6 h under continuous N_2(g) flow. The solution was then filtered to remove unreacted DCC and DMAP. Following rotary evaporation of DCM, the resulted PEG_{113}-CEPA mCTA was collected by precipitation into 500 mL of cold diethyl ether, redissolved in deionized water and dialyzed against DI water for 2 days (dialysis membrane MWCO = 1000 Da). The received PEG_{113}-CEPA mCTA solution was lyophilized to give a yellow solid as the final product (3.66 g, 0.70 mmol, 73%).^{1}H-NMR (400 MHz, $CDCl_3$): δ (ppm) 4.26 (m, 2H, CO_2-C***H₂***), 3.46-3.82 (m, 2H, C***H₂***O), 3.38 (s, 3H, O-C***H₃***), 3.34 (q, 2H, CH_3-C***H₂***), 2.65 (m, 2H, C***H₂***-CO_2), 2.37-2.54 (m, 2H, C(CN)-C***H₂***), 1.88 (s, 3H, C***H₃***-C(CN)), 1.36 (t, 3H, C***H₃***-CH_2). FT-IR (neat): ν (cm^{-1}) 2882 (C-H, PEG chain), 1736 (C=O), 1098 (C-O-C). SEC (5 mM NH_4BF_4 in DMF, λ = 309 nm) $M_{n,\,SEC\ RI}$ = 12.4 kg mol^{-1}, $Đ_{M\ RI}$ = 1.05.

Outer membrane protein F (OmpF) purification

Endogenous OmpF was isolated and purified from *Escherichia coli* BL21. Cells were grown at 37 °C in Luria-Bertani medium until late exponential phase, then harvested by centrifugation for 30 min at 6,000 × g and resuspended in PBS. The cells were lysed by passing through a microfluidiser (Constant Systems) and the membrane fraction was recovered by ultracentrifugation for 30 min at 100,000 × g. The outer membrane was enriched by washing the pellet twice with 0.5% (w/v) SDS in 50 mM Tris (pH = 7.4). The remaining pellet was resuspended in 50 mM Tris (pH = 7.4), 8M urea and 1% (w/v) dodecylmaltoside (DDM), then dialyzed at room temperature overnight against 50 mM Tris (pH = 7.4). Aggregated protein was removed by ultracentrifugation for 30 min at 100,000 × g, leaving OmpF in solution. Remaining bound lipids and LPS were removed by ethanol precipitation. OmpF was diluted 1:10 into cold 95% (v/v) ethanol, incubated at -20 °C for 30 min and then centrifuged for 15 min at 4 °C and 15,000 × g. The supernatant was discarded and the pellet air-dried before resuspending into 0.02%

(w/v) (= 0.39 mM) DDM in 20 mM sodium phosphate (pH = 6.0). SDS-PAGE and native mass spectrometry confirmed the purified OmpF was trimeric and SDS- and proteinase K-resistant.

OmpF SDS-PAGE and protease resistance assay test

Purified OmpF samples were loaded on to a 12% pre-cast SDS-PAGE gel (Serva), either with or without heating to 95 °C for 10 min. Non-boiled OmpF was resistant to unfolding by SDS and ran with an apparent molecular weight of 73 kDa. Boiled samples denatured to the monomer and ran at the expected molecular weight of 37 kDa. OmpF was also tested for protease resistance by incubating 100 μL of purified protein for 10 min with 10U of Proteinase K immobilized on Eupergit® C. The resin was removed by centrifugation and the OmpF loaded on to the SDS-PAGE gel with or without heating. Non-boiled OmpF was resistant to degradation by proteinase K.

Kinetic colorimetric analyses for determination of activity of HRP-loaded vesicles

Purified empty, HRP-loaded and OmpF-functionalized + HRP-loaded PEG_{113}-*b*-$PHPMA_{400}$ vesicles at 20× dilution (0.5 wt% solids content), 40× dilution (0.25 wt% solids content) or 100× dilution (0.1 wt% solids content) in 100 mM PB (pH = 5.5) (120 μL) were diluted with 100 mM PB (pH = 5.5) (20 μL) in a 96-well plate microwell. *O*-dianisidine (2 mM, 40 μL) was then added. Finally, a 35 wt% aqueous solution of hydrogen peroxide (20 μL) was added and the change in absorbance at λ = 492 nm was recorded every two minutes using a plate reader. All measurements were performed in quadruplicate.

Supplementary Data for PEG_{113}-*b*-$PHPMA_{400}$ Vesicles Formed in DI Water

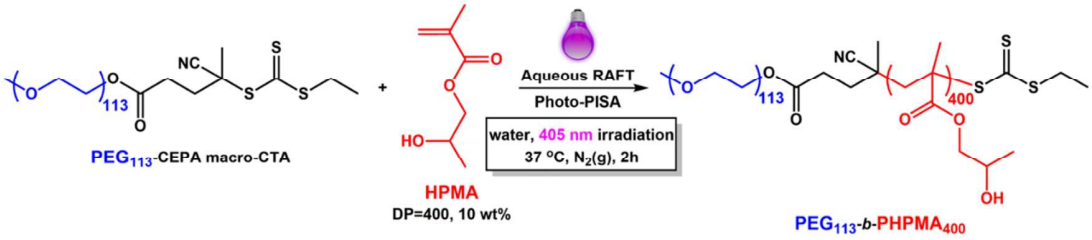

Scheme S1. Synthesis of PEG_{113}-*b*-$PHPMA_{400}$ diblock copolymer nano-objects by aqueous RAFT-mediated photo-PISA using PEG_{113}-CEPA mCTA and [HPMA] = 10 wt%.

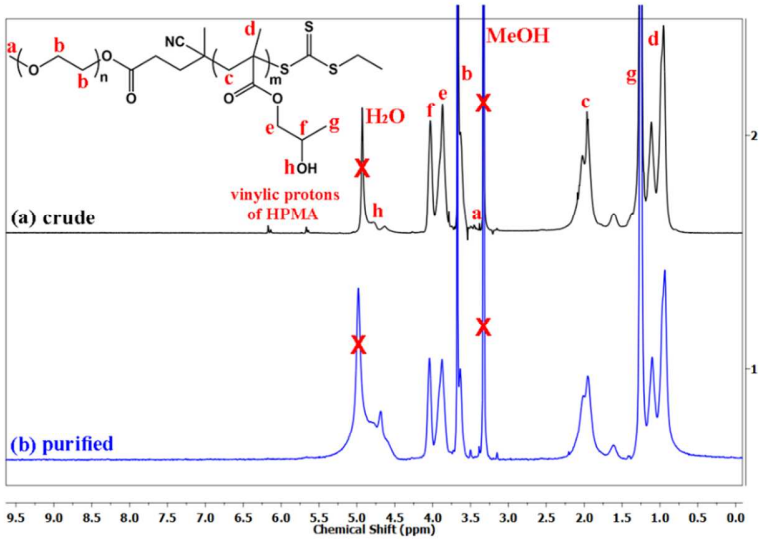

Figure S1. (a) Conversion ^{1}H-NMR spectrum of crude PEG_{113}-*b*-$PHPMA_{400}$ diblock copolymer in methanol-d_4. (b) ^{1}H-NMR spectrum of PEG_{113}-*b*-$PHPMA_{400}$ diblock copolymer in methanol-d_4 after purification by centrifugation/resuspension cycles in DI water for monomer removal.

Table S1. Molecular characteristics of PEG_{113}-CEPA mCTA and PEG_{113}-*b*-$PHPMA_{400}$ diblock copolymers formed in DI water, as determined by SEC analysis.

Sample	$M_{n,\ SEC\ RI}$[a] ($\times 10^3$ g mol^{-1})	$Đ_{M\ RI}$[a]	$M_{n,\ SEC\ UV}$[a] ($\times 10^3$ g mol^{-1})	$Đ_{M\ UV}$[a]
PEG_{113} mCTA	12.4	1.05	12.7	1.04
PEG_{113}-$PHPMA_{400}$ in DI water	80.1	1.25	79.0	1.23

[a]Calculated M_n and $Đ_M$ values from PMMA standards using 5 mM NH_4BF_4 in DMF as the eluent with UV detection at 309 nm

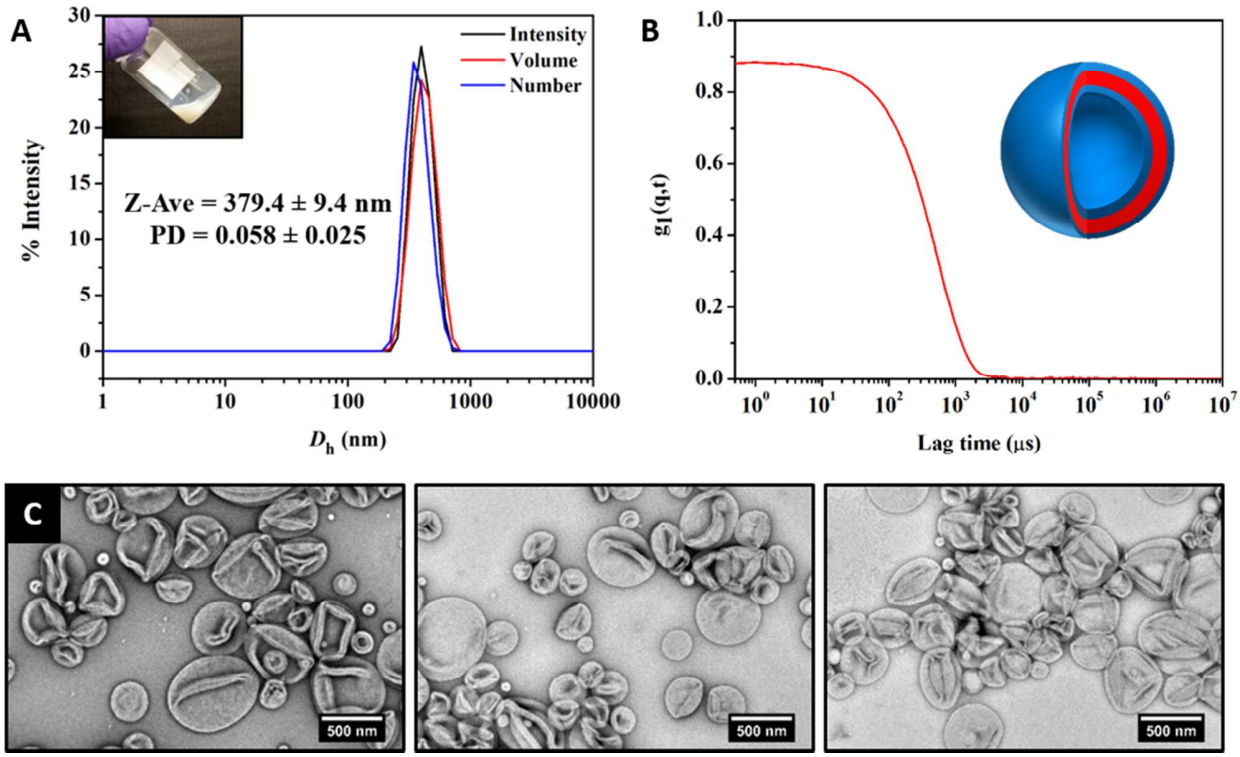

Figure S2. (A) Intensity-weighted size distributions of purified PEG_{113}-*b*-$PHPMA_{400}$ vesicles in DI water obtained by DLS, along with the average D_h and PD values (the error shows the standard deviation from 5 repeat measurements) (*inset:* vial containing PEG_{113}-*b*-$PHPMA_{400}$ vesicle solution after photo-PISA in DI water at 11 wt% solids content) and (B) DLS autocorrelation function. (C) Representative dry-state TEM images of purified PEG_{113}-*b*-$PHPMA_{400}$ vesicles in DI water, stained with 1 wt% UA.

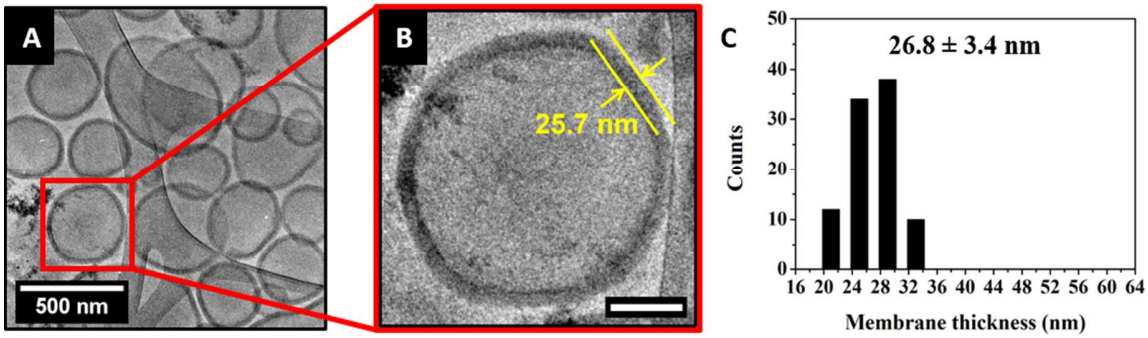

Figure S3. (A) Representative cryo-TEM image of purified PEG_{113}-*b*-$PHPMA_{400}$ unilamellar vesicles in deionized water. (B) Zoomed cryo-TEM image of an individual vesicle for the determination of bilayer membrane thickness from statistical analysis (the scale bar represents 100 nm). (C) Distribution of vesicles' membrane thicknesses measured from statistical analysis, along with the calculated average bilayer thickness (the error shows the standard deviation from ~100 particle membranes).

Supplementary Data for PEG_{113}-*b*-$PHPMA_{400}$ Nano-Objects Formed in Surfactant Solutions

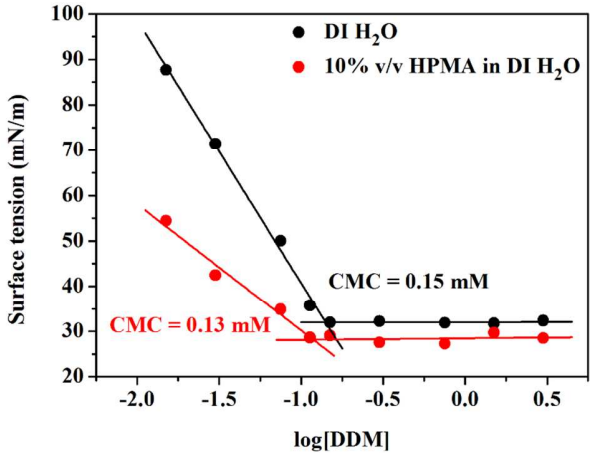

Figure S4. Surface tension measurements for the determination of CMC of DDM in DI water (black line) (*ca*. CMC = 0.15 mM) and 10% v/v HPMA in water (red line) (*ca*. CMC = 0.13 mM).

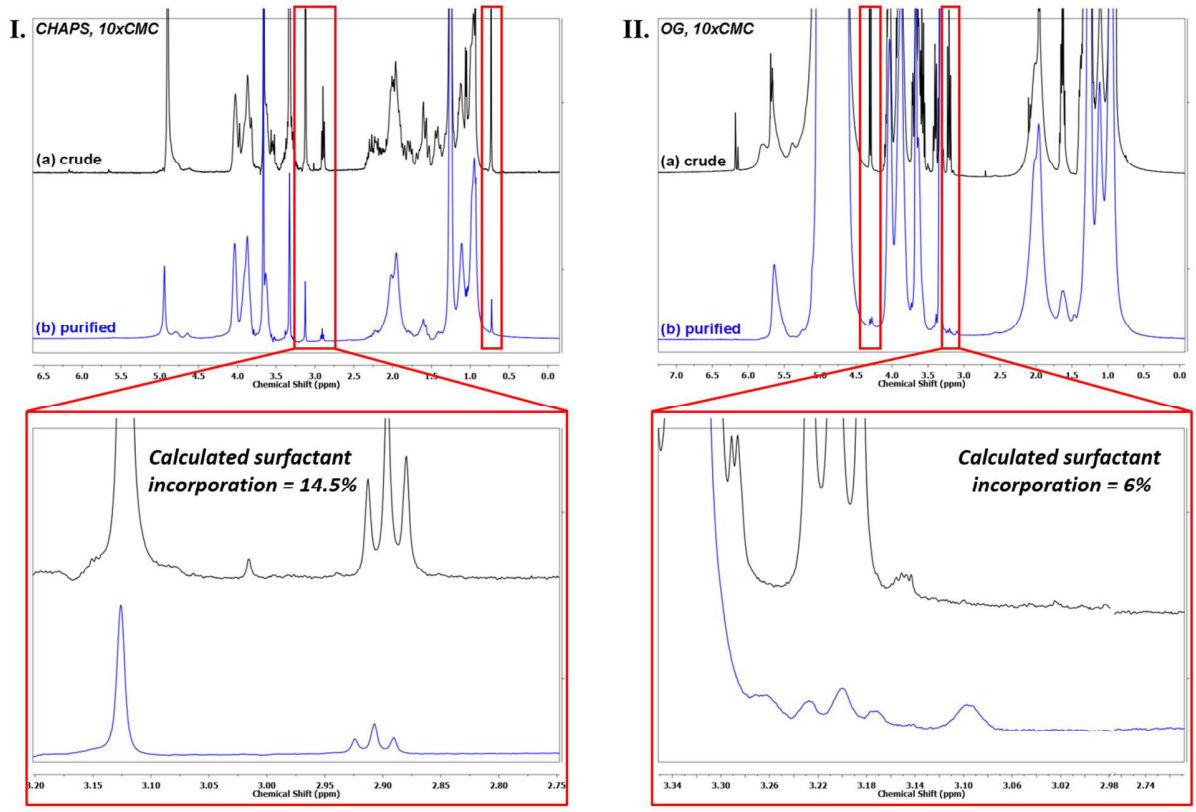

Figure S5. ^{1}H-NMR spectra of (a) crude and (b) purified PEG_{113}-*b*-$PHPMA_{400}$ diblock copolymers in methanol-d_4 at (I) [CHAPS] = 10×CMC and (II) [OG] = 10×CMC for estimation of surfactant incorporation (the peaks in red squares are solely attributed to surfactant molecules and were used in determination of incorporation in each case).

Table S2. Summary of final monomer conversions after photo-PISA in surfactant solutions as assessed by ^{1}H-NMR spectroscopy in methanol-d_4, after 2h of reaction.

Non-Ionic Surfactants					
[Triton™ X-100] (mM)	**Monomer Conversion**	**[DDM] (mM)**	**Monomer Conversion**	**[OG] (mM)**	**Monomer Conversion**
0.02	98%	0.015	> 99%	1.8	99%
0.04	99%	0.15 **(CMC)**	> 99%	18.0 **(CMC)**	> 99%
0.2 **(CMC)**	> 99%	0.3	99%	180.0	98%
0.4	98%	1.5	97%	-	-
2.0	98%	-	-	-	-
Ionic Surfactants					
[SDS] (mM)	**Monomer Conversion**	**[CTAB] (mM)**	**Monomer Conversion**		
0.82	97%	0.08	> 99%		
8.2 **(CMC)**	97%	0.8 **(CMC)**	> 99%		
82.0	96%	8.0	99%		
Zwitterionic Surfactants					
[DPC] (mM)	**Monomer Conversion**	**[CHAPS] (mM)**	**Monomer Conversion**		
0.15	> 99%	0.8	> 99%		
1.5 **(CMC)**	98%	8.0 **(CMC)**	> 99%		
2.0	98%	80.0	97%		
5.0	98%	160.0	70% - ***2h*** > 99% - ***18h***		
15.0	97%	-	-		
30.0	96%	-	-		

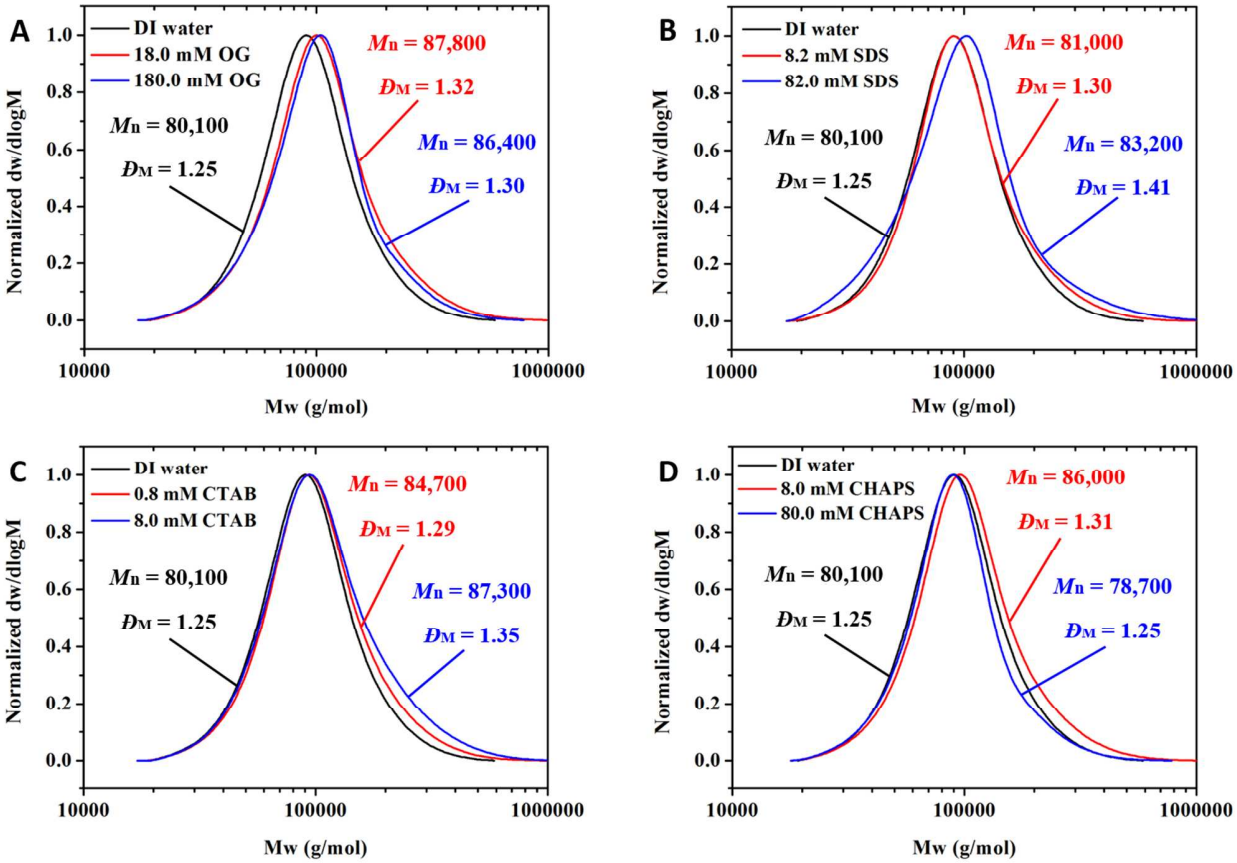

Figure S6. Representative SEC RI traces for PEG_{113}-*b*-$PHPMA_{400}$ diblock copolymers synthesized in presence of OG (A), SDS (B), CTAB (C) and CHAPS (D) at $C_{surf.}$ = CMC and 10×CMC in each case, along with the corresponding M_n (g mol^{-1}) and $Đ_M$ values. M_n and $Đ_M$ values were calculated from PMMA standards using 5 mM NH_4BF_4 in DMF as the eluent.

Supplementary dry-state TEM images:

Non-Ionic Surfactants:

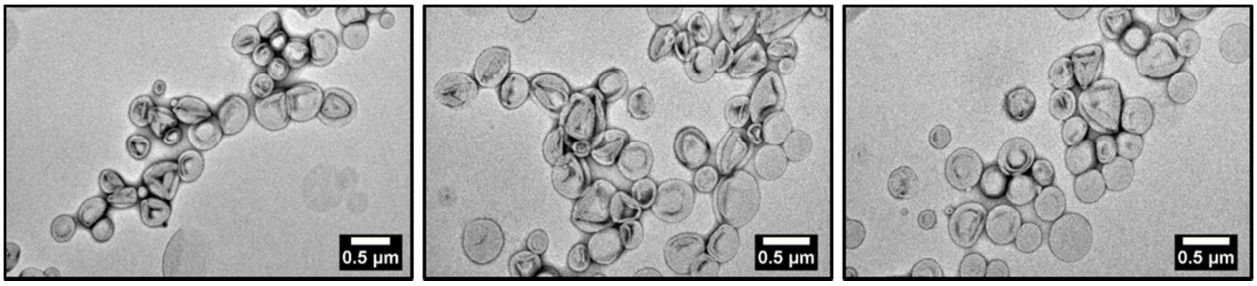

Figure S7. Representative dry-state TEM images of purified PEG_{113}-*b*-$PHPMA_{400}$ nano-objects formed in [Triton™ X-100] = 0.2 mM (= CMC), stained with 1 wt% UA. *Observed morphology:* ULVs.

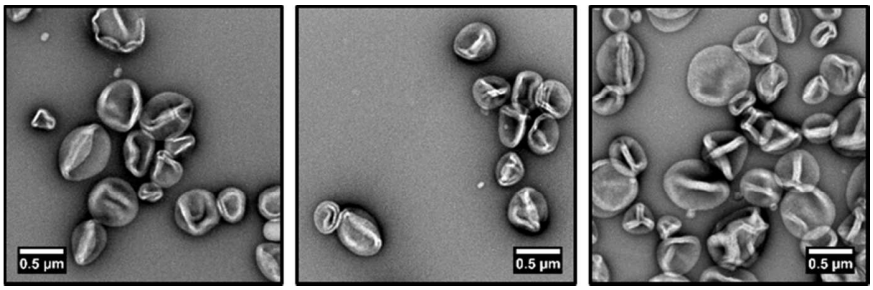

Figure S8. Representative dry-state TEM images of purified PEG_{113}-*b*-$PHPMA_{400}$ nano-objects formed in [Triton™ X-100] = 2.0 mM (= 10×CMC), stained with 1 wt% UA. *Observed morphology:* ULVs.

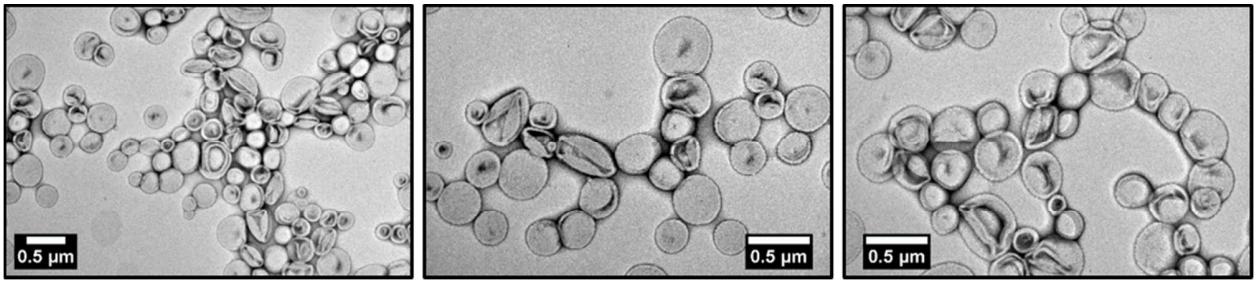

Figure S9. Representative dry-state TEM images of purified PEG_{113}-*b*-$PHPMA_{400}$ nano-objects formed in [DDM] = 0.15 mM (= CMC), stained with 1 wt% UA. *Observed morphology:* ULVs.

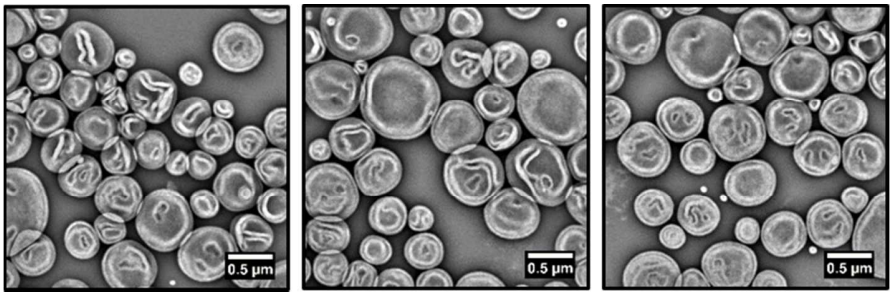

Figure S10. Representative dry-state TEM images of purified PEG_{113}-*b*-$PHPMA_{400}$ nano-objects formed in [DDM] = 1.5 mM (= 10×CMC), stained with 1 wt% UA. *Observed morphology:* ULVs.

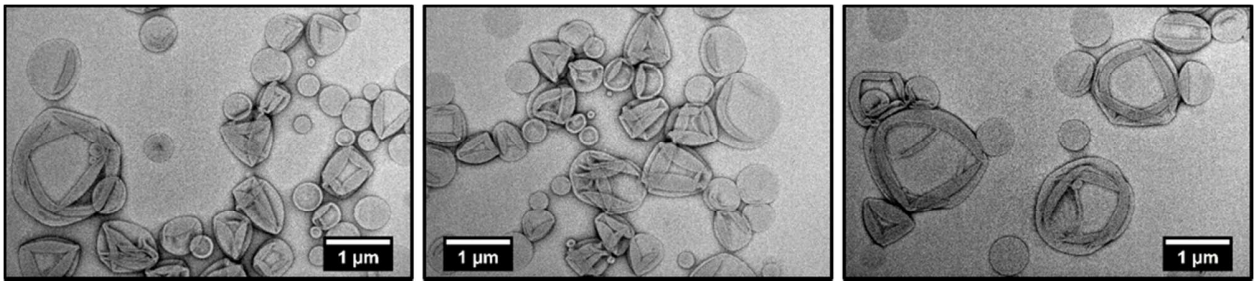

Figure S11. Representative dry-state TEM images of purified PEG_{113}-*b*-$PHPMA_{400}$ nano-objects formed in [OG] = 18.0 mM (= CMC), stained with 1 wt% UA. *Observed morphology:* GULVs.

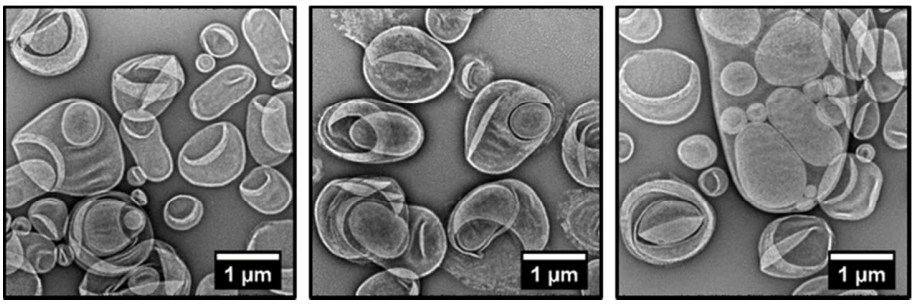

Figure S12. Representative dry-state TEM images of purified PEG_{113}-*b*-$PHPMA_{400}$ nano-objects formed in [OG] = 180.0 mM (= 10×CMC), stained with 1 wt% UA. *Observed morphology:* Mixed (GULVs + MLVs).

Ionic Surfactants:

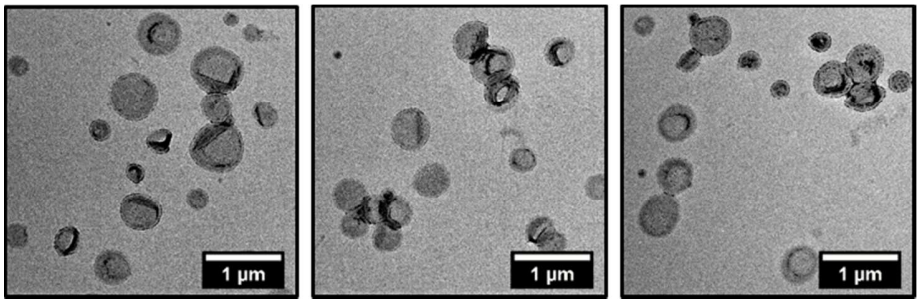

Figure S13. Representative dry-state TEM images of purified PEG_{113}-*b*-$PHPMA_{400}$ nano-objects formed in [SDS] = 0.82 mM (= 0.1×CMC), stained with 1 wt% UA. *Observed morphology:* ULVs.

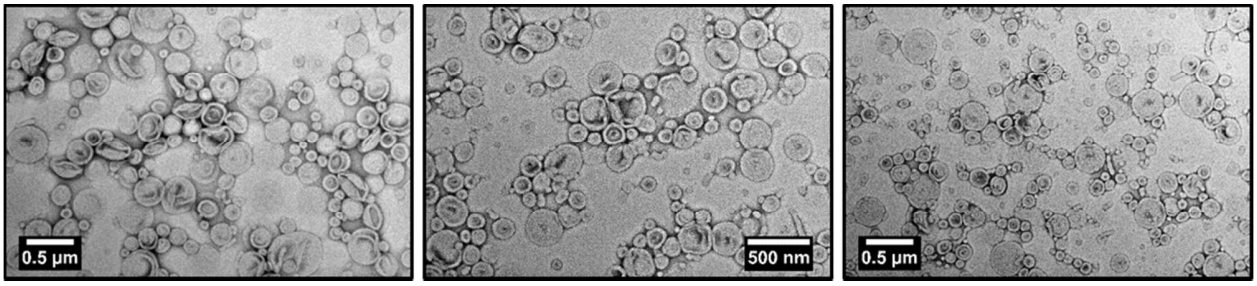

Figure S14. Representative dry-state TEM images of purified PEG_{113}-*b*-$PHPMA_{400}$ nano-objects formed in [SDS] = 8.2 mM (= CMC), stained with 1 wt% UA. *Observed morphology:* Mixed (S + W + ULVs).

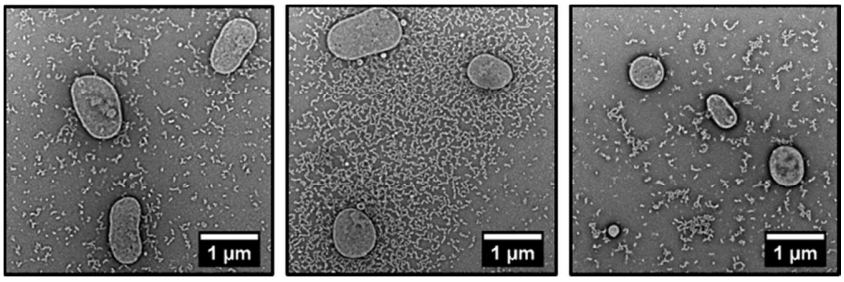

Figure S15. Representative dry-state TEM images of purified PEG_{113}-*b*-$PHPMA_{400}$ nano-objects formed in [SDS] = 82.0 mM (= 10×CMC), stained with 1 wt% UA. *Observed morphology:* Mixed (S + W + ULVs).

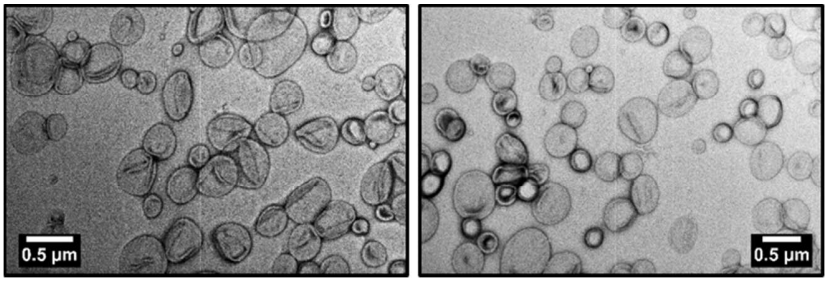

Figure S16. Representative dry-state TEM images of purified PEG_{113}-*b*-$PHPMA_{400}$ nano-objects formed in [CTAB] = 0.08 mM (= 0.1×CMC), stained with 1 wt% UA. *Observed morphology:* ULVs.

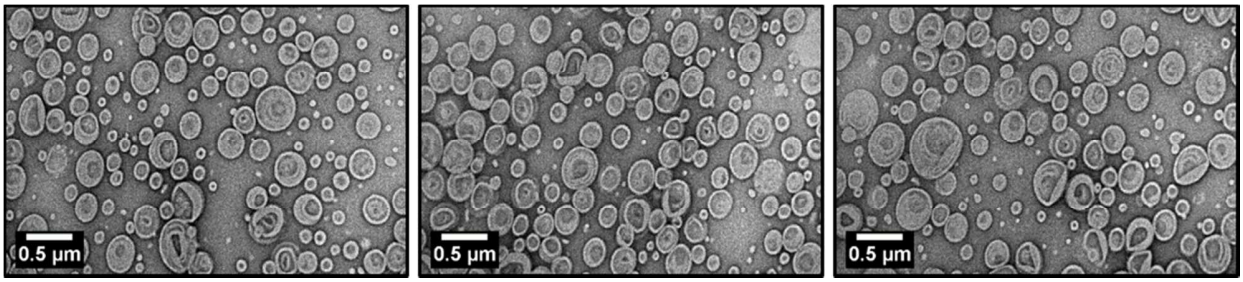

Figure S17. Representative dry-state TEM images of purified PEG_{113}-*b*-$PHPMA_{400}$ nano-objects formed in [CTAB] = 0.8 mM (= CMC), stained with 1 wt% UA. *Observed morphology:* Mixed (S + ULVs).

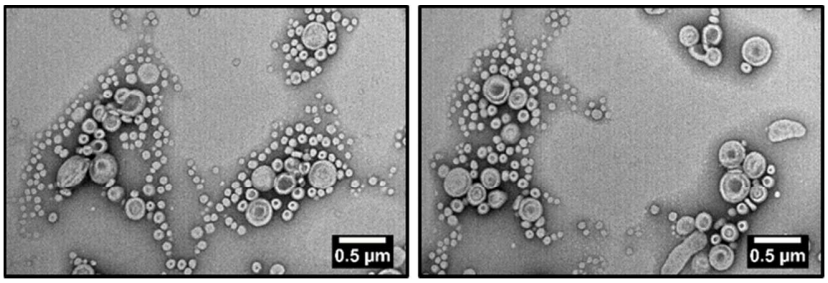

Figure S18. Representative dry-state TEM images of purified PEG_{113}-*b*-$PHPMA_{400}$ nano-objects formed in [CTAB] = 8.0 mM (= 10×CMC), stained with 1 wt% UA. *Observed morphology:* Mixed (S + ULVs).

Zwitterionic Surfactants:

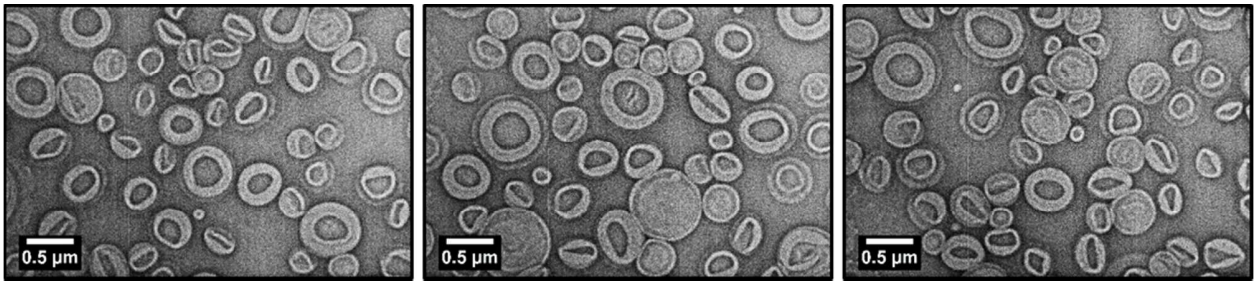

Figure S19. Representative dry-state TEM images of PEG_{113}-*b*-$PHPMA_{400}$ nano-objects formed in [CHAPS] = 8.0 mM (= CMC), stained with 1 wt% UA. *Observed morphology:* ULVs.

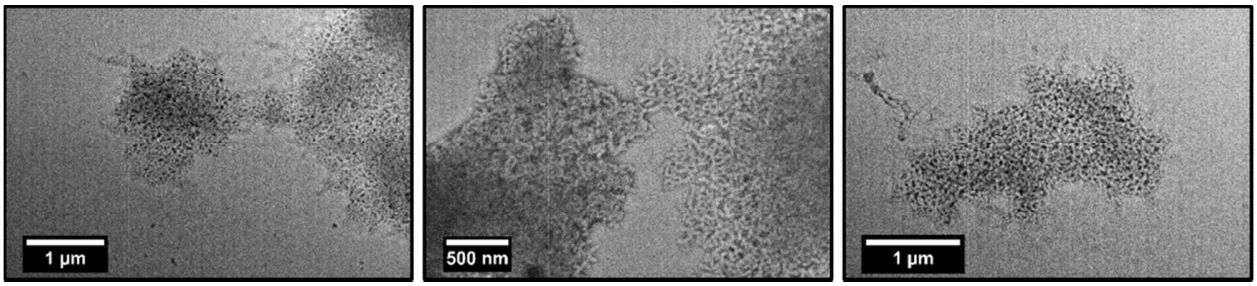

Figure S20. Representative dry-state TEM images of PEG_{113}-*b*-$PHPMA_{400}$ nano-objects formed in [CHAPS] = 80.0 mM (= 10×CMC), stained with 1 wt% UA. *Observed morphology:* W.

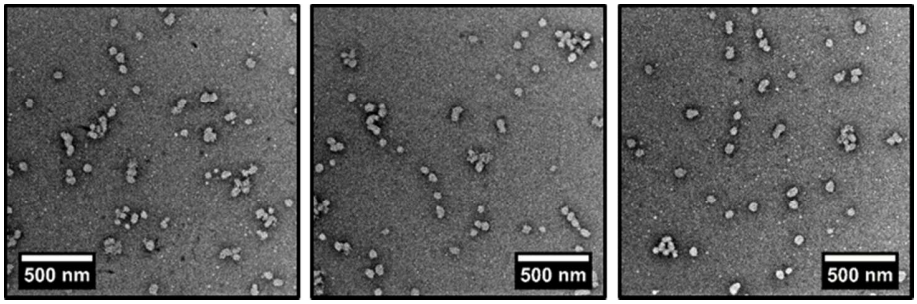

Figure S21. Representative dry-state TEM images of PEG_{113}-*b*-$PHPMA_{400}$ nano-objects formed in [CHAPS] = 160.0 mM (= 20×CMC) **after 2h** of reaction time, stained with 1 wt% UA. *Observed morphology:* S.

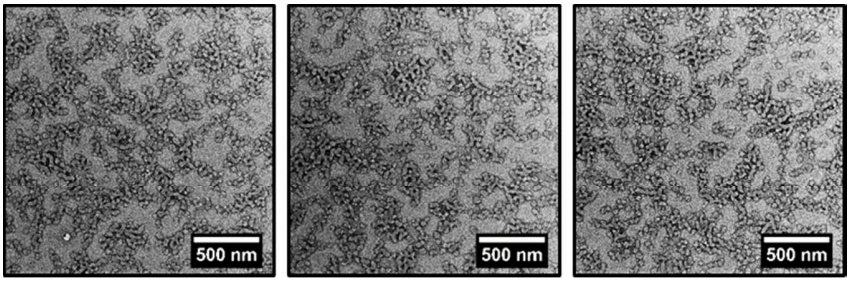

Figure S22. Representative dry-state TEM images of PEG_{113}-*b*-$PHPMA_{400}$ nano-objects formed in [CHAPS] = 160.0 mM (= 20×CMC) **after 18h** of reaction time, stained with 1 wt% UA. *Observed morphology:* Mixed (S + short W).

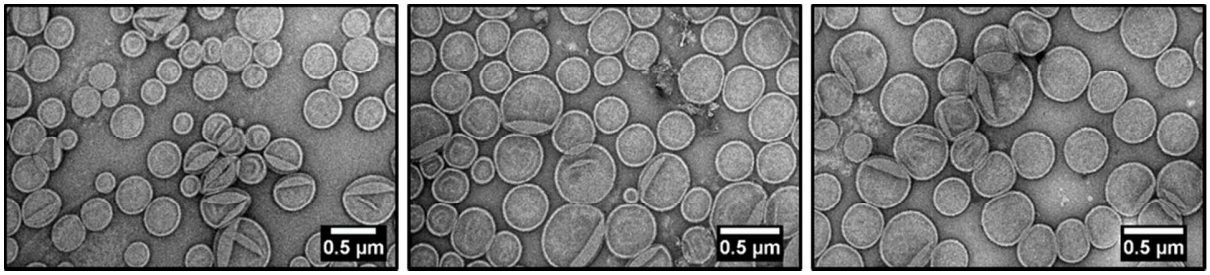

Figure S23. Representative dry-state TEM images of purified PEG_{113}-*b*-$PHPMA_{400}$ nano-objects formed in [DPC] = 1.5 mM (= CMC), stained with 1 wt% UA. *Observed morphology:* ULVs.

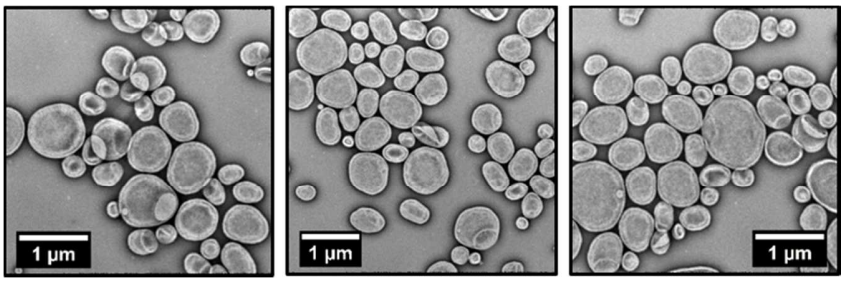

Figure S24. Representative dry-state TEM images of purified PEG_{113}-*b*-$PHPMA_{400}$ nano-objects formed in [DPC] = 15.0 mM (= 10×CMC), stained with 1 wt% UA. *Observed morphology:* ULVs.

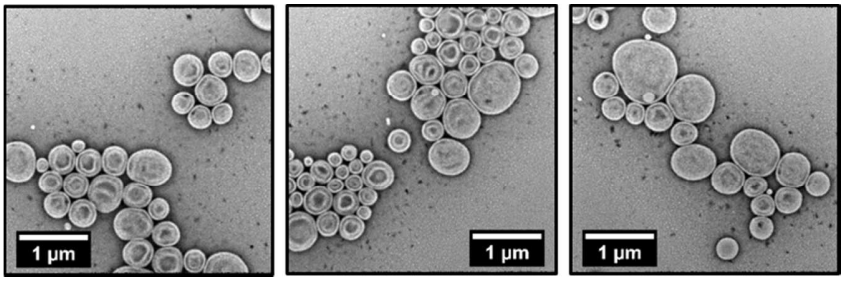

Figure S25. Representative dry-state TEM images of purified PEG_{113}-*b*-$PHPMA_{400}$ nano-objects formed in [DPC] = 30.0 mM (= 20×CMC), stained with 1 wt% UA. *Observed morphology:* ULVs.

Supplementary cryo-TEM images:

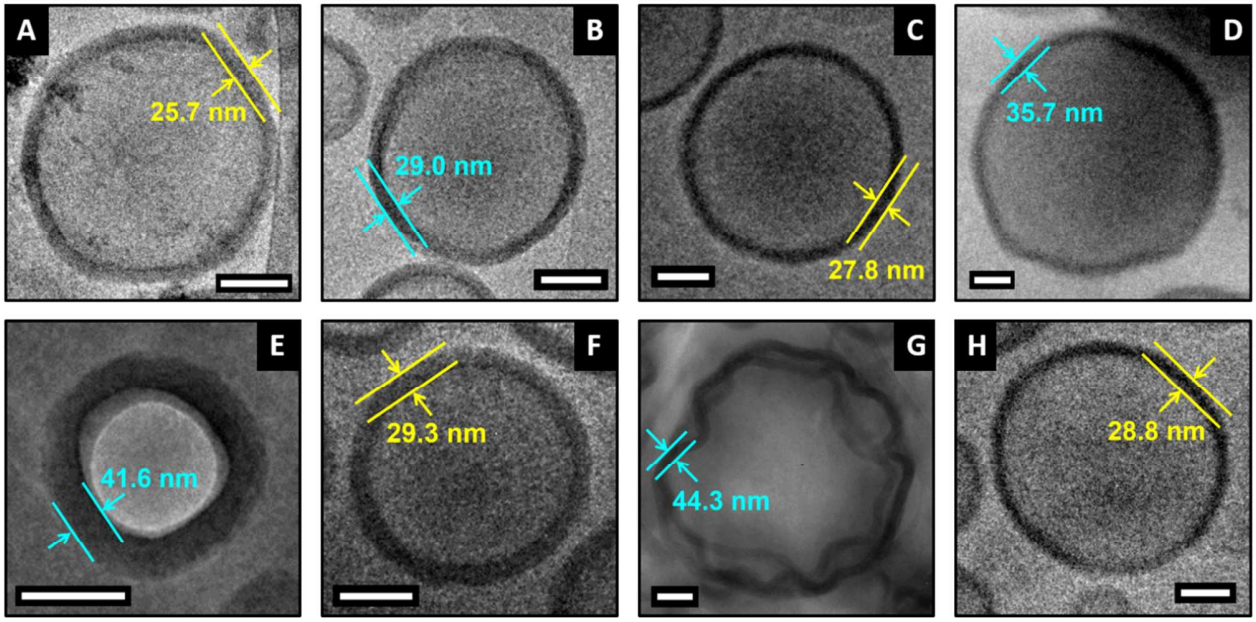

Figure S26. Representative zoomed cryo-TEM images of individual PEG_{113}-*b*-$PHPMA_{400}$ vesicles developed in DI water (A), Triton™ X-100 (B), DDM (C), OG (D), SDS (E), CTAB (F), CHAPS (G) and DPC (H) at $C_{surf.}$ = CMC for the determination of bilayer membrane thickness from statistical analysis (scale bars represent 100 nm in each case).

Table S3. Summary of observed morphologies of PEG_{113}-*b*-$PHPMA_{400}$ nano-objects developed by photo-PISA in different surfactant solutions, as judged by dry-state and cryogenic-transmission electron microscopy.

Non-Ionic Surfactants					
[Triton™ X-100] (mM)	**Morphology**	**[DDM] (mM)**	**Morphology**	**[OG] (mM)**	**Morphology**
0.02	ULVs	0.015	ULVs	1.8	ULVs
0.04	ULVs	0.15 **(CMC)**	ULVs	18.0 **(CMC)**	GULVs
0.2 **(CMC)**	ULVs	0.3	ULVs	180.0	GULVs + MLVs
0.4	ULVs	1.5	ULVs	-	-
2.0	ULVs	-	-	-	-
Ionic Surfactants					
[SDS] (mM)	**Morphology**	**[CTAB] (mM)**	**Morphology**		
0.82	ULVs	0.08	ULVs		
8.2 **(CMC)**	S + W + ULVs	0.8 **(CMC)**	S + ULVs		
82.0	S + W + ULVs	8.0	S + ULVs		
Zwitterionic Surfactants					
[DPC] (mM)	**Morphology**	**[CHAPS] (mM)**	**Morphology**		
0.15	ULVs	0.8	ULVs		
1.5 **(CMC)**	ULVs	8.0 **(CMC)**	ULVs		
2.0	ULVs	80.0	W		
5.0	ULVs	160.0	S - ***2h*** S + W - ***18h***		
15.0	ULVs	-	-		
30.0	ULVs	-	-		

Abbreviations - **S:** spherical micelles, **W:** worm-like micelles, **ULVs:** unilamellar vesicles, **GULVs:** giant unilamellar vesicles, **MLVs:** multilamellar vesicles

Supplementary Data for OmpF Porin Reconstitution into PEG_{113}-*b*-$PHPMA_{400}$ Vesicles

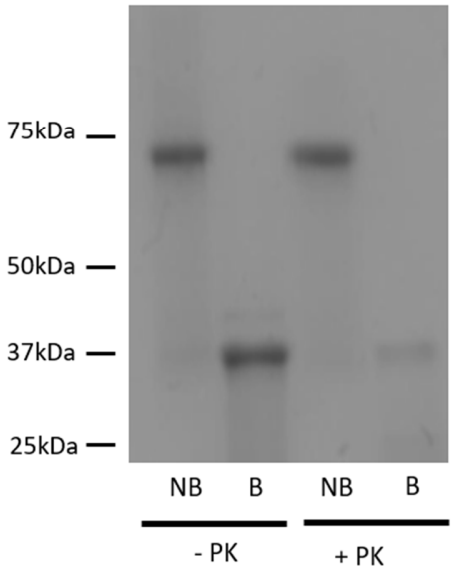

Figure S27. SDS-PAGE gel and protease resistance assay of purified folded (non-boiled, NB) and denatured (boiled, B) OmpF showing the trimer/monomer transition and OmpF trimer resistance to degradation by proteinase K.

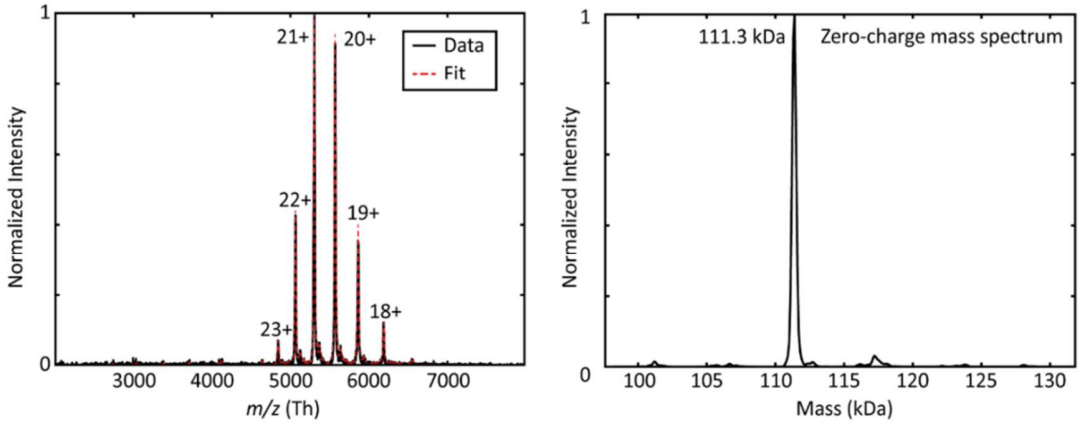

Figure S28. Native mass spectra of purified OmpF porin confirming the successful isolation of the trimeric structure (MW of trimer = 111.3 kDa).

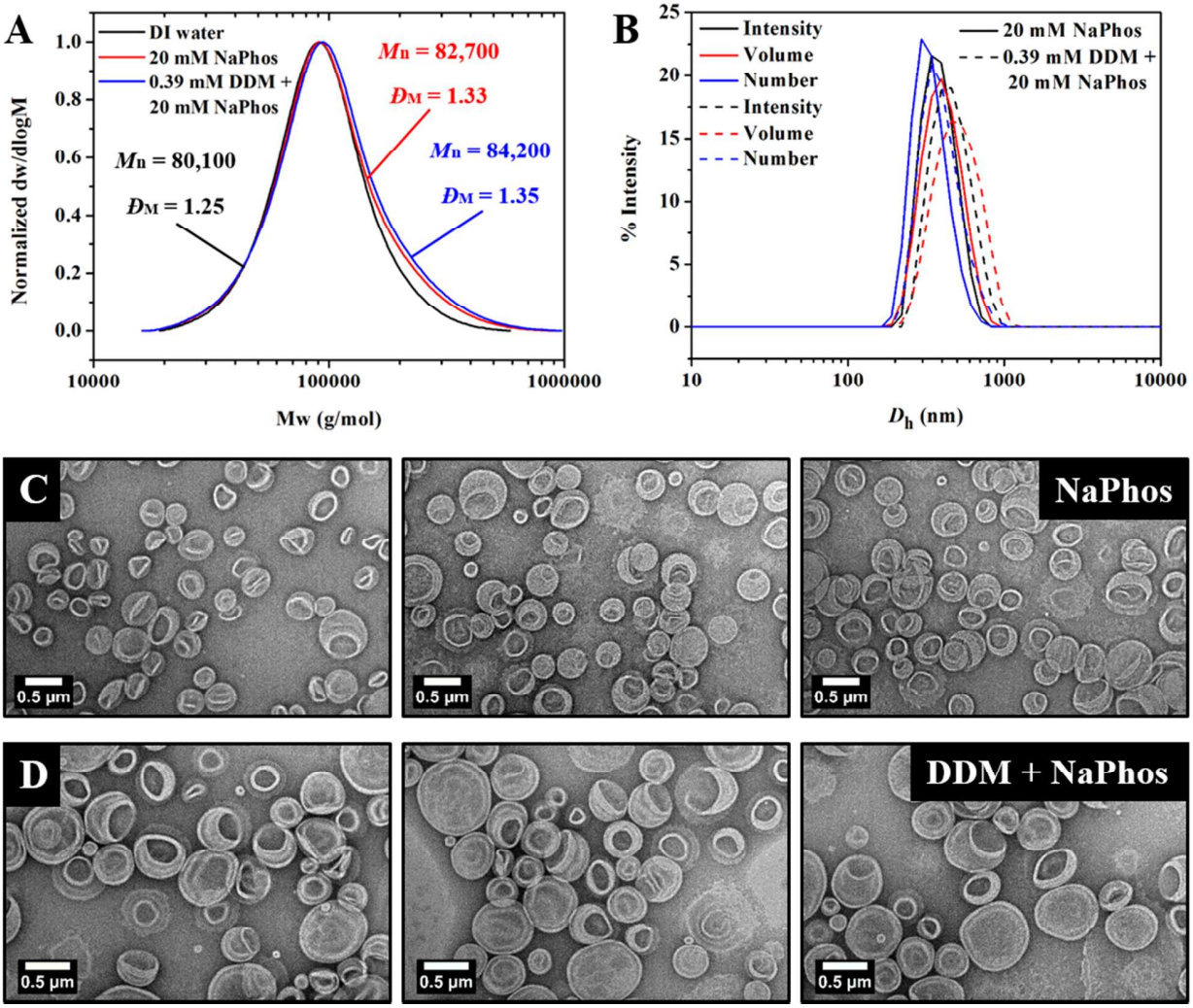

Figure S29. (A) Representative SEC RI traces for PEG_{113}-*b*-$PHPMA_{400}$ diblock copolymers synthesized in 20 mM NaPhos (pH = 6.0) and 0.39 mM DDM + 20 mM NaPhos (pH = 6.0), along with the corresponding M_n (g mol^{-1}) and $Đ_M$ values. M_n and $Đ_M$ values were calculated from PMMA standards using 5 mM NH_4BF_4 in DMF as the eluent. (B) Intensity-weighted size distributions of purified PEG_{113}-*b*-$PHPMA_{400}$ vesicles in 20 mM NaPhos (pH = 6.0) and 0.39 mM DDM + 20 mM NaPhos (pH = 6.0), obtained by DLS. (C) Representative dry-state TEM images of purified PEG_{113}-*b*-$PHPMA_{400}$ vesicles formed in 20 mM NaPhos (pH = 6.0), stained with 1 wt% UA. (D) Representative dry-state TEM images of purified PEG_{113}-*b*-$PHPMA_{400}$ vesicles formed in 0.39 mM DDM + 20 mM NaPhos (pH = 6.0), stained with 1 wt% UA.

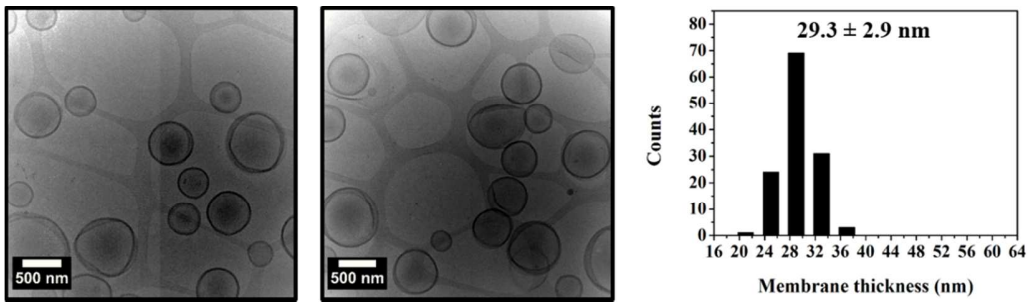

Figure S30. Representative cryo-TEM images of purified PEG_{113}-*b*-$PHPMA_{400}$ vesicles formed in 0.39 mM DDM + 20 mM NaPhos (pH = 6.0), and distribution of vesicles' membrane thicknesses measured from statistical analysis, along with the calculated average bilayer thickness (the error shows the standard deviation from ~150 particle membranes).

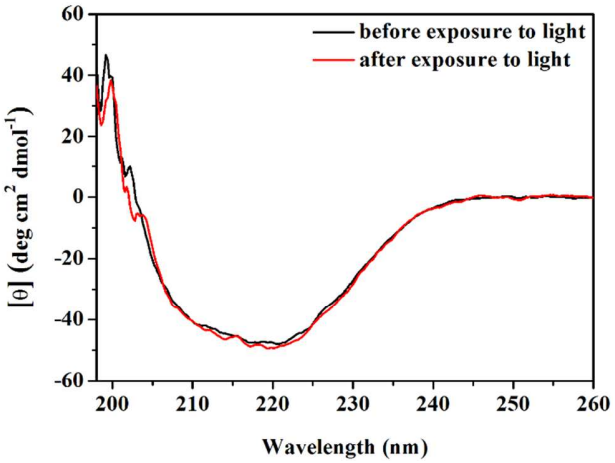

Figure S31. Circular dichroism (CD) spectra of OmpF porin stabilized in 0.39 mM DDM + 20 mM NaPhos (pH = 6.0) before (black line) and after (red line) exposure to 405 nm irradiation for 2 h, showing no light-induced change in secondary structure of OmpF.

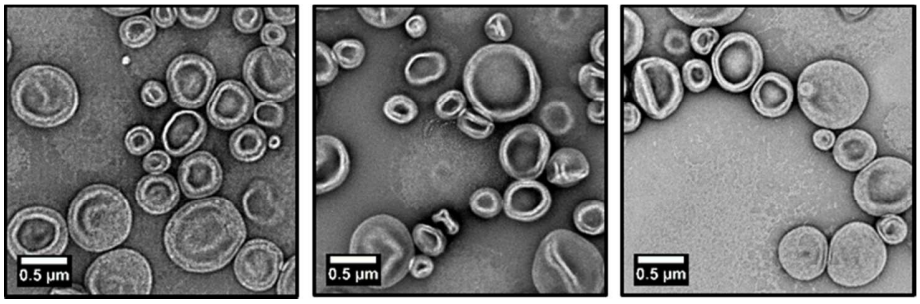

Figure S32. Representative dry-state TEM images of HRP-loaded + OmpF-functionalized PEG_{113}-*b*-$PHPMA_{400}$ unilamellar vesicles formed in DDM + NaPhos aqueous solution, stained with 1 wt% UA.

References

[1] Reading, E.; Liko, I.; Allison, T. M.; Benesch, J. L.; Laganowsky, A.; Robinson, C. V. The Role of the Detergent Micelle in Preserving the Structure of Membrane Proteins in the Gas Phase. *Angew. Chem. Int. Ed*. **2015**, *54*, 4577-4581.

[2] Johnson, R. N.; Burke, R. S.; Convertine, A. J.; Hoffman, A. S.; Stayton, P. S.; Pun, S. H. Synthesis of Statistical Copolymers Containing Multiple Functional Peptides for Nucleic Acid Delivery. *Biomacromolecules* **2010**, *11*, 3007-3013.

[3] Tan, J.; Sun, H.; Sumerlin, B. S.; Zhang, L. Photo-PISA: Shedding Light on Polymerization-Induced Self-Assembly. *ACS Macro Lett*. **2015**, *4*, 1249-1253.

[4] Blackman, L. D.; Doncom, K. E. B.; Gibson, M. I.; O'Reilly, R. K. Comparison of Photo- and Thermally Initiated Polymerization-Induced Self-Assembly: A Lack of End Group Fidelity Drives the Formation of Higher Order Morphologies. *Polym. Chem*. **2017**, *8*, 2860-2871.

Chapter 3. Tuning the Membrane Permeability of Polymersome Nanoreactors Developed by Aqueous Emulsion Polymerization-Induced Self-Assembly

3.1. Publication Details and Overview

Title: Tuning the membrane permeability of polymersome nanoreactors developed by aqueous emulsion polymerization-induced self-assembly

Authors: **Spyridon Varlas**,[†] Jeffrey C. Foster,[†] Panagiotis G. Georgiou,[†,‡] Robert Keogh,[†,‡] Jonathan T. Husband,[†] David S. Williams,[†,§] and Rachel K. O'Reilly*[,†]

Affiliations: [†]School of Chemistry, University of Birmingham, Edgbaston, Birmingham B15 2TT, United Kingdom

[‡]Department of Chemistry, University of Warwick, Gibbet Hill Road, Coventry CV4 7AL, United Kingdom

[§]Department of Chemistry, College of Science, Swansea University, Swansea SA2 8PP, United Kingdom

Journal: Nanoscale

Year: 2019

Volume: 11

Page Numbers: 12643-12654

DOI: 10.1039/C9NR02507C

Submitted: 22nd March 2019, **Published:** 15th June 2019

Coauthor Contributions: Part of the modification reactions of epoxy-functionalized polymersome nanoreactors using hydrophobic primary amines were performed with assistance from Mr. Panagiotis G. Georgiou at the University of Birmingham. Cryo-TEM imaging of polymersome nanoreactors was performed with assistance from Dr. Robert Keogh and Dr. Saskia Bakker at the University of Warwick. HPLC traces and MALDI-ToF mass spectra of HRP before and after reaction with glycidol were acquired by Mr. Jonathan T. Husband at the University of Birmingham. The design of Michaelis-Menten kinetics determination experiments and discussion of obtained kinetic data were carried out with assistance from Dr. Jeffrey C. Foster and Dr. David S. Williams at the University of Birmingham. Optical microscopy imaging of the initial monomer-in-water emulsion solution was performed with assistance from Dr. Maria C. Arno at the University of Birmingham. The design and construction of the photoreactor used for the photoinitiated polymerizations was carried out by Mr. Rod Wesson at the University of Warwick. Dr. Jeffrey C. Foster (University of Birmingham) and Dr. David S. Williams (Swansea

University) provided guidance and editing of this manuscript. Prof. Rachel K. O'Reilly (University of Birmingham) supervised the research project, provided guidance and editing of this manuscript.

Overview: Initial reports of our group on the design of enzyme-loaded polymersome nanoreactors *via* aqueous photo-PISA that could serve as rudimentary cell/organelle-mimicking models have revealed that the membranes of such nanostructures commonly presented inherent, unrestrained permeability toward small molecules (e.g., substrates and catalysis products) owing to the relatively hydrated core-forming PHPMA block. In this Chapter, a procedurally facile methodology is presented that allowed for precise control over the permeability and other main membrane characteristics of polymersome nanoreactors developed *via* aqueous RAFT-mediated photo-PISA, such as their chemical composition, hydrophobicity and thickness, that addresses this emerging challenge and, thus, extends the scope of such confined formulations in cell-mimicry, controlled drug delivery and other therapeutic applications.

In particular, our thoroughly investigated PEG-*b*-PHPMA polymersome system was further reformed upon introduction of water-immiscible glycidyl methacrylate (GlyMA) as a second core-forming co-monomer during aqueous emulsion photo-PISA under otherwise identical reaction conditions. Importantly, preparation of HRP-loaded PEG-*b*-P(HPMA-*co*-GlyMA) polymersomes with similar membrane thickness, but also increased core domain hydrophobicity compared to their PEG-*b*-PHPMA counterparts was achieved, resulting in nano-objects with reduced membrane permeability. In addition, the presence of pendant epoxide groups within the block copolymer nanostructures could further facilitate post-PISA membrane functionalization based on

simple epoxide ring-opening reactions using a series of primary amines of varying hydrophobicity. The utilized procedure was found to be non-detrimental for both the assemblies and the sensitive encapsulated cargo, whilst water-insoluble aromatic amines could also be effectively used in aqueous nanoparticle dispersions due to their sequestration within the hydrophobic polymersome membranes.

Careful selection of the amine modifiers used in this study has allowed for the identification of important structure-property relationships, enabling the correlation between the hydrophobicity of the nucleophile, the polymersome membrane thickness and, ultimately, their permeability toward small molecules, as judged by enzymatic activity determination assays. Notably, the most hydrophobic amines led to a marked increase in membrane thickness and density and, as an extent, to near complete blockage of the membrane diffusivity owing to the development of strong non-covalent interactions between introduced aromatic units within the polymer chains. Therefore, the approach discussed in Chapter 3 could be potentially applied for the design of size-selective compartmentalized nanoplatforms that would be able to retain small molecules, such as drugs, fluorophores, or ions, for prolonged periods of time for various biomedical applications, whereby sustained release of the encapsulated cargo is deemed of paramount importance. It should be also noted that attempts to introduce OmpF channels within the impermeable polymersomes developed in this Chapter to re-enable the passive diffusion of small molecules across their membranes, following the process described in Chapter 2, were not successful (data not shown) most possibly due to a significant mismatch between the length of the protein and the thickness of the polymersome membranes, preventing the proper function of reconstituted OmpF.

Nanoscale

PAPER

View Article Online
View Journal | View Issue

Cite this: *Nanoscale*, 2019, **11**, 12643

Tuning the membrane permeability of polymersome nanoreactors developed by aqueous emulsion polymerization-induced self-assembly†

Spyridon Varlas, [a] Jeffrey C. Foster, [a] Panagiotis G. Georgiou, [a,b] Robert Keogh,[a,b] Jonathan T. Husband, [a] David S. Williams[a,c] and Rachel K. O'Reilly *[a]

Polymeric vesicles (or polymersomes) are hollow bilayer structures consisting of an inner aqueous compartment enclosed by a hydrophobic membrane. Vesicular constructs are ubiquitous in nature and perform a variety of functions by compartmentalizing molecules into disparate environments. For polymer chemists, the synthesis of vesicles can be readily accomplished using polymerization-induced self-assembly (PISA), whereby pure vesicle morphologies can be easily accessed by tuning initial reaction parameters. Research into polymersomes is motivated primarily by the fact that hydrophilic cargo such as drug molecules, DNA, or enzymes can be encapsulated and protected from the often harsh conditions of the surrounding environment. A key factor governing the capability of vesicles to retain and protect their cargo is the permeability of their hydrophobic membrane. Herein, we demonstrate that membrane permeability of enzyme-loaded epoxy-functionalized polymersomes synthesized by aqueous emulsion PISA can be modulated *via* epoxide ring-opening with various diamine cross-linkers and hydrophobic primary amines. In general, membrane cross-linking or amine conjugation resulted in increased polymersome membrane thickness. Membrane modification was also found to decrease permeability in all cases, as measured by enzymatically-catalysed oxidation of an externally administered substrate. Functionalization with hydrophobic amines resulted in the largest reduction in enzyme activity, suggesting significant blocking of substrate diffusion into the central aqueous compartment. This procedurally facile strategy yields meaningful insight into how the chemical structure of the membrane influences permeability and thus could be generally applied to the formulation of polymeric vesicles for therapeutic applications.

Received 22nd March 2019,
Accepted 13th June 2019

DOI: 10.1039/c9nr02507c

rsc.li/nanoscale

Introduction

Structural organization is an essential feature of nature's toolbox for maintaining all forms of life. Evolution of compartmentalized environments on both cellular and subcellular level (*i.e.* organelles) allows for vital biological reactions to occur selectively in confined spaces that simultaneously separate and protect them from external detrimental agents.[1,2] Communication and transport of energy, nutrients and other signaling molecules between such compartments is achieved *via* metabolic pathways that in most cases involve diffusion through semi-permeable or stimuli-responsive membranes.[2–4]

Inspired by nature, researchers have developed methodologies to design minimal synthetic analogues that mimic these complex systems.[5] Among them, self-assembled bilayer nanostructures such as liposomes and amphiphilic block copolymer vesicles (also referred to as polymersomes) have been studied extensively for their application as functional artificial organelles and catalytic nanoreactors due to their ability to incorporate both hydrophilic and hydrophobic molecules into their domains.[6–12] Additionally, polymersomes have attracted significant research interest owing to their higher chemical versatility, physical stability and more facile functionalization in comparison to liposomes.[13–15]

Until recently, preparation of polymeric vesicles was achieved by multi-step conventional block copolymer self-assembly strategies in solution, such as solvent-switch or thin-film rehydration, at low polymer concentrations (≤1% w/w)

[a]*School of Chemistry, University of Birmingham, B15 2TT, Birmingham, UK. E-mail: r.oreilly@bham.ac.uk*
[b]*Department of Chemistry, University of Warwick, Gibbet Hill Road, CV4 7AL, Coventry, UK*
[c]*Department of Chemistry, College of Science, Swansea University, SA2 8PP, Swansea, UK*

†Electronic supplementary information (ESI) available: Materials and methods, supplementary NMR, FT-IR and DLS data, additional dry-state and cryo-TEM images, and HRP control experiment activity results. See DOI: 10.1039/c9nr02507c

that in the majority of cases require the use of organic solvents.[16–20] Over recent years, aqueous polymerization-induced self-assembly (PISA) has been established as a powerful single-step approach for *in situ* fabrication of block copolymer nano-objects at high solids concentrations (typically 10–30% w/w) that allows for access to higher-order morphologies, such as worm-like micelles and polymersomes, in a reproducible manner.[21–26]

In particular, development of single-phase block copolymer vesicles *via* PISA in dispersed aqueous media has been primarily achieved using reversible addition–fragmentation chain-transfer (RAFT) polymerization,[22,27,28] as well as non-radical methodologies such as ring-opening metathesis polymerization (ROMP).[29,30] However, a limited number of reports centered upon polymersomes prepared under emulsion PISA conditions have been introduced in the literature thus far,[31–34] while the factors that allow for higher-order morphologies other than kinetically trapped spheres to be accessed under emulsion polymerization conditions remain currently unclear.

Importantly, different methodologies to conduct visible-light initiated PISA (photo-PISA) for synthesis of nano-objects at ambient reaction temperatures either by using special photoinitiators and photoredox catalysts or *via* the "photoiniferter" mechanism of chain transfer agents (CTAs) have been recently reported.[35–41] Aqueous photo-PISA has enabled the direct non-disruptive encapsulation of inorganic nanoparticles,[36,42] as well as other sensitive (bio)molecules, such as fluorophores,[36,43] and proteins/enzymes,[43–48] into polymeric vesicles for the efficient construction of delivery vehicles, therapeutics, and catalytic nanoreactors with biologically relevant applications.[49]

To date, studies in the field of cell-mimicking enzyme-loaded polymersome nanoreactors have been pioneered and extensively investigated by the van Hest, Lecommandoux, Meier, Battaglia, and Voit groups.[50–54] The membranes of such nanoconstructs were rendered permeable toward substrate molecules and catalysis products upon incorporation of channel-forming transmembrane proteins,[52,55] DNA nanopores,[56] or stimuli-responsive moieties[51,54] into their hydrophobic domains. Furthermore, a few reports were based upon the inherent permeability of the polymersome membranes for passive diffusion of small molecules between their outer and inner aqueous compartments.[57,58]

More recently, our group has demonstrated the preparation of enzyme-loaded poly(ethylene glycol)-*b*-poly(2-hydroxypropyl methacrylate) (PEG-*b*-PHPMA) nanoreactors *via* one-pot aqueous photo-PISA that were able to communicate through their inherently permeable and relatively hydrated membranes, allowing for catalytic cascade reactions to occur inside separated compartments.[43] Moreover, encapsulation of a therapeutic enzyme into the same system resulted in nanoreactors intended for leukemia treatment, whilst protection of the cargo from antibody binding and proteolytic degradation owing to the size-selective permeability of the PHPMA membrane was also presented.[46] In a different study by our group, incorporation of a channel-forming porin protein into the membrane of PEG-*b*-PHPMA vesicles led to a significant permeability enhancement.[47] Other attempts to enhance the membrane permeability of PISA polymersomes by incorporating pH-responsive units into their core-forming blocks for drug release applications have also been reported recently.[59,60]

Herein, enzyme-loaded epoxy-functionalized polymersome nanoreactors of well-defined characteristics and inherent permeability were developed *via* aqueous RAFT-mediated emulsion photo-PISA at mild temperature using a mixture of 2-hydroxypropyl methacrylate (HPMA) and glycidyl methacrylate (GlyMA) as the core-forming monomers. The pendant epoxide groups of PGlyMA units provided a reactive handle for straightforward post-PISA functionalization of the membrane through nucleophilic ring-opening reactions induced by a series of primary amines and cross-linking diamines.[61–63] In all cases, modification of the chemical composition of the core-forming block resulted in a distinct increase of vesicular membrane thickness and as a consequence in less-hydrated nanoreactors with tunable permeability toward small molecule substrates, as determined by enzymatic assays. Enhanced blocking efficiency was evident upon increasing the hydrophobicity of the nucleophile employed, allowing for identification of valuable structure–property relationships. Overall, our findings expand the current knowledge on membrane characteristics of semi-permeable nanocompartments and could facilitate the design of biomembrane-mimicking nanostructures and artificial "nanofactories" with programmed size-selective permeability *via* one-pot PISA.

Experimental section

Materials and methods

Materials and characterization techniques used are included in the ESI.†

Synthetic procedures

Synthesis of poly(ethylene glycol)$_{113}$-based macromolecular chain transfer agent (PEG$_{113}$ macro-CTA). The synthesis of PEG$_{113}$ macro-CTA by *N*,*N*′-dicyclohexylcarbodiimide (DCC) coupling between poly(ethylene glycol) monomethyl ether (PEG$_{113}$-OH) and 4-cyano-4-[(ethylsulfanylthiocarbonyl)sulfanyl] pentanoic acid (CEPA) was performed according to previously reported experimental protocols by our group and others.[36,40]

Synthesis of PEG$_{113}$-*b*-P(HPMA$_{320}$-*co*-GlyMA$_{80}$) diblock copolymer vesicles by aqueous RAFT-mediated emulsion photoinitiated polymerization-induced self-assembly (photo-PISA). Photo-PISA reactions were performed in a custom-built photoreactor setup. This ensured the polymerization solutions were only exposed to the light from the 400–410 nm LED source placed underneath the vials. The detailed description of the photoreactor setup specifications is given in the ESI.†

A typical synthetic procedure to achieve epoxy-functionalized PEG$_{113}$-*b*-P(HPMA$_{320}$-*co*-GlyMA$_{80}$) diblock copolymer vesicles at [solids] = 10% w/w *via* aqueous RAFT-mediated emul-

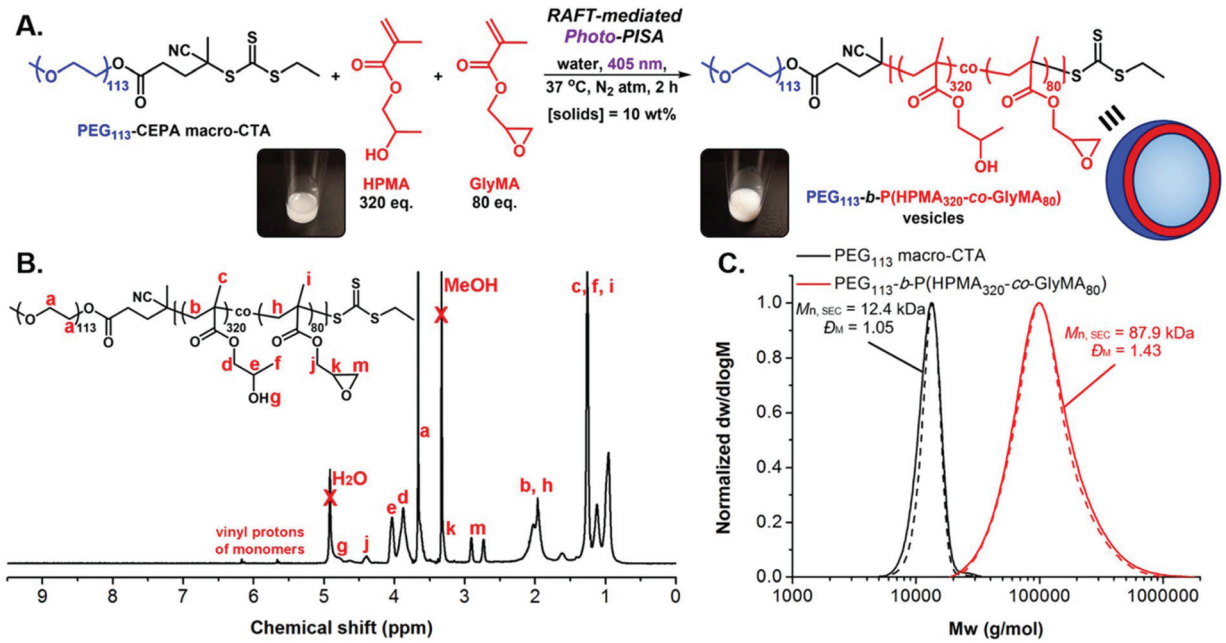

Fig. 1 (A) Schematic illustration of the synthetic route employed for the preparation of PEG_{113}-*b*-P($HPMA_{320}$-*co*-$GlyMA_{80}$) diblock copolymer vesicles at [solids] = 10% w/w *via* aqueous RAFT-mediated emulsion photo-PISA (405 nm irradiation), using a PEG_{113} macro-CTA. Insets show images of the polymerization solution vial before (left) and after (right) photo-PISA. (B) Conversion ^{1}H-NMR spectrum of crude PEG_{113}-*b*-P($HPMA_{320}$-*co*-$GlyMA_{80}$) diblock copolymer in methanol-d_4, showing near quantitative monomer consumption (>98%). (C) Normalized SEC RI (solid lines) and SEC UV (dashed lines) molecular weight distributions for PEG_{113} macro-CTA (black traces) and PEG_{113}-*b*-P($HPMA_{320}$-*co*-$GlyMA_{80}$) diblock copolymer (red traces), along with their corresponding M_n and $Đ_M$ values calculated based on PMMA standards using DMF + 5 mM NH_4BF_4 as the eluent.

sion photo-PISA is described (Fig. 1A).[43,47] PEG_{113} macro-CTA (9.1 mg, 1.7×10^{-6} mol, 1 eq.), HPMA (79 mg, 5.5×10^{-4} mol, 320 eq.) (80 mol%) and GlyMA (19.9 mg, 1.4×10^{-4} mol, 80 eq.) (20 mol%) were dispersed in deionized (DI) water (0.9 mL) with vigorous agitation using a vortex mixer for 2 min in a sealed 15 mL scintillation vial bearing a magnetic stirrer bar. The resulting monomer-in-water emulsion solution was degassed by sparging with N_2(g) for 15 min. The sealed vial was incubated at 37 °C with magnetic stirring under 405 nm light irradiation for 2 hours to ensure full monomer conversion. After this period, the reaction mixture was exposed to air and allowed to cool to room temperature. FT-IR, ^{1}H-NMR in methanol-d_4 and SEC analyses in DMF + 5 mM NH_4BF_4 of the pure diblock copolymers were performed after lyophilization of an aliquot of particles. DLS analysis and dry-state and cryo-TEM imaging were performed on samples after dilution to an appropriate analysis concentration. ^{1}H-NMR (400 MHz, methanol-d_4): δ (ppm) 4.78 (br s, O***H***), 4.40 (br s, CH_2 of PGlyMA side chain), 4.03 and 3.87 (br s, C***H*** and CH_2 of PHPMA side chain), 3.66 (br s, CH_2CH_2O of PEG), 3.33 (br s, C***H*** of PGlyMA epoxide ring), 2.91 and 2.73 (br s, CH_2 of PGlyMA epoxide ring) 2.30–1.80 (br m, CH_2 of PHPMA and PGlyMA backbone), 1.45–0.81 (br m, CH_3 of PHPMA and PGlyMA backbone and CH_3 of PHPMA side chain).

Encapsulation of horseradish peroxidase (HRP) into PEG_{113}-*b*-P($HPMA_{320}$-*co*-$GlyMA_{80}$) vesicles by one-pot aqueous RAFT-mediated emulsion photo-PISA. For the preparation of HRP-loaded PEG_{113}-*b*-P($HPMA_{320}$-*co*-$GlyMA_{80}$) nanoreactors by aqueous emulsion photo-PISA at 10% w/w solids content, a typical synthetic protocol was followed.[43] PEG_{113} macro-CTA (9.1 mg, 1.7×10^{-6} mol, 1 eq.), HPMA (79 mg, 5.5×10^{-4} mol, 320 eq.) (80 mol%) and GlyMA (19.9 mg, 1.4×10^{-4} mol, 80 eq.) (20 mol%) were dispersed in DI water (0.8 mL) with vigorous agitation using a vortex mixer for 2 min in a sealed 15 mL scintillation vial bearing a magnetic stirrer bar. Then, 0.1 mL of a 200 U mL^{-1} HRP solution in DI water was added. The resulting emulsion solution was degassed by sparging with N_2(g) for 15 min. The sealed vial was incubated at 37 °C with magnetic stirring under 405 nm light irradiation for 2 hours to ensure full monomer conversion. After this period, the reaction mixture was exposed to air and allowed to cool to room temperature. The resulting solution of HRP-loaded PEG_{113}-*b*-P($HPMA_{320}$-*co*-$GlyMA_{80}$) vesicles was then diluted 10-fold in DI water or 100 mM PB (pH = 5.5, PB 5.5) and purified, respectively, by three centrifugation/resuspension cycles in DI water or 100 mM PB 5.5 at 14 000 rpm for the removal of unreacted monomer and free HRP enzyme.

Post-PISA membrane functionalization of HRP-loaded PEG_{113}-*b*-P($HPMA_{320}$-*co*-$GlyMA_{80}$) vesicles *via* ring-opening of pendant epoxide groups using primary amines. Ring-opening of PGlyMA epoxide groups using a series of primary amines as nucleophiles for membrane functionalization of HRP-loaded PEG_{113}-*b*-P($HPMA_{320}$-*co*-$GlyMA_{80}$) vesicles was performed following a reported synthetic procedure.[61] In a typical experiment, benzylamine (6 mg, 5.6×10^{-5} mol) (BA) was added to a purified dispersion solution of HRP-loaded PEG_{113}-*b*-P

(HPMA$_{320}$-*co*-GlyMA$_{80}$) vesicles at 10× dilution (1% w/w solids content) in DI water (2 mL) ([amine]/[epoxide] molar ratio = 2.0). The mixture was then stirred at room temperature for 18 hours to allow for ring-opening of the epoxide groups and vesicle membrane functionalization. The resulting modified vesicles were then purified by one centrifugation/resuspension cycle in 100 mM PB 5.5 at 14 000 rpm prior to kinetic colorimetric analysis. Successful ring-opening of PGlyMA units was confirmed by FT-IR spectroscopy of a lyophilized sample. The above protocol was also followed for 1-naphthylmethylamine (NMA) and 1-adamantanemethylamine (AMA). In the case of cross-linking diamines poly(ethylene glycol)$_n$ diamine (n = 23, 46) (PEG$_n$DA), ethylenediamine (C$_2$DA), 1,3-diaminopropane (C$_3$DA), 1,4-diaminobutane (C$_4$DA), hexamethylenediamine (C$_6$DA), and *p*-xylylenediamine (PXDA), a [diamine]/[epoxide] molar ratio = 1.0 was maintained.

Kinetic colorimetric analyses for determination of the activity of HRP-loaded PEG$_{113}$-*b*-P(HPMA$_{320}$-*co*-GlyMA$_{80}$) vesicles before and after post-PISA membrane functionalization. Purified HRP-loaded PEG$_{113}$-*b*-P(HPMA$_{320}$-*co*-GlyMA$_{80}$) vesicles before and after post-PISA membrane functionalization at 20× dilution (0.5% w/w solids content) in 100 mM PB 5.5 (120 μL) were diluted with 100 mM PB 5.5 (20 μL) in a 96-well plate microwell. A fixed concentration of 3,3′-dimethoxybenzidine (DMB) (2 mM, 40 μL) was then added. Finally, a 35% w/v aqueous solution of hydrogen peroxide (20 μL) was added, and the change in absorbance at λ = 492 nm was recorded every minute for a period of 30 min using a plate reader. Absorbance values were corrected against particle absorbance at t = 0 min and reported as $\Delta Abs_{492\ nm}$.

For Michaelis–Menten kinetics determination, activity of purified HRP-loaded PEG$_{113}$-*b*-P(HPMA$_{320}$-*co*-GlyMA$_{80}$) vesicles before and after post-PISA membrane functionalization using BA, NMA, and PXDA was evaluated at different [DMB] (0–6 mM) with H_2O_2 under saturating conditions. Vesicles at 20× dilution (0.5% w/w solids content) in 100 mM PB 5.5 (120 μL) were diluted with 100 mM PB 5.5 (20 μL) in a 96-well plate microwell. DMB of appropriate concentration (0–30 mM, 40 μL) was then added. Finally, a 35% w/v aqueous solution of hydrogen peroxide (20 μL) was added, and the change in absorbance was monitored in an identical manner. Absorbance values were corrected against particle absorbance at t = 0 min and reported as $\Delta Abs_{492\ nm}$. In each case, the average initial slope of three repeat measurements (V_0) for the first 10 min of the assay was used for construction of Michaelis–Menten kinetic plots and was normalized against V_{max} (Table S3†). Calculated K_m^* values are presented as mean ± standard error.

A similar process was followed for activity testing of the free enzyme after a series of control experiments at appropriate [HRP]. The free HRP solutions at final [HRP] = 1 U mL^{-1} in 100 mM PB 5.5 (20 μL) were diluted with 100 mM PB 5.5 (120 μL) in a 96-well plate microwell. DMB (2 mM, 40 μL) was then added. Finally, a 35% w/v aqueous solution of hydrogen peroxide (20 μL) was added, and the change in absorbance was monitored in an identical manner. In all cases, measurements were performed in at least triplicate and results are reported as their average values.

Results and discussion

Synthesis of epoxy-functionalized PEG$_{113}$-*b*-P(HPMA$_{320}$-*co*-GlyMA$_{80}$) polymersomes *via* aqueous RAFT-mediated emulsion photo-PISA

Following related PISA studies previously reported by our group and others,[36,40] a water-soluble poly(ethylene glycol) macromolecular chain transfer agent (PEG$_{113}$ macro-CTA) was first synthesized through an esterification reaction between poly(ethylene glycol) monomethyl ether (PEG$_{113}$-OH) and an acid-functionalized CTA (esterification efficiency = 93%, $M_{n,\ SEC}$ = 12.4 kg mol^{-1}, $Đ_M$ = 1.05). Aqueous RAFT-mediated photoinitiated PISA (photo-PISA) of a mixture of commercially available water-miscible 2-hydroxypropyl methacrylate (HPMA) and water-immiscible glycidyl methacrylate (GlyMA) as the core-forming monomers was achieved under emulsion polymerization conditions, using PEG$_{113}$ macro-CTA as both the steric stabilizer block and the surfactant for stabilization of the heterogeneous monomer-in-water solution.[64] Dispersed monomer droplets of varying size (5–30 μm) were observed upon optical microscopy imaging of the formed emulsion solution prior to polymerization (Fig. S2†).

Single-phase epoxy-functionalized PEG$_{113}$-*b*-P(HPMA-*co*-GlyMA) diblock copolymer vesicles were developed upon irradiation of the polymerization solution under 405 nm visible light in the absence of an externally added photoinitiator or catalyst ("photoiniferter" mechanism of trithiocarbonates)[35,65,66] at 37 °C, targeting DP$_{PHPMA}$ = 320 (80 mol%) and DP$_{PGlyMA}$ = 80 (20 mol%) at 10% w/w solids content (Fig. 1A). Emulsion photo-PISA was carried out at mild temperature to ensure quantitative retention of epoxy functional groups, as epoxides can undergo partial hydrolysis in aqueous solution at elevated temperatures (60–100 °C).[61] Importantly, 99% of PGlyMA pendant epoxy groups remained intact after photo-PISA, as calculated from ^{1}H-NMR spectroscopy by comparing the integral ratio of the peaks corresponding to epoxy proton signals at 2.73 and 2.91 ppm ($I_{2.73/2.91\ ppm}$ = 1.98) to the peak of the methacrylic backbone –CH_2– protons at 1.50–2.30 ppm ($I_{1.50–2.30\ ppm}$ = 10.00) (Fig. S3†). A kinetic study revealed that near complete monomer conversion (>98%) was achieved after 2 hours of irradiation time, as calculated by ^{1}H-NMR spectroscopy, whilst the onset of particle micellization accompanied by an increase in polymerization rate was observed after ∼20 min of irradiation time (*ca.* 17% monomer conversion) (Fig. 1B and S4A†). The distribution of PGlyMA units along the growing polymer chain was also investigated during kinetics monitoring and the calculated HPMA/GlyMA molar ratio varied between 3 and 4 throughout the whole duration of photo-PISA, suggesting the formation of random copolymers (Fig. S4B†). The prepared PEG$_{113}$-*b*-P(HPMA$_{320}$-*co*-GlyMA$_{80}$) diblock copolymer possessed monomodal molecular weight distribution with

relatively low dispersity value, as determined by SEC analysis ($M_{n,\,SEC}$ = 87.9 kg mol^{-1}, $Đ_M$ = 1.43) (Fig. 1C).

Dynamic light scattering (DLS) analysis revealed the formation of nano-objects with a monomodal size distribution and mean hydrodynamic diameter (D_h) of 188.3 ± 5.6 nm, low polydispersity (PD = 0.18 ± 0.02) and a smooth, single exponential decay autocorrelation function with optimal signal-to-noise ratio (Y-intercept >0.9) (Fig. 2A and B). The absence of charges on the outer surface of the developed particles was confirmed by microelectrophoretic analysis at neutral pH (measured zeta-potential = −1.87 ± 0.10 mV). Dry-state transmission electron microscopy (TEM) imaging confirmed the successful development of well-defined PEG$_{113}$-*b*-P(HPMA$_{320}$-*co*-GlyMA$_{80}$) unilamellar vesicles of spherical shape and uniform size ($D_{dry\text{-}state}$ = 170.3 ± 23.0 nm) (Fig. 2C and S5A†). Additionally, the characteristics of PEG$_{113}$-*b*-P(HPMA$_{320}$-*co*-GlyMA$_{80}$) vesicles in solution were studied by cryogenic TEM (cryo-TEM) imaging. Average vesicle size measured from particle counting analysis based on cryo-TEM was in good agreement with values determined by DLS and dry-state TEM analyses (D_{cryo} = 175.5 ± 24.1 nm), while calculated average membrane thickness was M_{ave} = 28.0 ± 3.0 nm (Fig. 2D–F and S5B†).

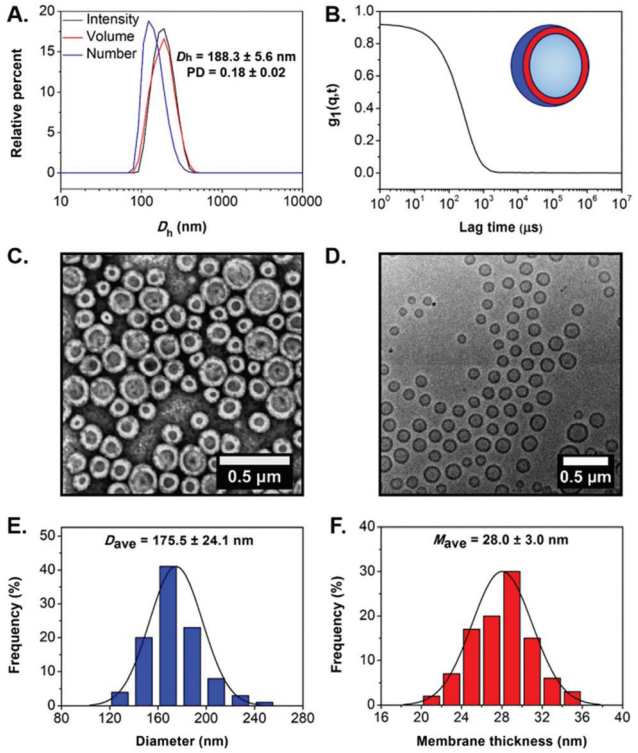

Fig. 2 (A) Intensity-weighted size distributions along with average D_h and PD values (the error shows the standard deviation from 5 repeat measurements), and (B) autocorrelation function obtained by DLS for empty PEG$_{113}$-*b*-P(HPMA$_{320}$-*co*-GlyMA$_{80}$) vesicles. (C) Representative dry-state TEM image, stained with 1 wt% uranyl acetate (UA) solution, and (D) representative cryo-TEM image of empty PEG$_{113}$-*b*-P(HPMA$_{320}$-*co*-GlyMA$_{80}$) vesicles. (E) Histogram of size distribution, and (F) histogram of membrane thickness distribution along with calculated average diameter and membrane thickness values, respectively, measured from particle analysis based on cryo-TEM images for empty PEG$_{113}$-*b*-P(HPMA$_{320}$-*co*-GlyMA$_{80}$) vesicles. In each case, at least 100 particles were analyzed.

Preparation of catalytic enzyme-loaded PEG$_{113}$-*b*-P(HPMA$_{320}$-*co*-GlyMA$_{80}$) polymersome nanoreactors *via* one-pot aqueous emulsion photo-PISA

Next, PEG$_{113}$-*b*-P(HPMA$_{320}$-*co*-GlyMA$_{80}$) polymersomes were used as a nanocarrier platform for loading of a model hydrophilic enzyme to prepare catalytically active epoxy-functionalized nanoreactors.[43,47] Enzyme horseradish peroxidase (HRP) was encapsulated into the inner aqueous compartment of the vesicles by performing a one-pot emulsion photo-PISA process under the same mild reaction conditions described herein in the presence of an aqueous HRP solution for the development of enzyme-loaded PEG$_{113}$-*b*-P(HPMA$_{320}$-*co*-GlyMA$_{80}$) polymersome nanoreactors. Purification of the vesicle sample for complete removal of free HRP was achieved by consecutive centrifugation/resuspension cycles in either deionized (DI) water or 100 mM phosphate buffer (pH = 5.5, PB 5.5).

Importantly, the encapsulation process of HRP into PEG$_{113}$-*b*-P(HPMA$_{320}$-*co*-GlyMA$_{80}$) polymersomes did not alter their overall characteristics as judged by DLS analysis and TEM imaging (Fig. S6†). Comparable D_h and PD values were measured for HRP-loaded vesicles with respect to non-HRP-loaded vesicles (D_h = 182.6 ± 2.5 nm, and PD = 0.14 ± 0.04), whilst average vesicle size and average membrane thickness measured from cryo-TEM images were D_{cryo} = 172.5 ± 25.5 nm and M_{ave} = 27.9 ± 2.6 nm, respectively.

HRP is known to catalyze the oxidation reaction of colourless substrate 3,3′-dimethoxybenzidine (DMB) to a coloured dimer product (red-brown), which can be monitored by measuring the change in absorbance at λ = 492 nm over time *via* kinetic colorimetric analysis. This assay provides a read-out of enzyme activity and consequently of polymersome membrane permeability. Notably, PEG$_{113}$-*b*-P(HPMA$_{320}$-*co*-GlyMA$_{80}$) vesicles were found to be inherently permeable toward small molecule DMB, although they presented reduced enzyme activity compared to their reported PEG$_{113}$-*b*-PHPMA$_{400}$ counterparts presumably due to increased membrane hydrophobicity in the former case.[43] Although nanoreactors with near identical membrane thickness values were developed in both cases, the presence of an additional hydrophobic core-block component in the case of PEG$_{113}$-*b*-P(HPMA$_{320}$-*co*-GlyMA$_{80}$) vesicles resulted in particles with less hydrated membranes and reduced permeability, making the exchange of substrates between their outer and inner compartment a more difficult process.[47] Control experiments to assess the activity of free HRP after incubation at 37 °C for 2 hours in 10% w/w HPMA or HPMA/GlyMA (80 : 20 molar ratio) monomer solutions in DI water under 405 nm irradiation (photo-PISA conditions) revealed quantitative retention of activity in both cases compared to untreated enzyme, showing that the enzyme function was not affected by either monomer (Fig. S7†). In addition, high-performance liquid chromatography (HPLC)

and matrix-assisted laser desorption/ionization time-of-flight mass spectrometry (MALDI-ToF MS) were employed to determine potential modification of HRP by ring-opening of the epoxide groups *via* its lysine residues. Notably, incubation of free HRP with a water-soluble small molecule epoxide (glycidol) for 2 hours in DI water showed no evident modification upon comparison with the untreated enzyme (Fig. S8†).

Membrane functionalization of enzyme-loaded PEG_{113}-*b*-P($HPMA_{320}$-*co*-$GlyMA_{80}$) vesicles *via* ring-opening of epoxide groups using primary amines

Incorporation of PGlyMA units and thus the presence of pendant epoxy groups within the hydrophobic membrane of prepared HRP-loaded nanoreactors provides a reactive handle that allows for post-PISA functionalization of the polymersomes with nucleophilic compounds. A commonly utilized procedure involves the ring-opening of epoxide groups by primary amines under mild reaction conditions.[61–63] To this extent, we envisioned that introducing hydrophobic or cross-linking moieties into the polymersome membrane would result in permeability reduction or nanoreactors completely impermeable toward small molecules.

A series of commercially available primary amines and diamines (cross-linking agents) of varying hydrophobicity were chosen as nucleophiles for ring-opening of PGlyMA epoxy groups and subsequent vesicle membrane modification (Scheme 1). Post-polymerization functionalization was achieved by mixing purified HRP-loaded PEG_{113}-*b*-P($HPMA_{320}$-*co*-$GlyMA_{80}$) vesicle solutions in DI water at [solids] = 1% w/w with different amines at room temperature for 18 hours. In all cases, the [amine]/[epoxide] molar ratio was constantly maintained at 2.0 (*i.e.* [diamine]/[epoxide] = 1.0).[61–63] Following this period, membrane-functionalized polymersomes were transferred into PB 5.5 (optimum pH value of HRP) by one centrifugation/resuspension cycle prior to kinetic colorimetric analysis for enzyme activity and nanoreactor permeability determination. FT-IR spectroscopy was used for the confirmation of successful ring-opening of PGlyMA units in each case by monitoring the characteristic asymmetric vibration peaks of epoxide groups at 849 and 909 cm^{-1} before and after ring-opening reactions (Fig. S11, S14 and S16†). It should also be noted that incubation of free HRP in DI water at room temperature for 18 hours as a control experiment resulted in no loss of enzyme activity (>99% retention of activity), compared to incubation of the enzyme in PB 5.5 for the same period of time (Fig. S9†). Additionally, a control experiment for comparison of the activity of non-epoxy-functionalized and purified HRP-loaded PEG_{113}-*b*-$PHPMA_{400}$ vesicles before and after incubation with the utilized primary amine and diamine molecules at room temperature for 18 hours in DI water, highlighted that the prolonged presence of amines in the particle dispersion solutions did not affect the catalytic activity of HRP (>95% retention of activity in all cases – control vesicle solutions after incubation with C_nDA cross-linkers could not be resuspended in PB 5.5 and hence their activity was not assessed) (Fig. S10†).

Ring-opening of PGlyMA units using linear poly(ethylene glycol) diamines (PEG_nDA) as cross-linkers. First, two water-soluble poly(ethylene glycol)-based diamine polymers of differing molecular weight (PEG_nDA, n = 23 or 46) were selected as cross-linking agents for post-PISA membrane functionalization of HRP-loaded PEG_{113}-*b*-P($HPMA_{320}$-*co*-$GlyMA_{80}$) nanoreactors following the above described process (Scheme 1). In both cases, efficient ring-opening of epoxy groups of PGlyMA using polymeric $PEG_{23/46}$DA as cross-linkers was confirmed by FT-IR spectroscopy (Fig. S11†) that resulted in a noticeable increase of nanostructure size. D_h values of

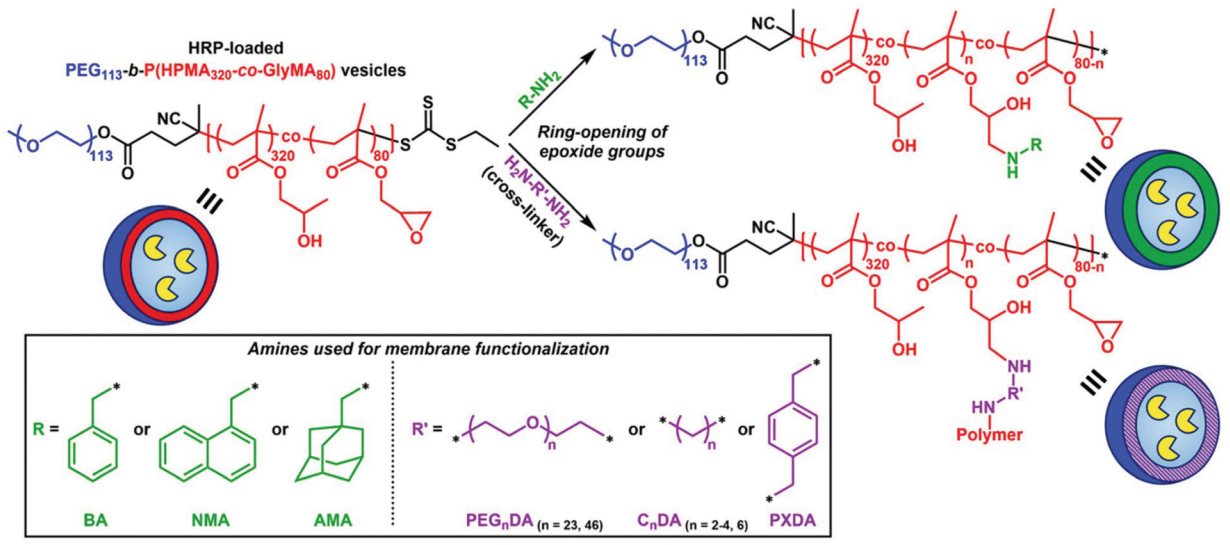

Scheme 1 Schematic illustration of the membrane functionalization procedure of HRP-loaded PEG_{113}-*b*-P($HPMA_{320}$-*co*-$GlyMA_{80}$) polymersome nanoreactors *via* ring-opening of pendant PGlyMA epoxide groups using a series of primary amines as nucleophiles to yield polymersomes with controlled permeability.

PEG$_n$DA-modified particles were approximately 240 nm (PD = 0.11–0.14), as measured by DLS analysis (Fig. 3A-I and B-I), whereas the hydrodynamic diameter of the original PEG$_{113}$-*b*-P(HPMA$_{320}$-*co*-GlyMA$_{80}$) polymersome platform was ~180 nm. No evident macroscopic precipitation of the particle solutions was observed that could imply inter-vesicular cross-linking. In particular, dry-state and cryo-TEM imaging revealed the retention of vesicular morphology in both cases with no apparent particle agglomeration, whilst average vesicle sizes determined from particle counting analysis based on cryo-TEM images were in excellent agreement with DLS results ($D_{\text{cryo, PEG}_{23}\text{DA}}$ = 224.0 ± 21.0 nm, and $D_{\text{cryo, PEG}_{46}\text{DA}}$ = 218.5 ± 22.3 nm) (Fig. 3A-II, B-II and S12†). The observed size increase can be explained by the hydrophilic nature of the PEG$_n$DA cross-linkers that could potentially lead to hydration of the vesicle membranes and as a result to partial swelling of the assemblies. Moreover, a measurable increase in average membrane thickness to ~32 nm was noticed in both cases compared to the non-functionalized vesicles (Fig. 3A-III and B-III).

Surprisingly, activity comparison between encapsulated HRP into inherently permeable PEG$_{113}$-*b*-P(HPMA$_{320}$-*co*-GlyMA$_{80}$) vesicles and PEG$_n$DA cross-linked PEG$_{113}$-*b*-P(HPMA$_{320}$-*co*-GlyMA$_{80}$) vesicles showed a significant enzyme activity decrease for the latter ones. More specifically, an absorbance decrease of 45 ± 5% was measured from kinetic colorimetric analysis after 30 min in the case of cross-linked PEG$_{113}$-*b*-P(HPMA$_{320}$-*co*-GlyMA$_{80}$) + PEG$_{23}$DA vesicles compared to their non-functionalized epoxide-containing counterparts, while a further absorbance decrease of 69 ± 4% was identified upon increasing the molecular weight of the PEG$_n$DA cross-linker (n = 46) (Fig. 3C and S13†). The observed decrease in HRP activity demonstrates the permeability reduction of PEG$_n$DA-functionalized nanoreactors toward DMB and hydrogen peroxide. Contrary to the observed particle swelling that would suggest a potential permeability enhancement, this can be understood in terms of the considerably thicker and more densely packed vesicular membranes after cross-linking that create an additional diffusive barrier which in turn hinders the passage of small molecule substrates to reach the active enzyme site.[43]

Ring-opening of PGlyMA units using linear aliphatic diamines (C$_n$DA) as cross-linkers. Next, a series of linear aliphatic diamine small molecules with increasing chain length (C$_n$DA, n = 2, 3, 4, 6) were selected as cross-linkers for ring-opening of epoxy groups located in the hydrophobic domain of HRP-loaded PEG$_{113}$-*b*-P(HPMA$_{320}$-*co*-GlyMA$_{80}$) vesicles (Scheme 1). We hypothesized that increasing the hydrophobicity of the cross-linking moiety compared to PEG$_n$DA would result in a more pronounced enzyme activity reduction similar to the background activity (~0%) of empty vesicles. This would allow for fabrication of nanoreactors that are effectively impermeable toward substrate molecules, whereby their encapsulated cargo is isolated from the outer aqueous surrounding environment of the particles.

FT-IR spectroscopy was used to confirm the successful modification of the polymersome membrane (*i.e.* dis-

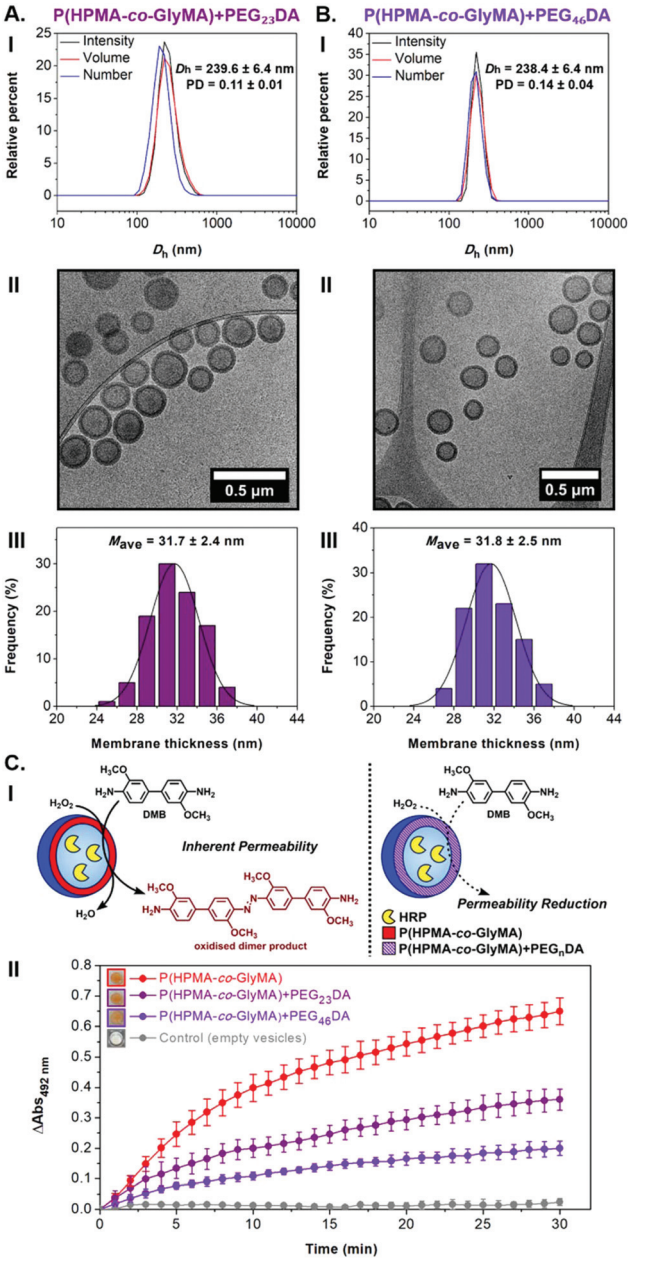

Fig. 3 (A) For HRP-loaded PEG$_{113}$-*b*-P(HPMA$_{320}$-*co*-GlyMA$_{80}$) + PEG$_{23}$DA vesicles, and (B) for HRP-loaded PEG$_{113}$-*b*-P(HPMA$_{320}$-*co*-GlyMA$_{80}$) + PEG$_{46}$DA vesicles: (I) Intensity-weighted size distributions along with average D_h and PD values obtained by DLS (the error shows the standard deviation from 5 repeat measurements), (II) representative cryo-TEM images, and (III) histograms of membrane thickness distribution along with calculated average membrane thickness values measured from particle analysis based on cryo-TEM images. In each case, at least 100 particles were analyzed. (C) Schematic illustration of HRP-catalyzed oxidation reaction of DMB to a red-brown dimer product, detected by kinetic colorimetric assay, taking place inside inherently permeable HRP-loaded PEG$_{113}$-*b*-P(HPMA$_{320}$-*co*-GlyMA$_{80}$) vesicles *versus* cross-linked HRP-loaded PEG$_{113}$-*b*-P(HPMA$_{320}$-*co*-GlyMA$_{80}$) + PEG$_n$DA vesicles (I), and enzymatic activity of the purified empty (grey line), HRP-loaded (red line), and HRP-loaded PEG$_n$DA-functionalized (purple lines) PEG$_{113}$-*b*-P(HPMA$_{320}$-*co*-GlyMA$_{80}$) vesicles (end point = 30 min, λ = 492 nm) (the insets show the end-point microwells in each case) (II).

appearance of the characteristic bands of epoxide groups at 849 and 909 cm^{-1}) (Fig. S14†). Interestingly, DLS analysis of the C_nDA-functionalized HRP-loaded polymersomes revealed a size decrease to 125–130 nm (PD = 0.12–0.13) for the shorter C_2DA and C_3DA cross-linkers compared to the original PEG_{113}-*b*-P($HPMA_{320}$-*co*-$GlyMA_{80}$) vesicles which was attributed to shrinkage of the particles upon cross-linking with hydrophobic compounds that results in exclusion of water molecules from the membrane. In the case of longer C_4DA and C_6DA cross-linkers, a vast D_h increase was measured to 1497 ± 266 nm and 1389 ± 149 nm, respectively, accompanied by a noticeable polydispersity increase (PD = 0.23–0.24) (Fig. 4A). These findings suggest the occurrence of particle agglomeration in the latter cases due to the development of inter-vesicular interactions resulting in the apparent population of particles with increased size. This was also evident by visual inspection of the PISA solutions upon functionalization after one week, where macroscopic precipitation was visible to some extent for PEG_{113}-*b*-P($HPMA_{320}$-*co*-$GlyMA_{80}$) + $C_{4/6}$DA assemblies, implying the occurrence of time-dependent coagulation in aqueous media. The morphology retention of HRP-loaded PEG_{113}-*b*-P($HPMA_{320}$-*co*-$GlyMA_{80}$) + C_nDA polymersomes was also verified by dry-state and cryo-TEM imaging after post-PISA functionalization (D_{cryo} = 116–120 nm), for which near identical vesicle formulations were observed in all cases. A negligible population of aggregated particles could only be observed in the case of C_4DA and C_6DA-functionalized polymersomes that supports the DLS findings described above. The average membrane thickness of the prepared nanoreactors was also calculated from particle counting analysis in each case. Increased membrane thickness values of M_{ave} = 30–32 nm were measured in all cases, comparable to PEG_nDA-functionalized vesicles (Fig. 4B and S15†).

Similar to PEG_nDA cross-linked vesicles, assessment of the enzyme activity of HRP-loaded PEG_{113}-*b*-P($HPMA_{320}$-*co*-$GlyMA_{80}$) + C_nDA nanoreactors through kinetic colorimetric analysis revealed an absorbance decrease ranging from 50% to 61% depending on the cross-linker molecule used as compared to their PEG_{113}-*b*-P($HPMA_{320}$-*co*-$GlyMA_{80}$) counterparts (Fig. 4C). The absorbance decrease measured was approximately the same in all cases, whilst there was no apparent trend based on the length of the cross-linker used for ring-opening of PGlyMA units (*i.e.* increasing the C_nDA length didn't result in an analogous HRP activity decrease). Overall, membrane cross-linking of the vesicles using C_nDA molecules and subsequent introduction of additional hydrophobicity yielded particles with thicker and possibly less hydrated membranes with markedly reduced permeability.

Ring-opening of PGlyMA units using other hydrophobic primary amines as nucleophiles. As a next step, a more hydrophobic cross-linking xylylene-based diamine (PXDA) was selected for ring-opening of PGlyMA epoxy groups along with three other hydrophobic compounds bearing a single amino group in their structure (*i.e.* BA, NMA, and AMA) to prevent formation of linkages and agglomeration of the vesicles, as observed for longer C_nDA cross-linkers, and to achieve com-

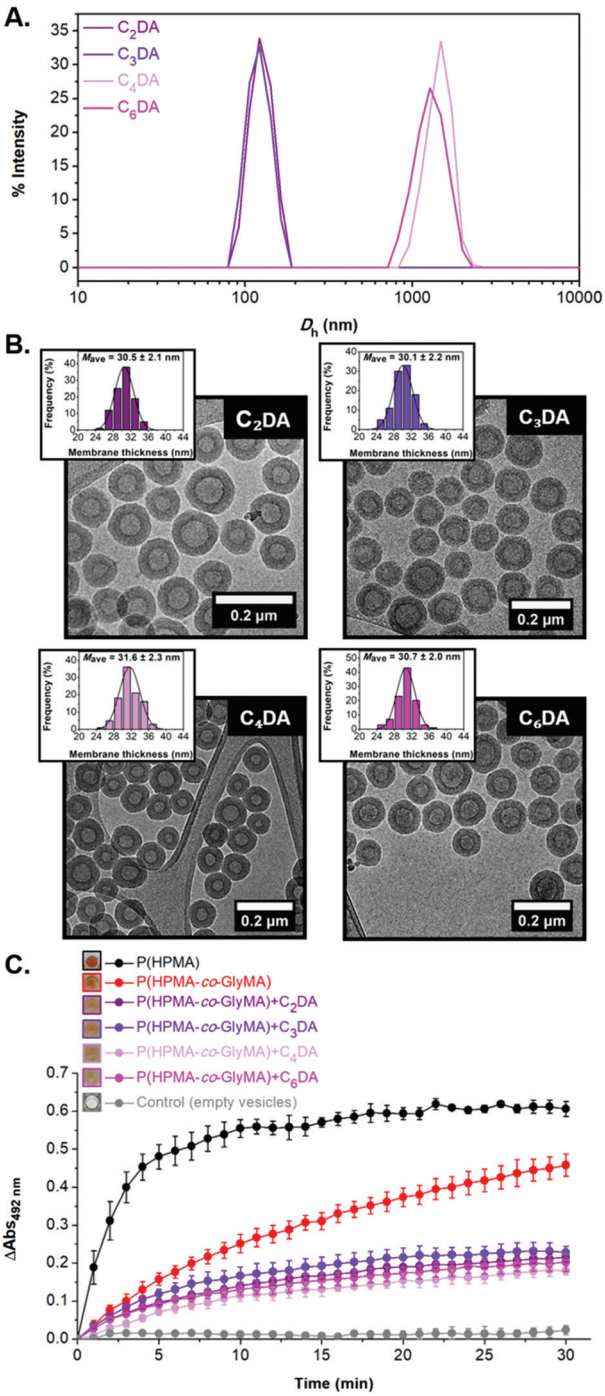

Fig. 4 (A) Intensity-weighted size distributions along with average D_h and PD values obtained by DLS (the error shows the standard deviation from 5 repeat measurements) for HRP-loaded PEG_{113}-*b*-P($HPMA_{320}$-*co*-$GlyMA_{80}$) + C_nDA (n = 2, 3, 4, 6) vesicles. (B) Representative cryo-TEM images of HRP-loaded PEG_{113}-*b*-P($HPMA_{320}$-*co*-$GlyMA_{80}$) + C_nDA vesicles, and corresponding histograms of membrane thickness distribution along with calculated average membrane thickness values measured from particle analysis based on cryo-TEM images. In each case, at least 100 particles were analyzed. (C) Enzymatic activity of the purified empty (grey line), HRP-loaded (red line), and HRP-loaded C_nDA-functionalized (purple/pink lines) PEG_{113}-*b*-P($HPMA_{320}$-*co*-$GlyMA_{80}$) vesicles, and HRP-loaded PEG_{113}-*b*-$P(HPMA)_{400}$ vesicles (black line) (end point = 30 min, λ = 492 nm) (the insets show the end-point microwells in each case).

plete reduction of membrane permeability for enzyme-loaded PEG_{113}-*b*-P($HPMA_{320}$-*co*-$GlyMA_{80}$) polymersome nanoreactors (Scheme 1). Notably, the majority of selected amines resulted in fabrication of stable nanoparticle dispersions, except for AMA, where prominent macroscopic precipitation and formation of a film at the bottom of the vial was observed after epoxide ring-opening reaction, implying instability of the nano-objects in this case due to significantly increased hydrophobicity. In all cases, FT-IR spectroscopic analysis confirmed the successful ring-opening of PGlyMA epoxide groups (Fig. S16†).

In the case of BA-functionalized vesicles, D_h and PD values comparable with those of the original HRP-loaded vesicles were measured from DLS analysis (D_h = 203.4 ± 2.8 nm and PD = 0.08) (Fig. 5A-I and II). Dry-state TEM imaging was first used to confirm that post-PISA functionalization did not alter their morphology and uniform size (Fig. 5A-III and S17A-I†), while size and membrane thickness measurements were carried out from particle counting analysis based on cryo-TEM images (Fig. 5A-IV to VI and S17A-II†). Importantly, the average diameter of BA membrane-modified vesicles was in good agreement with DLS results ($D_{cryo,\ BA}$ = 175.4 ± 27.7 nm), whereas a significant increase in average membrane thickness was also observed ($M_{ave,\ BA}$ = 33.2 ± 2.9 nm) compared to PEG_{113}-*b*-P($HPMA_{320}$-*co*-$GlyMA_{80}$) vesicles.

Near identical well-defined vesicle formulations of low PD and similar D_h values were identified by DLS analysis and dry-state TEM imaging in the case of NMA and PXDA amines (Fig. 5B-I to III, C-I to III and S17†). Similar to HRP-loaded PEG_{113}-*b*-P($HPMA_{320}$-*co*-$GlyMA_{80}$) + BA nanoreactors, average D_{cryo} values were in good agreement with light scattering results, whilst an increased average membrane thickness was calculated for PXDA-functionalized vesicles ($M_{ave,\ PXDA}$ = 31.1 ± 2.7 nm). Additionally, a further membrane thickness increase to $M_{ave,\ NMA}$ = 37.6 ± 2.8 nm was calculated upon PGlyMA ring-opening using a more hydrophobic amine (*i.e.* NMA), showing an evident relationship between the structure/hydrophobicity of the nucleophile and the membrane thickness of the resulting vesicles (Fig. 5B-IV to VI, C-IV to VI and S17†).

The activity of HRP-loaded PEG_{113}-*b*-P($HPMA_{320}$-*co*-$GlyMA_{80}$) + BA/NMA/PXDA polymersomes was assessed by kinetic colorimetric analysis, monitoring the enzyme-catalyzed peroxidation of DMB in line with above described assays (Fig. 6A). The rate of DMB peroxidation was clearly affected by the physicochemical nature of the polymersome (particularly M_{ave}), with reductions in substrate processing correlating to increasing thickness of the diffusional barriers provided by the functionalized membrane. At a fixed substrate concentration (0.4 mM DMB and 1.1 M H_2O_2), there was a small reduction in product formation for the PXDA cross-linked polymersomes of 31 ± 4% upon comparison with the original HRP-loaded PEG_{113}-*b*-P($HPMA_{320}$-*co*-$GlyMA_{80}$) vesicles that dropped to >80% in the case of BA and NMA-functionalized nanoreactors (Fig. 6B). Although these values correlate well with measured M_{ave} values (*i.e.* NMA > BA > PXDA > PGlyMA) and showcase how post-PISA chemical modification affects the membrane character altering its relative permeability, it was important to expand this data to explore the effect of substrate concentration; measuring the observable permeability. No change to the actual K_m of the intact enzyme was taken into consider-

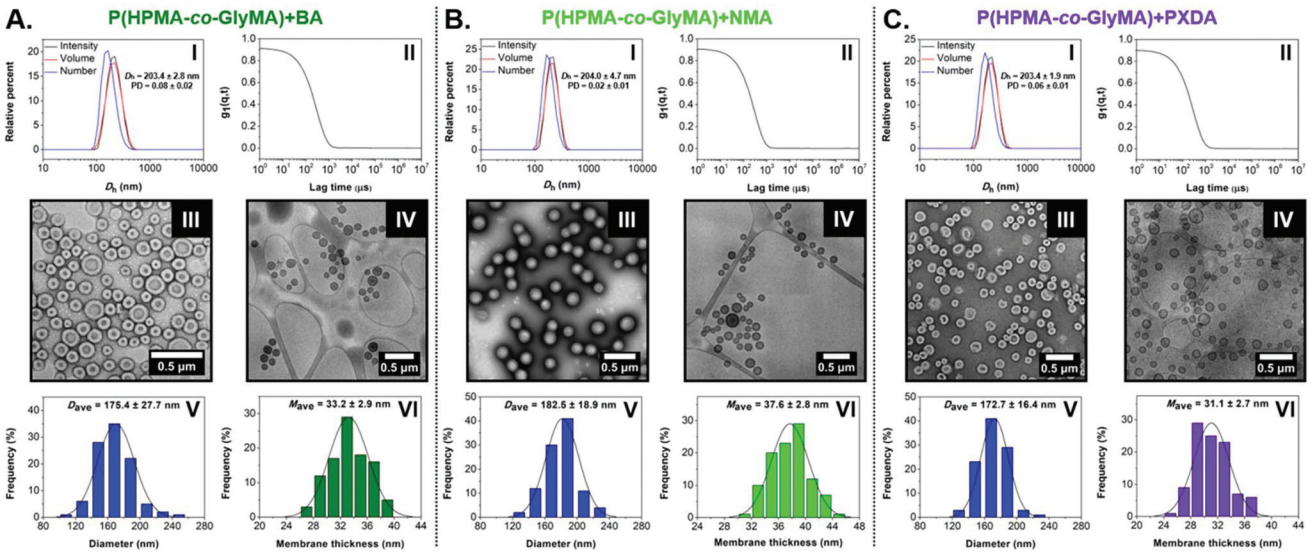

Fig. 5 (A) For HRP-loaded PEG_{113}-*b*-P($HPMA_{320}$-*co*-$GlyMA_{80}$) + BA vesicles, (B) for HRP-loaded PEG_{113}-*b*-P($HPMA_{320}$-*co*-$GlyMA_{80}$) + NMA vesicles, and (C) for HRP-loaded PEG_{113}-*b*-P($HPMA_{320}$-*co*-$GlyMA_{80}$) + PXDA vesicles: (I) Intensity-weighted size distributions along with average D_h and PD values (the error shows the standard deviation from 5 repeat measurements), and (II) autocorrelation functions obtained by DLS, (III) representative dry-state TEM images, stained with 1 wt% UA solution, and (IV) representative cryo-TEM images, (V) histograms of size distribution, and (VI) histograms of membrane thickness distribution along with calculated average diameter and membrane thickness values, respectively, measured from particle analysis based on cryo-TEM images. In each case, at least 100 particles were analyzed.

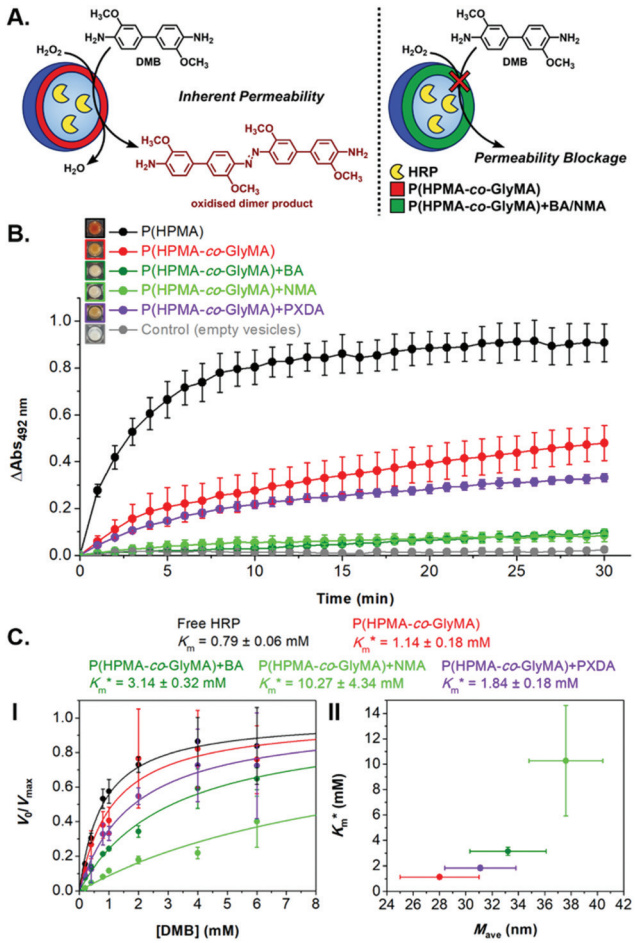

Fig. 6 (A) Schematic illustration of HRP-catalyzed oxidation reaction of DMB to a red-brown dimer product, detected by kinetic colorimetric assay, taking place inside inherently permeable HRP-loaded PEG_{113}-*b*-P($HPMA_{320}$-*co*-$GlyMA_{80}$) vesicles *versus* impermeable HRP-loaded PEG_{113}-*b*-P($HPMA_{320}$-*co*-$GlyMA_{80}$) + BA/NMA vesicles, and (B) enzymatic activity of the purified empty (grey line), HRP-loaded (red line), HRP-loaded PXDA-functionalized (purple line), and HRP-loaded BA/NMA-functionalized (green lines) PEG_{113}-*b*-P($HPMA_{320}$-*co*-$GlyMA_{80}$) vesicles, and HRP-loaded PEG_{113}-*b*-$P(HPMA)_{400}$ vesicles (black line) (end point = 30 min, λ = 492 nm) (the insets show the end-point microwells in each case). (C) Normalized Michaelis–Menten kinetic plots of free HRP and HRP-loaded PEG_{113}-*b*-P($HPMA_{320}$-*co*-$GlyMA_{80}$) + BA/NMA/PXDA vesicles (I), and calculated K_m^* values (mean ± standard error) for each sample as a function of average nanoreactor membrane thickness (M_{ave}) (II).

ation as such fundamental changes to activity are not generally associated with encapsulation.[67] Normalized kinetic data was presented in terms of V_0/V_{max} due to the focus on comparisons between equilibrium substrate dissociation constant (K_m) of the nanoreactor-loaded enzyme rather than absolute activity; an [enzyme]-dependent parameter.

Systematically varying [DMB] (with $[H_2O_2]$ under saturating conditions) gave a more detailed insight into the effect of membrane modification on the performance of nanoreactors, where the trend identified previously was confirmed and could be elucidated with greater detail (Fig. 6C-I and S18†). As compared to the K_m value of the free enzyme at 0.79 ± 0.06 mM, the K_m^* of HRP-loaded PEG_{113}-*b*-P($HPMA_{320}$-*co*-$GlyMA_{80}$) nanoreactors increased by *ca.* 30% (up to 1.14 ± 0.18 mM) as a result of enzyme compartmentalization within the semi-permeable P($HPMA_{320}$-*co*-$GlyMA_{80}$) membrane. This effect could be tuned by introducing cross-linking or chemical modification. PXDA cross-linking of polymersomes further increased K_m^* by *ca.* 30% (up to 1.84 ± 0.18 mM), in accordance with earlier data under fixed substrate concentration conditions. Interestingly, using such kinetic assays, we were able to resolve the effect of BA and NMA modification on the permeability of the polymersome membrane. Indeed, post-PISA membrane modification and insertion of benzylic (BA) groups gave rise to a 70% increase in K_m^*, which increased by a further 230% when using bulkier naphthyl (NMA) groups (up to 3.14 ± 0.32 & 10.27 ± 4.34 mM, respectively). Overall, the observed rate of substrate turnover of the unmodified polymersomes was *ca.* 90% higher than that of the NMA-functionalized nanoreactors. Relating these values for K_m^* to the measured values of average membrane thickness (M_{ave}), it is apparent that their relationship is non-linear, which means that the physicochemical origin of this tunability cannot be fully explicated by the influence of chemical modifier upon the membrane dimensions but is also related to the nature of the new membrane (Fig. 6C-II). In this instance, we can understand the increasing K_m^* value (and decreasing permeability) between BA and NMA membranes arising due to the increasing non-covalent aromatic interactions between polymer chains (*i.e.* increasing the density and reducing the porosity of the bilayer).

Overall, our findings provide a more in depth understanding of how relatively simple chemistries, used for the functionalization of polymersome membranes with increasingly more hydrophobic moieties, can tune the passive diffusion of small molecules into their aqueous inner lumen. This strategy has been utilized to achieve greater control over substrate processing by enzymes encapsulated within a polymersome nanoreactor.

Conclusions

In summary, we report a facile strategy to modulate the membrane permeability of polymeric vesicles. Epoxy-containing, enzyme-loaded vesicle nanoreactors obtained *via* aqueous emulsion PISA were functionalized with a series of diamine cross-linkers or hydrophobic primary amines using a simple procedure. Membrane modification resulted in increased thickness and reduced permeability relative to the non-functionalized particles. Of the compounds tested, the hydrophobic amines exhibited the most dramatic blocking effect on the vesicle membranes, reducing permeability by over 80% as determined by a colorimetric assay involving substrate oxidation by the encapsulated enzymes. This fundamental study reveals important insight into the relationship between membrane thickness, cross-linking density, or hydrophobicity and

permeability. Such fine control over the diffusion of substrates across inherently permeable vesicular membranes has rarely been demonstrated and should inform particle design in future studies.

Conflicts of interest

There are no conflicts to declare.

Acknowledgements

This work was supported by the ERC (grant number 615142), EPSRC, and the University of Birmingham. D. S. W. thanks the Ser Cymru II programme for support; this project received funding from the European Union's Horizon 2020 research and innovation under the Marie Skłodowska-Curie grant agreement no. 663830. Advanced BioImaging Research Technology Platform, BBSRC ALERT14 award BB/M01228X/1, is thanked for supporting cryo-TEM characterization and Dr S. Bakker (University of Warwick) is thanked for cryo-TEM assistance. Dr M. C. Arno (University of Birmingham) is thanked for optical microscopy assistance.

Notes and references

1 J. W. Szostak, D. P. Bartel and P. L. Luisi, *Nature*, 2001, **409**, 387–390.
2 W. Martin, *Philos. Trans. R. Soc., B*, 2010, **365**, 847–855.
3 K. Sugano, M. Kansy, P. Artursson, A. Avdeef, S. Bendels, L. Di, G. F. Ecker, B. Faller, H. Fischer, G. Gerebtzoff, H. Lennernaes and F. Senner, *Nat. Rev. Drug Discovery*, 2010, **9**, 597–614.
4 N. J. Yang and M. J. Hinner, in *Site-Specific Protein Labeling: Methods and Protocols*, ed. A. Gautier and M. J. Hinner, Springer New York, New York, NY, 2015, pp. 29–53, DOI: 10.1007/978-1-4939-2272-7_3.
5 M. Marguet, C. Bonduelle and S. Lecommandoux, *Chem. Soc. Rev.*, 2013, **42**, 512–529.
6 R. Roodbeen and J. C. M. van Hest, *BioEssays*, 2009, **31**, 1299–1308.
7 R. J. R. W. Peters, I. Louzao and J. C. M. van Hest, *Chem. Sci.*, 2012, **3**, 335–342.
8 J. Xu, F. J. Sigworth and D. A. LaVan, *Adv. Mater.*, 2010, **22**, 120–127.
9 J. Gaitzsch, X. Huang and B. Voit, *Chem. Rev.*, 2016, **116**, 1053–1093.
10 B. C. Buddingh' and J. C. M. van Hest, *Acc. Chem. Res.*, 2017, **50**, 769–777.
11 P. A. Gale, J. T. Davis and R. Quesada, *Chem. Soc. Rev.*, 2017, **46**, 2497–2519.
12 A. Belluati, I. Craciun, C. E. Meyer, S. Rigo and C. G. Palivan, *Curr. Opin. Biotechnol.*, 2019, **60**, 53–62.
13 J. F. Le Meins, O. Sandre and S. Lecommandoux, *Eur. Phys. J. E*, 2011, **34**, 14.
14 C. G. Palivan, R. Goers, A. Najer, X. Zhang, A. Car and W. Meier, *Chem. Soc. Rev.*, 2016, **45**, 377–411.
15 E. Rideau, R. Dimova, P. Schwille, F. R. Wurm and K. Landfester, *Chem. Soc. Rev.*, 2018, **47**, 8572–8610.
16 B. M. Discher, Y.-Y. Won, D. S. Ege, J. C. M. Lee, F. S. Bates, D. E. Discher and D. A. Hammer, *Science*, 1999, **284**, 1143–1146.
17 D. E. Discher and A. Eisenberg, *Science*, 2002, **297**, 967–973.
18 J. Rodríguez-Hernández, F. Chécot, Y. Gnanou and S. Lecommandoux, *Prog. Polym. Sci.*, 2005, **30**, 691–724.
19 S. Sugihara, A. Blanazs, S. P. Armes, A. J. Ryan and A. L. Lewis, *J. Am. Chem. Soc.*, 2011, **133**, 15707–15713.
20 Y. Mai and A. Eisenberg, *Chem. Soc. Rev.*, 2012, **41**, 5969–5985.
21 A. Blanazs, J. Madsen, G. Battaglia, A. J. Ryan and S. P. Armes, *J. Am. Chem. Soc.*, 2011, **133**, 16581–16587.
22 N. J. Warren and S. P. Armes, *J. Am. Chem. Soc.*, 2014, **136**, 10174–10185.
23 N. J. Warren, O. O. Mykhaylyk, D. Mahmood, A. J. Ryan and S. P. Armes, *J. Am. Chem. Soc.*, 2014, **136**, 1023–1033.
24 N. J. Warren, O. O. Mykhaylyk, A. J. Ryan, M. Williams, T. Doussineau, P. Dugourd, R. Antoine, G. Portale and S. P. Armes, *J. Am. Chem. Soc.*, 2015, **137**, 1929–1937.
25 W. Zhou, Q. Qu, Y. Xu and Z. An, *ACS Macro Lett.*, 2015, **4**, 495–499.
26 J. C. Foster, S. Varlas, B. Couturaud, Z. Coe and R. K. O'Reilly, *J. Am. Chem. Soc.*, 2019, **141**, 2742–2753.
27 S. L. Canning, G. N. Smith and S. P. Armes, *Macromolecules*, 2016, **49**, 1985–2001.
28 X. Wang and Z. An, *Macromol. Rapid Commun.*, 2019, **40**, 1800325.
29 D. B. Wright, M. A. Touve, M. P. Thompson and N. C. Gianneschi, *ACS Macro Lett.*, 2018, **7**, 401–405.
30 J. C. Foster, S. Varlas, L. D. Blackman, L. A. Arkinstall and R. K. O'Reilly, *Angew. Chem., Int. Ed.*, 2018, **57**, 10672–10676.
31 W. Zhang, F. D'Agosto, O. Boyron, J. Rieger and B. Charleux, *Macromolecules*, 2012, **45**, 4075–4084.
32 W. Zhang, F. D'Agosto, P.-Y. Dugas, J. Rieger and B. Charleux, *Polymer*, 2013, **54**, 2011–2019.
33 S. Y. Khor, N. P. Truong, J. F. Quinn, M. R. Whittaker and T. P. Davis, *ACS Macro Lett.*, 2017, **6**, 1013–1019.
34 J. Tan, X. Dai, Y. Zhang, L. Yu, H. Sun and L. Zhang, *ACS Macro Lett.*, 2019, **8**, 205–212.
35 J. Yeow and C. Boyer, *Adv. Sci.*, 2017, **4**, 1700137.
36 J. Tan, H. Sun, M. Yu, B. S. Sumerlin and L. Zhang, *ACS Macro Lett.*, 2015, **4**, 1249–1253.
37 J. Tan, Y. Bai, X. Zhang, C. Huang, D. Liu and L. Zhang, *Macromol. Rapid Commun.*, 2016, **37**, 1434–1440.
38 J. Yeow, O. R. Sugita and C. Boyer, *ACS Macro Lett.*, 2016, **5**, 558–564.
39 J. Tan, D. Liu, Y. Bai, C. Huang, X. Li, J. He, Q. Xu, X. Zhang and L. Zhang, *Polym. Chem.*, 2017, **8**, 1315–1327.
40 L. D. Blackman, K. E. B. Doncom, M. I. Gibson and R. K. O'Reilly, *Polym. Chem.*, 2017, **8**, 2860–2871.

41 B. Couturaud, P. G. Georgiou, S. Varlas, J. R. Jones, M. C. Arno, J. C. Foster and R. K. O'Reilly, *Macromol. Rapid Commun.*, 2019, **40**, 1800460.
42 J. Tan, D. Liu, X. Zhang, C. Huang, J. He, Q. Xu, X. Li and L. Zhang, *RSC Adv.*, 2017, **7**, 23114–23121.
43 L. D. Blackman, S. Varlas, M. C. Arno, A. Fayter, M. I. Gibson and R. K. O'Reilly, *ACS Macro Lett.*, 2017, **6**, 1263–1267.
44 J. Tan, D. Liu, Y. Bai, C. Huang, X. Li, J. He, Q. Xu and L. Zhang, *Macromolecules*, 2017, **50**, 5798–5806.
45 J. Tan, X. Zhang, D. Liu, Y. Bai, C. Huang, X. Li and L. Zhang, *Macromol. Rapid Commun.*, 2017, **38**, 1600508.
46 L. D. Blackman, S. Varlas, M. C. Arno, Z. H. Houston, N. L. Fletcher, K. J. Thurecht, M. Hasan, M. I. Gibson and R. K. O'Reilly, *ACS Cent. Sci.*, 2018, **4**, 718–723.
47 S. Varlas, L. D. Blackman, H. E. Findlay, E. Reading, P. J. Booth, M. I. Gibson and R. K. O'Reilly, *Macromolecules*, 2018, **51**, 6190–6201.
48 S. Varlas, P. G. Georgiou, P. Bilalis, J. R. Jones, N. Hadjichristidis and R. K. O'Reilly, *Biomacromolecules*, 2018, **19**, 4453–4462.
49 G. Cheng and J. Pérez-Mercader, *Macromol. Rapid Commun.*, 2019, **40**, 1800513.
50 R. J. R. W. Peters, M. Marguet, S. Marais, M. W. Fraaije, J. C. M. van Hest and S. Lecommandoux, *Angew. Chem., Int. Ed.*, 2014, **53**, 146–150.
51 H. Che, S. Cao and J. C. M. van Hest, *J. Am. Chem. Soc.*, 2018, **140**, 5356–5359.
52 C. Nardin, S. Thoeni, J. Widmer, M. Winterhalter and W. Meier, *Chem. Commun.*, 2000, 1433–1434.
53 J. Gaitzsch, D. Appelhans, L. Wang, G. Battaglia and B. Voit, *Angew. Chem., Int. Ed.*, 2012, **51**, 4448–4451.
54 D. Gräfe, J. Gaitzsch, D. Appelhans and B. Voit, *Nanoscale*, 2014, **6**, 10752–10761.
55 T. Einfalt, R. Goers, I. A. Dinu, A. Najer, M. Spulber, O. Onaca-Fischer and C. G. Palivan, *Nano Lett.*, 2015, **15**, 7596–7603.
56 L. Messager, J. R. Burns, J. Kim, D. Cecchin, J. Hindley, A. L. B. Pyne, J. Gaitzsch, G. Battaglia and S. Howorka, *Angew. Chem., Int. Ed.*, 2016, **55**, 11106–11109.
57 S. F. M. van Dongen, M. Nallani, J. J. L. M. Cornelissen, R. J. M. Nolte and J. C. M. van Hest, *Chem. – Eur. J.*, 2009, **15**, 1107–1114.
58 I. Louzao and J. C. M. van Hest, *Biomacromolecules*, 2013, **14**, 2364–2372.
59 W.-J. Zhang, C.-Y. Hong and C.-Y. Pan, *ACS Appl. Mater. Interfaces*, 2017, **9**, 15086–15095.
60 X.-F. Xu, C.-Y. Pan, W.-J. Zhang and C.-Y. Hong, *Macromolecules*, 2019, **52**, 1965–1975.
61 P. Chambon, A. Blanazs, G. Battaglia and S. P. Armes, *Langmuir*, 2012, **28**, 1196–1205.
62 J. R. Lovett, L. P. D. Ratcliffe, N. J. Warren, S. P. Armes, M. J. Smallridge, R. B. Cracknell and B. R. Saunders, *Macromolecules*, 2016, **49**, 2928–2941.
63 F. L. Hatton, J. R. Lovett and S. P. Armes, *Polym. Chem.*, 2017, **8**, 4856–4868.
64 S. Piogé, T. N. Tran, T. G. McKenzie, S. Pascual, M. Ashokkumar, L. Fontaine and G. Qiao, *Macromolecules*, 2018, **51**, 8862–8869.
65 S. Muthukrishnan, E. H. Pan, M. H. Stenzel, C. Barner-Kowollik, T. P. Davis, D. Lewis and L. Barner, *Macromolecules*, 2007, **40**, 2978–2980.
66 M. Chen, M. Zhong and J. A. Johnson, *Chem. Rev.*, 2016, **116**, 10167–10211.
67 L. M. P. E. van Oppen, L. K. E. A. Abdelmohsen, S. E. van Emst-de Vries, P. L. W. Welzen, D. A. Wilson, J. A. M. Smeitink, W. J. H. Koopman, R. Brock, P. H. G. M. Willems, D. S. Williams and J. C. M. van Hest, *ACS Cent. Sci.*, 2018, **4**, 917–928.

3.2. Appendix – Supporting Information Material

Electronic Supplementary Information

Tuning the membrane permeability of polymersome nanoreactors developed by aqueous emulsion polymerization-induced self-assembly

Spyridon Varlas,[a] *Jeffrey C. Foster,*[a] *Panagiotis G. Georgiou,*[a,b] *Robert Keogh,*[a,b] *Jonathan T. Husband,*[a] *David S. Williams,*[a,c] *and Rachel K. O'Reilly*[a]*

[a] School of Chemistry, University of Birmingham, B15 2TT, Birmingham, UK

[b] Department of Chemistry, University of Warwick, Gibbet Hill Road, CV4 7AL, Coventry, UK

[c] Department of Chemistry, College of Science, Swansea University, SA2 8PP, Swansea, UK

*Corresponding Author: r.oreilly@bham.ac.uk (R.K.O.R.)

Contents

Experimental Section S2
Materials and Methods S2
Materials S2
Characterization Techniques S2
Photoreactor Setup Specifications S6
Supplementary Characterization Data S7

Experimental Section

Materials and Methods

Materials

Poly(ethylene glycol) methyl ether (average M_n = 5,000 g mol^{-1}, PEG-OH), carbon disulfide (anhydrous, ≥99%), sodium ethanethiolate, *N,N′*-dicyclohexylcarbodiimide (99%, DCC), 4-(dimethylamino)pyridine (≥98%, DMAP), benzylamine (99%, BA), 1-naphthylmethylamine (97%, NMA), ethylenediamine (≥99%, C_2DA), 1,3-diaminopropane (≥99%, C_3DA), 1,4-diaminobutane (99%, C_4DA), hexamethylenediamine (98%, C_6DA), poly(ethylene glycol) diamine (average M_n = 2,000 g mol^{-1}), glycidol (96%) and 3,3′-dimethoxybenzidine (DMB) were purchased from Sigma Aldrich and were used without further purification. Glycidyl methacrylate (97%, GlyMA) was also purchased from Sigma-Aldrich and was passed through a column of basic alumina to remove inhibitor prior to use. Iodine, diethyl ether and dichloromethane (DCM) were purchased from Fisher Scientific. 4,4'-Azobis(4-cyanovaleric acid) (98%, ACVA) and poly(ethylene glycol) diamine (average M_n = 1,000 g mol^{-1}) were obtained from Alfa Aesar. 2-Hydroxypropyl methacrylate (mixture of isomers, 98%, HPMA) was also purchased from Alfa Aesar and was passed through a column of basic alumina to remove inhibitor prior to use. 1-Adamantanemethylamine (98%, AMA) was purchased from Acros Organics. *p*-Xylylenediamine (>99.0%, PXDA) was obtained from Tokyo Chemical Industry UK. Hydrogen peroxide (35%) was purchased from Lancaster Synthesis. The enzyme peroxidase from *Amoracia rusticana* (type VI, essentially salt free) (HRP) was purchased from Sigma Aldrich, divided into aliquots at 200 U mL^{-1} in deionized water and stored at -20 °C. Nunc™ 96-well microplates were purchased from ThermoFisher Scientific. Formvar and lacey-carbon coated copper grids were purchased from EM Resolutions.

Characterization Techniques

NMR Spectroscopy. ^{1}H-NMR and ^{13}C-NMR spectra were recorded at a 400 MHz on a Bruker DPX-400 spectrometer, with chloroform-*d* ($CDCl_3$) or methanol-d_4 (CD_3OD) as the solvent. Chemical shifts of protons are reported as δ in parts per million (ppm) and are relative to tetramethylsilane (TMS) at δ = 0 ppm when using $CDCl_3$ or solvent residual peak (CH_3OH, δ = 3.31 ppm).

FT-IR Spectroscopy. Fourier Transform-Infrared (FT-IR) spectroscopy measurements were carried out using an Agilent Cary 630 FT-IR spectrometer, in the range of 650 to 4000 cm^{-1}, after lyophilization of an aliquot of sample.

Size Exclusion Chromatography. Size exclusion chromatography (SEC) analysis was performed on a system composed of a Varian 390-LC-Multi detector suite equipped with a Varian Polymer Laboratories guard column (PLGel 5 μM, 50 × 7.5 mm), two Mixed-C Varian Polymer Laboratories columns (PLGel 5 μM, 300 × 7.5 mm) and a PLAST RT auto-sampler. Detection was conducted using a differential refractive index (RI) and an ultraviolet (UV) detector set to λ = 309 nm. The mobile phase used was DMF (HPLC grade) containing 5 mM NH_4BF_4 at 50 °C at flow rate of 1.0 mL min^{-1}. Poly(methyl methacrylate) (PMMA) standards were used for calibration. Number average molecular weights (M_n), weight average molecular weights (M_w) and dispersities ($Đ_M = M_w/M_n$) were determined using Cirrus v3.3 SEC software.

High-Performance Liquid Chromatography. Reverse phase high-pressure liquid chromatography (RP-HPLC) was carried out using a Shim-pack GISS 5 μm C18 (4.6 × 125 mm) column on a Shimadzu instrument using the following modules: LC-20AD solvent delivery module, SIL-20AC HT autosampler, CTO-20AC column oven and SPD-M20A photodiode array UV-Vis detector. The 222 nm peptide bond absorbance was extracted from the PDA detector. The mobile phases used were H_2O (18.2 MΩ·cm + 0.04% v/v formic acid)/MeCN (HPLC grade + 0.04% v/v formic acid). A range of mobile phase gradients was investigated. The optimized gradient was ran at 0.8 mL min^{-1} at 30 °C and is shown in Table S1.

Table S1. Mobile phase composition used for HPLC analysis.

Time (min)	% H_2O	% MeCN
0	95	5
3	80	20
16	25	75
20	5	95
21	95	5
25	95	5

Matrix-Assisted Laser Desorption/Ionization Time-of-Flight Mass Spectrometry. MALDI-ToF MS was conducted on a Bruker Ultraflex MALDI TOF/TOF mass spectrometer. A solution of HRP (0.2 mg ml^{-1}) was spotted onto a 96-spot steel plate followed by an equal volume of sinapic acid matrix (15 mg in 0.5 mL of water, 0.5 mL of acetonitrile and 1 μL of trifluoroacetic acid (TFA)). The solvent was evaporated before the recording of spectra and analysis using flexControl software.

Dynamic Light Scattering. Hydrodynamic diameters (D_h) and size distributions of particles were determined by dynamic light scattering (DLS) using a Malvern Zetasizer Nano ZS with a 4 mW He-Ne 633 nm laser module operating at 25 °C. Measurements were carried out at an angle of 173° (back scattering), and results were analyzed using Malvern DTS 7.03 software. All determinations were repeated 5 times with at least 10 measurements recorded for each run. D_h values were calculated using the Stokes-Einstein equation where particles are assumed to be spherical.

Zeta Potential Analysis. Zeta potential was measured by the technique of microelectrophoresis, using a Malvern Zetasizer Nano ZS instrument, at room temperature at 633 nm. All reported measurements were the average of at least five runs. Zeta potential was calculated from the corresponding electrophoretic mobilities (μ_E) by using the Henry's correction of the Smoluchowski equation ($\mu_E = 4\pi\ \varepsilon_0\ \varepsilon_r\ \zeta\ (1+\kappa r)/6\pi\ \mu$).

Optical Microscopy. Images of the monomer-in-water emulsion solution prior to polymerization were captured using a Leica DM IL LED optical microscope equipped with a Leica MC170 HD colour camera at 10× magnification. 10 μL of the freshly prepared sample was added on a glass slide and imaged within 5 min after emulsion formation.

Transmission Electron Microscopy. Dry-state stained TEM imaging was performed on either a JEOL JEM-2000 FX or a JEOL JEM-2100Plus microscope operating at an acceleration voltage of 200 kV and a JEOL JEM-1400 microscope operating at an acceleration voltage of 80 kV. All dry-state samples were diluted with deionized water and then deposited onto formvar-coated copper grids. After roughly 1 min, excess sample was blotted from the grid and the grid was stained with an aqueous 1 wt% uranyl acetate (UA) solution for 1 min prior to blotting, drying and microscopic analysis.
Cryogenic transmission electron microscopy (cryo-TEM) imaging was performed on a JEOL JEM-2100Plus microscope operating at an acceleration voltage of 200 kV. Samples for cryo-TEM imaging were prepared at 0.5% w/w solids content in deionized water by depositing 8 μL sample onto plasma-

treated lacey-carbon coated grids followed by blotting for approximately 5 s and plunging into a pool of liquid ethane, cooled using liquid nitrogen, to vitrify the samples. Transfer into a pre-cooled cryo-TEM holder was performed under liquid nitrogen temperatures prior to microscopic analysis. For the determination of average size and membrane thickness of the vesicles at least 100 particles were analyzed in each case.

Kinetic Colorimetric Analysis. Kinetic colorimetric analysis was performed in 96-well Nunclon™ plates and measured on a BMG Labtech FLUOstar OPTIMA plate reader running in absorbance mode with a filter of $\lambda = 492$ nm. Absorbance values at this wavelength were measured every minute for a period of 30 min. All measurements were performed in at least triplicate.

Photoreactor Setup Specifications

The LED source for the visible-light initiated PISA reactions (TruOpto OSV5X3CAC1E, 4.5 W) was purchased from Rapid Electronics and had a radiant flux of 800 mW@400 mA at 12V DC operating at a wavelength of 400–410 nm. This was fitted to a custom-built setup equipped with a dimmer switch for controlling the output light intensity. The vial base is located 19 mm above the light source to limit heating which creates a 40° cone of light from the center of the LED giving 76% intensity at the perimeter of the sample. In the present study, all photo-PISA reactions were carried out at full output light intensity.

Figure S1. Digital photographs of photoreactor system used in the present study to carry out photo-PISA reactions under 405 nm irradiation.

Supplementary Characterization Data

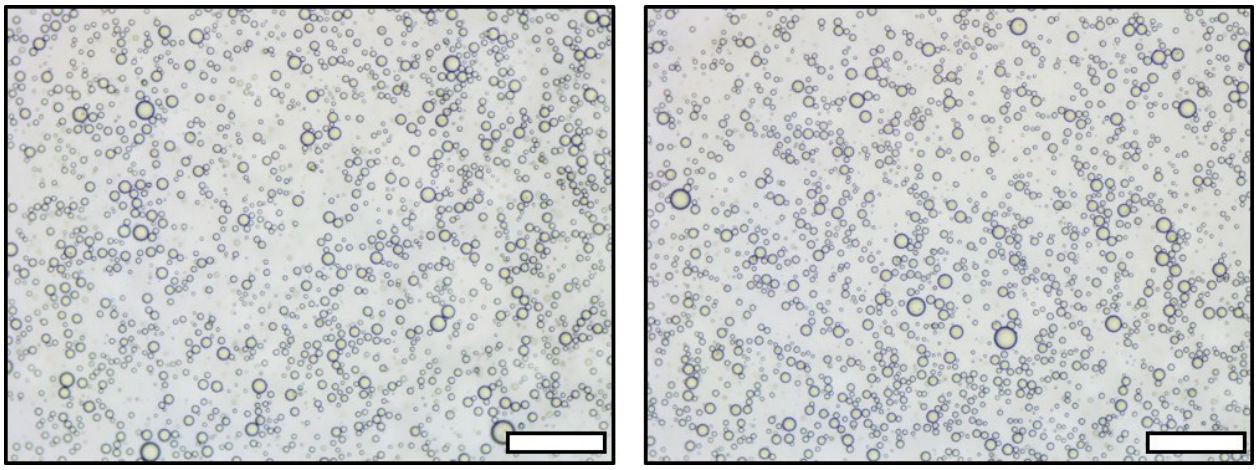

Figure S2. Representative optical microscopy images of initial monomer-in-water emulsion stabilized by PEG_{113} macro-CTA prior to photo-PISA. Scale bars represent 200 μm.

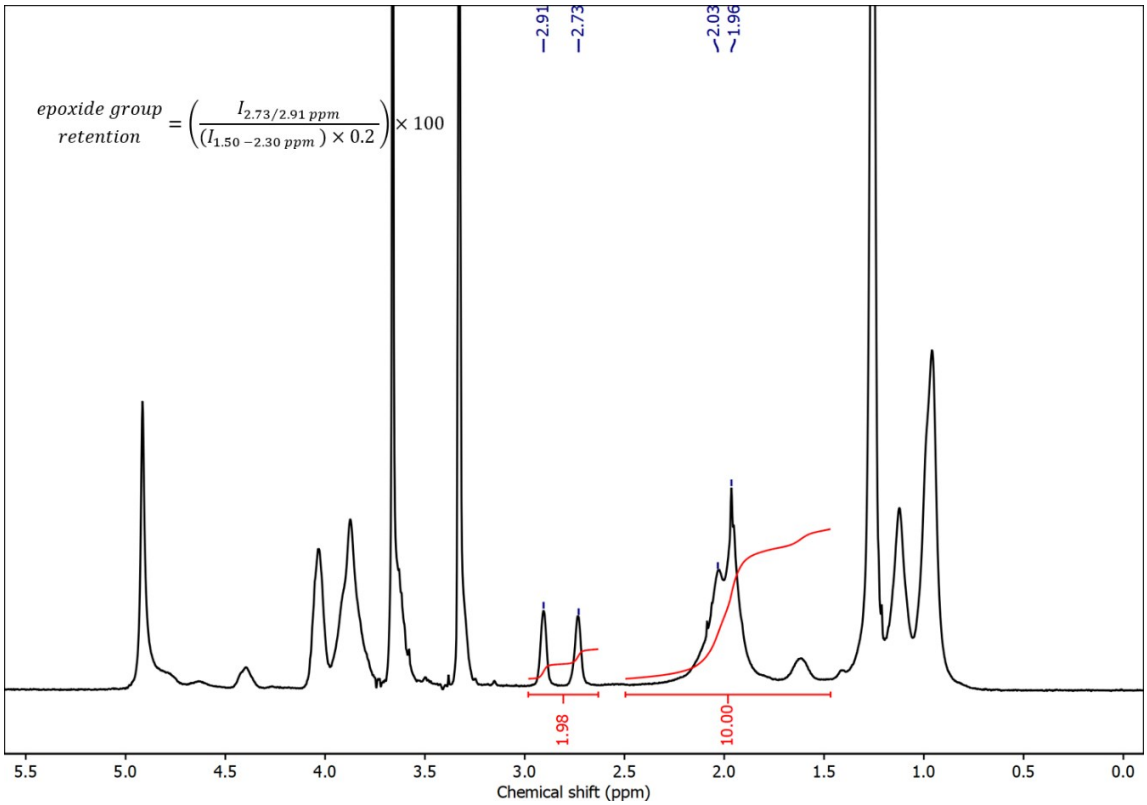

Figure S3. ^{1}H-NMR spectrum of crude PEG_{113}-*b*-P($HPMA_{320}$-*co*-$GlyMA_{80}$) diblock copolymer in methanol-d_4 for calculation of epoxide group retention efficiency after aqueous RAFT-mediated emulsion photo-PISA.

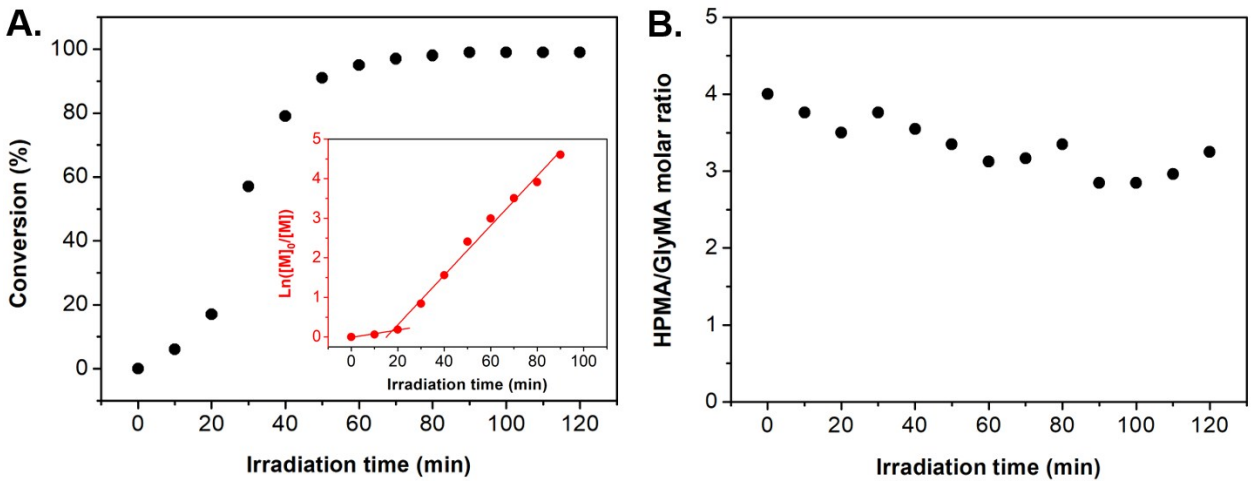

Figure S4. (A) Polymerization kinetics for aqueous RAFT-mediated emulsion photo-PISA of HPMA/GlyMA (80:20 molar ratio) using a PEG_{113} macro-CTA at [solids] = 10% w/w (target DP_{PHPMA} = 320 and DP_{PGlyMA} = 80) (inset: $\ln([M]_0/[M])$ versus irradiation time kinetic plot). (B) Relative HPMA/GlyMA monomer molar ratio as a function of photo-PISA irradiation time, as calculated by conversion ^{1}H-NMR analysis in methanol-d_4.

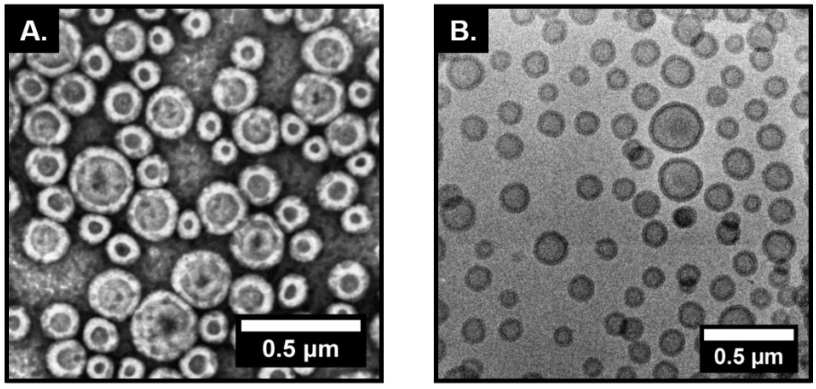

Figure S5. (A) Representative dry-state TEM image, stained with 1 wt% uranyl acetate (UA) solution, and (B) representative cryo-TEM image of empty PEG_{113}-*b*-P($HPMA_{320}$-*co*-$GlyMA_{80}$) vesicles.

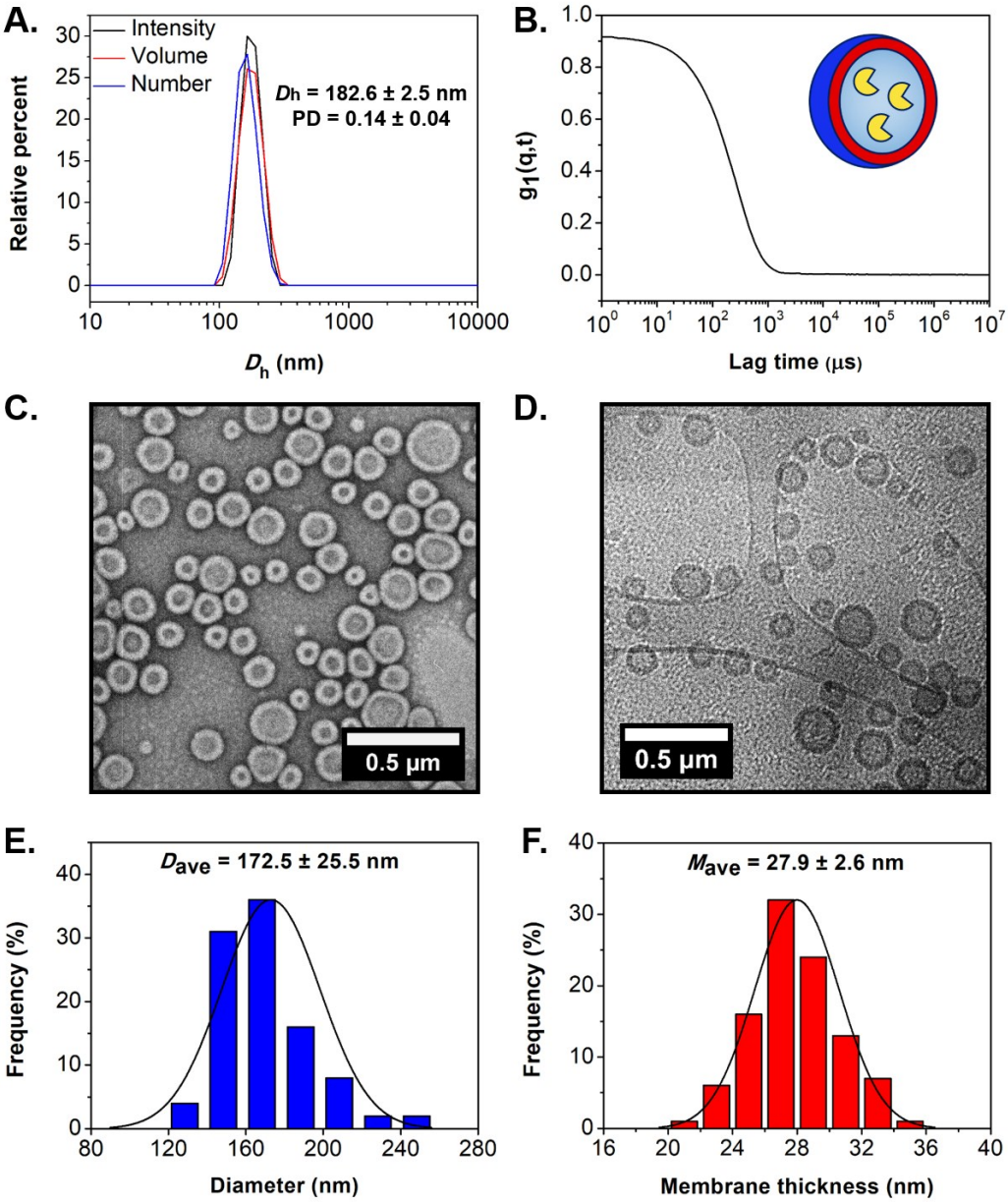

Figure S6. Characterization of purified HRP-loaded PEG_{113}-*b*-P($HPMA_{320}$-*co*-$GlyMA_{80}$) vesicles. (A) Intensity-weighted size distributions along with average D_h and PD values (the error shows the standard deviation from 5 repeat measurements), and (B) autocorrelation function obtained by DLS. (C) Representative dry-state TEM image, stained with 1 wt% UA solution, and (D) representative cryo-TEM image. (E) Histogram of size distribution, and (F) histogram of membrane thickness distribution along with calculated average diameter and membrane thickness values, respectively, measured from particle analysis based on cryo-TEM images. In each case, at least 100 particles were analyzed.

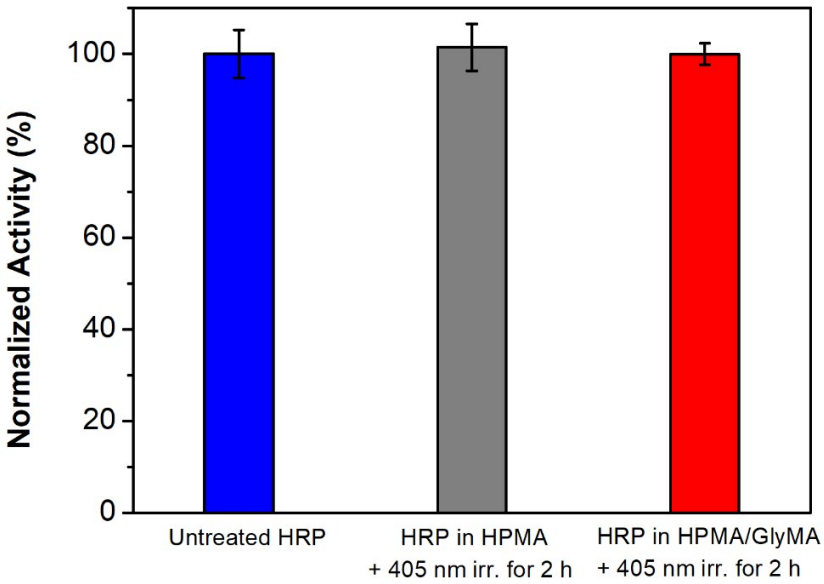

Figure S7. Control experiments comparing the activity of free HRP after incubation at 37 °C for 2 hours under 405 nm irradiation in either 10% w/w HPMA solution in DI water or 10% w/w HPMA/GlyMA (80:20 molar ratio) solution in DI water against untreated enzyme ($[HRP]_{reaction}$ = 20 U mL^{-1}), as determined at the end point of the colorimetric assay (end point = 30 min, λ = 492 nm), showing no loss of HRP activity under aqueous emulsion photo-PISA conditions.

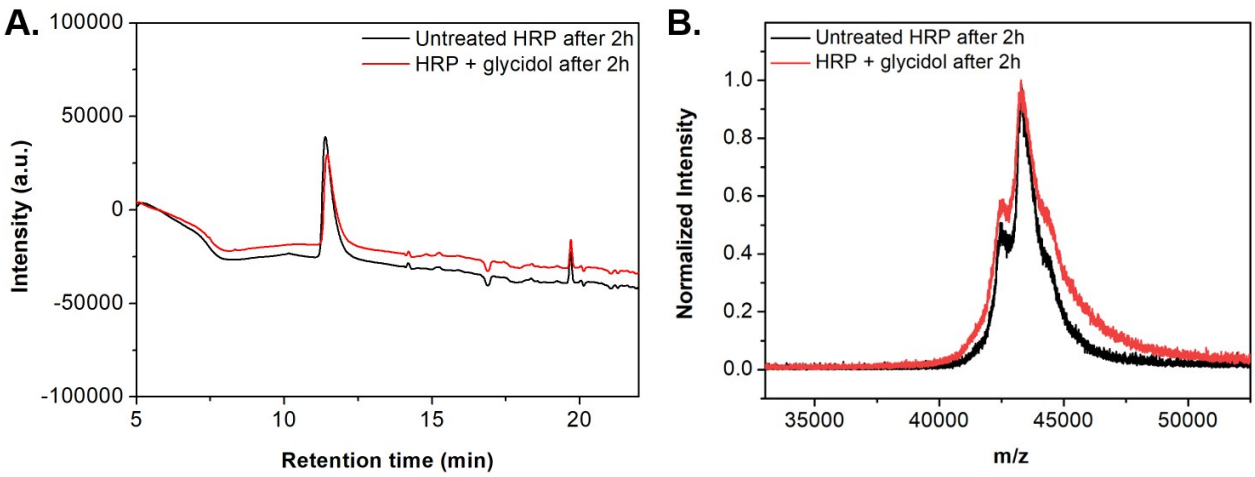

Figure S8. (A) HPLC traces and (B) MALDI-ToF mass spectra of untreated HRP (black traces) and HRP after reaction with water-soluble glycidol (0.14 mmol mL^{-1}) for 2 hours in DI water (red traces) ($[HRP]_{reaction}$ = 20 U mL^{-1}), showing no apparent modification of HRP by ring-opening of the epoxide groups *via* its lysine residues.

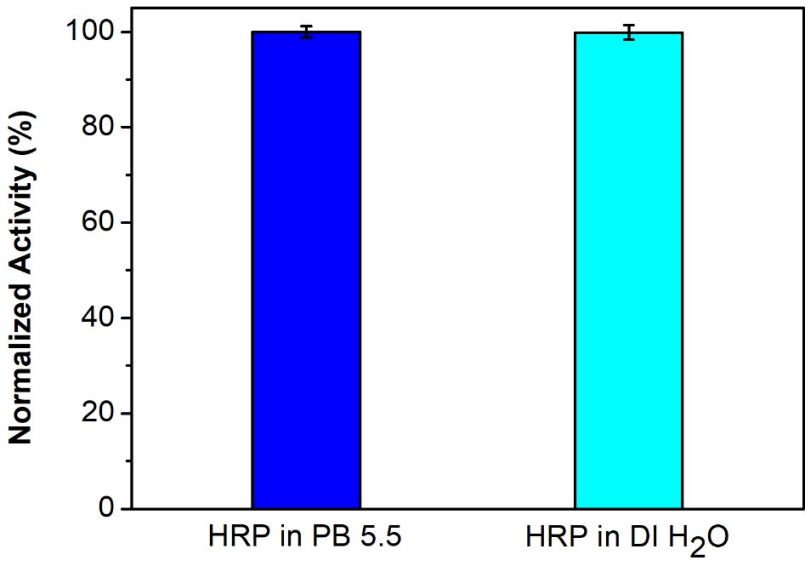

Figure S9. Control experiment comparing the activity of free HRP after incubation at room temperature for 18 hours in either PB 5.5 (optimum pH value of the enzyme) or DI water ($[HRP]_{reaction}$ = 2 U mL^{-1}), as determined at the end point of the colorimetric assay (end point = 30 min, λ = 492 nm), showing no loss of HRP activity under the epoxide ring-opening reaction conditions.

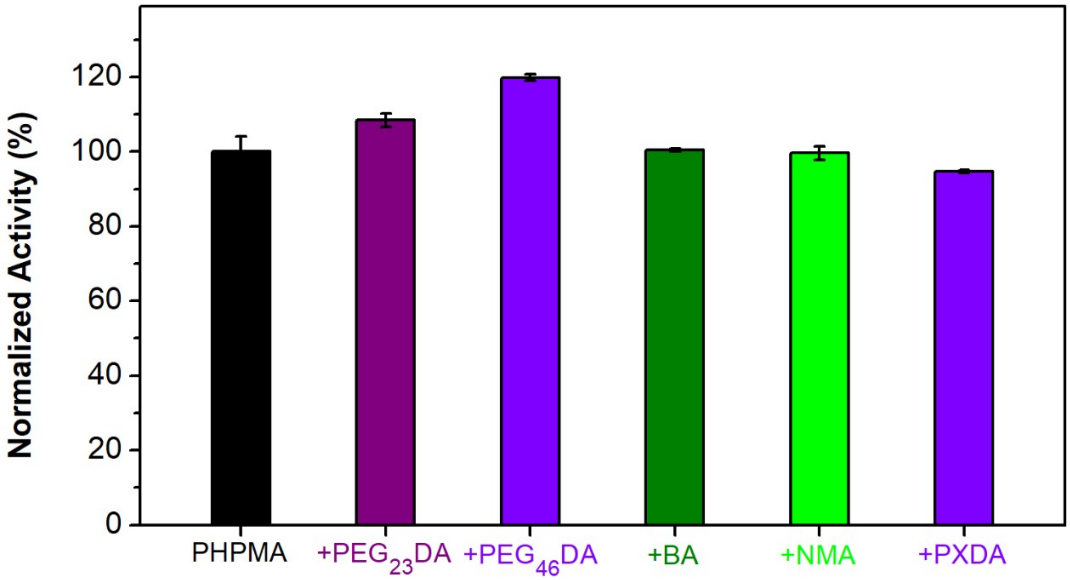

Figure S10. Control experiment comparing the activity of purified HRP-loaded PEG_{113}-*b*-$PHPMA_{400}$ vesicles before and after incubation with a series of primary amine and diamine molecules at room temperature for 18 hours in DI water, as determined at the end point of the colorimetric assay (end point = 30 min, λ = 492 nm), showing no negative effect of utilized amines on the HRP catalytic activity.

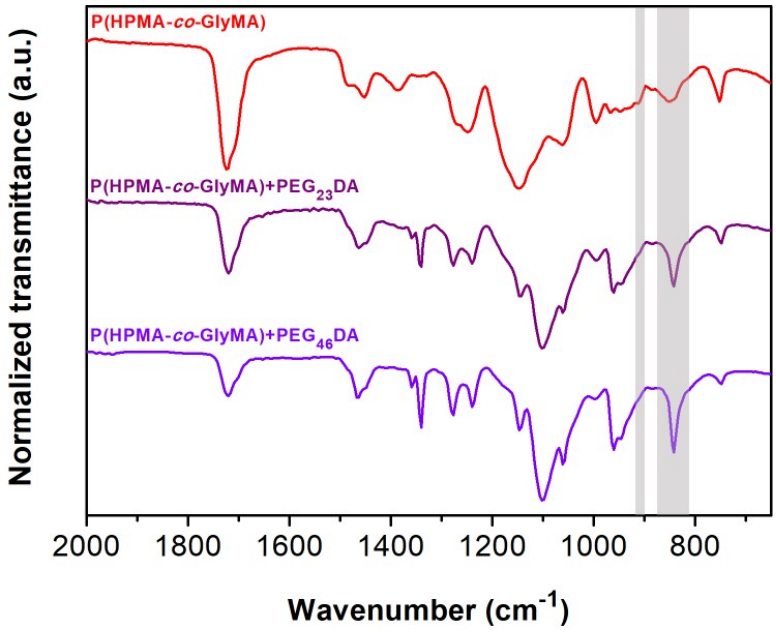

Figure S11. FT-IR spectra recorded for PEG_{113}-*b*-P($HPMA_{320}$-*co*-$GlyMA_{80}$) vesicles prior to membrane functionalization, and cross-linked PEG_{113}-*b*-P($HPMA_{320}$-*co*-$GlyMA_{80}$)+PEG_nDA vesicles showing the disappearance of the characteristic asymmetric vibration peaks of PGlyMA epoxy groups at 849 and 909 cm^{-1} after ring-opening reactions using PEG_nDA (n = 23, 46).

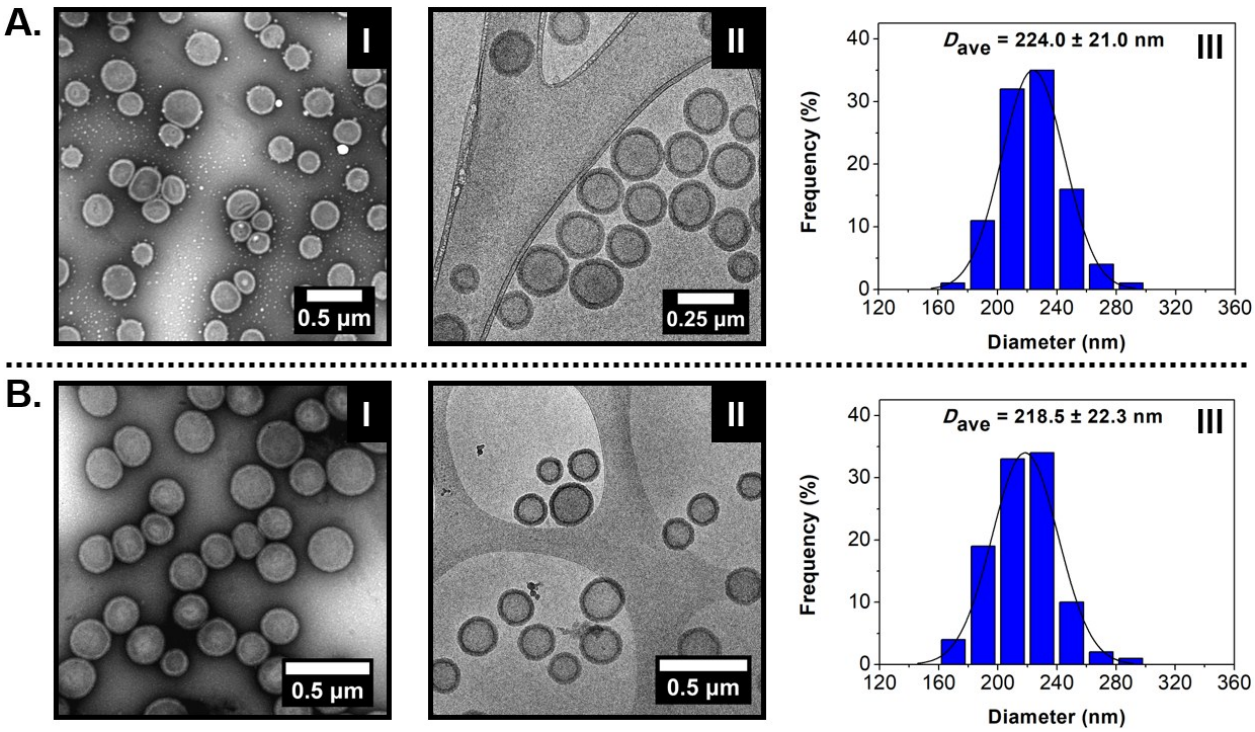

Figure S12. (A) For cross-linked HRP-loaded PEG_{113}-*b*-P($HPMA_{320}$-*co*-$GlyMA_{80}$)+$PEG_{23}DA$ vesicles, and (B) for cross-linked HRP-loaded PEG_{113}-*b*-P($HPMA_{320}$-*co*-$GlyMA_{80}$)+$PEG_{46}DA$ vesicles: (I) Representative dry-state TEM images, stained with 1 wt% UA solution, (II) representative cryo-TEM images, and (III) histograms of size distribution along with calculated average diameter values measured from particle analysis based on cryo-TEM images. In each case, at least 100 particles were analysed.

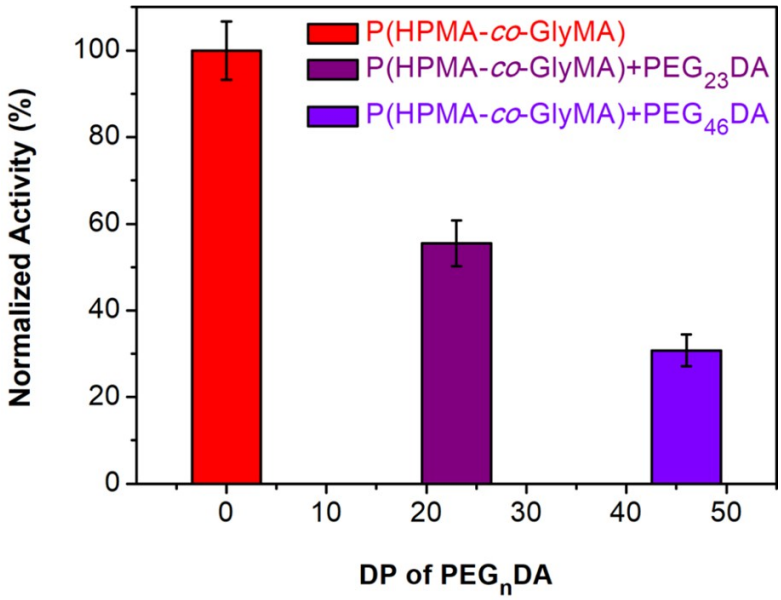

Figure S13. Normalized activities of PEG_nDA (n = 23, 46) cross-linked HRP-loaded PEG_{113}-*b*-P($HPMA_{320}$-*co*-$GlyMA_{80}$) vesicles compared to non-functionalized HRP-loaded PEG_{113}-*b*-P($HPMA_{320}$-*co*-$GlyMA_{80}$) vesicles at the end point of the enzymatic assay (end point = 30 min, λ = 492 nm), showing activity decrease upon increasing length of PEG_nDA (error bars show the standard deviation from four repeat measurements).

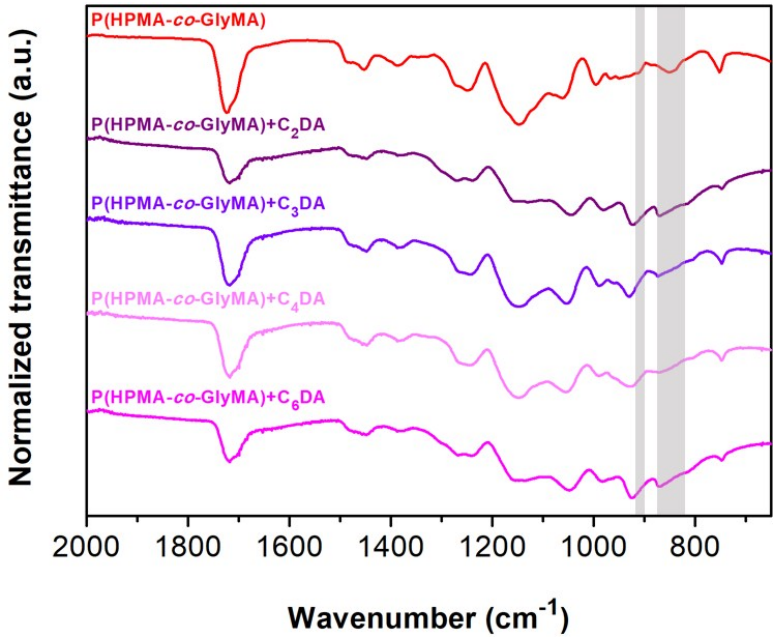

Figure S14. FT-IR spectra recorded for PEG_{113}-*b*-P($HPMA_{320}$-*co*-$GlyMA_{80}$) vesicles prior to membrane functionalization, and cross-linked PEG_{113}-*b*-P($HPMA_{320}$-*co*-$GlyMA_{80}$)+C_nDA vesicles showing the disappearance of the characteristic asymmetric vibration peaks of PGlyMA epoxy groups at 849 and 909 cm^{-1} after ring-opening reactions using C_nDA (n = 2-4, 6).

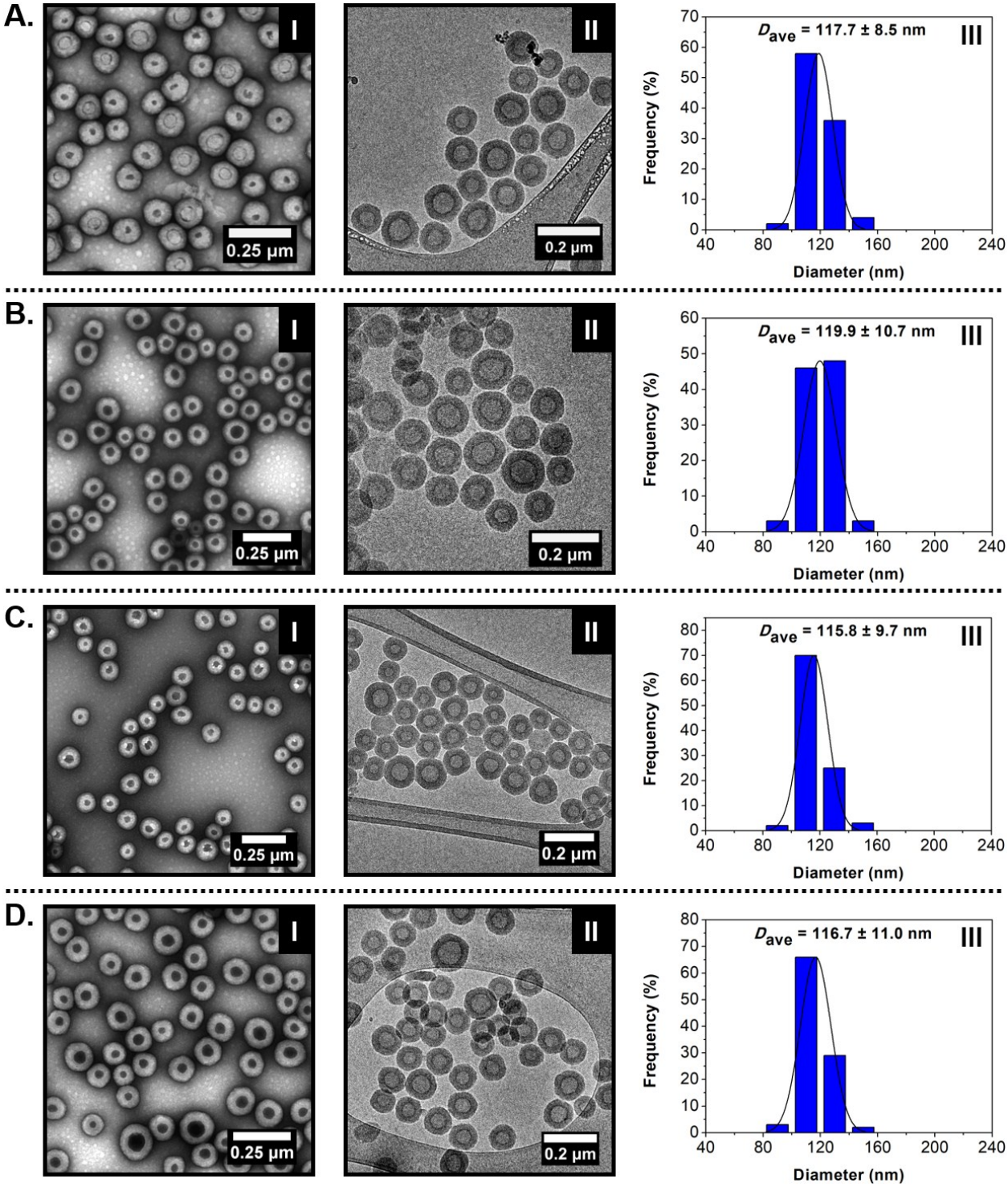

Figure S15. (A) For cross-linked HRP-loaded PEG_{113}-*b*-P($HPMA_{320}$-*co*-$GlyMA_{80}$)+C_2DA vesicles, (B) for cross-linked HRP-loaded PEG_{113}-*b*-P($HPMA_{320}$-*co*-$GlyMA_{80}$)+C_3DA vesicles, (C) for cross-linked HRP-loaded PEG_{113}-*b*-P($HPMA_{320}$-*co*-$GlyMA_{80}$)+C_4DA vesicles and (D) for cross-linked HRP-loaded

PEG_{113}-*b*-P($HPMA_{320}$-*co*-$GlyMA_{80}$)+C_6DA vesicles: (I) Representative dry-state TEM images, stained with 1 wt% UA solution, (II) representative cryo-TEM images, and (III) histograms of size distribution along with calculated average diameter values measured from particle analysis based on cryo-TEM images. In each case, at least 100 particles were analysed.

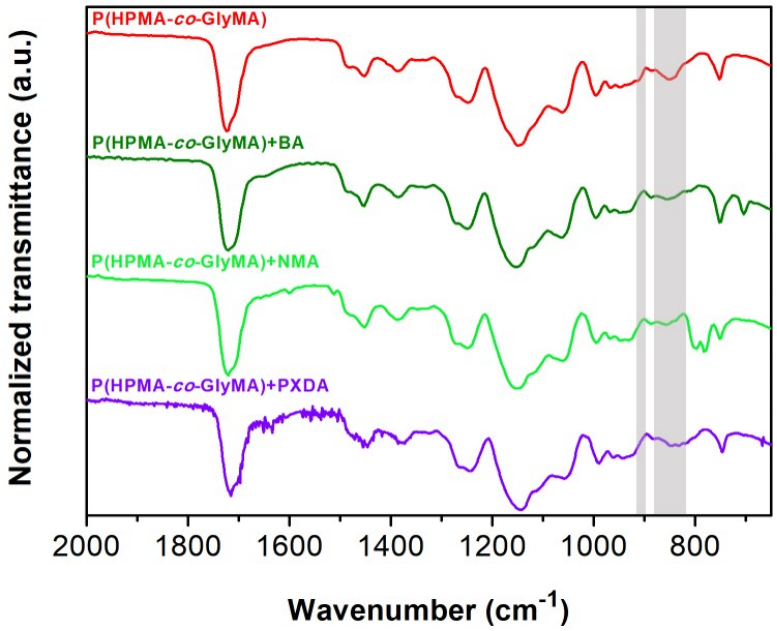

Figure S16. FT-IR spectra recorded for PEG_{113}-*b*-P($HPMA_{320}$-*co*-$GlyMA_{80}$) vesicles prior to membrane functionalization, BA/NMA-functionalized PEG_{113}-*b*-P($HPMA_{320}$-*co*-$GlyMA_{80}$) vesicles, and PXDA cross-linked PEG_{113}-*b*-P($HPMA_{320}$-*co*-$GlyMA_{80}$) vesicles showing the disappearance of the characteristic asymmetric vibration peaks of PGlyMA epoxy groups at 849 and 909 cm^{-1} after ring-opening reactions using BA, NMA or PXDA.

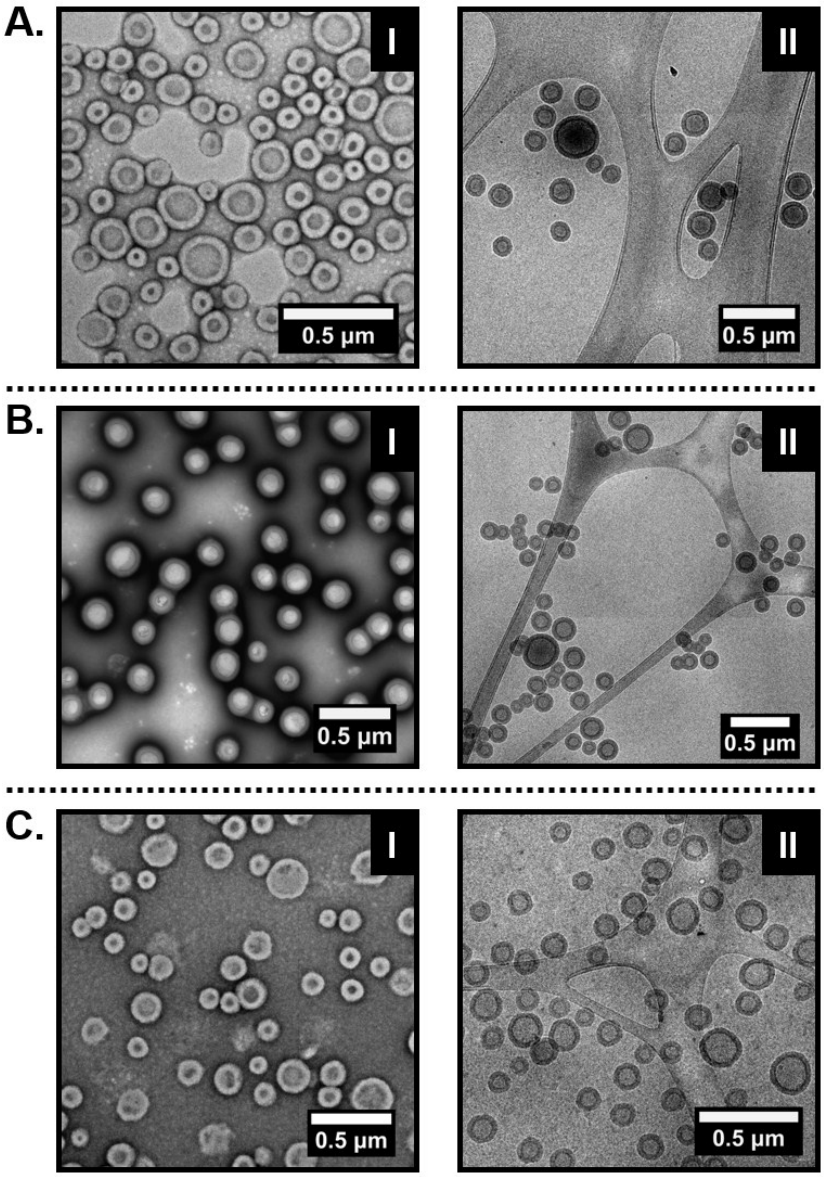

Figure S17. (A) For HRP-loaded PEG_{113}-*b*-P($HPMA_{320}$-*co*-$GlyMA_{80}$)+BA vesicles, (B) for HRP-loaded PEG_{113}-*b*-P($HPMA_{320}$-*co*-$GlyMA_{80}$)+NMA vesicles, and (C) for cross-linked HRP-loaded PEG_{113}-*b*-P($HPMA_{320}$-*co*-$GlyMA_{80}$)+PXDA vesicles: (I) Representative dry-state TEM images, stained with 1 wt% UA solution, and (II) representative cryo-TEM images.

Table S2. Summary of size, PD, and membrane thickness values for empty PEG_{113}-*b*-P($HPMA_{320}$-*co*-$GlyMA_{80}$) vesicles (*), and HRP-loaded PEG_{113}-*b*-P($HPMA_{320}$-*co*-$GlyMA_{80}$) vesicles before and after membrane functionalization using a series of primary amines, as determined by DLS analysis and TEM imaging, respectively.

Amine	D_h[a] (nm)	PD[a]	$D_{dry\text{-}state}$[b] (nm)	D_{cryo}[c] (nm)	M_{ave}[c] (nm)
-(*)	188.3 ± 5.6	0.18 ± 0.02	170.3 ± 23.0	175.5 ± 24.1	28.0 ± 3.0
-	182.6 ± 2.5	0.14 ± 0.04	171.9 ± 17.8	172.5 ± 25.5	27.9 ± 2.6
$PEG_{23}DA$	239.6 ± 6.4	0.11 ± 0.01	229.5 ± 33.2	224.0 ± 21.0	31.7 ± 2.4
$PEG_{46}DA$	238.4 ± 6.4	0.14 ± 0.04	233.3 ± 32.3	218.5 ± 22.3	31.8 ± 2.5
C_2DA	128.4 ± 3.8	0.13 ± 0.01	122.7 ± 8.3	117.7 ± 8.5	30.5 ± 2.1
C_3DA	123.8 ± 0.6	0.12 ± 0.02	122.2 ± 9.9	119.9 ± 10.7	30.1 ± 2.2
C_4DA	1497 ± 266	0.24 ± 0.04	122.3 ± 8.9	115.8 ± 9.7	31.6 ± 2.3
C_6DA	1389 ± 149	0.23 ± 0.06	123.1 ± 10.1	116.7 ± 11.0	30.7 ± 2.0
PXDA	203.4 ± 1.9	0.06 ± 0.01	181.3 ± 22.9	172.7 ± 16.4	31.1 ± 2.7
BA	203.4 ± 2.8	0.08 ± 0.02	164.6 ± 26.8	175.4 ± 27.7	33.2 ± 2.9
NMA	204.0 ± 4.7	0.02 ± 0.01	190.7 ± 16.2	182.5 ± 18.9	37.6 ± 2.8
AMA	*Macroscopic precipitation – unstable particles*				

[a]D_h and PD values measured from DLS analysis. [b]Average diameter values measured from particle analysis based on dry-state TEM images. [c]Average diameter and membrane thickness values measured from particle analysis based on cryo-TEM images. In each case, at least 100 particles were analyzed.

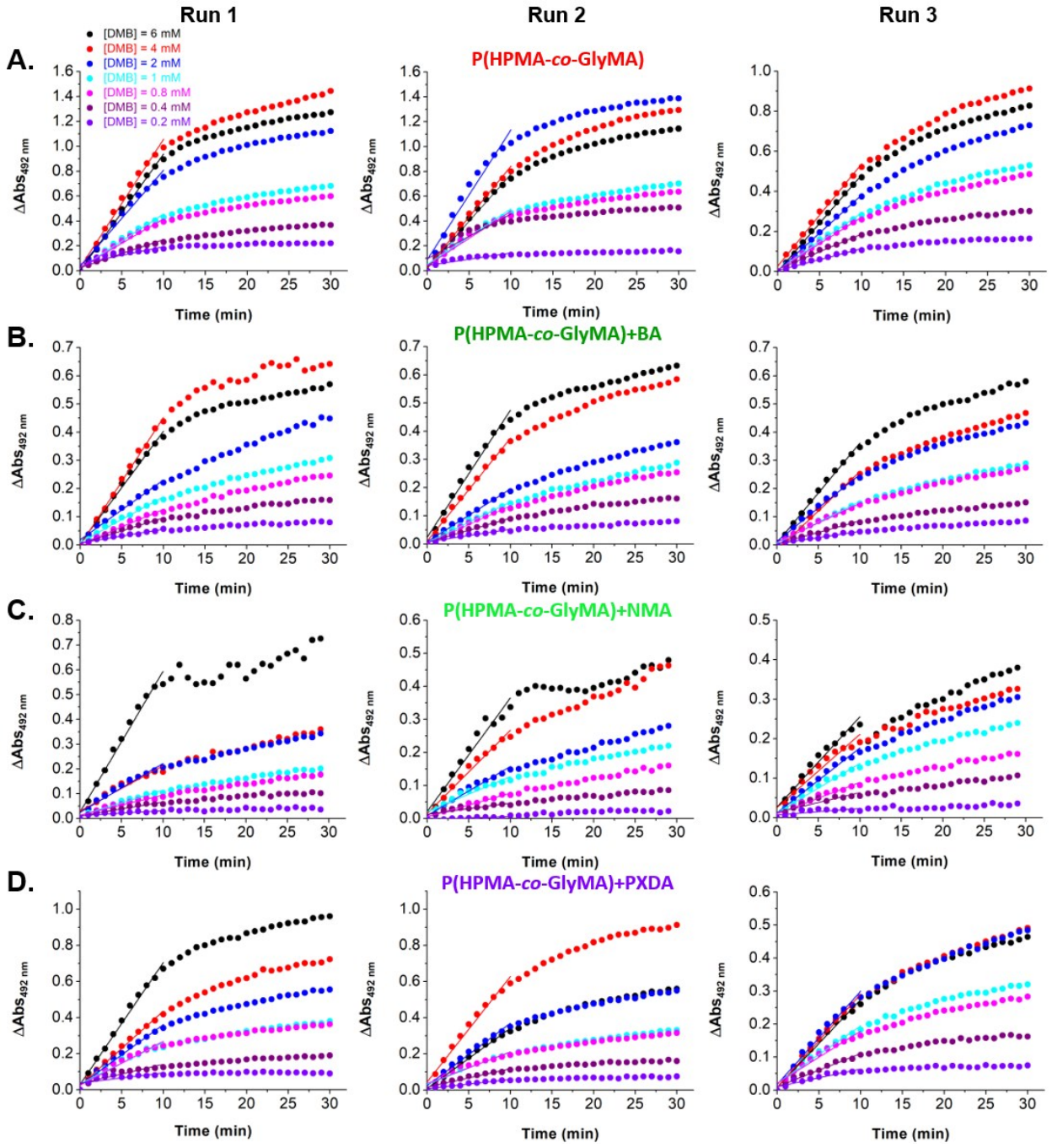

Figure S18. Enzymatic activity of (A) HRP-loaded PEG_{113}-*b*-P($HPMA_{320}$-*co*-$GlyMA_{80}$) vesicles, (B) HRP-loaded PEG_{113}-*b*-P($HPMA_{320}$-*co*-$GlyMA_{80}$)+BA vesicles, (C) HRP-loaded PEG_{113}-*b*-P($HPMA_{320}$-*co*-$GlyMA_{80}$)+NMA vesicles, and (D) HRP-loaded PEG_{113}-*b*-P($HPMA_{320}$-*co*-$GlyMA_{80}$)+PXDA vesicles at different [DMB] (with [H_2O_2] under saturating conditions) (end point = 30 min, λ = 492 nm). In each case, the average initial slope of three repeat measurements (V_0) for the first 10 min of the assay was used for construction of Michaelis-Menten kinetic plots and was normalized against V_{max}.

Table S3. Summary of enzyme activity curve fitting analysis for HRP-loaded PEG_{113}-*b*-P($HPMA_{320}$-*co*-$GlyMA_{80}$) and HRP-loaded PEG_{113}-*b*-P($HPMA_{320}$-*co*-$GlyMA_{80}$)+BA/NMA/PXDA vesicles utilized for construction of Michaelis-Menten kinetic plots.

Sample	[DMB] (mM)	Slope Run 1	Slope Run 2	Slope Run 3	Average Slope	Standard Deviation
PEG_{113}-*b*-P($HPMA_{320}$-*co*-$GlyMA_{80}$)	6	0.0938	0.0760	0.0481	0.0726	0.0188
	4	0.1031	0.0817	0.0511	0.0786	0.0214
	2	0.0774	0.1046	0.0378	0.0733	0.0274
	1	0.0435	0.0448	0.0284	0.0389	0.0074
	0.8	0.0392	0.0438	0.0263	0.0364	0.0074
	0.4	0.0227	0.0360	0.0176	0.0254	0.0077
	0.2	0.0138	0.0103	0.0109	0.0116	0.0015
PEG_{113}-*b*-P($HPMA_{320}$-*co*-$GlyMA_{80}$)+BA	6	0.0398	0.0450	0.0354	0.0401	0.0039
	4	0.0453	0.0365	0.0279	0.0366	0.0071
	2	0.0212	0.0186	0.0237	0.0212	0.0020
	1	0.0161	0.0143	0.0147	0.0150	0.0008
	0.8	0.0124	0.0133	0.0137	0.0132	0.0005
	0.4	0.0091	0.0086	0.0082	0.0086	0.0004
	0.2	0.0049	0.0045	0.0045	0.0046	0.0002
PEG_{113}-*b*-P($HPMA_{320}$-*co*-$GlyMA_{80}$)+NMA	6	0.0568	0.0344	0.0229	0.0380	0.0141
	4	0.0183	0.0252	0.0186	0.0207	0.0031
	2	0.0197	0.0149	0.0165	0.0170	0.0020
	1	0.0102	0.0106	0.0125	0.0111	0.0010
	0.8	0.0082	0.0072	0.0080	0.0078	0.0004
	0.4	0.0057	0.0034	0.0050	0.0047	0.0009
	0.2	0.0020	0.0009	0.0017	0.0015	0.0005
PEG_{113}-*b*-P($HPMA_{320}$-*co*-$GlyMA_{80}$)+PXDA	6	0.0676	0.0333	0.0266	0.0425	0.0180
	4	0.0413	0.0583	0.0282	0.0426	0.0124
	2	0.0335	0.0346	0.0282	0.0321	0.0028
	1	0.0229	0.0181	0.0173	0.0195	0.0024
	0.8	0.0243	0.0175	0.0158	0.0192	0.0037
	0.4	0.0107	0.0102	0.0010	0.0073	0.0045
	0.2	0.0057	0.0051	0.0054	0.0054	0.0002

Chapter 4. Predicting Monomers for Use in Aqueous Ring-Opening Metathesis Polymerization-Induced Self-Assembly

4.1. Publication Details and Overview

Title: Predicting Monomers for Use in Aqueous Ring-Opening Metathesis Polymerization-Induced Self-Assembly

Authors: **Spyridon Varlas**,[†] Jeffrey C. Foster,[†] Lucy A. Arkinstall,[†] Joseph R. Jones,[†] Robert Keogh,[†,‡] Robert T. Mathers,*[,§] and Rachel K. O'Reilly*[,†]

Affiliations: [†]School of Chemistry, University of Birmingham, Edgbaston, Birmingham B15 2TT, United Kingdom

[‡]Department of Chemistry, University of Warwick, Gibbet Hill Road, Coventry CV4 7AL, United Kingdom

[§]Department of Chemistry, Pennsylvania State University, New Kensington, Pennsylvania 15068, United States

Journal: ACS Macro Letters

Year: 2019

Volume: 8

Page Numbers: 466-472

DOI: 10.1021/acsmacrolett.9b00117

Submitted: 16th February 2019, **Published:** 3rd April 2019

Coauthor Contributions: Synthesis of norbornene-based monomers used in this study was performed with assistance from Dr. Jeffrey C. Foster and Ms. Lucy A. Arkinstall at the University of Birmingham. SAXS measurements were performed by Dr. Steven Huband at the University of Warwick, while SAXS data analysis and discussion were performed by Dr. Joseph R. Jones at the University of Birmingham. Cryo-TEM imaging of polymersomes was performed with assistance from Dr. Robert Keogh and Dr. Saskia Bakker at the University of Warwick. LogP_{oct}/SA calculations for reported and predicted monomers, as well as for their corresponding oligomers were performed by Prof. Robert T. Mathers at the Pennsylvania State University. MicroDSC analysis was performed with assistance from Mr. Zachary Coe at the University of Birmingham. Dr. Jeffrey C. Foster (University of Birmingham) and Prof. Robert T. Mathers (Pennsylvania State University) provided guidance and editing of this manuscript. Prof. Rachel K. O'Reilly (University of Birmingham) supervised the research project, provided guidance and editing of this chapter.

Overview: In this Chapter, aqueous ROMP-mediated PISA is employed as a powerful and robust methodology for the *in situ* fabrication of polynorbornene-based block copolymer nano-objects with tunable morphology and core-forming block chemistry, but also distinctly different characteristics as compared to their (meth)acrylate/acrylamide-based counterparts, typically prepared *via* RAFT-mediated PISA, in an effort to unravel the potential of this underexplored field in catalysis, drug delivery and biomimicry.

In our initial report on controlled ROMP in acidic aqueous media using a macroinitiator approach and the realization of ROMPISA upon selection of suitable core-forming monomers that produce water-immiscible polymers under the same polymerization conditions, it was intriguing to observe that access to uniquely small higher-order nanostructures (i.e., worm-like micelles and vesicles) could be readily achieved *via* this strategy. We hypothesized this behavior emerges due to the high rigidity and T_g of PNBs that, in turn, induce high degrees of chain stretching, low unimer mobility and decreased interfacial curvature between the corona- and core-forming domains, giving rise to higher-order morphologies during the early stages of the ROMPISA process. The primary focus of Chapter 4 was to expand the pool of available corona- and core-forming ROMPISA monomers in order to evaluate the universality of this self-assembly behavior and, additionally, enable control over the core-block hydrophobicity and functionality of the developed nano-objects for future biotechnological applications.

First, theoretical identification of new ROMPISA monomers was achieved *via* an *in silico* methodology, previously utilized in aqueous RAFT-mediated PISA by our group, that involved LogP_{oct}/SA calculations for a series of NB-based monomers and their corresponding oligomeric models. Positive LogP_{oct}/SA values correspond to hydrophobic oligomers that preferably partition into the octanol phase and, as such, can comprise the

core-forming block in an amphiphilic block copolymer formulation, whereas the opposite behavior indicates candidates for use in corona-forming blocks. Next, experimental validation was successfully carried out for the whole series of predicted monomers upon synthesis of diblock copolymer nano-objects using our established two-step macroinitiator approach for conducting ROMPISA in aqueous media, followed by thorough characterization of the prepared nanoassemblies. Importantly, a set of nano-objects with similar physical characteristics were obtained, whilst useful structure-property relationships could be also identified with higher-order nanostructures being accessed upon increasing oligomer hydrophobicity for a certain core-block DP.

In this contribution, we were particularly interested in monitoring the evolution of vesicular nanostructures, as well as investigating their properties. Their uniquely small size, along with their distinctly thin membranes (3-10 nm) and the wide range of functionalities introduced within their core-forming domains, that enable a range of potential post-PISA transformations, could significantly expand the application breadth of such assemblies. The preliminary findings highlighted herein were used as a groundwork for the project discussed in Chapter 5, while they also constitute the main area of focus in studies currently ongoing within our group.

ACS Macro Letters

Letter

Cite This: ACS Macro Lett. 2019, 8, 466−472

pubs.acs.org/macroletters

Predicting Monomers for Use in Aqueous Ring-Opening Metathesis Polymerization-Induced Self-Assembly

Spyridon Varlas,[†] Jeffrey C. Foster,[†] Lucy A. Arkinstall,[†] Joseph R. Jones,[†] Robert Keogh,[†,‡] Robert T. Mathers,*[,§] and Rachel K. O'Reilly*[,†]

[†]School of Chemistry, University of Birmingham, Edgbaston, Birmingham B15 2TT, U.K.

[‡]Department of Chemistry, University of Warwick, Gibbet Hill Road, Coventry CV4 7AL, U.K.

[§]Department of Chemistry, Pennsylvania State University, New Kensington, Pennsylvania 15068, United States

Supporting Information

ABSTRACT: Aqueous polymerization-induced self-assembly (PISA) is a well-established methodology enabling *in situ* synthesis of polymeric nanoparticles of controllable morphology. Notably, PISA *via* ring-opening metathesis polymerization (ROMPISA) is an emerging technology for block copolymer self-assembly, mainly due to its high versatility and robustness. However, a limited number of monomers suitable for core-forming blocks in aqueous ROMPISA have been reported to date. In this work, we identified seven monomers for use as either corona- or core-forming blocks during aqueous ROMPISA by *in silico* calculation of relative hydrophobicity for corresponding oligomeric models. The predicted monomers were validated experimentally by conducting ROMPISA using our previously reported two-step approach. In addition to predictive data, our computational model was exploited to identify trends between polymer hydrophobicity and the morphology of the self-assembled nano-objects they formed. We expect that this methodology will greatly expand the scope of aqueous ROMPISA, as monomers can be easily identified based on the structure−property relationships observed herein.

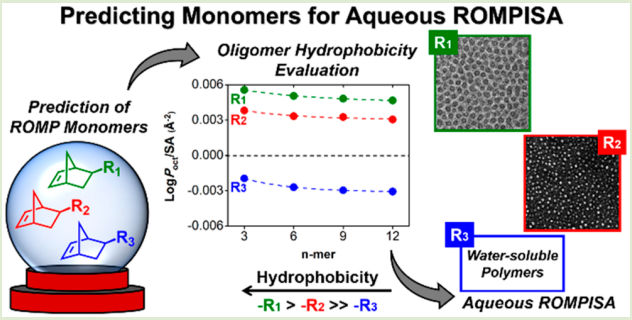

Conventional preparative methodologies for solution self-assembly of block copolymers have been extensively applied in modern polymer science.[1−4] These involve the synthesis of a block copolymer in organic solvent and multiple steps for its transition into a selective solvent for one or more blocks to allow for the formation of nanostructures. In general, such strategies are often limited by low polymer concentration (≤1% w/w) and precise morphology control issues.[5,6] Recently, polymerization-induced self-assembly (PISA) has been introduced as an alternative one-pot procedure for *in situ* development of nano-objects with tunable morphologies at high solid concentrations (typically 10−30% w/w).[7−10] During block copolymer PISA, direct nanoparticle fabrication is achieved as a solvent-soluble corona-forming block is chain extended using specific solvent-miscible (dispersion PISA) or solvent-immiscible (emulsion PISA) monomers that form a second, insoluble core block.[11]

To date, the majority of literature reports on PISA has been dominated by reversible-deactivation radical polymerization (RDRP) techniques, mainly involving atom transfer radical polymerization (ATRP)[12,13] and reversible addition−fragmentation chain-transfer (RAFT) polymerization,[14−17] in both aqueous and organic media. However, PISA mediated by ring-opening metathesis polymerization (ROMPISA) has recently emerged as a nonradical technology for block copolymer self-assembly. This growing research interest is facilitated by the robust nature of commercially available Ru-based catalysts, fast polymerization kinetics, and the ability to conduct polymerizations under air at ambient temperature in either organic or aqueous milieu.[18−20]

Since ROMPISA is a newly established concept, a very limited number of monomers that are able to undergo the described solubility transition upon polymerization to achieve *in situ* self-assembly are known, especially in dispersed aqueous media. In particular, a few monomers that undergo ROMPISA in organic solvent or under aqueous emulsion conditions have been reported thus far,[21−25] while Gianneschi's group introduced a quaternary amine-based phenyl norbornene dicarboximide monomer as the core-forming block in aqueous dispersion ROMPISA.[26,27] In addition, *exo*-5-norbornenecarboxylic acid and a di(oligo(ethylene glycol))-based norbornene monomer have been reported by our group for use in aqueous dispersion ROMPISA *via* a water-soluble macroinitiator approach.[28] Hence, opportunities exist for identification of new core-forming ROMPISA monomers.

Recently, our group reported an *in silico* method that allows for prediction of monomers that could be used either as

Received: February 16, 2019
Accepted: March 19, 2019
Published: April 3, 2019

corona- or core-forming blocks in aqueous RAFT-mediated PISA through oligomer hydrophobicity evaluation, as well as for prediction of morphologies for PISA systems implemented with different monomer chemistries.[29] Herein, this process is applied to predict a set of norbornene monomers with various functionalities for use in aqueous ROMPISA. Diblock copolymer nano-objects were successfully developed *via* one-pot ROMPISA using the predicted monomers as core-forming blocks and the same hydrophilic stabilizer block as the macroinitiator, following our recently reported procedure for controlled ROMP in aqueous media.[28] The order of resulting morphologies increased upon respective degree of polymerization (DP) and relative hydrophobicity increase, while structure−property relationships were also identified based on our monomer design.

The predictive methodology followed for identifying whether a monomer will be able to undergo aqueous ROMPISA is based on *in silico* determination of hydrophobicity for corresponding oligomeric models by calculating octanol−water partition coefficients ($Log P_{oct}$). This analysis has been well-established for small molecules, while transitioning to larger polymer molecules benefits from normalization of $Log P_{oct}$ values by solvent-accessible surface area (SA) to minimize molecular weight and end-group discrepancies.[30−32] Olefin end-groups were chosen for the oligomer models in all calculations for simplicity. While end-group hydrophobicity contributes to the $Log P_{oct}$/SA value for short oligomers (i.e., DP < 10), the influence of end-groups becomes negligible as DP increases.[30] Positive $Log P_{oct}$/SA values correspond to hydrophobic polymers that primarily partition into the octanol phase and as such can be used in core-forming blocks during ROMPISA in aqueous media. On the contrary, water-soluble polymers possess negative $Log P_{oct}$/SA values, indicating their ability to be used in corona-forming blocks. The importance of the sign of $Log P_{oct}$/SA can be understood by comparing homopolymer solubility; for example, homopolymers synthesized using **M8** or **M9** were completely insoluble in water, whereas **P(M10)** could be readily dissolved.

Using the described predictive methodology (see Supporting Information for detailed description), $Log P_{oct}$/SA values of ROMP oligomers ranging from 3-mers to 12-mers were calculated for a series of norbornene-based monomers bearing a wide range of functional groups. A correlation between oligomer $Log P_{oct}$/SA and monomer $Log P_{oct}$ was also identified, giving insight into the water solubility of their respective homopolymers (Figure S1). Monomers used in our study were mainly selected based on their relatively facile one- or two-step syntheses from commercially available precursor compounds. We also hypothesized that hydrophobicity trends for this wide range of monomers with different anchor or terminal functional groups would elicit important structure−property relationships. For comparison, $Log P_{oct}$/SA analysis of previously reported monomers used in aqueous ROMPISA (**MX** = **M1**, **M4**, **M7**, and **M11**) was also carried out.[26,28] The hydrophobicity evaluation results for $\mathbf{P(MX)}_n$ (**MX** = **M1**−**M11**) ROMP oligomers as a function of increasing chain length along with their corresponding monomer structures are shown in Figure 1.

A plethora of studied monomers (**M1**−**M9**) were predicted to be suitable for core-forming blocks in aqueous ROMPISA as their respective oligomers possess positive $Log P_{oct}$/SA values across all chain lengths. In general, the imide-based oligomers (**M4**−**M6** and **M9**) were less hydrophobic than the ester-/amide-based ones (**M1**−**M3** and **M8**), while multiple polar functional groups or charges were required to achieve negative oligomer $Log P_{oct}$/SA values suitable for hydrophilic corona-forming blocks (**M10** and **M11**).

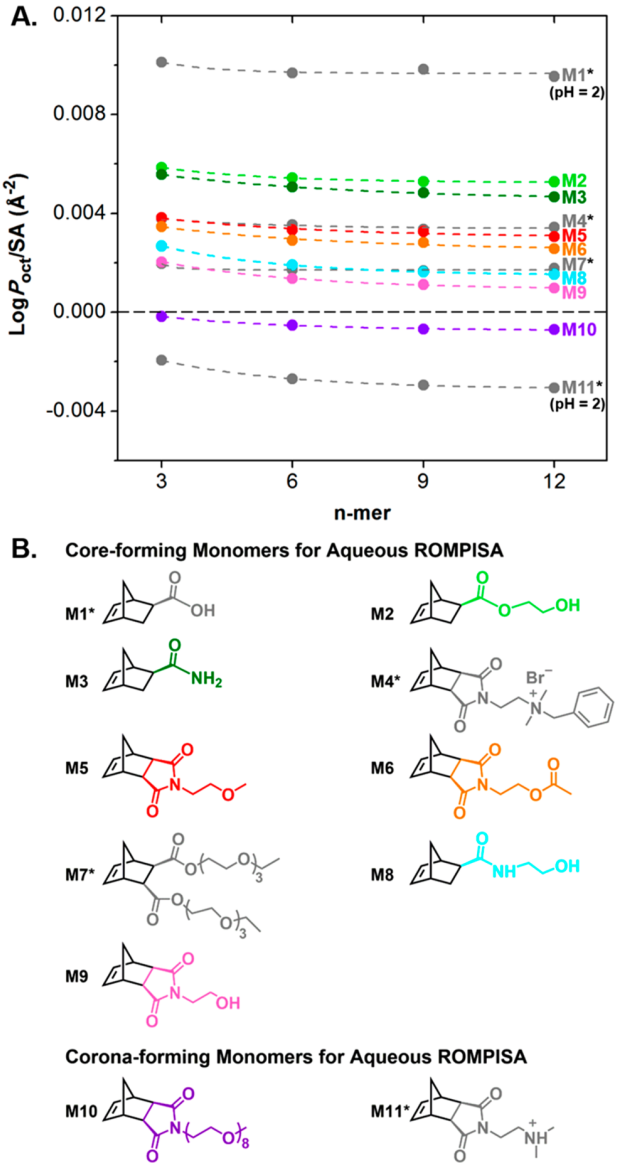

Figure 1. (A) Evolution of $\mathbf{P(MX)}_n$ (**MX** = **M1**−**M11**) ROMP oligomer hydrophobicity as a function of the length of the oligomer. $Log P_{oct}$ values (ALogP98 method) were calculated using an atom-based approach and normalized by solvent-accessible surface area (SA) using Materials Studio 2018. The $Log P_{oct}$/SA > 0 region corresponds to core-forming blocks, while the $Log P_{oct}$/SA < 0 region corresponds to corona-forming blocks. (B) Core- and corona-forming norbornene-based monomer structures for aqueous ROMPISA. Monomers marked with an asterisk (*) have been reported in the literature.

To correlate computational hydrophobicity trends with experimental results, two criteria were envisioned for monomer design. First, the ease of monomer synthesis was considered. Monomers **M2**, **M3**, **M5**, **M6**, and **M8**−**M11** were synthesized following simple imide formation or esterification/amidation procedures (see Supporting Information for experimental details). Second, the solubility of prepared monomers in aqueous media was of major significance. Importantly, the

DOI: 10.1021/acsmacrolett.9b00117
ACS Macro Lett. 2019, 8, 466−472

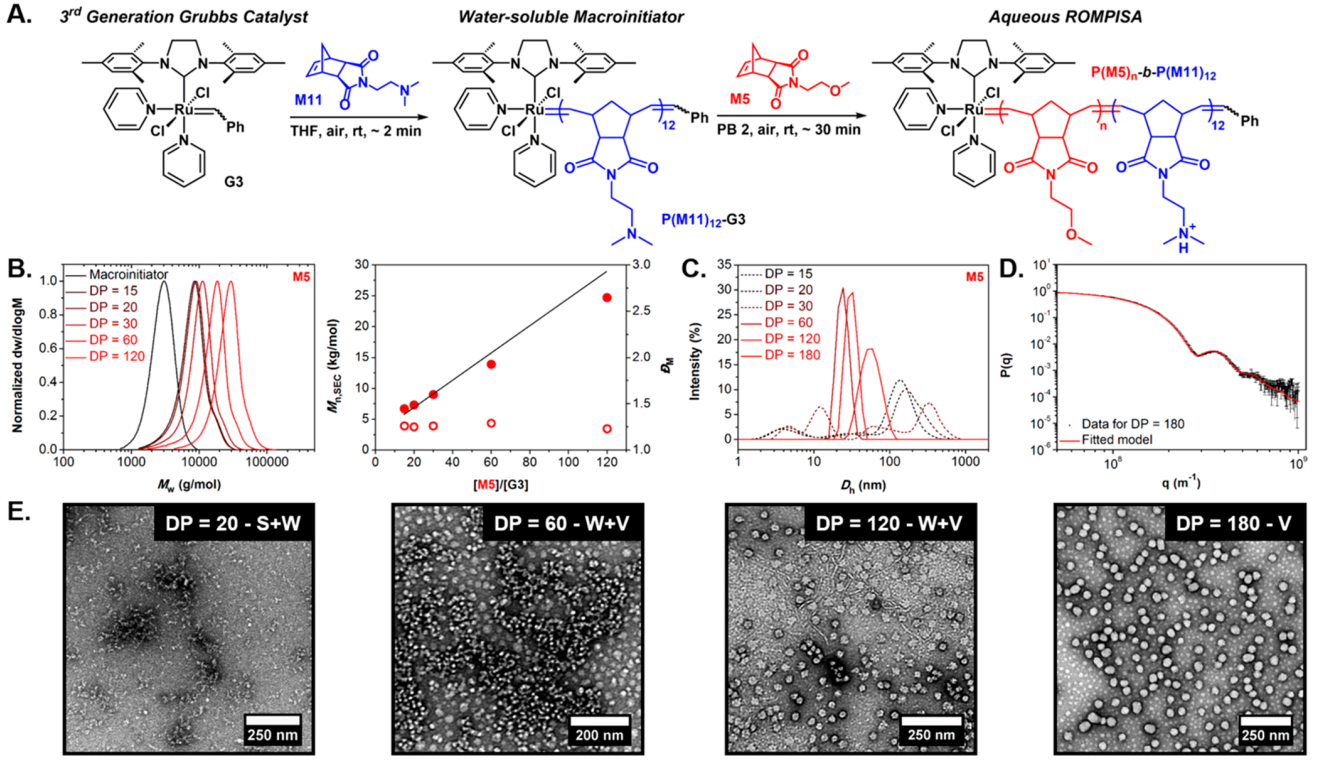

Figure 2. (A) Schematic representation of the synthetic route followed for the development of $\mathbf{P(M11)_{12}}$-*b*-$\mathbf{P(M5)}_n$ (n = 15, 20, 30, 60, 120, and 180) diblock copolymer nano-objects *via* aqueous ROMPISA using a water-soluble $\mathbf{P(M11)_{12}}$ macroinitiator. (B) Normalized SEC RI molecular weight distributions, and evolution of M_n (filled circles) and $Đ_M$ (empty circles) values calculated from SEC analysis with increasing targeted $DP_{P(M5)}$ for $\mathbf{P(M11)_{12}}$-*b*-$\mathbf{P(M5)}_n$ diblock copolymers. The solid line represents expected M_n values calculated using the monomer feed ratio, assuming full monomer conversion. M_n and $Đ_M$ values were calculated from PS standards using THF + 2% v/v NEt_3 as the eluent. (C) Intensity weighted size distributions obtained by DLS for $\mathbf{P(M11)_{12}}$-*b*-$\mathbf{P(M5)}_n$ diblock copolymer nano-objects. (D) Fitted model to SAXS data recorded for $\mathbf{P(M11)_{12}}$-*b*-$\mathbf{P(M5)_{180}}$. (E) Representative dry-state TEM images of $\mathbf{P(M11)_{12}}$-*b*-$\mathbf{P(M5)}_n$ diblock copolymer nano-objects, stained with 1 wt% uranyl acetate (UA) solution.

majority of monomers in Figure 1B were found to be water-miscible at [**MX**] = 1 wt%, underlying their ability to be used in aqueous dispersion ROMPISA. Based on these findings, we chose to evaluate diblock copolymer ROMPISA using monomers **M2**, **M3**, **M5**, **M6**, **M8**, and **M9** as core-forming blocks and **M11** as the corona-forming block following our reported methodology to conduct well-controlled, open-to-air ROMP in aqueous media using a macroinitiator approach.[28]

A **P(M11)** macroinitiator was first synthesized *via* ROMP, under air, in a water-miscible organic solvent (i.e., THF) using the commercially available third-generation Grubbs catalyst (G3) ($DP_{P(M11)}$ = 12, $M_{n,NMR}$ = 2.8 kDa, $M_{n,SEC}$ = 2.6 kDa, $Đ_M$ = 1.17, Table S1). An aliquot of the resulting macroinitiator in THF was then added to a solution of a second core-forming monomer (**MX** = **M2**, **M3**, **M5**, **M6**, **M8**, or **M9**) in acidic phosphate buffer (pH = 2, PB 2) (PB/THF = 9:1, [**MX**] = 1 wt%), where ionization of the pendant tertiary amine groups of **P(M11)** occurred yielding the charged hydrophilic stabilizer block (see Figure S2 for pH-dependent solubility of **P(M11)** oligomers). The presence of acid also promoted pyridine ligand dissociation to generate the active form of the G3 catalyst. Chain extensions for the development of $\mathbf{P(M11)_{12}}$-*b*-$\mathbf{P(MX)}_n$ diblock copolymer nano-objects *via* ROMPISA targeting increasing DP of **P(MX)** were fast and typically completed within a 2−30 min time scale, depending on the monomer. As a representative example, the obtained characterization results from aqueous ROMPISA of **M5** are given in detail in Figure 2.

Based on the described synthetic route, a series of aqueous ROMPISA reactions using **M5** were conducted over a range of DPs of **P(M5)** core-forming blocks by varying the initial [**M5**]/[G3] feed ratio, using a water-soluble $\mathbf{P(M11)_{12}}$ macroinitiator (Figure 2A). A gradual turbidity increase was noticed for polymerization solutions with increasing $DP_{P(M5)}$, indicating the onset of particle micellization. Quantitative monomer conversions (>99%) were achieved in all cases after approximately 30 min, as determined by ^{1}H NMR spectroscopic analysis in methanol-d_4 of the crude samples. SEC analysis of $\mathbf{P(M11)_{12}}$-*b*-$\mathbf{P(M5)}_n$ diblock copolymers, using THF + 2% v/v triethylamine (NEt_3) as the eluent, revealed the well-controlled character of the aqueous ROMPISA process using **M5**. Specifically, symmetrical, monomodal molecular weight distributions were observed, shifting linearly toward higher molecular weight (M_n) values upon increasing the DP of **P(M5)**. Calculated M_n values agreed well with theoretically expected values, while dispersity ($Đ_M$) values remained low ($Đ_M$ < 1.30) throughout (Figure 2B and Table S4).

DLS analysis of $\mathbf{P(M11)_{12}}$-*b*-$\mathbf{P(M5)}_n$ ROMPISA solutions revealed the formation of particles with multiple populations and high polydispersity (PD) values for the lower DPs of **P(M5)**, suggesting the development of worm-like micelles or nano-objects with mixed morphologies, while single particle populations with low PD were observed for $DP_{P(M5)} \geq 60$

DOI: 10.1021/acsmacrolett.9b00117
ACS Macro Lett. 2019, 8, 466−472

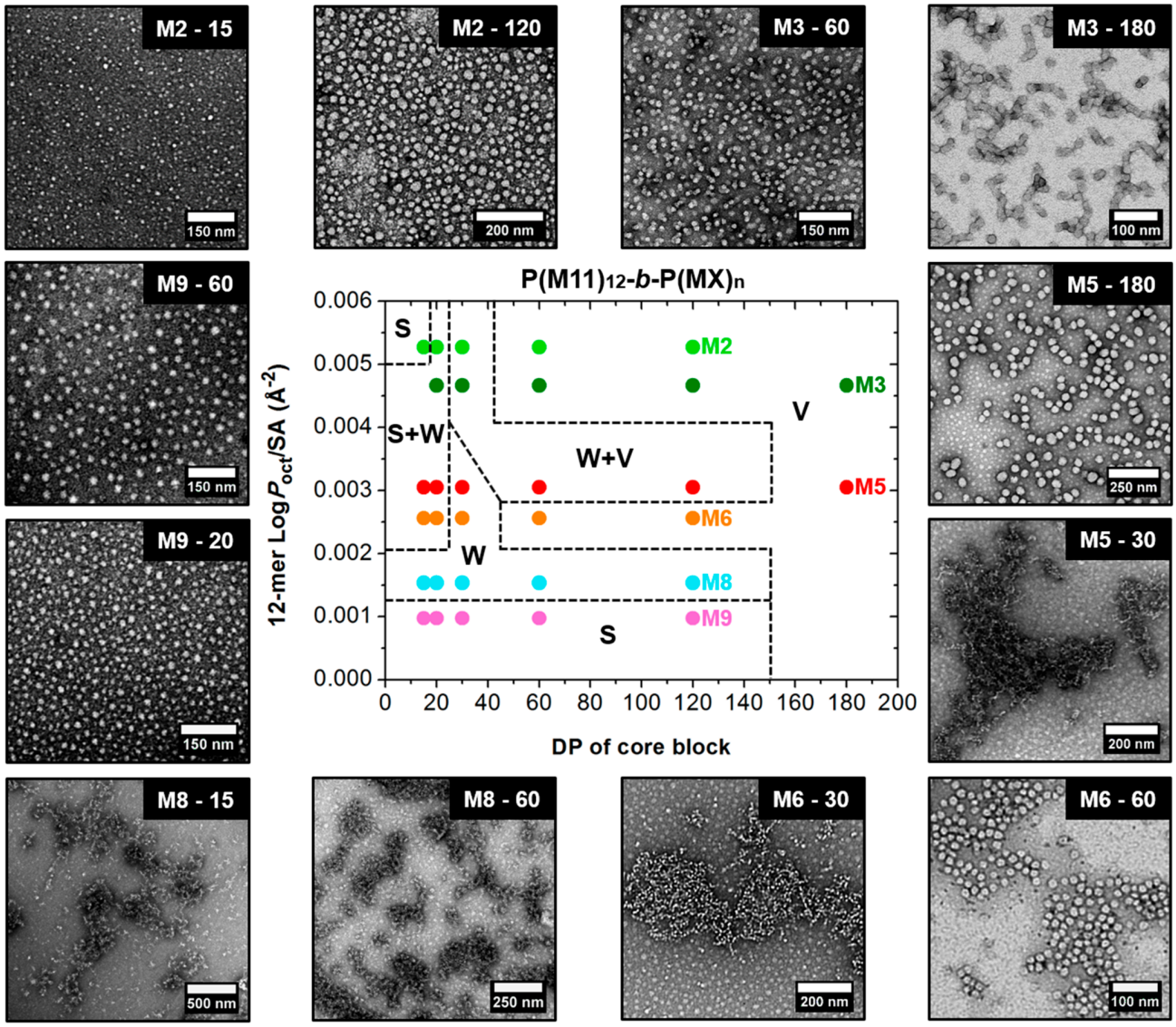

Figure 3. Detailed phase diagram for $\mathbf{P(M11)_{12}}$-*b*-$\mathbf{P(MX)_n}$ (**MX** = **M2**, **M3**, **M5**, **M6**, **M8**, and **M9**) diblock copolymer nano-objects prepared *via* aqueous ROMPISA by varying the DP of the $\mathbf{P(MX)}$ core block as a function of corresponding 12-mer LogP_{oct}/SA values, along with representative dry-state TEM images of different formulations stained with 1 wt% uranyl acetate (UA) solution (Key: S, spherical micelles; W, worm-like micelles; V, vesicles).

indicating the formation of uniform assemblies (Figure 2C and Table S12). Dry-state and cryo-TEM imaging further supported the DLS findings and showed an evolution in morphology from spheres and short worms ($DP_{P(M5)} \leq 30$) to mixed morphologies of worms and vesicles ($60 \leq DP_{P(M5)} \leq 120$) and finally to single-phase vesicles of uniform size ($DP_{P(M5)} = 180$) as the DP of the core-forming block increased (Figures 2E, S28, and S32). The observed pure worm ($DP_{P(M5)} = 30$) and vesicle ($DP_{P(M5)} = 180$) morphologies were further investigated by small-angle X-ray scattering (SAXS) analysis (Figures 2D and S33). For $DP_{P(M5)} = 180$, the scattering data were consistent with a parsimonious model for scattering by spherical particles, and fitted values to describe the particle size distribution were consistent with TEM imaging observations. However, the existence of an inner aqueous compartment could not be verified from SAXS data, as parameters within the parsimonious model could potentially mask its existence, especially if the size of this compartment is on the order of variability in particle size (i.e., a few nanometers). Notably, our theoretical model correctly predicted that the rest of the monomers with positive oligomer LogP_{oct}/SA values (**MX** = **M2**, **M3**, **M6**, **M8**, and **M9**) could also be used as hydrophobic core blocks during ROMPISA in aqueous media. Similar analysis with comparable results was performed for $\mathbf{P(M11)_{12}}$-*b*-$\mathbf{P(MX)_n}$ diblock copolymer nano-objects prepared *via* aqueous ROMPISA using the other predicted core-forming monomers (see Supporting Information for characterization results). In contrast, predicted monomer **M10** with negative oligomer LogP_{oct}/SA values could be successfully utilized as the corona-forming block since it only formed water-soluble polymers, while its ability to be chain-extended in a controlled manner under the same aqueous ROMP conditions was further confirmed (Figure S24 and Tables S8–S9).

According to our previous report on predicting new monomers for use in aqueous RAFT-mediated PISA, we applied the LogP_{oct}/SA analysis to reliably predict ROMPISA

DOI: 10.1021/acsmacrolett.9b00117
ACS Macro Lett. 2019, 8, 466–472

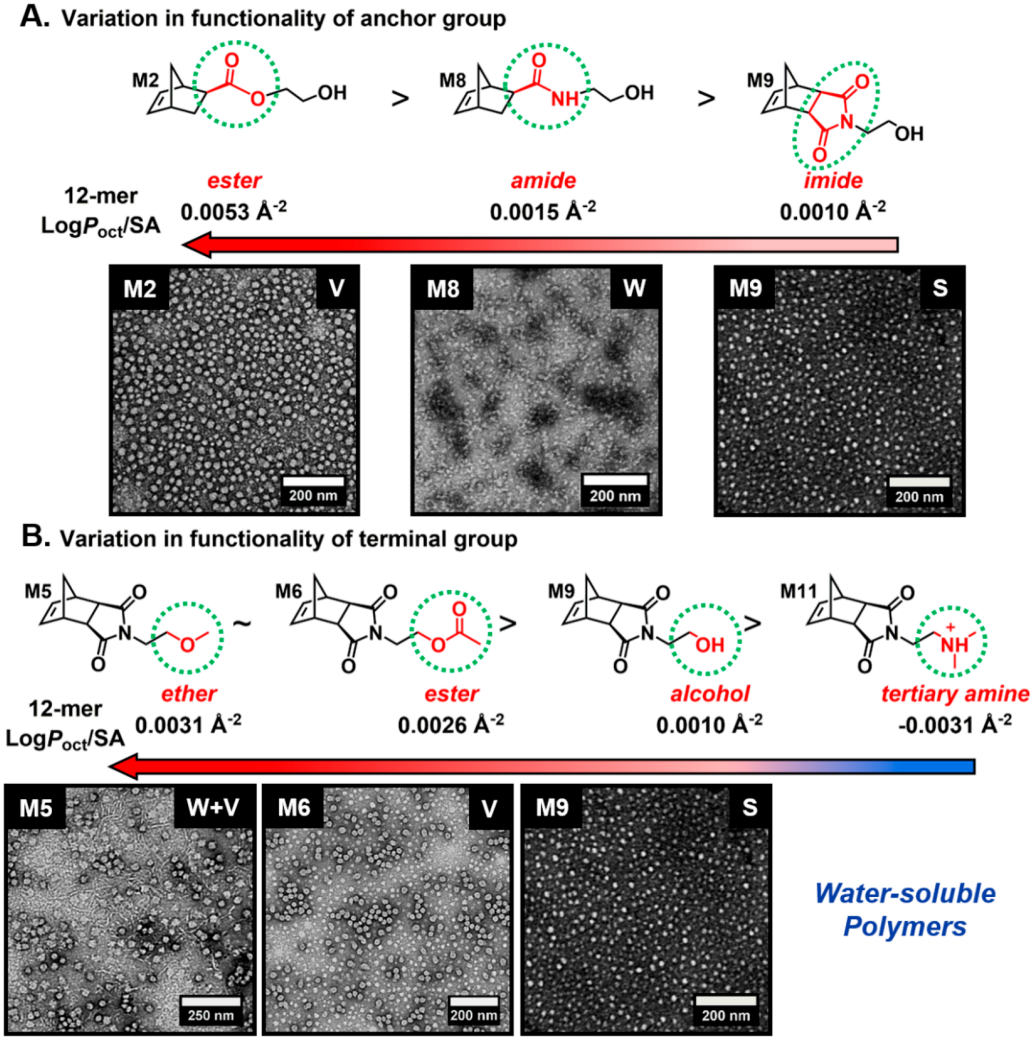

Figure 4. Hydrophobicity trends for different anchor groups (A) and different terminal groups (B) for norbornene-based monomers involved in aqueous ROMPISA based on LogP_{oct}/SA analysis from Materials Studio 2018 and corresponding dry-state TEM images for **P(M11)**$_{12}$-*b*-**P(MX)**$_n$ diblock copolymer nano-objects at DP$_{P(MX)}$ = 120 showing higher-order morphologies upon increasing polymer hydrophobicity.

morphologies.[29] Herein, contrary to traditional phase diagrams for PISA formulations that show morphology progression as a function of increasing DP and solid content, a phase diagram for **P(M11)**$_{12}$-*b*-**P(MX)**$_n$ diblock copolymer nano-objects was constructed based on the relative hydrophobicity of **P(MX)**$_n$ homopolymers. To assist comparisons across the phase diagram, all ROMPISA reactions were carried out at the same solid concentration (Figure 3).

We hypothesized that nano-object morphology would evolve toward higher-order structures with increasing DP of the core block and LogP_{oct}/SA value for the same oligomer length (i.e., up and to the right of the phase diagram). Confirming this hypothesis, small spherical micelles were generally observed for low hydrophobicity values and low DPs of **P(MX)**, while worm-like micelles or mixed morphologies mostly occupied the middle region of the phase diagram. Finally, TEM imaging revealed the formation of vesicular structures for high DPs and high 12-mer LogP_{oct}/SA values (Figures S26−S32). The vesicle morphologies were confirmed to contain inner compartments by cryo-TEM. It is worth mentioning that some polymers did not conform perfectly to this trend. This discrepancy did not arise from differences in polymer T_g values, as confirmed by microDSC (Figure S23). Instead, morphological exceptions could originate from differences in polymerization kinetics of the various monomers. For instance, imide norbornene monomers are known to polymerize more slowly compared to their ester or amide counterparts, as could be the case with **M5**.[33−35] As such, the morphologies obtained using **M2** and **M3** could be kinetically trapped and may not represent equilibrium structures. Despite that, there is still an overall trend of higher-order structures obtained as LogP_{oct}/SA increases for a certain DP of **P(MX)** that agrees well with our predictive methodology.

Based on our sophisticated monomer design, the investigation of potential hydrophobicity trends for ROMPISA monomers which differ solely in terms of anchor or terminal group functionality has yielded meaningful insight into structure−property relationships. First, the variation in functionality of the anchor group for monomers with the same terminal alcohol group was considered (Figure 4A). LogP_{oct}/SA analysis for ROMP oligomers showed that the ester anchor group of **M2** was more hydrophobic than the amide linkage of **M8**, which in turn was more hydrophobic than the respective imide group of **M9**. Aqueous ROMPISA

DOI: 10.1021/acsmacrolett.9b00117
ACS Macro Lett. 2019, 8, 466−472

reactions for the synthesis of $\mathbf{P(M11)_{12}}$-*b*-$\mathbf{P(MX)_n}$ diblock copolymer nano-objects using **MX** = **M2**, **M8**, and **M9** were conducted targeting the same DP of the core-froming block ($DP_{P(MX)}$ = 120) to confirm this trend. Prepared diblock copolymers had similar length, although the morphologies of obtained PISA formulations differed significantly and trended based on polymer hydrophobicity. For the most hydrophobic monomer, **M2**, spherical vesicles were formed at DP = 120, while networks of worm-like micelles were developed for less hydrophobic **M8** and small spherical micelles for **M9** at the same DP.

Next, hydrophobicity trends for monomers with the same imide anchor group and different terminal functional groups were studied (Figure 4B). In particular, our model suggested that the ether terminal group of **M5** was more hydrophobic than the methyl ester group of **M6** and the respective alcohol group of **M9**, while the protonated tertiary amine group of **M11** was the most hydrophilic, forming water-soluble polymers regardless of block length. Indeed, for $\mathbf{P(M11)_{12}}$-*b*-$\mathbf{P(MX)_n}$ nano-objects using **MX** = **M5**, **M6**, and **M9** with comparable block lengths, higher-order morphologies were obtained with increasing magnitude of 12-mer $\mathrm{Log}P_{oct}$/SA values at the same DP of **P(MX)**.

To conclude, we report an *in silico* predictive methodology based on oligomer hydrophobicity calculations for successful identification of new monomers with a wide range of functionalities for use in aqueous ROMPISA as corona- or core-forming blocks. Upon ROMPISA using the predicted monomers, common nano-object morphologies were accessed that were found to evolve toward higher-order structures with increasing DP and oligomer hydrophobicity values. Importantly, valuable oligomer hydrophobicity trends were identified based on different monomer structures that allow for reliable morphology prediction. Overall, our study could further expand the field of PISA beyond RDRP techniques and pave the way for discovering new monomers that undergo ROMPISA.

■ ASSOCIATED CONTENT

Supporting Information

The Supporting Information is available free of charge on the ACS Publications website at DOI: 10.1021/acsmacrolett.9b00117.

Materials and characterization techniques, oligomer hydrophobicity evaluation details, synthetic procedures, additional SEC data of diblock copolymers, additional microDSC, DLS, and SAXS data, and dry-state and cryo-TEM images of nano-objects (PDF)

■ AUTHOR INFORMATION

Corresponding Authors

*E-mail: rtm11@psu.edu (R.T.M.).
*E-mail: r.oreilly@bham.ac.uk (R.K.O.R.).

ORCID

Spyridon Varlas: 0000-0002-4171-7572
Robert T. Mathers: 0000-0002-0503-4571
Rachel K. O'Reilly: 0000-0002-1043-7172

Author Contributions

The manuscript was written through contributions of all authors. All authors have given approval to the final version of the manuscript.

Notes

The authors declare no competing financial interest.

■ ACKNOWLEDGMENTS

This work was supported by the ERC (grant number 615142), EPSRC, and the University of Birmingham. Mr. Z. Coe (University of Birmingham) is thanked for microDSC assistance, and Dr. S. Bakker (University of Warwick) is thanked for cryo-TEM assistance. Advanced BioImaging Research Technology Platform, BBSRC ALERT14 award BB/M01228X/1, is thanked for supporting cryo-TEM characterization. Steven Huband at the University of Warwick X-ray Diffraction Research Technology Platform is thanked for assisting with SAXS measurements.

■ REFERENCES

(1) Blanazs, A.; Armes, S. P.; Ryan, A. J. Self-Assembled Block Copolymer Aggregates: From Micelles to Vesicles and their Biological Applications. *Macromol. Rapid Commun.* **2009**, *30*, 267−277.

(2) Mai, Y.; Eisenberg, A. Self-assembly of block copolymers. *Chem. Soc. Rev.* **2012**, *41*, 5969−5985.

(3) Rodríguez-Hernández, J.; Chécot, F.; Gnanou, Y.; Lecommandoux, S. Toward 'smart' nano-objects by self-assembly of block copolymers in solution. *Prog. Polym. Sci.* **2005**, *30*, 691−724.

(4) Brendel, J. C.; Schacher, F. H. Block Copolymer Self-Assembly in Solution—Quo Vadis? *Chem. - Asian J.* **2018**, *13*, 230−239.

(5) Patterson, J. P.; Robin, M. P.; Chassenieux, C.; Colombani, O.; O'Reilly, R. K. The analysis of solution self-assembled polymeric nanomaterials. *Chem. Soc. Rev.* **2014**, *43*, 2412−2425.

(6) Charleux, B.; Delaittre, G.; Rieger, J.; D'Agosto, F. Polymerization-Induced Self-Assembly: From Soluble Macromolecules to Block Copolymer Nano-Objects in One Step. *Macromolecules* **2012**, *45*, 6753−6765.

(7) Warren, N. J.; Armes, S. P. Polymerization-Induced Self-Assembly of Block Copolymer Nano-objects via RAFT Aqueous Dispersion Polymerization. *J. Am. Chem. Soc.* **2014**, *136*, 10174−10185.

(8) Yeow, J.; Boyer, C. Photoinitiated Polymerization-Induced Self-Assembly (Photo-PISA): New Insights and Opportunities. *Adv. Sci.* **2017**, *4*, 1700137.

(9) Wang, X.; An, Z. New Insights into RAFT Dispersion Polymerization-Induced Self-Assembly: From Monomer Library, Morphological Control, and Stability to Driving Forces. *Macromol. Rapid Commun.* **2019**, *40*, 1800325.

(10) Liu, X.; Sun, M.; Sun, J.; Hu, J.; Wang, Z.; Guo, J.; Gao, W. Polymerization Induced Self-Assembly of a Site-Specific Interferon α-Block Copolymer Conjugate into Micelles with Remarkably Enhanced Pharmacology. *J. Am. Chem. Soc.* **2018**, *140*, 10435−10438.

(11) Canning, S. L.; Smith, G. N.; Armes, S. P. A Critical Appraisal of RAFT-Mediated Polymerization-Induced Self-Assembly. *Macromolecules* **2016**, *49*, 1985−2001.

(12) Wang, G.; Schmitt, M.; Wang, Z.; Lee, B.; Pan, X.; Fu, L.; Yan, J.; Li, S.; Xie, G.; Bockstaller, M. R.; Matyjaszewski, K. Polymerization-Induced Self-Assembly (PISA) Using ICAR ATRP at Low Catalyst Concentration. *Macromolecules* **2016**, *49*, 8605−8615.

(13) Wang, J.; Wu, Z.; Wang, G.; Matyjaszewski, K. In Situ Crosslinking of Nanoparticles in Polymerization-Induced Self-Assembly via ARGET ATRP of Glycidyl Methacrylate. *Macromol. Rapid Commun.* **2019**, *40*, 1800332.

(14) Warren, N. J.; Mykhaylyk, O. O.; Mahmood, D.; Ryan, A. J.; Armes, S. P. RAFT aqueous dispersion polymerization yields poly(ethylene glycol)-based diblock copolymer nano-objects with predictable single phase morphologies. *J. Am. Chem. Soc.* **2014**, *136*, 1023−1033.

(15) Ng, G.; Yeow, J.; Xu, J.; Boyer, C. Application of oxygen tolerant PET-RAFT to polymerization-induced self-assembly. *Polym. Chem.* **2017**, *8*, 2841−2851.

DOI: 10.1021/acsmacrolett.9b00117
ACS Macro Lett. 2019, 8, 466−472

(16) Blackman, L. D.; Varlas, S.; Arno, M. C.; Fayter, A.; Gibson, M. I.; O'Reilly, R. K. Permeable Protein-Loaded Polymersome Cascade Nanoreactors by Polymerization-Induced Self-Assembly. *ACS Macro Lett.* **2017**, *6*, 1263−1267.
(17) Varlas, S.; Blackman, L. D.; Findlay, H. E.; Reading, E.; Booth, P. J.; Gibson, M. I.; O'Reilly, R. K. Photoinitiated Polymerization-Induced Self-Assembly in the Presence of Surfactants Enables Membrane Protein Incorporation into Vesicles. *Macromolecules* **2018**, *51*, 6190−6201.
(18) Bielawski, C. W.; Grubbs, R. H. Highly Efficient Ring-Opening Metathesis Polymerization (ROMP) Using New Ruthenium Catalysts Containing N-Heterocyclic Carbene Ligands. *Angew. Chem., Int. Ed.* **2000**, *39*, 2903−2906.
(19) Sutthasupa, S.; Shiotsuki, M.; Sanda, F. Recent advances in ring-opening metathesis polymerization, and application to synthesis of functional materials. *Polym. J.* **2010**, *42*, 905.
(20) Radzinski, S. C.; Foster, J. C.; Matson, J. B. Synthesis of bottlebrush polymers via transfer-to and grafting-through approaches using a RAFT chain transfer agent with a ROMP-active Z-group. *Polym. Chem.* **2015**, *6*, 5643−5652.
(21) Zhang, L.; Song, C.; Yu, J.; Yang, D.; Xie, M. One-pot synthesis of polymeric nanoparticle by ring-opening metathesis polymerization. *J. Polym. Sci., Part A: Polym. Chem.* **2010**, *48*, 5231−5238.
(22) Liu, J.; Liao, Y.; He, X.; Yu, J.; Ding, L.; Xie, M. Facile One-Pot Approach for Preparing Functionalized Polymeric Nanoparticles via ROMP. *Macromol. Chem. Phys.* **2011**, *212*, 55−63.
(23) Yoon, K.-Y.; Lee, I.-H.; Kim, K. O.; Jang, J.; Lee, E.; Choi, T.-L. One-Pot in Situ Fabrication of Stable Nanocaterpillars Directly from Polyacetylene Diblock Copolymers Synthesized by Mild Ring-Opening Metathesis Polymerization. *J. Am. Chem. Soc.* **2012**, *134*, 14291−14294.
(24) Wright, D. B.; Touve, M. A.; Adamiak, L.; Gianneschi, N. C. ROMPISA: Ring-Opening Metathesis Polymerization-Induced Self-Assembly. *ACS Macro Lett.* **2017**, *6*, 925−929.
(25) Torres-Rocha, O. L.; Wu, X.; Zhu, C.; Crudden, C. M.; Cunningham, M. F. Polymerization-Induced Self-Assembly (PISA) of 1,5-Cyclooctadiene Using Ring Opening Metathesis Polymerization. *Macromol. Rapid Commun.* **2019**, *40*, 1800326.
(26) Wright, D. B.; Touve, M. A.; Thompson, M. P.; Gianneschi, N. C. Aqueous-Phase Ring-Opening Metathesis Polymerization-Induced Self-Assembly. *ACS Macro Lett.* **2018**, *7*, 401−405.
(27) Wright, D. B.; Thompson, M. P.; Touve, M. A.; Carlini, A. S.; Gianneschi, N. C. Enzyme-Responsive Polymer Nanoparticles via Ring-Opening Metathesis Polymerization-Induced Self-Assembly. *Macromol. Rapid Commun.* **2019**, *40*, 1800467.
(28) Foster, J. C.; Varlas, S.; Blackman, L. D.; Arkinstall, L. A.; O'Reilly, R. K. Ring-Opening Metathesis Polymerization in Aqueous Media Using a Macroinitiator Approach. *Angew. Chem., Int. Ed.* **2018**, *57*, 10672−10676.
(29) Foster, J. C.; Varlas, S.; Couturaud, B.; Jones, J. R.; Keogh, R.; Mathers, R. T.; O'Reilly, R. K. Predicting Monomers for Use in Polymerization-Induced Self-Assembly. *Angew. Chem., Int. Ed.* **2018**, *57*, 15733−15737.
(30) Magenau, A. J. D.; Richards, J. A.; Pasquinelli, M. A.; Savin, D. A.; Mathers, R. T. Systematic Insights from Medicinal Chemistry To Discern the Nature of Polymer Hydrophobicity. *Macromolecules* **2015**, *48*, 7230−7236.
(31) Yildirim, E.; Dakshinamoorthy, D.; Peretic, M. J.; Pasquinelli, M. A.; Mathers, R. T. Synthetic Design of Polyester Electrolytes Guided by Hydrophobicity Calculations. *Macromolecules* **2016**, *49*, 7868−7876.
(32) Dharmaratne, N. U.; Jouaneh, T. M. M.; Kiesewetter, M. K.; Mathers, R. T. Quantitative Measurements of Polymer Hydrophobicity Based on Functional Group Identity and Oligomer Length. *Macromolecules* **2018**, *51*, 8461−8468.
(33) Radzinski, S. C.; Foster, J. C.; Chapleski, R. C.; Troya, D.; Matson, J. B. Bottlebrush Polymer Synthesis by Ring-Opening Metathesis Polymerization: The Significance of the Anchor Group. *J. Am. Chem. Soc.* **2016**, *138*, 6998−7004.
(34) Slugovc, C.; Demel, S.; Riegler, S.; Hobisch, J.; Stelzer, F. The Resting State Makes the Difference: The Influence of the Anchor Group in the ROMP of Norbornene Derivatives. *Macromol. Rapid Commun.* **2004**, *25*, 475−480.
(35) Chang, A. B.; Lin, T.-P.; Thompson, N. B.; Luo, S.-X.; Liberman-Martin, A. L.; Chen, H.-Y.; Lee, B.; Grubbs, R. H. Design, Synthesis, and Self-Assembly of Polymers with Tailored Graft Distributions. *J. Am. Chem. Soc.* **2017**, *139*, 17683−17693.

DOI: 10.1021/acsmacrolett.9b00117
ACS Macro Lett. 2019, 8, 466−472

4.2. Appendix – Supporting Information Material

Supporting Information

"Predicting Monomers for Use in Aqueous Ring-Opening Metathesis Polymerization-Induced Self-Assembly (ROMPISA)"

Spyridon Varlas,[†] *Jeffrey C. Foster,*[†] *Lucy A. Arkinstall,*[†] *Joseph R. Jones,*[†] *Robert Keogh,*[†,‡] *Robert T. Mathers,*[*,§] *and Rachel K. O'Reilly*[*,†]

[†]School of Chemistry, University of Birmingham, Edgbaston, Birmingham, B15 2TT, UK

[‡]Department of Chemistry, University of Warwick, Gibbet Hill Road, Coventry, CV4 7AL, UK

[§]Department of Chemistry, Pennsylvania State University, New Kensington, PA 15068, USA

*<u>*Corresponding Authors*</u>: rtm11@psu.edu (R.T.M.) and r.oreilly@bham.ac.uk (R.K.O.R.)

Contents

Experimental Section S2
Materials and Methods S2
Materials S2
Characterization Techniques S2
Evaluation of Oligomer Hydrophobicity S5
Synthetic Methods S9
Supplementary Characterization Data for **P(M11)$_{12}$-*b*-P(MX)$_n$** Diblock Copolymers S24
Supplementary Characterization Data for Water-Soluble **P(M10)$_{11}$-*b*-P(M10)$_n$** Diblock Copolymers S30
Supplementary Characterization Data for **P(M11)$_{12}$-*b*-P(MX)$_n$** Diblock Copolymer Nano-Objects Developed by Aqueous ROMPISA S32
References S42

Experimental Section

Materials and Methods

Materials

Grubbs Catalyst™ 3rd Generation (G3) ($(H_2IMes)(pyr)_2(Cl)_2Ru=CHPh$), *exo*-5-norbornenecarboxylic acid (97%), *cis*-5-norbornene-*exo*-2,3-dicarboxylic anhydride (95%), ethylene glycol (anhydrous, 99.8%), *N,N′*-dicyclohexylcarbodiimide (99%, DCC), 4-(dimethylamino)pyridine (≥98%, DMAP), acetyl chloride (98%), 2-methoxyethylamine (99%), ethanolamine (≥99.5%), poly(ethylene glycol) methyl ether (M_n ~ 350 g mol^{-1}, $mPEG_8$-OH), *N*-hydroxysuccinimide (98%), urea (98%), sodium phosphate monobasic (≥99.0%) and *N,N*-dimethylethylenediamine (95%) were purchased from Sigma-Aldrich and were used without further purification. Acetonitrile, triethylamine (for HPLC, NEt_3) and dichloromethane (DCM) were purchased from Fisher Scientific. DCM was dried over calcium hydride overnight and then distilled before use. Tetrahydrofuran (THF) (HPLC grade) was purchased from VWR Chemicals and was purified *via* passage through a column of basic alumina prior to use. *N*-(3-Dimethylaminopropyl)-*N′*-ethylcarbodiimide hydrochloride (crystalline, EDC.HCl) was purchased from Carbosynth. Diisopropyl azodicarboxylate (94%, DIAD) was purchased from Alfa Aesar. Triphenylphosphine (99%, PPh_3) was obtained from Acros Organics. Formvar-carbon coated (300 mesh), graphene oxide (GO) coated (300 mesh) and lacey-carbon coated (400 mesh) copper grids were purchased from EM Resolutions.

Characterization Techniques

NMR Spectroscopy. ^{1}H-NMR and ^{13}C-NMR spectra were recorded at 300 MHz or 400 MHz on a Bruker DPX-300 or a Bruker DPX-400 spectrometer, using chloroform-*d* ($CDCl_3$), DMSO-d_6 or methanol-d_4 (CD_3OD) as the solvent. Chemical shifts of protons are reported as δ in parts per million (ppm) and are relative to tetramethylsilane (TMS) at δ = 0 ppm when using $CDCl_3$ or solvent residual peaks (DMSO, δ = 2.50 ppm, CH_3OH, δ = 3.31 ppm).

High-Resolution Mass Spectrometry. HRMS spectra were recorded by the MS Analytical Facility Service at the University of Birmingham on a Waters Xevo G2-XS QTof Quadrupole Time-of-Flight mass spectrometer.

Size Exclusion Chromatography. Size exclusion chromatography (SEC) analysis was performed on a system composed of an Agilent 1260 Infinity II LC system equipped with an Agilent guard column (PLGel 5 μM, 50 × 7.5 mm) and two Agilent Mixed-C columns (PLGel 5 μM, 300 × 7.5 mm). The mobile phase used was either DMF (HPLC grade) containing 5 mM NH_4BF_4 at 50 °C at flow rate of 1.0 mL min^{-1} (poly(methyl methacrylate) (PMMA) standards used for calibration), or THF (HPLC grade) containing 2% v/v NEt_3 at 40 °C at flow rate of 1.0 mL min^{-1} (polystyrene (PS) standards used for calibration). Number average molecular weights (M_n), weight average molecular weights (M_w) and dispersities ($Đ_M = M_w/M_n$) were determined using either Wyatt ASTRA v7.1.3 or Agilent GPC/SEC software.

Micro-Differential Scanning Calorimetry. Determination of Glass Transition Temperature (T_g) for **P(M11)$_{12}$-*b*-P(M5)$_{120}$** and **P(M11)$_{12}$-*b*-P(M6)$_{120}$** diblock copolymer samples was performed using a TA Instruments NANO-DSC differential scanning calorimeter by heating the samples in solution from 0 °C to 100 °C at a rate of 1.5 °C/min. Samples were degassed for 10 min prior to injection of 600 μL into the instrument and corrected against a background of DI water. Collected data were processed using NanoAnaylze Software.

Dynamic Light Scattering. Hydrodynamic diameters (D_h) and size distributions (PD) of nano-objects were determined by dynamic light scattering (DLS) using a Malvern Zetasizer Nano ZS with a 4 mW He-Ne 633 nm laser module operating at 25 °C. Measurements were carried out at an angle of 173° (back scattering), and results were analyzed using Malvern DTS v7.03 software. All determinations were repeated 5 times with at least 10 measurements recorded for each run. D_h values were calculated using the Stokes-Einstein equation where particles are assumed to be spherical, while for worm-like particles DLS was used to detect multiple populations and obtain dispersity information.

Small-Angle X-Ray Scattering. SAXS measurements were made using a Xenocs Xeuss 2.0 equipped with a micro-focus Cu K_α source collimated with Scatterless slits. The scattering was measured using a Pilatus 300k detector with a pixel size of 0.172 mm × 0.172 mm. The distance between the detector and the sample was calibrated using silver behenate ($AgC_{22}H_{43}O_2$), giving a value 2.481(5) m. Samples at 10 mg/mL were mounted in 1mm borosilicate glass capillaries. The magnitude of the scattering vector was calculated from $q = (4\pi/\lambda) \cdot \sin(\theta/2)$, where θ is the angle between the incident and scattered X-rays and λ is the wavelength of the incident X-rays. The accessible range was therefore $4 \times 10^7 \leq q \leq 1.6 \times 10^9$ m^{-1}. A radial integration as a function of q was performed on the 2-dimensional scattering profile and the resulting data corrected for the absorption and background from the sample holder. Modelling of the

scattering form factor was achieved by parameterization and fitting of several different models drawn from Pedersen,[1] using R statistical software[2] and the library 'FME'.[3]

Transmission Electron Microscopy. Dry-state stained transmission electron microscopy (TEM) imaging was performed on a JEOL JEM-1400 microscope operating at an acceleration voltage of 80 kV. All dry-state samples were diluted with deionized water to appropriate analysis concentration and then deposited onto formvar-coated or GO-coated copper grids. After roughly 1 min, excess sample was blotted from the grid and the grid was stained with an aqueous 1 wt% uranyl acetate (UA) solution for 1 min prior to blotting, drying and microscopic analysis.

Cryogenic transmission electron microscopy (cryo-TEM) imaging was performed on a JEOL JEM-2100Plus microscope operating at an acceleration voltage of 200 kV. Vesicle samples for cryo-TEM analysis were prepared, after dilution with deionized water, by depositing 8 μL of sample onto a lacey-carbon grid followed by blotting for approximately 5 s and plunging into a pool of liquid ethane, cooled using liquid nitrogen, to vitrify the sample. Transfer into a pre-cooled cryo-TEM holder was performed under liquid nitrogen temperatures prior to microscopic analysis.

Evaluation of Oligomer Hydrophobicity

LogP_{oct} Analysis. Octanol-water partition coefficients (LogP_{oct}) were calculated for monomers and oligomeric models in Materials Studio 2018,[4] using an atom-based approach (ALogP98 method)[5] for all molecular models containing C, H, N, and O atoms.

Surface Area Analysis. Octanol-water partition coefficients (LogP_{oct}) were normalized by solvent accessible surface area (SA) using Materials Studio 2018.[4] First, single oligomers were subjected to a Geometry Optimization procedure using the Forcite Molecular Dynamics (MD) module with a COMPASS II force field. The force field contains information on important parameters, like preferred bond lengths, bond angles, torsion angles, partial charges, and van der Waals radii that influence the conformation.[6-8] To minimize energy and determine a preferred conformation, these simulations ran until the energy of the oligomer decreased below predetermined convergence criteria (1×10^{-4} kcal mol^{-1} energy convergence, 0.005 kcal mol^{-1}/Å force convergence, and 5×10^{-5} Å displacement convergence). Second, these SA values represent solvent accessible surface area created by an algorithm that rolls a ball over the surface of the oligomer. To ensure the SA values are meaningful in the context of octanol-water partition coefficients (LogP_{oct}), the probe had a 1.4 Å radius to match the size of a water molecule. Third, to monitor variations in surface area calculations as the *n*-mer size increased, oligomers were annealed for 25 cycles using a sinusoidal temperature ramp (300 – 500 K) to maximize variability in SA values. After averaging SA values for cycles 21-25, the standard deviation ranged from 0.3-2.9% with an average of 1.2%.

Models. Scheme S1 depicts a representative sample of imide-based oligomers ranging from 3-mers to 12-mers. The size of the largest models approached molecular weight values for polymers that allow aqueous ROMPISA. Although the functional groups varied depending on the monomer, a consistent *cis/trans* ratio (~1:1) and vinyl end-groups mimicked experimental conditions.

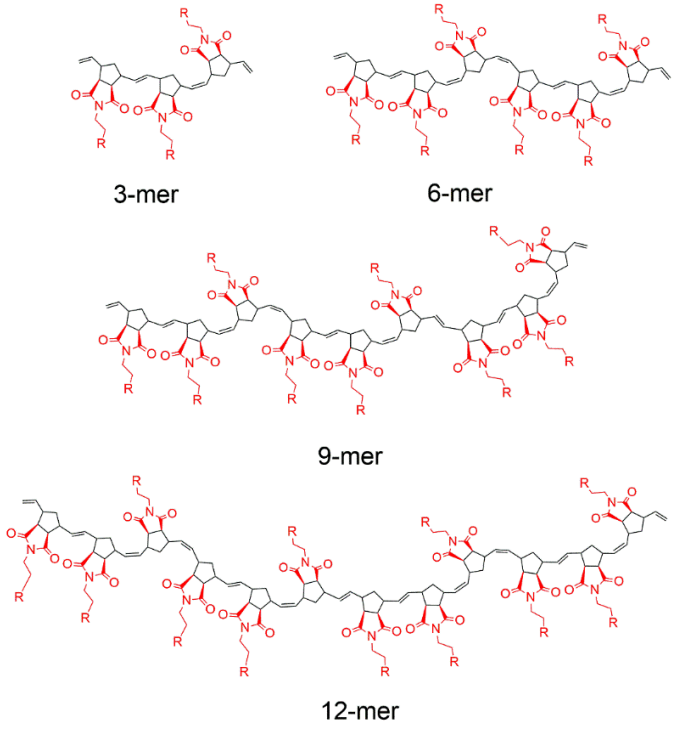

Scheme S1. Representative sample of imide-based oligomers ranging from 3-mers to 12-mers for hydrophobicity analysis of aqueous ROMPISA.

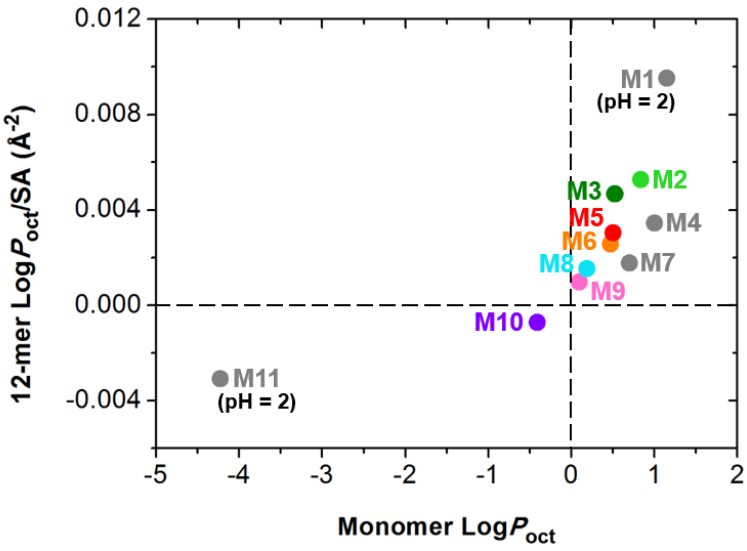

Figure S1. 12-mer LogP_{oct}/SA values as a function of LogP_{oct} values of their respective monomers. Data points located in the upper right quadrant correspond to monomers that can be used to form hydrophobic polymers, while those in the lower left quadrant correspond to monomers that produce water-soluble polymers.

LogP_{oct} Adjustment for Monomers with Ionizable and Charged Groups. Although calculating LogP_{oct} values for neutral monomers (**M1**-**M3**, **M5**-**M10**) is relatively straightforward, the hydrophobicity of monomers with functional groups that can ionize depends with pH. In the medicinal chemistry field, adjusting LogP_{oct} values of ionizable groups at a particular pH has been accomplished with a modified version of the Henderson-Hasselbalch (HH) equation. As shown in equation 1, this correction for dissociation (C_D) quantifies how protonation of amines lowers LogP_{oct} values.[9]

$$C_D = \text{Log}[1/(1 + 10^{(pKa-pH)})] \qquad (1)$$

For tertiary amines (**M11**), the ALogP98 values were corrected for pH with a dissociation constant (C_D) according to equations 1 and 2. Carboxylic acid groups (**M1**) were assumed to be fully protonated at pH = 2 and no correction for dissociation was required. The hydrophobicity of ammonium-based monomers (**M4**) was adjusted by comparing experimental LogP_{oct} values of a series of model compounds with ALogP98 values.

In equation 2, we hypothesized that incorporating C_D values into the LogP_{oct}/SA values will provide a first approximation of the influence of certain pH ranges for known values of pKa. Experimental validation of models based on HH equations indicate a broad range of pH values for phenols (pH = 3-9)[10] and amines (pH > 2)[11]. However the extreme pH ranges, such as pH < 2 or > 10, typically produce deviations due to common-ion effects or aggregation.

$$(\text{Log}P_{oct} + nC_D)/SA \qquad (2)$$

In order to improve the predictive capability of equation 2, precise knowledge of solution pH and pK_a of functional groups is required. For small molecules, typical pKa values for aliphatic (~10-11), benzyl (~9), and aromatic (~4-5) amines are well known.[12] Interestingly, pKa values for aliphatic amines on polymers are lower since neighboring groups influence each other. For example, the dimethylamino groups in poly(dimethylaminoethyl methylmethacrylate) (PDMAEMA) have pKa values ~7.0-7.5.[13-15] Using a pKa value of 7.0 for the dimethylamino group of monomer **M11**, a substantial decrease in hydrophobicity is noted in Figure S2 as pH decreases.

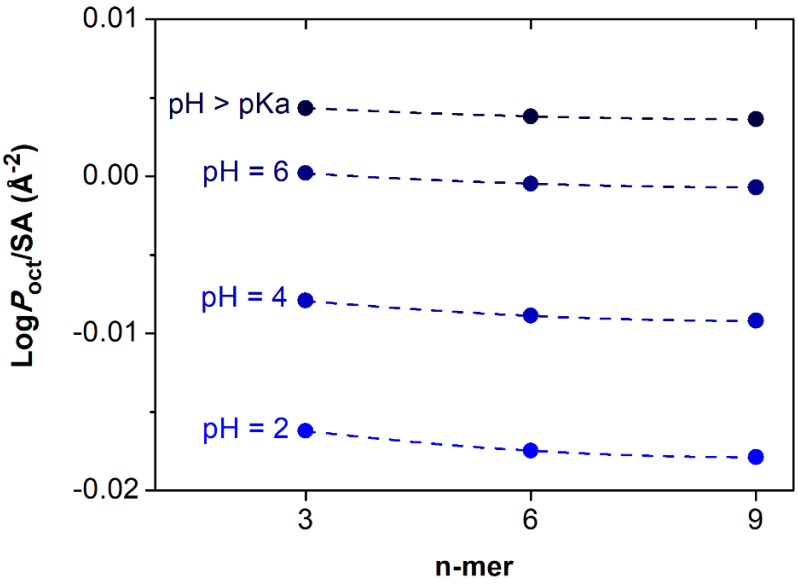

Figure S2. Effect of pH variation on hydrophobicity of ROMP oligomers for **M11** bearing dimethylamino pendant groups.

Synthetic Methods

Synthesis of ***exo*-5-Norbornene carboxylic ester alcohol – M2**

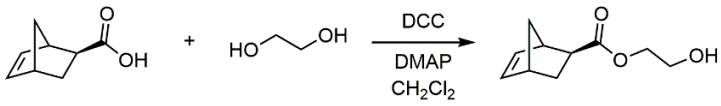

A round bottom flask was charged with *exo*-5-norbornenecarboxylic acid (0.50 g, 3.6 mmol, 1 eq), ethylene glycol (0.60 mL, 11 mmol, 3 eq), DMAP (44 mg, 0.36 mmol, 0.1 eq), and 20 mL of CH_2Cl_2. Then, DCC (0.75 g, 3.6 mmol, 1 eq) was added to the flask in one portion. The reaction mixture was stirred overnight at room temperature. The following day, the precipitated dicyclohexyl urea was removed by filtration and the crude product was concentrated under reduced pressure and purified by column chromatography using silica gel as the stationary phase and a gradient from 0-50% EtOAc in hexane as the eluent to afford the pure product as a colorless oil (0.18 g, 37%).[1]H-NMR (400 MHz, $CDCl_3$): δ (ppm) 6.13 (m, 2H), 4.23 (m, 2H), 3.84 (q, 2H), 3.06 (s, 1H), 2.93 (s, 1H), 2.28 (m, 1H), 1.94 (m, 2H), 1.54 (d, 1H), 1.38 (m, 2H). [13]C-NMR (400 MHz, $CDCl_3$): δ (ppm) 176.8, 138.1, 135.7, 66.1, 61.2, 46.7, 46.3, 43.0, 41.6, 30.4. The characterization agreed with a previous literature report.[16]

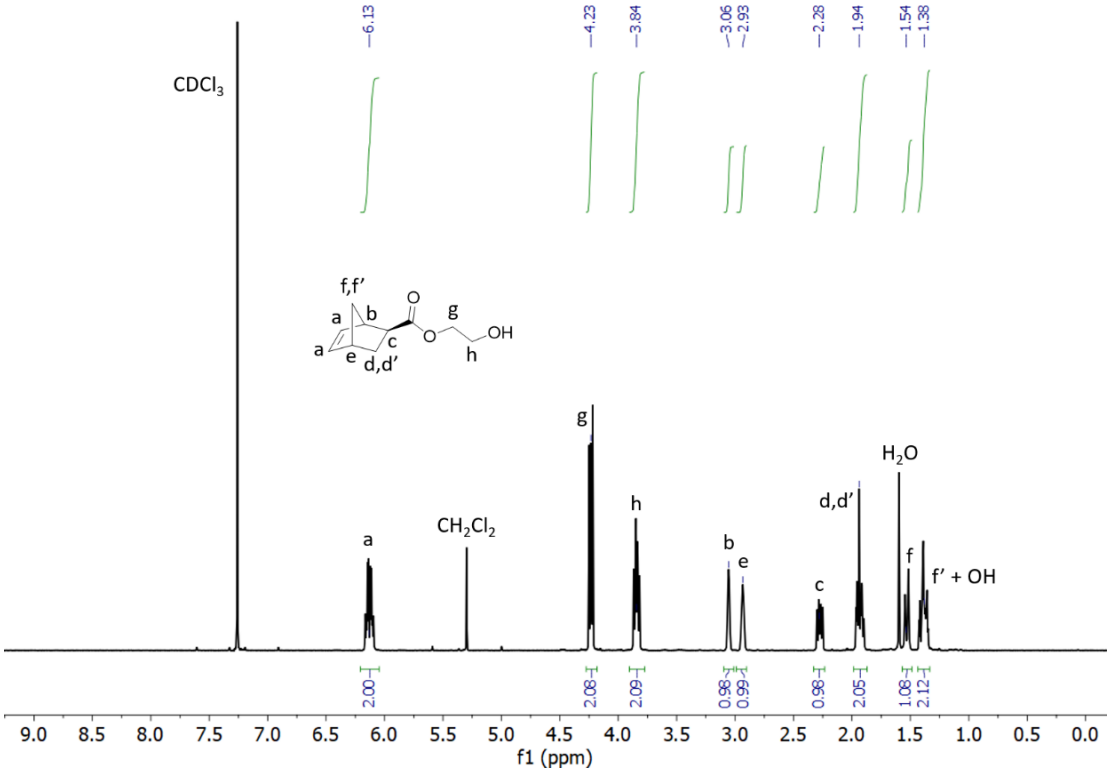

Figure S3. [1]H-NMR spectrum of *exo*-5-norbornene carboxylic ester alcohol (**M2**) in $CDCl_3$.

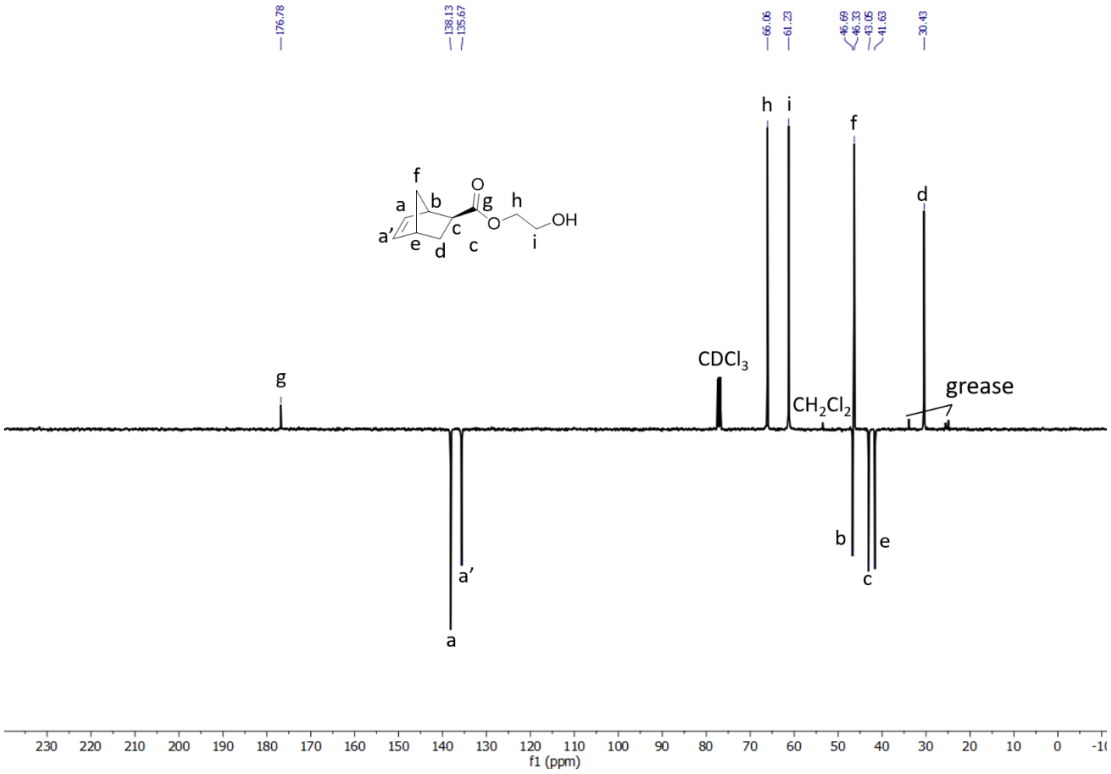

Figure S4. ^{13}C-NMR spectrum of *exo*-5-norbornene carboxylic ester alcohol (**M2**) in $CDCl_3$.

Synthesis of ***exo*-5-Norbornene NHS-ester**

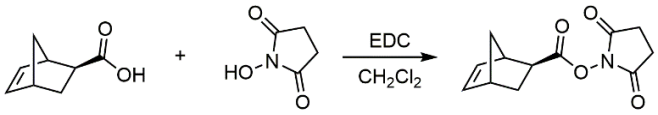

exo-5-Norbornenecarboxylic acid (2.00 g, 14.5 mmol, 1 eq), EDC.HCl (3.47 g, 18.1 mmol, 1.25 eq) and 1-hydroxypyrrolidine-2,5-dione (2.08 g, 18.1 mmol, 1.25 eq) were stirred in CH_2Cl_2 (50 mL) overnight at room temperature. The mixture was diluted with water (50 mL) and then the aqueous mixture was extracted with CH_2Cl_2 (2 × 25 mL). Afterwards, the combined organic phases were washed twice with saturated aq. $NaHCO_3$ (2 × 50 mL), followed by saturated aq. NH_4Cl (2 × 50 mL) and brine (50 mL). The organic phase was dried over $MgSO_4$ and the solvent was removed *in vacuo* to yield an off-white solid. The solid was recrystallized from ethanol to afford the pure product as white crystals (1.62 g, 47%).[1]H-NMR (400 MHz, $CDCl_3$): δ (ppm) 6.17 (m, 2H), 3.28 (s, 1H), 3.00 (s, 1H), 2.83 (d, 4H), 2.51 (m, 1H), 2.05 (m, 1H), 1.55-1.45 (m, 3H). ^{13}C-NMR (400 MHz, $CDCl_3$): δ (ppm) 171.7, 169.3, 138.6, 135.3, 47.2, 46.4, 41.8, 40.3, 31.0, 25.6. The characterization agreed with a previous literature report.[17]

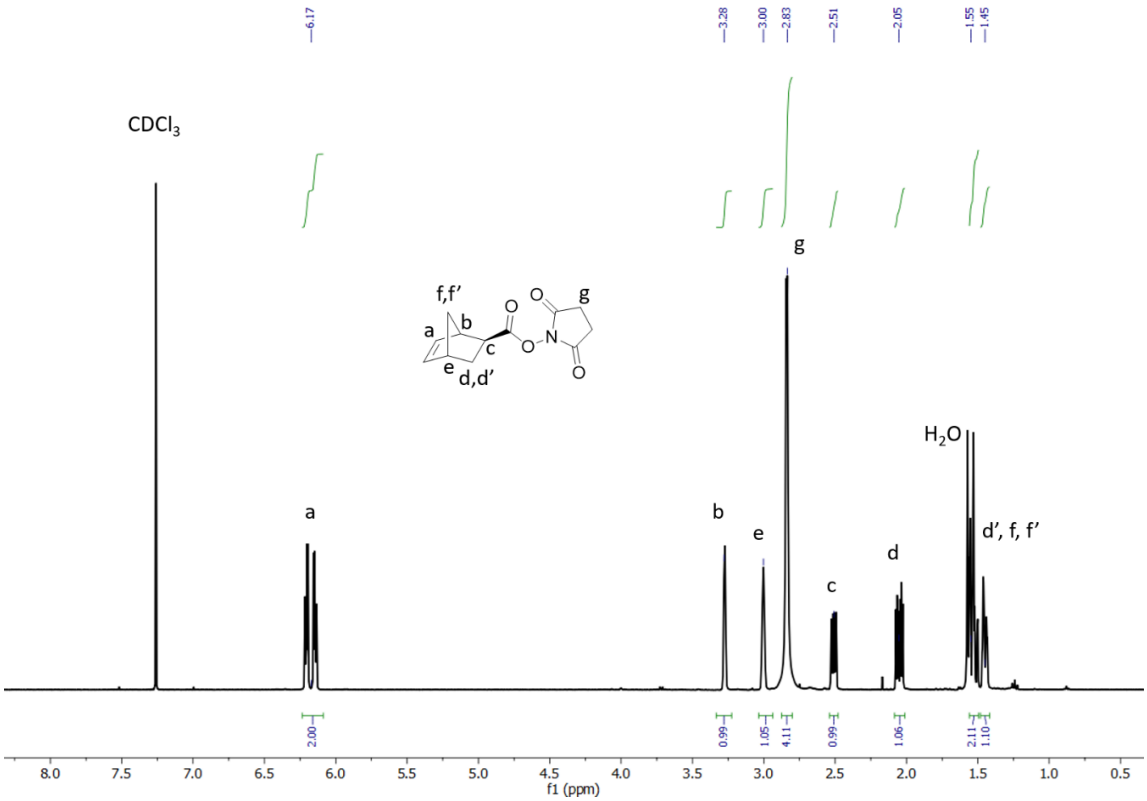

Figure S5. ^{1}H NMR spectrum of *exo*-5-norbornene NHS-ester in $CDCl_3$.

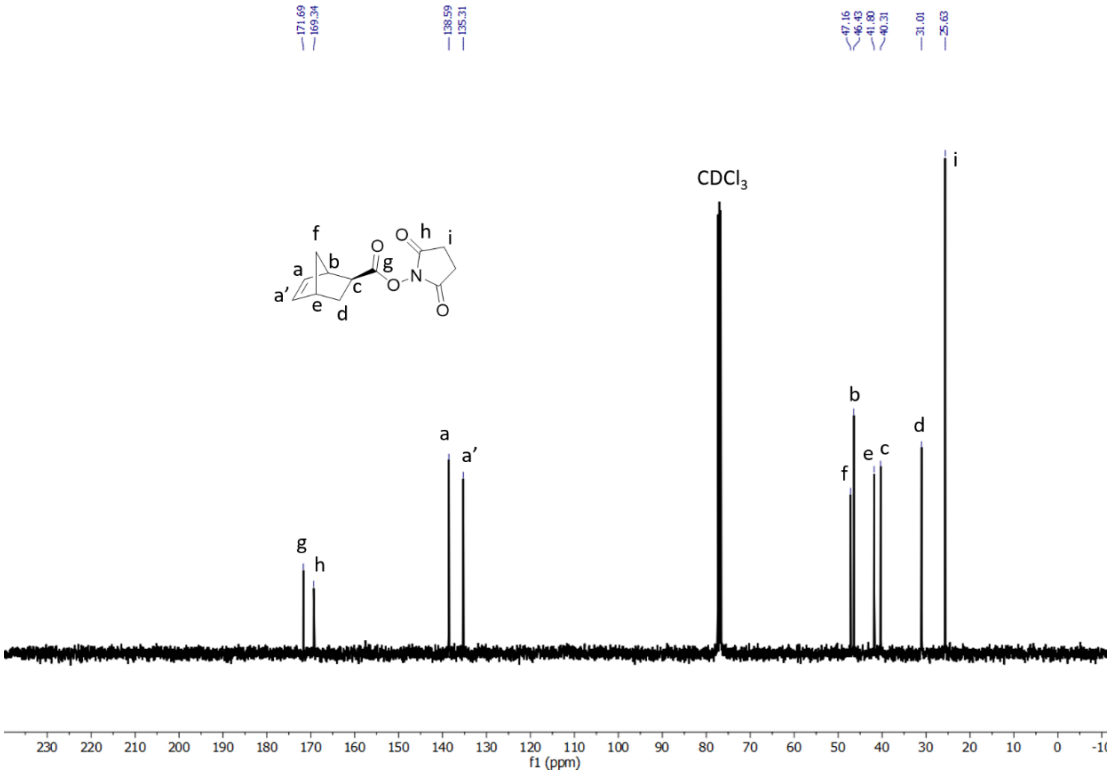

Figure S6. ^{13}C-NMR spectrum of *exo*-5-norbornene NHS-ester in $CDCl_3$.

Synthesis of ***exo*-5-Norbornenecarboxamide – M3**

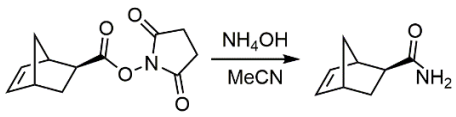

exo-5-Norbornene NHS-ester (1.0 g, 4.3 mmol, 1 eq) was dissolved in 50 mL of MeCN in a round bottom flask. Then, 40 mL of NH_4OH solution (28% in H_2O) were added to the flask. The reaction mixture was stirred for 30 min at room temperature. The reaction mixture was then diluted with 100 mL of DI H_2O. The flask was placed in an ice bath, and the solution was acidified to pH ~ 7 using concentrated HCl solution. The aqueous solution was then extracted with CH_2Cl_2 (2 × 50 mL), and the combined organic layers were dried over $MgSO_4$ and concentrated under reduced pressure to afford the pure product as a white powder (0.57 g, 97%). ^{1}H-NMR (400 MHz, $CDCl_3$): δ (ppm) 6.09 (m, 2H), 2.94 (s, 1H), 2.89 (s, 1H), 2.06 (m, 1H), 1.87 (m, 1H), 1.60 (d, 1H), 1.32 (m, 2H). ^{13}C-NMR (400 MHz, $CDCl_3$): δ (ppm) 178.2, 138.4, 135.9, 47.0, 46.4, 44.1, 41.6, 30.6. The characterization agreed with a previous literature report.[18]

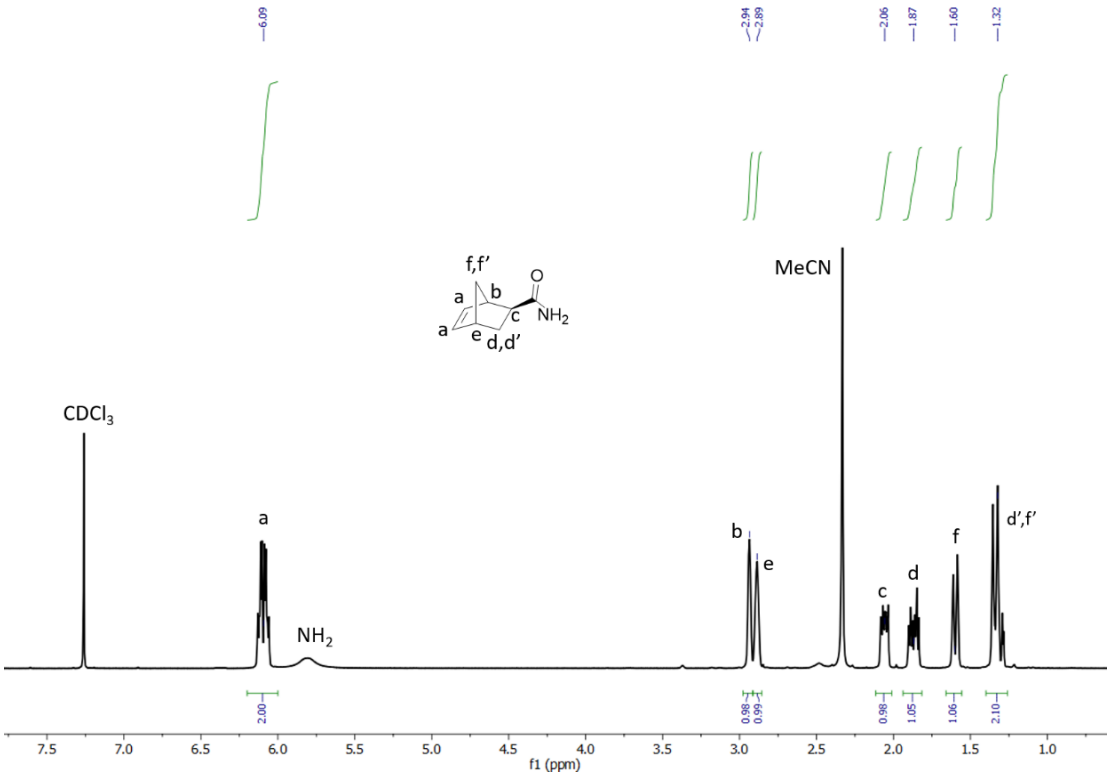

Figure S7. ^{1}H-NMR spectrum of *exo*-5-norbornenecarboxamide (**M3**) in $CDCl_3$.

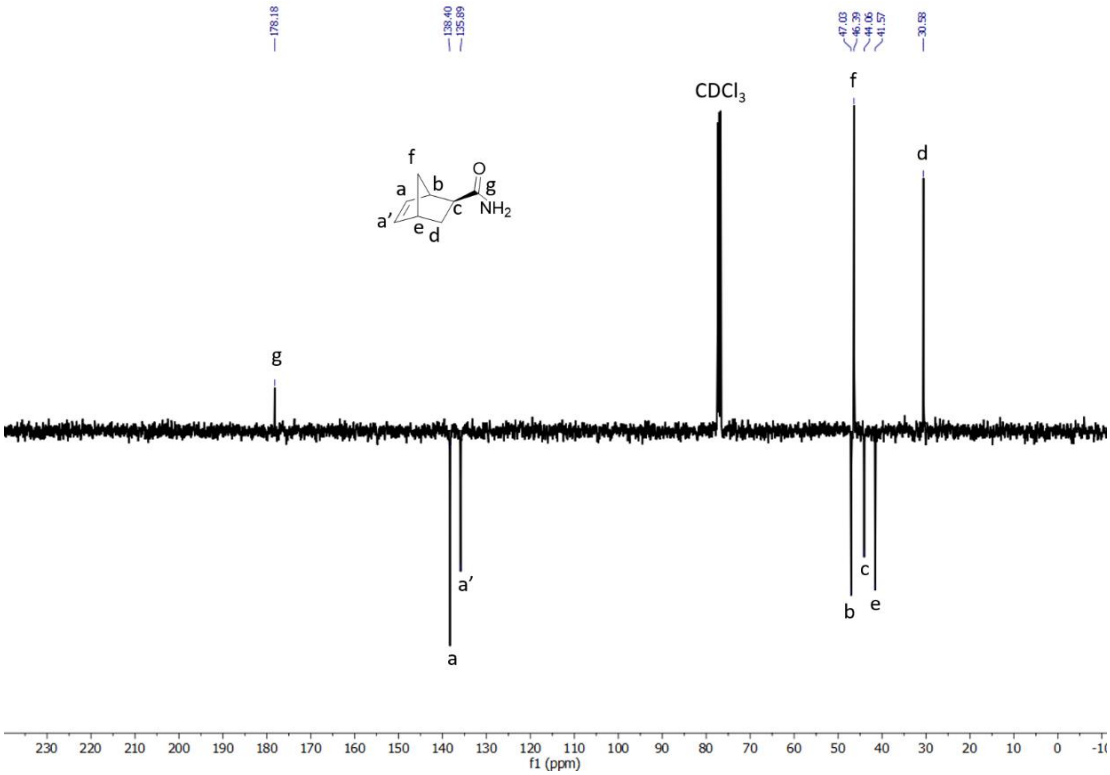

Figure S8. ^{13}C-NMR spectrum of *exo*-5-norbornenecarboxamide (**M3**) in $CDCl_3$.

Synthesis of ***exo*-Norbornene imide methyl ether – M5**

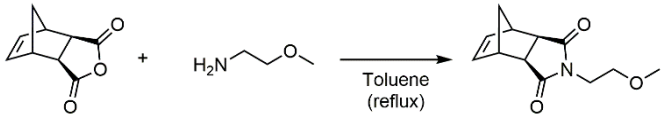

cis-5-Norbornene-*exo*-2,3-dicarboxylic anhydride (1.0 g, 6.1 mmol, 1 eq) was dissolved in 15 mL of toluene in a round bottom flask. 2-Methoxyethylamine (0.59 mL, 6.7 mmol, 1.1 eq) was then added to the flask. The flask was fitted with an air-cooled condenser and the reaction mixture was heated at reflux for 4 h. The reaction mixture was then cooled to room temperature and concentrated under reduced pressure. The resulting residue was redissolved in 30 mL of EtOAc, and the EtOAc solution was washed with 1M HCl solution (30 mL) and brine, dried over $MgSO_4$, and concentrated under reduced pressure to afford the pure product as a colorless oil (1.3 g, 99%). ^{1}H-NMR (400 MHz, $CDCl_3$): δ (ppm) 6.29 (s, 2H), 3.70 (t, 2H), 3.56 (t, 2H), 3.31 (s, 3H), 3.28 (s, 2H), 2.69 (s, 2H), 1.48 (d, 1H), 1.35 (d, 1H).^{13}C-NMR (400 MHz, $CDCl_3$): δ (ppm) 178.1, 137.8, 68.5, 58.5, 47.8, 45.3, 42.6, 37.9. HRMS: m/z $[C_{12}H_{15}NO_3+H]^+$ calc. 222.1130 g mol^{-1}, exp. 222.1132 g mol^{-1}.

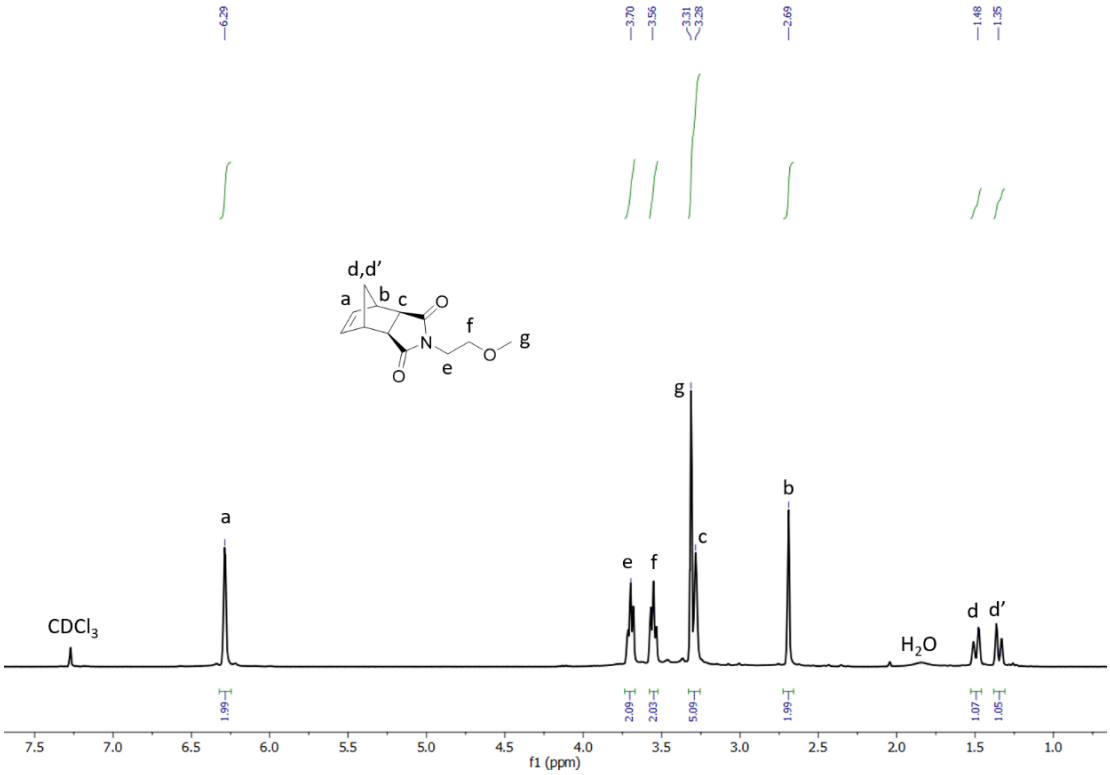

Figure S9. ^{1}H-NMR spectrum of *exo*-norbornene imide methyl ether (**M5**) in $CDCl_3$.

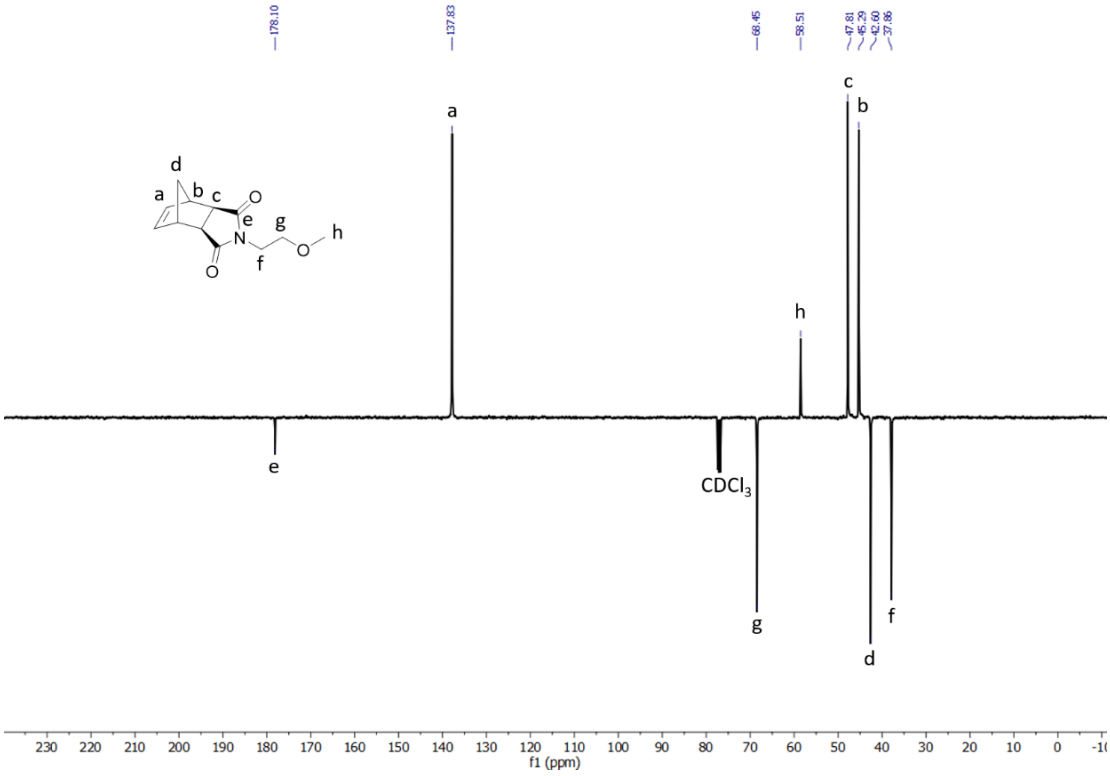

Figure S10. ^{13}C-NMR spectrum of *exo*-norbornene imide methyl ether (**M5**) in $CDCl_3$.

Synthesis of ***exo*-Norbornene imide alcohol methyl ester – M6**

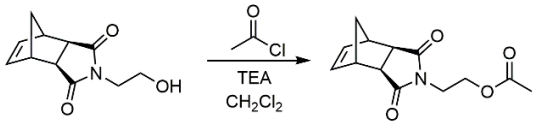

A round bottom flask was charged with *exo*-norbornene imide alcohol (**M9**) (0.20 g, 0.97 mmol, 1 eq), triethylamine (160 µL, 1.2 mmol, 1.2 eq), and 5 mL of CH_2Cl_2. The flask was placed in an ice bath. Acetyl chloride (90 µL, 1.0 mmol, 1.1 eq) was added dropwise *via* a glass syringe. The reaction mixture was allowed to warm to room temperature and was stirred overnight. The reaction mixture was then concentrated under reduced pressure and the resulting residue was redissolved in 20 mL of CH_2Cl_2. The CH_2Cl_2 solution was washed with 1M HCl solution (20 mL) and brine, dried over $MgSO_4$, and concentrated under reduced pressure to give the product as a colorless oil (0.22 g, 93%). ^{1}H-NMR (400 MHz, $CDCl_3$): δ (ppm) 6.27 (t, 2H), 4.21 (t, 2H), 3.73 (t, 2H), 3.26 (s, 2H), 2.69 (s, 2H), 1.98 (s, 3H), 1.50 (d, 1H), 1.30 (d, 1H). ^{13}C-NMR (400 MHz, $CDCl_3$): δ (ppm) 176.86, 169.67, 136.80, 59.65, 46.82, 44.24, 41.62, 36.51, 19.71. HRMS: m/z $[C_{13}H_{15}NO_4+Na]^+$ calc. 272.0899 g mol^{-1}, exp. 272.0903 g mol^{-1}.

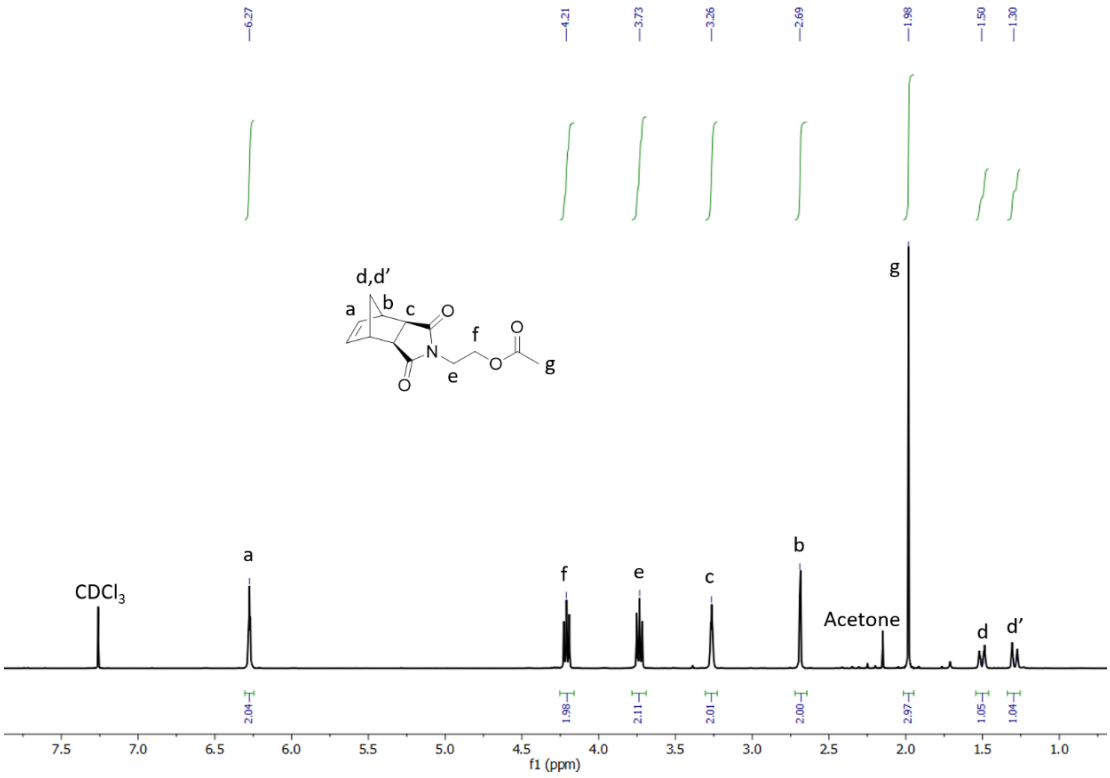

Figure S11. ^{1}H-NMR spectrum of *exo*-norbornene imide alcohol methyl ester (**M6**) in $CDCl_3$.

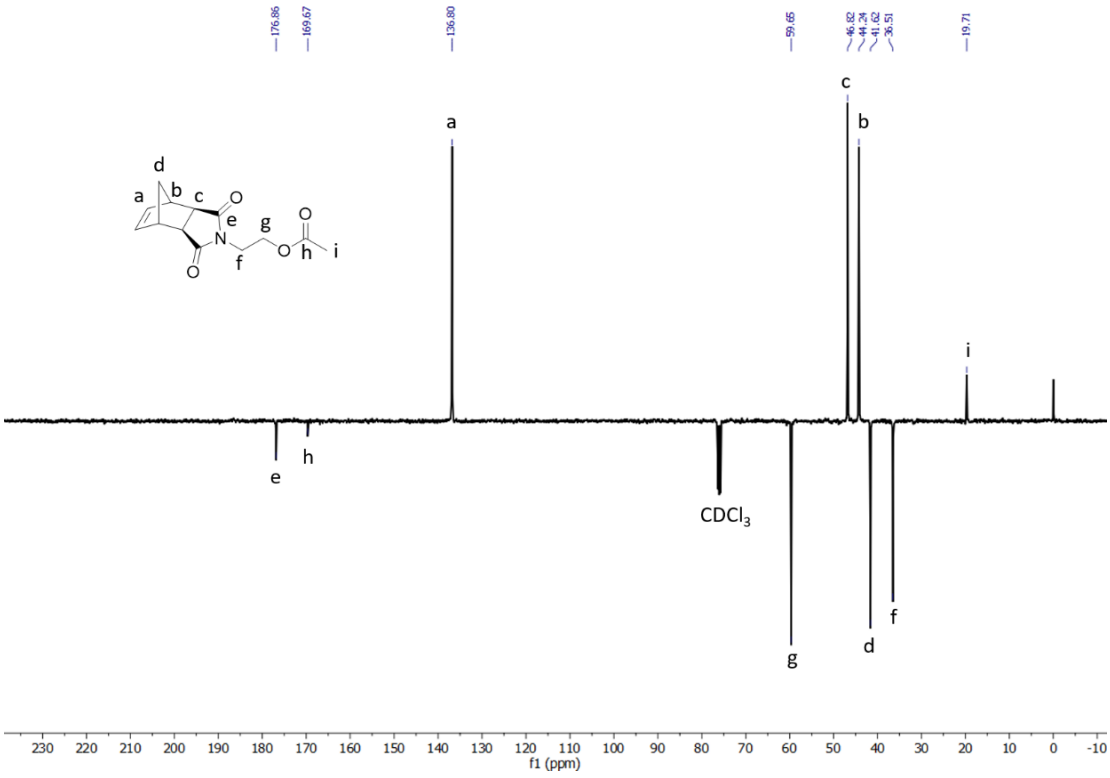

Figure S12. ^{13}C-NMR spectrum of *exo*-norbornene imide alcohol methyl ester (**M6**) in $CDCl_3$.

Synthesis of ***exo*-5-Norbornene carboxylic amide alcohol – M8**

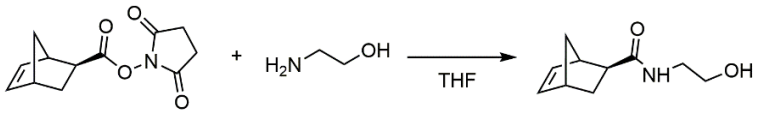

exo-5-Norbornene NHS-ester (0.30 g, 1.3 mmol, 1 eq) was dissolved in THF in a round bottom flask. Ethanolamine (160 µL, 2.6 mmol, 2 eq) was then added to the flask. A white precipitate immediately formed following this addition. The reaction mixture was stirred for an additional period of 2 h at room temperature. The precipitated solids were removed by filtration and the filtrate was further dried under vacuum. The crude product was further purified by successive azeotropic distillations using toluene to remove the excess ethanolamine, giving the pure product as a colorless oil (0.23 g, 98%). ^{1}H-NMR (400 MHz, $CDCl_3$): δ (ppm) 6.27 (br s, 1H), 6.06 (m, 2H), 3.64 (t, 2H), 3.42 (s, 1H), 3.36 (m, 2H), 2.86 (s, 2H), 1.98 (m, 1H), 1.83 (m, 1H), 1.63 (d, 1H), 1.28 (m, 2H). ^{13}C-NMR (400 MHz, $CDCl_3$): δ (ppm) 176.2, 137.2, 135.0, 61.3, 46.2, 45.3, 43.6, 41.5, 40.6, 29.6. HRMS: m/z $[C_{10}H_{15}NO_2+H]^+$ calc. 182.1181 g mol^{-1}, exp. 182.1184 g mol^{-1}.

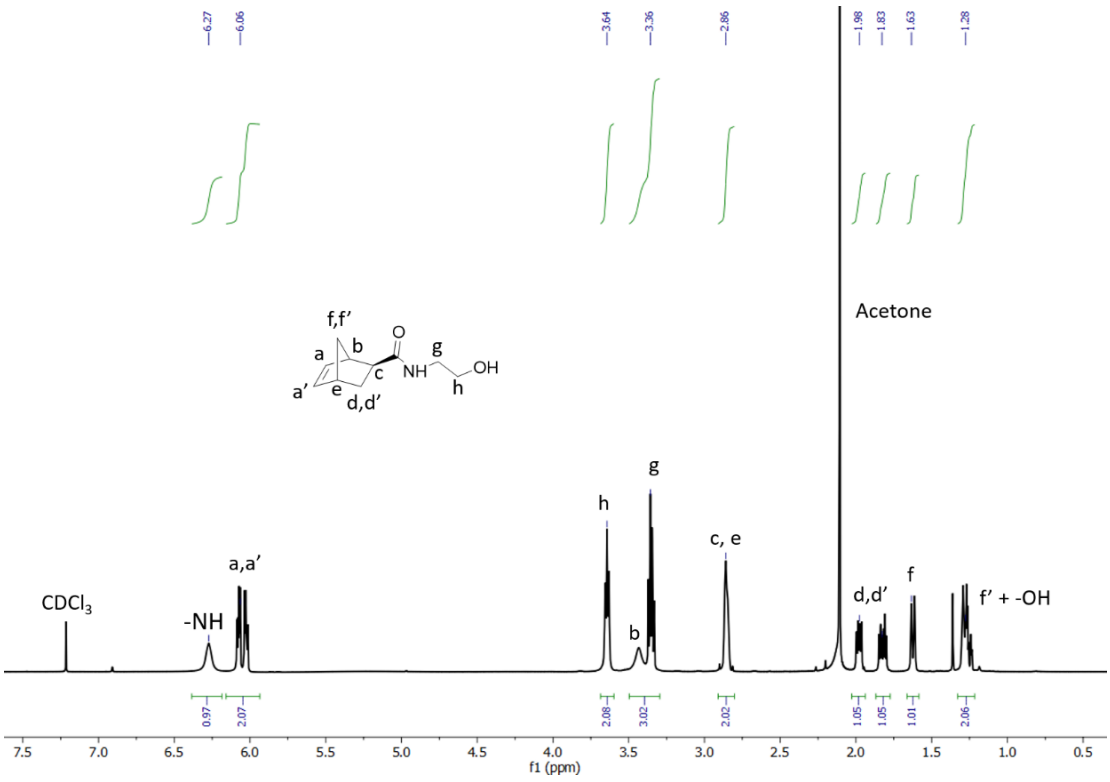

Figure S13. ^{1}H-NMR spectrum of *exo*-5-norbornene carboxylic amide alcohol (**M8**) in $CDCl_3$.

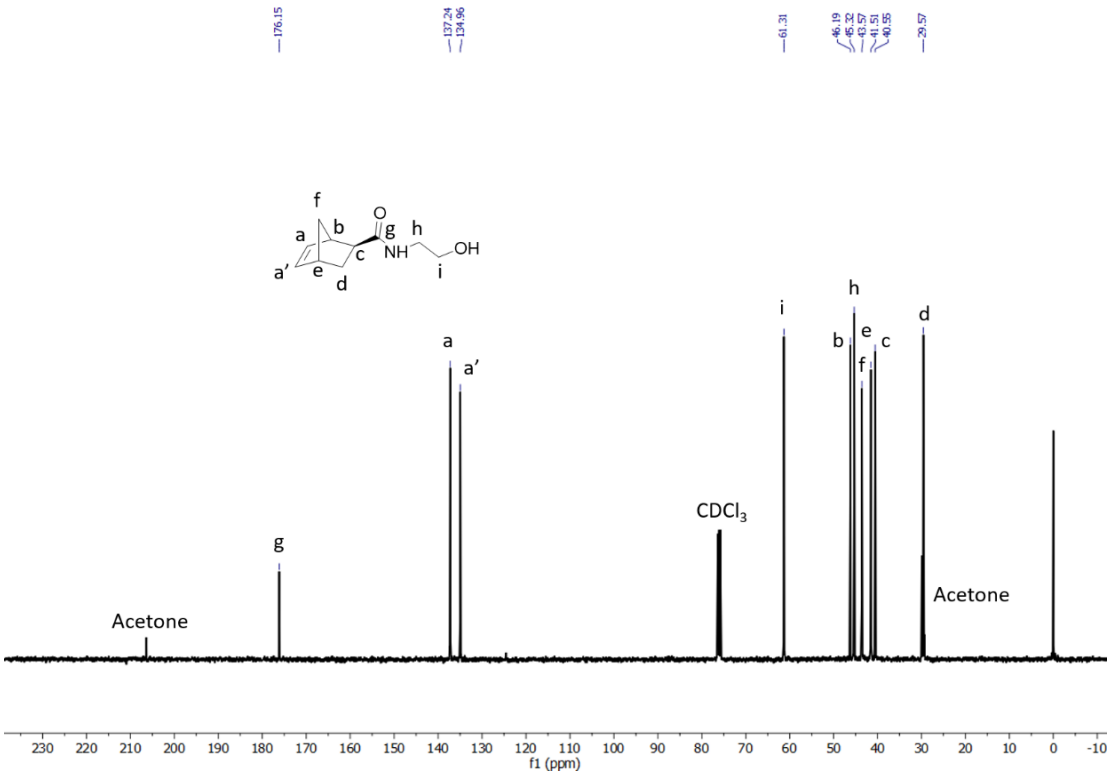

Figure S14. ^{13}C-NMR spectrum of *exo*-5-norbornene carboxylic amide alcohol (**M8**) in $CDCl_3$.

Synthesis of ***exo*-Norbornene imide alcohol – M9**

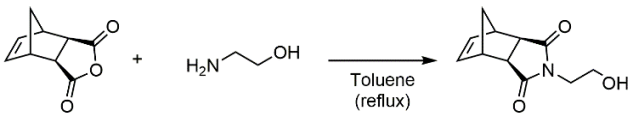

The synthesis of *exo*-norbornene imide alcohol (**M9**) was carried out according to a previously described process.[16] *cis*-5-Norbornene-*exo*-2,3-dicarboxylic anhydride (5.00 g, 30.5 mmol, 1 eq) was dissolved in 40 mL of toluene in a round bottom flask. Ethanolamine (2.20 mL, 36.6 mmol, 1.2 eq) was then added to the flask. The flask was fitted with an air-cooled condenser and the reaction mixture was heated at reflux for 4 h. The reaction mixture was then cooled to room temperature and concentrated under reduced pressure. The resulting residue was redissolved in 30 mL of EtOAc, and the EtOAc solution was washed with 1M HCl solution (30 mL) and brine, dried over $MgSO_4$, and concentrated under reduced pressure to afford the pure product as colorless crystals (5.62 g, 89%).^{1}H-NMR (400 MHz, $CDCl_3$): δ (ppm) 6.23 (s, 2H), 3.70 (t, 2H), 3.62 (t, 2H), 3.21 (s, 2H), 2.66 (s, 2H), 1.43 (d, 1H), 1.28 (d, 1H). ^{13}C-NMR (400 MHz, $CDCl_3$): δ (ppm) 178.8, 137.8, 60.1, 47.9, 45.3, 42.8, 41.3.

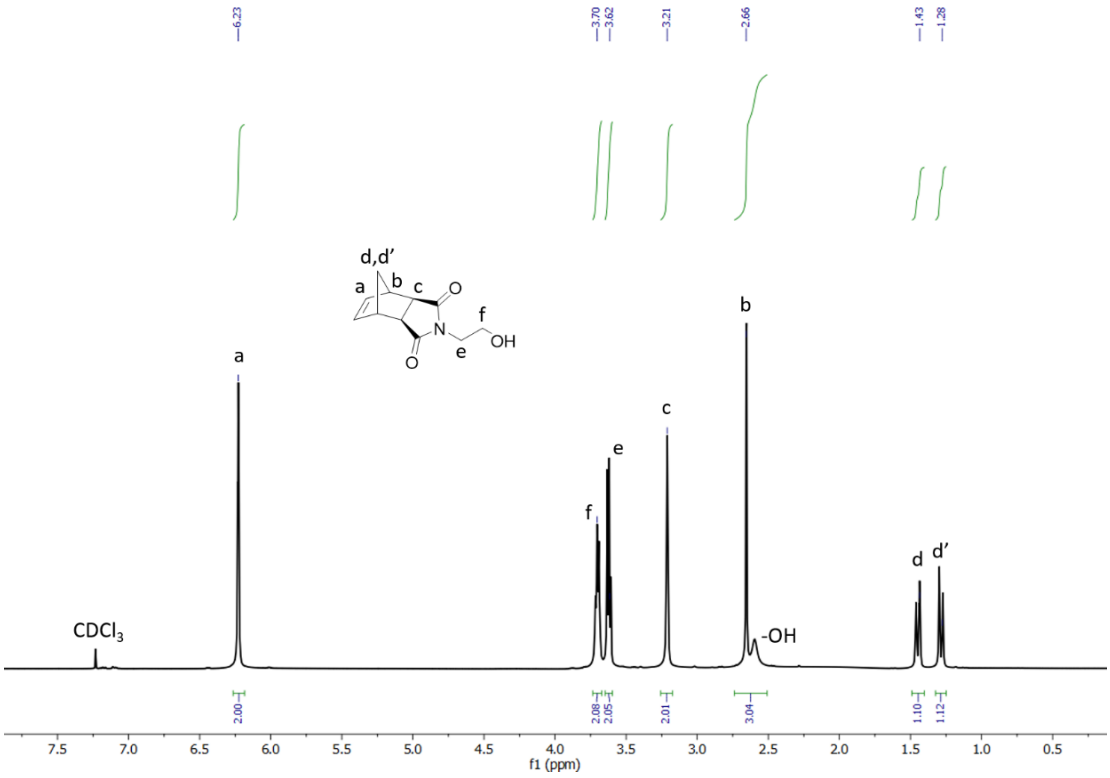

Figure S15. ^{1}H-NMR spectrum of *exo*-norbornene imide alcohol (**M9**) in $CDCl_3$.

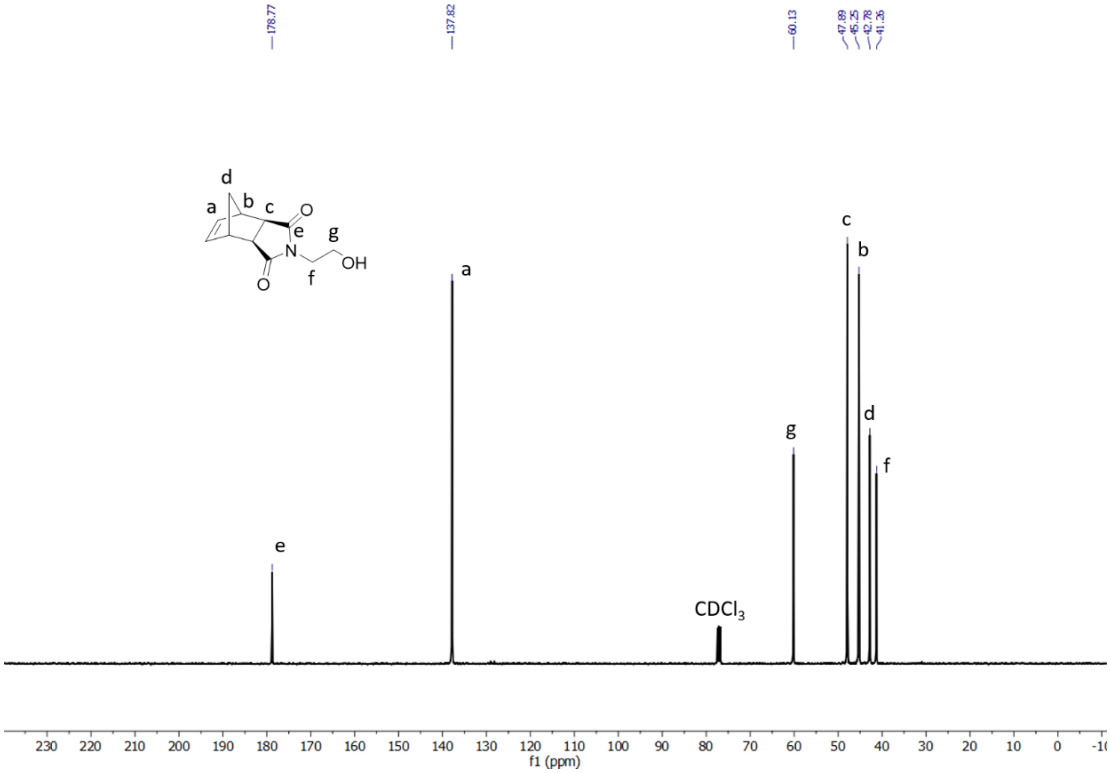

Figure S16. ^{13}C-NMR spectrum of *exo*-norbornene imide alcohol (**M9**) in $CDCl_3$.

Synthesis of ***exo*-Norbornene imide mPEG$_8$ – M10**

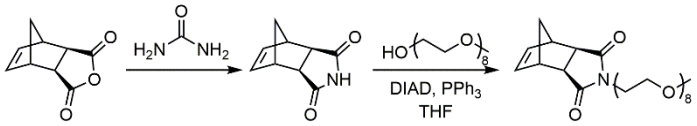

An Erlenmeyer flask was charged with *cis*-5-norbornene-*exo*-2,3-dicarboxylic anhydride (3.0 g, 18 mmol, 1 eq) and urea (1.2 g, 19 mmol, 1.1 eq). The flask was placed in an oil bath that had been pre-heated to 160 °C. The solids melted, and gas evolution was observed that continued until the completion of the reaction. The reaction mixture was heated at 160 °C for 20 min. Boiling hot H_2O (75 mL) was added to the flask, and the suspension was stirred at reflux until all of the solids dissolved. The flask was then removed from the oil bath and was allowed to cool to room temperature. The product crystallized upon cooling, and was isolated *via* vacuum filtration to yield *exo*-5-norbornene imide, which was dried under vacuum and used in the next step without further purification.

A 2-necked round bottom flask was charged with *exo*-5-norbornene imide (2.25 g, 13.8 mmol, 1.2 eq), poly(ethylene glycol) methyl ether (M_n ~ 350 Da, 4.00 g, 11.5 mmol, 1 eq), PPh_3 (3.62 g, 13.8 mmol, 1.2 eq) and 80 mL of THF. The flask was sealed with a rubber septum and placed under N_2 atmosphere. Once all solids had dissolved, DIAD (2.7 mL, 13.8 mmol, 1.2 eq) was added dropwise *via* a glass syringe. The reaction mixture was stirred at room temperature overnight. MeOH (10 mL) was added to quench the reaction. The reaction mixture was concentrated under reduced pressure. H_2O (50 mL) and hexane (50 mL) were then added to the flask and the precipitated solids, which were assumed to be PPh_3=O, were removed by vacuum filtration. The biphasic mixture was transferred to a separatory funnel, and the H_2O layer was extracted with CH_2Cl_2 (2 × 50 mL). The organic layers were combined, washed with brine, dried over $MgSO_4$, and concentrated under reduced pressure. The crude product was further purified by column chromatography using silica gel as the stationary phase and a gradient from 0-5% MeOH in EtOAc as the eluent to afford the pure product as a colorless viscous oil (4.21 g, 74%).^{1}H-NMR (300 MHz, $CDCl_3$): δ (ppm) 6.27 (s, 2H), 3.63 (br m, 33H), 3.37 (s, 3H), 3.26 (s, 2H), 2.67 (s, 2H), 1.49 (d, 1H), 1.34 (d, 1H).

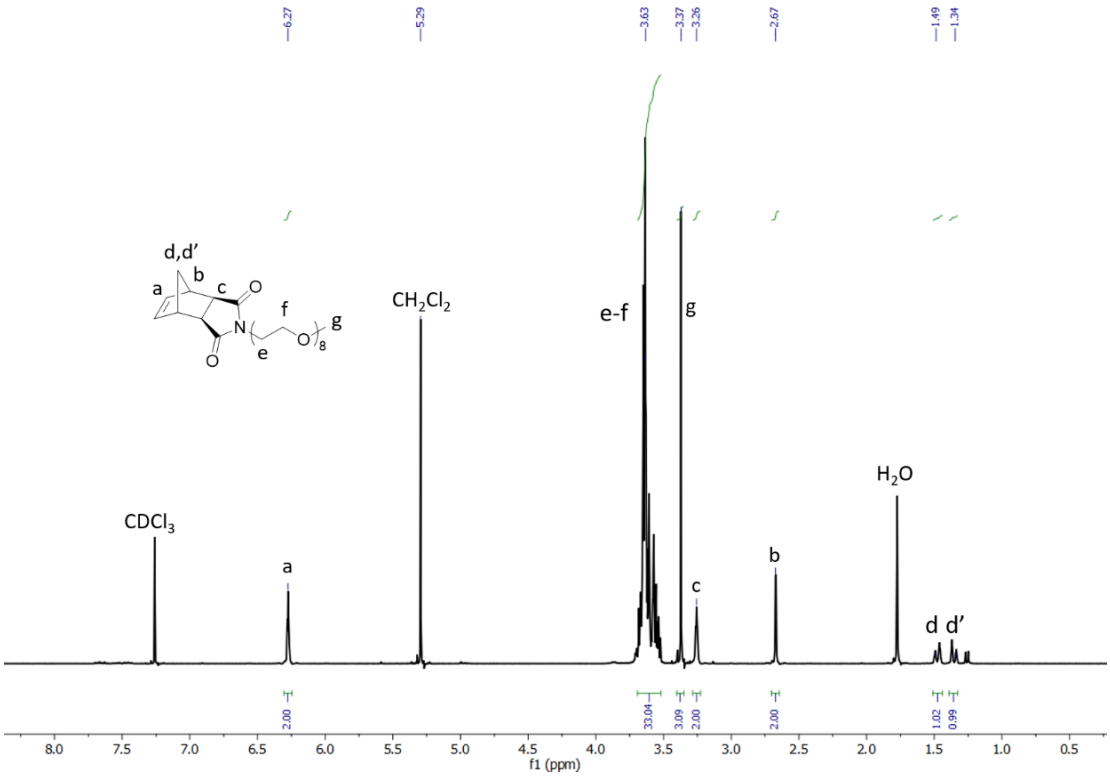

Figure S17. ^{1}H-NMR spectrum of *exo*-norbornene imide mPEG$_8$ (**M10**) in $CDCl_3$.

Synthesis of ***exo*-Norbornene imide tertiary amine – M11**

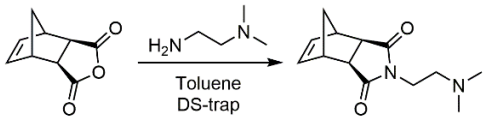

The synthesis of *exo*-norbornene imide tertiary amine (**M11**) was carried out according to a previously described process from our group.[19] ^{1}H-NMR (400 MHz, $CDCl_3$): δ (ppm) 6.29 (s, 2H), 3.59 (t, 2H), 3.26 (s, 2H), 2.67 (s, 2H), 2.47 (t, 2H), 2.22 (s, 6H), 1.45 (s, 2H). ^{13}C-NMR (400 MHz, $CDCl_3$): δ (ppm) 178.1, 137.8, 56.1, 47.8, 45.4, 45.3, 42.6, 36.6.

Synthesis of P(M11)$_{12}$-*b*-P(MX)$_n$ Diblock Copolymer Nano-Objects by Aqueous Ring-Opening Metathesis Polymerization-Induced Self-Assembly (ROMPISA)

A typical procedure for the synthesis of **P(M11)$_{12}$-*b*-P(M5)$_n$** (n = 15, 20, 30, 60, 120, and 180) diblock copolymer nano-objects *via* aqueous ROMPISA is described.[19] Three stock solutions were first prepared: (1) a solution of 35.3 mg of **M11** in 300 μL of filtered THF; (2) a solution of 11 mg of **G3** in 200 μL of filtered THF; and (3) a 11.1 mg/mL solution of **M5** in phosphate buffer (pH = 2). Then, solution (1) was added to a vial equipped with a stir bar. Solution (2) was then added to the vial of solution (1) with rapid stirring for the synthesis of **P(M11)** macroinitiator (final [**M11**] = 70.6 mg/mL, final [**G3**] = 21.9 mg/mL, [**M11**]/[**G3**] = 10). ^{1}H-NMR (300 MHz, DMSO-d_6) $M_{n,\,NMR}$ = 2,800 g mol^{-1}, DP$_{\mathbf{P(M11)}}$ = 12. SEC (THF + 2% v/v NEt_3) $M_{n,\,SEC\ RI}$ = 2,600 g mol^{-1}, $Đ_{M,\,SEC\ RI}$ = 1.17. SEC (DMF + 5 mM NH_4BF_4) $M_{n,\,SEC\ RI}$ = 5,100 g mol^{-1}, $Đ_{M,\,SEC\ RI}$ = 1.19.

After ~2 min, aliquots of 100, 75, 50, 25, 12.5, and 8.3 μL of the **P(M11)$_{12}$** macroinitiator solution were transferred to six new vials equipped with stir bars. The aliquots were then diluted to 100 μL total volume using filtered THF. 900 μL of solution (3) were then added *via* pipette to each of the six vials. Each polymerization solution was thoroughly mixed following this addition by drawing up the entire volume into the pipette tip and ejecting the liquid back into the vial (4×) and stirred for ~30 min prior to ^{1}H-NMR and SEC analyses. In the case of ROMPISA polymerizations, the reaction mixtures were dialyzed against DI water (MWCO = 3.5-5 kDa) for 48 h to remove residual catalyst and the THF co-solvent prior to DLS or SAXS analyses, and TEM imaging. A similar approach for aqueous ROMPISA of **P(M11)$_{12}$-*b*-P(MX)$_n$** nano-objects was followed in the case of core-forming monomers **MX** = **M2**, **M3**, **M6**, **M8**, and **M9** (monomer **M2** required heating and sonication for dispersion in aqueous media).

Synthesis of Water-Soluble P(M10)$_{11}$-*b*-P(M10)$_n$ Diblock Copolymers by Aqueous Ring-Opening Metathesis Polymerization (ROMP)

For corona-forming monomer **MX** = **M10**, a typical procedure for the synthesis of water-soluble **P(M10)$_{11}$-*b*-P(M10)$_n$** (n = 15, 20, 30, 60, and 120) diblock copolymers *via* aqueous ROMP chain-extensions was followed using a **P(M10)$_{11}$** macroinitiator.[19] Three stock solutions were first prepared: (1) a solution of 33.3 mg of **M10** in 300 μL of filtered THF; (2) a solution of 9 mg of **G3** in 200 μL of filtered THF; and (3) a 11.1 mg/mL solution of **M10** in phosphate buffer (pH = 2). Then, solution (1) was added to a vial equipped with a stir bar. Solution (2) was then added to the vial of solution (1) with rapid stirring

for the synthesis of **P(M10)** macroinitiator (final [**M10**] = 66.7 mg/mL, final [**G3**] = 18.1 mg/mL, [**M10**]/[**G3**] = 10). ^{1}H-NMR (300 MHz, methanol-d_4) $M_{n,\,NMR}$ = 5,500 g mol^{-1}, $DP_{\mathbf{P(M10)}}$ = 11. SEC (THF + 2% v/v NEt_3) $M_{n,\,SEC\,RI}$ = 5,600 g mol^{-1}, $Đ_{M,\,SEC\,RI}$ = 1.13. SEC (DMF + 5 mM NH_4BF_4) $M_{n,\,SEC\,RI}$ = 8,200 g mol^{-1}, $Đ_{M,\,SEC\,RI}$ = 1.18.

After ~2 min, aliquots of 100, 75, 50, 25, and 12.5 μL of the **P(M10)$_{11}$** macroinitiator solution were transferred to five new vials equipped with stir bars. The aliquots were then diluted to 100 μL total volume using filtered THF. 900 μL of solution (3) were then added *via* pipette to each of the five vials. Each polymerization solution was thoroughly mixed following this addition by drawing up the entire volume into the pipette tip and ejecting the liquid back into the vial (4×) and stirred for ~5 min prior to ^{1}H-NMR and SEC analyses.

Supplementary Characterization Data for P(M11)$_{12}$-*b*-P(MX)$_n$ Diblock Copolymers

Table S1. Molecular characteristics of **P(M11)$_{12}$** macroinitiator prepared *via* ROMP in THF, as determined by ^{1}H-NMR spectroscopy and SEC analysis.

[M11]/[G3]	% Conv.[a]	$M_{n,\,theo.}$ (kDa)[b]	$M_{n,\,NMR}$ (kDa)[c]	$M_{n,\,SEC\ RI}$ (kDa)[d]	$Đ_{M,\,SEC\ RI}$[d]	$M_{n,\,SEC\ RI}$ (kDa)[e]	$Đ_{M,\,SEC\ RI}$[e]
10	>99	2.3	2.8	2.6	1.17	5.1	1.19

[a]Monomer conversion calculated from ^{1}H-NMR spectroscopy in DMSO-d_6. [b]Calculated from conversion. [c]Calculated using end group analysis from ^{1}H-NMR spectroscopy. [d]Mn and $Đ_M$ values calculated from PS standards using THF + 2% v/v NEt_3 as the eluent. [e]Mn and $Đ_M$ values calculated from PMMA standards using DMF + 5 mM NH_4BF_4 as the eluent.

Table S2. Molecular characteristics of **P(M11)$_{12}$-*b*-P(M2)$_n$** diblock copolymers prepared *via* aqueous ROMPISA, as determined by ^{1}H-NMR spectroscopy and SEC analysis.

[M2]/[G3]	% Conv.[a]	$M_{n,\,theo.}$ (kDa)[b]	$M_{n,\,SEC\ RI}$ (kDa)[c]	$Đ_{M,\,SEC\ RI}$[c]
15	>99	5.1	5.5	1.39
20	>99	6.0	5.9	1.44
30	>99	7.8	7.8	1.46
60	>99	13.3	12.3	1.60
120	>99	24.2	20.6	1.41

[a]Monomer conversion calculated from ^{1}H-NMR spectroscopy in methanol-d_4. [b]Calculated from conversion. [c]Mn and $Đ_M$ values calculated from PS standards using THF + 2% v/v NEt_3 as the eluent.

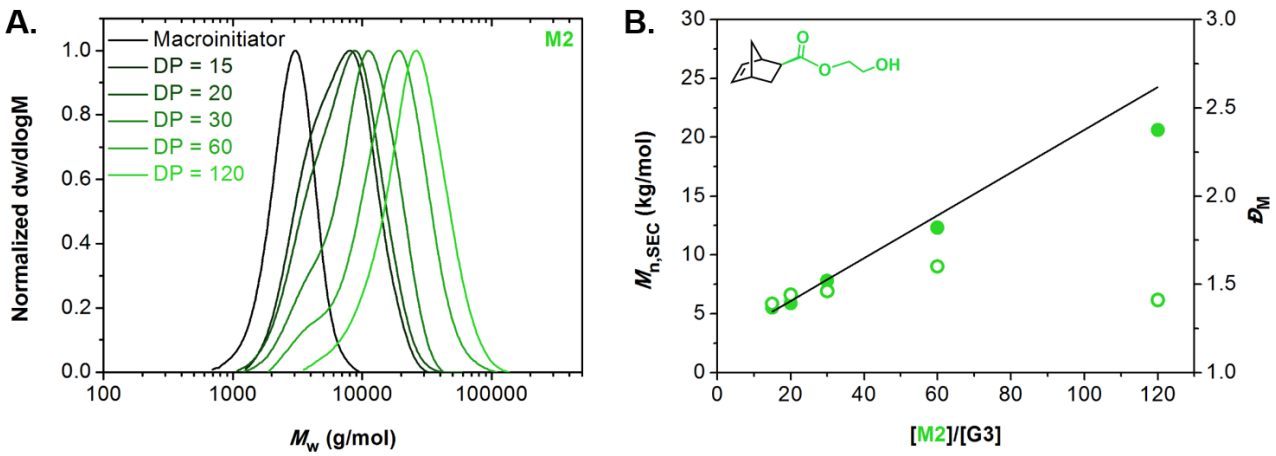

Figure S18. (A) Normalized SEC RI molecular weight distributions for **P(M11)$_{12}$-*b*-P(M2)$_n$** diblock copolymers (n = 15, 20, 30, 60, and 120). (B) Evolution of M_n (filled circles) and $Đ_M$ (empty circles) values calculated from SEC RI analysis with increasing targeted DP$_{P(M2)}$ for **P(M11)$_{12}$-*b*-P(M2)$_n$** diblock

copolymers prepared *via* aqueous ROMPISA. The solid line represents expected M_n values calculated using the monomer feed ratio. M_n and $Đ_M$ values were calculated from PS standards using THF + 2% v/v NEt_3 as the eluent.

Table S3. Molecular characteristics of **P(M11)$_{12}$-*b*-P(M3)$_n$** diblock copolymers prepared *via* aqueous ROMPISA, as determined by ^{1}H-NMR spectroscopy and SEC analysis.

[M3]/[G3]	% Conv.[a]	$M_{n,\,theo.}$ (kDa)[b]	$M_{n,\,SEC\ RI}$ (kDa)[c]	$Đ_{M,\,SEC\ RI}$[c]
20	>99	5.1	9.2	1.36
30	>99	6.5	10.1	1.36
60	>99	10.6	12.5	1.57
120	>99	18.8	15.4	1.87
180	>99	27.0	19.7	2.17

[a]Monomer conversion calculated from ^{1}H-NMR spectroscopy in methanol-d_4. [b]Calculated from conversion. [c]*M*n and $Đ_M$ values calculated from PMMA standards using DMF + 5 mM NH_4BF_4 as the eluent.

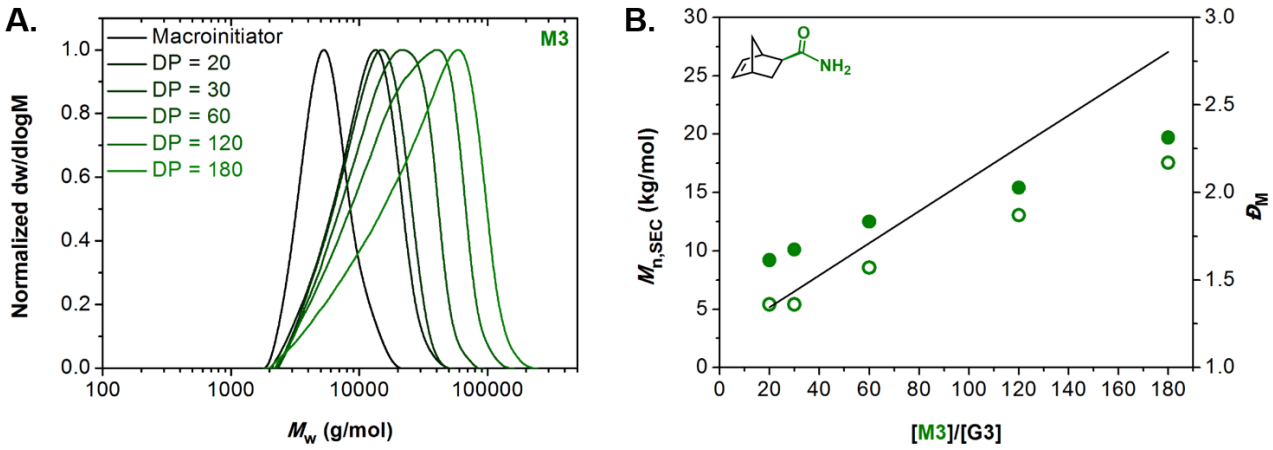

Figure S19. (A) Normalized SEC RI molecular weight distributions for **P(M11)$_{12}$-*b*-P(M3)$_n$** diblock copolymers (n = 20, 30, 60, 120, and 180). (B) Evolution of M_n (filled circles) and $Đ_M$ (empty circles) values calculated from SEC RI analysis with increasing targeted DP$_{P(M3)}$ for **P(M11)$_{12}$-*b*-P(M3)$_n$** diblock copolymers prepared *via* aqueous ROMPISA. The solid line represents expected M_n values calculated using the monomer feed ratio. M_n and $Đ_M$ values were calculated from PMMA standards using DMF + 5 mM NH_4BF_4 as the eluent. The deviation from expected M_n values is attributed to increased interactions between the amide groups of the polymers and the stationary phase of the columns affecting their elution time.[20]

Table S4. Molecular characteristics of **P(M11)$_{12}$-*b*-P(M5)$_n$** diblock copolymers prepared *via* aqueous ROMPISA, as determined by ^{1}H-NMR spectroscopy and SEC analysis.

[M5]/[G3]	% Conv.[a]	$M_{n,\text{theo.}}$ (kDa)[b]	$M_{n,\text{SEC RI}}$ (kDa)[c]	$Đ_{M,\text{SEC RI}}$[c]
15	>99	5.7	6.7	1.26
20	>99	6.8	7.3	1.25
30	>99	9.0	9.0	1.26
60	>99	15.6	13.9	1.29
120	>99	28.9	24.7	1.23
180	>99	42.1	--[d]	--[d]

[a]Monomer conversion calculated from ^{1}H-NMR spectroscopy in methanol-d_4. [b]Calculated from conversion. [c]Mn and $Đ_M$ values calculated from PS standards using THF + 2% v/v NEt$_3$ as the eluent. [d]Polymer was insoluble in SEC mobile phase.

Table S5. Molecular characteristics of **P(M11)$_{12}$-*b*-P(M6)$_n$** diblock copolymers prepared *via* aqueous ROMPISA, as determined by ^{1}H-NMR spectroscopy and SEC analysis.

[M6]/[G3]	% Conv.[a]	$M_{n,\text{theo.}}$ (kDa)[b]	$M_{n,\text{SEC RI}}$ (kDa)[c]	$Đ_{M,\text{SEC RI}}$[c]
15	>99	6.1	7.7	1.32
20	>99	7.3	8.3	1.35
30	>99	9.8	10.9	1.38
60	>99	17.3	18.3	1.48
120	>99	32.2	32.2	1.20

[a]Monomer conversion calculated from ^{1}H-NMR spectroscopy in methanol-d_4. [b]Calculated from conversion. [c]Mn and $Đ_M$ values calculated from PS standards using THF + 2% v/v NEt$_3$ as the eluent.

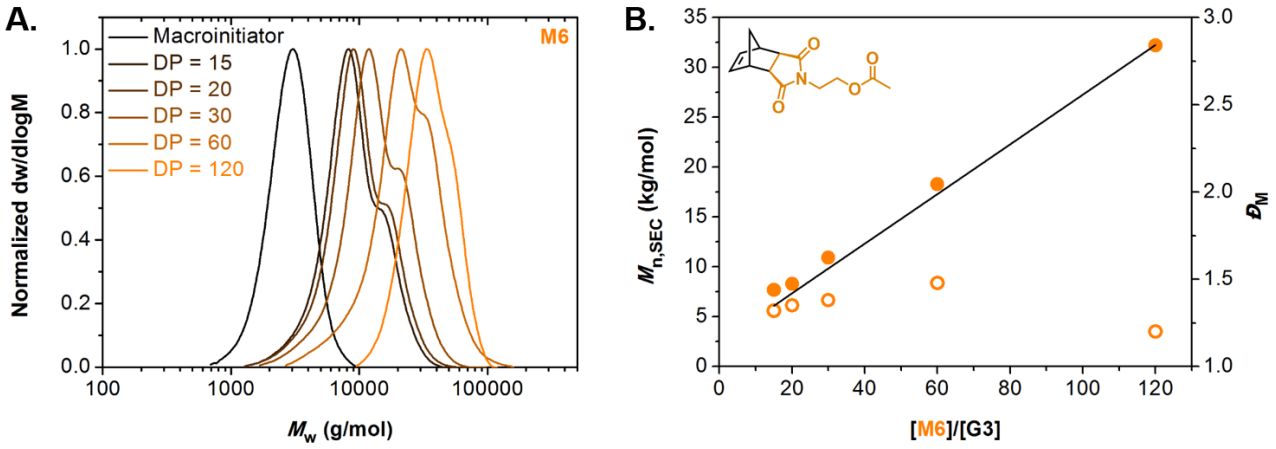

Figure S20. (A) Normalized SEC RI molecular weight distributions for **P(M11)$_{12}$-*b*-P(M6)$_n$** diblock copolymers (n = 15, 20, 30, 60, and 120). (B) Evolution of M_n (filled circles) and $Đ_M$ (empty circles)

values calculated from SEC RI analysis with increasing targeted $DP_{P(M6)}$ for **P(M11)$_{12}$-*b*-P(M6)$_n$** diblock copolymers prepared *via* aqueous ROMPISA. The solid line represents expected M_n values calculated using the monomer feed ratio. M_n and $Đ_M$ values were calculated from PS standards using THF + 2% v/v NEt_3 as the eluent.

Table S6. Molecular characteristics of **P(M11)$_{12}$-*b*-P(M8)$_n$** diblock copolymers prepared *via* aqueous ROMPISA, as determined by ^{1}H-NMR spectroscopy and SEC analysis.

[M8]/[G3]	% Conv.[a]	$M_{n,\,theo.}$ (kDa)[b]	$M_{n,\,SEC\ RI}$ (kDa)[c]	$Đ_{M,\,SEC\ RI}$[c]
15	>99	5.1	10.2	1.25
20	>99	6.0	10.8	1.27
30	>99	7.8	11.9	1.32
60	>99	13.2	13.1	1.42
120	>99	24.1	17.2	1.48

[a]Monomer conversion calculated from ^{1}H-NMR spectroscopy in methanol-d_4. [b]Calculated from conversion. [c]*M*n and $Đ_M$ values calculated from PMMA standards using DMF + 5 mM NH_4BF_4 as the eluent.

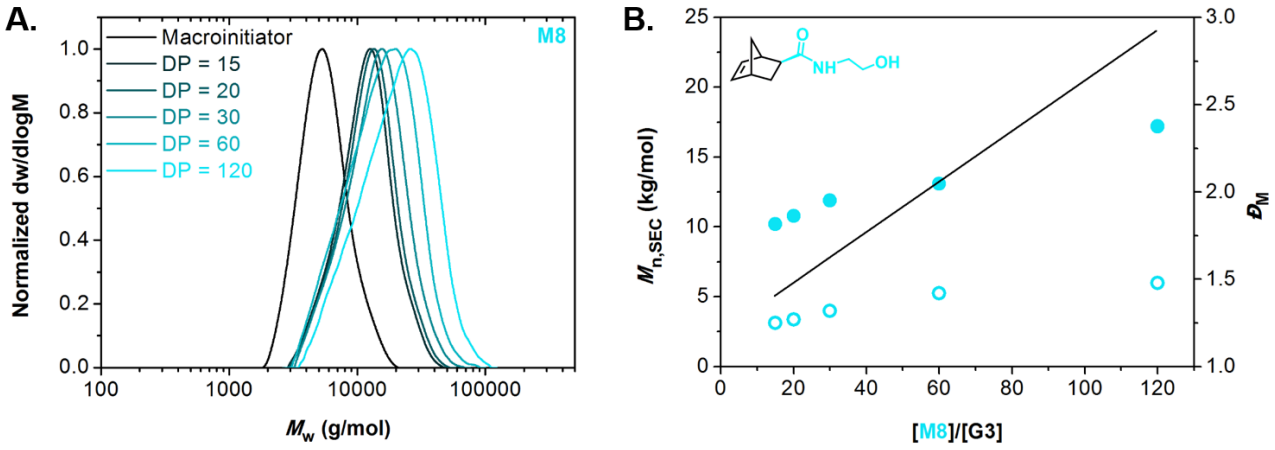

Figure S21. (A) Normalized SEC RI molecular weight distributions for **P(M11)$_{12}$-*b*-P(M8)$_n$** diblock copolymers (n = 15, 20, 30, 60, and 120). (B) Evolution of M_n (filled circles) and $Đ_M$ (empty circles) values calculated from SEC RI analysis with increasing targeted $DP_{P(M8)}$ for **P(M11)$_{12}$-*b*-P(M8)$_n$** diblock copolymers prepared *via* aqueous ROMPISA. The solid line represents expected M_n values calculated using the monomer feed ratio. M_n and $Đ_M$ values were calculated from PMMA standards using DMF + 5 mM NH_4BF_4 as the eluent. The deviation from expected M_n values is attributed to increased interactions between the amide groups of the polymers and the stationary phase of the columns affecting their elution time.[20]

Table S7. Molecular characteristics of **P(M11)$_{12}$-*b*-P(M9)$_n$** diblock copolymers prepared *via* aqueous ROMPISA, as determined by ^{1}H-NMR spectroscopy and SEC analysis.

[M9]/[G3]	% Conv.[a]	$M_{n,\,theo.}$ (kDa)[b]	$M_{n,\,SEC\ RI}$ (kDa)[c]	$Đ_{M,\,SEC\ RI}$[c]
15	>99	5.5	9.3	1.34
20	>99	6.5	10.0	1.34
30	>99	8.6	11.6	1.41
60	>99	14.8	15.5	1.50
120	>99	27.2	25.3	1.55

[a]Monomer conversion calculated from ^{1}H-NMR spectroscopy in methanol-d_4. [b]Calculated from conversion. [c]Mn and $Đ_M$ values calculated from PMMA standards using DMF + 5 mM NH_4BF_4 as the eluent.

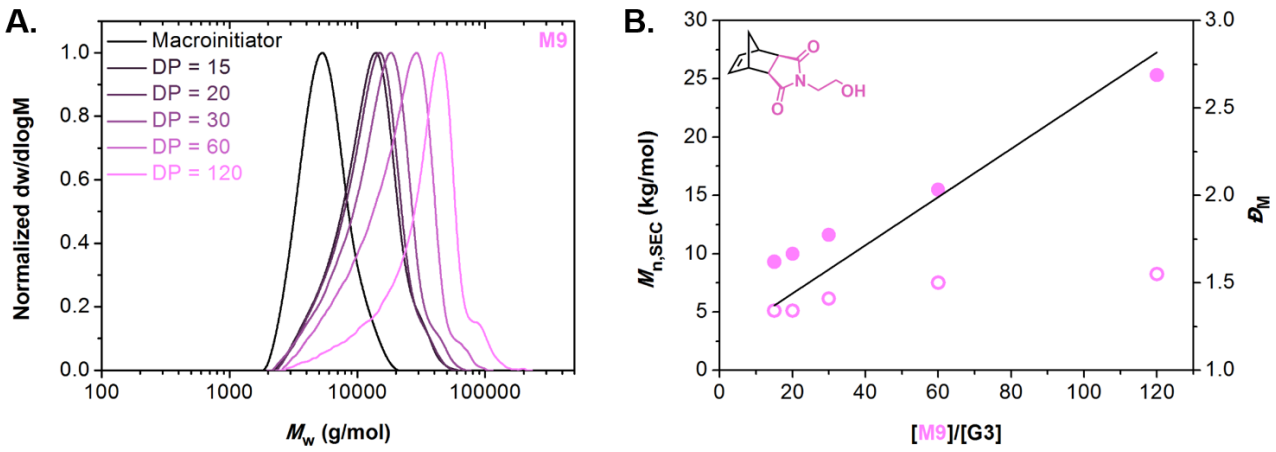

Figure S22. (A) Normalized SEC RI molecular weight distributions for **P(M11)$_{12}$-*b*-P(M9)$_n$** diblock copolymers (n = 15, 20, 30, 60, and 120). (B) Evolution of M_n (filled circles) and $Đ_M$ (empty circles) values calculated from SEC RI analysis with increasing targeted DP$_{P(M11)}$ for **P(M11)$_{12}$-*b*-P(M9)$_n$** diblock copolymers prepared *via* aqueous ROMPISA. The solid line represents expected M_n values calculated using the monomer feed ratio. M_n and $Đ_M$ values were calculated from PMMA standards using DMF + 5 mM NH_4BF_4 as the eluent.

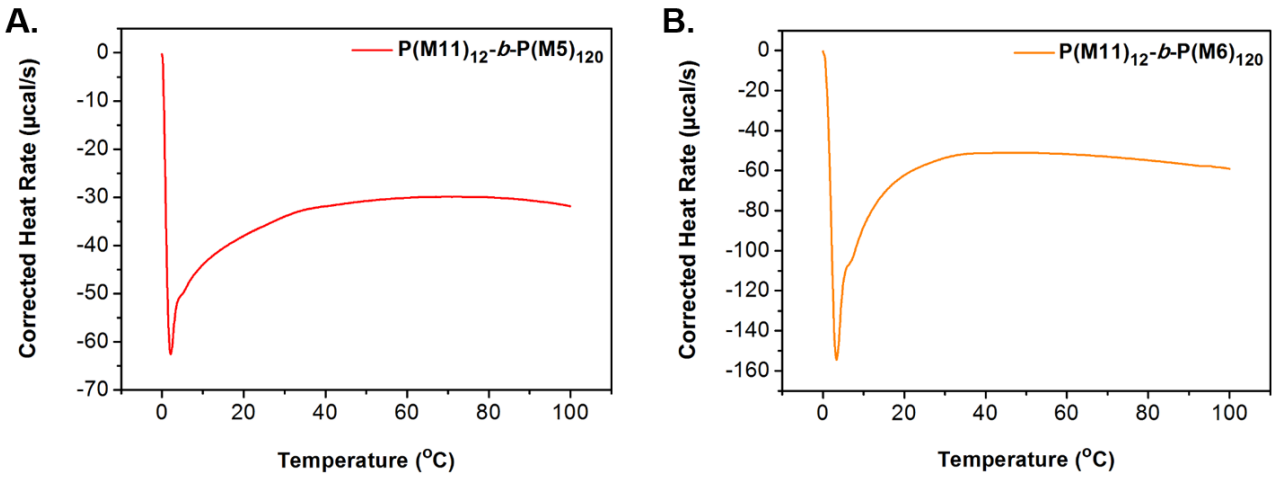

Figure S23. DSC thermograms of (A) **P(M11)$_{12}$-*b*-P(M5)$_{120}$** and (B) **P(M11)$_{12}$-*b*-P(M6)$_{120}$** diblock copolymers in solution (heating rate 1.5 °C/min). The endothermic peak at ca. 5 °C is attributed to absorption of heat by the solvent. For both samples, there were no observable thermodynamic events within the tested temperature range, implying that T_g values for both polymers likely reside above 100 °C.

Supplementary Characterization Data for Water-Soluble P(M10)$_{11}$-*b*-P(M10)$_n$ Diblock Copolymers

Table S8. Molecular characteristics of **P(M10)$_{11}$** macroinitiator prepared *via* ROMP in THF, as determined by ^{1}H-NMR spectroscopy and SEC analysis.

[M10]/[G3]	% Conv.[a]	$M_{n,\,theo.}$ (kDa)[b]	$M_{n,\,NMR}$ (kDa)[c]	$M_{n,\,SEC\ RI}$ (kDa)[d]	$Đ_{M,\,SEC\ RI}$[d]	$M_{n,\,SEC\ RI}$ (kDa)[e]	$Đ_{M,\,SEC\ RI}$[e]
10	>99	5.0	5.5	5.6	1.13	8.2	1.18

[a]Monomer conversion calculated from ^{1}H-NMR spectroscopy in methanol-d_4. [b]Calculated from conversion. [c]Calculated using end group analysis from ^{1}H-NMR spectroscopy. [d]Mn and $Đ_M$ values calculated from PS standards using THF + 2% v/v NEt_3 as the eluent. [e]Mn and $Đ_M$ values calculated from PMMA standards using DMF + 5 mM NH_4BF_4 as the eluent.

Table S9. Molecular characteristics of **P(M10)$_{11}$-*b*-P(M10)$_n$** diblock copolymers prepared *via* aqueous ROMP, as determined by ^{1}H-NMR spectroscopy and SEC analysis.

[M10]/[G3]	% Conv.[a]	$M_{n,\,theo.}$ (kDa)[b]	$M_{n,\,SEC\ RI}$ (kDa)[c]	$Đ_{M,\,SEC\ RI}$[c]
15	>99	12.4	11.9	1.12
20	>99	14.9	13.0	1.11
30	>99	19.8	16.8	1.09
60	>99	34.7	25.5	1.10
120	>99	64.4	39.2	1.08

[a]Monomer conversion calculated from ^{1}H-NMR spectroscopy in methanol-d_4. [b]Calculated from conversion. [c]Mn and $Đ_M$ values calculated from PS standards using THF + 2% v/v NEt_3 as the eluent.

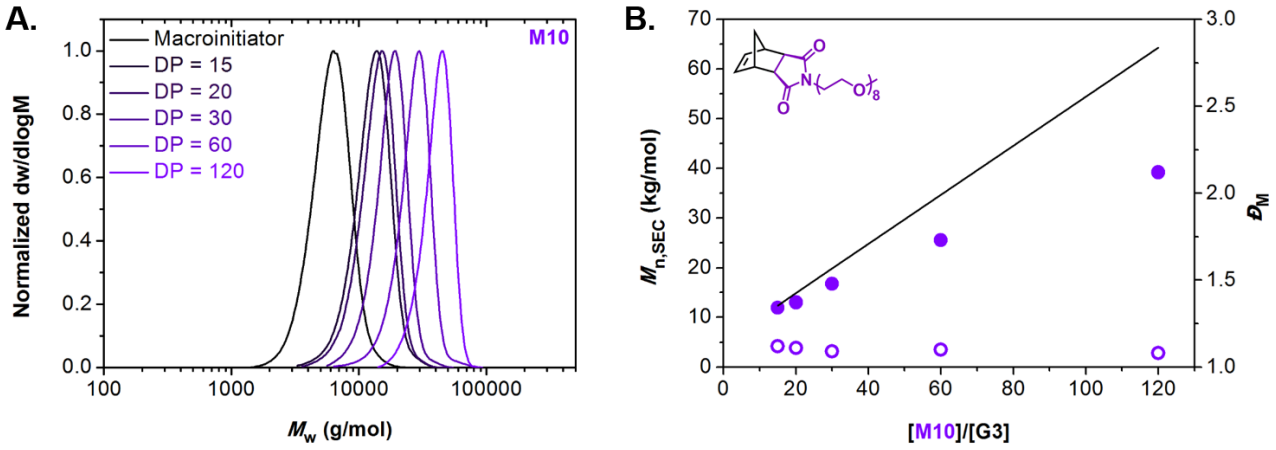

Figure S24. (A) Normalized SEC RI molecular weight distributions for **P(M10)$_{11}$-*b*-P(M10)$_n$** diblock copolymers (n = 15, 20, 30, 60, and 120). (B) Evolution of M_n (filled circles) and $Đ_M$ (empty circles)

values calculated from SEC RI analysis with increasing targeted $DP_{P(M10)}$ for **P(M10)$_{11}$-*b*-P(M10)$_n$** diblock copolymers prepared *via* aqueous ROMP. The solid line represents expected M_n values calculated using the monomer feed ratio. M_n and $Đ_M$ values were calculated from PS standards using THF + 2% v/v NEt_3 as the eluent. The deviation from expected M_n values is attributed to formation of highly branched polymers which appear to have smaller hydrodynamic volume compared to linear polymers.

Supplementary Characterization Data for P(M11)$_{12}$-*b*-P(MX)$_n$ Diblock Copolymer Nano-Objects Developed by Aqueous ROMPISA

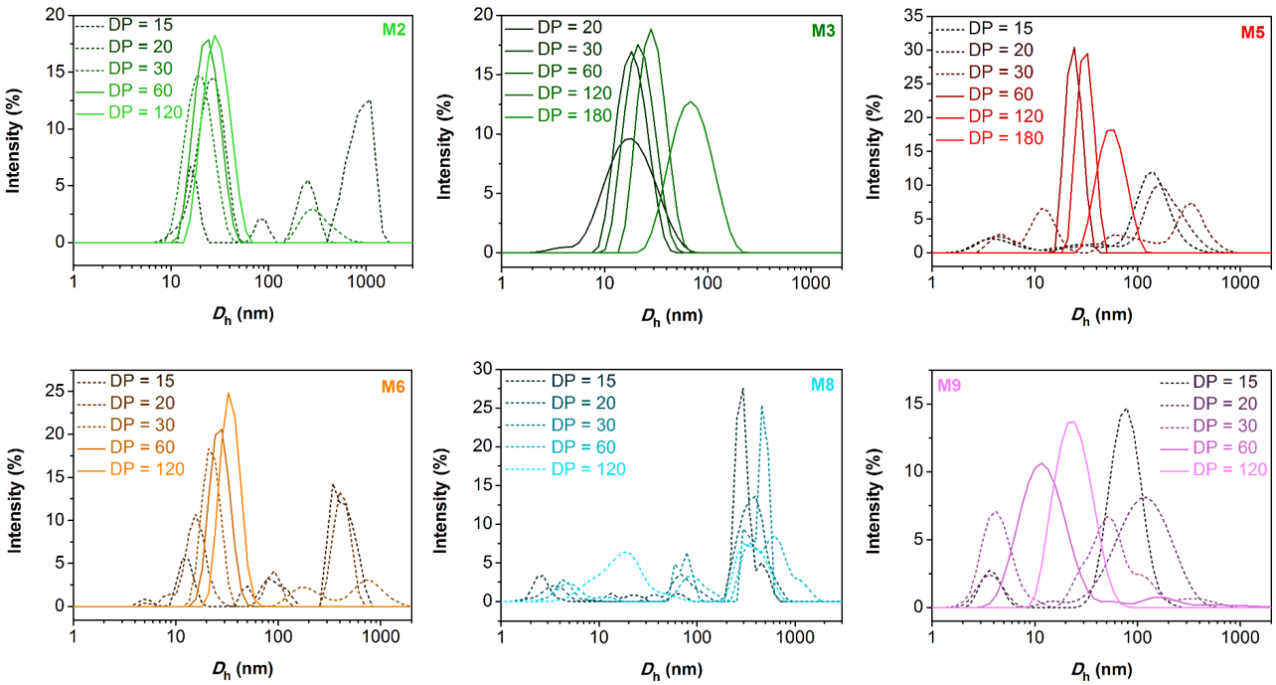

Figure S25. Intensity-weighted size distributions obtained by DLS for **P(M11)$_{12}$-*b*-P(MX)$_n$** (**MX** = **M2**, **M3**, **M5**, **M6**, **M8**, and **M9**) diblock copolymer nano-objects developed *via* aqueous ROMPISA. The dashed lines indicate worm-like micelles or morphologies with high PD.

Table S10. Summary of *D*h, and PD values and observed morphologies for **P(M11)$_{12}$-*b*-P(M2)$_n$** diblock copolymer nano-objects prepared *via* aqueous ROMPISA reactions, as determined by DLS analysis and dry-state TEM imaging, respectively.

[M2]/[G3]	D_h (nm)[a]	PD[a]	Morphology[b]
15	627.7 ± 130.9	0.72 ± 0.19	S
20	34.1 ± 5.3	0.36 ± .011	S+W
30	49.2 ± 18.3	0.28 ± 0.12	W+V
60	29.4 ± 5.2	0.26 ± 0.05	ill-defined V
120	29.0 ± 0.5	0.16 ± 0.02	V

[a]D_h and PD values measured from DLS analysis (the error shows the standard deviation from 5 repeat measurements). [b]Morphologies observed from dry-state TEM imaging, using 1 wt% uranyl acetate (UA) solution for staining (Key: S – spherical micelles, W – worm-like micelles, V – vesicles).

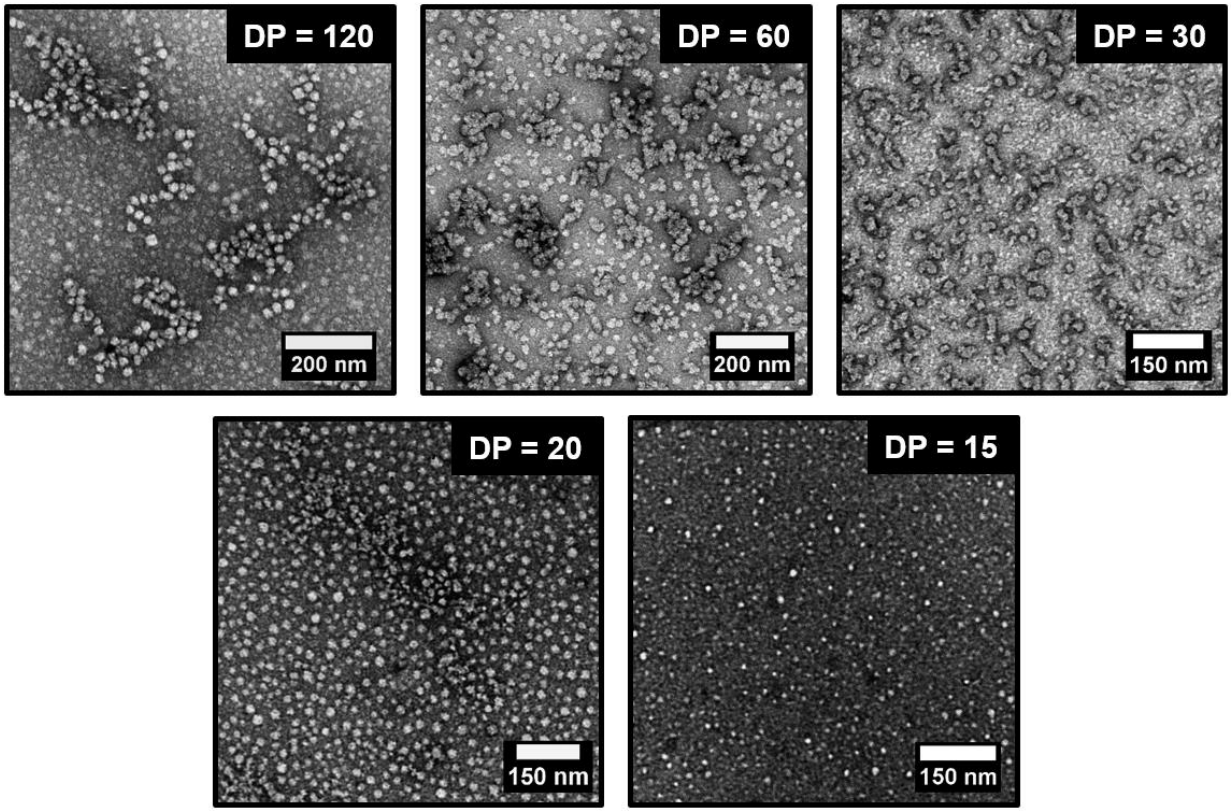

Figure S26. Representative dry-state TEM images of **P(M11)$_{12}$-*b*-P(M2)$_n$** (n = 15, 20, 30, 60, and 120) diblock copolymer nano-objects developed *via* aqueous ROMPISA, stained with 1 wt% UA solution.

Table S11. Summary of *D*h, and PD values and observed morphologies for **P(M11)$_{12}$-*b*-P(M3)$_n$** diblock copolymer nano-objects prepared *via* aqueous ROMPISA reactions, as determined by DLS analysis and dry-state TEM imaging, respectively.

[M3]/[G3]	D_h (nm)[a]	PD[a]	Morphology[b]
20	16.7 ± 0.8	0.33 ± 0.01	S+W
30	18.6 ± 0.3	0.20 ± 0.01	W+V
60	21.3 ± 0.4	0.15 ± 0.02	V
120	27.4 ± 0.8	0.08 ± 0.02	V
180	63.2 ± 1.0	0.16 ± 0.01	V

[a]D_h and PD values measured from DLS analysis (the error shows the standard deviation from 5 repeat measurements). [b]Morphologies observed from dry-state TEM imaging, using 1 wt% UA solution for staining (Key: S – spherical micelles, W – worm-like micelles, V – vesicles).

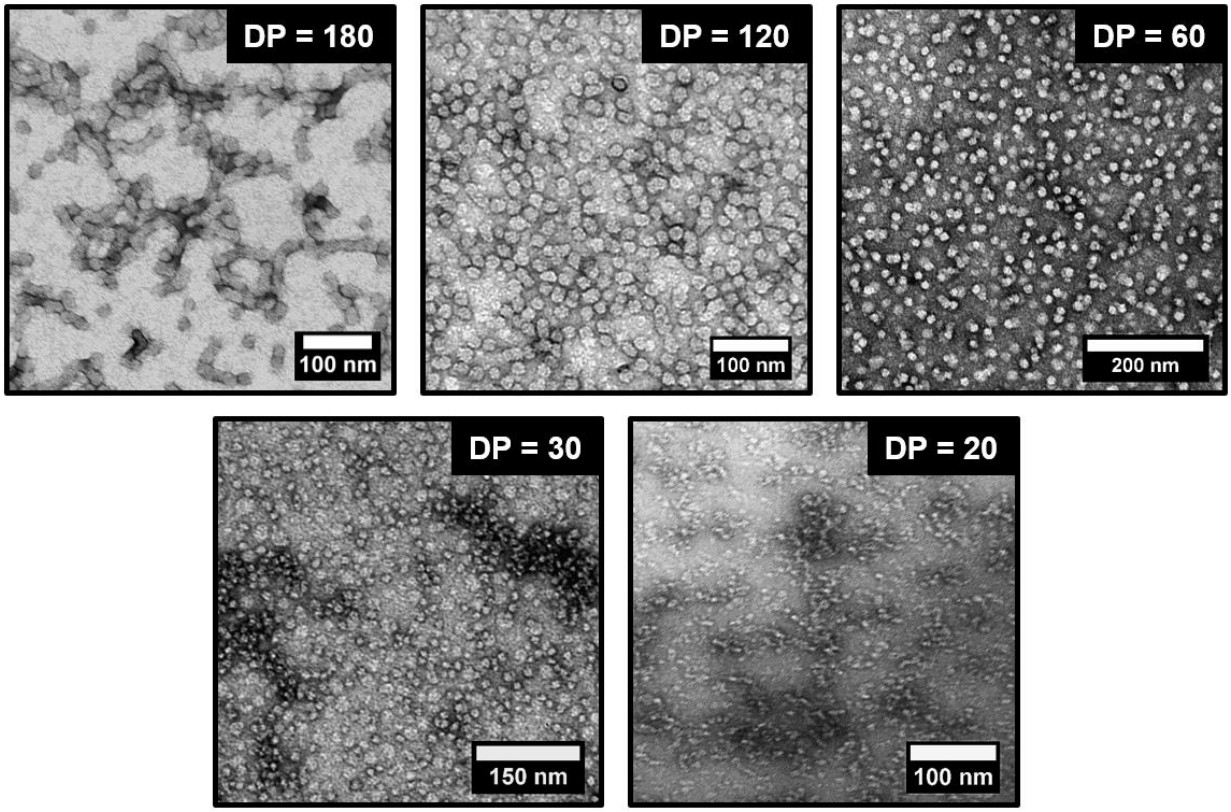

Figure S27. Representative dry-state TEM images of **P(M11)$_{12}$-*b*-P(M3)$_n$** (n = 20, 30, 60, 120, and 180) diblock copolymer nano-objects developed *via* aqueous ROMPISA, stained with 1 wt% UA solution.

Table S12. Summary of *D*h, and PD values and observed morphologies for **P(M11)$_{12}$-*b*-P(M5)$_n$** diblock copolymer nano-objects prepared *via* aqueous ROMPISA reactions, as determined by DLS analysis and dry-state TEM imaging, respectively.

[M5]/[G3]	D_h (nm)[a]	PD[a]	Morphology[b]
15	169.7 ± 54.2	0.35 ± 0.16	S+W
20	140.5 ± 86.1	0.57 ± 0.27	S+W
30	118.8 ± 83.9	0.45 ± 0.17	W
60	24.8 ± 0.5	0.15 ± 0.03	W+V
120	31.1 ± 0.5	0.08 ± 0.01	W+V
180	53.4 ± 0.7	0.08 ± 0.01	V

[a]D_h and PD values measured from DLS analysis (the error shows the standard deviation from 5 repeat measurements). [b]Morphologies observed from dry-state TEM imaging, using 1 wt% UA solution for staining (Key: S – spherical micelles, W – worm-like micelles, V – vesicles).

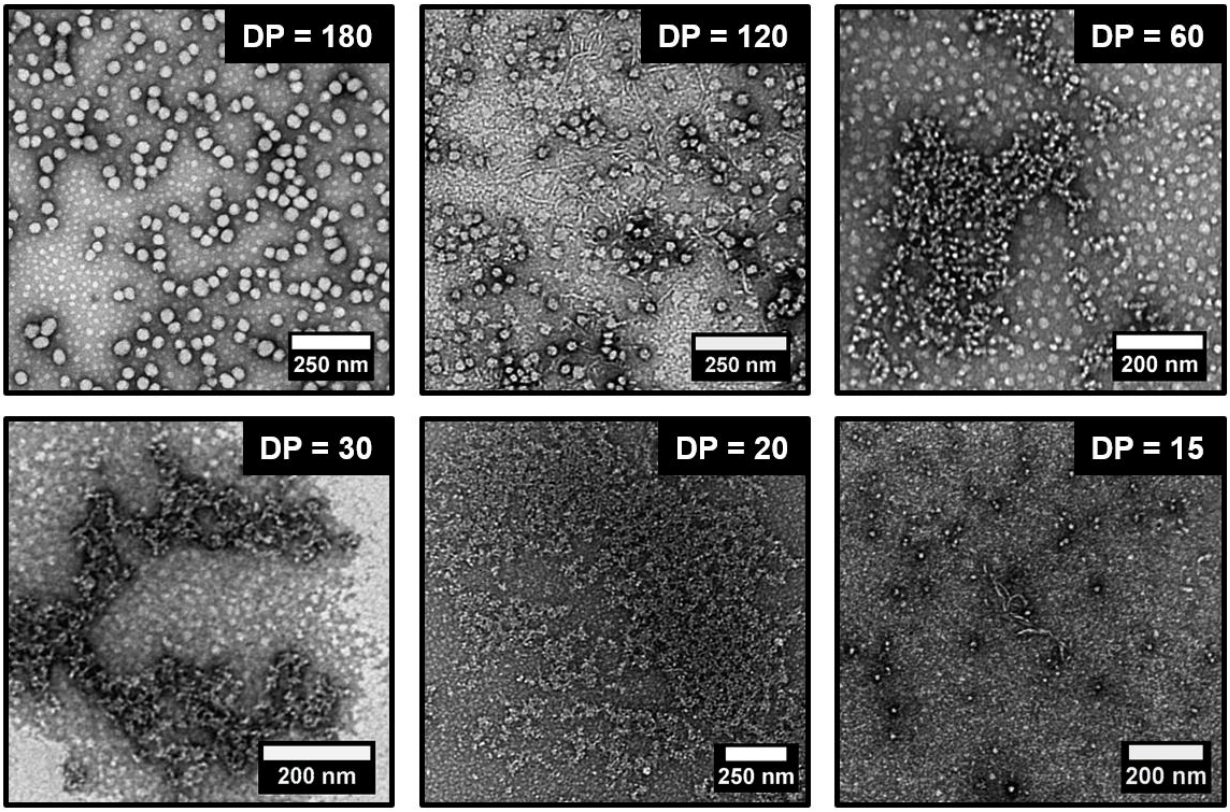

Figure S28. Representative dry-state TEM images of **P(M11)$_{12}$-*b*-P(M5)$_n$** (n = 15, 20, 30, 60, 120, and 180) diblock copolymer nano-objects developed *via* aqueous ROMPISA, stained with 1 wt% UA solution.

Table S13. Summary of *D*h, and PD values and observed morphologies for **P(M11)$_{12}$-*b*-P(M6)$_n$** diblock copolymer nano-objects prepared *via* aqueous ROMPISA reactions, as determined by DLS analysis and dry-state TEM imaging, respectively.

[M6]/[G3]	D_h (nm)[a]	PD[a]	Morphology[b]
15	329.1 ± 30.1	0.50 ± 0.03	S+W
20	175.6 ± 46.5	0.36 ± 0.03	S+W
30	38.6 ± 0.9	0.47 ± 0.02	W
60	33.5 ± 0.8	0.14 ± 0.01	V
120	37.1 ± 1.8	0.12 ± 0.02	V

[a]D_h and PD values measured from DLS analysis (the error shows the standard deviation from 5 repeat measurements). [b]Morphologies observed from dry-state TEM imaging, using 1 wt% UA solution for staining (Key: S – spherical micelles, W – worm-like micelles, V – vesicles).

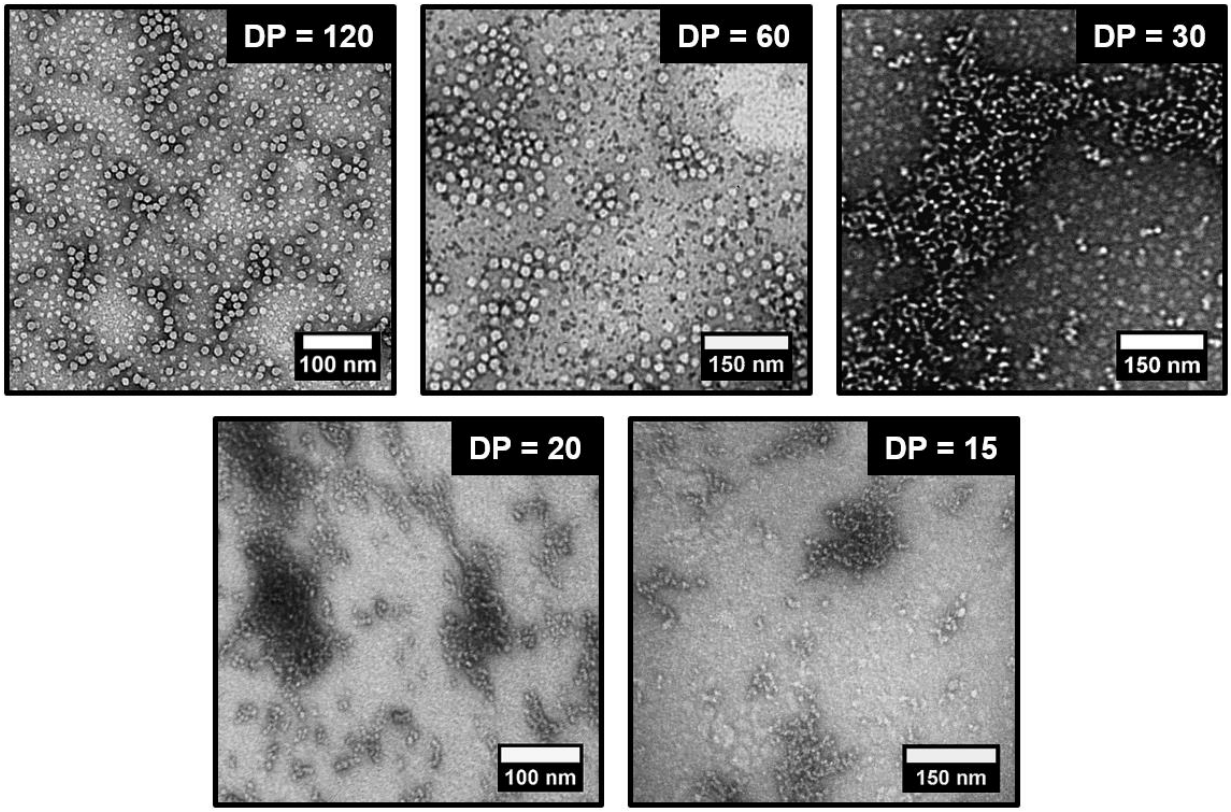

Figure S29. Representative dry-state TEM images of **P(M11)$_{12}$-*b*-P(M6)$_{n}$** (n = 15, 20, 30, 60, and 120) diblock copolymer nano-objects developed *via* aqueous ROMPISA, stained with 1 wt% UA solution.

Table S14. Summary of *D*h, and PD values and observed morphologies for **P(M11)$_{12}$-*b*-P(M8)$_{n}$** diblock copolymer nano-objects prepared *via* aqueous ROMPISA reactions, as determined by DLS analysis and dry-state TEM imaging, respectively.

[M8]/[G3]	D_h (nm)[a]	PD[a]	Morphology[b]
15	1146 ± 227.4	0.83 ± 0.10	W
20	577.9 ± 93.7	0.60 ± 0.03	W
30	468 ± 57.9	0.58 ± 0.05	W
60	686.3 ± 140.1	0.73 ± 0.14	W
120	324.1 ± 91.8	0.46 ± 0.08	W

[a]D_h and PD values measured from DLS analysis (the error shows the standard deviation from 5 repeat measurements). [b]Morphologies observed from dry-state TEM imaging, using 1 wt% UA solution for staining (Key: S – spherical micelles, W – worm-like micelles, V – vesicles).

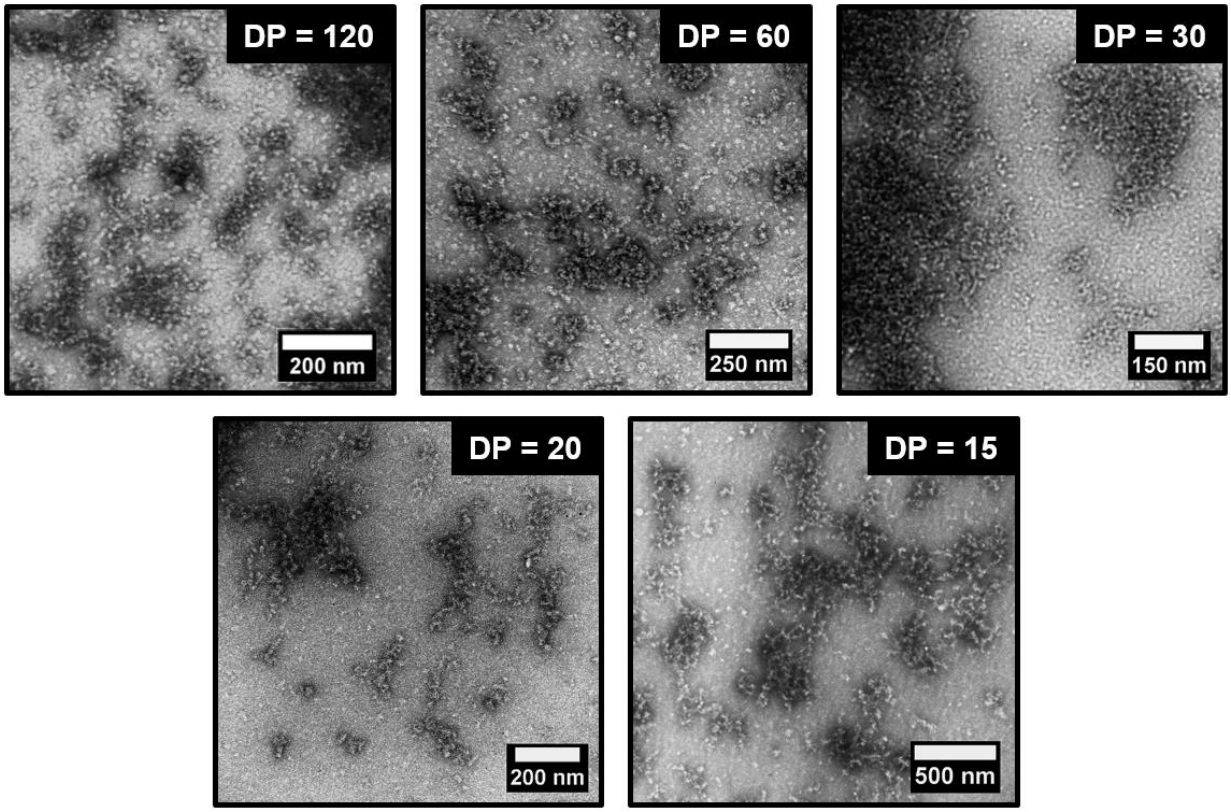

Figure S30. Representative dry-state TEM images of **P(M11)$_{12}$-*b*-P(M8)$_n$** (n = 15, 20, 30, 60, and 120) diblock copolymer nano-objects developed *via* aqueous ROMPISA, stained with 1 wt% UA solution.

Table S15. Summary of *D*h, and PD values and observed morphologies for **P(M11)$_{12}$-*b*-P(M9)$_n$** diblock copolymer nano-objects prepared *via* aqueous ROMPISA reactions, as determined by DLS analysis and dry-state TEM imaging, respectively.

[M9]/[G3]	D_h (nm)[a]	PD[a]	Morphology[b]
15	95.8 ± 49.4	0.36 ± 0.18	S
20	58.3 ± 8.5	0.73 ± 0.18	S
30	160.1 ± 63.5	0.46 ± 0.13	S
60	13.5 ± 0.8	0.34 ± 0.04	S
120	22.9 ± 0.5	0.17 ± 0.01	S

[a]D_h and PD values measured from DLS analysis (the error shows the standard deviation from 5 repeat measurements). [b]Morphologies observed from dry-state TEM imaging, using 1 wt% UA solution for staining (Key: S – spherical micelles, W – worm-like micelles, V – vesicles).

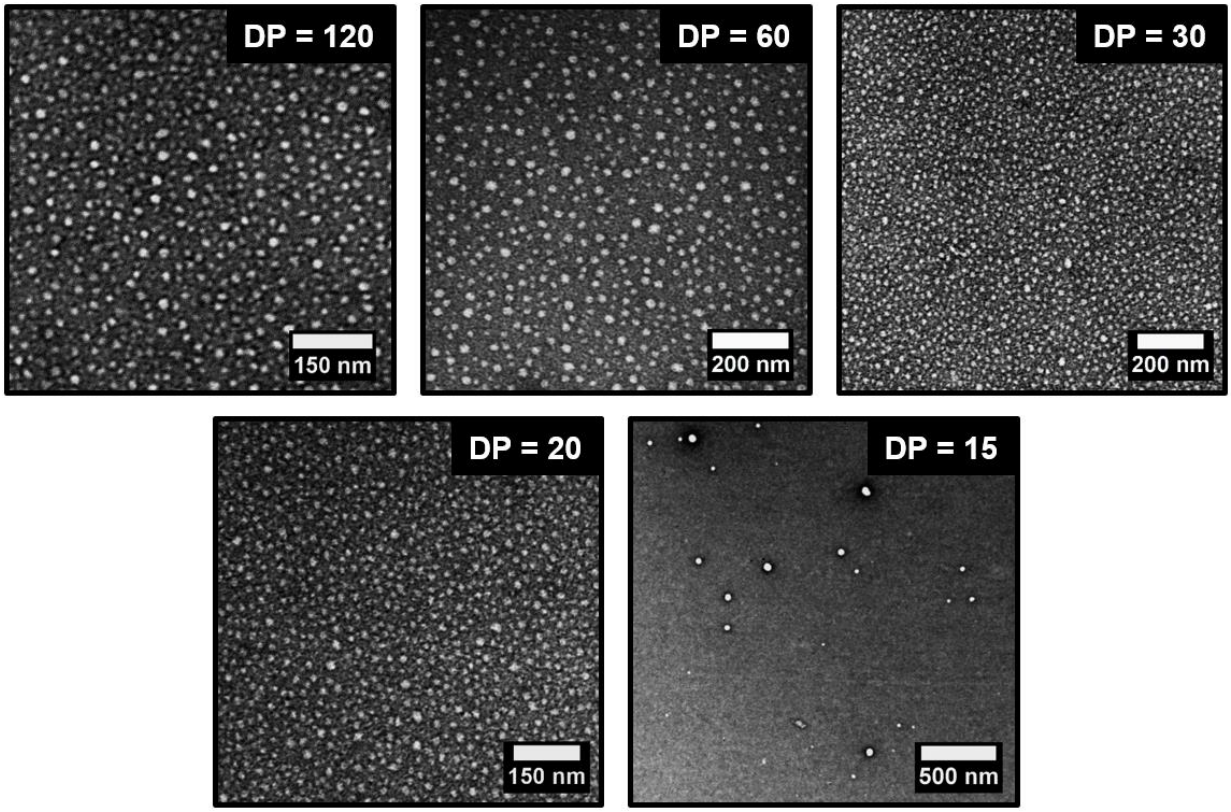

Figure S31. Representative dry-state TEM images of **P(M11)$_{12}$-*b*-P(M9)$_{n}$** (n = 15, 20, 30, 60, and 120) diblock copolymer nano-objects developed *via* aqueous ROMPISA, stained with 1 wt% UA solution.

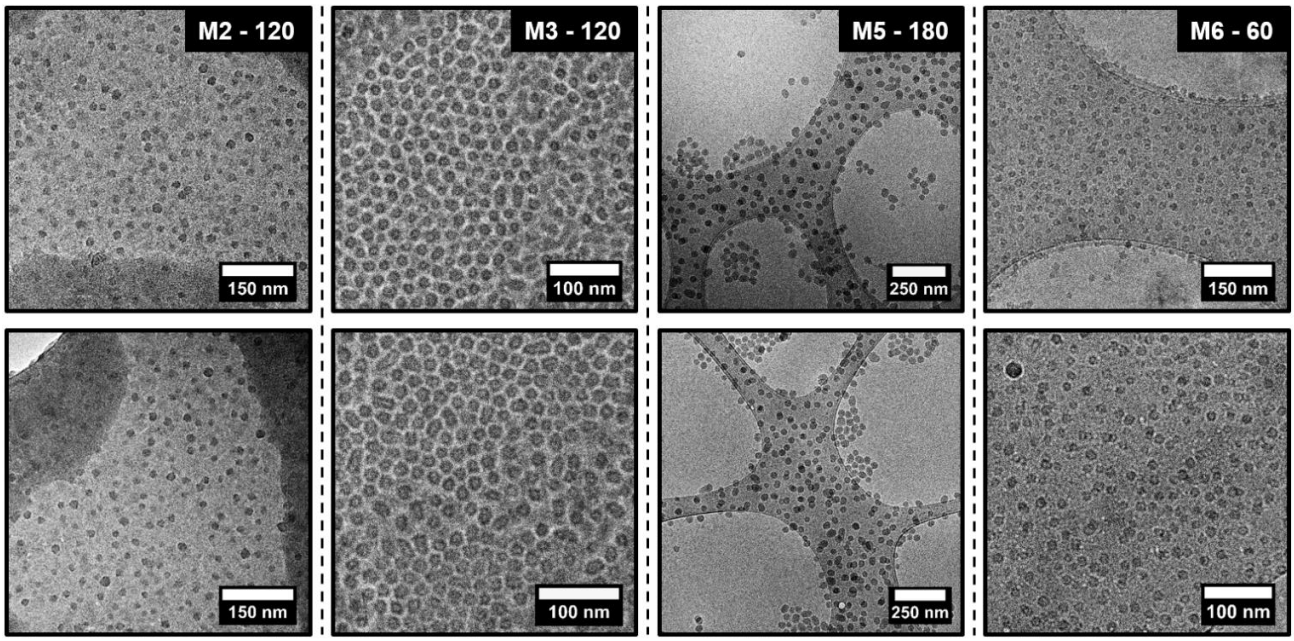

Figure S32. Representative cryo-TEM images of selected vesicular morphologies for **P(M11)$_{12}$-*b*-P(MX)$_n$** (**MX** = **M2**, **M3**, **M5**, and **M6**) diblock copolymer nano-objects developed *via* aqueous ROMPISA.

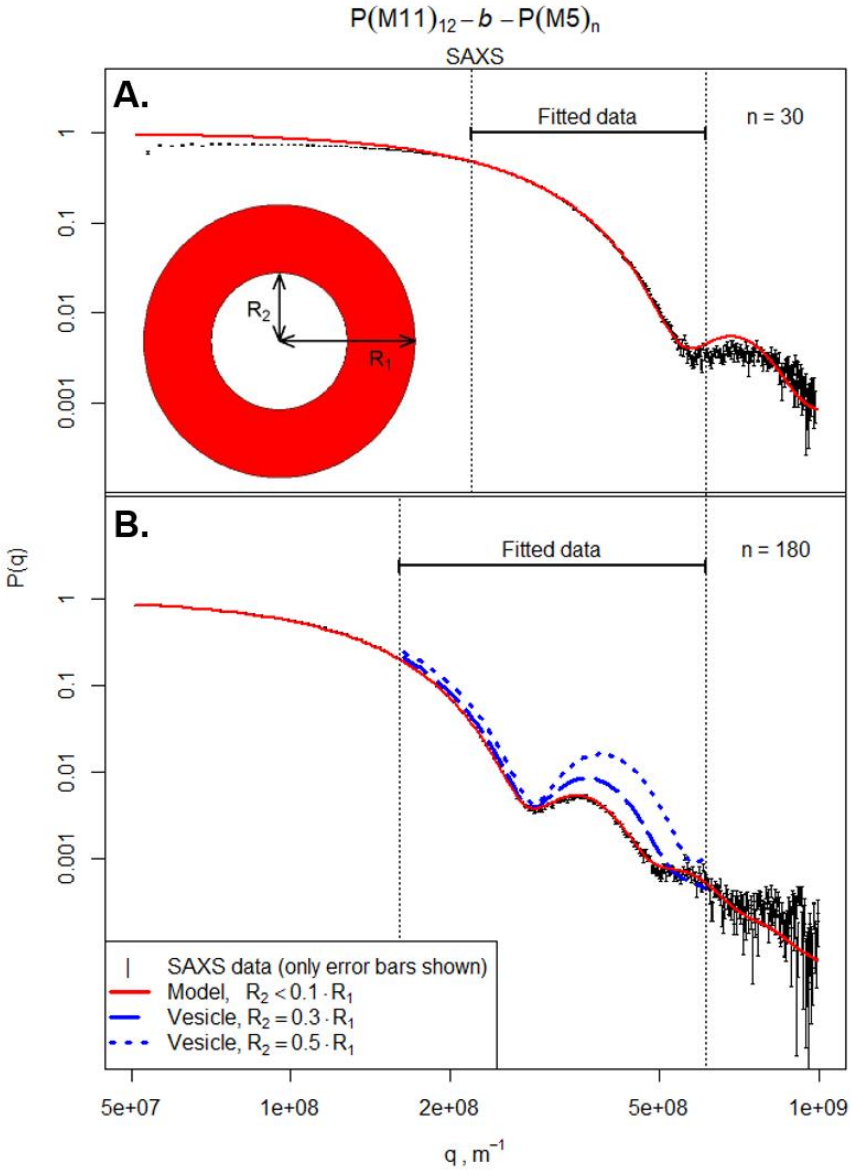

Figure S33. (A) SAXS data recorded for **P(M11)$_{12}$-*b*-P(M5)$_{30}$** particles appeared to be consistent with a model for homogeneous spheres ($R_2 \approx 0$) where there is a distribution of particle sizes, $\varepsilon_i R_1$, such that $\ln(\varepsilon_i) \sim N$ ($\mu = 0$, $\sigma = 0.11$). (B) SAXS data recorded for **P(M11)$_{12}$-*b*-P(M5)$_{180}$** particles appeared to be consistent with a model for homogeneous spheres. For comparison, example form factors, $P(q; R_1, R_2, \sigma)$, are shown to indicate how the data might otherwise be expected to appear in the case of these particles being vesicular structures that incorporate a non-trivial central void, $R_2 = 0.3R_1$ or $R_2 = 0.5R_1$.

To test our assessments made by inspection of dry-state and cryo-TEM images, two examples of the ROMPISA solutions were selected for further investigation by SAXS analysis from the bulk sample. We

found that in each case, **P(M11)$_{12}$-*b*-P(M5)$_{30}$** and **P(M11)$_{12}$-*b*-P(M5)$_{180}$**, the data recorded was not consistent with any of several differently parameterized models for scattering by long worm or vesicular structures. Indeed, the best fits were obtained *via* the parsimonious model: spherical particles of homogeneous density of non-uniform size, i.e. incorporating a parameter to measure the particle size distribution. According to the fitted model, the intensity weighted average particle size (external radius, R_Z) for **P(M11)$_{12}$-*b*-P(M5)$_{30}$** was $R_Z = 8.4 \pm 0.0$ nm, while for **P(M11)$_{12}$-*b*-P(M5)$_{180}$** was $R_Z = 16.8 \pm 0.1$ nm. These sizes were judged to be consistent with the imaging data.

References

1. Pedersen, J., In *Neutron, X-rays and Light. Scattering Methods Applied to Soft Condensed Matter.*, Zemb, T. L. P., Ed. Elsevier: North Holland, **2002**.

2. Team, R. C. R foundation for statistical computing. *Vienna, Austria* **2013**, *3*.

3. Soetaert, K.; Petzoldt, T. Inverse Modelling, Sensitivity and Monte Carlo Analysis in R Using Package FME. *J. Stat. Softw.* **2010**, *33*, 28.

4. *Materials Studio 2018*, Accelrys Software Inc., Materials Studio 2018: San Diego, **2018**.

5. Ghose, A. K.; Viswanadhan, V. N.; Wendoloski, J. J. Prediction of Hydrophobic (Lipophilic) Properties of Small Organic Molecules Using Fragmental Methods: An Analysis of ALOGP and CLOGP Methods. *J. Phys. Chem. A* **1998**, *102*, 3762-3772.

6. Sun, H.; Jin, Z.; Yang, C. W.; Akkermans, R. L. C.; Robertson, S. H.; Spenley, N. A.; Miller, S.; Todd, S. M. COMPASS II: extended coverage for polymer and drug-like molecule databases. *J. Mol. Model.* **2016**, *22*, 47.

7. Yang, J.; Ren, Y.; Tian, A.-m.; Sun, H. COMPASS Force Field for 14 Inorganic Molecules, He, Ne, Ar, Kr, Xe, H2, O2, N2, NO, CO, CO2, NO2, CS2, and SO2, in Liquid Phases. *J. Phys. Chem. B* **2000**, *104*, 4951-4957.

8. Sun, H. COMPASS: An ab Initio Force-Field Optimized for Condensed-Phase Applications-Overview with Details on Alkane and Benzene Compounds. *J. Phys. Chem. B* **1998**, *102*, 7338-7364.

9. Scherrer, R. A.; Howard, S. M. Use of distribution coefficients in quantitative structure-activity relations. *J. Med. Chem.* **1977**, *20*, 53-58.

10. Kuramochi, H.; Kawamoto, K.; Sakai, S.-i. Effects of pH on the water solubility and 1-octanol–water partition coefficient of 2,4,6-tribromophenol. *J. Environ. Monit.* **2008**, *10*, 206-210.

11. Völgyi, G.; Baka, E.; Box, K. J.; Comer, J. E. A.; Takács-Novák, K. Study of pH-dependent solubility of organic bases. Revisit of Henderson-Hasselbalch relationship. *Anal. Chim. Acta* **2010**, *673*, 40-46.

12. R. Crampton, M.; A. Robotham, I. Acidities of Some Substituted Ammonium Ions in Dimethyl Sulfoxide. *J. Chem. Research (S)* **1997**, 22-23.

13. Li, Y.; Wang, Z.; Wei, Q.; Luo, M.; Huang, G.; Sumer, B. D.; Gao, J. Non-covalent interactions in controlling pH-responsive behaviors of self-assembled nanosystems. *Polym. Chem.* **2016**, *7*, 5949-5956.

14. Du, L.; Wang, C.; Meng, L.; Cheng, Q.; Zhou, J.; Wang, X.; Zhao, D.; Zhang, J.; Deng, L.; Liang, Z.; Dong, A.; Cao, H. The study of relationships between pKa value and siRNA delivery efficiency based on tri-block copolymers. *Biomaterials* **2018**, *176*, 84-93.

15. Omer, M.; Khan, M.; Kim, Y. K.; Lee, J. H.; Kang, I.-K.; Park, S.-Y. Biosensor utilizing a liquid crystal/water interface functionalized with poly(4-cyanobiphenyl-4′-oxyundecylacrylate-b-((2-dimethyl amino) ethyl methacrylate)). *Colloids Surf. B Biointerfaces* **2014**, *121*, 400-408.

16. Radzinski, S. C.; Foster, J. C.; Chapleski, R. C.; Troya, D.; Matson, J. B. Bottlebrush Polymer Synthesis by Ring-Opening Metathesis Polymerization: The Significance of the Anchor Group. *J. Am. Chem. Soc.* **2016**, *138*, 6998-7004.

17. Strong, L. E.; Kiessling, L. L. A General Synthetic Route to Defined, Biologically Active Multivalent Arrays. *J. Am. Chem. Soc.* **1999**, *121*, 6193-6196.

18. Kolonko, E. M.; Pontrello, J. K.; Mangold, S. L.; Kiessling, L. L. General Synthetic Route to Cell-Permeable Block Copolymers via ROMP. *J. Am. Chem. Soc.* **2009**, *131*, 7327-7333.

19. Foster, J. C.; Varlas, S.; Blackman, L. D.; Arkinstall, L. A.; O'Reilly, R. K. Ring-Opening Metathesis Polymerization in Aqueous Media Using a Macroinitiator Approach. *Angew. Chem. Int. Ed.* **2018**, *57*, 10672-10676.

20. Chen, J.; Radke, W.; Pasch, H. Analysis of polyamides by size exclusion chromatography and laser light scattering. *Macromol. Symp.* **2003**, *193*, 107-118.

Additional Discussion on Characterization Data

As shown in Figures S18-S21 of Chapter 4, SEC analysis of **P(M11)$_{12}$-*b*-P(MX)$_n$** diblock copolymers developed *via* ROMPISA in acidic aqueous media (pH = 2) revealed that the corresponding molecular weight distributions were rather broad ($Đ_M \geq 1.25$) with traces that were either bimodal or possessed tails/shoulders at high or low molecular weight values depending on the core-forming monomer utilized in each case. This behavior could be attributed to numerous factors primarily involving the nature of developed polymers, as well as the inherent limitations of Ru-catalyzed ROMP in aqueous media.

In particular, polyamides such as the PNB-based diblock copolymers developed using **M3** and **M8** as the core-forming monomers are known to possess very limited solubility in a wide range of common organic solvents (including DMF + 5 mM NH_4BF_4 that was used as the mobile phase during SEC analysis in this case). This phenomenon is attributed to the strong intermolecular H-bonding developed between the amide groups, conferring increased solvent resistance to the polymers and rendering their solution characterization a rather strenuous process. Thus, it is evident that the limited solubility of this series of diblock copolymers and the occurrence of potential aggregation phenomena in the SEC mobile phase are primarily responsible for their poor separation upon increasing the core-block DP, the evident low molecular weight tailing and the deviation of calculated M_n values from the theoretically expected ones. It should be noted that **P(M11)$_{12}$-*b*-P(M3)$_n$** and **P(M11)$_{12}$-*b*-P(M8)$_n$** diblock copolymers were insoluble in the alternative mobile phase of THF + 2% NEt_3 that was available in our lab.

Additionally, a recently published study by our group (*J. Am. Chem. Soc*. **2020**, DOI: 10.1021/jacs.0c05499) provided valuable insight into the performance of common Ru-

based catalysts during ROMP in aqueous media containing varying concentrations of H^+ and Cl^- ions, as well as catalyst deactivation pathways arising from chloride ligand displacement by OH^- and H_2O species. Importantly, it was demonstrated that the extent of polymerization control and final monomer conversion achieved were directly dependent on $[H^+]$ and $[Cl^-]$ with higher concentrations of H^+ (i.e., lower pH values) promoting pyridine/phosphine ligand dissociation toward the formation of the metathesis-active catalytic species, while increased concentrations of Cl^- limiting the exchange of labile Cl ligands on the Ru center with OH^- and the formation of ROMP-inactive Ru-$(OH)_n$ complexes. However, it should be noted that in all cases polymers prepared *via* aqueous ROMP possessed higher $Đ_M$ values than those synthesized by living ROMP in organic solvent. To a certain extent, nucleophilic addition to the Ru center by bases or electron donor molecules (e.g., OH^-, H_2O, monomer functional groups such as alcohols and amines) was speculated to occur during aqueous ROMPISA reactions carried out in Chapter 4, leading to reduced catalyst turnover and poorer chain-extensions as compared to polymerizations conducted in organic media. Finally, the potential coexistence of multiple catalytic species with distinctly different metathetical activities could result in polymerizations with various propagation rates and synthesis of copolymers with bimodal molecular weight distributions (i.e., presence of low- or high-MW shoulders on the SEC traces). The deviation of aqueous ROMPISA reactions using the set of core-forming monomers predicted in Chapter 4 from the living character of ROMP is evidently demonstrated in the SEC traces for **P(M11)$_{12}$-*b*-P(MX)$_n$** diblock copolymers given in Figures S18-S21.

Chapter 5. Polymerization-Induced Polymersome Fusion

5.1. Publication Details and Overview

Title: Polymerization-Induced Polymersome Fusion

Authors: **Spyridon Varlas**,[†] Robert Keogh,[†] Yujie Xie,[†,‡] Sarah L. Horswell,[†] Jeffrey C. Foster,*[,†] and Rachel K. O'Reilly*[,†]

Affiliations: [†]School of Chemistry, University of Birmingham, Edgbaston, Birmingham B15 2TT, United Kingdom

[‡]Department of Chemistry, University of Warwick, Gibbet Hill Road, Coventry CV4 7AL, United Kingdom

Journal: Journal of the American Chemical Society

Year: 2019

Volume: 141

Page Numbers: 20234-20248

DOI: 10.1021/jacs.9b10152

Submitted: 19th September 2019, **Published:** 29th November 2019

Permissions: This article and its supporting information are available on the ACS Publications website at https://pubs.acs.org/doi/abs/10.1021/jacs.9b10152. Further permissions related to the material excerpted should be directed to the ACS Publications Support.

Coauthor Contributions: ROMPISA kinetic experiments, *in situ* turbidimetric analysis and characterization of obtained kinetic samples by DLS was carried out with assistance from Dr. Robert Keogh at the University of Birmingham. Dry-state TEM image analysis was performed with assistance from Dr. Jeffrey C. Foster at the University of Birmingham. Cryo-TEM imaging of spherical and tubular polymersomes was performed with assistance from Dr. Robert Keogh and Dr. Saskia Bakker at the University of Warwick. Synthesis of ACM- and RhB-functionalized norbornene monomers was carried out with assistance from Ms. Yujie Xie and synthesis of ACM- and RhB-containing triblock copolymer nano-objects was performed with assistance from Dr. Robert Keogh at the University of Birmingham. Steady-state fluorescence spectroscopy and fluorescence lifetime measurements were performed by Ms. Yujie Xie at the University of Birmingham. Confocal microscopy imaging of dye-loaded samples was carried out with assistance from Ms. Yujie Xie at the University of Birmingham. SLS analysis was carried out by Dr. Robert Keogh at the University of Birmingham. SAXS measurements were performed by Dr. Steven Huband at the University of Warwick, while SAXS data analysis was performed by Dr. Sarah L. Horswell at the University of Birmingham. DSC analysis was performed with assistance from Ms. Irem Akar at the University of Birmingham. Dr. Jeffrey C. Foster (University of Birmingham) and Prof. Rachel K.

O'Reilly (University of Birmingham) supervised the research project, provided guidance and editing of this manuscript.

Overview: In this Chapter, the preliminary findings and observations that were identified during the study discussed in Chapter 4 are further explored, providing valuable insight into the morphological evolution of polynorbornene-based polymersomes developed *via* aqueous ROMPISA upon simultaneously varying the chemistry of the hydrophilic steric stabilizer block and the core-forming block length, as well as revealing an unprecedented self-assembly behavior of such amphiphilic formulations based on intervesicular fusion.

In particular, it was previously observed that small polymersomes of spherical shape and near identical size could be obtained *via* ROMPISA over a broad range of core block DPs and chemistries, and LogP_{oct}/SA values. As a result, a considerable amount of energy was speculated to be getting accumulated within the hydrophobic membranes of the particles upon increasing the DP of their constituent rigid rod-like chains. In stark contrast to membrane rearrangement pathways followed in polymersome formulations developed *via* RDRP-mediated PISA, whereby formation of higher-order multilamellar or large compound nano-objects is typically favored, initial evidence suggested the occurrence of polymersome fusion events during ROMPISA as potential rearrangement mechanism for the system to release the high membrane tension developed and minimize its overall energy. However, it was hypothesized that the presence of protonated tertiary amine groups and, as an extent, positive charges on the corona layer of the assemblies prepared in Chapter 4 were drastically limiting interparticle adhesion and further morphological evolution *via* fusion.

Therefore, in this Chapter, two distinct approaches for controlling the structure of hydrophilic corona of the polymersomes were followed (i.e., by either conducting ROMPISA in the presence of NaCl or by using a PEG-based corona-forming monomer) in order to screen/eliminate their surface charge and facilitate the occurrence of "productive" inelastic collisions between particles. In both cases, anisotropic polymersomes of tubular shape – tubesomes – were developed *in situ* during ROMPISA, as an outcome of spontaneous 1D fusion events between their spherical counterparts. Importantly, mechanistic investigations provided valuable insight into the distinct polymerization, principal amphiphile self-assembly and interparticle fusion phenomena.

In particular, it was demonstrated that tubesome development could be solely achieved during ROMPISA, whereby the main driving force for their formation was the continuously increasing tension generated within the polymersome membranes upon polymerization with increasing core block length above a critical DP. Occurrence of polymersome fusion was confirmed to be the most energetically favorable pathway for the release of such significant membrane tension build-up. Moreover, kinetic monitoring revealed that morphological transition toward tubesomes was lagging behind the rapid polymerization process (second-order kinetics *vs* first-order kinetics, respectively), suggesting the formation of kinetically-trapped, yet stable, morphologies consisted of rod-like polymer chains with high T_g and limited mobility. Interestingly, the purity and length distribution of the tubesomes were found to precisely follow a "step-growth-like" relationship, whereby "monomeric" spherical polymersomes fused in a step-wise manner to generate "polymeric" products of tubular shape. Finally, model methodologies were established that allowed for successful monitoring of basic fusion-derived processes, such

as the blending of the vesicular membranes and the mixing of their interior aqueous compartments.

Overall, the findings discussed in Chapter 5 highlight ROMPISA as an ideal platform for facile access to tubular polymersomes and the potential application of such formulations in small molecule trafficking, selective catalysis and drug delivery, owing to the superior characteristics of highly anisotropic nanostructures compared to their spherical counterparts (e.g., improved biodistribution, increased cellular uptake, and prolonged circulation times *in vivo*).

JACS JOURNAL OF THE AMERICAN CHEMICAL SOCIETY

Article

Cite This: J. Am. Chem. Soc. 2019, 141, 20234−20248

pubs.acs.org/JACS

Polymerization-Induced Polymersome Fusion

Spyridon Varlas,[†] Robert Keogh,[†] Yujie Xie,[†,‡] Sarah L. Horswell,[†] Jeffrey C. Foster,*[,†] and Rachel K. O'Reilly*[,†]

[†]School of Chemistry, University of Birmingham, Edgbaston, Birmingham B15 2TT, United Kingdom

[‡]Department of Chemistry, University of Warwick, Gibbet Hill Road, Coventry CV4 7AL, United Kingdom

Supporting Information

ABSTRACT: The dynamic interactions of membranes, particularly their fusion and fission, are critical for the transmission of chemical information between cells. Fusion is primarily driven by membrane tension built up through membrane deformation. For artificial polymersomes, fusion is commonly induced via the external application of a force field. Herein, fusion-promoted development of anisotropic tubular polymersomes (tubesomes) was achieved in the absence of an external force by exploiting the unique features of aqueous ring-opening metathesis polymerization-induced self-assembly (ROMPISA). The out-of-equilibrium tubesome morphology was found to arise spontaneously during polymerization, and the composition of each tubesome sample (purity and length distribution) could be manipulated simply by targeting different core-block degrees of polymerization (DPs). The evolution of tubesomes was shown to occur via fusion of "monomeric" spherical polymersomes, evidenced most notably by a step-growth-like relationship between the fraction of tubular to spherical nano-objects and the average number of fused particles per tubesome (analogous to monomer conversion and DP, respectively). Fusion was also confirmed by Förster resonance energy transfer (FRET) studies to show membrane blending and confocal microscopy imaging to show mixing of the polymersome lumens. We term this unique phenomenon polymerization-induced polymersome fusion, which operates via the buildup of membrane tension exerted by the growing polymer chains. Given the growing body of evidence demonstrating the importance of nanoparticle shape on biological activity, our methodology provides a facile route to reproducibly obtain samples containing mixtures of spherical and tubular polymersomes, or pure samples of tubesomes, of programmed length. Moreover, the capability to mix the interior aqueous compartments of polymersomes during polymerization-induced fusion also presents opportunities for its application in catalysis, small molecule trafficking, and drug delivery.

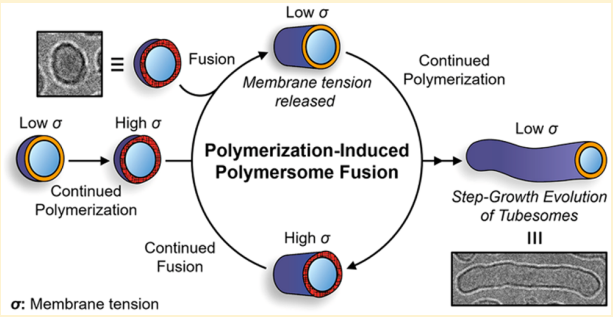

INTRODUCTION

The fusion of biological membranes is an essential process governing endo- and exocytosis, protein trafficking, fertilization, and viral infection in eukaryotic cells.[1−3] Proteins and other (macro)molecules are distributed throughout a cell, released into or internalized from the extracellular space via the action of membrane-bound vesicles.[4] Such vesicle-mediated transport occurs via the budding of new vesicular compartments from a cellular membrane and their downstream fusion with another membrane.[5] Vesicle budding and fusion processes do not transpire spontaneously, as lipid bilayer vesicles (liposomes) repel one another through electrostatic forces and possess membranes that are stabilized against deformation by a strong hydrophobic effect. Thus, the mechanisms of vesicle budding and fusion require an input of energy to occur. In biological systems, this energy is supplied by "**SNAP REceptor**", SNARE, proteins, which bring vesicles into close contact with the target surface and induce deformations in their membranes.[6−9] The tension built up through such elastic deformations is hypothesized to serve as the main driving force for vesicle fusion,[10] originating from an overall reduction in the tension-induced bending energy (E_b) of the system upon each fusion event.[11]

Although vesicle fusion is contingent on the action of proteins in biological systems, dissipative particle dynamics (DPD) simulations have shown that fusion between vesicles can occur spontaneously in the absence of proteins when two criteria are satisfied: (1) the particles can adhere to one another and maintain close contact and (2) there is sufficient membrane tension to overcome energetic barriers of fusion, of which the membrane bending energy dominates.[12] The bending energy of a membrane (E_b) is defined in eq 1

$$E_b = \sigma \Delta A + \oint \frac{k}{2} C^2 \, dA \quad (1)$$

where σ is the membrane tension, ΔA is the change in membrane surface area, k is the membrane bending rigidity, a

Received: September 19, 2019
Published: November 29, 2019

polymer specific property, and C is the local membrane curvature.[13,14] From this equation, it is clear that a buildup of tension within a vesicular membrane increases its bending energy, and the alleviation of this tension provides a significant driving force for vesicle fusion as it reduces the overall E_b of the system. Membrane tension is typically generated via the exertion of an external force. In biological systems, this force is applied by fusion proteins, although other mechanisms have also been discovered.[10]

Both experimental and DPD simulations have rigorously demonstrated the impact of membrane tension on the vesicular morphology and dynamics, showing that tension can be released by a number of pathways including vesicle hemifusion, fusion, membrane deformation, or membrane rupture.[12,15−18] For vesicles with σ sufficiently low that spontaneous membrane rupture occurs over prohibitively long time scales, fusion is the most probable pathway to release their membrane tension. Importantly, the mechanism of vesicle fusion appears to depend upon the nature of the membrane's amphiphilic constituents. Thus, fusion of liposomes occurs in a distinctly different manner compared to the fusion processes of amphiphilic block copolymer vesicles (also referred to as polymersomes) composed of either coil−coil or rod−coil blocks.[19−21] In the latter case, additional membrane tension is provided by the tendency of rod-like polymers to align, resisting the formation of nanostructures with high interfacial curvature. Indeed, DPD studies on fusion of rod−coil polymersome systems have shown that membrane tension scales with the length of the rod-like block.[18]

While the fusion mechanisms of liposomes and their application in biological systems have been studied extensively,[22−25] a very limited number of experimental studies have been carried out regarding the fusion of polymersomes.[26,27] This is due, in part, to the fact that polymersomes are most often prepared using conventional block copolymer self-assembly methodologies, such as solvent-switch or thin-film rehydration, operating under thermodynamically favorable conditions and thus their membranes are formed with low membrane tension, preventing their spontaneous fusion.[28−30] An alternative one-step route that allows for preparation of polymersomes at high concentrations is polymerization-induced self-assembly (PISA).[31−38] During PISA, amphiphilic block copolymer nano-objects are developed spontaneously upon chain-extension of a solvophilic steric stabilizer block using specific solvent-miscible monomers that gradually form solvophobic polymers as the length of the core-forming block increases, driving *in situ* self-assembly.[39−43] Based on the rate of polymerization propagation relative to self-assembly dynamics, kinetically trapped morphologies with high membrane tensions could theoretically be generated via PISA.[44]

Morphology diagrams have been constructed for PISA systems by varying externally controlled experimental parameters, such as the targeted degree of polymerization (DP) of the core-forming block, the overall solids concentration, or the core-block solubility, providing a roadmap to readily obtain pure polymersome nano-objects.[39,45,46] Typically, polymersomes occupy a narrow region of the phase space, requiring high solids concentrations and high DPs for their formation. In our recent report on aqueous ring-opening metathesis polymerization-induced self-assembly (ROMPISA), we observed that polymersomes occupied a uniquely broad region of the phase space over a wide range of core-forming monomers and targeted DPs.[47] This phenomenon was mainly attributed to the influence of the rigid rod-like nature of polynorbornenes on their packing within the assembled nanostructures, disfavoring higher interfacial curvature structures, such as spherical or worm-like micelles. In addition to the unique morphology evolution observed for nano-objects prepared by ROMPISA,[47] it was also apparent that the developed polymersomes were of similar size and shape over a broad range of targeted core block DPs. This result was in stark contrast to polymersomes obtained via PISA mediated by reversible addition−fragmentation chain transfer (RAFT) polymerization, which generally increase in size or evolve toward more complex morphologies, such as multicomponent vesicles or lamellae, as the core block DP is further increased.[48−51] Since it did not appear that polymersomes prepared via ROMPISA could minimize their bending energies through membrane rearrangement processes (no observable changes in ΔA or C), we wondered whether the nano-object membranes were becoming "charged" with high tension during polymerization as the length of their constituent polymers increased to compensate for their static curvature and surface area. Thus, we envisioned that ROMPISA may represent an ideal platform for studying the fusion behavior of polymersomes formed from rod-like polymers.

As discussed above, good intervesicle adhesion and increased membrane tension must both be present to allow for membrane fusion events to occur. Our previous studies on aqueous ROMPISA were carried out using a polyamine corona-forming block, which, under the experimental conditions utilized, produced nano-objects with positive surface charge.[47,52] As a result, no evidence of polymersome adhesion and fusion was observed in these systems, as these processes were effectively prohibited by strong interparticle repulsion. We therefore hypothesized that the structure of the hydrophilic stabilizer block could be tuned to modulate the fusion behavior of ROMPISA polymersomes, inducing the evolution of large and/or non-spherical bilayer structures.

Herein, we evaluate this hypothesis by investigating the influence of macroinitiator chemistry, reaction conditions, and targeted core block DP upon the morphology of diblock copolymer nano-objects prepared via aqueous dispersion ROMPISA. In particular, it was found that the absence of charges on the outer surface of the developed nano-objects facilitated polymerization-induced polymersome fusion and *in situ* evolution of an increasing population of progressively longer tubular polymersomes−tubesomes−upon increasing targeted DP of the core-forming block. Polymerization kinetic monitoring and exhaustive nano-object characterization revealed that the onset of polymersome fusion occurred at a critical core block DP followed by an acceleration in rate of tubesome growth. Importantly, the development of kinetically favorable tubesomes via polymerization-induced fusion of spherical polymersome building blocks was found to precisely follow a step-growth-like motif, where a larger number of fusion events per particle was noticed for samples with larger tubesome fractions. Overall, our study provides insight into the fusion mechanisms of artificial polymeric vesicles and access to facile one-pot preparation of anisotropic tubular polymersomes via aqueous ROMPISA, establishing them as an attractive alternative nanoplatform for numerous biomedical applications owing to their well-documented superior physicochemical properties compared to their spherical counterparts.[53−57]

DOI: 10.1021/jacs.9b10152
J. Am. Chem. Soc. 2019, 141, 20234−20248

RESULTS

ROMP-mediated PISA in aqueous environment requires solubilization of the utilized metathesis catalyst through modification of one or more of its surrounding ligands with hydrophilic moieties.[52,58,59] While several strategies have been developed thus far to generate water-soluble Ru-based metathesis catalysts, often through transformations involving either *N*-heterocyclic carbene (NHC) or pyridine ligands,[60,61] such catalysts typically suffer from reduced activity compared to the unmodified precursor in organic solvent.[62] In this study, rapid polymerization kinetics were desired to obtain kinetically trapped morphologies during ROMPISA; thus, our previously reported open-to-air two-step ROMPISA procedure was adopted, involving the synthesis of a hydrophilic macroinitiator via ROMP in organic media prior to PISA, which affords fast and controllable polymerization in aqueous media, as shown in Scheme 1.[52]

Scheme 1. Schematic Representation of the Synthetic Route Followed for the Development of P(NB-R)$_{11}$-*b*-P(NB-MEG)$_n$ Diblock Copolymer Nano-Objects via Aqueous Dispersion ROMPISA, Using Either a Water-Soluble P(NB-Amine)$_{11}$ or P(NB-PEG)$_{11}$ Macroinitiator

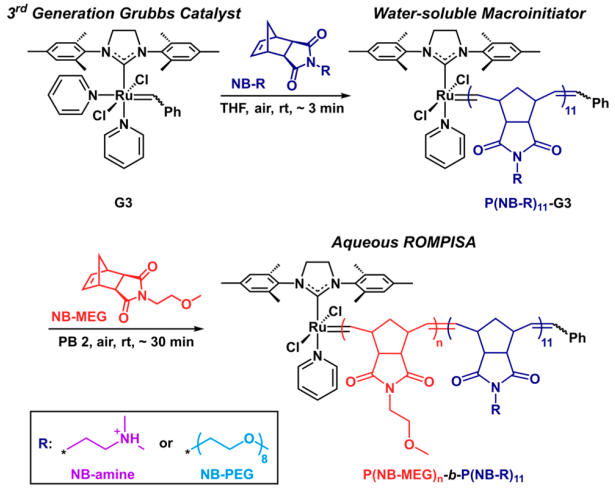

To perform aqueous ROMPISA using a macroinitiator approach, a water-soluble polymer was first prepared by polymerizing a hydrophilic monomer, in this case either a tertiary amine functional norbornene (**NB-amine**) or a PEGylated norbornene (**NB-PEG**), via ROMP in a water-miscible solvent (i.e., THF) using the commercially available third-generation Grubbs catalyst (**G3**). The resulting macroinitiator was subsequently chain-extended upon dilution with an acidic aqueous solution of the core-forming monomer (**NB-MEG**), resulting in the *in situ* formation of amphiphilic diblock copolymer nano-objects under dispersion polymerization conditions. The presence of acid is of vital importance for controlled aqueous ROMP using **G3**, as it promotes pyridine ligand dissociation to generate the active catalyst species and limits catalyst deactivation by OH^- species.[52,60,63]

Previously, we demonstrated that typical PISA morphologies (i.e., spherical micelles, worm-like micelles, and vesicles) could be readily accessed using this macroinitiator approach and that uniquely small, spherical polymersomes were obtained over a broad range of compositions for **P(NB-amine)**$_{12}$-*b*-**P(NB-X)**$_n$ diblock copolymers with $60 \leq n \leq 180$.[47] In this study, our efforts initially focused on further extending the core block DP beyond 180 to determine whether the system would evolve beyond vesicles toward other higher-order morphologies. We hypothesized that the cationic amine corona would provide an additional barrier against morphological transitions beyond spherical polymersomes due to electrostatic repulsive forces between particles, effectively limiting fusion events and other interparticle assembly pathways.[64] Toward this end, a series of ROMPISA reactions were carried out using a **P(NB-amine)**$_{11}$ macroinitiator ($M_{n,NMR}$ = 2.5 kDa, $M_{n,SEC}$ = 2.6 kDa, $Đ_M$ = 1.22, Figures S7–S9, and Table S2) targeting DPs of 120, 180, 240, 300, and 420 for the core-forming **P(NB-MEG)** block by varying the initial [**NB-MEG**]/[**G3**] feed ratio. All polymerizations were performed in acidic phosphate buffer (pH 2, PB2) at a total solids concentration of 1 wt % in the presence of 10% v/v THF. Following ROMPISA, **P(NB-amine)**$_{11}$-*b*-**P(NB-MEG)**$_n$ diblock copolymers were analyzed by ^{1}H-NMR spectroscopy for monomer conversion calculation, and size-exclusion chromatography (SEC) to determine number-average molecular weight (M_n) and dispersity ($Đ_M$) values, while the resulting nano-objects were characterized by dynamic light scattering (DLS), zeta potential analysis, and transmission electron microscopy (TEM) imaging. A summary of the obtained results is provided in Figure 1 and in the Supporting Information (Figures S10 and S14–S17 and Tables S3 and S5).

In particular, controlled polymerizations were achieved in all cases, with quantitative monomer conversions (>99%) achieved after ~30 min of polymerization time yielding **P(NB-amine)**$_{11}$-*b*-**P(NB-MEG)**$_n$ diblock copolymers with narrow and symmetrical molecular weight distributions, low dispersity values ($Đ_M \leq 1.14$), and $M_{n,SEC}$ that increased linearly with the initial feed ratio of monomer to catalyst (Figure 1A,B and Table S3). Consistent with our previous report, a uniform population of spherical polymersomes with D_h = 47.8 ± 1.7 nm was obtained when targeting DP$_{\mathbf{P(NB\text{-}MEG)}}$ = 180, as judged by DLS analysis and TEM imaging. As the targeted core block DP was further increased to 240 and 300, only a slight increase in the average hydrodynamic diameter of the polymersomes to 59.9 ± 0.3 and 61.4 ± 1.2 nm, respectively, was observed, whereas at DP$_{\mathbf{P(NB\text{-}MEG)}}$ = 420, ill-defined non-spherical nano-objects with D_h = 83.2 ± 0.9 nm were developed. In all cases, zeta potential analysis confirmed the presence of positive charges on the outer surface of the obtained nano-objects and their cationic character under ROMPISA-mimicking conditions (zeta potential > + 21 mV, at pH 2.0; Figures 1C,D,F, S14, and S17 and Table S5).

To gain further insight into the self-assembly process, dry-state TEM images were analyzed using image processing software to calculate average particle length (L_{ave}, the distance in nm along the longest nano-object axis), average maximum dimension (S_{ave}, diameter for spherical polymersomes or length for non-spherical ones) and average circularity values (C_{ave}) for each formulation. A full description of the image analysis methodology applied herein is provided in the Supporting Information. As shown in Figures 1F, S15 and S16, S_{ave} values increased concurrently with D_h, although these values were systematically lower than the diameters measured by DLS likely due to particle shrinkage upon drying. In addition, the nano-object C_{ave} values—a ratio of the particle's area to its perimeter—remained relatively constant, ranging between 0.65 and 0.8 across the series with the exception of

DOI: 10.1021/jacs.9b10152
J. Am. Chem. Soc. 2019, 141, 20234–20248

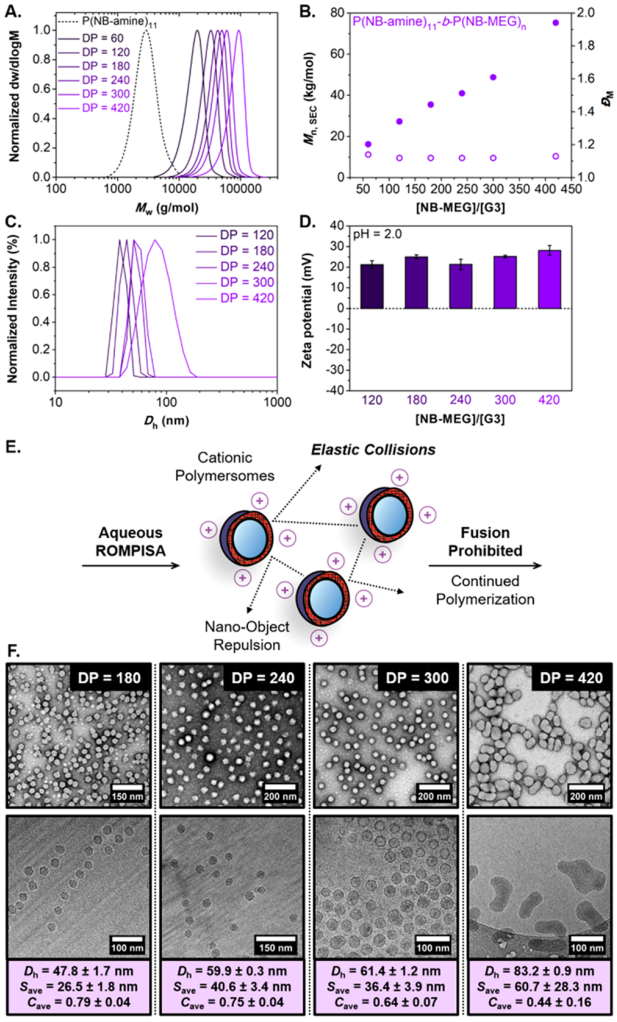

Figure 1. Characterization summary for the series of **P(NB-amine)**$_{11}$-*b*-**P(NB-MEG)**$_n$ diblock copolymer nano-objects. (A) Normalized SEC RI molecular weight distributions, and (B) evolution of M_n (filled circles) and $Đ_M$ (empty circles) values with increasing targeted $DP_{P(NB\text{-}MEG)}$ calculated from SEC analysis for **P(NB-amine)**$_{11}$-*b*-**P(NB-MEG)**$_n$ diblock copolymers prepared via aqueous ROMPISA. $M_{n,\,SEC}$ and $Đ_M$ values were calculated from PS standards using THF + 2% v/v NEt_3 as the eluent. (C) Normalized intensity-weighted size distributions obtained by DLS for **P(NB-amine)**$_{11}$-*b*-**P(NB-MEG)**$_n$ diblock copolymer nano-objects. (D) Zeta potential values for **P(NB-amine)**$_{11}$-*b*-**P(NB-MEG)**$_n$ diblock copolymer nano-objects measured from microelectrophoretic analysis in PB2. (E) Schematic representation of interpolymersome repulsion restricting fusion events and further morphological evolution. (F) Representative dry-state (top row) and cryo-TEM (bottom row) images of **P(NB-amine)**$_{11}$-*b*-**P(NB-MEG)**$_n$ diblock copolymer nano-objects, and summary of D_h values determined from DLS, and S_{ave} and C_{ave} values calculated from image analysis of the dry-state TEM images. Dry-state samples were stained using 1 wt % uranyl acetate (UA) solution.

the **P(NB-amine)**$_{11}$-*b*-**P(NB-MEG)**$_{420}$ nanostructures. A dramatic decrease in C_{ave} to 0.44 ± 0.16 was measured for this sample, where the predominant morphology appeared to be of non-spherical shape. Taken together, these data support our hypothesis that electrostatic repulsive forces originating from cationic charges within the particle coronae resist morphological evolution via pathways involving interactions between multiple nano-objects (i.e., fusion; Figure 1E).

To promote fusion, it was apparent that surface charge should be minimized to facilitate adhesive collisions between nano-objects. We envisioned that, by changing the chemistry of the stabilizer block pendant groups from cationic tertiary amines to non-ionic poly(ethylene glycol) (PEG, $M_n \approx 350$ g mol^{-1}) units, the energy barrier of polymersome fusion would be reduced, rendering fusion the operative pathway of morphological evolution. To this extent, a series of **P(NB-PEG)**$_{11}$-*b*-**P(NB-MEG)**$_n$ diblock copolymer nano-objects were prepared using the same two-step ROMPISA methodology as previously discussed, this time employing **NB-PEG** as the corona-forming monomer to prepare a water-soluble **P(NB-PEG)**$_{11}$ macroinitiator ($M_{n,NMR}$ = 5.5 kDa, $M_{n,SEC}$ = 5.3 kDa, $Đ_M$ = 1.20, Figures S25−S27 and Table S8). As before, aqueous ROMPISA reactions using **NB-MEG** as the core-forming monomer were conducted at [solids] = 1 wt % in 90:10 PB2/THF. Core-block DPs of 40, 60, 120, 140, 180, 240, 260, and 300 were targeted to accurately monitor the evolution of particle morphology as a function of copolymer composition.

Similar to the **P(NB-amine)**-based formulations, ^{1}H-NMR spectroscopic analysis showed complete monomer conversions (>99%) after ∼30 min, and SEC analysis of the resulting **P(NB-PEG)**$_{11}$-*b*-**P(NB-MEG)**$_n$ diblock copolymers confirmed excellent polymerization control across the series ($Đ_M \leq 1.16$; Figures 2A,B and S28 and Table S9). In addition, TEM imaging and DLS analysis revealed the formation of small spherical polymersomes with D_h values of 25.9 ± 1.9 nm, 34.9 ± 3.6 nm and 47.5 ± 1.1 nm when targeting $DP_{P(NB\text{-}MEG)}$ = 40, 60 and 120, respectively (Figures 2C,F and S35−S38 and Table S11). It is supposed that the membrane thickness of the polymersomes rapidly increases inward upon targeting higher core-block DPs, reducing the volume of their inner aqueous compartments, analogous to a previous study on polymersomes developed via RAFT-mediated PISA.[33] Due to the uniquely small size of the polymersomes prepared herein, it was sometimes difficult to identify the presence of their inner lumen and accurately determine their membrane thickness from the acquired TEM images. To further prove the polymersome morphology, static light scattering (SLS) analysis was carried out on the spherical polymersome samples with $DP_{P(NB\text{-}MEG)}$ = 40 and 60. In particular, measured R_g/R_h values were 0.87 and 0.82, respectively, with calculated N_{agg} values of 439 and 827 (Figures S32 and S33 and Table S12). Based on the fact that the measured R_g/R_h values are intermediate between what would be typically expected for hollow spherical polymersomes (R_g/R_h = 1.0) and spherical core−shell micelles ($R_g/R_h \approx 0.78$), as well as the markedly high N_{agg} values compared to expected values for spherical micelles,[85] these results support our hypothesis of hollow nanostructures with rather small inner compartments. Moreover, the observed decrease in R_g/R_h ratio with increasing $DP_{P(NB\text{-}MEG)}$ is consistent with our proposal of assemblies of similar hydrodynamic volume but progressively increasing membrane thickness, and as a consequence reduced inner lumen volume.

In stark contrast to the **P(NB-amine)**-based series, significant nano-object elongation was clearly evident when the targeted core-block DP was increased above 120, based on observations from acquired dry-state and cryo-TEM images. In fact, for the **P(NB-PEG)**$_{11}$-*b*-**P(NB-MEG)**$_n$ samples where n = 140, 180, 240, and 260, tubular polymersomes (so-called

DOI: 10.1021/jacs.9b10152
J. Am. Chem. Soc. 2019, 141, 20234−20248

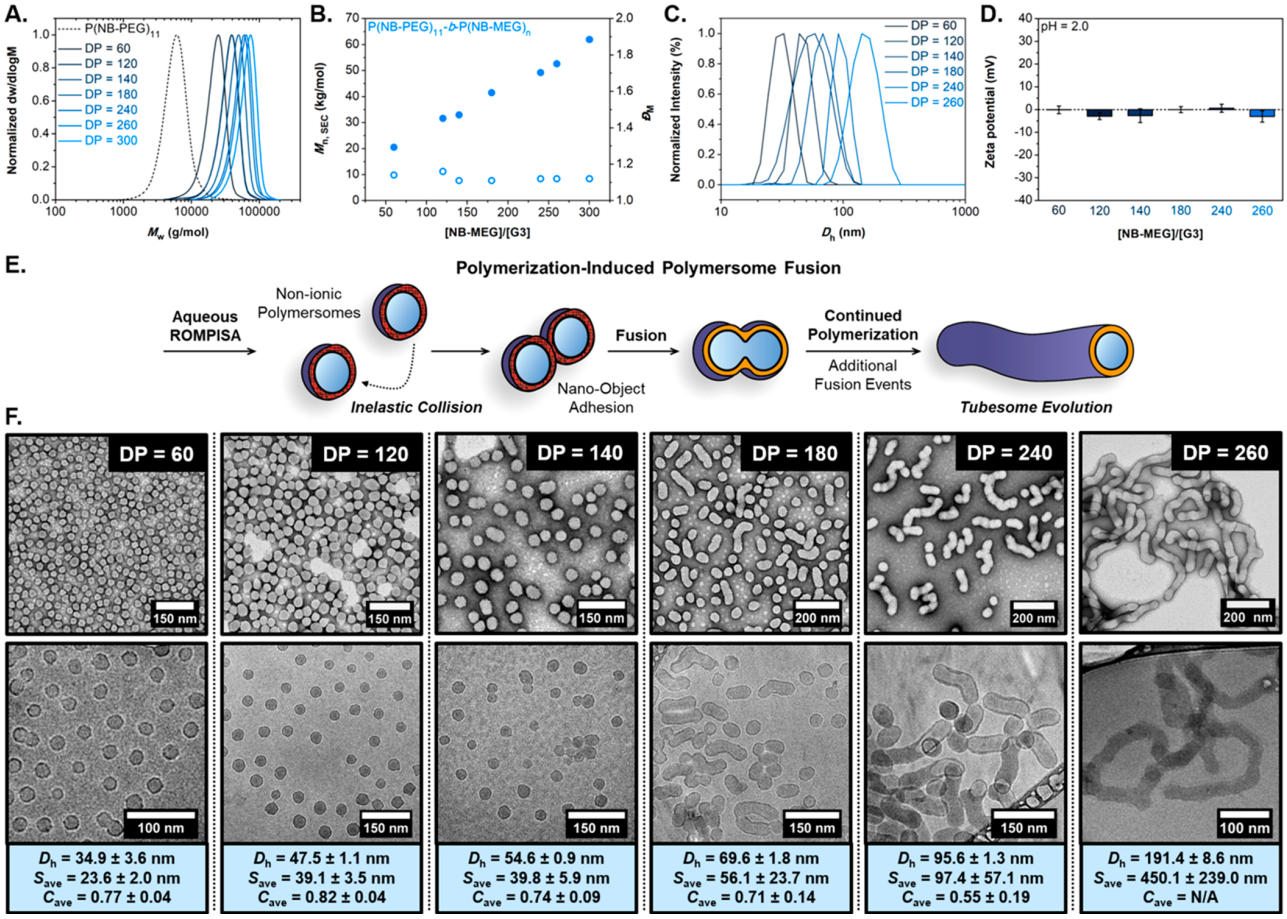

Figure 2. Characterization summary for the series of $\mathbf{P(NB\text{-}PEG)_{11}}$-*b*-$\mathbf{P(NB\text{-}MEG)_n}$ diblock copolymer nano-objects. (A) Normalized SEC RI molecular weight distributions, and (B) evolution of M_n (filled circles) and $Đ_M$ (empty circles) values with increasing targeted $DP_{P(NB\text{-}MEG)}$ calculated from SEC analysis for $\mathbf{P(NB\text{-}PEG)_{11}}$-*b*-$\mathbf{P(NB\text{-}MEG)_n}$ diblock copolymers prepared via aqueous ROMPISA. $M_{n,\,SEC}$ and $Đ_M$ values were calculated from PS standards using THF + 2% v/v NEt_3 as the eluent. (C) Normalized intensity-weighted size distributions obtained by DLS for $\mathbf{P(NB\text{-}PEG)_{11}}$-*b*-$\mathbf{P(NB\text{-}MEG)_n}$ diblock copolymer nano-objects. (D) Zeta potential values for $\mathbf{P(NB\text{-}PEG)_{11}}$-*b*-$\mathbf{P(NB\text{-}MEG)_n}$ diblock copolymer nano-objects measured from microelectrophoretic analysis in PB2. (E) Schematic representation of tubesome evolution via polymerization-induced polymersome fusion. (F) Representative dry-state (top row) and cryo-TEM (bottom row) images of $\mathbf{P(NB\text{-}PEG)_{11}}$-*b*-$\mathbf{P(NB\text{-}MEG)_n}$ diblock copolymer nano-objects, and summary of D_h values determined from DLS, and S_{ave} and C_{ave} values calculated from image analysis of the dry-state TEM images. Dry-state samples were stained using 1 wt % uranyl acetate (UA) solution.

"tubesomes") of increasing length were obtained, as evidenced by both DLS and TEM image analyses (Figures 2C,F and S35–S38 and Table S11). Typically, cryo-TEM serves as the main imaging tool for observation of non-spherical polymersomes, as morphological discrepancies of nano-objects can occur during the drying process. However, in our case the morphology of tubular nanostructures could be effectively retained under dry-state TEM conditions, owing to the high glass transition temperature (T_g) values of polynorbornene-based polymers (T_g of $\mathbf{P(NB\text{-}MEG)_{180}}$ homopolymer = 118.2 °C, Figure S6).

From dry-state TEM image processing, the calculated S_{ave} values also increased with increasing targeted $DP_{P(NB\text{-}MEG)}$, while C_{ave} values decreased consistently across the series (note that circularity could not be accurately calculated for the $\mathbf{P(NB\text{-}PEG)_{11}}$-*b*-$\mathbf{P(NB\text{-}MEG)_{260}}$ sample due to the lack of a sufficient number of "well-isolated" particles in the TEM images). It was also apparent that the populations of spherical and tubular polymersomes became increasingly biased toward the latter upon gradually increasing the targeted core block DP. Indeed, a nearly pure morphology of highly anisotropic tubesomes was present in the $\mathbf{P(NB\text{-}PEG)_{11}}$-*b*-$\mathbf{P(NB\text{-}MEG)_{260}}$ sample. In this case, cryo-TEM imaging was challenging to perform as the tubesomes were located in relatively thick vitrified ice layers owing to their large size and irregular shape.[57] It should also be noted that the average width of formed tubesomes did not appear to significantly vary beyond the critical $DP_{P(NB\text{-}MEG)}$ = 140 sample, whereas a further increase of the core-forming block beyond DP = 260 resulted in macroscopic precipitation due to instability of the developed nano-objects, most likely owing to their exceedingly increased length and hydrophobicity. Contrary to the zeta potential values measured for $\mathbf{P(NB\text{-}amine)_{11}}$-*b*-$\mathbf{P(NB\text{-}MEG)_n}$ nano-objects, the presence of non-ionic PEG chains on the outer layer of both the $\mathbf{P(NB\text{-}PEG)_{11}}$-*b*-$\mathbf{P(NB\text{-}MEG)_n}$ spherical and tubular polymersomes was readily reflected on the findings from microelectrophoretic analysis, as zeta potential values of approximately 0 mV were measured in all cases (Figure 2D and Table S11). These results support the idea that reduced interparticle repulsion, affected by changes in

DOI: 10.1021/jacs.9b10152
J. Am. Chem. Soc. 2019, 141, 20234–20248

corona chemistry and particle surface charge, led to notable polymersome fusion during ROMPISA, implying that morphological evolution was now occurring by a different pathway than that observed in the case of the **P(NB-amine)**-based system (Figure 2E).

As a final illustration of the importance of particle corona chemistry on the self-assembly behavior, the ROMPISA reactions for preparation of **P(NB-amine)**$_{11}$-*b*-**P(NB-MEG)**$_n$ nano-objects were repeated in the presence of a high concentration of NaCl in PB2 (i.e., [NaCl] = 100 mM). We supposed that the presence of salt would act to partially screen the positive charge in the nano-object coronae, facilitating the occurrence of productive inelastic collisions and thus increasing the incidence of fusion events. Full characterization of the synthesized diblock copolymers and the resulting nanostructures is provided in detail in the Supporting Information (Figures S20−S24 and Tables S6 and S7). In brief, polymerization control was not affected by the presence of NaCl in the reaction medium; however, particle fusion was observed between polymersomes with **P(NB-amine)** coronae in this case, with the onset of fusion shifted toward higher core-block DP relative to the **P(NB-PEG)**-based series. Indeed, nearly pure morphologies of long, tubular polymersomes could be obtained for the **P(NB-amine)** system in the presence of NaCl, highlighting the importance of the role of corona chemistry in determining the assembly pathway during ROMPISA.

While marked differences in corona charge between the **P(NB-amine)**- and **P(NB-PEG)**-based samples represented a probable explanation for the noticeable variation in the assemblies developed for each series, we also considered that the unique tubesome morphology could potentially arise from differences in ROMPISA kinetics between the two series. To compare the relative rates of both polymerization and morphological evolution processes, kinetic monitoring experiments were performed using complementary characterization techniques. Aqueous ROMPISA reactions targeting either **P(NB-amine)**$_{11}$-*b*-**P(NB-MEG)**$_{300}$ or **P(NB-PEG)**$_{11}$-*b*-**P(NB-MEG)**$_{260}$—polymers with approximately the same M_n and $Đ_M$ values—were sampled at various time intervals over a period of 30 min, and the sample aliquots were quenched via the addition of ethyl vinyl ether (EVE) for deactivation of the Ru-based catalyst (Figures S11 and S29). In both cases, these samples were then analyzed by ^{1}H-NMR spectroscopic and SEC analyses to determine polymerization conversion and "livingness", while DLS analysis of samples diluted immediately after quenching was used to monitor changes in nano-object size as polymerization progressed. It should be mentioned that dry-state TEM imaging of the quenched samples was also attempted, although significant discrepancies were observed in the TEM images compared with those shown in Figures 1 and 2, attributed to the presence of plasticizing EVE molecules incorporated within the polymersome membranes leading to equilibration of the samples toward more thermodynamically favored products upon drying on the TEM grids (Figure S41). However, dry-state TEM imaging of samples taken after completion of each kinetic run without addition of EVE agreed well with our previous findings for aqueous ROMISA reactions targeting DP$_{\text{P(NB-MEG)}}$ = 300 or 260, respectively.

Based on the original plots of monomer conversion vs time (Figures S12 and S30), it was found in both cases that the onset of nano-object micellization occurred at a very early stage of the polymerization (i.e., at *ca.* 0.3 min and 35% **NB-MEG** conversion), before which the rate of polymerization in solution appeared to be faster compared to polymerization within the nano-object cores.[66,67] Thus, we considered monomer conversion after this nucleation point in our subsequent analysis. As shown in Figure 3A, both polymerization processes exhibited pseudo-first order kinetics after the point of nucleation, as judged by the semilogarithmic plots, with quantitative conversions (>99%) achieved after 30 min. Importantly, propagation rates for both samples were found not to vary significantly ($t_{1/2}$ = 1.9 and 2.5 min were calculated for **P(NB-amine)**- and **P(NB-PEG)**-based formulations, respectively). Thus, we were able to rule out differential

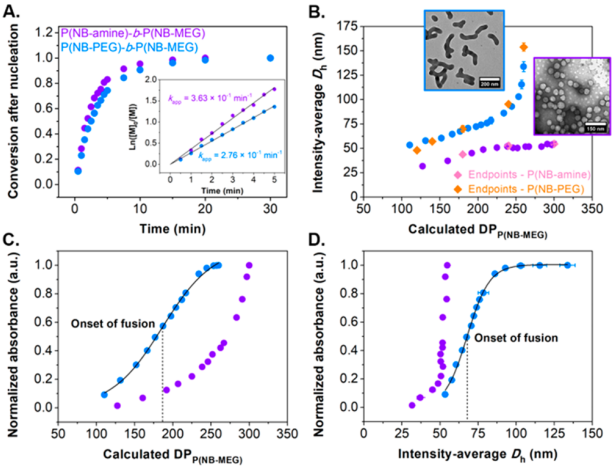

Figure 3. Summary of aqueous ROMPISA kinetic monitoring experiments. (A) Monomer conversion after particle nucleation vs polymerization time kinetic plots for synthesis of **P(NB-amine)**$_{11}$-*b*-**P(NB-MEG)**$_{300}$ (purple circles) and **P(NB-PEG)**$_{11}$-*b*-**P(NB-MEG)**$_{260}$ (blue circles) diblock copolymers via aqueous ROMPISA, as determined by ^{1}H-NMR spectroscopy in DMSO-d_6 with 1,3,5-trioxane as an external standard. The inset shows the corresponding semilogarithmic plots for the determination of pseudo-first-order kinetic constants (k_{app}). (B) Evolution of intensity-average D_h, as determined by DLS analysis of aliquots for the same **P(NB-amine)**$_{11}$-*b*-**P(NB-MEG)**$_{300}$ (purple circles) and **P(NB-PEG)**$_{11}$-*b*-**P(NB-MEG)**$_{260}$ (blue circles) diblock copolymer nano-objects withdrawn during kinetic monitoring, as a function of DP$_{\text{P(NB-MEG)}}$ calculated from conversion. The insets show representative dry-state TEM images of samples obtained after completion of each ROMPISA process without EVE addition. The pink and orange diamonds represent D_h values determined from the end-point measurements shown in Figures 1 and 2 for the **P(NB-amine)**- and **P(NB-PEG)**-based samples, respectively. (C) Normalized absorbance, as determined by *in situ* turbidimetric analysis during each polymerization for synthesis of **P(NB-amine)**$_{11}$-*b*-**P(NB-MEG)**$_{300}$ (purple circles) and **P(NB-PEG)**$_{11}$-*b*-**P(NB-MEG)**$_{260}$ (blue circles) diblock copolymer nano-objects, as a function of DP$_{\text{P(NB-MEG)}}$ calculated from conversion. The black line corresponds to a standard sigmoidal logistic fit, showing an inflection point at DP$_{\text{P(NB-MEG)}}$ ≈ 185 highlighted by the dashed line that corresponds to the onset of polymersome fusion (R^2 = 0.998). (D) Normalized absorbance, as determined by *in situ* turbidimetric analysis during each polymerization for synthesis of **P(NB-amine)**$_{11}$-*b*-**P(NB-MEG)**$_{300}$ (purple circles) and **P(NB-PEG)**$_{11}$-*b*-**P(NB-MEG)**$_{260}$ (blue circles) diblock copolymer nano-objects, vs intensity-average D_h measured from DLS analysis. The black line corresponds to a standard sigmoidal logistic fit, with an inflection point at D_h ≈ 68 nm highlighted by the dashed line that corresponds to the onset of polymersome fusion (R^2 = 0.998).

DOI: 10.1021/jacs.9b10152
J. Am. Chem. Soc. 2019, 141, 20234−20248

polymerization kinetics as an explanation for the distinct differences in fusion behavior between the two nano-object series. Moreover, SEC analysis of selected samples obtained from kinetic monitoring experiments revealed the linear evolution of $M_{n,\,SEC}$ values with increasing **NB-MEG** conversion and verified the living character of both ROMPISA processes (Figures S13 and S31 and Tables S4 and S10).

In contrast to the ^{1}H-NMR spectroscopic analysis, a significant difference was observed in the slopes of the plots showing the time-dependent evolution of intensity-average D_h values, as measured by DLS (Figures S18A and S39A). To further emphasize this difference, the average diameter values corresponding to the developed diblock copolymer nano-objects at each time point were correlated to the core block DP calculated from conversion (Figure 3B). For the **P(NB-amine)**-based samples, it was evident that intensity-average D_h values increased linearly up to *ca.* $DP_{P(NB\text{-}MEG)}$ = 210, after which the measured diameter remained constant independent of the DP of the growing **P(NB-MEG)** block. By comparison, a similar linear D_h increase was observed early in the polymerization of the **P(NB-PEG)**-based system; however, above a similar $DP_{P(NB\text{-}MEG)}$ threshold, the average nano-object diameter increased exponentially with increasing polymer DP. These data are consistent with the observations made by TEM imaging (Figures 1 and 2), where the **P(NB-PEG)$_{11}$-*b*-P(NB-MEG)$_n$** nanostructure composition approached a pure morphology of long, tubular polymersomes as the DP of core-forming **P(NB-MEG)** was increased from 180 to 260, while **P(NB-amine)$_{11}$-*b*-P(NB-MEG)$_n$** diblock copolymers only yielded small spherical polymersomes with minor size differences as the targeted core block DP varied between 180 and 300.

As a final method for direct kinetic comparison, both ROMPISA procedures were monitored via *in situ* turbidimetric analysis using UV−vis spectroscopy. Variations in transmitted light (% transmittance) at λ = 550 nm were measured over the course of the reactions, and the observed reduction in % transmittance (or increase in absorbance) was assumed to arise from increased scattering of the incident light by the growing particles in solution (Figures S18B and S39B). For Rayleigh scattering, relevant for particles smaller than the wavelength of the incident light, the scattering intensity can be correlated to the diameter of the scattering species through a power law relationship.[68] Thus, the decrease in transmitted light intensity can be viewed in the lens of increasing particle size. Upon comparing the data obtained from turbidimetric analysis to those obtained from ^{1}H-NMR spectroscopy and DLS analysis, a few key relationships evidently emerged. Figure 3C shows the change in absorbance (related in this case to scattering intensity) as a function of the core block DP calculated from conversion. For the **P(NB-amine)**-based sample, the curve scaled according to a power law relationship, consistent with increased scattering by particles of progressively increasing size. In contrast, a sigmoidal relationship was noticed for the **P(NB-PEG)**-based sample, with an initial slope of power-law scaling and an inflection at $DP_{P(NB\text{-}MEG)} \approx 185$. The DP value at this inflection point is of great significance, as it corresponds to the critical DP at which the onset of polymersome fusion was also observed in previous end-point experiments (Figure 2). This result can be rationalized as follows: (1) spherical polymersomes initially increase in diameter, leading to increased scattering according to the expected power law relationship, (2) above a certain DP threshold, fusion of spherical polymersome building blocks begins favoring the development of tubesomes, and (3) the rate of change in the size of the particles increases dramatically, but is also accompanied by a proportional decrease in the overall number of particles, with the net effect being a decreased dependence of the scattered light intensity on the polymer DP. The same trends were observed when comparing the intensity-average D_h of the prepared diblock copolymer nano-objects, as measured by DLS analysis, to their corresponding absorbance values (Figure 3D), with an inflection point being evident for the **P(NB-PEG)$_{11}$-*b*-P(NB-MEG)$_n$** sample at $D_h \approx 68$ nm corresponding to a $DP_{P(NB\text{-}MEG)}$ of approximately 180 and to the time at which the onset of polymersome fusion occurs.

The above experiments provide indirect evidence of polymerization-induced polymersome fusion based on the exponential size increase of the tubesomes with increasing DP of the core-forming block and the presence of apparent intermediate fusion stages in the obtained TEM images (Figure S40). To directly verify and monitor polymersome fusion, a series of Förster resonance energy transfer (FRET) experiments were carried out, which involve the non-radiative transfer of absorbed energy from a donor to an acceptor fluorophore. The excited acceptor then emits a photon, with the net effect being that excitation of the donor fluorophore results in fluorescence emission of the acceptor. Importantly, the FRET process requires the two species to be in close contact for the energy transfer to occur (i.e., distances ≤10 nm). Thus, FRET provides a distance-dependent measurement of the dynamic activity of the two fluorescent compounds on the nanoscale.[69]

To evaluate polymersome membrane fusion using FRET in our **P(NB-PEG)-*b*-P(NB-MEG)** system, donor and acceptor fluorophores, that form a FRET pair when in close proximity, were incorporated into the developed polymer nanostructures. In particular, aminochloromaleimide (ACM) was chosen as the donor molecule based on its synthetic simplicity, small size, and high quantum yield in non-polar environments.[70] To provide good spectral overlap, Rhodamine B (RhB) was employed as the acceptor fluorophore (Figure 4B). Both species were introduced via coupling to norbornene moieties for the synthesis of **NB-ACM** and **NB-RhB** monomers, respectively, such that they could be directly polymerized and would remain covalently linked to the prepared copolymers during ROMPISA, avoiding a false indication of FRET behavior arising from diffusion of free fluorophore molecules between nano-objects. Our previously described aqueous ROMPISA procedure was then appropriately modified to introduce a short run of each fluorescent monomer as an intermediate block between the corona- and core-forming segments. In brief, **NB-PEG** was first polymerized via solution ROMP in THF using **G3** for synthesis of a **P(NB-PEG)$_{11}$** macroinitiator. Then, a solution of either **NB-ACM** or **NB-RhB** monomer in THF was added to the macroinitiator solution for synthesis of the second fluorophore-containing block (Figures S44 and S45 and Table S13). In the final step, each diblock copolymer macroinitiator was chain-extended using an acidic aqueous solution of **NB-MEG**, resulting in development of **P(NB-PEG)$_{11}$-*b*-P(NB-ACM)$_m$-*b*-P(NB-MEG)$_n$** and **P(NB-PEG)$_{11}$-*b*-P(NB-RhB)$_{m/2}$-*b*-P(NB-MEG)$_n$** triblock copolymer nano-objects via ROMPISA (**NB-ACM**/**NB-RhB** molar ratio = 2:1; Figure 4A-I).

As shown in Figure 4A-II, we hypothesized that FRET would arise between ACM- and RhB-functionalized particles

DOI: 10.1021/jacs.9b10152
J. Am. Chem. Soc. 2019, 141, 20234−20248

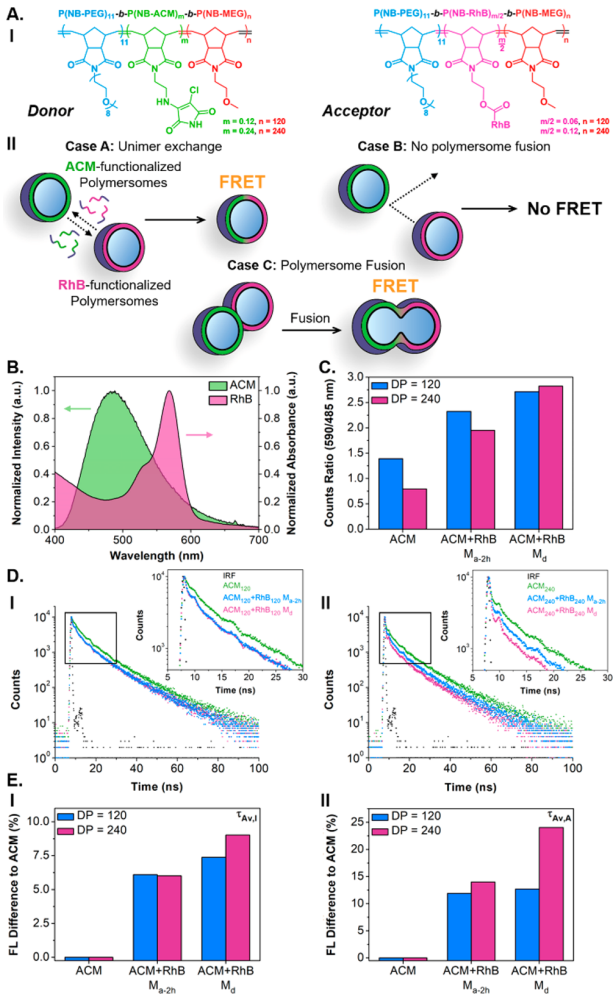

Figure 4. Summary of FRET results for pure $\mathbf{P(NB\text{-}PEG)_{11}}$-*b*-$\mathbf{P(NB\text{-}ACM)_m}$-*b*-$\mathbf{P(NB\text{-}MEG)_n}$ triblock copolymer nano-objects (ACM_n), and resulting ACM_n+RhB_n $M_{a\text{-}2h}$ and ACM_n+RhB_n M_d samples (n = 120 and 240) for direct monitoring of polymersome membrane fusion. (A) Structures of $\mathbf{P(NB\text{-}PEG)_{11}}$-*b*-$\mathbf{P(NB\text{-}ACM)_m}$-*b*-$\mathbf{P(NB\text{-}MEG)_n}$ (donor) and $\mathbf{P(NB\text{-}PEG)_{11}}$-*b*-$\mathbf{P(NB\text{-}RhB)_{m/2}}$-*b*-$\mathbf{P(NB\text{-}MEG)_n}$ (acceptor) triblock copolymers prepared via aqueous ROMPISA (I), and schematic representation of potential outcomes from polymersome mixing experiments (II). (B) Spectral overlap between ACM fluorescence emission and RhB absorption spectra. For ACM_n, ACM_n+RhB_n $M_{a\text{-}2h}$ and ACM_n+RhB_n M_d samples: (C) Counts ratio of the donor ($\lambda_{em.\ ACM}$ = 485 nm) and acceptor ($\lambda_{em.\ RhB}$ = 590 nm) fluorescence emission peaks. (D) Fluorescence lifetime decay profiles of (I) n = 120 and (II) n = 240 samples. (E) Comparison of average fluorescence lifetime values, expressed as % difference relative to the pure ACM_n nano-objects, obtained using (I) $\tau_{Av,I}$, and (II) $\tau_{Av,A}$ fitting models.

only when (1) unimer exchange between particles was occurring on the time scale of the experiment; or (2) fusion between spherical polymersomes occurred, creating regions of close fluorophore contact within the fused tubular polymersome membranes. In the absence of both, no FRET would be expected. Since we were operating under the assumption that fusion events only occurred during polymerization, it was important to compare samples containing each fluorophore that were mixed during ROMPISA prior to the point at which full monomer conversion was reached, to those mixed after completion of the polymerization in order to confirm this hypothesis.

Thus, two sets of ROMPISA reactions targeting **P(NB-MEG)** DPs of 120 (below fusion threshold) and 240 (above fusion threshold) were carried out using either $\mathbf{P(NB\text{-}PEG)_{11}}$-*b*-$\mathbf{P(NB\text{-}ACM)_m}$ or $\mathbf{P(NB\text{-}PEG)_{11}}$-*b*-$\mathbf{P(NB\text{-}RhB)_{m/2}}$ diblock copolymer macroinitiator under otherwise identical polymerization conditions. Equal amounts of pure ACM- and RhB-containing samples were then mixed after 1 min of polymerization time (*ca.* ∼ 50% **NB-MEG** conversion), at which point initial particle nucleation had occurred but polymerization was still incomplete. These samples, mixed during polymerization (M_d), were compared against the corresponding ones in which the ACM- and RhB-functionalized triblock copolymer nano-objects were mixed after polymerization for either 2h ($M_{a\text{-}2h}$) or 24h ($M_{a\text{-}24h}$). In the latter case, no fusion was expected to occur for either sample due to the lack of a driving force. Detailed characterization of resulting triblock copolymers and nano-objects is provided in the Supporting Information (Figures S46−S51 and Tables S14−S16).

In summary, successful attachment of the fluorophore molecules on the formed polymers was confirmed by performing SEC analysis of the diblock macroinitiators with UV detection at λ_{ACM} = 360 nm or λ_{RhB} = 545 nm where complete overlap between the RI and UV traces was observed. Importantly, DLS analysis and dry-state TEM imaging of the pure ACM- and RhB-functionalized samples, as well as the $M_{a\text{-}24h}$ and M_d mixed samples, showed that the triblock copolymer architecture did not affect the self-assembly process of the resulting nano-objects in all cases, with spherical polymersomes of ∼50 nm in diameter being observed for targeted $DP_{P(NB\text{-}MEG)}$ = 120, and a mixture of spherical and tubular polymersomes being formed for $DP_{P(NB\text{-}MEG)}$ = 240.

A simple comparison of the relative FRET efficiency of the various samples could be made using the ratio of the maximum intensities of the donor (ACM) and acceptor (RhB) peaks in the fluorescence spectra, with higher values representing a greater FRET efficiency. The calculated ratios for the pure and mixed nano-object samples when excited at $\lambda_{ex.}$ = 360 nm are shown in Figure 4C. In general, the FRET ratio was higher for the mixed samples than for the pure ACM-functionalized nano-objects. A more evident increase in this ratio can be noticed when comparing the $M_{a\text{-}2h}$ and M_d samples for the polymerizations targeting $DP_{P(NB\text{-}MEG)}$ = 240 than for those targeting $DP_{P(NB\text{-}MEG)}$ = 120. Since the molar concentration of each fluorophore remained constant in both series, these findings indicate a higher relative FRET efficiency for the mixed samples with **P(NB-MEG)** DP of 240, implying closer contact between the fluorophores in this case and as a consequence a great extent of membrane blending.

To further evaluate differences in FRET behavior of triblock copolymer nano-objects with $DP_{P(NB\text{-}MEG)}$ = 120 and 240, fluorescence lifetimes (FL) corresponding to the ACM fluorophore for pure and mixed samples were measured. Figure 4D-I,D-II show fluorescence lifetime decay curves for the ACM-functionalized particles alone (ACM_n) and mixed with RhB-functionalized particles either during (ACM_n+RhB_n M_d) or after polymerization (ACM_n+RhB_n $M_{a\text{-}2h}$; n = 120 and 240, respectively). In particular, no change in FL could be observed when comparing the decay curves for the ACM_{120}+RhB_{120} $M_{a\text{-}2h}$ and ACM_{120}+RhB_{120} M_d mixed samples, consistent with our observation that no fusion events occur at this **P(NB-MEG)** DP. In contrast, a faster FL decay

DOI: 10.1021/jacs.9b10152
J. Am. Chem. Soc. 2019, 141, 20234−20248

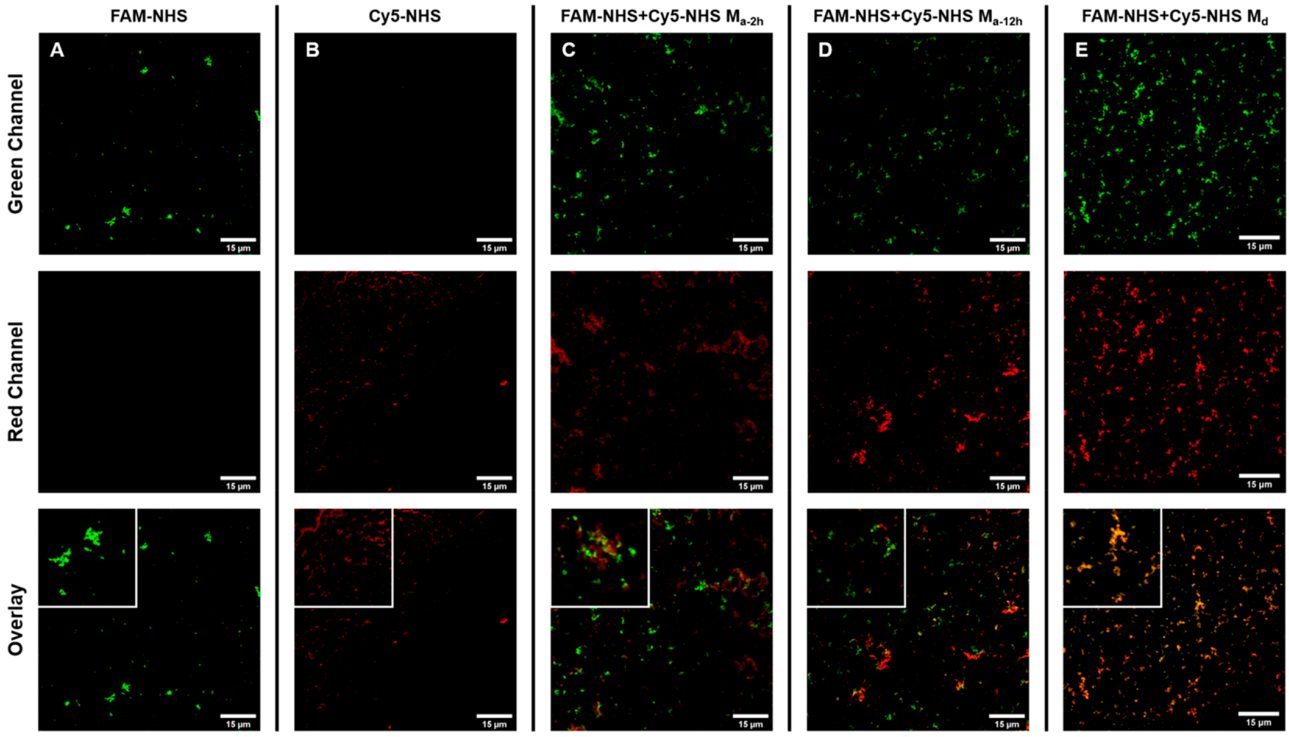

Figure 5. Representative confocal microscopy images for pure FAM-NHS-loaded (green; A) and Cy5-NHS-loaded (red; B) **P(NB-PEG)$_{11}$-*b*-P(NB-MEG)$_{240}$** diblock copolymer nano-objects, and resulting FAM-NHS+Cy5-NHS M$_{a-2h/12h}$ (C and D) and FAM-NHS+Cy5-NHS M$_d$ (E) samples for investigation of inner aqueous lumen mixing of polymersomes during tubesome development. In all cases, the scale bars represent 15 μm and the size of the insets is 20 μm × 20 μm.

was observed for the samples that were mixed during polymerization targeting DP$_{P(NB-MEG)}$ = 240, where extensive membrane fusion was expected to occur. The observed FL differences revealed a change in the surrounding microenvironment of ACM molecules due to the close presence of RhB moieties and subsequent occurrence of energy transfer phenomena.[69] To further emphasize this difference in FRET behavior, the decay curves were fit using both $\tau_{Av,I}$ and $\tau_{Av,A}$ methods to determine intensity-average and amplitude-average FL values, respectively, for each sample (Table S16). A comparison of average fluorescence lifetimes for the ACM$_n$+RhB$_n$ M$_{a-2h}$ and ACM$_n$+RhB$_n$ M$_d$ mixed samples relative to that of the pure ACM$_n$ nano-objects, taken as a percentage difference, is shown in Figure 4E. Here, a more dramatic difference can be observed between the ACM$_{120}$+RhB$_{120}$ and ACM$_{240}$+RhB$_{240}$ samples that were mixed during polymerization. Owing to the fact that FRET efficiency depends on the distance separating the donor and acceptor species, it can be concluded that a notably higher proportion of these fluorophores are in close contact for nano-objects with DP$_{P(NB-MEG)}$ = 240 compared to the ones with DP$_{P(NB-MEG)}$ = 120, further supporting the concept of polymerization-induced polymersome fusion.

Contrary to the above FRET findings, comparison of average FL values for samples mixed after polymerization either for 2h or 24h showed the opposite trend for ACM$_{120}$+RhB$_{120}$ and ACM$_{240}$+RhB$_{240}$ samples, with a decrease in FL observed between the ACM$_{120}$+RhB$_{120}$ M$_{a-2h}$ and ACM$_{120}$+RhB$_{120}$ M$_{a-24h}$ samples but no noticeable difference between FL decay profiles for the DP$_{P(NB-MEG)}$ = 240 samples (Figure S51). This suggests a limited occurrence of unimer exchange for the DP$_{P(NB-MEG)}$ = 120 samples and essentially no unimer exchange for the kinetically "frozen" ACM$_{240}$+RhB$_{240}$ nanostructures over prolonged periods of time.

In addition to the membrane fusion studies, it was of paramount importance to investigate whether the interior aqueous lumens of individual spherical polymersomes were also able to mix to form a single aqueous compartment during fusion processes. To this extent, two water-soluble fluorescent dyes with distinctly different fluorescent profiles chosen to avoid FRET (i.e., FAM-NHS (green-emitting dye), and Cy5-NHS (red-emitting dye)) were encapsulated within the lumens of **P(NB-PEG)$_{11}$-*b*-P(NB-MEG)$_n$** diblock copolymer nano-objects.[71] Since fusion events were shown to be driven by polymerization, it was projected that lumen and hence dye mixing would only occur when samples were mixed in early stages of ROMPISA prior to tubesome development, whereas exchange of cargoes for samples mixed after completion of the polymerization could only occur via diffusion of the dyes between discrete nano-objects. Similar to the methodology followed in FRET studies, the two dyes were directly encapsulated into separate formulations via aqueous ROMPISA targeting DP of **P(NB-MEG)** = 240 (above fusion threshold), and FAM-NHS- and Cy5-NHS-loaded samples were mixed either after 1 min of polymerization time (*ca.* ~ 50% monomer conversion) (FAM-NHS+Cy5-NHS M$_d$) or after polymerization for a period of 2h (FAM-NHS+Cy5-NHS M$_{a-2h}$) and 12h (FAM-NHS+Cy5-NHS M$_{a-12h}$). The developed pure and mixed FAM-NHS- and Cy5-NHS-loaded samples were purified by dialysis against DI water (pH 7.0) for removal of unencapsulated dye and were subsequently imaged using TEM and confocal microscopy.

DOI: 10.1021/jacs.9b10152
J. Am. Chem. Soc. 2019, 141, 20234−20248

In all cases, the morphologies formed from this series of dye-loaded nano-objects agreed well with previously described di- or triblock copolymer systems targeting the same core-block DP with a mixture of long tubesomes and a small population of spherical non-fused polymersomes being observed by dry-state TEM imaging (Figure S43). Moreover, confocal microscopy imaging of the purified FAM-NHS- and Cy5-NHS-loaded **P(NB-PEG)$_{11}$-*b*-P(NB-MEG)$_{240}$** nano-objects confirmed the successful encapsulation of either dye within discrete compartmentalized nanostructures, detected using either a green or a red channel, respectively (Figures 5A,B). Importantly, comparison of the green and red channel overlay for acquired images of FAM-NHS+Cy5-NHS $M_{a\text{-}2h/12h}$ and FAM-NHS+Cy5-NHS M_d samples revealed that extensive fusion between polymersome lumens was achieved in the latter case, where near complete color overlap was clearly observed in the merged image, suggesting the co-localization of the two fluorescent dyes in the same aqueous microenvironment (Figure 5E). In contrast, merged confocal microscopy images for dye-loaded samples mixed after polymerization showed no observable color overlap after 2h and 12h of mixing, implying that no fusion had occurred nor had the two dyes become co-localized via diffusion processes. These experiments serve as further validation of our original hypothesis of polymerization-promoted fusion (Figure 5C,D).

DISCUSSION

On the basis of our original experimental design, it was possible to promote fusion of spherical polymersomes prepared via aqueous ROMPISA and induce morphological transitions toward the formation of higher-order tubular polymersomes by altering the chemistry of the corona-forming stabilizer block. In particular, it was observed that inelastic collisions and fusion phenomena between cationic **P(NB-amine)$_{11}$-*b*-P(NB-MEG)$_n$** diblock copolymer polymersomes were effectively prohibited for a wide range of targeted core block DPs, preventing the morphological evolution of the prepared vesicular nanostructures. On the contrary, the energetic barrier that needed to be surpassed to allow for one-dimensional collisions between individual polymersomes was readily reduced when a non-ionic **P(NB-PEG)**-based macroinitiator was utilized for preparation of nano-objects with minimal surface charge, driving the occurrence of extensive fusion events during polymerization and *in situ* development of cylindrical tubesomes (Figures 1 and 2). The preparation of tubular polymersomes has been previously reported via manipulation of spherical precursors by changes in osmotic pressure, pH, or supramolecular complexation,[55,56,72,73] by purification of mixed morphologies containing tubesomes and other nanostructures,[74] through assembly of liquid-crystalline block copolymers,[75,76] or through self-assembly in solvent mixtures containing high concentrations of PEG.[77,78] In these examples, no control over the length or sample composition was demonstrated. In contrast, tubesomes of controllable length were reproducibly achieved in our system under standard aqueous ROMPISA conditions in the absence of external manipulation, originating instead from polymerization-induced polymersome fusion.

Comparison of the TEM image analysis data for the various samples shown above revealed that the average maximum dimension (S_{ave}) values of **P(NB-amine)**-based formulations remained nearly constant with increasing DP of core-forming **P(NB-MEG)** block, suggesting limited fusion in this case. In stark contrast, the calculated S_{ave} values and the corresponding non-spherical fraction for diblock copolymer nano-objects bearing **P(NB-PEG)$_{11}$** and **P(NB-amine)$_{11}$+NaCl** coronae were found to gradually increase with increasing targeted core block DP, whereas C_{ave} values followed the opposite trend, providing initial evidence for our hypothesis of polymersome fusion. Importantly, in the case of the **P(NB-PEG)$_{11}$-*b*-P(NB-MEG)$_{260}$** nano-objects, an S_{ave} of approximately 450 nm and a non-spherical fraction close to 1.0 evidently showed the development of a near uniform population of long tubular polymersomes with unique physicochemical characteristics owing to their shape anisotropy.[53−57] Determination of the fraction of non-spherical nano-objects from TEM image analysis for each series also indicated that the onset of polymersome fusion in the case of **P(NB-amine)**-based nano-objects prepared in the presence of NaCl occurred at a higher core-block DP compared to the **P(NB-PEG)**-based series (Figures 6A,B, S15−S16, S23−S24, and S36−S37).

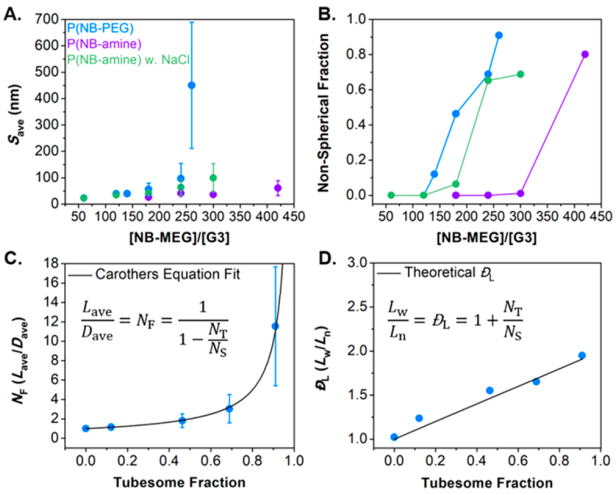

Figure 6. Summary of image analysis data as calculated from acquired dry-state TEM images. (A) Evolution of S_{ave} values with increasing targeted $DP_{P(NB\text{-}MEG)}$ for **P(NB-PEG)$_{11}$-*b*-P(NB-MEG)$_n$** (blue circles) and **P(NB-amine)$_{11}$-*b*-P(NB-MEG)$_n$** diblock copolymer nano-objects developed via aqueous ROMPISA in the absence (purple circles) or presence (green circles) of NaCl. (B) Sample composition, expressed as the fraction of non-spherical nano-objects, as a function of targeted $DP_{P(NB\text{-}MEG)}$ for the same samples. For **P(NB-PEG)$_{11}$-*b*-P(NB-MEG)$_n$** diblock copolymer nano-objects: C) Evolution of N_F (= L_{ave}/D_{ave}) values, the average number of fused particles per tubesome, as a function of the fraction of cylindrical tubesomes in the sample. The black line represents a "step-growth-like" fit of the data using a modified version of Carothers equation (R^2 = 0.997). (D) Evolution of tubesome length dispersity, $Đ_L$, (= L_w/L_n) values with increasing cylindrical tubesome fraction. The black line represents theoretically expected $Đ_L$ values calculated from a "step-growth-like" fit of the data using a modified version of Carothers equation (R^2 = 0.981).

In order to gain further insight into the fusion process of **P(NB-PEG)$_{11}$-*b*-P(NB-MEG)$_n$** diblock copolymer nano-objects, a data fitting process was developed based on the dry-state TEM image analysis data relating the particle shape distribution to the average tubesome length. First, the average number of spherical polymersomes that had fused per tubesome (N_F) was calculated for each diblock copolymer composition by dividing the average particle length (L_{ave}) (or

DOI: 10.1021/jacs.9b10152
J. Am. Chem. Soc. 2019, 141, 20234−20248

D_{ave} for samples where only spherical polymersomes were observed) by a fixed particle diameter value. This diameter value was chosen to be the calculated D_{ave} of the **P(NB-PEG)$_{11}$-*b*-P(NB-MEG)$_{140}$** sample at the onset of polymersome fusion (i.e., $D_{ave} \approx 39$ nm) with the assumption that the average width of fused tubesomes remained relatively constant once fusion had begun. This was further validated by performing manual particle counting measurements for determination of average tubesome width values for each sample, which did not notably vary across the series. The determined N_F values were then correlated to the fraction of cylindrical tubesomes over spherical particles ($F_C = N_T/N_S$, where N_T and N_S represent the number of tubular and spherical polymersomes, respectively; Figure 6C).

Interestingly, it was found that the most accurate fit of the obtained image analysis data resulted from a modified version of Carothers equations for step-growth polymerization that correlate the average degree of polymerization (X_n) and polymer dispersity ($Đ_M$) with monomer conversion (p) (i.e., $X_n = 1/(1 - p)$ and $Đ_M = 1 + p$, respectively).[79] In complete analogy to step-growth polymerization, single spherical polymersomes were considered to be "monomeric building blocks" for the fusion-driven synthesis of tubesome "macromolecules", composed of two or more fused particles. In addition, N_F was considered as the "degree of polymersome fusion" and the ratio N_T/N_S was considered as the "monomer conversion". Finally, the tubesome length dispersity values ($Đ_L = 1 + F_C$) were calculated by dividing the measured weight-average length values (L_w) by the corresponding number-average length values (L_n) for every **P(NB-PEG)$_{11}$-*b*-P(NB-MEG)$_n$** nano-object composition and were found to agree well with theoretically expected values obtained from a modified Carothers equation for polymer dispersity determination (Figure 6D).[79] On the basis of these findings, it is evident that polymersome fusion mirrors a step-growth-like motif. Thus, the proposed polymersome fusion methodology can be utilized as a straightforward guide for targeting a specific nano-object composition (i.e., ratio between tubular and spherical polymersomes) in this system via tuning of the targeted core block DP of the nanoassemblies.

Apart from investigation of polymersome fusion via TEM imaging of end-point ROMPISA reactions targeting a certain DP of **P(NB-MEG)**, alternative characterization techniques were also utilized to *in situ* monitor and definitively confirm the occurrence of polymerization-induced fusion events. First, ROMPISA kinetic monitoring via ^{1}H-NMR spectroscopy was performed for synthesis of **P(NB-amine)$_{11}$-*b*-P(NB-MEG)$_{300}$** and **P(NB-PEG)$_{11}$-*b*-P(NB-MEG)$_{260}$** diblock copolymers with effectively the same molecular weight and dispersity values, eliminating the speculation that observed differences in the fusion behavior could potentially arise from discrepancies in polymerization kinetics. In both cases, aqueous ROMPISA processes followed pseudo-first-order kinetics with similar polymerization rate constants and quantitative monomer conversions achieved after 30 min of polymerization. Additionally, monitoring of changes in average nano-object diameter and % transmittance values upon polymerization progression by DLS and *in situ* turbidimetric analysis, respectively, allowed for direct evaluation of fusion behavior and tubesome formation in the **P(NB-PEG)$_{11}$**-based system (Figure 3).

Following detailed assessment of the polymersome fusion procedure, the polymerization time (t = 2.55 min) and as a consequence the critical DP of **P(NB-MEG)** (DP ≈ 185) at which the onset of fusion occurred were able to be accurately determined. These values were subsequently correlated to intensity-average D_h values measured from DLS kinetic analysis, revealing that nano-objects of approximately 68 nm in size were present in solution at the onset of polymersome fusion prior to evolution of tubesomes. Similar to the methodology followed for analysis of dry-state TEM images for **P(NB-PEG)$_{11}$-*b*-P(NB-MEG)$_n$** diblock copolymer nano-objects, all intensity-average D_h values measured for intermediate time points and core-forming block DPs during kinetic monitoring were divided by this fixed D_h value in order to determine the extent of fusion and conversion of spherical polymersomes by DLS analysis. Finally, DLS conversion values were appropriately normalized so that the fraction of cylindrical tubesomes (F_C) (i.e., conversion) at the final time point was equal to the one calculated for the same end-point **P(NB-PEG)$_{11}$-*b*-P(NB-MEG)$_{260}$** formulation from TEM image analysis, since DLS operates under the assumption that incident light is scattered by hard spheres, often underestimating the actual average dimension values for nanoparticles of cylindrical shape (Figure 7A).

To further investigate differences between polymerization and fusion kinetics, the rates corresponding to each process were initially plotted as semilogarithmic relationships assuming pseudo-first-order kinetics. Interestingly, it was found that this

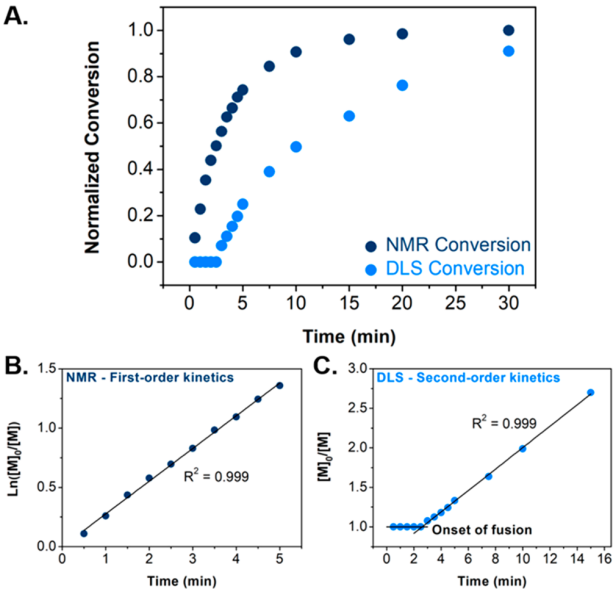

Figure 7. Comparison between polymerization and fusion kinetics for synthesis of **P(NB-PEG)$_{11}$-*b*-P(NB-MEG)$_{260}$** tubesomes. (A) Monomer conversion after particle nucleation (dark blue circles) and spherical polymersome conversion (light blue circles) vs polymerization time kinetic plots for synthesis of **P(NB-PEG)$_{11}$-*b*-P(NB-MEG)$_{260}$** diblock copolymer tubesomes via aqueous ROMPISA, as determined by ^{1}H-NMR spectroscopy and DLS analysis, respectively. (B) Ln([M]$_0$/[M]) vs polymerization time kinetic plot, as determined by ^{1}H-NMR spectroscopy, showing that the ROMPISA polymerization followed pseudo-first-order kinetics (R^2 = 0.999). (C) [M]$_0$/[M] vs polymerization time kinetic plot, as determined by DLS analysis, showing that the polymersome fusion process followed second-order kinetics with the onset of fusion observed at *ca.* 2.55 min (R^2 = 0.999).

DOI: 10.1021/jacs.9b10152
J. Am. Chem. Soc. 2019, 141, 20234−20248

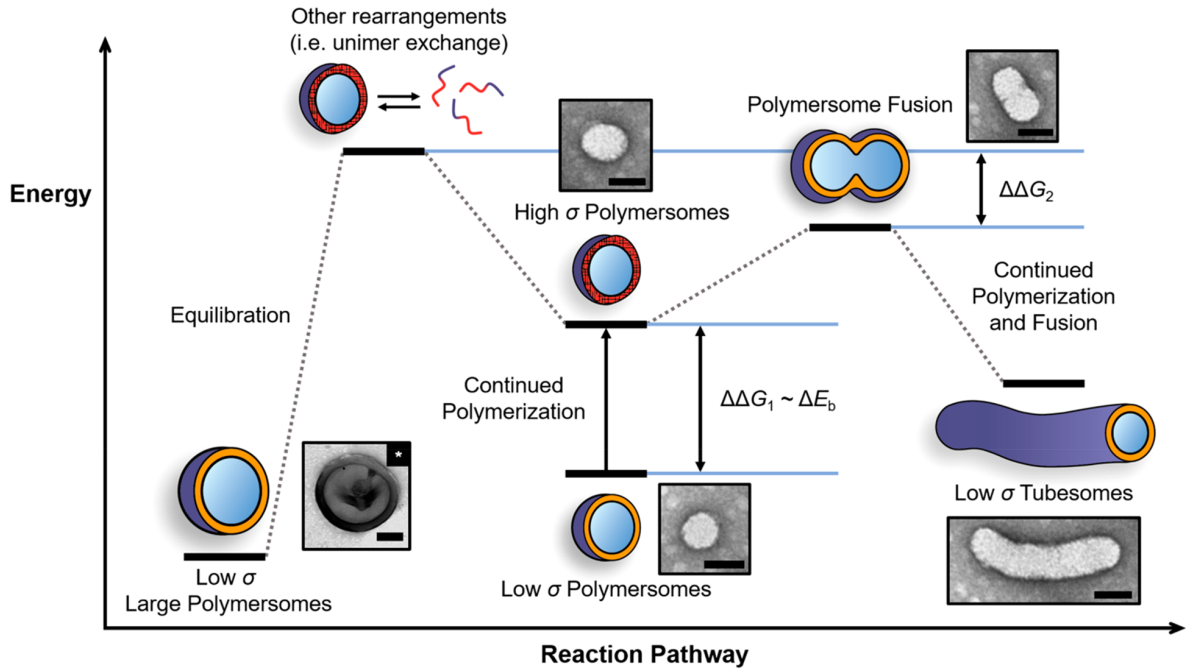

Figure 8. Proposed assembly pathway for polymerization-induced fusion of spherical polymersomes and *in situ* membrane tension-driven morphological evolution toward kinetically favored tubesomes for **P(NB-PEG)**$_{11}$-*b*-**P(NB-MEG)**$_n$ diblock copolymer nano-objects. Other rearrangements (i.e., unimer exchange) and equilibration procedures promote the formation of thermodynamically favored nanostructures. The scale bars for the dry-state TEM image insets represent 50 nm, except for the image marked with an asterisk (*) where the scale bar represents 100 nm.

first-order fitting was only precisely applicable in the case of ROMPISA kinetics, whereas a poor data fit was obtained in the case of polymersome fusion kinetics (Figure 7B). Indeed, the rate of polymerization-induced polymersome fusion was best fit using a second-order kinetic equation (Figure 7C). As shown in Figure 7C, the kinetic plot of $[M]_0/[M]$ vs polymerization time using size values obtained from DLS analysis was separated into two regimes. For the first regime from 0 to 2.55 min, spherical polymersomes of growing size were developed with no evident fusion events occurring, whereas for the second regime, a dramatic acceleration in rate was observed after 2.55 min that was attributed to the onset of polymerization-induced polymersome fusion resulting in a progressively larger population of tubular vesicles with increasing conversion.

We believe that the evidently faster polymerization kinetics as compared to fusion kinetics is of paramount importance for the development of kinetically trapped morphologies with slow chain mobility during aqueous ROMPISA in the case of **P(NB-PEG)**$_{11}$-based formulations. In particular, out-of-equilibrium evolution of tubular polymersomes as the kinetically favorable product driven by 1D inelastic collisions between spherical polymersome building blocks with high membrane tension was solely observed during ROMPISA, whereas other self-assembly methodologies (e.g., solvent-switch or plasticization by EVE molecules) that allow for slow rearrangement and equilibration of polymer chains resulted in the formation of different thermodynamically favorable morphologies, such as large spherical polymersomes or donut-shaped particles (Figure S41).

Confirmation of our originally proposed rationale that fusion events were only promoted during ROMPISA and were more pronounced at higher core-block DPs was achieved by a series of experiments involving either the direct attachment or encapsulation of fluorescent molecules within the membrane or inner aqueous lumen domains of polymersomes, respectively, that were used as markers for fusion monitoring. In the first case, ACM- and RhB-functionalized triblock copolymer nano-objects were prepared containing either fluorophore between the corona- and core-forming blocks with targeted $DP_{P(NB\text{-}MEG)}$ below or above the fusion threshold. This approach allowed for monitoring of fusion events of polymersome membranes occurring during ROMPISA process. For samples mixed during ROMPISA, a distinctly faster FL decay was observed for ACM-containing nano-objects when targeting core block DP = 240 as compared to the samples with $DP_{P(NB\text{-}MEG)}$ = 120 owing to occurrence of extensive fusion events and hence presence of the two fluorophores in close proximity in the former case. FL decay profiles for samples mixed after polymerization for 2h revealed no significant energy transfer and fusion phenomena in either case, whereas measurements after mixing for an extended period of time (24h) showed that minimum unimer exchange took place for the $DP_{P(NB\text{-}MEG)}$ = 240 sample (Figures 4 and S51).

Moreover, following the previously described concept of sample mixing during polymerization prior to the onset of fusion or after completion of polymerization and fusion procedures, the polymerization-induced mixing of polymersome inner lumens was also verified by confocal microscopy imaging via the observed co-localization of the utilized water-soluble FAM-NHS and Cy5-NHS fluorescent dyes within the same aqueous microenvironment for the **P(NB-PEG)**$_{11}$-*b*-**P(NB-MEG)**$_{240}$ diblock copolymer nano-object samples mixed during polymerization. On the contrary, limited cargo exchange and hence minimum lumen fusion and membrane permeability was observed for samples mixed after ROMPISA,

DOI: 10.1021/jacs.9b10152
J. Am. Chem. Soc. 2019, 141, 20234−20248

as FAM-NHS and Cy5-NHS dyes were found to be located in distinctly disparate domains (Figure 5). In addition, the evidently rapid monomer consumption is supposed to also limit plasticization of the nano-object hydrophobic domains by the core-forming monomer in the early ROMPISA stages, minimizing unimer and cargo exchange between particles.

Finally, dry-state TEM imaging and analysis of the acquired images for both **P(NB-amine)**- and **P(NB-PEG)**-based samples of different compositions aged for a period of 4 weeks were carried out for determination of S_{ave} values and non-spherical nano-object fractions (Figures S19 and S42). In both cases, average particle dimensions and non-spherical fractions of the aged samples were found not to vary significantly compared to the originally developed samples, clearly showing their high stability under storage conditions in aqueous media as well as the prevention of equilibration phenomena or additional fusion events after polymerization over prolonged periods of time due to the lack of a driving force.

Based on these observations, our proposed assembly pathway for polymerization-induced polymersome fusion and *in situ* step-growth-like formation of tubesomes in the case of **P(NB-PEG)$_{11}$-*b*-P(NB-MEG)$_n$** diblock copolymer nano-objects is schematically illustrated in Figure 8. We rationalize the fusion phenomenon in terms of polymersome membrane energy. Small spherical polymersomes of low σ arise in early stages of polymerization. The rapid increase of block copolymer chain length and concurrent increase in copolymer hydrophobicity as ROMPISA progresses leads to a buildup of polymersome membrane tension ($\Delta\Delta G_1$, high σ polymersomes). This tension cannot be alleviated by unimer exchange or other dissipative pathways, evidenced by the long-term stability of the tubular nanostructures, likely due to the glassy nature of the membranes (T_g of **P(NB-MEG)$_{180}$** homopolymer = 118.2 °C, Figure S6) and the poor water solubility of the constituent polymer chains. Such a pathway would allow access to the equilibrium morphology, which was shown to consist of large spherical polymersomes prepared via a solvent-switch methodology. Instead, membrane tension is alleviated by fusion between two (or more) polymersomes. Upon continued polymerization and fusion events, tubesomes form preferentially to reduce the overall surface area of the system. Ideally, an energetic minimum would be reached for spherical polymersomes with membranes under no tension. However, the bending rigidity of the constituent polymer chains reduces the amount of membrane curvature that is allowed, and a fine balance is struck between membrane tension and bending rigidity to generate highly anisotropic, low σ tubesomes as kinetic products that persist beyond the completion of the polymerization.

CONCLUSIONS

In summary, we present a novel two-step strategy to induce spontaneous fusion of small spherical polymersomes and concurrent morphological evolution toward tubular block copolymer nanostructures via aqueous ROMP-mediated PISA without the requirement of further external processing. Variations in corona chemistry (i.e., ionic vs non-ionic coronae) and core-forming block length/hydrophobicity in combination with the unique characteristics of ROMPISA, such as the exceedingly fast polymerization kinetics and the synthesis of rod-like poly(norbornene)-based block copolymers with rigid backbone and high T_g values, were found to be the main factors in dictating the occurrence of "controlled" fusion phenomena and the development of kinetically trapped tubesomes. Such features are typically absent in the vast majority of cases for extensively studied RAFT-mediated PISA processes, explaining why such an intriguing assembly behavior has not been observed thus far. Importantly, preparation of a progressively larger population of anisotropic tubesomes was supposed to occur through internal buildup of polymersome membrane tension with continued polymerization and was observed to accurately follow a step-growth-like polymersome fusion model. Overall, we expect that our unprecedented polymerization-induced polymersome fusion methodology will lead the way toward exploring a wide range of nature-mimicking processes via the application of block copolymer nano-objects of distinct characteristics in on-demand catalysis, artificial organelle development, and drug/protein delivery among others.

ASSOCIATED CONTENT

Supporting Information

The Supporting Information is available free of charge at https://pubs.acs.org/doi/10.1021/jacs.9b10152.

Materials and characterization techniques, synthetic procedures, supplementary NMR and SEC analysis data of di- and triblock copolymers, additional DLS, SLS, FL and turbidimetric analysis data, and representative dry-state and cryo-TEM images of nano-objects, full characterization of **P(NB-amine)$_{11}$-*b*-P(NB-MEG)$_n$** diblock copolymer nano-objects developed via ROMPISA in the presence of NaCl (PDF)

AUTHOR INFORMATION

Corresponding Authors

*j.c.foster@bham.ac.uk
*r.oreilly@bham.ac.uk

ORCID

Jeffrey C. Foster: 0000-0002-9097-8680
Rachel K. O'Reilly: 0000-0002-1043-7172

Notes

The authors declare no competing financial interest.

ACKNOWLEDGMENTS

This work was supported by the ERC (Grant No. 615142), EPSRC, and the University of Birmingham. Y.X. acknowledges Chancellor's International Scholarship (University of Warwick) for funding. Ms. I. Akar (University of Birmingham) is thanked for DSC assistance. Dr. S. Bakker (University of Warwick) is thanked for cryo-TEM assistance, and Advanced BioImaging Research Technology Platform, BBSRC ALERT14 award BB/M01228X/1, is thanked for supporting cryo-TEM characterization. Dr. S. Huband at the University of Warwick X-ray Diffraction Research Technology Platform is thanked for assisting with SAXS measurements.

REFERENCES

(1) Lucy, J. A. The Fusion of Biological Membranes. *Nature* **1970**, *227*, 815−817.
(2) Wickner, W.; Schekman, R. Membrane fusion. *Nat. Struct. Mol. Biol.* **2008**, *15*, 658−664.
(3) Chernomordik, L. V.; Kozlov, M. M. Mechanics of membrane fusion. *Nat. Struct. Mol. Biol.* **2008**, *15*, 675−683.

DOI: 10.1021/jacs.9b10152
J. Am. Chem. Soc. 2019, 141, 20234−20248

(4) Alberts, B.; Johnson, A.; Lewis, J.; Raff, M.; Roberts, K.; Walter, P. *Mol. Biol. Cell*, 4th ed.; Garland Science: New York, 2002.
(5) Mashburn-Warren, L. M.; Whiteley, M. Special delivery: vesicle trafficking in prokaryotes. *Mol. Microbiol.* **2006**, *61*, 839−846.
(6) Rothman, J. E.; Wieland, F. T. Protein Sorting by Transport Vesicles. *Science* **1996**, *272*, 227−234.
(7) Fasshauer, D.; Sutton, R. B.; Brunger, A. T.; Jahn, R. Conserved structural features of the synaptic fusion complex: SNARE proteins reclassified as Q- and R-SNAREs. *Proc. Natl. Acad. Sci. U. S. A.* **1998**, *95*, 15781−15786.
(8) Chen, Y. A.; Scheller, R. H. SNARE-mediated membrane fusion. *Nat. Rev. Mol. Cell Biol.* **2001**, *2*, 98−106.
(9) Jahn, R.; Grubmüller, H. Membrane fusion. *Curr. Opin. Cell Biol.* **2002**, *14*, 488−495.
(10) Kozlov, M. M.; Chernomordik, L. V. Membrane tension and membrane fusion. *Curr. Opin. Struct. Biol.* **2015**, *33*, 61−67.
(11) Shillcock, J. C.; Lipowsky, R. Tension-induced fusion of bilayer membranes and vesicles. *Nat. Mater.* **2005**, *4*, 225−228.
(12) Gao, L.; Lipowsky, R.; Shillcock, J. Tension-induced vesicle fusion: pathways and pore dynamics. *Soft Matter* **2008**, *4*, 1208−1214.
(13) Lasic, D. D. On the thermodynamic stability of liposomes. *J. Colloid Interface Sci.* **1990**, *140*, 302−304.
(14) Lipowsky, R. Spontaneous tubulation of membranes and vesicles reveals membrane tension generated by spontaneous curvature. *Faraday Discuss.* **2013**, *161*, 305−331.
(15) Venturoli, M.; Maddalena Sperotto, M.; Kranenburg, M.; Smit, B. Mesoscopic models of biological membranes. *Phys. Rep.* **2006**, *437*, 1−54.
(16) Müller, M.; Katsov, K.; Schick, M. Biological and synthetic membranes: What can be learned from a coarse-grained description? *Phys. Rep.* **2006**, *434*, 113−176.
(17) Gao, L.; Shillcock, J.; Lipowsky, R. Improved dissipative particle dynamics simulations of lipid bilayers. *J. Chem. Phys.* **2007**, *126*, 015101.
(18) Lin, Y.-L.; Chang, H.-Y.; Sheng, Y.-J.; Tsao, H.-K. The fusion mechanism of small polymersomes formed by rod−coil diblock copolymers. *Soft Matter* **2014**, *10*, 1500−1511.
(19) Nieva, J. L.; Goni, F. M.; Alonso, A. Liposome fusion catalytically induced by phospholipase C. *Biochemistry* **1989**, *28*, 7364−7367.
(20) Rørvig-Lund, A.; Bahadori, A.; Semsey, S.; Bendix, P. M.; Oddershede, L. B. Vesicle Fusion Triggered by Optically Heated Gold Nanoparticles. *Nano Lett.* **2015**, *15*, 4183−4188.
(21) Ries, O.; Löffler, P. M. G.; Rabe, A.; Malavan, J. J.; Vogel, S. Efficient liposome fusion mediated by lipid−nucleic acid conjugates. *Org. Biomol. Chem.* **2017**, *15*, 8936−8945.
(22) Malinin, V. S.; Frederik, P.; Lentz, B. R. Osmotic and Curvature Stress Affect PEG-Induced Fusion of Lipid Vesicles but Not Mixing of Their Lipids. *Biophys. J.* **2002**, *82*, 2090−2100.
(23) Dimova, R.; Riske, K. A.; Aranda, S.; Bezlyepkina, N.; Knorr, R. L.; Lipowsky, R. Giant vesicles in electric fields. *Soft Matter* **2007**, *3*, 817−827.
(24) Henderson, I. M.; Paxton, W. F. Salt, Shake, Fuse—Giant Hybrid Polymer/Lipid Vesicles through Mechanically Activated Fusion. *Angew. Chem., Int. Ed.* **2014**, *53*, 3372−3376.
(25) Kliesch, T.-T.; Dietz, J.; Turco, L.; Halder, P.; Polo, E.; Tarantola, M.; Jahn, R.; Janshoff, A. Membrane tension increases fusion efficiency of model membranes in the presence of SNAREs. *Sci. Rep.* **2017**, *7*, 12070.
(26) Su, W.; Luo, Y.; Yan, Q.; Wu, S.; Han, K.; Zhang, Q.; Gu, Y.; Li, Y. Photoinduced Fusion of Micro-Vesicles Self-Assembled from Azobenzene-Containing Amphiphilic Diblock Copolymers. *Macromol. Rapid Commun.* **2007**, *28*, 1251−1256.
(27) Chang, H.-Y.; Sheng, Y.-J.; Tsao, H.-K. Structural and mechanical characteristics of polymersomes. *Soft Matter* **2014**, *10*, 6373−6381.
(28) Rodríguez-Hernández, J.; Chécot, F.; Gnanou, Y.; Lecommandoux, S. Toward 'smart' nano-objects by self-assembly of block copolymers in solution. *Prog. Polym. Sci.* **2005**, *30*, 691−724.
(29) Mai, Y.; Eisenberg, A. Self-assembly of block copolymers. *Chem. Soc. Rev.* **2012**, *41*, 5969−5985.
(30) Palivan, C. G.; Goers, R.; Najer, A.; Zhang, X.; Car, A.; Meier, W. Bioinspired polymer vesicles and membranes for biological and medical applications. *Chem. Soc. Rev.* **2016**, *45*, 377−411.
(31) Blanazs, A.; Madsen, J.; Battaglia, G.; Ryan, A. J.; Armes, S. P. Mechanistic Insights for Block Copolymer Morphologies: How Do Worms Form Vesicles? *J. Am. Chem. Soc.* **2011**, *133*, 16581−16587.
(32) Warren, N. J.; Armes, S. P. Polymerization-Induced Self-Assembly of Block Copolymer Nano-objects via RAFT Aqueous Dispersion Polymerization. *J. Am. Chem. Soc.* **2014**, *136*, 10174−10185.
(33) Warren, N. J.; Mykhaylyk, O. O.; Ryan, A. J.; Williams, M.; Doussineau, T.; Dugourd, P.; Antoine, R.; Portale, G.; Armes, S. P. Testing the Vesicular Morphology to Destruction: Birth and Death of Diblock Copolymer Vesicles Prepared via Polymerization-Induced Self-Assembly. *J. Am. Chem. Soc.* **2015**, *137*, 1929−1937.
(34) Zhang, W.-J.; Hong, C.-Y.; Pan, C.-Y. Artificially Smart Vesicles with Superior Structural Stability: Fabrication, Characterizations, and Transmembrane Traffic. *ACS Appl. Mater. Interfaces* **2017**, *9*, 15086−15095.
(35) Blackman, L. D.; Varlas, S.; Arno, M. C.; Houston, Z. H.; Fletcher, N. L.; Thurecht, K. J.; Hasan, M.; Gibson, M. I.; O'Reilly, R. K. Confinement of Therapeutic Enzymes in Selectively Permeable Polymer Vesicles by Polymerization-Induced Self-Assembly (PISA) Reduces Antibody Binding and Proteolytic Susceptibility. *ACS Cent. Sci.* **2018**, *4*, 718−723.
(36) Varlas, S.; Blackman, L. D.; Findlay, H. E.; Reading, E.; Booth, P. J.; Gibson, M. I.; O'Reilly, R. K. Photoinitiated Polymerization-Induced Self-Assembly in the Presence of Surfactants Enables Membrane Protein Incorporation into Vesicles. *Macromolecules* **2018**, *51*, 6190−6201.
(37) Varlas, S.; Foster, J. C.; Georgiou, P. G.; Keogh, R.; Husband, J. T.; Williams, D. S.; O'Reilly, R. K. Tuning the membrane permeability of polymersome nanoreactors developed by aqueous emulsion polymerization-induced self-assembly. *Nanoscale* **2019**, *11*, 12643−12654.
(38) Chen, M.; Li, J.-W.; Zhang, W.-J.; Hong, C.-Y.; Pan, C.-Y. pH- and Reductant-Responsive Polymeric Vesicles with Robust Membrane-Cross-Linked Structures: In Situ Cross-Linking in Polymerization-Induced Self-Assembly. *Macromolecules* **2019**, *52*, 1140−1149.
(39) Charleux, B.; Delaittre, G.; Rieger, J.; D'Agosto, F. Polymerization-Induced Self-Assembly: From Soluble Macromolecules to Block Copolymer Nano-Objects in One Step. *Macromolecules* **2012**, *45*, 6753−6765.
(40) Tan, J.; Sun, H.; Yu, M.; Sumerlin, B. S.; Zhang, L. Photo-PISA: Shedding Light on Polymerization-Induced Self-Assembly. *ACS Macro Lett.* **2015**, *4*, 1249−1253.
(41) Canning, S. L.; Smith, G. N.; Armes, S. P. A Critical Appraisal of RAFT-Mediated Polymerization-Induced Self-Assembly. *Macromolecules* **2016**, *49*, 1985−2001.
(42) Yeow, J.; Boyer, C. Photoinitiated Polymerization-Induced Self-Assembly (Photo-PISA): New Insights and Opportunities. *Adv. Sci.* **2017**, *4*, 1700137.
(43) Penfold, N. J. W.; Yeow, J.; Boyer, C.; Armes, S. P. Emerging Trends in Polymerization-Induced Self-Assembly. *ACS Macro Lett.* **2019**, *8*, 1029−1054.
(44) Sun, J.-T.; Hong, C.-Y.; Pan, C.-Y. Formation of the block copolymer aggregates via polymerization-induced self-assembly and reorganization. *Soft Matter* **2012**, *8*, 7753−7767.
(45) Foster, J. C.; Varlas, S.; Couturaud, B.; Coe, Z.; O'Reilly, R. K. Getting into Shape: Reflections on a New Generation of Cylindrical Nanostructures' Self-Assembly Using Polymer Building Blocks. *J. Am. Chem. Soc.* **2019**, *141*, 2742−2753.
(46) Foster, J. C.; Varlas, S.; Couturaud, B.; Jones, J. R.; Keogh, R.; Mathers, R. T.; O'Reilly, R. K. Predicting Monomers for Use in Polymerization-Induced Self-Assembly. *Angew. Chem., Int. Ed.* **2018**, *57*, 15733−15737.

DOI: 10.1021/jacs.9b10152
J. Am. Chem. Soc. 2019, 141, 20234−20248

(47) Varlas, S.; Foster, J. C.; Arkinstall, L. A.; Jones, J. R.; Keogh, R.; Mathers, R. T.; O'Reilly, R. K. Predicting Monomers for Use in Aqueous Ring-Opening Metathesis Polymerization-Induced Self-Assembly. *ACS Macro Lett.* **2019**, *8*, 466−472.
(48) Blackman, L. D.; Doncom, K. E. B.; Gibson, M. I.; O'Reilly, R. K. Comparison of photo- and thermally initiated polymerization-induced self-assembly: a lack of end group fidelity drives the formation of higher order morphologies. *Polym. Chem.* **2017**, *8*, 2860−2871.
(49) Tan, J.; Huang, C.; Liu, D.; Li, X.; He, J.; Xu, Q.; Zhang, L. Polymerization-Induced Self-Assembly of Homopolymer and Diblock Copolymer: A Facile Approach for Preparing Polymer Nano-Objects with Higher-Order Morphologies. *ACS Macro Lett.* **2017**, *6*, 298−303.
(50) Huang, C.; Tan, J.; Xu, Q.; He, J.; Li, X.; Liu, D.; Zhang, L. Adding a solvophilic comonomer to the polymerization-induced self-assembly of block copolymer and homopolymer: a cooperative strategy for preparing large compound vesicles. *RSC Adv.* **2017**, *7*, 46069−46081.
(51) Varlas, S.; Georgiou, P. G.; Bilalis, P.; Jones, J. R.; Hadjichristidis, N.; O'Reilly, R. K. Poly(sarcosine)-Based Nano-Objects with Multi-Protease Resistance by Aqueous Photoinitiated Polymerization-Induced Self-Assembly (Photo-PISA). *Biomacromolecules* **2018**, *19*, 4453−4462.
(52) Foster, J. C.; Varlas, S.; Blackman, L. D.; Arkinstall, L. A.; O'Reilly, R. K. Ring-Opening Metathesis Polymerization in Aqueous Media Using a Macroinitiator Approach. *Angew. Chem., Int. Ed.* **2018**, *57*, 10672−10676.
(53) Yang, X.; Grailer, J. J.; Rowland, I. J.; Javadi, A.; Hurley, S. A.; Steeber, D. A.; Gong, S. Multifunctional SPIO/DOX-loaded wormlike polymer vesicles for cancer therapy and MR imaging. *Biomaterials* **2010**, *31*, 9065−9073.
(54) Lai, M.-H.; Jeong, J. H.; DeVolder, R. J.; Brockman, C.; Schroeder, C.; Kong, H. Ellipsoidal Polyaspartamide Polymersomes with Enhanced Cell-Targeting Ability. *Adv. Funct. Mater.* **2012**, *22*, 3239−3246.
(55) van Oers, M. C. M.; Rutjes, F. P. J. T.; van Hest, J. C. M. Tubular Polymersomes: A Cross-Linker-Induced Shape Transformation. *J. Am. Chem. Soc.* **2013**, *135*, 16308−16311.
(56) Toebes, B. J.; Abdelmohsen, L. K. E. A.; Wilson, D. A. Enzyme-driven biodegradable nanomotor based on tubular-shaped polymeric vesicles. *Polym. Chem.* **2018**, *9*, 3190−3194.
(57) Wong, C. K.; Stenzel, M. H.; Thordarson, P. Non-spherical polymersomes: formation and characterization. *Chem. Soc. Rev.* **2019**, *48*, 4019−4035.
(58) Wright, D. B.; Touve, M. A.; Thompson, M. P.; Gianneschi, N. C. Aqueous-Phase Ring-Opening Metathesis Polymerization-Induced Self-Assembly. *ACS Macro Lett.* **2018**, *7*, 401−405.
(59) Torres-Rocha, O. L.; Wu, X.; Zhu, C.; Crudden, C. M.; Cunningham, M. F. Polymerization-Induced Self-Assembly (PISA) of 1,5-Cyclooctadiene Using Ring Opening Metathesis Polymerization. *Macromol. Rapid Commun.* **2019**, *40*, 1800326.
(60) Tomasek, J.; Schatz, J. Olefin metathesis in aqueous media. *Green Chem.* **2013**, *15*, 2317−2338.
(61) Sabatino, V.; Ward, T. R. Aqueous olefin metathesis: recent developments and applications. *Beilstein J. Org. Chem.* **2019**, *15*, 445−468.
(62) Varlas, S.; Foster, J. C.; O'Reilly, R. K. Ring-opening metathesis polymerization-induced self-assembly (ROMPISA). *Chem. Commun.* **2019**, *55*, 9066−9071.
(63) Lynn, D. M.; Mohr, B.; Grubbs, R. H. Living Ring-Opening Metathesis Polymerization in Water. *J. Am. Chem. Soc.* **1998**, *120*, 1627−1628.
(64) Semsarilar, M.; Ladmiral, V.; Blanazs, A.; Armes, S. P. Cationic Polyelectrolyte-Stabilized Nanoparticles via RAFT Aqueous Dispersion Polymerization. *Langmuir* **2013**, *29*, 7416−7424.
(65) Patterson, J. P.; Robin, M. P.; Chassenieux, C.; Colombani, O.; O'Reilly, R. K. The analysis of solution self-assembled polymeric nanomaterials. *Chem. Soc. Rev.* **2014**, *43*, 2412−2425.
(66) Novak, B. M.; Grubbs, R. H. Catalytic organometallic chemistry in water: the aqueous ring-opening metathesis polymerization of 7-oxanorbornene derivatives. *J. Am. Chem. Soc.* **1988**, *110*, 7542−7543.
(67) Hillmyer, M. A.; Lepetit, C.; McGrath, D. V.; Novak, B. M.; Grubbs, R. H. Aqueous ring-opening metathesis polymerization of carboximide-functionalized 7-oxanorbornenes. *Macromolecules* **1992**, *25*, 3345−3350.
(68) Wyatt, P. J. Measurement of Special Nanoparticle Structures by Light Scattering. *Anal. Chem.* **2014**, *86*, 7171−7183.
(69) Clegg, R. M. Förster resonance energy transfer—FRET what is it, why do it, and how it's done. In *Laboratory Techniques in Biochemistry and Molecular Biology*; Elsevier: Amsterdam, 2009; Vol. *33*, pp 1−57.
(70) Xie, Y.; Husband, J. T.; Torrent-Sucarrat, M.; Yang, H.; Liu, W.; O'Reilly, R. K. Rational design of substituted maleimide dyes with tunable fluorescence and solvafluorochromism. *Chem. Commun.* **2018**, *54*, 3339−3342.
(71) Grumelard, J.; Taubert, A.; Meier, W. Soft nanotubes from amphiphilic ABA triblock macromonomers. *Chem. Commun.* **2004**, 1462−1463.
(72) Abdelmohsen, L. K. E. A.; Williams, D. S.; Pille, J.; Ozel, S. G.; Rikken, R. S. M.; Wilson, D. A.; van Hest, J. C. M. Formation of Well-Defined, Functional Nanotubes via Osmotically Induced Shape Transformation of Biodegradable Polymersomes. *J. Am. Chem. Soc.* **2016**, *138*, 9353−9356.
(73) Chen, X.; Liu, L.; Huo, M.; Zeng, M.; Peng, L.; Feng, A.; Wang, X.; Yuan, J. Direct Synthesis of Polymer Nanotubes by Aqueous Dispersion Polymerization of a Cyclodextrin/Styrene Complex. *Angew. Chem., Int. Ed.* **2017**, *56*, 16541−16545.
(74) Robertson, J. D.; Yealland, G.; Avila-Olias, M.; Chierico, L.; Bandmann, O.; Renshaw, S. A.; Battaglia, G. pH-Sensitive Tubular Polymersomes: Formation and Applications in Cellular Delivery. *ACS Nano* **2014**, *8*, 4650−4661.
(75) Wong, C. K.; Mason, A. F.; Stenzel, M. H.; Thordarson, P. Formation of non-spherical polymersomes driven by hydrophobic directional aromatic perylene interactions. *Nat. Commun.* **2017**, *8*, 1240.
(76) Mondal, T.; Sakurai, T.; Yoneda, S.; Seki, S.; Ghosh, S. Semiconducting Nanotubes by Intrachain Folding Following Macroscopic Assembly of a Naphthalene−Diimide (NDI) Appended Polyurethane. *Macromolecules* **2015**, *48*, 879−888.
(77) Gao, C.; Zhou, H.; Qu, Y.; Wang, W.; Khan, H.; Zhang, W. In Situ Synthesis of Block Copolymer Nanoassemblies via Polymerization-Induced Self-Assembly in Poly(ethylene glycol). *Macromolecules* **2016**, *49*, 3789−3798.
(78) Ding, Z.; Ding, M.; Gao, C.; Boyer, C.; Zhang, W. In Situ Synthesis of Coil−Coil Diblock Copolymer Nanotubes and Tubular Ag/Polymer Nanocomposites by RAFT Dispersion Polymerization in Poly(ethylene glycol). *Macromolecules* **2017**, *50*, 7593−7602.
(79) Flory, P. J. Fundamental Principles of Condensation Polymerization. *Chem. Rev.* **1946**, *39*, 137−197.

DOI: 10.1021/jacs.9b10152
J. Am. Chem. Soc. 2019, 141, 20234−20248

5.2. Appendix – Supporting Information Material

Supporting Information

"Polymerization-Induced Polymersome Fusion"

Spyridon Varlas,[†] *Robert Keogh,*[†] *Yujie Xie,*[†,‡] *Sarah L. Horswell,*[†] *Jeffrey C. Foster,*[*,†] *and Rachel K. O'Reilly*[*,†]

[†]School of Chemistry, University of Birmingham, Edgbaston, Birmingham, B15 2TT, UK

[‡]Department of Chemistry, University of Warwick, Gibbet Hill Road, Coventry, CV4 7AL, UK

*<u>*Corresponding Authors*</u>: j.c.foster@bham.ac.uk (J.C.F.) and r.oreilly@bham.ac.uk (R.K.O.R.)

Contents

Experimental Section S2

Materials and Methods S2

Materials S2

Characterization Techniques S2

Synthetic Methods S11

Supplementary Characterization Data for **P(NB-MEG)$_{180}$** Homopolymer S23

Supplementary Characterization Data for **P(NB-amine)$_{11}$-*b*-P(NB-MEG)$_n$** Diblock Copolymer Nano-Objects Developed by Aqueous ROMPISA S24

Supplementary Characterization Data for **P(NB-amine)$_{11}$-*b*-P(NB-MEG)$_n$** Diblock Copolymer Nano-Objects Developed by Aqueous ROMPISA in the Presence of NaCl S35

Supplementary Characterization Data for **P(NB-PEG)$_{11}$-*b*-P(NB-MEG)$_n$** Diblock Copolymer Nano-Objects Developed by Aqueous ROMPISA S40

Supplementary Characterization Data for **P(NB-PEG)$_{11}$-*b*-P(NB-ACM)$_m$-*b*-P(NB-MEG)$_n$** and **P(NB-PEG)$_{11}$-*b*-P(NB-RhB)$_{m/2}$-*b*-P(NB-MEG)$_n$** Triblock Copolymer Nano-Objects Developed by Aqueous ROMPISA S54

References S63

Experimental Section

Materials and Methods

Materials

Grubbs Catalyst™ 2nd Generation (**G2**) ($(H_2IMes)(PCy_3)(Cl)_2Ru{=}CHPh$), ethyl vinyl ether (EVE) (99%), *N*-Boc-ethylenediamine (≥98.0%), rhodamine B (RhB) (≥95%), 4-(dimethylamino)pyridine (DMAP) (≥99%), *N,N′*-dicyclohexylcarbodiimide (DCC) (99%), sodium phosphate monobasic (≥99.0%) and 1,3,5-trioxane (≥99%) were purchased from Sigma-Aldrich and were used without further purification. *cis*-5-Norbornene-*exo*-2,3-dicarboxylic anhydride (97%) and trifluoroacetic acid (TFA) (99%) were purchased from Alfa Aesar. Cyanine5 NHS ester (Cy5-NHS) was purchased from Lumiprobe. Sodium chloride (99%), 5/6-carboxyfluorescein succinimidyl ester (FAM-NHS) and dichloromethane (DCM) were purchased from Fisher Scientific. DCM was dried over calcium hydride overnight and then distilled before use. SnakeSkin™ dialysis tubing (MWCO = 3.5 kDa) was also purchased from Fisher Scientific. Tetrahydrofuran (THF) (HPLC grade) was purchased from VWR Chemicals and was purified *via* passage through a column of basic alumina prior to use. Grubbs Catalyst™ 3rd Generation (**G3**) ($(H_2IMes)(pyr)_2(Cl)_2Ru{=}CHPh$) was prepared from **G2** according to a previously described procedure and was used within 2-3 days.[1] The synthesis of *exo*-norbornene imide tertiary amine (**NB-amine**), *exo*-norbornene imide alcohol (**NB-alcohol**), *exo*-norbornene imide poly(ethylene glycol) methyl ether (M_n ~ 350 g mol^{-1}) (**NB-PEG**) and *exo*-norbornene imide ethylene glycol monomethyl ether (**NB-MEG**) was carried out according to previously described processes from our group.[2, 3] Formvar-carbon coated (300 mesh) and lacey-carbon coated (400 mesh) copper grids were purchased from EM Resolutions.

Characterization Techniques

NMR Spectroscopy. ^{1}H-NMR and ^{13}C-NMR spectra were recorded at 300 MHz or 400 MHz on a Bruker DPX-300 or a Bruker DPX-400 spectrometer, using chloroform-*d* ($CDCl_3$), DMSO-d_6 or methanol-d_4 (CD_3OD) as the solvent. Chemical shifts of protons are reported as δ in parts per million (ppm) and are relative to tetramethylsilane (TMS) at δ = 0 ppm when using $CDCl_3$ or solvent residual peaks when using DMSO-d_6 (DMSO, δ = 2.50 ppm) or methanol-d_4 (CH_3OH, δ = 3.31 ppm). For polymerization kinetics determination, ^{1}H-NMR spectra were recorded using $CDCl_3$ or DMSO-d_6 containing a known concentration of 1,3,5-trioxane (δ = 5.1 ppm) as an external standard.

High-Resolution Mass Spectrometry. HRMS spectra were recorded by the MS Analytical Facility Service at the University of Birmingham on a Waters Xevo G2-XS QTof Quadrupole Time-of-Flight mass spectrometer.

Size Exclusion Chromatography. Size exclusion chromatography (SEC) analysis was performed on a system composed of an Agilent 1260 Infinity II LC system equipped with an Agilent guard column (PLGel 5 μM, 50 × 7.5 mm) and two Agilent Mixed-C columns (PLGel 5 μM, 300 × 7.5 mm). The mobile phase used was THF (HPLC grade) containing 2% v/v NEt_3 at 40 °C at flow rate of 1.0 mL min^{-1} (polystyrene (PS) standards were used for calibration). Detection was conducted using a differential refractive index (RI) detector, whereas for **P(NB-PEG)$_{11}$-*b*-P(NB-ACM)$_{m}$-*b*-P(NB-MEG)$_{n}$** and **P(NB-PEG)$_{11}$-*b*-P(NB-RhB)$_{m/2}$-*b*-P(NB-MEG)$_{n}$** triblock copolymers an ultraviolet (UV) detector set to either λ_{ACM} = 360 nm or λ_{RhB} = 545 nm, respectively, was also used. Number-average molecular weights (M_n), weight-average molecular weights (M_w) and dispersities ($Đ_M = M_w/M_n$) were determined using the Agilent GPC/SEC software.

Differential Scanning Calorimetry. Determination of the glass transition temperature (T_g) for **P(NB-MEG)$_{180}$** homopolymer was performed using a Mettler Toledo DSC 3 differential scanning calorimeter by heating the sample from 25 °C to 190 °C at a rate of 10 °C/min for two heating/cooling cycles. The T_g was determined from the inflection point in the second heating cycle of DSC. Collected data were processed using STARe software.

Turbidimetry. Turbidimetric analysis was performed on a Thermo Scientific Evolution™ 350 UV-Vis spectrophotometer equipped with a Peltier heating and cooling system. *In situ* ROMPISA kinetic analysis was performed by monitoring changes in transmittance of each polymerization solution at λ = 550 nm every 6 s over a period of 20 min at 25 °C. A solution of appropriately diluted **P(NB-amine)$_{11}$** or **P(NB-PEG)$_{11}$** macroinitiator in phosphate buffer at pH = 2.0 (PB 2) was used as a reference sample.

Dynamic Light Scattering. Hydrodynamic diameters (D_h) and size distributions (PD) of nano-objects were determined by dynamic light scattering (DLS) using a Malvern Zetasizer Nano ZS with a 4 mW He-Ne 633 nm laser module operating at 25 °C. Measurements were carried out at an angle of 173° (back scattering), and results were analyzed using Malvern DTS v7.03 software. All determinations were repeated 4 times with at least 10 measurements recorded for each run. D_h values were calculated using the Stokes-Einstein equation where particles are assumed to be spherical, while for cylindrical particles DLS was used to detect multiple populations and obtain dispersity information.

Zeta Potential Analysis. Zeta potential was measured by the technique of microelectrophoresis, using a Malvern Zetasizer Nano ZS instrument, at room temperature at 633 nm. Owing to the high conductivity (>5 mS/cm) of the analysis media (phosphate buffer at pH = 2.0 with or without 100 mM NaCl), monomodal mode was selected for measurements using an applied voltage of 10 V. All reported zeta potential values were the average of at least three runs with at least 40 measurements recorded for each run. Zeta potential was calculated from the corresponding electrophoretic mobilities (μ_E) by using the Henry's correction of the Smoluchowski equation ($\mu_E = 4\pi\ \varepsilon_0\ \varepsilon_r\ \zeta\ (1+\kappa r)/6\pi\ \mu$).

Static Light Scattering. Static light scattering (SLS) analysis was performed using an ALV/CGS-3 compact goniometer system. 0.1 mg mL^{-1} solutions were filtered through 0.45 μm nylon filters prior to light scattering analysis at multiple angles ranging from 35° to 150° against a toluene standard. The wavelength of the incident beam was λ = 633 nm and for each angle, runs of at least 60 s were carried out at 20 °C. d*n*/dc values were determined using a DnDc1260 differential refractometer supplied by PSS GmbH (laser λ = 620 nm, T = 20 °C) at concentrations in the range 0.1 mg $ml^{-1} \leq c \leq$ 0.5 mg ml^{-1}.
For each sample, the resulting $g_2(q, t)$ autocorrelation functions from DLS analysis for each angle were analyzed by the REPES algorithm to determine a relaxation time, τ. The determined τ values at each angle were plotted against the square of the scattering wave vector, q, to determine the apparent diffusion coefficient, D, according to the following equation:[4]

$$\tau^{-1} = q^2 D$$

Apparent hydrodynamic radii (R_h) were then calculated using the Stokes-Einstein equation:

$$R_h = \frac{k_B T}{6\pi\eta D},$$

where η is the solvent viscosity, k_B is the Boltzmann constant and T is the absolute temperature.
Using SLS analysis at the same angles, partial Zimm plots were obtained and the radius of gyration (R_g) and the apparent aggregation number, N_{agg}, for each sample were calculated using the following equations:[4]

$$\frac{Kc}{R_\theta} \approx \frac{q^2 {R_g}^2}{3M_{w,particle}} + \frac{1}{M_{w,particle}}$$

$$N_{agg} = \frac{M_{w,particle}}{M_{w,polymer}}$$

For SLS analysis, the intensity of the scattered light (I_{sample}) was used to calculate Kc/R_θ for each angle, where c is the polymer concentration and the Rayleigh ratio, R_θ, and K are defined by the following equations:

$$R_\theta = \frac{I_{sample} - I_{solvent}}{I_{standard}} R_{\theta,standard}$$

$$K = \frac{4\pi^2 {n_{standard}}^2 \left(\frac{dn}{dc}\right)^2}{N_A \lambda^4},$$

where λ is the wavelength of the laser, $n_{standard}$ is the refractive index of the standard, dn/dc is the refractive index increment of the sample and N_A is Avogadro's number.

Small-Angle X-Ray Scattering. Small-angle X-ray scattering (SAXS) measurements were performed using a Xenocs Xeuss 2.0 equipped with a micro-focus Cu K_α source collimated with Scatterless slits. The scattering was measured using a Pilatus 300k detector with a pixel size of 0.172 mm × 0.172 mm. The distance between the detector and the sample was calibrated using silver behenate ($AgC_{22}H_{43}O_2$), giving a value of 2.481(5) m. **P(NB-PEG)$_{11}$-*b*-P(NB-MEG)$_{60}$** sample at 10 mg mL^{-1} was mounted in a 1 mm borosilicate glass capillary prior to analysis. A Guinier plot of the acquired SAXS data for the range $qR_g < 1.3$ was linear, giving R_g = 130 Å.

Transmission Electron Microscopy. Dry-state stained transmission electron microscopy (TEM) imaging was performed on a JEOL JEM-1400 microscope operating at an acceleration voltage of 80 kV. All dry-state samples were diluted with deionized water to appropriate analysis concentration (0.01% w/w solids content) and then deposited onto formvar-coated copper grids. After roughly 1 min, excess sample was blotted from the grid and the grid was stained with an aqueous 1 wt% uranyl acetate (UA) solution for 1 min prior to blotting, drying and microscopic analysis.

Cryogenic transmission electron microscopy (cryo-TEM) imaging was performed on a JEOL JEM-2100Plus microscope operating at an acceleration voltage of 200 kV. Samples for cryo-TEM analysis were prepared, after 200-fold dilution with deionized water, by depositing 8 μL of sample onto a lacey-carbon grid followed by blotting for approximately 5 s and plunging into a pool of liquid ethane, cooled using liquid nitrogen, to vitrify the samples. Transfer into a pre-cooled cryo-TEM holder was performed under liquid nitrogen temperatures prior to microscopic analysis.

Transmission Electron Microscopy Image Analysis. Dry-state TEM images were processed using ImageJ image analysis software to determine the population distribution of spherical and tubular polymersomes, the average maximum dimension (S_{ave}) (diameter for spherical polymersomes or length for tubesomes) of each sample, and the average tubesome length (L_{ave}). Using ImageJ, the image threshold was first adjusted such that individual particles could be clearly resolved as dark shapes against a white background. The area (a) and perimeter (p) of each particle were then determined using the Analyze Particles feature, adjusting the area (a) and circularity (C) parameters such that a representative sample of particles was selected from each image. Image masks generated *via* this process are shown herein.

Next, circularity (C) values were calculated from the generated nano-object areas and perimeters using the equation shown in Figure S1. The circularity of each particle was exploited to differentiate its morphology – in general, particles with $1 \geq C > 0.7$ were assumed to be spherical polymersomes, whilst those with $C \leq 0.7$ were assigned as cylindrical tubesomes. Based on this initial calculation, the fraction of cylindrical particles over spherical particles (F_C) was determined, which was then benchmarked against the original dry-state TEM images by manually counting the number of spherical polymersomes (N_S) and cylindrical tubesomes (N_T) in a given area over multiple images. In some cases, the threshold value of $C = 0.7$ was adjusted such that the calculated cylindrical particle fraction matched the value obtained from manual counting.

The radius (r) for spherical polymersomes or length (l) for cylindrical tubesomes was then calculated from their areas using the corresponding equations shown in Figure S1 and averaged across the entire population to determine D_{ave} and L_{ave}, respectively. In all cases, a population of at least 300 particles were analyzed. For the **P(NB-PEG)$_{11}$-*b*-P(NB-MEG)$_{260}$** sample, the tubesome fraction and L_{ave} were determined by manually measuring the length of each particle over several images, as individual particles could not be isolated using the Analyze Particles feature of ImageJ software.

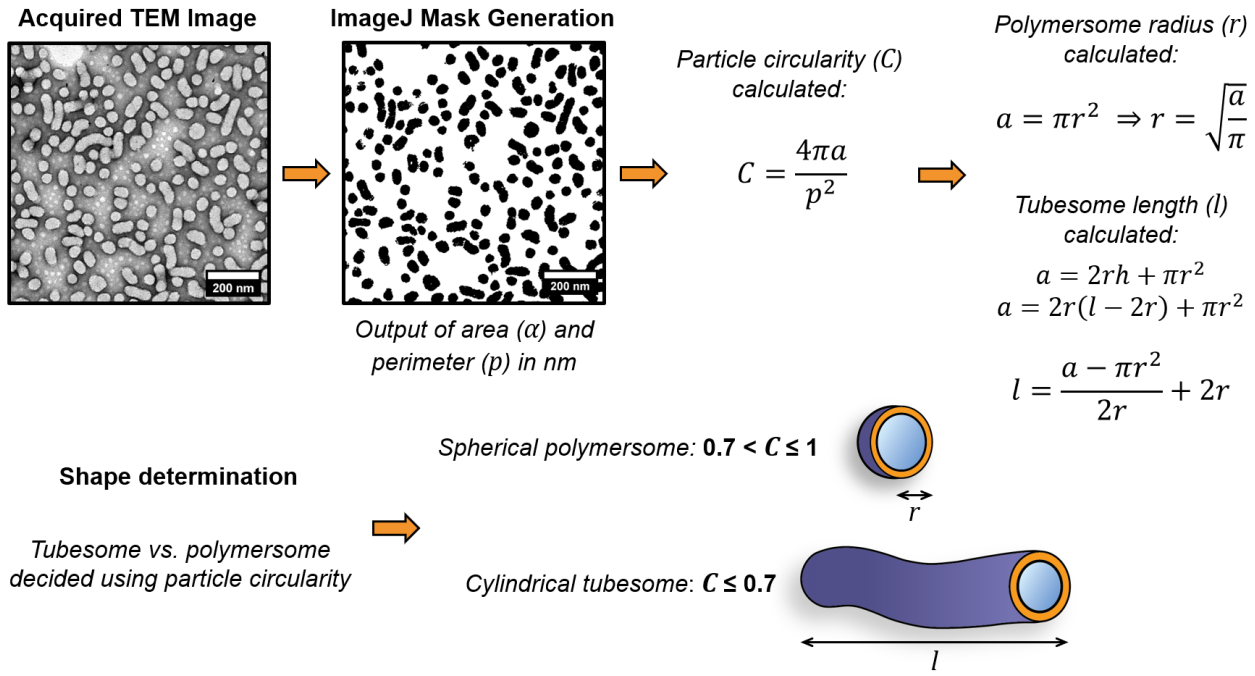

Figure S1. Description of dry-state TEM image analysis procedure and equations utilized for calculation of nano-object circularity (*C*), radius (*r*) (for spherical polymersomes) and length (*l*) (for cylindrical tubesomes) values, using ImageJ image processing software.

Step-Growth Fitting of Image Analysis Data. For **P(NB-PEG)$_{11}$-*b*-P(NB-MEG)$_n$** diblock copolymer nano-objects, a process to generate step-growth fits relating the particle shape distribution to the average tubesome length was developed. For samples in which fusion was observed, the average number of spherical polymersomes that had fused per tubesome (N_F) was calculated by dividing L_{ave} by a fixed diameter, D_C. This diameter was taken as the D_{ave} of the sample prior to the onset of fusion, with the assumption that the width of the tubesomes remained constant across the series of targeted DPs once fusion began to occur. This assumption was supported by manual tubesome width measurements, which were found not to vary significantly over a large number of analyzed images. Carothers equations provide a relationship between monomer conversion, the degree of polymerization and the polymer dispersity for step-growth polymerizations. In our system, we treated the average number of polymersomes that had fused to make each tubesome ($N_F = L_{ave}/D_{ave}$) and the fraction of cylindrical particles over spherical particles (F_C) as analogies for the degree of polymerization and conversion, respectively. In this way, non-fused spherical polymersomes were considered to be "monomers", and tubesomes, comprised of two or more fused polymersomes, represented "polymers". Thus, a plot of L_{ave}/D_{ave} as a function of cylindrical tubesome fraction (F_C) was fit using the following equation derived from original Carothers equation:

$$\frac{L_{\mathrm{ave}}}{D_{\mathrm{ave}}} = N_F = \frac{1}{1 - F_C} = \frac{1}{1 - \frac{N_{\mathrm{T}}}{N_{\mathrm{S}}}}$$

To further the analogy, the tubesome length dispersity, $Đ_{\mathrm{L}}$, was calculated from the image analysis data using the following expressions:

$$L_{\mathrm{n}} = \frac{\sum L_i}{\sum n_i}$$

$$L_{\mathrm{w}} = \frac{\sum L_i^4}{\sum L_i^3}$$

$$Đ_L = \frac{L_{\mathrm{w}}}{L_{\mathrm{n}}}$$

where L_{i} corresponds to the length of each individual tubesome. $Đ_{\mathrm{L}}$ was then plotted against the cylindrical tubesome fraction (F_{C}), which was fit with the following linear relationship, also derived from Carothers equations:

$$Đ_L = 1 + F_C = 1 + \frac{N_{\mathrm{T}}}{N_{\mathrm{S}}}$$

Confocal Laser Scanning Microscopy. Freshly prepared and purified solutions of FAM-NHS-loaded (green-emitting dye), Cy5-NHS-loaded (red-emitting dye) and mixed **P(NB-PEG)$_{11}$-*b*-P(NB-MEG)$_{240}$** diblock copolymer nano-objects at 100-fold dilution were deposited on a glass slide and imaged by confocal laser scanning microscopy (CLSM) after evaporation of the solvent. Images were acquired using an Olympus FV3000 confocal laser Scanning Microscope. Samples were imaged at 60× magnification upon excitation using a 488 nm laser (green channel) and a 640 nm laser (red channel). Images were processed using cellSens (Olympus) and ImageJ image processing software.

Steady-State Fluorescence Spectroscopy. Steady-state fluorescence excitation and emission spectra were recorded on an Edinburgh Instruments FS5 spectrofluorometer using 10 mm path length quartz cuvettes with four transparent polished faces (Starna Cells, type: 3-Q-10), and were analyzed using Fluoracle software (Edinburgh Instruments). For **P(NB-PEG)$_{11}$-*b*-P(NB-ACM)$_{m}$-*b*-P(NB-MEG)$_{n}$** triblock copolymer nano-objects $\lambda_{\mathrm{ex.}}$ = 360 nm and $\lambda_{\mathrm{em.}}$ = 485 nm were selected, whereas for **P(NB-PEG)$_{11}$-*b*-**

P(NB-RhB)$_{m/2}$-*b*-P(NB-MEG)$_n$ triblock copolymer nano-objects $\lambda_{ex.}$ = 360 nm and $\lambda_{em.}$ = 590 nm were selected (slit width ex. = 2.5 nm, slit width em. = 2.5 nm).

Fluorescence Lifetime Spectroscopy. Time-correlated single photon counting (TCSPC) was employed to obtain all fluorescence lifetime (FL) spectra. FL spectra of **P(NB-PEG)$_{11}$-*b*-P(NB-ACM)$_m$-*b*-P(NB-MEG)$_n$** triblock copolymer nano-objects at 10-fold dilution and mixed samples at 5-fold dilution (**NB-ACM**/**NB-RhB** molar ratio 2:1) were recorded on an Edinburgh Instruments FS5 spectrofluorometer equipped with 375 ± 10 nm ps pulsed diode laser source (PicoQuant) using 10 mm path length quartz cuvettes with four transparent polished faces (Starna Cells, type: 3-Q-10). In all cases, fluorescence emission was monitored at $\lambda_{em.}$ = 485 nm. Instrument response functions (IRF) were determined from scattering signal of a Ludox HS-40 colloidal silica solution (10% w/w particles in water). Pulse frequency was 2.5 MHz, and maximum power was 5 mW (attenuated by variable neutral density filters to prevent count pile up and maintain counting rates below 25 kcps). Analysis was performed on Fluoracle software (Edinburgh Instruments). All IRF deconvolved exponential fits were performed with the 3 or 4 exponents selected for completeness of fit as determined by bootstrap Chi-square analysis in Fluoracle using the following equations:

Exponential model function:

$$S(t) = \int_0^t E(t')R(t-t')dt'$$

S(t): Measured fluorescence decay;

E(t'): Measured instrumental response function;

R(t - t'): Theoretical sample decay model function;

$$R(t) = A_1 exp\left\{-\frac{t}{\tau_1}\right\} + A_2 exp\left\{-\frac{t}{\tau_2}\right\} + A_3 exp\left\{-\frac{t}{\tau_3}\right\}$$

Reduced Chi-square:

$$\chi^2 = \sum_k W_k^2 \frac{(F_k - S_k)^2}{N}$$

W_k: Weighting factors for the individual data points;

S_k: Measurement data points;

F_k: Data points of the fitted curve;

N: The number of the free parameters which is approximately the number of fitted data points subtracted by the number of lifetime parameters used in the fit.

Intensity-average fluorescence lifetime ($\tau_{Av,I}$) and amplitude-average fluorescence lifetime ($\tau_{Av,A}$) values were determined from the fitting parameters according to the following equations:

$$\tau_{\mathrm{Av,I}} = \frac{\sum A_i \tau_i^2}{\sum A_i \tau_i}$$

$$\tau_{\mathrm{Av,A}} = \frac{\sum A_i \tau_i}{\sum A_i}$$

Synthetic Methods

Synthesis of *exo*-Norbornene imide aminochloromaleimide (NB-ACM)

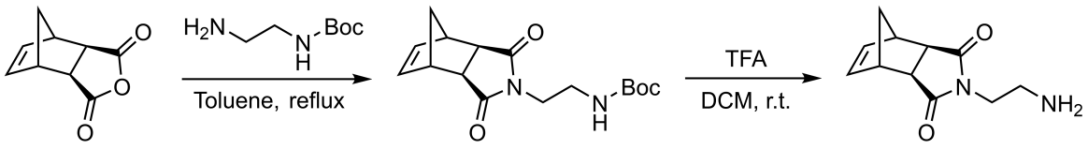

1 **2**

The synthesis of the amino-functionalized norbornene imide precursor **2** was carried out according to a previously described process.[5] First, to a solution of *cis*-5-norbornene-*exo*-2,3-dicarboxylic anhydride (1.0 g, 6.08 mmol, 1 eq) in 40 mL of dry toluene was added *N*-Boc-ethylenediamine (1.17 g, 7.30 mmol, 1.2 eq) in 5 mL of dry toluene. The flask was fitted with a Dean-Stark trap and the reaction mixture was heated at reflux for 18 h. Upon cooling to room temperature, the reaction mixture was washed with 1 M HCl (×3) followed by sat. $NaHCO_3$ (×1). The organic layer was dried over Na_2SO_4, filtered and concentrated to dryness under reduced pressure to afford a light brown solid as the pure product **1** (1.33 g, 72%). ^{1}H-NMR (400 MHz, $CDCl_3$): δ (ppm) 6.29 (t, 2H), 3.69 – 3.56 (m, 2H), 3.35 (q, 2H), 3.28 (p, 2H), 2.70 (d, 2H), 1.53 – 1.51 (d, 1H), 1.42 (s, 9H), 1.27 – 1.25 (d, 1H). ^{13}C-NMR (400 MHz, $CDCl_3$): δ (ppm) 178.2, 155.9, 137.8, 79.5, 47.9, 45.2, 42.9, 39.1, 38.5, 28.3. MS: m/z $[M+Na]^+$ calc. 329.14 g mol^{-1}, exp. 329.16 g mol^{-1}.

Next, the *N*-Boc protected amino *exo*-norbornene imide **1** (1.0 g, 3.2 mmol) was dissolved in a 1:1 TFA:CH_2Cl_2 solution (50 mL) and stirred at room temperature for 4 h. The reaction mixture was concentrated to dryness under reduced pressure to afford a brown residue that was precipitated by the addition of diethyl ether. Removal of the solvent resulted to isolation of the amino deprotected product **2** as a white solid (0.65 g, 98%). ^{1}H-NMR (400 MHz, methanol-d_4): δ (ppm) 6.24 (t, 2H), 4.76 (s, 4H), 3.69 (t, 2H), 3.15 – 3.09 (m, 2H), 3.05 (t, 2H), 2.68 (d, 2H), 1.41 – 1.39 (d, 1H), 1.17 – 1.14 (d, 1H). ^{13}C-NMR (400 MHz, methanol-d_4): δ (ppm) 178.5, 137.6, 45.0, 42.3, 37.7, 35.6. MS: m/z $[M+H]^+$ calc. 207.11 g mol^{-1}, exp. 207.12 g mol^{-1}.

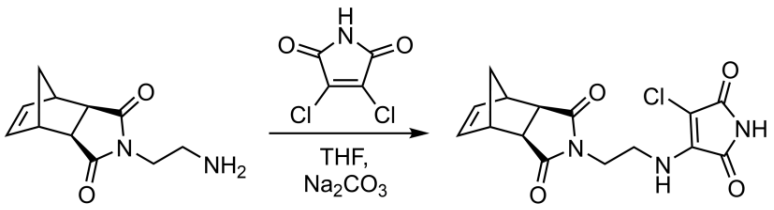

2 **3 (NB-ACM)**

The synthesis of *exo*-norbornene imide aminochloromaleimide (**NB-ACM**) monomer was performed according to a previously reported protocol by our group with slight modification.[6] 2,3- dichloromaleimide (0.5 g, 3.0 mmol, 1 eq), sodium carbonate (0.8 g, 7.5 mmol, 2.5 eq) and amino *exo*-norbornene imide **2** (0.65 g, 3.15 mmol, 1.05 eq) were dissolved in THF (25 mL) at room temperature. Consumption of 2,3-dichloromaleimide was monitored by TLC and the reaction was completed within 30 min. The solvent was then evaporated under reduced pressure and the residue was taken up with 100 mL of CH_2Cl_2. The resulting solution was washed with H_2O (2 × 100 mL) and dried over Na_2SO_4. The crude product was further purified *via* column chromatography using silica gel as the stationary phase and a mixture of petroleum ether/ethyl acetate 1:1 as the eluent to afford the pure product **3** (**NB-ACM**) as a yellow solid (0.47 g, 45%). ^{1}H-NMR (400 MHz, $CDCl_3$): δ (ppm) 7.03 (br s, 1H), 6.30 (t, 2H), 5.69 (br s, 1H), 3.82 (m, 4H), 3.29 (s, 2H), 2.75 (s, 2H), 1.55 – 1.52 (d, 1H), 1.17 – 1.14 (d, 1H). ^{13}C-NMR (400 MHz, $CDCl_3$): δ (ppm) 178.3, 166.4, 164.5, 140.7, 137.8, 48.0, 45.3, 42.9, 42.0, 38.5. HRMS: m/z $[M+H]^+$ calc. 336.0746 g mol^{-1}, exp. 336.0743 g mol^{-1}.

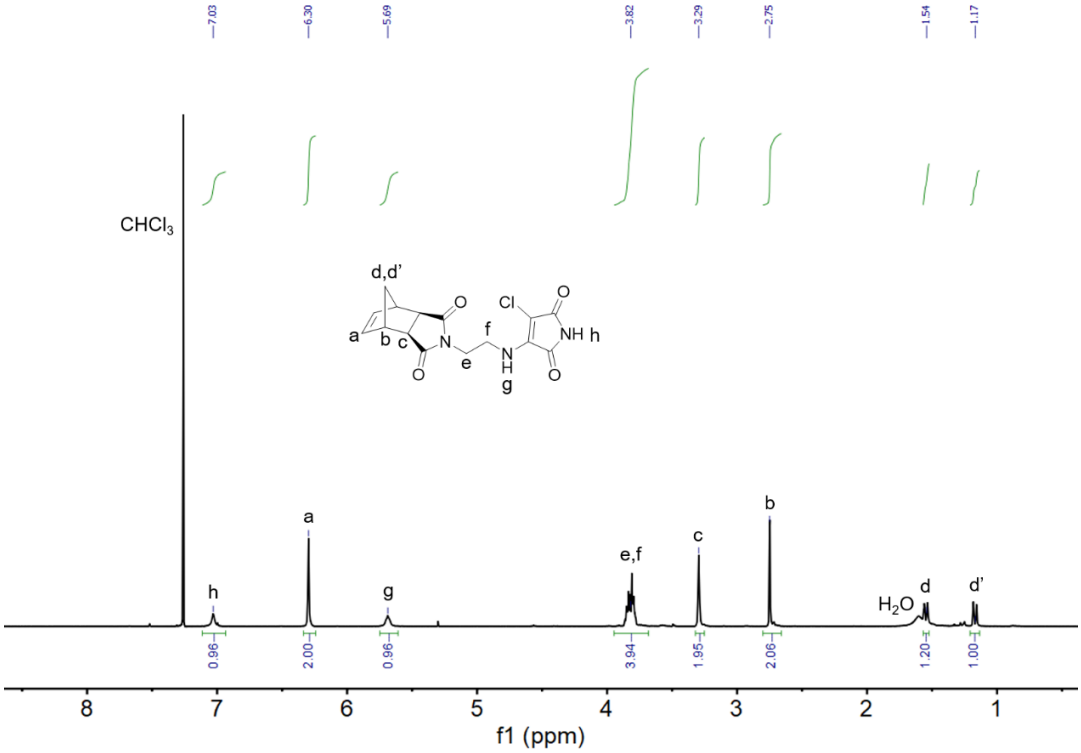

Figure S2. ^{1}H-NMR spectrum of *exo*-norbornene imide aminochloromaleimide (**NB-ACM**) in $CDCl_3$.

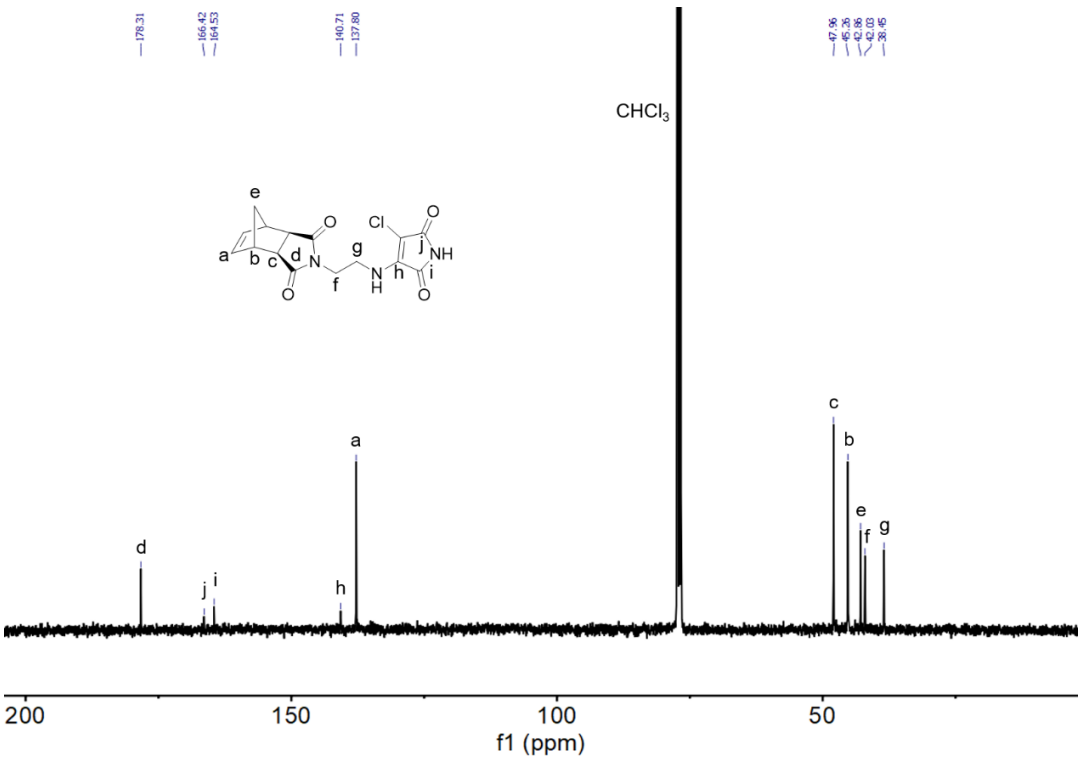

Figure S3. ^{13}C-NMR spectrum of *exo*-norbornene imide aminochloromaleimide (**NB-ACM**) in $CDCl_3$.

Synthesis of *exo*-Norbornene imide Rhodamine B (NB-RhB)

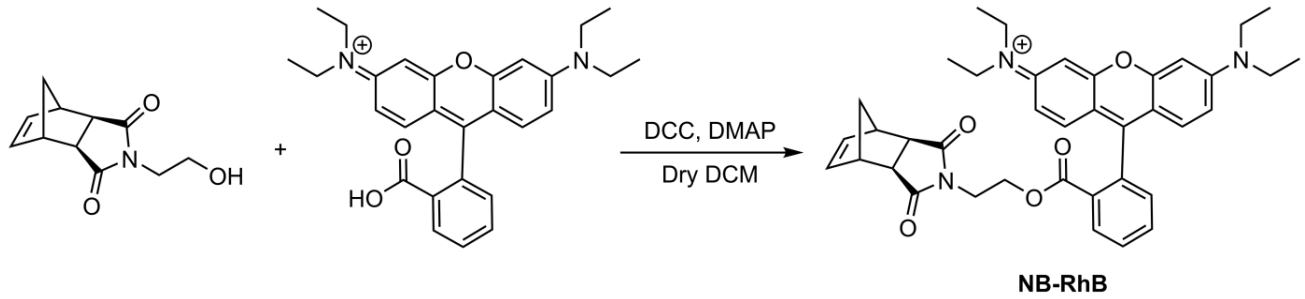

NB-RhB

The synthesis of *exo*-norbornene imide rhodamine B (**NB-RhB**) monomer was performed according to a previously described process with slight modification.[7] *exo*-Norbornene imide alcohol (205 mg, 1 mmol, 1 eq), rhodamine B (985 mg, 2 mmol, 2 eq) and DMAP (30.5 mg, 0.25 mmol. 0.25 eq) were dissolved in 10 mL of anhydrous DCM under a nitrogen atmosphere. A solution of DCC (412 mg, 2 mmol, 2 eq) in 5 mL of anhydrous DCM was added dropwise to the reaction mixture over a period of 30 min. The mixture was stirred for 24 h at room temperature, concentrated under reduced pressure, and purified *via* column chromatography using silica gel as the stationary phase and a mixture of CH_2Cl_2/MeOH 90:10 as the eluent to to afford the pure product of **NB-RhB** as a a purple solid (0.28 g, 45%). ^{1}H-NMR (400 MHz, $CDCl_3$): δ (ppm) 8.17 (d, 1H), 7.82 (t, 1H), 7.72 (t, 1H), 7.29 (d, 1H), 7.04 (d, 2H), 6.90 (m, 2H), 6.79 (d, 2H), 6.27 (s, 2H), 4.21 (t, 2H), 3.70 (t, 2H), 3.62 (q, 8H), 3.23 (s, 2H), 2.67 (s, 2H), 1.48 (d, 1H), 1.31 (t, 12H), 1.23 (d, 1H). ^{13}C-NMR (400 MHz, $CDCl_3$): δ (ppm) 177.7, 164.3, 158.9, 157.8, 155.6, 137.8, 134.2, 133.5, 131.4, 131.3, 130.4, 129.0, 114.3, 113.5, 96.3, 62.1, 47.8, 46.2, 45.3, 42.7, 37.3, 12.7. HRMS: m/z $[M+H]^+$ calc. 632.3119 g mol^{-1}, exp. 632.3120 g mol^{-1}.

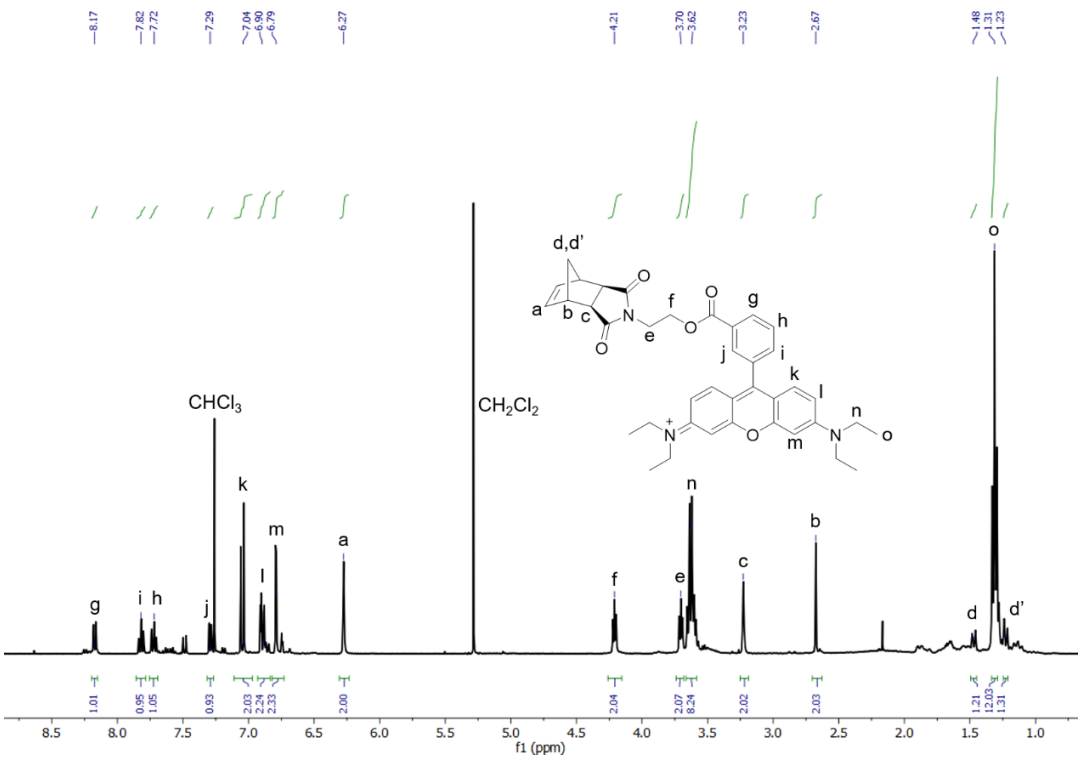

Figure S4. ^{1}H-NMR spectrum of *exo*-norbornene imide Rhodamine B (NB-RhB) in $CDCl_3$.

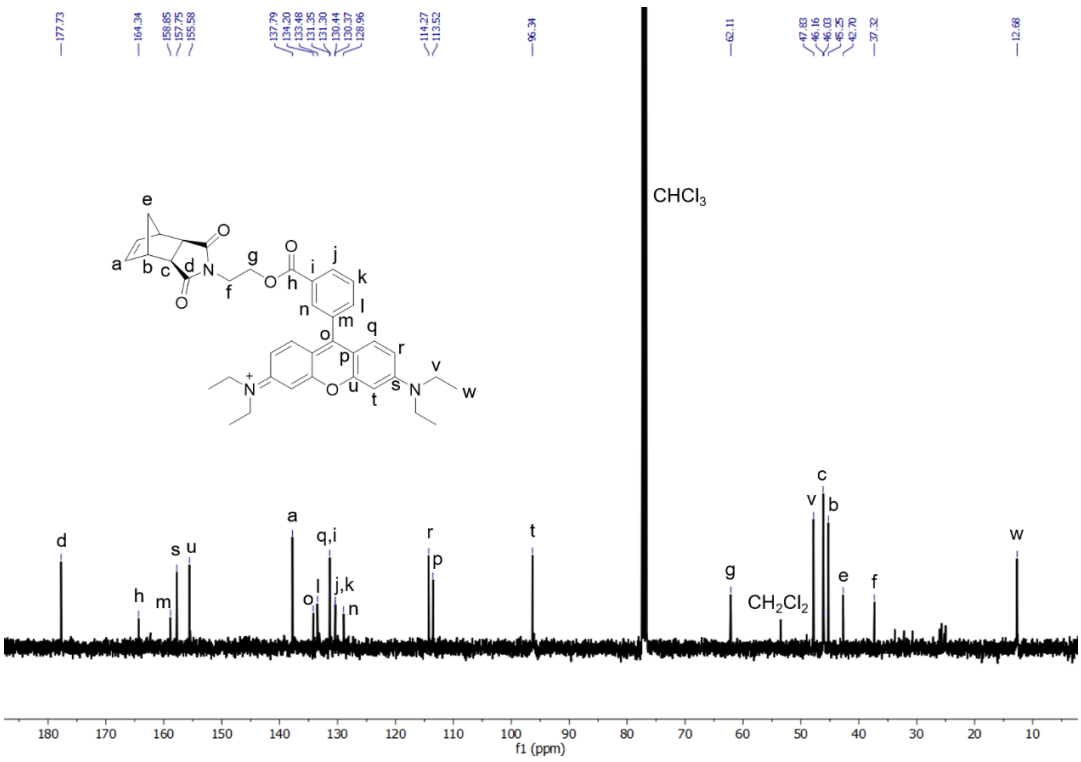

Figure S5. ^{13}C-NMR spectrum of *exo*-norbornene imide Rhodamine B (NB-RhB) in $CDCl_3$.

Synthesis of P(NB-MEG)$_{180}$ Homopolymer *via* Solution Ring-Opening Metathesis Polymerization (ROMP)

A typical procedure for the synthesis of **P(NB-MEG)$_{180}$** homopolymer *via* solution ROMP is described. A stock solution of 9.1 mg/mL of **G3** in DCM and a solution of 50 mg of **NB-MEG** in 900 μL of DCM were first prepared. Then, 100 μL of **G3** stock solution were added to the vial of **NB-MEG** monomer solution with rapid stirring and polymerization was allowed to proceed at room temperature for 1 h (final [**NB-MEG**] = 50 mg/mL, final [**G3**] = 0.91 mg/mL, [**NB-MEG**]/[**G3**] = 180). Polymerization was quenched by addition of a few drops of ethyl vinyl ether and **P(NB-MEG)$_{180}$** homopolymer was precipitated from methanol, isolated by vacuum filtration and dried under vacuum prior to ^{1}H-NMR, SEC and DSC analyses. ^{1}H-NMR (400 MHz, $CDCl_3$) $M_{n,\,theo.}$ = 39,800 g mol^{-1}. SEC (THF + 2% v/v NEt_3) $M_{n,\,SEC}$ = 41,000 g mol^{-1}, $Đ_{M,\,SEC}$ = 1.10.

Synthesis of P(NB-amine)$_{11}$-*b*-P(NB-MEG)$_n$ Diblock Copolymer Nano-Objects *via* Aqueous Ring-Opening Metathesis Polymerization-Induced Self-Assembly (ROMPISA)

A typical procedure for the synthesis of **P(NB-amine)$_{11}$-*b*-P(NB-MEG)$_n$** (n = 60, 120, 180, 240, 300, and 420) diblock copolymer nano-objects *via* aqueous dispersion ROMPISA is described.[2, 3] Three stock solutions were first prepared: (1) a solution of 21.2 mg of **NB-amine** in 100 μL of filtered THF; (2) a solution of 6.6 mg of **G3** in 100 μL of filtered THF; and (3) a 11.1 mg/mL solution of **NB-MEG** in acidic phosphate buffer (pH = 2, PB 2) in the (a) absence or (b) presence of 100 mM NaCl. Then, solution (1) was added to a vial equipped with a stir bar. Solution (2) was then added to the vial of solution (1) with rapid stirring for the synthesis of **P(NB-amine)** macroinitiator (final [**NB-amine**] = 105.8 mg/mL, final [**G3**] = 32.8 mg/mL, [**NB-amine**]/[**G3**] = 10). ^{1}H-NMR (300 MHz, DMSO-d_6) $M_{n,\,NMR}$ = 2,500 g mol^{-1}, $DP_{\mathbf{P(NB\text{-}amine)}}$ = 11. SEC (THF + 2% v/v NEt_3) $M_{n,\,SEC}$ = 2,600 g mol^{-1}, $Đ_{M,\,SEC}$ = 1.22.

After ~3 min, aliquots of 8.3, 4.2, 2.8, 2.1, 1.7, and 1.2 μL of the **P(NB-amine)$_{11}$** macroinitiator solution were transferred to six new vials equipped with 2×5 mm stir bars. The aliquots were then diluted to 50 μL total volume using filtered THF. 450 μL of either solution (3a) or (3b) were then added *via* a pipette to each of the six vials (PB/THF = 9:1, [**NB-MEG**] = 1 wt%). Each polymerization solution was thoroughly mixed following this addition by drawing up the entire volume into the pipette tip and ejecting the liquid

back into the vial (4×) and stirred at 1000 rpm for ~30 min prior to ^{1}H-NMR and SEC analyses. ROMPISA solutions at 200× dilution in DI water were further characterized by DLS analysis and TEM imaging.

Synthesis of P(NB-PEG)$_{11}$-*b*-P(NB-MEG)$_n$ Diblock Copolymer Nano-Objects *via* Aqueous Ring-Opening Metathesis Polymerization-Induced Self-Assembly (ROMPISA)

A typical procedure for the synthesis of **P(NB-PEG)$_{11}$-*b*-P(NB-MEG)$_n$** (n = 40, 60, 120, 140, 180, 240, 260, and 300) diblock copolymer nano-objects *via* aqueous dispersion ROMPISA is described.[2, 3] Three stock solutions were first prepared: (1) a solution of 44.8 mg of **NB-PEG** in 100 μL of filtered THF; (2) a solution of 6.6 mg of **G3** in 100 μL of filtered THF; and (3) a 11.1 mg/mL solution of **NB-MEG** in acidic phosphate buffer (pH = 2, PB 2). Then, solution (1) was added to a vial equipped with a stir bar. Solution (2) was then added to the vial of solution (1) with rapid stirring for the synthesis of **P(NB-PEG)** macroinitiator (final [**NB-PEG**] = 223.8 mg/mL, final [**G3**] = 32.8 mg/mL, [**NB-PEG**]/[**G3**] = 10). ^{1}H-NMR (300 MHz, DMSO-d_6) $M_{n,\,NMR}$ = 5,500 g mol^{-1}, DP$_{\mathbf{P(NB\text{-}PEG)}}$ = 11. SEC (THF + 2% v/v NEt_3) $M_{n,\,SEC}$ = 5,300 g mol^{-1}, $Đ_{M,\,SEC}$ = 1.20.

After ~3 min, aliquots of 12.5, 8.3, 4.2, 3.6, 2.8, 2.1, 1.9, and 1.7 μL of the **P(NB-PEG)$_{11}$** macroinitiator solution were transferred to eight new vials equipped with 2×5 mm stir bars. The aliquots were then diluted to 50 μL total volume using filtered THF. 450 μL of solution (3) were then added *via* a pipette to each of the eight vials (PB/THF = 9:1, [**NB-MEG**] = 1 wt%). Each polymerization solution was thoroughly mixed following this addition by drawing up the entire volume into the pipette tip and ejecting the liquid back into the vial (4×) and stirred at 1000 rpm for ~30 min prior to ^{1}H-NMR and SEC analyses. ROMPISA solutions at 200× dilution in DI water were further characterized by DLS analysis and TEM imaging. It should be noted that ROMPISA polymerizations targeting DP$_{\mathbf{P(NB\text{-}MEG)}}$ > 260 resulted in unstable nano-object solutions that precipitated out of solution during or immediately after polymerization.

Kinetic Study of P(NB-amine)$_{11}$ and P(NB-PEG)$_{11}$ Macroinitiator Syntheses *via* Solution ROMP

A typical procedure for kinetics determination of **P(NB-amine)$_{11}$** and **P(NB-PEG)$_{11}$** macroinitiator syntheses *via* solution ROMP is described. A solution of 17.6 mg of **NB-amine** (or 37.3 mg of **NB-PEG**) in 800 μL of filtered THF was first prepared in a vial equipped with a stir bar. In a second vial, 5.5 mg of **G3** were dissolved in 200 μL of filtered THF. Then, **G3** solution was added to the monomer solution vial

with rapid stirring for the synthesis of **P(NB-amine)** (or **P(NB-PEG)**) macroinitiator ([**NB-amine**]/[**G3**] = 10, [**NB-PEG**]/[**G3**] = 10). At 30 s time points over a period of 3 min, 100 μL aliquots were withdrawn from the polymerization solution and were added into vials containing a few drops of ethyl vinyl ether for polymerization quenching. Kinetic monitoring samples were diluted immediately after quenching using a stock solution of $CDCl_3$ containing a known concentration of 1,3,5-trioxane as an external standard and were analyzed by ^{1}H-NMR spectroscopy for monomer conversion calculation.

Kinetic Study of Aqueous ROMPISA for Preparation of P(NB-amine)$_{11}$-*b*-P(NB-MEG)$_{300}$ Diblock Copolymer Nano-Objects

A typical kinetic monitoring procedure for synthesis of **P(NB-amine)$_{11}$-*b*-P(NB-MEG)$_{300}$** diblock copolymer nano-objects *via* aqueous dispersion ROMPISA is described.[2, 3] Three stock solutions were first prepared: (1) a solution of 21.2 mg of **NB-amine** in 100 μL of filtered THF; (2) a solution of 6.6 mg of **G3** in 100 μL of filtered THF; and (3) a 11.1 mg/mL solution of **NB-MEG** in acidic phosphate buffer (pH = 2, PB 2). Then, solution (1) was added to a vial equipped with a stir bar. Solution (2) was then added to the vial of solution (1) with rapid stirring for the synthesis of **P(NB-amine)** macroinitiator (final [**NB-amine**] = 105.8 mg/mL, final [**G3**] = 32.8 mg/mL, [**NB-amine**]/[**G3**] = 10).

After ~3 min, an aliquot of 13.6 μL of the **P(NB-amine)** macroinitiator solution was transferred to a new vial equipped with a 2×5 mm stir bar. The aliquot was then diluted to 400 μL total volume using filtered THF. 3.6 mL of solution (3) were then added *via* a pipette to the macroinitiator vial (PB/THF = 9:1, [**NB-MEG**] = 1 wt%) and the resulting polymerization solution was thoroughly mixed following this addition by drawing up the entire volume into the pipette tip and ejecting the liquid back into the vial (4×) and stirred at 1000 rpm. At various time points over a period of 30 min, 200 μL aliquots were withdrawn from the polymerization solution and were added into vials containing a few drops of ethyl vinyl ether for polymerization quenching. Kinetic monitoring samples were diluted immediately after quenching using either (a) a stock solution of DMSO-d_6 containing a known concentration of 1,3,5-trioxane as an external standard and were analyzed by ^{1}H-NMR spectroscopy for monomer conversion calculation, (b) a solution of THF + 2% v/v NEt_3 eluent for SEC analysis, or (c) DI water for further characterization by DLS analysis and TEM imaging.

Kinetic Study of Aqueous ROMPISA for Preparation of P(NB-PEG)$_{11}$-*b*-P(NB-MEG)$_{260}$ Diblock Copolymer Nano-Objects

A typical kinetic monitoring procedure for synthesis of **P(NB-PEG)$_{11}$-*b*-P(NB-MEG)$_{260}$** diblock copolymer nano-objects *via* aqueous dispersion ROMPISA is described.[2, 3] Three stock solutions were first prepared: (1) a solution of 44.8 mg of **NB-PEG** in 100 μL of filtered THF; (2) a solution of 6.6 mg of **G3** in 100 μL of filtered THF; and (3) a 11.1 mg/mL solution of **NB-MEG** in acidic phosphate buffer (pH = 2, PB 2). Then, solution (1) was added to a vial equipped with a stir bar. Solution (2) was then added to the vial of solution (1) with rapid stirring for the synthesis of **P(NB-PEG)** macroinitiator (final [**NB-PEG**] = 223.8 mg/mL, final [**G3**] = 32.8 mg/mL, [**NB-PEG**]/[**G3**] = 10).

After ~3 min, an aliquot of 15.2 μL of the **P(NB-PEG)** macroinitiator solution was transferred to a new vial equipped with a 2×5 mm stir bar. The aliquot was then diluted to 400 μL total volume using filtered THF. 3.6 mL of solution (3) were then added *via* a pipette to the macroinitiator vial (PB/THF = 9:1, [**NB-MEG**] = 1 wt%) and the resulting polymerization solution was thoroughly mixed following this addition by drawing up the entire volume into the pipette tip and ejecting the liquid back into the vial (4×) and stirred at 1000 rpm. At various time points over a period of 30 min, 200 μL aliquots were withdrawn from the polymerization solution and were added into vials containing a few drops of ethyl vinyl ether for polymerization quenching. Kinetic monitoring samples were diluted immediately after quenching using either (a) a stock solution of DMSO-d_6 containing a known concentration of 1,3,5-trioxane as an external standard and were analyzed by ^{1}H-NMR spectroscopy for monomer conversion calculation, (b) a solution of THF + 2% v/v NEt_3 eluent for SEC analysis, or (c) DI water for further characterization by DLS analysis and TEM imaging.

Aqueous ROMPISA Monitoring *via In situ* Turbidimetric Analysis for Preparation of P(NB-amine)$_{11}$-*b*-P(NB-MEG)$_{300}$ and P(NB-PEG)$_{11}$-*b*-P(NB-MEG)$_{260}$ Diblock Copolymer Nano-Objects

A typical procedure for *in situ* turbidimetric analysis during aqueous ROMPISA for synthesis of **P(NB-amine)$_{11}$-*b*-P(NB-MEG)$_{300}$** (or **P(NB-PEG)$_{11}$-*b*-P(NB-MEG)$_{260}$**) diblock copolymer nano-objects is described. Three stock solutions were first prepared: (1) a solution of 21.2 mg of **NB-amine** (or 44.8 mg of **NB-PEG**) in 100 μL of filtered THF; (2) a solution of 6.6 mg of **G3** in 100 μL of filtered THF; and (3) a 11.1 mg/mL solution of **NB-MEG** in acidic phosphate buffer (pH = 2, PB 2). Then, solution (1) was added to a vial equipped with a stir bar. Solution (2) was then added to the vial of solution (1) with rapid

stirring for the synthesis of **P(NB-amine)** (or **P(NB-PEG)**) macroinitiator ([**NB-amine**]/[**G3**] = 10, [**NB-PEG**]/[**G3**] = 10).

After ~3 min, an aliquot of 6.8 μL of the **P(NB-amine)** (or 7.6 μL of the **P(NB-PEG)**) macroinitiator solution was transferred to a 10 mm path length quartz cuvette equipped with a 2×5 mm stir bar. The aliquot was then diluted to 200 μL total volume using filtered THF. 1.8 mL of solution (3) were then added *via* a pipette to the cuvette containing the macroinitiator solution (PB/THF = 9:1, [**NB-MEG**] = 1 wt%) and the resulting polymerization solution was thoroughly mixed following this addition by drawing up the entire volume into the pipette tip and ejecting the liquid back into the vial (4×). *In situ* ROMPISA turbidimetric analysis was performed by monitoring changes in transmittance of each polymerization solution at λ = 550 nm every 6 s over a period of 20 min at 25 °C, using a UV-Vis spectrophotometer equipped with a Peltier temperature controlling system (stir rate = 10). A solution of appropriately diluted **P(NB-amine)** (or **P(NB-PEG)**) macroinitiator in phosphate buffer at pH = 2.0 (PB 2) was used as a reference sample.

Self-Assembly of P(NB-PEG)$_{11}$-*b*-P(NB-MEG)$_{260}$ Diblock Copolymer Nano-Objects *via* Solvent-Switch

First, the synthesis of **P(NB-PEG)$_{11}$-*b*-P(NB-MEG)$_{260}$** diblock copolymer tubesomes was achieved *via* aqueous ROMPISA following the above described procedure (final [polymer] = 10 mg/mL). The sample was then centrifuged at 14,000 rpm and dried *via* lyophilization. Subsequently, 5 mg of **P(NB-PEG)$_{11}$-*b*-P(NB-MEG)$_{260}$** diblock copolymer were dissolved in 50 μL of filtered THF and stirred for 1 hour prior to slow addition of 450 μL of DI water under rapid stirring using a syringe pump at a rate of 1 mL/h for self-assembly of **P(NB-PEG)$_{11}$-*b*-P(NB-MEG)$_{260}$** diblock copolymer nano-objects under thermodynamic equilibrium (final volume ratio between water and organic solvent = 9:1). Nano-object dispersion solution at 100× dilution in DI water was further characterized by TEM imaging.

Synthesis of FAM-NHS- and Cy5-NHS-Loaded P(NB-PEG)$_{11}$-*b*-P(NB-MEG)$_{240}$ Diblock Copolymer Nano-Objects and Mixed Samples *via* Aqueous ROMPISA

A typical procedure for the synthesis of FAM-NHS- and Cy5-NHS-loaded **P(NB-PEG)$_{11}$-*b*-P(NB-MEG)$_{240}$** diblock copolymer nano-objects and their resulting mixed samples *via* aqueous dispersion ROMPISA is described. Four stock solutions were first prepared: (1) a solution of 9.3 mg of **NB-PEG** in

450 μL of filtered THF; (2) a solution of 1.4 mg of **G3** in 50 μL of filtered THF; (3) a solution of 2.0 mg/mL of FAM-NHS (a) or Cy5-NHS (b) in filtered THF; and (4) a 11.1 mg/mL solution of **NB-MEG** in acidic phosphate buffer (pH = 2, PB 2). Then, solution (1) was added to a vial equipped with a stir bar. Solution (2) was then added to the vial of solution (1) with rapid stirring for the synthesis of **P(NB-PEG)** macroinitiator ([**NB-PEG**]/[**G3**] = 10).

After ~3 min, 50 μL of either solution (3a) or (3b) were added to a new vial containing 50 μL of the resulting macroinitiator solution equipped with a 2×5 mm stir bar. 900 μL of solution (4) were then added *via* a pipette to the macroinitiator vial (PB/THF = 9:1, [**NB-MEG**] = 1 wt%) and the resulting polymerization solution was thoroughly mixed following this addition by drawing up the entire volume into the pipette tip and ejecting the liquid back into the vial (4×) and stirred at 1000 rpm for ~30 min (final [FAM-NHS] = 0.1 mg/mL (= 0.21 mM), final [Cy5-NHS] = 0.1 mg/mL (= 0.15 mM)).

Diblock copolymer samples mixed during ROMPISA were prepared upon mixing 330 μL of FAM-NHS-loaded **P(NB-PEG)$_{11}$-*b*-P(NB-MEG)$_{240}$** with 330 μL of Cy5-NHS-loaded **P(NB-PEG)$_{11}$-*b*-P(NB-MEG)$_{240}$** after 1 min of polymerization time (*ca*. ~50% **NB-MEG** conversion) into a new vial equipped with a 2×5 mm stir bar and stirring at 1000 rpm for ~30 min.

Pure and mixed samples were subsequently dialysed against DI water (dialysis membrane MWCO = 3.5 kDa) for approximately 14 h for removal of non-encapsulated dye molecules (final pH value of each solutions was ~7.0) prior to TEM and confocal microscopy imaging.

Synthesis of P(NB-PEG)$_{11}$-*b*-P(NB-ACM)$_m$-*b*-P(NB-MEG)$_n$ and P(NB-PEG)$_{11}$-*b*-P(NB-RhB)$_{m/2}$-*b*-P(NB-MEG)$_n$ Triblock Copolymer Nano-Objects and Mixed Samples *via* Aqueous ROMPISA

A typical procedure for the synthesis of **P(NB-PEG)$_{11}$-*b*-P(NB-ACM)$_m$-*b*-P(NB-MEG)$_n$** and **P(NB-PEG)$_{11}$-*b*-P(NB-RhB)$_{m/2}$-*b*-P(NB-MEG)$_n$** (m = 0.12, n = 120, and m = 0.24, n = 240) triblock copolymer nano-objects and their resulting mixed samples *via* aqueous dispersion ROMPISA is described. For the synthesis of triblock copolymers with DP$_{\mathbf{P(NB\text{-}MEG)}}$ = 120, four stock solutions were first prepared: (1) a solution of 18.7 mg of **NB-PEG** in 850 μL of filtered THF; (2) a solution of 2.7 mg of **G3** in 100 μL of filtered THF; (3) a solution of 3.0 mg/mL of **NB-ACM** (or 2.8 mg/mL of **NB-RhB**) in filtered THF; and (4) a 11.1 mg/mL solution of **NB-MEG** in acidic phosphate buffer (pH = 2, PB 2). Then, solution (1) was added to a vial equipped with a stir bar. Solution (2) was then added to the vial of solution (1) with rapid stirring for the synthesis of **P(NB-PEG)** macroinitiator ([**NB-PEG**]/[**G3**] = 10). After ~3 min, 50 μL of

solution (3) were added to the macroinitiator vial and stirred at 500 rpm for synthesis of **P(NB-PEG)$_{11}$-*b*-P(NB-ACM)$_{m}$** (or **P(NB-PEG)$_{11}$-*b*-P(NB-RhB)$_{m/2}$**) diblock macroinitiator ([**NB-ACM**]/[**G3**] = 0.12, [**NB-RhB**]/[**G3**] = 0.06, **NB-ACM**/**NB-RhB** molar ratio = 2:1).

For the synthesis of triblock copolymers with DP$_{\mathbf{P(NB\text{-}MEG)}}$ = 240, four stock solutions were first prepared: (1) a solution of 9.3 mg of **NB-PEG** in 850 μL of filtered THF; (2) a solution of 1.4 mg of **G3** in 100 μL of filtered THF; (3) a solution of 3.0 mg/mL of **NB-ACM** (or 2.8 mg/mL of **NB-RhB**) in filtered THF; and (4) a 11.1 mg/mL solution of **NB-MEG** in acidic phosphate buffer (pH = 2, PB 2). Then, solution (1) was added to a vial equipped with a stir bar. Solution (2) was then added to the vial of solution (1) with rapid stirring for the synthesis of **P(NB-PEG)** macroinitiator ([**NB-PEG**]/[**G3**] = 10). After ~3 min, 50 μL of solution (3) were added to the macroinitiator vial and stirred at 500 rpm for synthesis of **P(NB-PEG)$_{11}$-*b*-P(NB-ACM)$_{m}$** (or **P(NB-PEG)$_{11}$-*b*-P(NB-RhB)$_{m/2}$**) diblock macroinitiator ([**NB-ACM**]/[**G3**] = 0.24, [**NB-RhB**]/[**G3**] = 0.12, **NB-ACM**:**NB-RhB** molar ratio = 2:1).

After ~3 min, an aliquot of 100 μL of the **P(NB-PEG)$_{11}$-*b*-P(NB-ACM)$_{m}$** (or **P(NB-PEG)$_{11}$-*b*-P(NB-RhB)$_{m/2}$**) diblock macroinitiator solution was transferred to a new vial equipped with a 2×5 mm stir bar. 900 μL of solution (4) were then added *via* a pipette to the macroinitiator vial (PB/THF = 9:1, [**NB-MEG**] = 1 wt%) and the resulting polymerization solution was thoroughly mixed following this addition by drawing up the entire volume into the pipette tip and ejecting the liquid back into the vial (4×) and stirred at 1000 rpm for ~30 min prior to ^{1}H-NMR and SEC analyses. ROMPISA solutions at 200× dilution in DI water were further characterized by DLS analysis and TEM imaging.

Triblock copolymer samples mixed during ROMPISA were prepared upon mixing 330 μL of **P(NB-PEG)$_{11}$-*b*-P(NB-ACM)$_{m}$-*b*-P(NB-MEG)$_{n}$** with 330 μL of **P(NB-PEG)$_{11}$-*b*-P(NB-RhB)$_{m/2}$-*b*-P(NB-MEG)$_{n}$** (m = 0.12, n = 120, and m = 0.24, n = 240) after 1 min of polymerization time (*ca*. ~50% **NB-MEG** conversion) into a new vial equipped with a 2×5 mm stir bar and stirring at 1000 rpm for ~30 min.

Supplementary Characterization Data for P(NB-MEG)$_{180}$ Homopolymer

Table S1. Molecular characteristics of **P(NB-MEG)$_{180}$** homopolymer prepared *via* ROMP in DCM, as determined by ^{1}H-NMR spectroscopy and SEC analysis.

[NB-MEG]/[G3]	% Conv.[a]	$M_{n,\,theo.}$ (kDa)[b]	$M_{n,\,SEC}$ (kDa)[c]	$Đ_{M,\,SEC}$[c]
180	>99	39.8	41.0	1.10

[a]Monomer conversion calculated from ^{1}H-NMR spectroscopy in $CDCl_3$. [b]Calculated from conversion. [c]*M*n and $Đ_M$ values calculated from PS standards using THF + 2% v/v NEt_3 as the eluent.

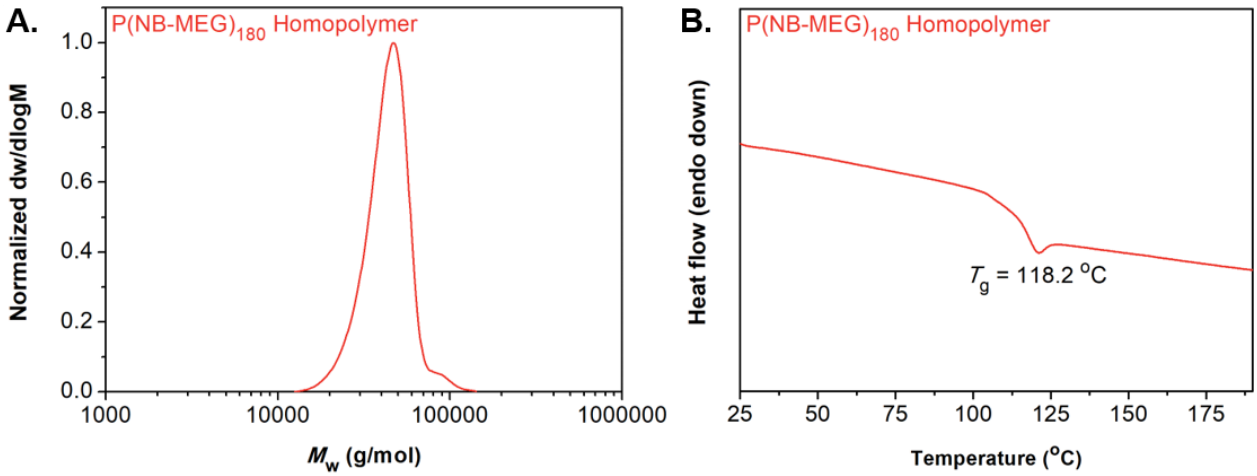

Figure S6. (A) Normalized SEC RI molecular weight distribution for **P(NB-MEG)$_{180}$** homopolymer. (B) DSC thermogram of **P(NB-MEG)$_{180}$** homopolymer (heating rate 10 °C/min). The endothermic peak observed at *ca*. 118.2 °C corresponds to the T_g of the polymer.

Supplementary Characterization Data for P(NB-amine)$_{11}$-*b*-P(NB-MEG)$_n$ Diblock Copolymer Nano-Objects Developed by Aqueous ROMPISA

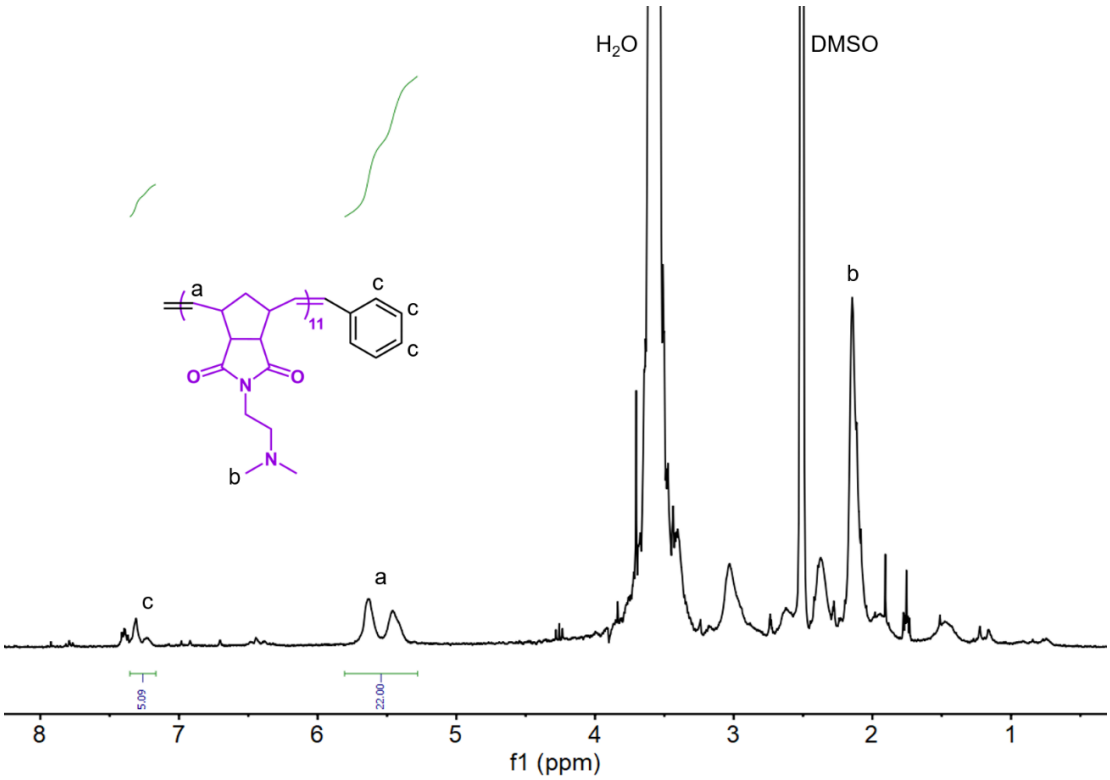

Figure S7. ^{1}H-NMR spectrum of **P(NB-amine)$_{11}$** macroinitiator in DMSO-d_6.

Table S2. Molecular characteristics of **P(NB-amine)$_{11}$** macroinitiator prepared *via* ROMP in THF, as determined by ^{1}H-NMR spectroscopy and SEC analysis.

[NB-amine]/[G3]	% Conv.[a]	$M_{n,\,theo.}$ (kDa)[b]	$M_{n,\,NMR}$ (kDa)[c]	$M_{n,\,SEC}$ (kDa)[d]	$Đ_{M,\,SEC}$[d]
10	>99	2.3	2.5	2.6	1.22

[a]Monomer conversion calculated from ^{1}H-NMR spectroscopy in DMSO-d_6. [b]Calculated from conversion. [c]Calculated using end group analysis from ^{1}H-NMR spectroscopy. [d]Mn and $Đ_M$ values calculated from PS standards using THF + 2% v/v NEt_3 as the eluent.

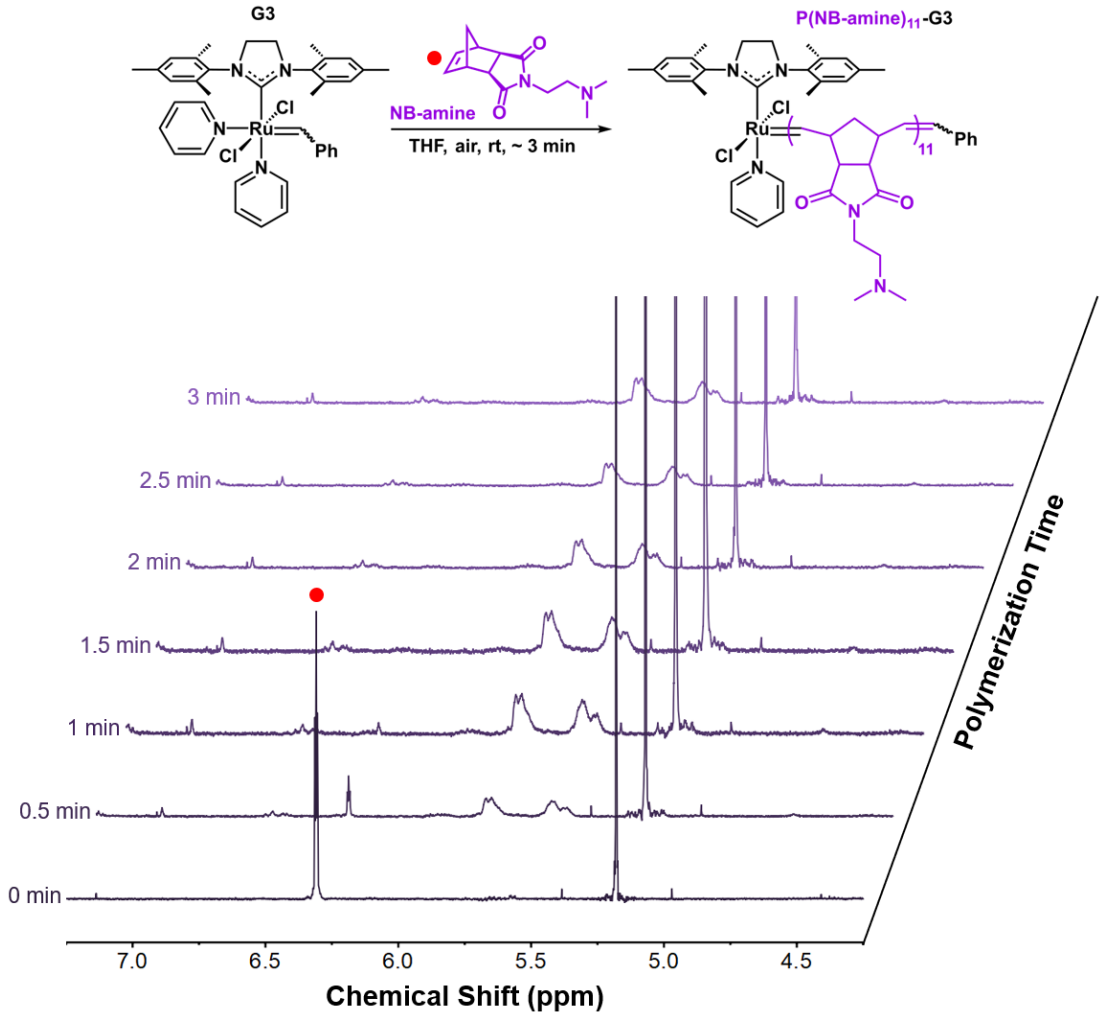

Figure S8. Stacked ^{1}H-NMR spectra obtained during kinetic monitoring of **P(NB-amine)$_{11}$** macroinitiator synthesis *via* solution ROMP as a function of polymerization time (solvent: $CDCl_3$ + 1,3,5-trioxane). The red circle denotes the **NB-amine** monomer peak at 6.30 ppm.

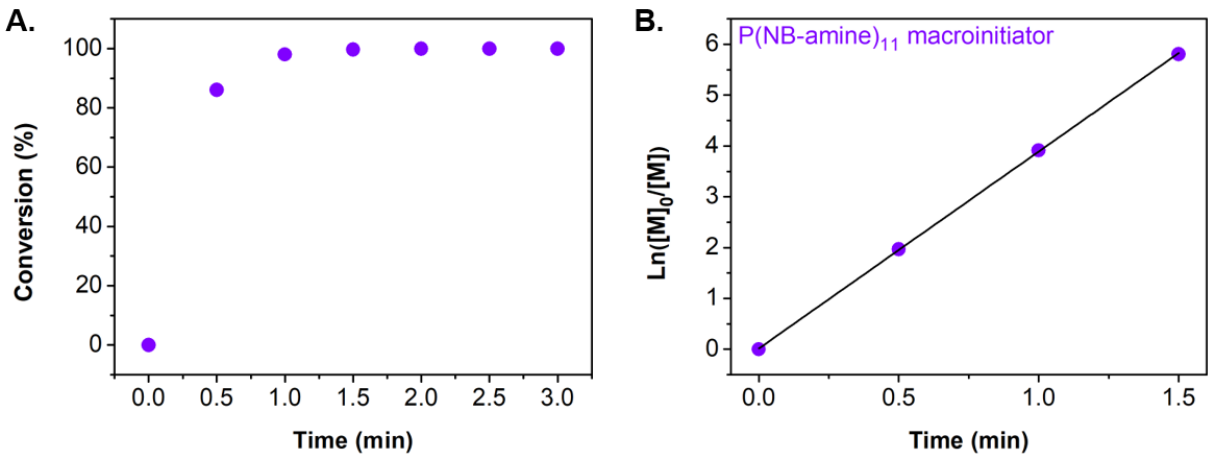

Figure S9. (A) Monomer conversion *vs*. polymerization time, and (B) ln([M]$_0$/[M]) *vs*. polymerization time kinetic plots for synthesis of **P(NB-amine)$_{11}$** macroinitiator *via* solution ROMP, as determined by ^{1}H-NMR spectroscopy in $CDCl_3$ + 1,3,5-trioxane.

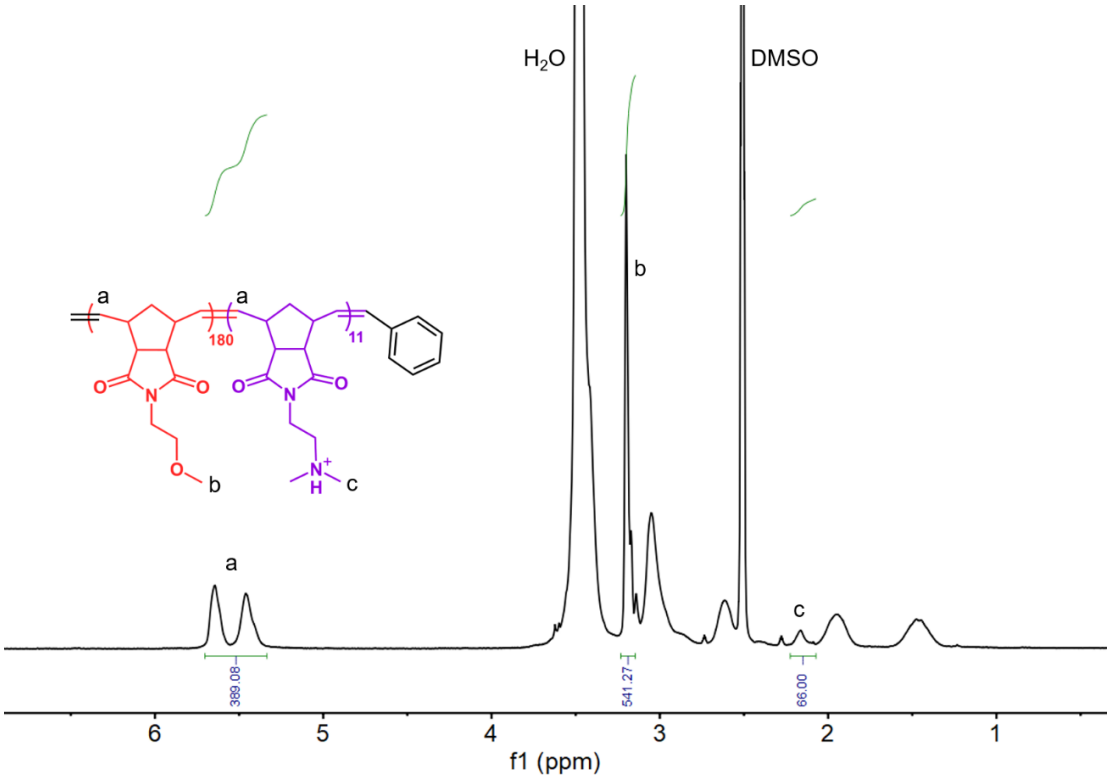

Figure S10. ^{1}H-NMR spectrum of **P(NB-amine)$_{11}$-*b*-P(NB-MEG)$_{180}$** diblock copolymer in DMSO-d_6.

Table S3. Molecular characteristics of **P(NB-amine)$_{11}$-*b*-P(NB-MEG)$_n$** diblock copolymers prepared *via* aqueous ROMPISA using different initial [**NB-MEG**]/[**G3**] ratios, as determined by ^{1}H-NMR spectroscopy and SEC analysis.

[NB-MEG]/[G3]	% Conv.[a]	$M_{n,\,theo.}$ (kDa)[b]	$M_{n,\,SEC}$ (kDa)[c]	$Đ_{M,\,SEC}$[c]
60	>99	15.8	16.2	1.14
120	>99	29.1	27.3	1.12
180	>99	42.4	35.5	1.12
240	>99	55.6	41.0	1.12
300	>99	68.9	48.8	1.12
420	>99	95.4	75.3	1.13

[a]Monomer conversion calculated from ^{1}H-NMR spectroscopy in DMSO-d_6. [b]Calculated from conversion. [c]Mn and $Đ_M$ values calculated from PS standards using THF + 2% v/v NEt$_3$ as the eluent.

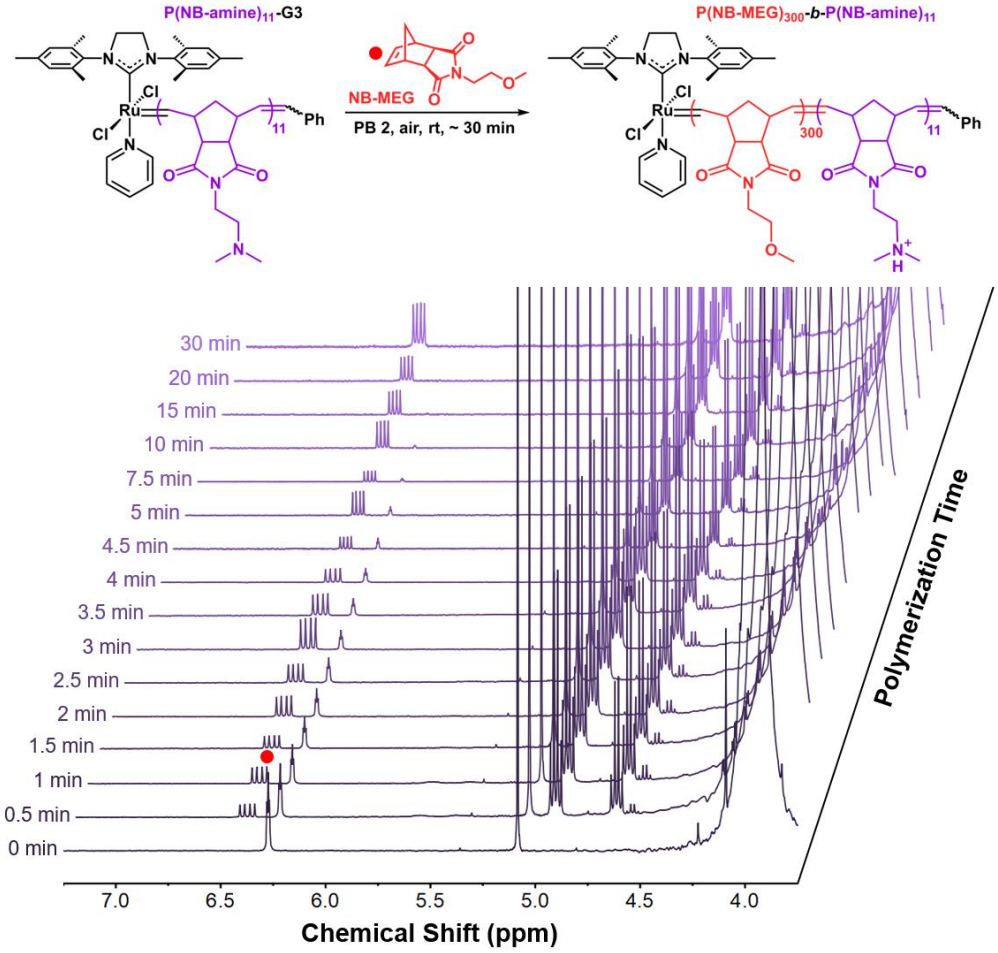

Figure S11. Stacked ^{1}H-NMR spectra obtained during kinetic monitoring of **P(NB-amine)$_{11}$-*b*-P(NB-MEG)$_{300}$** diblock copolymer synthesis *via* aqueous ROMPISA as a function of polymerization time (solvent: DMSO-d_6 + 1,3,5-trioxane). The red circle denotes the **NB-MEG** monomer peak at 6.28 ppm.

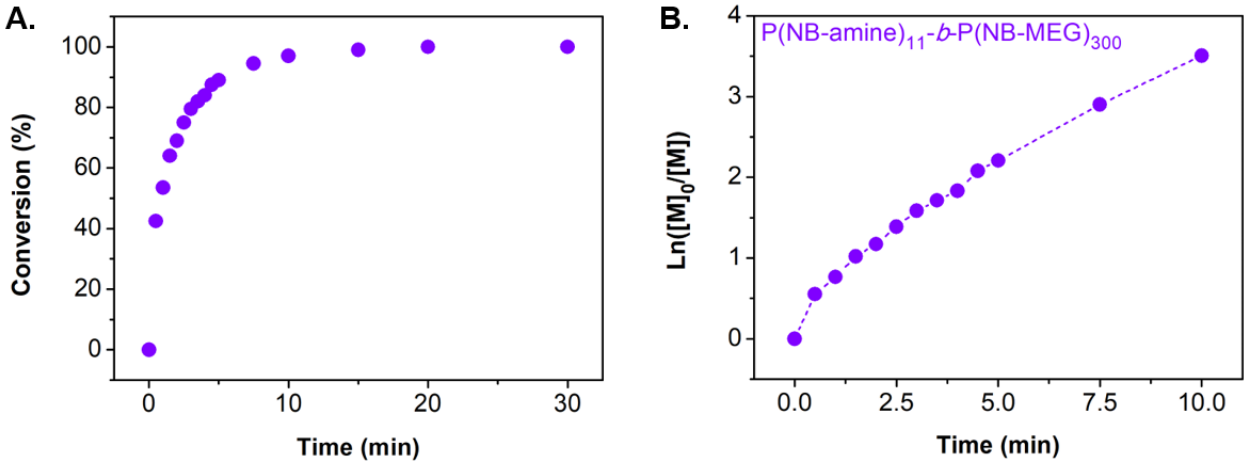

Figure S12. (A) Monomer conversion *vs*. polymerization time, and (B) ln([M]$_0$/[M]) *vs*. polymerization time kinetic plots for synthesis of **P(NB-amine)$_{11}$-*b*-P(NB-MEG)$_{300}$** diblock copolymers *via* aqueous ROMPISA, as determined by ^{1}H-NMR spectroscopy in DMSO-d_6 + 1,3,5-trioxane.

Table S4. Evolution of molecular characteristics with increasing **NB-MEG** conversion for **P(NB-amine)$_{11}$-*b*-P(NB-MEG)$_{300}$** diblock copolymers prepared *via* aqueous ROMPISA, as determined by ^{1}H-NMR spectroscopic and SEC kinetic analysis.

% Conv.[a]	**Calc. DP**[b]	$M_{n,\,theo.}$ **(kDa)**[b]	$M_{n,\,SEC}$ **(kDa)**[c]	$Đ_{M,\,SEC}$[c]
42.5	128	30.9	28.4	1.05
64	192	45.0	41.7	1.06
79.5	239	55.4	51.0	1.06
87.5	263	60.7	55.9	1.06
100	300	68.9	63.2	1.07

[a]Monomer conversion calculated from ^{1}H-NMR spectroscopy in DMSO-d_6 + 1,3,5-trioxane. [b]Calculated from conversion. [c]*M*n and $Đ_M$ values calculated from PS standards using THF + 2% v/v NEt$_3$ as the eluent.

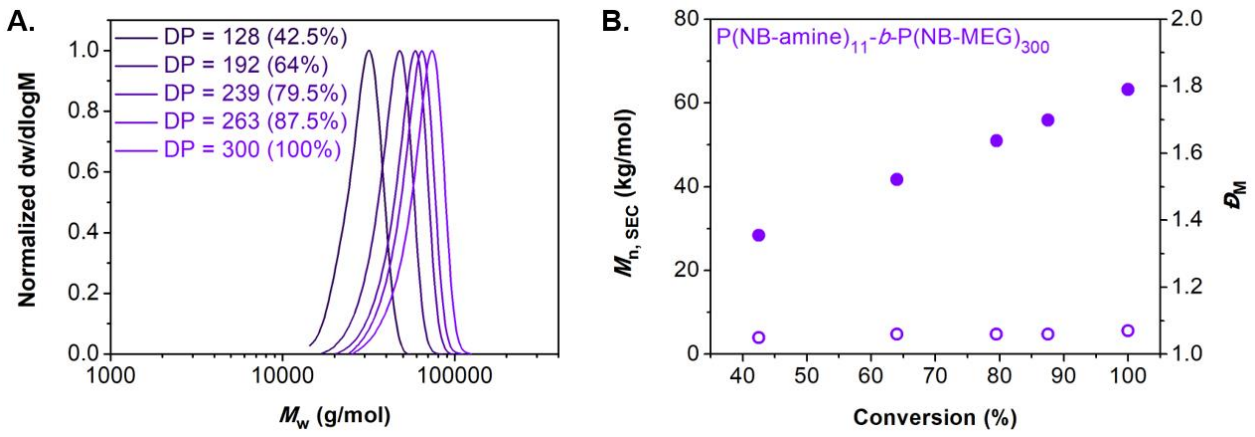

Figure S13. (A) Normalized SEC RI molecular weight distributions, and (B) evolution of M_n (filled circles) and $Đ_M$ (empty circles) values with increasing **NB-MEG** conversion calculated from SEC kinetic analysis for synthesis of **P(NB-amine)$_{11}$-*b*-P(NB-MEG)$_{300}$** diblock copolymers *via* aqueous ROMPISA. M_n and $Đ_M$ values were calculated from PS standards using THF + 2% v/v NEt_3 as the eluent.

Table S5. Summary of D_h, PD and zeta potential values and observed morphologies for **P(NB-amine)$_{11}$-*b*-P(NB-MEG)$_n$** diblock copolymer nano-objects prepared *via* aqueous ROMPISA, as determined by DLS, microelectrophoretic analysis and dry-state TEM imaging, respectively.

[NB-MEG] /[G3]	D_h (nm)[a]	PD[a]	Intensity-average D_h (nm)[a]	Zeta potential (mV)[b]	Morphology[c]
60	123.6 ± 22.8	0.21 ± 0.02	152.2 ± 83.2	+ 24.25 ± 3.11	W+V
120	41.9 ± 1.1	0.21 ± 0.03	38.6 ± 0.6	+ 21.28 ± 1.81	W+V
180	47.8 ± 1.7	0.23 ± 0.02	43.8 ± 1.1	+ 25.03 ± 0.91	V
240	59.9 ± 0.3	0.28 ± 0.06	52.7 ± 3.1	+ 21.37 ± 2.51	V
300	61.4 ± 1.2	0.25 ± 0.02	54.6 ± 0.8	+ 25.17 ± 0.66	V
420	83.2 ± 0.9	0.21 ± 0.01	84.7 ± 1.6	+ 28.13 ± 2.35	ill-defined V + T

[a]D_h and PD values measured from DLS analysis (the error shows the standard deviation from 4 repeat measurements). [b]Zeta potential values measured from microelectrophoretic analysis at pH = 2.0, using PB 2 (the error shows the standard deviation from at least 3 repeat measurements). [c]Morphologies observed from dry-state TEM imaging, using 1 wt% uranyl acetate (UA) solution for staining (Key: W – worm-like micelles, V – vesicles, T – tubesomes).

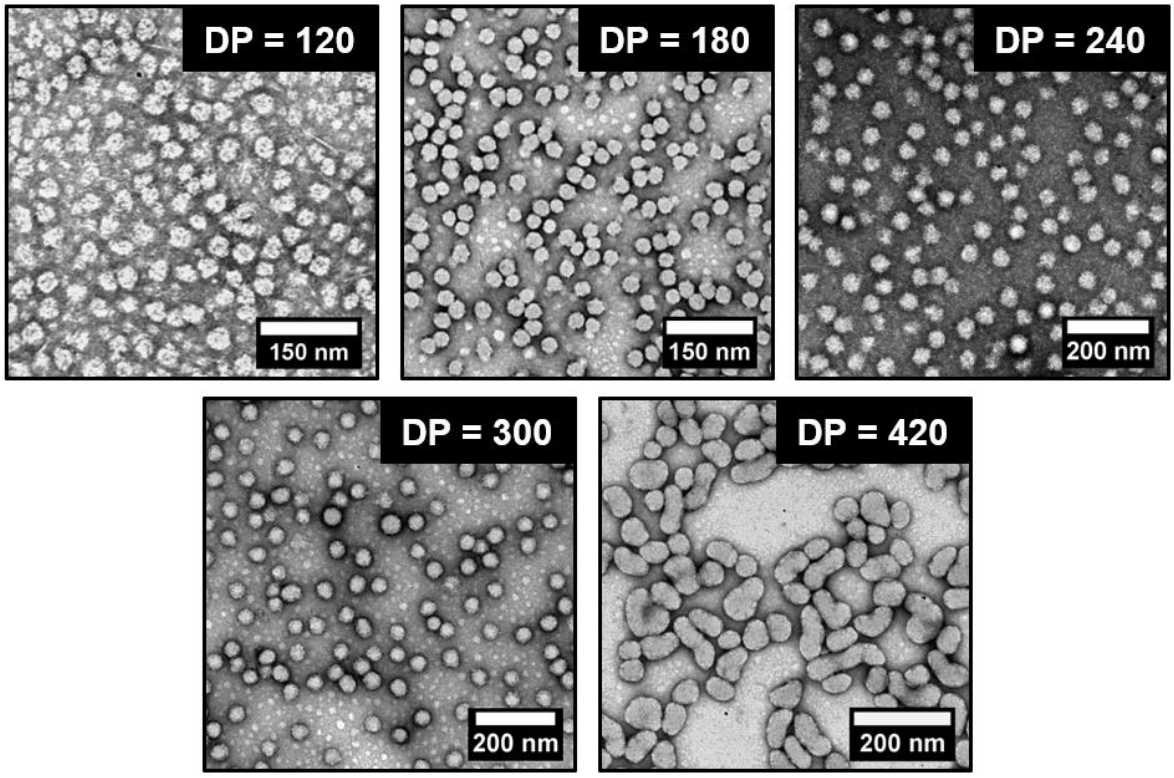

Figure S14. Representative dry-state TEM images of **P(NB-amine)$_{11}$-*b*-P(NB-MEG)$_n$** (n = 120, 180, 240, 300, and 420) diblock copolymer nano-objects developed *via* aqueous ROMPISA, stained with 1 wt% UA solution.

P(NB-amine)$_{11}$-*b*-P(NB-MEG)$_{180}$

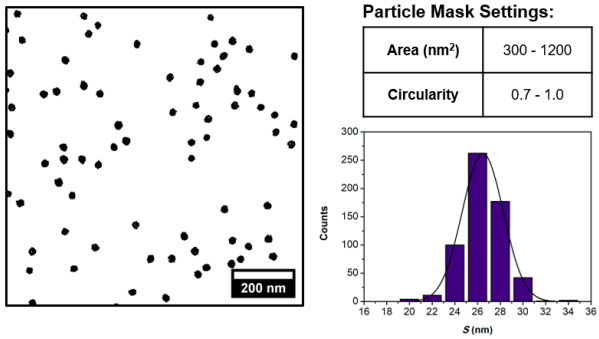

Particles Analyzed	D_{ave} (nm)	C_{ave}	Non-Spherical Fraction	S_{ave} (nm)	L_{ave} (nm)
599	26.5 ± 1.8	0.79 ± 0.04	N/A	26.5 ± 1.8	N/A

P(NB-amine)$_{11}$-*b*-P(NB-MEG)$_{240}$

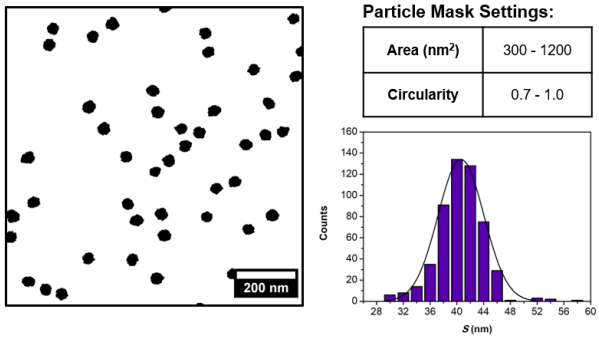

Particles Analyzed	D_{ave} (nm)	C_{ave}	Non-Spherical Fraction	S_{ave} (nm)	L_{ave} (nm)
527	40.6 ± 3.4	0.75 ± 0.04	N/A	40.6 ± 3.4	N/A

P(NB-amine)$_{11}$-*b*-P(NB-MEG)$_{300}$

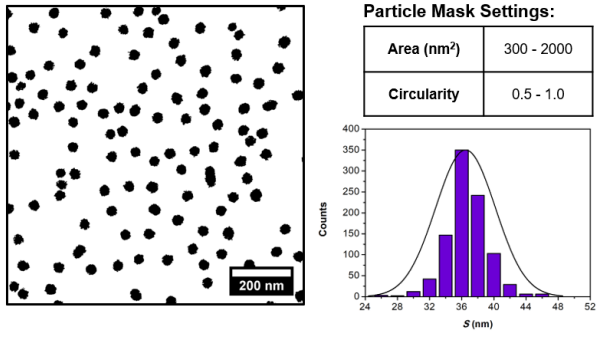

Particles Analyzed	D_{ave} (nm)	C_{ave}	Non-Spherical Fraction	S_{ave} (nm)	L_{ave} (nm)
949	36.7 ± 2.6	0.64 ± 0.07	0.01	36.4 ± 3.9	36.8 ± 1.8

P(NB-amine)$_{11}$-*b*-P(NB-MEG)$_{420}$

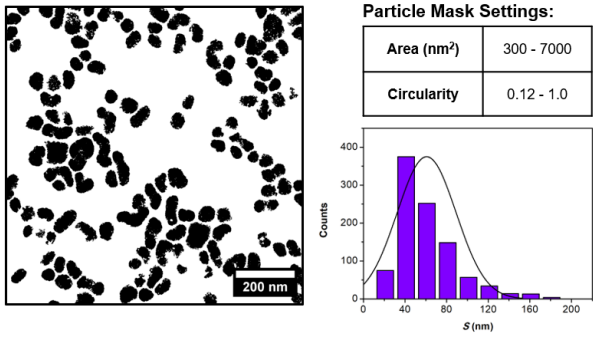

Particles Analyzed	D_{ave} (nm)	C_{ave}	Non-Spherical Fraction	S_{ave} (nm)	L_{ave} (nm)
972	48.4 ± 8.6	0.44 ± 0.16	0.80	60.7 ± 28.3	63.8 ± 30.6

Figure S15. Summary of dry-state TEM image analysis results for **P(NB-amine)$_{11}$-*b*-P(NB-MEG)$_{n}$** (n = 180, 240, 300, and 420) diblock copolymer nano-objects developed *via* aqueous ROMPISA, as determined by image processing using ImageJ analysis software.

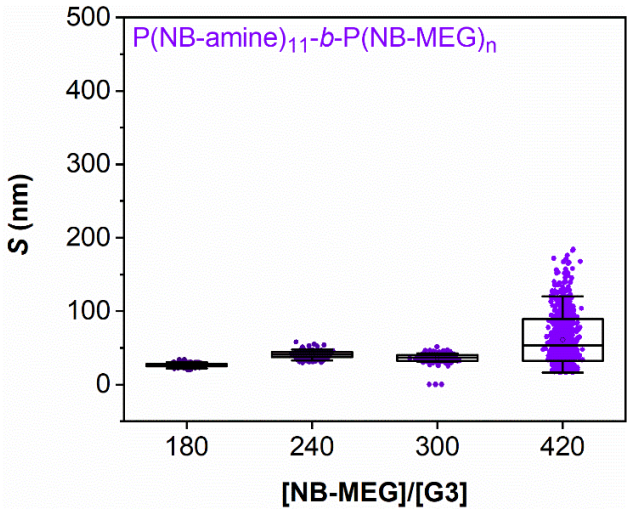

Figure S16. Box plots showing the size distribution of maximum dimension (*S*) with increasing $DP_{P(NB\text{-}MEG)}$ for **P(NB-amine)$_{11}$-*b*-P(NB-MEG)$_n$** (n = 180, 240, 300, and 420) diblock copolymer nano-objects developed *via* aqueous ROMPISA, as determined by dry-state TEM image analysis (the horizontal line within each box indicates the median).

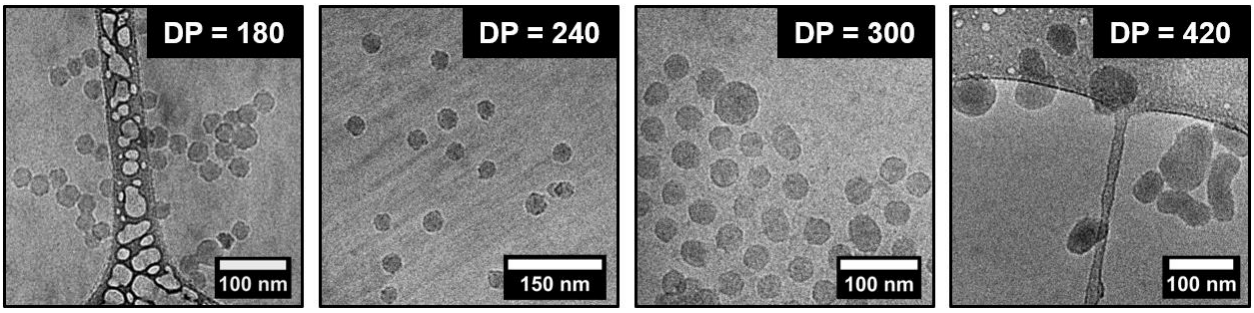

Figure S17. Representative cryo-TEM images of **P(NB-amine)$_{11}$-*b*-P(NB-MEG)$_n$** (n = 180, 240, 300, and 420) diblock copolymer nano-objects developed *via* aqueous ROMPISA.

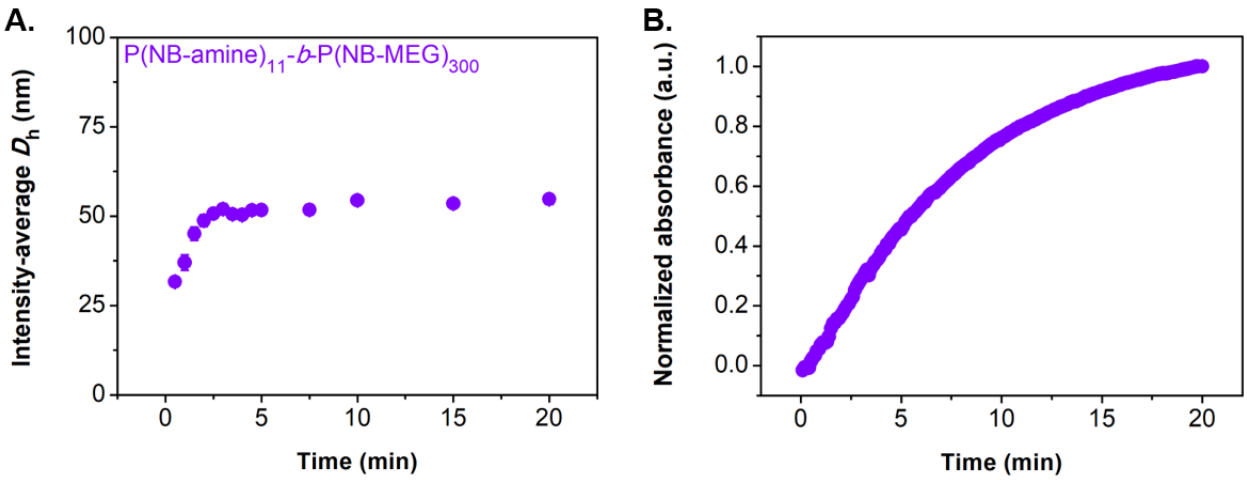

Figure S18. (A) Evolution of intensity-average D_h as a function of polymerization time for synthesis of **P(NB-amine)$_{11}$-*b*-P(NB-MEG)$_{300}$** diblock copolymer nano-objects *via* aqueous ROMPISA, as determined by DLS analysis of nano-object aliquots withdrawn during kinetic monitoring. (B) Normalized absorbance as a function of polymerization time for synthesis of **P(NB-amine)$_{11}$-*b*-P(NB-MEG)$_{300}$** diblock copolymer nano-objects *via* aqueous ROMPISA, as determined by *in situ* turbidimetric analysis during polymerization.

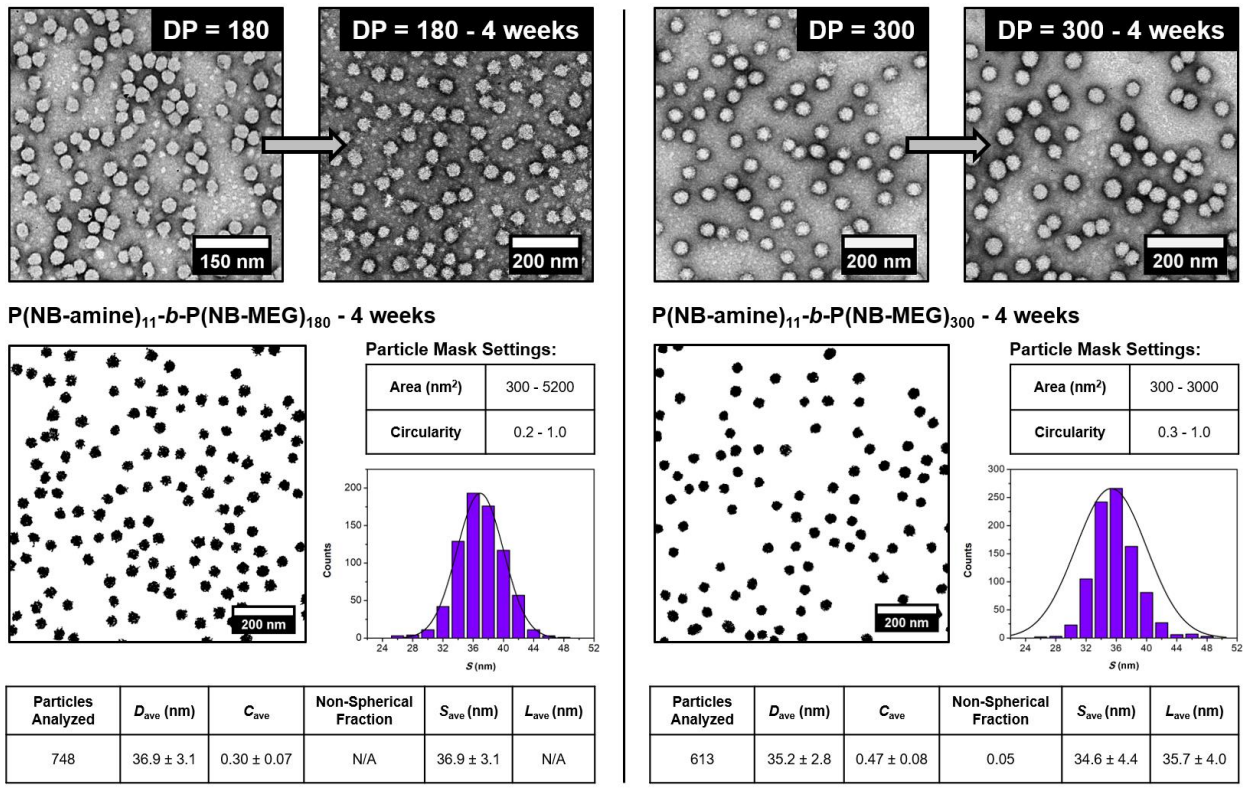

Particles Analyzed	D_{ave} (nm)	C_{ave}	Non-Spherical Fraction	S_{ave} (nm)	L_{ave} (nm)
748	36.9 ± 3.1	0.30 ± 0.07	N/A	36.9 ± 3.1	N/A

Particles Analyzed	D_{ave} (nm)	C_{ave}	Non-Spherical Fraction	S_{ave} (nm)	L_{ave} (nm)
613	35.2 ± 2.8	0.47 ± 0.08	0.05	34.6 ± 4.4	35.7 ± 4.0

Figure S19. Representative dry-state TEM images of original **P(NB-amine)$_{11}$-*b*-P(NB-MEG)$_n$** (n = 180, and 300) diblock copolymer nano-objects developed *via* aqueous ROMPISA and samples after aging for 4 weeks, stained with 1 wt% UA solution, along with summary of dry-state TEM image analysis results for aged **P(NB-amine)$_{11}$-*b*-P(NB-MEG)$_n$** diblock copolymer nano-objects, as determined by image processing using ImageJ analysis software.

Supplementary Characterization Data for P(NB-amine)$_{11}$-*b*-P(NB-MEG)$_n$ Diblock Copolymer Nano-Objects Developed by Aqueous ROMPISA in the Presence of NaCl

Table S6. Molecular characteristics of **P(NB-amine)$_{11}$-*b*-P(NB-MEG)$_n$** diblock copolymers prepared *via* aqueous ROMPISA in the presence of 100 mM NaCl using different initial [**NB-MEG**]/[**G3**] ratios, as determined by ^{1}H-NMR spectroscopy and SEC analysis.

[NB-MEG]/[G3]	% Conv.[a]	$M_{n,\,theo.}$ (kDa)[b]	$M_{n,\,SEC}$ (kDa)[c]	$Đ_{M,\,SEC}$[c]
60	>99	15.8	15.7	1.14
120	>99	29.1	26.5	1.12
180	>99	42.4	37.7	1.11
240	>99	55.6	43.4	1.12
300	>99	68.9	49.4	1.11
420	>99	95.4	74.9	1.12

[a]Monomer conversion calculated from ^{1}H-NMR spectroscopy in DMSO-d_6. [b]Calculated from conversion. [c]Mn and $Đ_M$ values calculated from PS standards using THF + 2% v/v NEt$_3$ as the eluent.

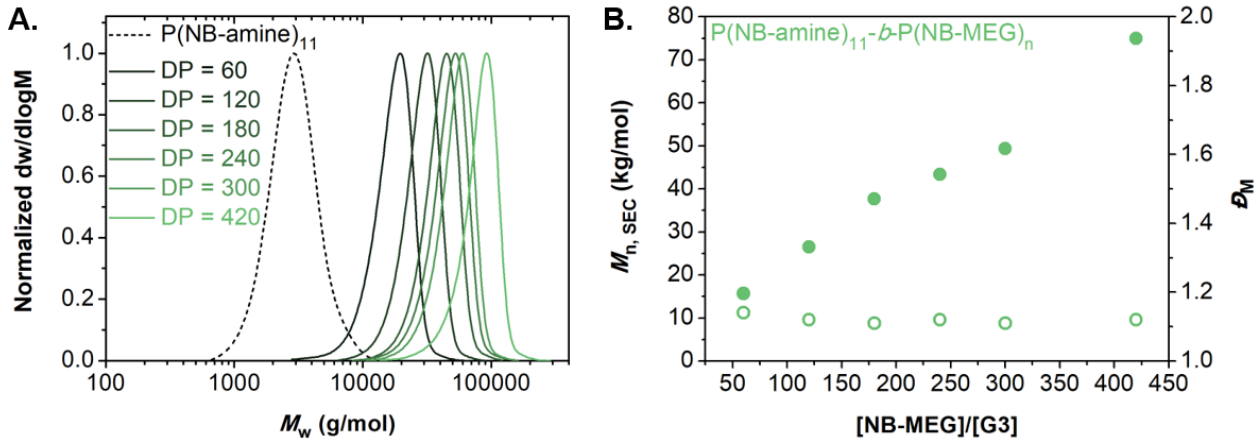

Figure S20. (A) Normalized SEC RI molecular weight distributions for **P(NB-amine)$_{11}$-*b*-P(NB-MEG)$_n$** diblock copolymers (n = 60, 120, 180, 240, 300, and 420). (B) Evolution of M_n (filled circles) and $Đ_M$ (empty circles) values with increasing targeted DP$_{P(NB\text{-}MEG)}$ calculated from SEC analysis for **P(NB-amine)$_{11}$-*b*-P(NB-MEG)$_n$** diblock copolymers prepared *via* aqueous ROMPISA in the presence of 100 mM NaCl. M_n and $Đ_M$ values were calculated from PS standards using THF + 2% v/v NEt$_3$ as the eluent.

Table S7. Summary of D_h, PD and zeta potential values and observed morphologies for **P(NB-amine)$_{11}$-*b*-P(NB-MEG)$_n$** diblock copolymer nano-objects prepared *via* aqueous ROMPISA in the presence of 100 mM NaCl, as determined by DLS, microelectrophoretic analysis and dry-state TEM imaging, respectively.

[NB-MEG] /[G3]	D_h (nm)[a]	PD[a]	Intensity-average D_h (nm)[a]	Zeta potential (mV)[b]	Morphology[c]
60	34.0 ± 0.6	0.26 ± 0.01	32.1 ± 0.5	+ 19.00 ± 1.08	V
120	53.8 ± 7.1	0.19 ± 0.05	47.5 ± 4.3	+ 14.44 ± 4.11	V
180	57.2 ± 0.9	0.20 ± 0.04	57.8 ± 1.8	+ 18.13 ± 1.47	V
240	140.3 ± 2.4	0.25 ± 0.01	186.5 ± 4.1	+ 19.27 ± 2.99	V + T
300	100.8 ± 1.5	0.17 ± 0.03	110.4 ± 2.3	+ 16.43 ± 0.90	V + T
420	1025 ± 90	0.41 ± 0.04	1157 ± 218	+ 20.10 ± 0.50	T + L

[a]D_h and PD values measured from DLS analysis (the error shows the standard deviation from 4 repeat measurements). [b]Zeta potential values measured from microelectrophoretic analysis at pH = 2.0, using PB 2 + 100 mM NaCl (the error shows the standard deviation from at least 3 repeat measurements). [c]Morphologies observed from dry-state TEM imaging, using 1 wt% uranyl acetate (UA) solution for staining (Key: V – vesicles, T – tubesomes, L – lamellae).

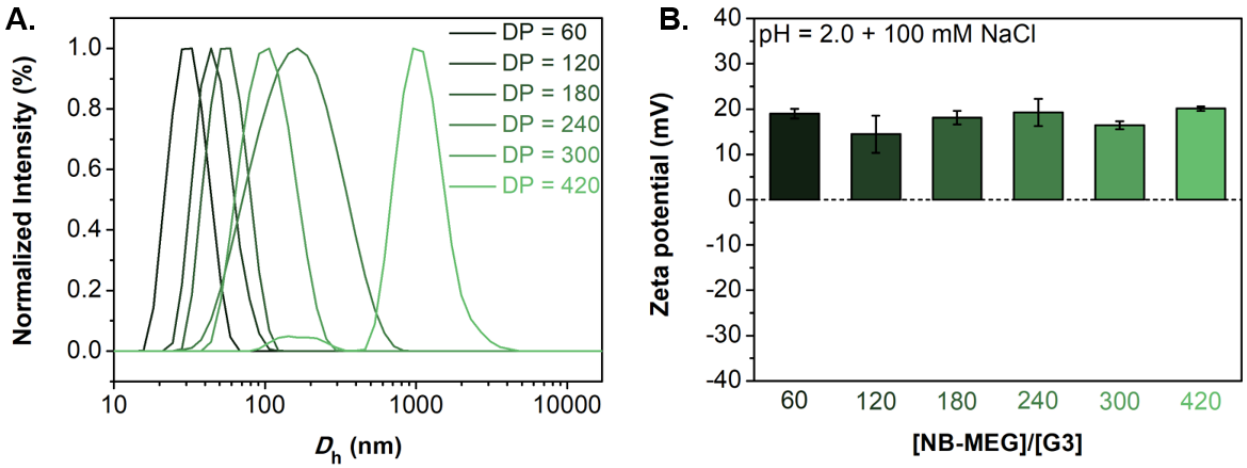

Figure S21. (A) Normalized intensity-weighted size distributions obtained by DLS for **P(NB-amine)$_{11}$-*b*-P(NB-MEG)$_n$** diblock copolymer nano-objects developed *via* aqueous ROMPISA in the presence of 100 mM NaCl. (B) Zeta potential values for **P(NB-amine)$_{11}$-*b*-P(NB-MEG)$_n$** diblock copolymer nano-objects measured from microelectrophoretic analysis under aqueous ROMPISA-mimicking conditions (pH = 2 + 100 mM NaCl).

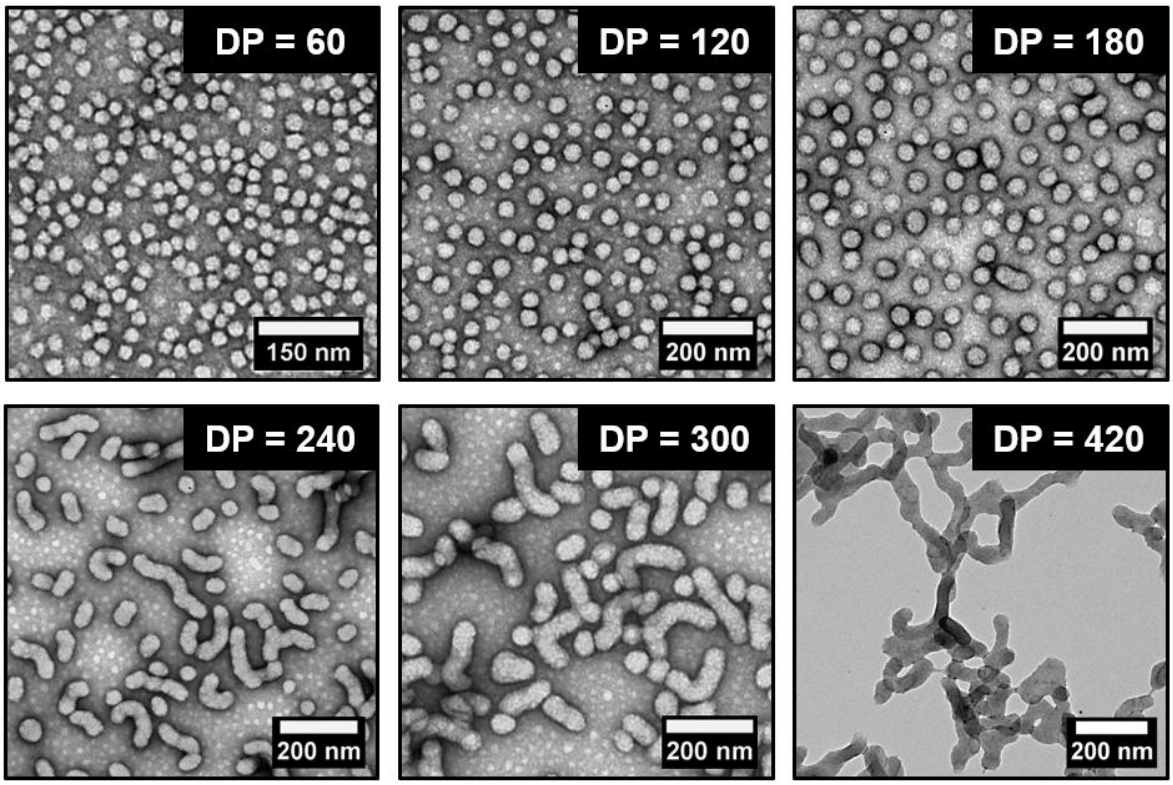

Figure S22. Representative dry-state TEM images of **P(NB-amine)$_{11}$-*b*-P(NB-MEG)$_n$** (n = 60, 120, 180, 240, 300, and 420) diblock copolymer nano-objects developed *via* aqueous ROMPISA in the presence of 100 mM NaCl, stained with 1 wt% UA solution.

P(NB-amine)$_{11}$-*b*-P(NB-MEG)$_{60}$

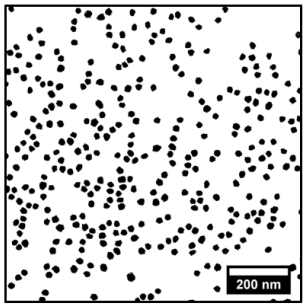

Particle Mask Settings:

Area (nm^2)	300 - 1200
Circularity	0.7 - 1.0

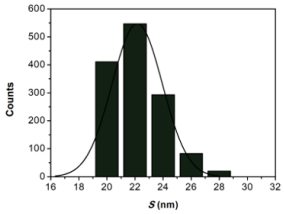

Particles Analyzed	D_{ave} (nm)	C_{ave}	Non-Spherical Fraction	S_{ave} (nm)	L_{ave} (nm)
1355	22.2 ± 1.8	0.78 ± 0.05	N/A	22.2 ± 1.8	N/A

P(NB-amine)$_{11}$-*b*-P(NB-MEG)$_{120}$

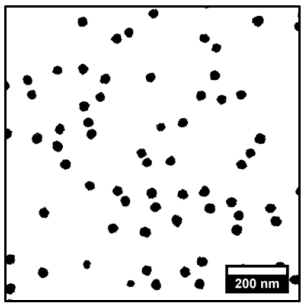

Particle Mask Settings:

Area (nm^2)	300 - 2000
Circularity	0.7 - 1.0

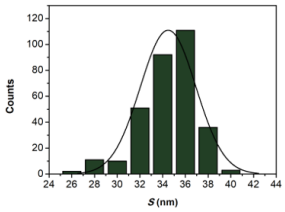

Particles Analyzed	D_{ave} (nm)	C_{ave}	Non-Spherical Fraction	S_{ave} (nm)	L_{ave} (nm)
316	34.5 ± 2.4	0.74 ± 0.03	N/A	34.5 ± 2.4	N/A

P(NB-amine)$_{11}$-*b*-P(NB-MEG)$_{180}$

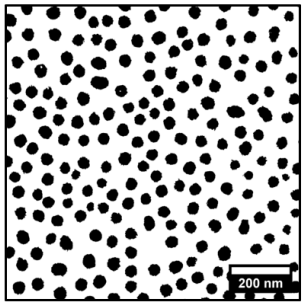

Particle Mask Settings:

Area (nm^2)	300 - 3000
Circularity	0.5 - 1.0

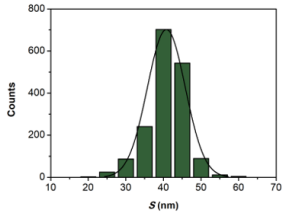

Particles Analyzed	D_{ave} (nm)	C_{ave}	Non-Spherical Fraction	S_{ave} (nm)	L_{ave} (nm)
1704	41.2 ± 4.5	0.74 ± 0.09	0.06	40.8 ± 5.1	37.1 ± 8.6

P(NB-amine)$_{11}$-*b*-P(NB-MEG)$_{240}$

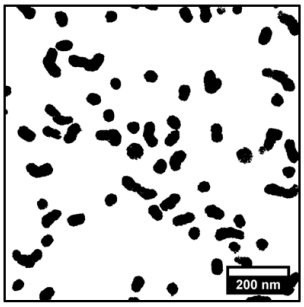

Particle Mask Settings:

Area (nm^2)	400 - 5000
Circularity	0.12 - 1.0

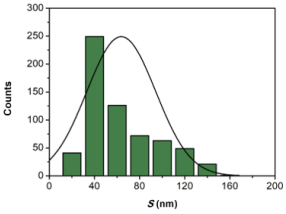

Particles Analyzed	D_{ave} (nm)	C_{ave}	Non-Spherical Fraction	S_{ave} (nm)	L_{ave} (nm)
622	45.4 ± 6.4	0.55 ± 0.20	0.65	63.7 ± 30.5	73.4 ± 33.7

P(NB-amine)$_{11}$-*b*-P(NB-MEG)$_{300}$

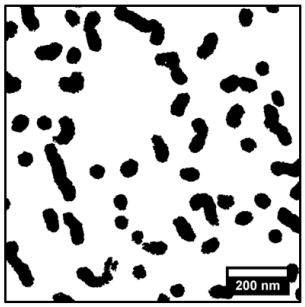

Particle Mask Settings:

Area (nm^2)	800 - 10000
Circularity	0.12 - 1.0

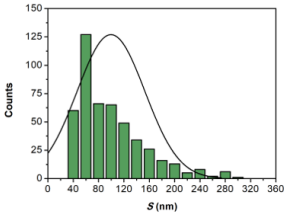

Particles Analyzed	D_{ave} (nm)	C_{ave}	Non-Spherical Fraction	S_{ave} (nm)	L_{ave} (nm)
478	53.1 ± 5.3	0.63 ± 0.15	0.69	99.6 ± 53.5	120.6 ± 52.2

Figure S23. Summary of dry-state TEM image analysis results for **P(NB-amine)$_{11}$-*b*-P(NB-MEG)$_{n}$** (n = 60, 120, 180, 240, and 300) diblock copolymer nano-objects developed *via* aqueous ROMPISA in the presence of 100 mM NaCl, as determined by image processing using ImageJ analysis software.

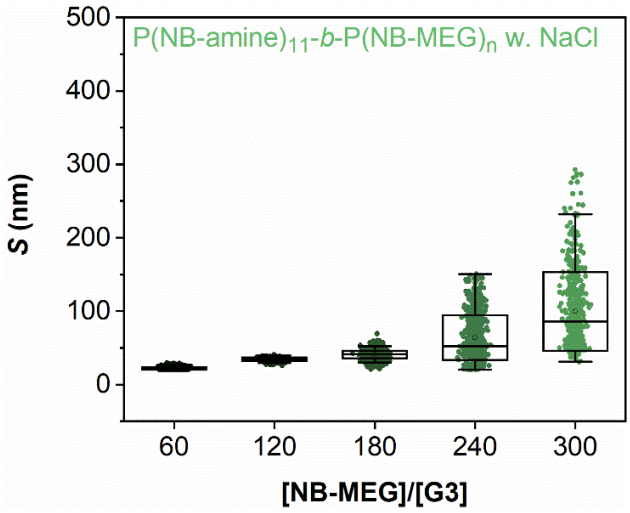

Figure S24. Box plots showing the size distribution of maximum dimension (*S*) with increasing $DP_{P(NB\text{-}MEG)}$ for **P(NB-amine)$_{11}$-*b*-P(NB-MEG)$_n$** (n = 60, 120, 180, 240, and 300) diblock copolymer nano-objects developed *via* aqueous ROMPISA in the presence of 100 mM NaCl, as determined by dry-state TEM image analysis (the horizontal line within each box indicates the median).

Supplementary Characterization Data for P(NB-PEG)$_{11}$-*b*-P(NB-MEG)$_n$ Diblock Copolymer Nano-Objects Developed by Aqueous ROMPISA

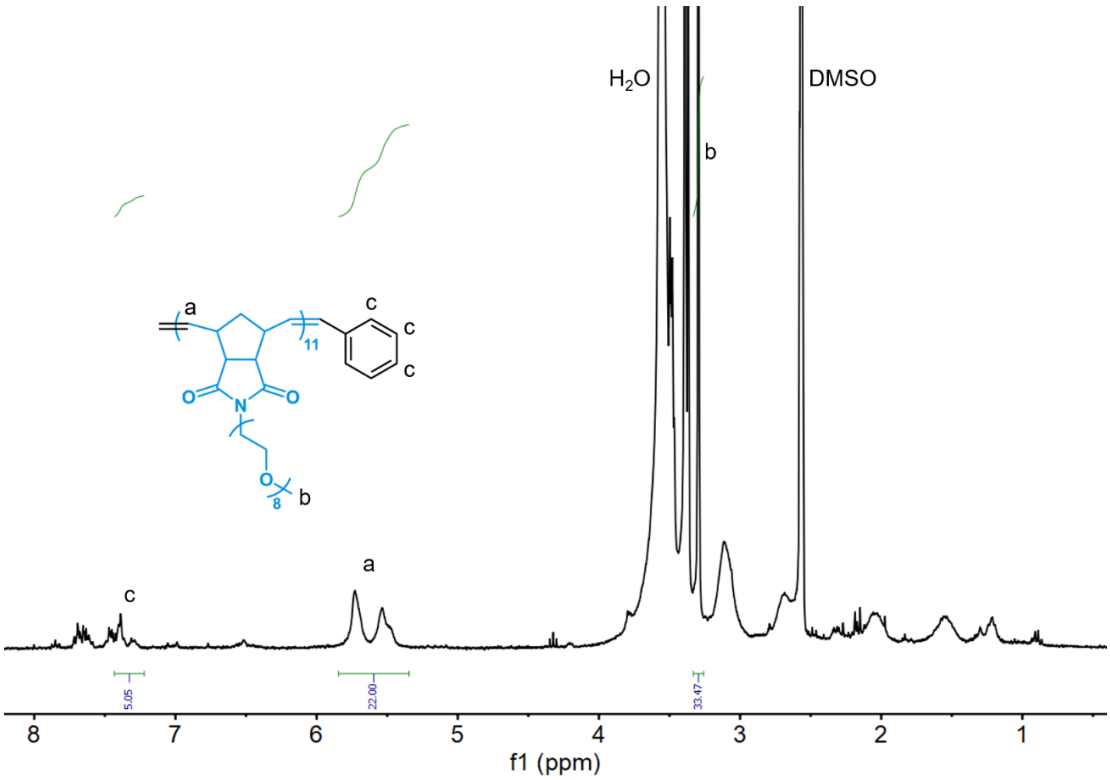

Figure S25. ^{1}H-NMR spectrum of **P(NB-PEG)$_{11}$** macroinitiator in DMSO-d_6.

Table S8. Molecular characteristics of **P(NB-PEG)$_{11}$** macroinitiator prepared *via* ROMP in THF, as determined by ^{1}H-NMR spectroscopy and SEC analysis.

[NB-PEG]/[G3]	% Conv.[a]	$M_{n,\,theo.}$ (kDa)[b]	$M_{n,\,NMR}$ (kDa)[c]	$M_{n,\,SEC}$ (kDa)[d]	$Đ_{M,\,SEC}$[d]
10	>99	5.0	5.5	5.3	1.20

[a]Monomer conversion calculated from ^{1}H-NMR spectroscopy in DMSO-d_6. [b]Calculated from conversion. [c]Calculated using end group analysis from ^{1}H-NMR spectroscopy. [d]Mn and $Đ_M$ values calculated from PS standards using THF + 2% v/v NEt_3 as the eluent.

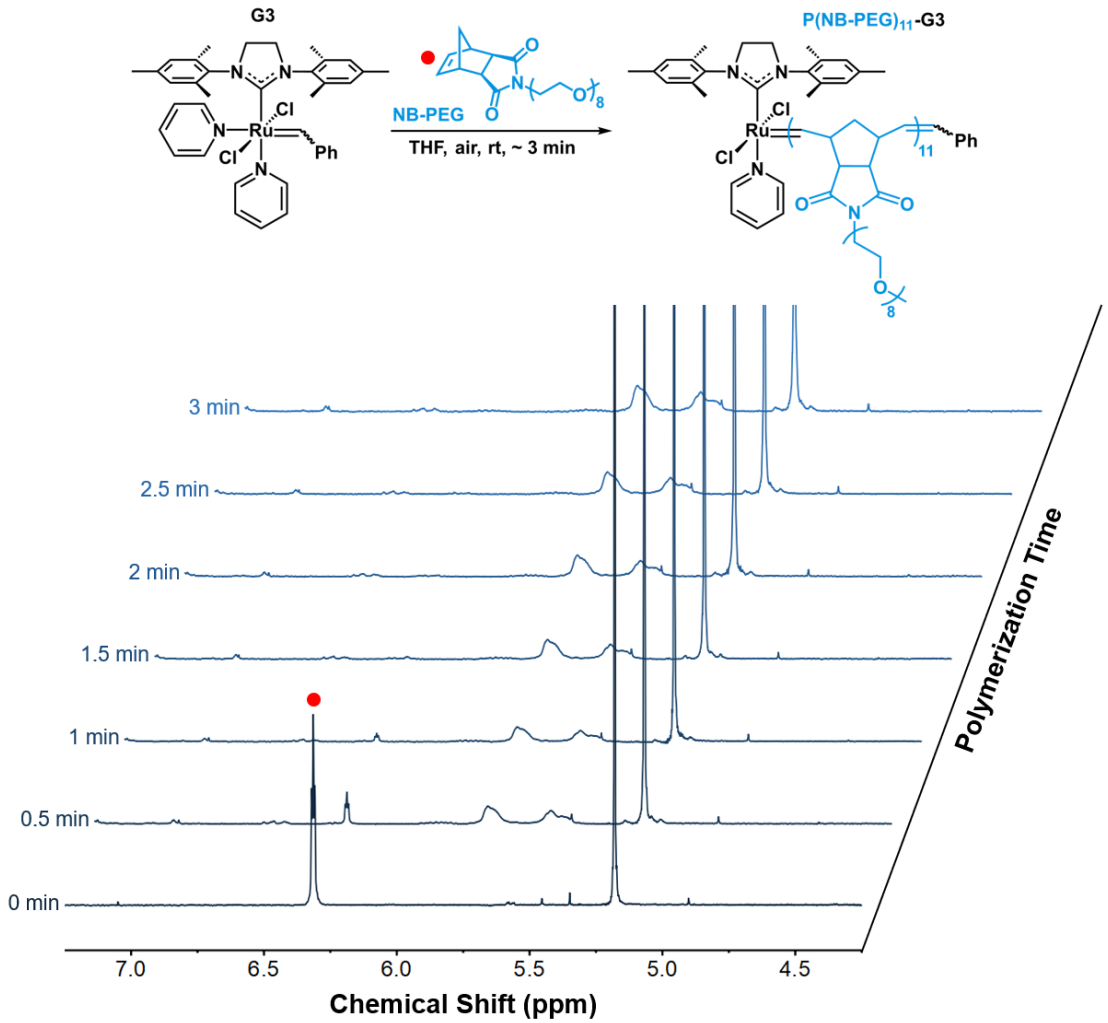

Figure S26. Stacked ^{1}H-NMR spectra obtained during kinetic monitoring of **P(NB-PEG)$_{11}$** macroinitiator synthesis *via* solution ROMP as a function of polymerization time (solvent: $CDCl_3$ + 1,3,5-trioxane). The red circle denotes the **NB-PEG** monomer peak at 6.30 ppm.

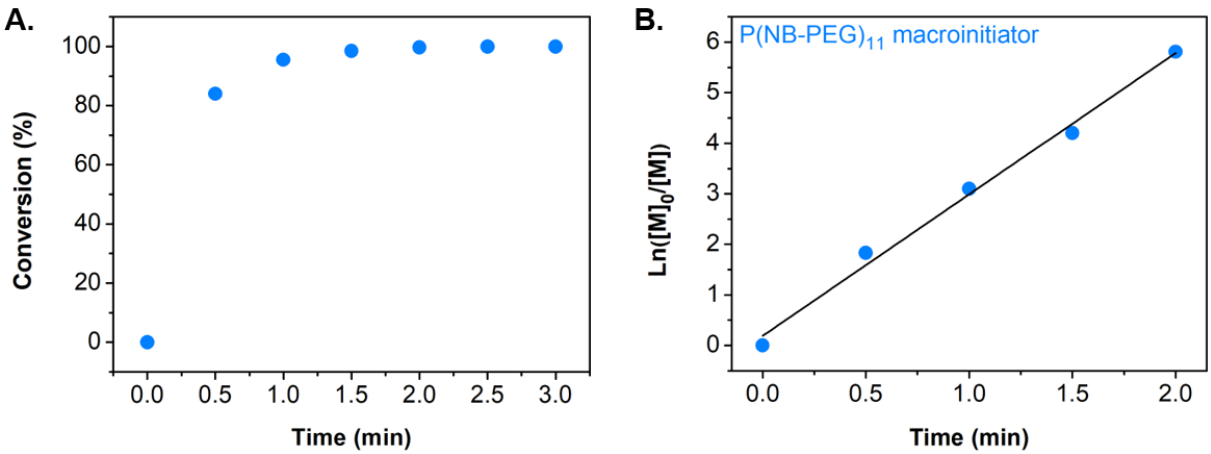

Figure S27. (A) Monomer conversion *vs*. polymerization time, and (B) ln([M]$_0$/[M]) *vs*. polymerization time kinetic plots for synthesis of **P(NB-PEG)$_{11}$** macroinitiator *via* solution ROMP, as determined by ^{1}H-NMR spectroscopy in $CDCl_3$ + 1,3,5-trioxane.

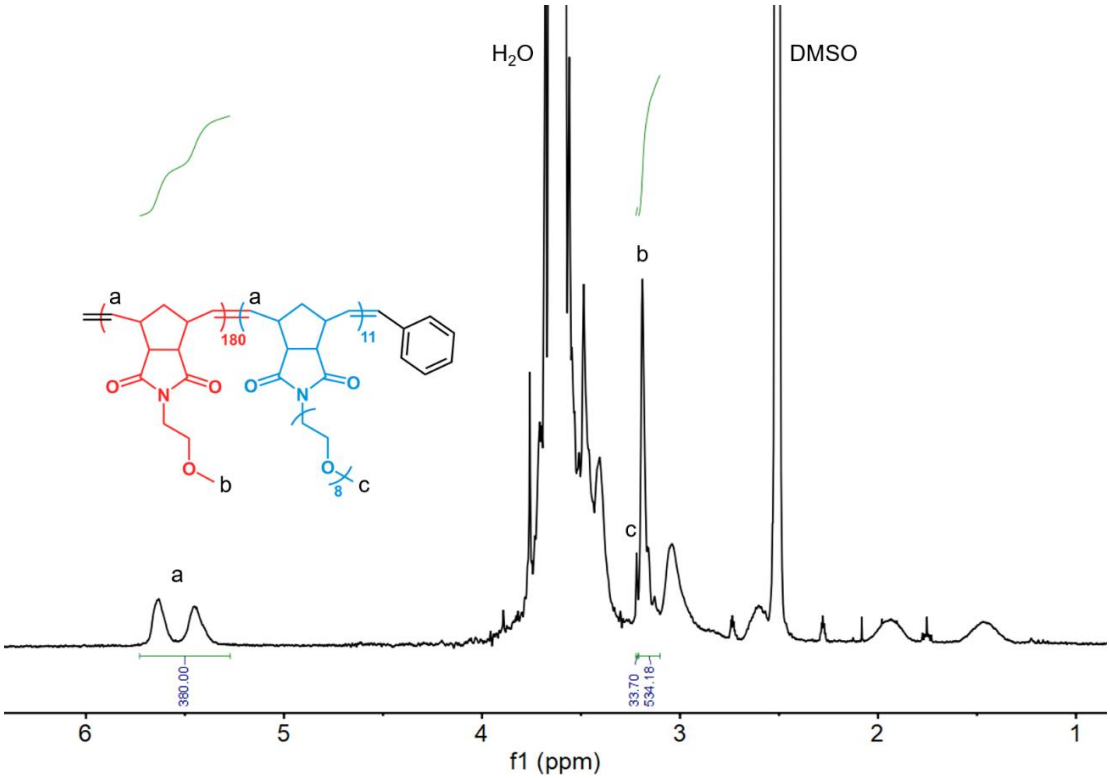

Figure S28. ^{1}H-NMR spectrum of **P(NB-PEG)$_{11}$-*b*-P(NB-MEG)$_{180}$** diblock copolymer in DMSO-d_6.

Table S9. Molecular characteristics of **P(NB-PEG)$_{11}$-*b*-P(NB-MEG)$_n$** diblock copolymers prepared *via* aqueous ROMPISA using different initial [**NB-MEG**]/[**G3**] ratios, as determined by ^{1}H-NMR spectroscopy and SEC analysis.

[NB-MEG]/[G3]	% Conv.[a]	$M_{n,\,theo.}$ (kDa)[b]	$M_{n,\,SEC}$ (kDa)[c]	$Đ_{M,\,SEC}$[c]
40	>99	14.3	14.4	1.15
60	>99	18.7	20.5	1.14
120	>99	32.0	31.6	1.16
140	>99	36.4	32.9	1.11
180	>99	45.2	41.5	1.11
240	>99	58.5	49.2	1.12
260	>99	63.0	52.6	1.12
300	>99	71.7	61.9	1.12

[a]Monomer conversion calculated from ^{1}H-NMR spectroscopy in DMSO-d_6. [b]Calculated from conversion. [c]Mn and $Đ_M$ values calculated from PS standards using THF + 2% v/v NEt_3 as the eluent.

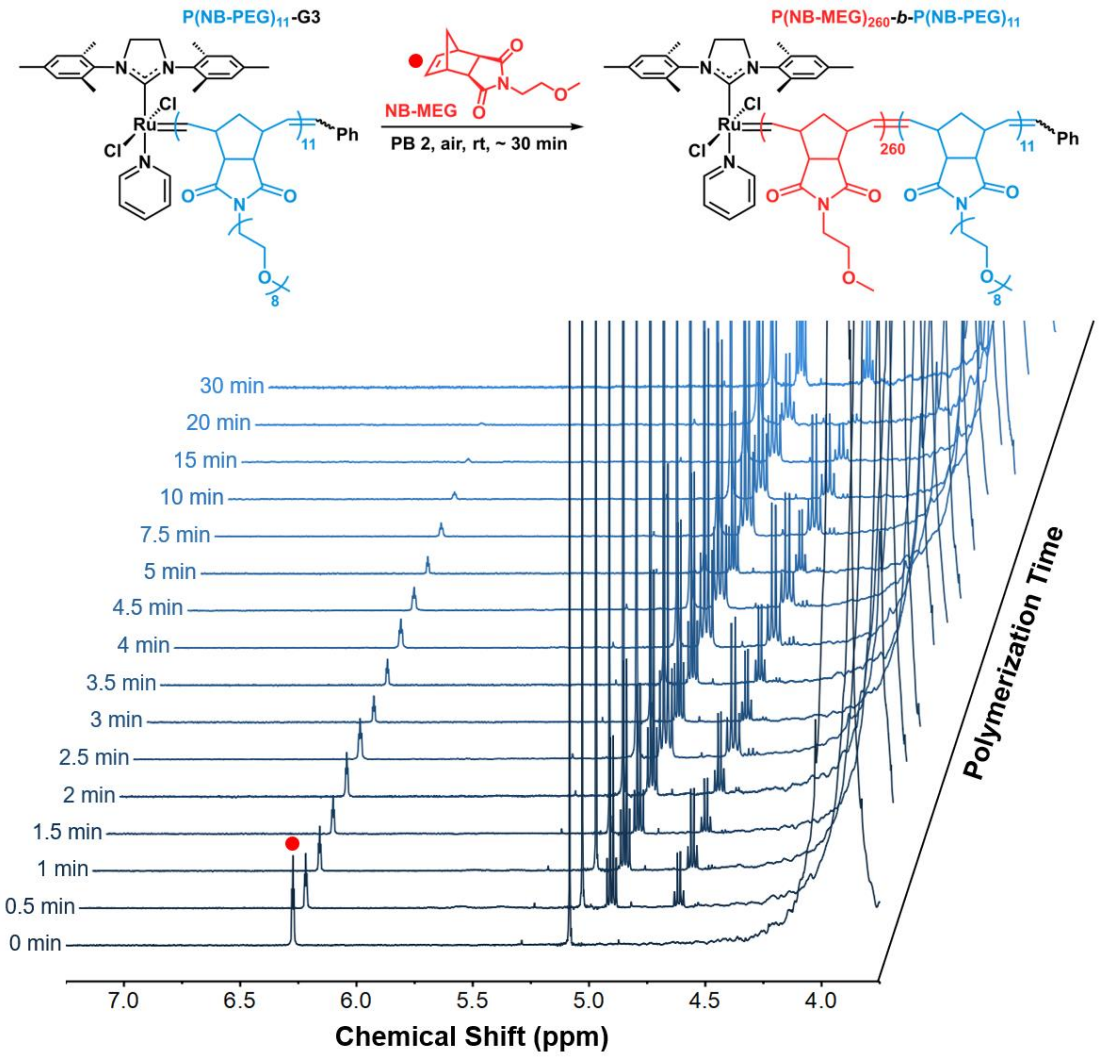

Figure S29. Stacked ^{1}H-NMR spectra obtained during kinetic monitoring of **P(NB-PEG)$_{11}$-*b*-P(NB-MEG)$_{260}$** diblock copolymer synthesis *via* aqueous ROMPISA as a function of polymerization time (solvent: DMSO-d_6 + 1,3,5-trioxane). The red circle denotes the **NB-MEG** monomer peak at 6.28 ppm.

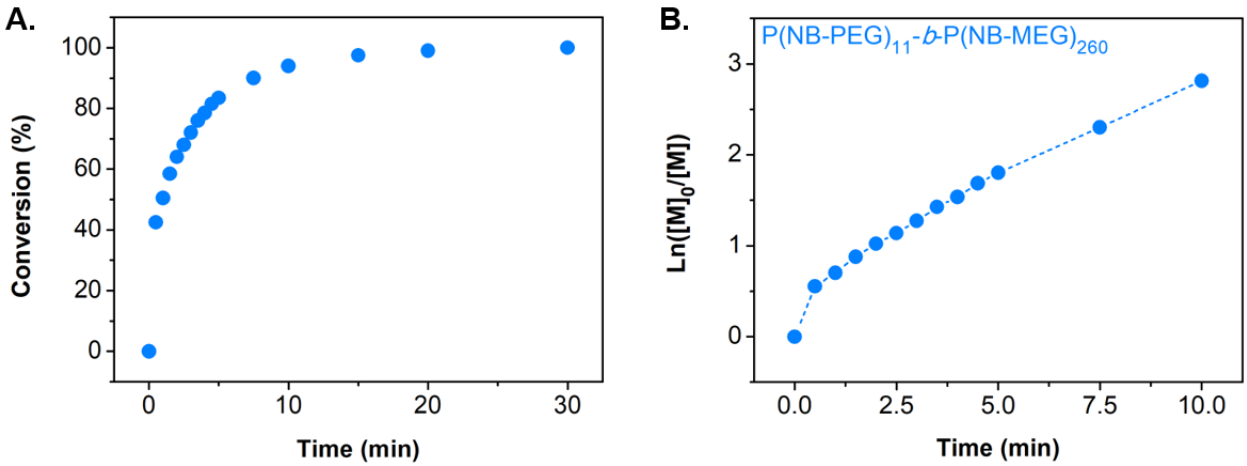

Figure S30. (A) Monomer conversion *vs*. polymerization time, and (B) ln([M]$_0$/[M]) *vs*. polymerization time kinetic plots for synthesis of **P(NB-PEG)$_{11}$-*b*-P(NB-MEG)$_{260}$** diblock copolymers *via* aqueous ROMPISA, as determined by ^{1}H-NMR spectroscopy in DMSO-d_6 + 1,3,5-trioxane.

Table S10. Evolution of molecular characteristics with increasing **NB-MEG** conversion for **P(NB-PEG)$_{11}$-*b*-P(NB-MEG)$_{260}$** diblock copolymers prepared *via* aqueous ROMPISA, as determined by ^{1}H-NMR spectroscopic and SEC kinetic analysis.

% Conv.[a]	**Calc. DP**[b]	$M_{n,\,theo.}$ **(kDa)**[b]	$M_{n,\,SEC}$ **(kDa)**[c]	$Đ_{M,\,SEC}$[c]
42.5	111	30.0	25.9	1.09
50.5	131	34.5	33.7	1.06
68	177	44.6	45.5	1.06
94	244	59.4	60.0	1.08
100	260	63.0	63.6	1.08

[a]Monomer conversion calculated from ^{1}H-NMR spectroscopy in DMSO-d_6 + 1,3,5-trioxane. [b]Calculated from conversion. [c]Mn and $Đ_M$ values calculated from PS standards using THF + 2% v/v NEt$_3$ as the eluent.

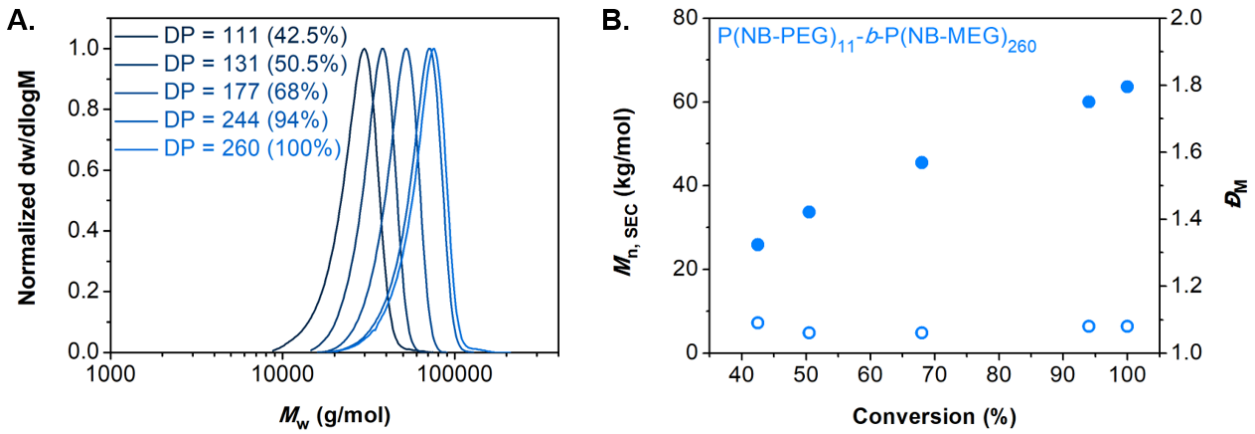

Figure S31. (A) Normalized SEC RI molecular weight distributions, and (B) evolution of M_n (filled circles) and $Đ_M$ (empty circles) values with increasing **NB-MEG** conversion calculated from SEC kinetic analysis for synthesis of **P(NB-PEG)$_{11}$-*b*-P(NB-MEG)$_{260}$** diblock copolymers *via* aqueous ROMPISA. M_n and $Đ_M$ values were calculated from PS standards using THF + 2% v/v NEt_3 as the eluent.

Table S11. Summary of D_h, PD and zeta potential values and observed morphologies for **P(NB-PEG)$_{11}$-*b*-P(NB-MEG)$_n$** diblock copolymer nano-objects prepared *via* aqueous ROMPISA, as determined by DLS, microelectrophoretic analysis and dry-state TEM imaging, respectively.

[NB-MEG] /[G3]	D_h (nm)[a]	PD[a]	Intensity-average D_h (nm)[a]	Zeta potential (mV)[b]	Morphology[c]
40	25.9 ± 1.9	0.09 ± 0.01	25.8 ± 1.3	+ 0.64 ± 3.93	V
60	34.9 ± 3.6	0.18 ± 0.04	31.9 ± 0.6	- 0.14 ± 1.70	V
120	47.5 ± 1.1	0.10 ± 0.01	47.6 ± 1.1	- 2.94 ± 1.49	V
140	54.6 ± 0.9	0.19 ± 0.01	57.1 ± 1.0	- 2.72 ± 3.03	V
180	69.6 ± 1.8	0.14 ± 0.03	69.9 ± 3.4	- 0.04 ± 1.29	V + T
240	95.6 ± 1.3	0.08 ± 0.02	95.8 ± 1.5	+ 0.61 ± 1.77	V + T
260	191.4 ± 8.6	0.34 ± 0.02	153.8 ± 4.3	- 3.09 ± 2.49	T
300	*Macroscopic precipitation – Unstable particles*				

[a]D_h and PD values measured from DLS analysis (the error shows the standard deviation from 4 repeat measurements). [b]Zeta potential values measured from microelectrophoretic analysis at pH = 2.0, using PB 2 (the error shows the standard deviation from at least 3 repeat measurements). [c]Morphologies observed from dry-state TEM imaging, using 1 wt% uranyl acetate (UA) solution for staining (Key: V – vesicles, T – tubesomes).

Table S12. Summary of R_h, R_g and N_{agg} values for spherical **P(NB-PEG)$_{11}$-*b*-P(NB-MEG)$_n$** polymersomes prepared *via* aqueous ROMPISA, as determined by multiple angle DLS and SLS analysis.

[NB-MEG] /[G3]	d*n*/dc (mL g^{-1})	$R_{h,\ 173°}$ (nm)[a]	$R_{h,\ multiple}$ (nm)[b]	R_g (nm)[c]	R_g/R_h	N_{agg}[d]
40	0.121 ± 0.003	12.9 ± 0.7	14.7 ± 0.7	12.7 ± 0.6	0.87	439
60	0.116 ± 0.003	17.5 ± 1.8	19.4 ± 1.0	15.9 ± 0.8	0.82	827

[a]R_h values measured from DLS analysis at a fixed angle of 173° (the error shows the standard deviation from 4 repeat measurements). [b]R_h values calculated from multiple angle DLS analysis using the Stokes-Einstein equation (mean ± 5%). [c]R_g values calculated from multiple angle SLS analysis (mean ± 5%). [d]N_{agg} values calculated from multiple angle SLS analysis.

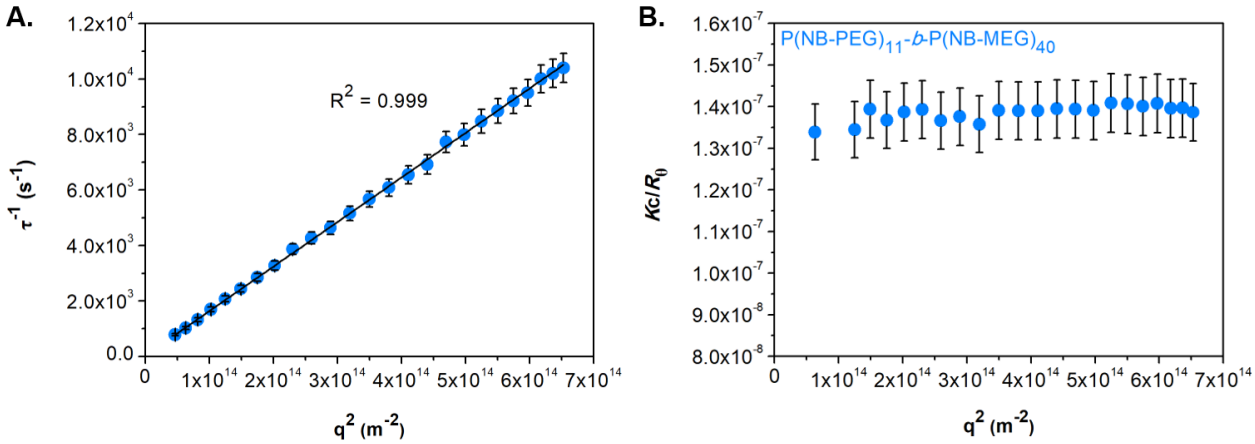

Figure S32. Multiple angle dynamic (A) and static (B) light scattering analysis of spherical **P(NB-PEG)$_{11}$-*b*-P(NB-MEG)$_{40}$** polymersomes at 0.1 mg mL^{-1}.

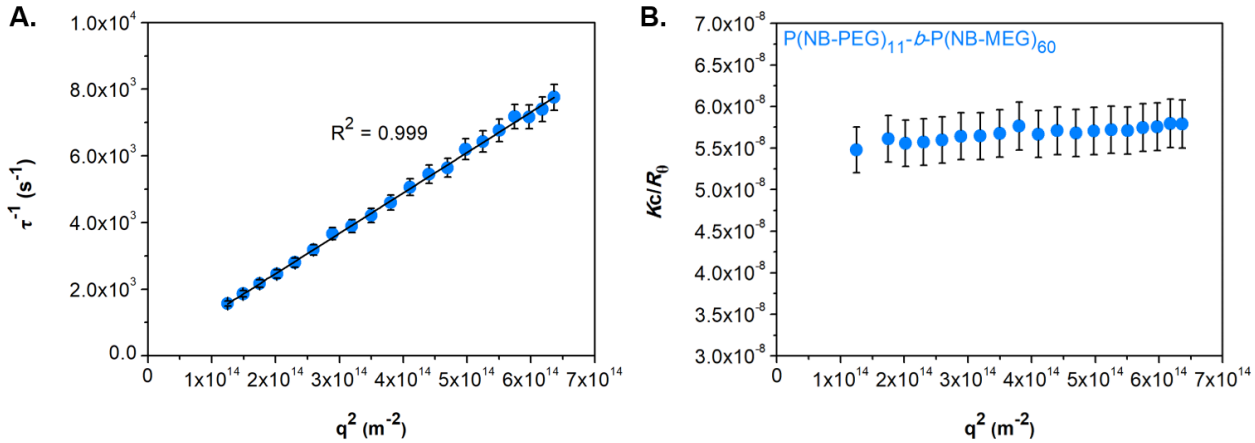

Figure S33. Multiple angle dynamic (A) and static (B) light scattering analysis of spherical **P(NB-PEG)$_{11}$-*b*-P(NB-MEG)$_{60}$** polymersomes at 0.1 mg mL^{-1}.

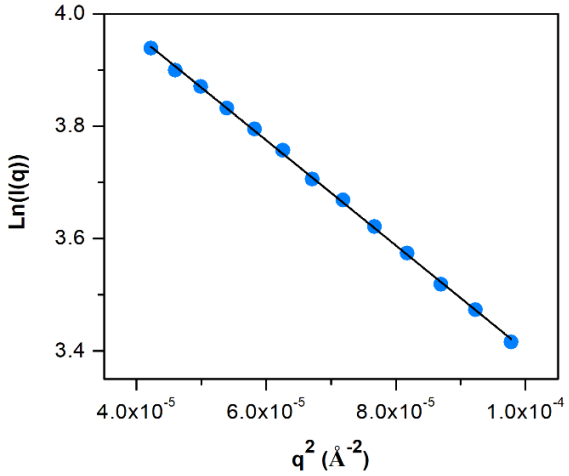

Figure S34. Guinier plot from SAXS data acquired for **P(NB-PEG)$_{11}$-*b*-P(NB-MEG)$_{60}$** polymersomes, giving R_g = 130 Å. For spherical particles, the resulting diameter is 31.8 nm.

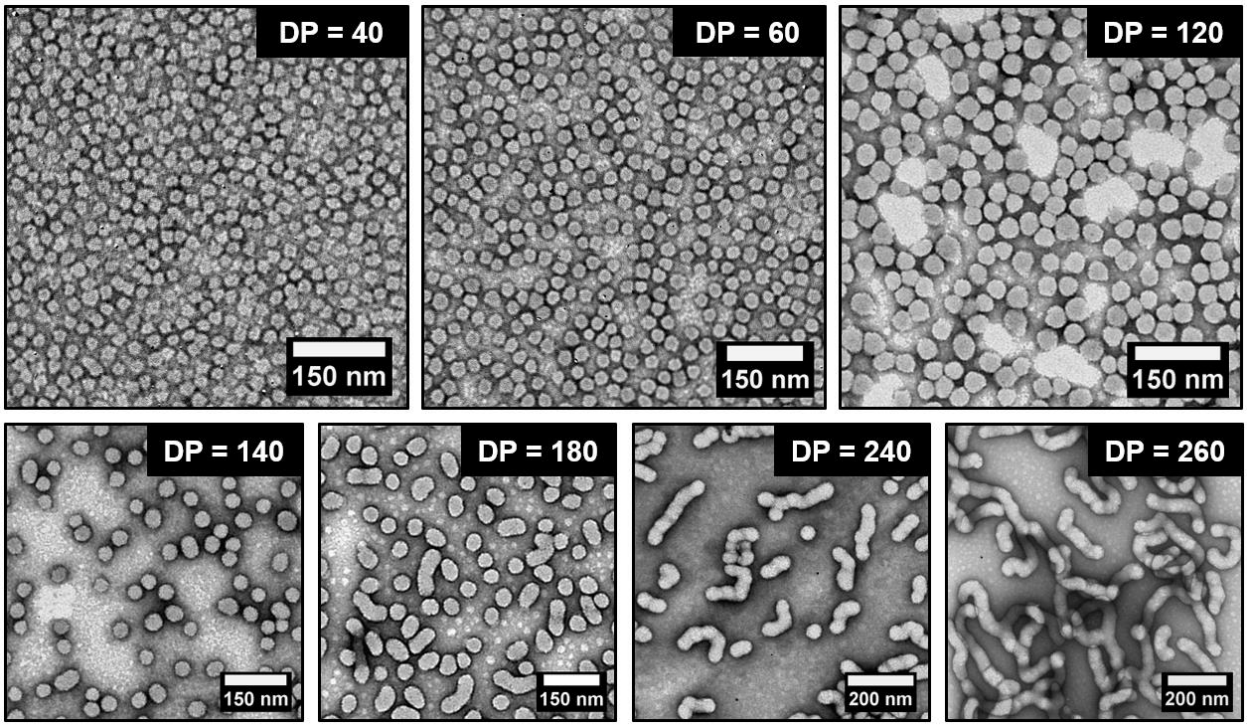

Figure S35. Representative dry-state TEM images of **P(NB-PEG)$_{11}$-*b*-P(NB-MEG)$_n$** (n = 40, 60, 120, 140, 180, 240, and 260) diblock copolymer nano-objects developed *via* aqueous ROMPISA, stained with 1 wt% UA solution.

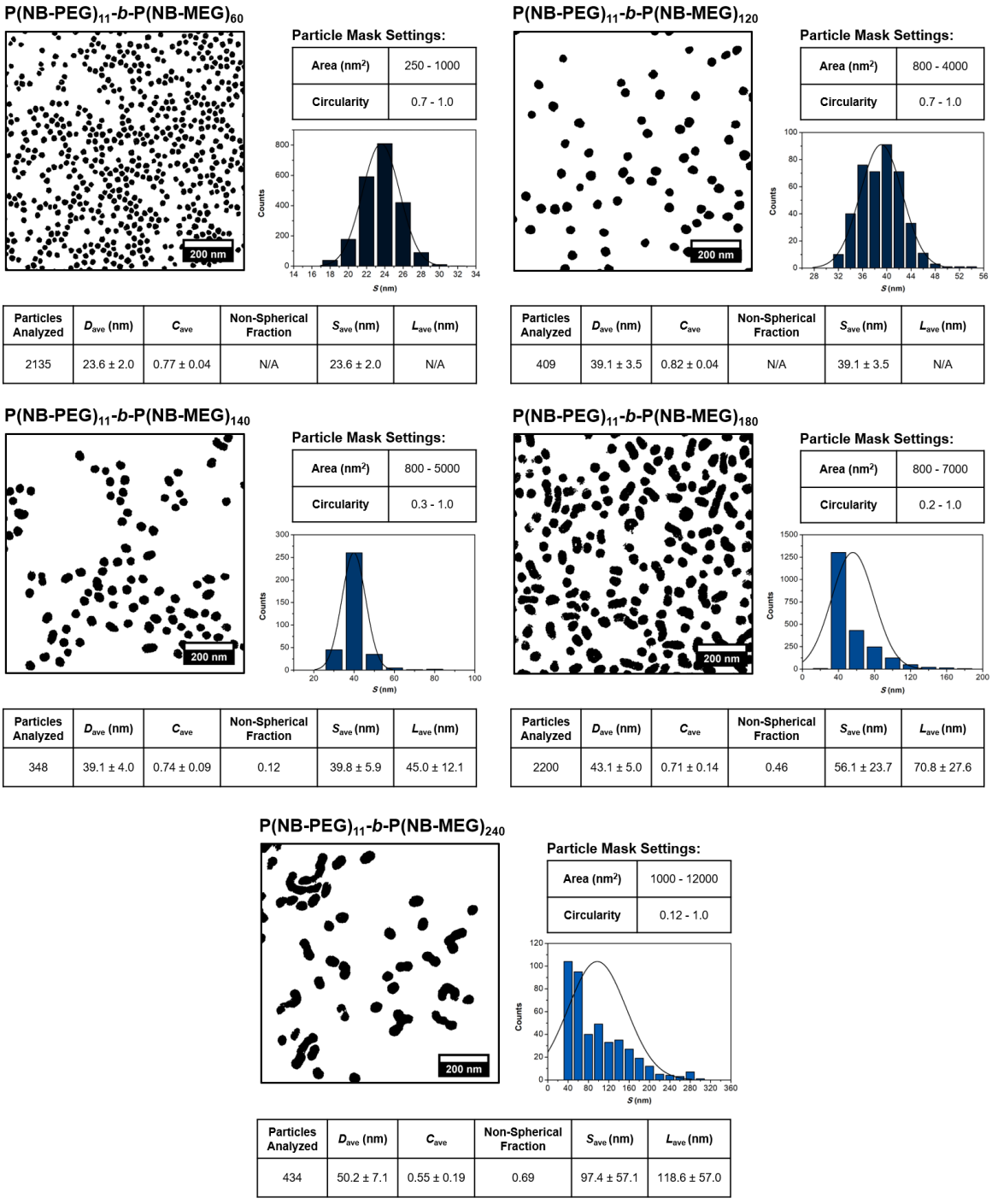

Figure S36. Summary of dry-state TEM image analysis results for **P(NB-PEG)$_{11}$-*b*-P(NB-MEG)$_{n}$** (n = 60, 120, 140, 180, and 240) diblock copolymer nano-objects developed *via* aqueous ROMPISA, as determined by image processing using ImageJ analysis software.

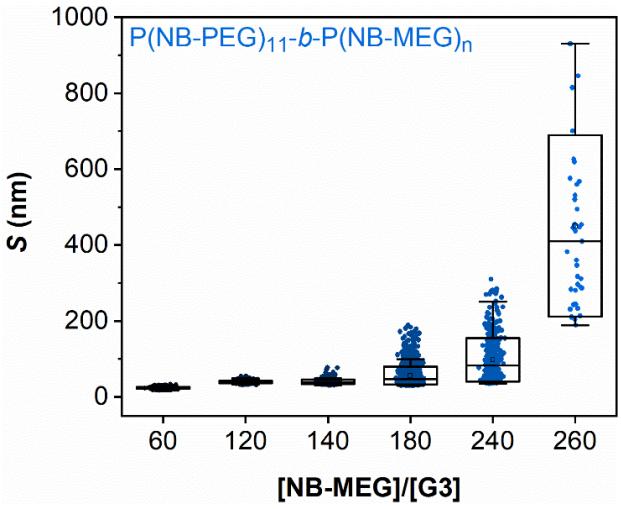

Figure S37. Box plots showing the size distribution of maximum dimension (*S*) with increasing $DP_{P(NB\text{-}MEG)}$ for **P(NB-PEG)$_{11}$-*b*-P(NB-MEG)$_n$** (n = 60, 120, 140, 180, 240, and 260) diblock copolymer nano-objects developed *via* aqueous ROMPISA, as determined by dry-state TEM image analysis (the horizontal line within each box indicates the median).

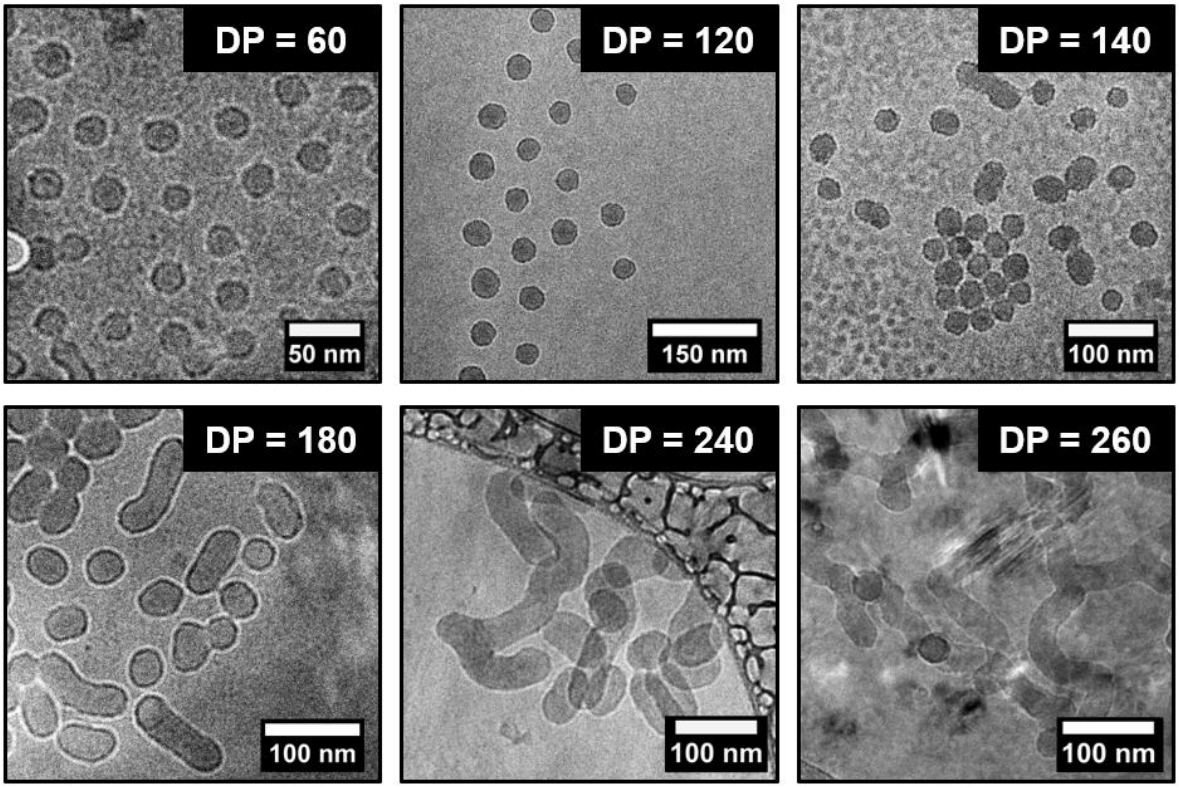

Figure S38. Representative cryo-TEM images of **P(NB-PEG)$_{11}$-*b*-P(NB-MEG)$_n$** (n = 60, 120, 140, 180, 240, and 260) diblock copolymer nano-objects developed *via* aqueous ROMPISA.

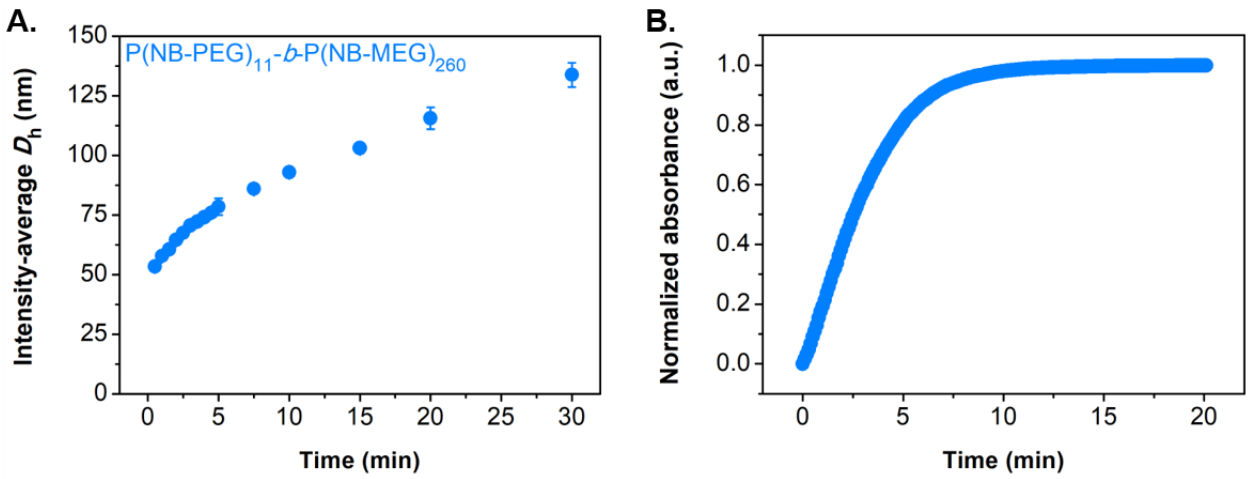

Figure S39. (A) Evolution of intensity-average D_h as a function of polymerization time for synthesis of **P(NB-PEG)$_{11}$-*b*-P(NB-MEG)$_{260}$** diblock copolymer nano-objects *via* aqueous ROMPISA, as determined by DLS analysis of nano-object aliquots withdrawn during kinetic monitoring. (B) Normalized absorbance as a function of polymerization time for synthesis of **P(NB-PEG)$_{11}$-*b*-P(NB-MEG)$_{260}$** diblock copolymer nano-objects *via* aqueous ROMPISA, as determined by *in situ* turbidimetric analysis during polymerization.

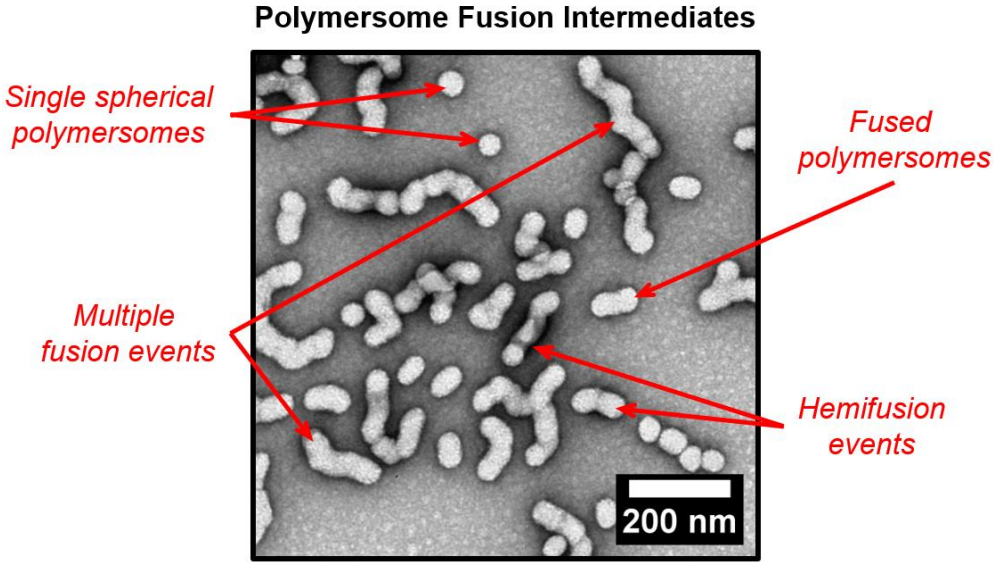

Figure S40. Representative dry-state TEM images of **P(NB-PEG)$_{11}$-*b*-P(NB-MEG)$_{240}$** diblock copolymer nano-objects developed *via* aqueous ROMPISA, stained with 1 wt% UA solution, showing various intermediate stages of polymerization-induced polymersome fusion.

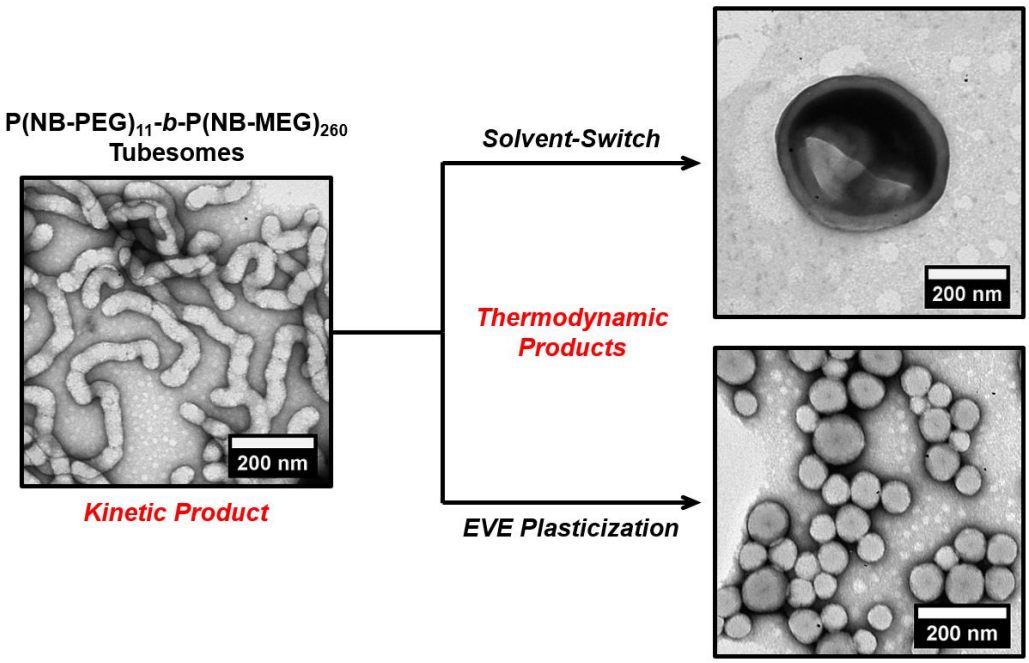

Figure S41. Representative dry-state TEM images of kinetically favored **P(NB-PEG)$_{11}$-*b*-P(NB-MEG)$_{260}$** diblock copolymer tubesomes developed *via* aqueous ROMPISA (left), and resulting thermodynamically favored **P(NB-PEG)$_{11}$-*b*-P(NB-MEG)$_{260}$** diblock copolymer nano-objects developed either *via* solvent-switch or upon treatment with plasticizing EVE molecules (right).

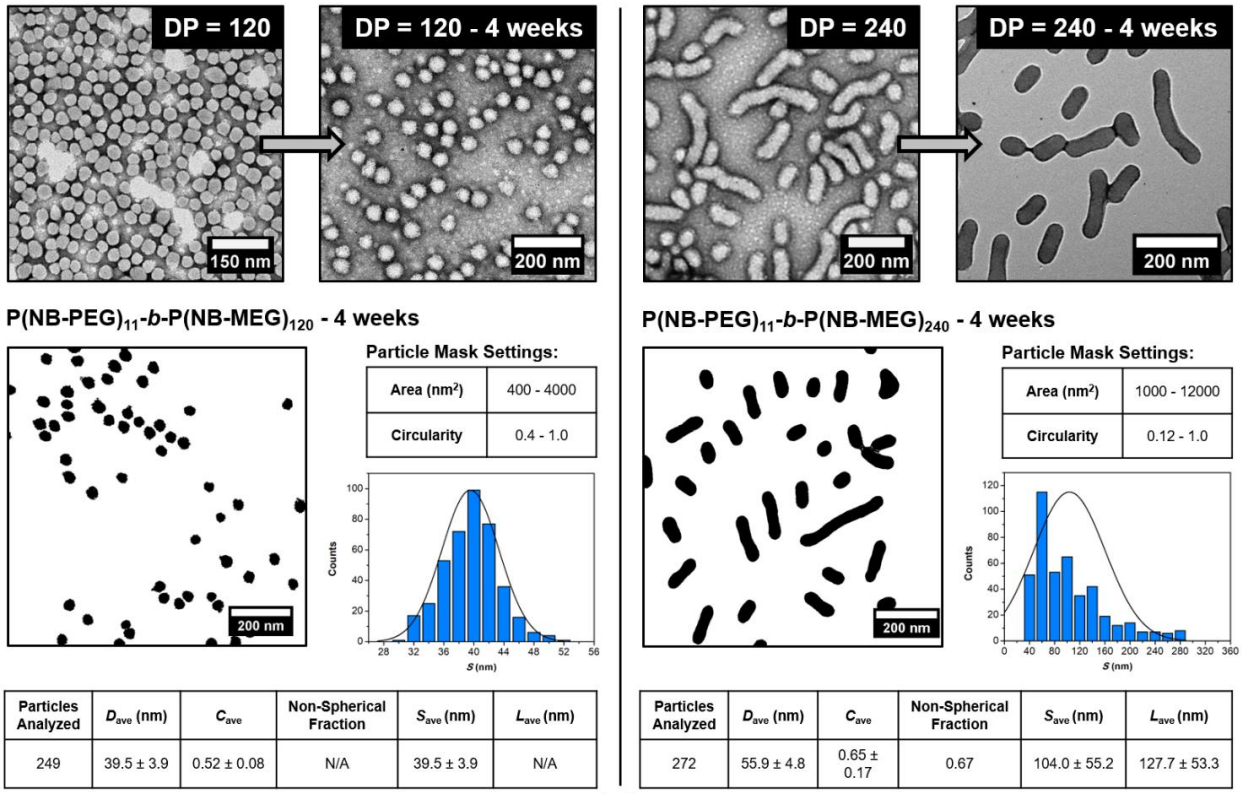

Figure S42. Representative dry-state TEM images of original **P(NB-PEG)$_{11}$-*b*-P(NB-MEG)$_{n}$** (n = 120, and 240) diblock copolymer nano-objects developed *via* aqueous ROMPISA and samples after aging for 4 weeks, stained with 1 wt% UA solution, along with summary of dry-state TEM image analysis results for aged **P(NB-PEG)$_{11}$-*b*-P(NB-MEG)$_{n}$** diblock copolymer nano-objects, as determined by image processing using ImageJ analysis software.

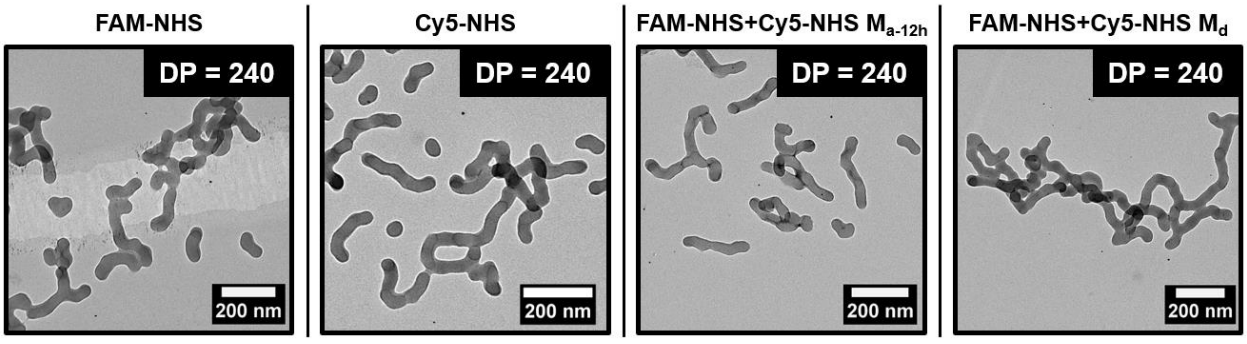

Figure S43. Representative dry-state TEM images of FAM-NHS- and Cy5-NHS-loaded **P(NB-PEG)$_{11}$-*b*-P(NB-MEG)$_{240}$** diblock copolymer nano-objects developed *via* aqueous ROMPISA and resulting $M_{a\text{-}12h}$ and M_d mixed samples, stained with 1 wt% UA solution.

Supplementary Characterization Data for P(NB-PEG)$_{11}$-*b*-P(NB-ACM)$_m$-*b*-P(NB-MEG)$_n$ and P(NB-PEG)$_{11}$-*b*-P(NB-RhB)$_{m/2}$-*b*-P(NB-MEG)$_n$ Triblock Copolymer Nano-Objects Developed by Aqueous ROMPISA and Mixed Samples

Abbreviation	Sample
ACM_n	**P(NB-PEG)$_{11}$-*b*-P(NB-ACM)$_m$-*b*-P(NB-MEG)$_n$** (n = 120, and 240)
RhB_n	**P(NB-PEG)$_{11}$-*b*-P(NB-RhB)$_{m/2}$-*b*-P(NB-MEG)$_n$** (n = 120, and 240)
ACM_n+RhB_n M_d	Samples ACM_n+RhB_n mixed **during** aqueous ROMPISA after 1 min
ACM_n+RhB_n $M_{a\text{-}2h}$	Samples ACM_n+RhB_n mixed **after** aqueous ROMPISA **for 2 hours**
ACM_n+RhB_n $M_{a\text{-}24h}$	Samples ACM_n+RhB_n mixed **after** aqueous ROMPISA **for 24 hours**

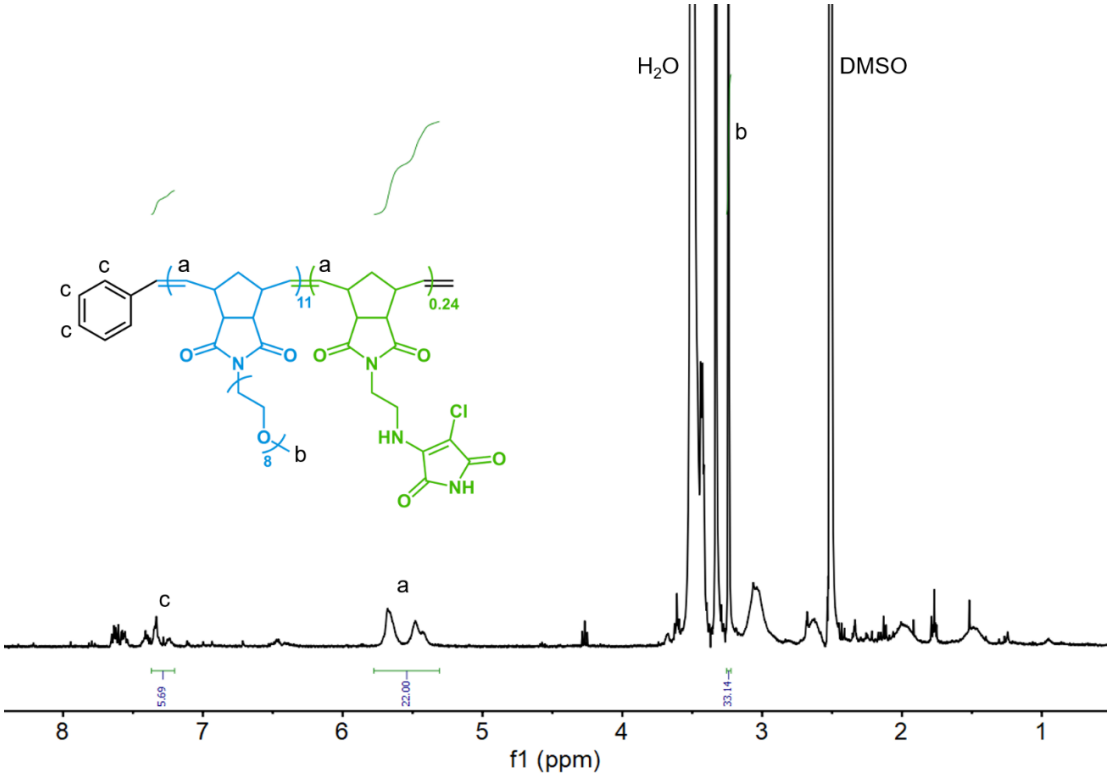

Figure S44. ^{1}H-NMR spectrum of **P(NB-PEG)$_{11}$-*b*-P(NB-ACM)$_{0.24}$** diblock copolymer macroinitiator in DMSO-d_6.

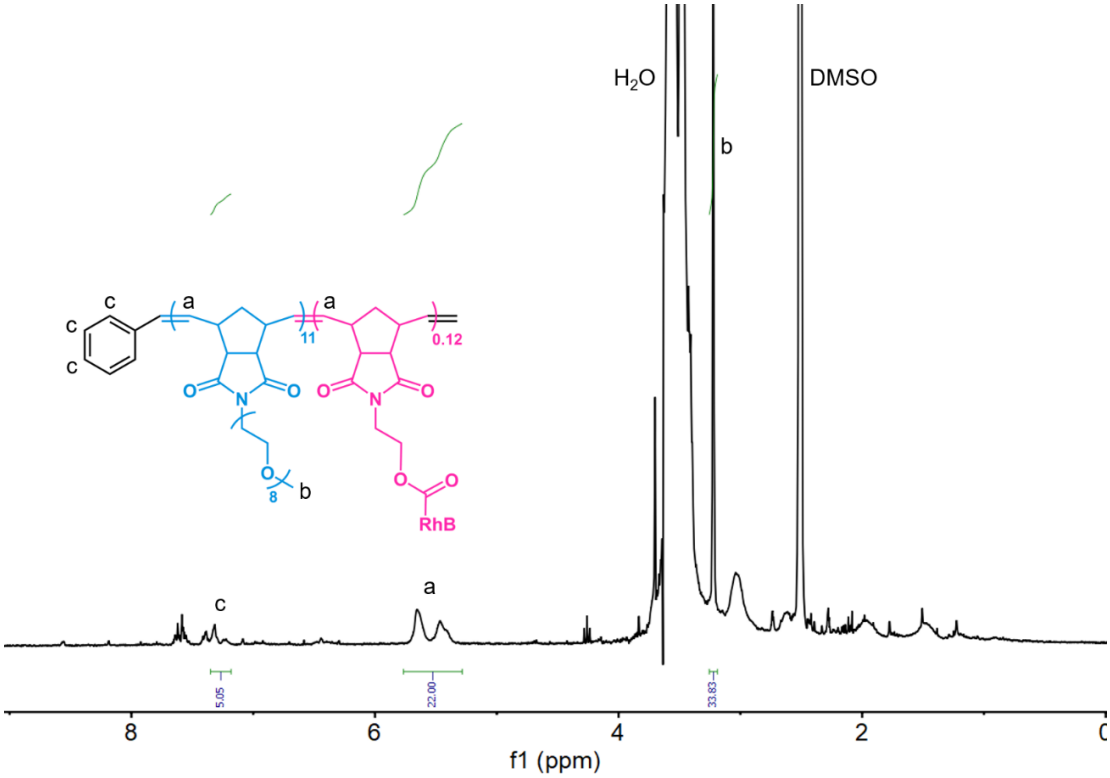

Figure S45. ^{1}H-NMR spectrum of **P(NB-PEG)$_{11}$-*b*-P(NB-RhB)$_{0.12}$** diblock copolymer macroinitiator in DMSO-d_6.

Table S13. Molecular characteristics of **P(NB-PEG)$_{11}$-*b*-P(NB-ACM)$_{m}$** and **P(NB-PEG)$_{11}$-*b*-P(NB-RhB)$_{m/2}$** (m = 0.12, and 0.24) diblock copolymer macroinitiators prepared *via* ROMP in THF, as determined by ^{1}H-NMR spectroscopy and SEC analysis.

[NB-PEG]/[G3]	[NB-ACM]/[G3]	[NB-RhB]/[G3]	% Conv.[a]	$M_{n,\,theo.}$ (kDa)[b]	$M_{n,\,SEC}$ (kDa)[c]	$Đ_{M,\,SEC}$[c]
10	**0.12**	-	>99	5.0	5.1	1.17
10	**0.24**	-	>99	5.0	5.7	1.16
10	-	**0.06**	>99	5.0	5.3	1.17
10	-	**0.12**	>99	5.0	5.8	1.16

[a]Monomer conversion calculated from ^{1}H-NMR spectroscopy in DMSO-d_6. [b]Calculated from conversion. [c]*M*n and $Đ_M$ values calculated from PS standards using THF + 2% v/v NEt_3 as the eluent.

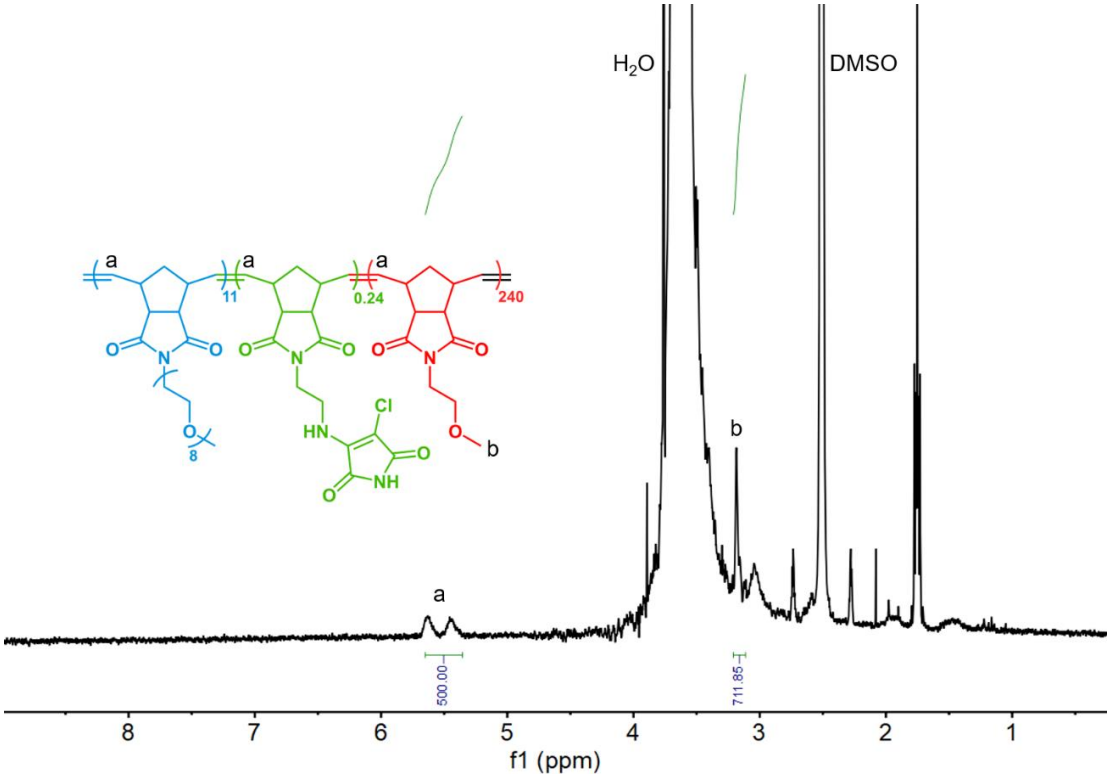

Figure S46. ^{1}H-NMR spectrum of **P(NB-PEG)$_{11}$-*b*-P(NB-ACM)$_{0.24}$-*b*-P(NB-MEG)$_{240}$** triblock copolymer in DMSO-d_6.

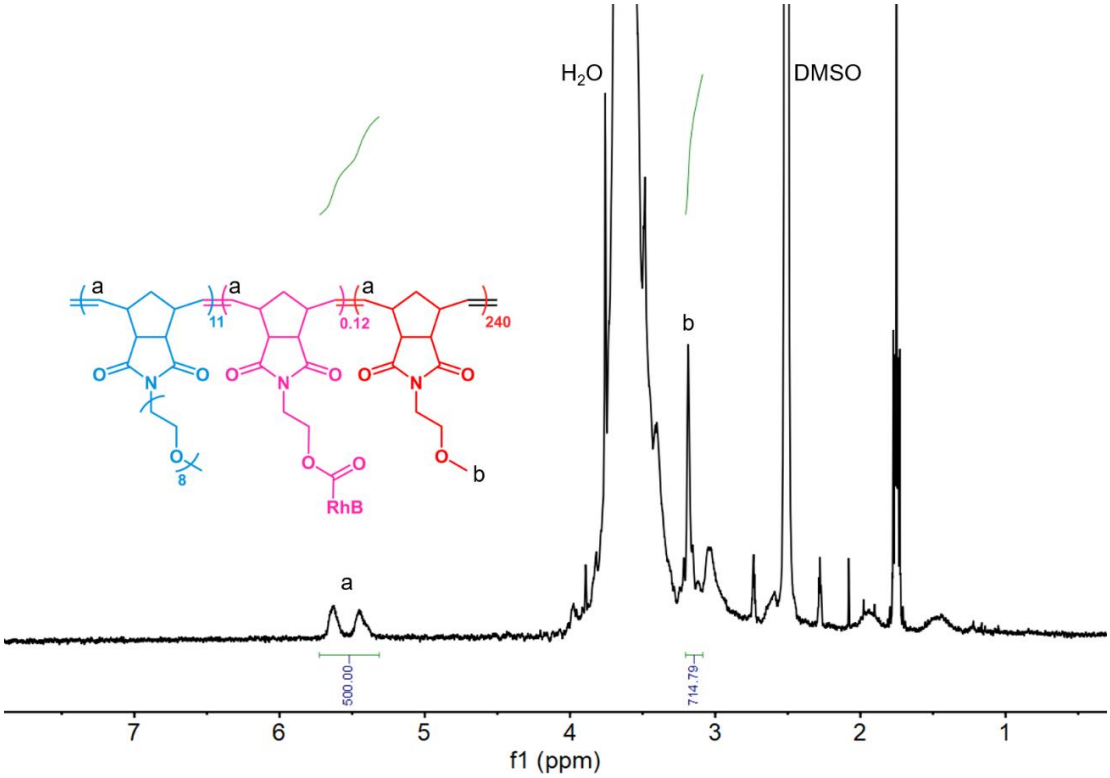

Figure S47. ^{1}H-NMR spectrum of **P(NB-PEG)$_{11}$-*b*-P(NB-RhB)$_{0.12}$-*b*-P(NB-MEG)$_{240}$** triblock copolymer in DMSO-d_6.

Table S14. Molecular characteristics of **P(NB-PEG)$_{11}$-*b*-P(NB-ACM)$_{m}$-*b*-P(NB-MEG)$_{n}$** and **P(NB-PEG)$_{11}$-*b*-P(NB-RhB)$_{m/2}$-*b*-P(NB-MEG)$_{n}$** triblock copolymers and resulting M_d mixed triblock copolymers prepared *via* aqueous ROMPISA using different initial [**NB-MEG**]/[**G3**] ratios, as determined by ^{1}H-NMR spectroscopy and SEC analysis.

Sample	[NB-MEG]/[G3]	% Conv.[a]	$M_{n,\,theo.}$ (kDa)[b]	$M_{n,\,SEC}$ (kDa)[c]	$Đ_{M,\,SEC}$[c]
ACM$_{120}$	**120**	>99	32.0	25.0	1.18
ACM$_{240}$	**240**	>99	58.5	47.4	1.23
RhB$_{120}$	**120**	>99	32.0	24.6	1.16
RhB$_{240}$	**240**	>99	58.5	46.6	1.24
ACM$_{120}$+RhB$_{120}$ M$_d$	**120**	>99	32.0	24.2	1.19
ACM$_{240}$+RhB$_{240}$ M$_d$	**240**	>99	58.5	44.8	1.22

[a]Monomer conversion calculated from ^{1}H-NMR spectroscopy in DMSO-d_6. [b]Calculated from conversion. [c]Mn and $Đ_M$ values calculated from PS standards using THF + 2% v/v NEt$_3$ as the eluent (with UV detection at λ_{ACM} = 360 nm or λ_{RhB} = 545 nm).

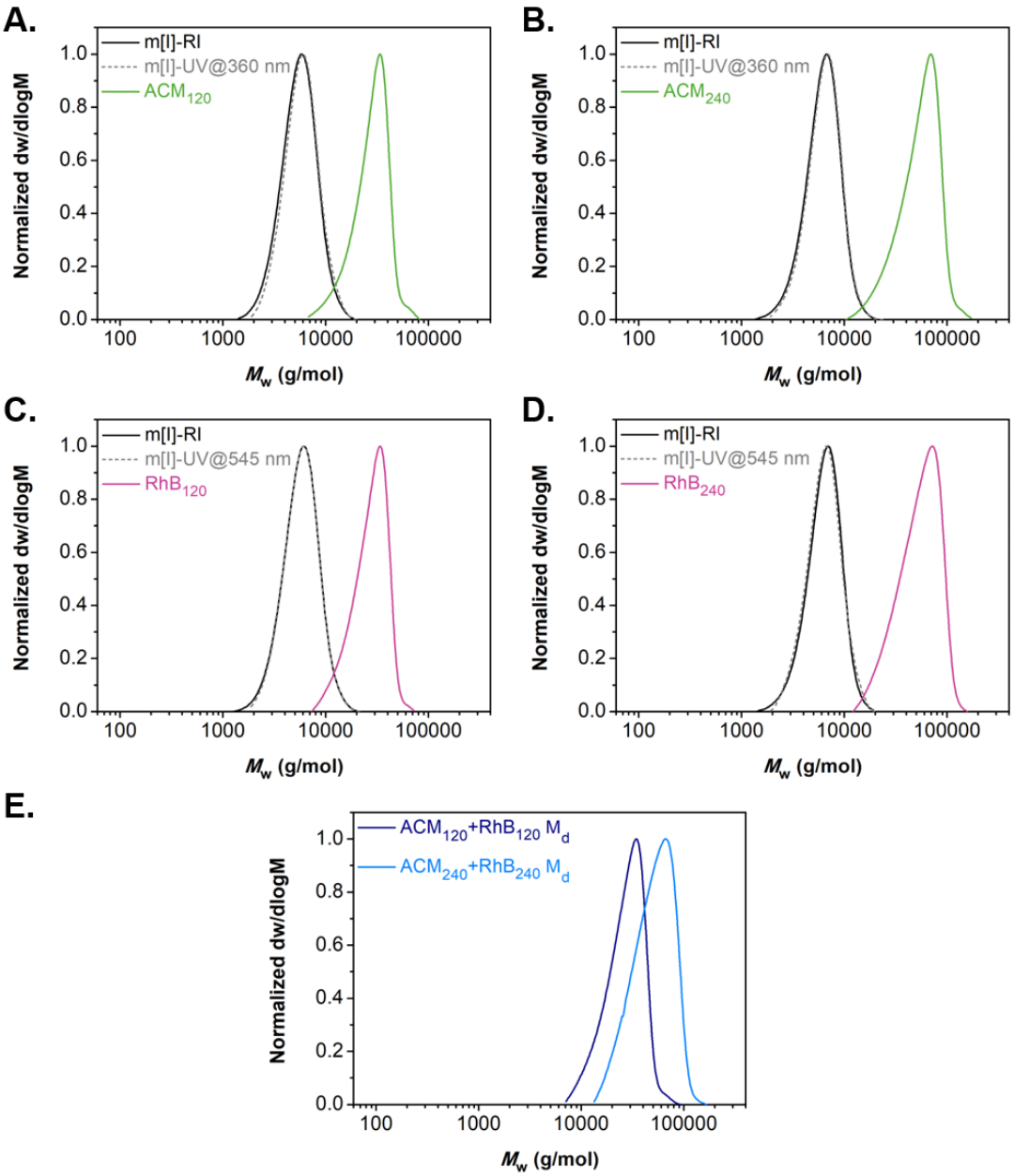

Figure S48. Normalized SEC molecular weight distributions for **P(NB-PEG)$_{11}$-*b*-P(NB-ACM)$_{m}$** diblock copolymer macroinitiators and **P(NB-PEG)$_{11}$-*b*-P(NB-ACM)$_{m}$-*b*-P(NB-MEG)$_{n}$** triblock copolymers (A-B), **P(NB-PEG)$_{11}$-*b*-P(NB-RhB)$_{m/2}$** diblock copolymer macroinitiators and **P(NB-PEG)$_{11}$-*b*-P(NB-RhB)$_{m/2}$-*b*-P(NB-MEG)$_{n}$** triblock copolymers (C-D) (m = 0.12, n = 120, and m = 0.24, n = 240), and resulting M_d mixed triblock copolymers (E) prepared *via* solution ROMP and aqueous ROMPISA, respectively. M_n and $Đ_M$ values were calculated from PS standards using THF + 2% v/v NEt_3 as the eluent (with UV detection at λ_{ACM} = 360 nm or λ_{RhB} = 545 nm).

Table S15. Summary of D_h and PD values and observed morphologies for **P(NB-PEG)$_{11}$-*b*-P(NB-ACM)$_m$-*b*-P(NB-MEG)$_n$** and **P(NB-PEG)$_{11}$-*b*-P(NB-RhB)$_{m/2}$-*b*-P(NB-MEG)$_n$** triblock copolymer nano-objects prepared *via* aqueous ROMPISA and resulting $M_{a\text{-}24h}$ and M_d mixed samples, as determined by DLS analysis and dry-state TEM imaging, respectively.

Sample	D_h (nm)[a]	PD[a]	Intensity-average D_h (nm)[a]	Morphology[b]
ACM_{120}	47.7 ± 0.9	0.10 ± 0.01	52.2 ± 1.3	V
ACM_{240}	152.1 ± 2.2	0.18 ± 0.03	161.9 ± 5.7	V + T
RhB_{120}	48.8 ± 1.9	0.20 ± 0.06	49.2 ± 2.6	V
RhB_{240}	464.9 ± 13.3	0.32 ± 0.05	189.2 ± 23.6	V + T
ACM_{120}+RhB_{120} $M_{a\text{-}24h}$	48.8 ± 0.8	0.17 ± 0.03	50.8 ± 1.2	V
ACM_{240}+RhB_{240} $M_{a\text{-}24h}$	280.4 ± 4.5	0.39 ± 0.05	183.4 ± 21.1	V + T
ACM_{120}+RhB_{120} M_d	49.6 ± 1.6	0.17 ± 0.02	51.9 ± 2.4	V
ACM_{240}+RhB_{240} M_d	649.9 ± 18.5	0.48 ± 0.03	190.2 ± 41.9	V + T

[a]D_h and PD values measured from DLS analysis (the error shows the standard deviation from 4 repeat measurements. [b]Morphologies observed from dry-state TEM imaging, using 1 wt% uranyl acetate (UA) solution for staining (Key: V – vesicles, T – tubesomes).

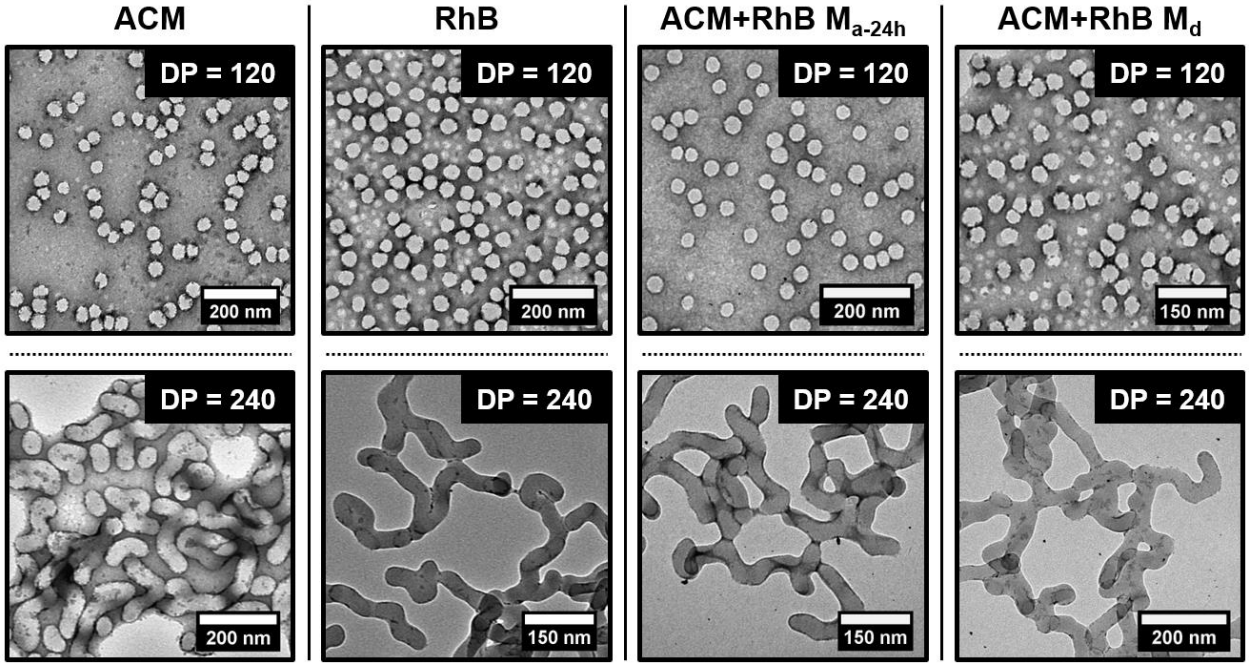

Figure S49. Representative dry-state TEM images of **P(NB-PEG)$_{11}$-*b*-P(NB-ACM)$_m$-*b*-P(NB-MEG)$_n$** and **P(NB-PEG)$_{11}$-*b*-P(NB-RhB)$_{m/2}$-*b*-P(NB-MEG)$_n$** (m = 0.12, and 0.24, n = 120, and 240) triblock copolymer nano-objects developed *via* aqueous ROMPISA and resulting $M_{a\text{-}24h}$ and M_d mixed samples, stained with 1 wt% UA solution.

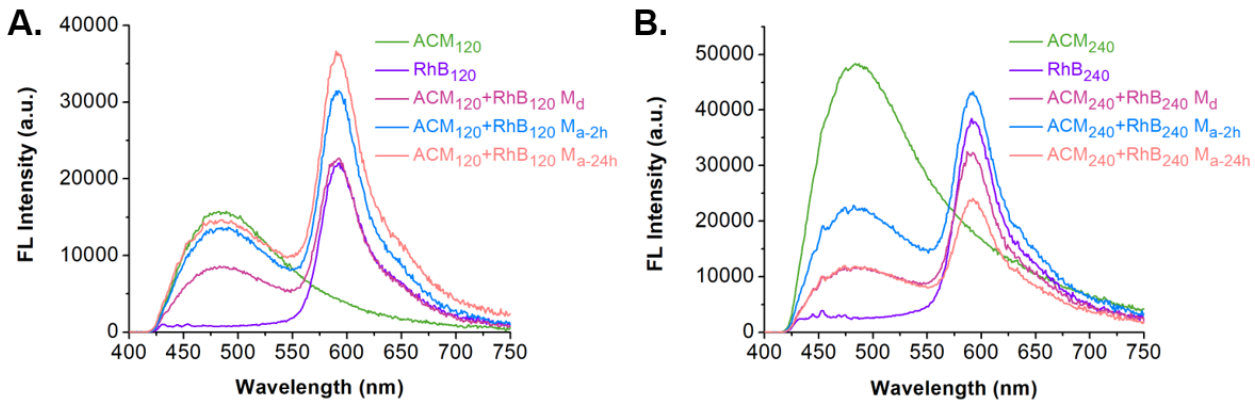

Figure S50. Fluorescence emission spectra of **P(NB-PEG)$_{11}$-*b*-P(NB-ACM)$_{m}$-*b*-P(NB-MEG)$_{n}$** and **P(NB-PEG)$_{11}$-*b*-P(NB-RhB)$_{m/2}$-*b*-P(NB-MEG)$_{n}$** ((A) n = 120, and (B) n = 240) triblock copolymer nano-objects developed *via* aqueous ROMPISA and resulting M_d, $M_{a\text{-}2h}$, and $M_{a\text{-}24h}$ mixed samples ($\lambda_{ex.}$ = 360 nm, slit width ex. = 2.5 nm, slit width em. = 2.5 nm).

Table S16. Summary of fitted parameters and intensity-average fluorescence lifetime ($\tau_{Av,I}$) and amplitude-average fluorescence lifetime ($\tau_{Av,A}$) values for **P(NB-PEG)$_{11}$-*b*-P(NB-ACM)$_m$-*b*-P(NB-MEG)$_n$** triblock copolymer nano-objects and resulting $M_{a\text{-}2h}$, $M_{a\text{-}24h}$, and M_d samples upon mixing with **P(NB-PEG)$_{11}$-*b*-P(NB-RhB)$_{m/2}$-*b*-P(NB-MEG)$_n$** triblock copolymer nano-objects, calculated from fluorescence lifetime spectroscopy.

Sample	Param.	Value (ns)	Std. D. (ns)	Rel. %	χ^2	$\tau_{Av,I}$	Std. D. (ns)	$\tau_{Av,A}$	Std. D. (ns)
ACM_{120}	τ_1 τ_2 τ_3 τ_4	1.00 5.30 14.01 -	0.05 0.11 0.12 -	6.72 41.47 51.81 -	2.25	11.91	0.11	9.52	0.11
ACM_{240}	τ_1 τ_2 τ_3 τ_4	0.22 3.55 12.96 -	0.01 0.05 0.07 -	9.85 31.49 58.66 -	1.98	11.73	0.06	8.74	0.06
ACM_{120}+RhB_{120} $M_{a\text{-}2h}$	τ_1 τ_2 τ_3 τ_4	0.20 3.43 12.54 -	0.01 0.04 0.06 -	6.79 35.65 57.56 -	1.90	11.20	0.05	8.45	0.05
ACM_{240}+RhB_{240} $M_{a\text{-}2h}$	τ_1 τ_2 τ_3 τ_4	0.17 3.10 12.23 -	0.01 0.05 0.07 -	15.05 30.83 54.12 -	1.93	11.04	0.06	7.60	0.05
ACM_{120}+RhB_{120} $M_{a\text{-}24h}$	τ_1 τ_2 τ_3 τ_4	0.05 3.02 11.99 -	0.00 0.05 0.07 -	14.38 30.42 55.20 -	1.72	10.89	0.06	7.54	0.05
ACM_{240}+RhB_{240} $M_{a\text{-}24h}$	τ_1 τ_2 τ_3 τ_4	0.05 3.10 12.05 -	0.00 0.05 0.08 -	15.81 30.99 53.21 -	1.72	10.87	0.07	7.38	0.06
ACM_{120}+RhB_{120} M_d	τ_1 τ_2 τ_3 τ_4	0.22 3.41 12.35 -	0.01 0.04 0.06 -	6.97 34.88 58.15 -	1.97	11.06	0.05	8.39	0.05
ACM_{240}+RhB_{240} M_d	τ_1 τ_2 τ_3 τ_4	0.16 2.89 11.83 -	0.01 0.05 0.08 -	20.93 28.20 50.87 -	2.27	10.71	0.07	6.87	0.06

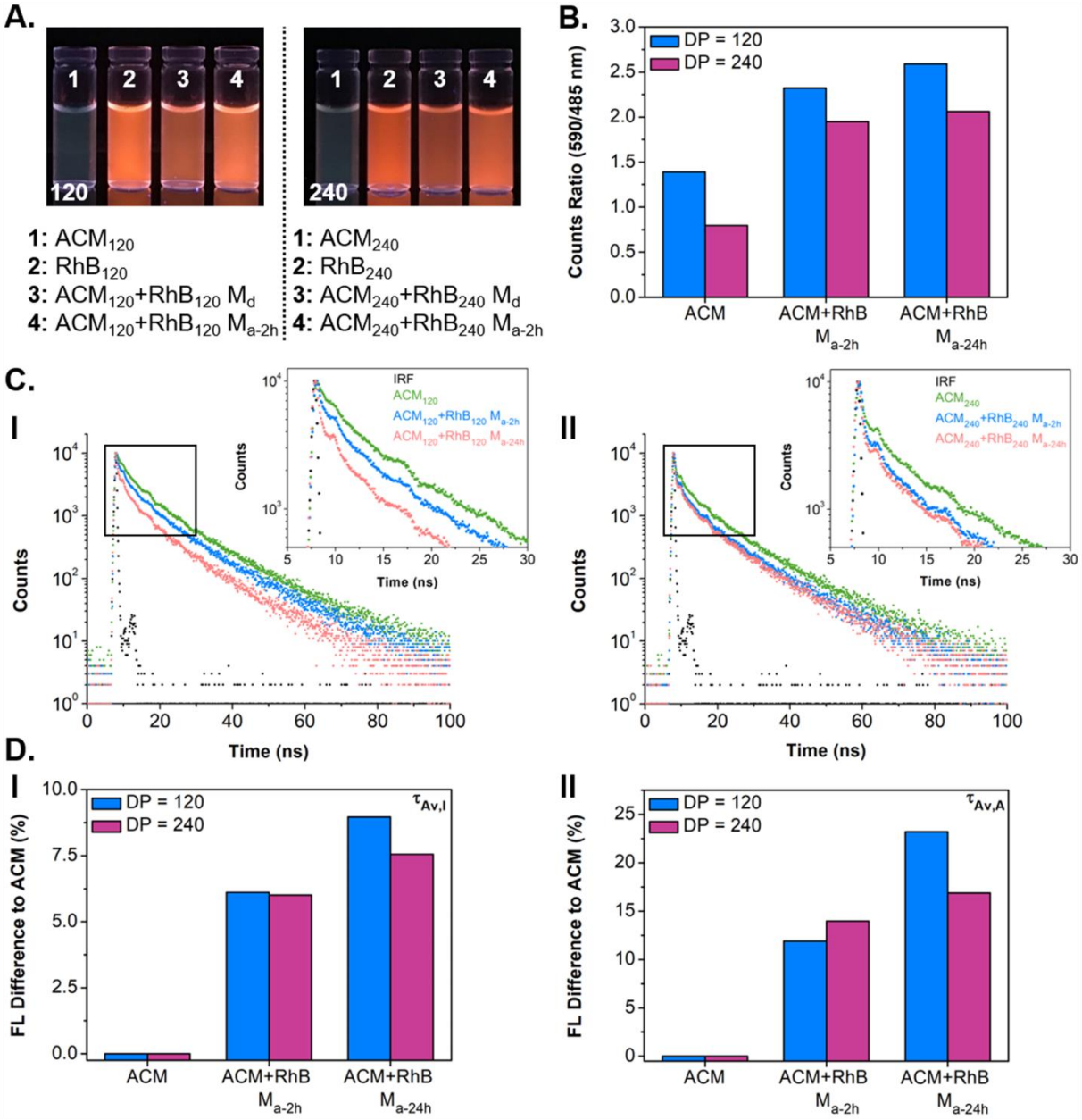

Figure S51. (A) Images of ACM_n, RhB_n, ACM_n+RhB_n M_d, and ACM_n+RhB_n $M_{a\text{-}2h}$ (n = 120, and 240) triblock copolymer nano-object solutions under UV light exposure (λ = 365 nm). For ACM_n, ACM_n+RhB_n $M_{a\text{-}2h}$, and ACM_n+RhB_n $M_{a\text{-}24h}$ triblock copolymer nano-objects: (B) Counts ratio of the donor ($\lambda_{em.\ ACM}$ = 485 nm) and acceptor ($\lambda_{em.\ RhB}$ = 590 nm) fluorescence emission peaks. (C) Fluorescence lifetime decay profiles of (I) n = 120, and (II) n = 240 samples. (D) Comparison of average fluorescence lifetime values, expressed as % difference relative to the pure ACM_n nano-objects, obtained using (I) $\tau_{Av,I}$, and (II) $\tau_{Av,A}$ fitting models.

References

1. Radzinski, S. C.; Foster, J. C.; Scannelli, S. J.; Weaver, J. R.; Arrington, K. J.; Matson, J. B., Tapered Bottlebrush Polymers: Cone-Shaped Nanostructures by Sequential Addition of Macromonomers. *ACS Macro Lett.* **2017,** *6*, 1175-1179.
2. Foster, J. C.; Varlas, S.; Blackman, L. D.; Arkinstall, L. A.; O'Reilly, R. K., Ring-Opening Metathesis Polymerization in Aqueous Media Using a Macroinitiator Approach. *Angew. Chem. Int. Ed.* **2018,** *57*, 10672-10676.
3. Varlas, S.; Foster, J. C.; Arkinstall, L. A.; Jones, J. R.; Keogh, R.; Mathers, R. T.; O'Reilly, R. K., Predicting Monomers for Use in Aqueous Ring-Opening Metathesis Polymerization-Induced Self-Assembly. *ACS Macro Lett.* **2019,** *8*, 466-472.
4. Patterson, J. P.; Robin, M. P.; Chassenieux, C.; Colombani, O.; O'Reilly, R. K., The analysis of solution self-assembled polymeric nanomaterials. *Chem. Soc. Rev.* **2014,** *43*, 2412-2425.
5. Thompson, M. P.; Randolph, L. M.; James, C. R.; Davalos, A. N.; Hahn, M. E.; Gianneschi, N. C., Labelling polymers and micellar nanoparticles via initiation, propagation and termination with ROMP. *Polym. Chem.* **2014,** *5*, 1954-1964.
6. Xie, Y.; Husband, J. T.; Torrent-Sucarrat, M.; Yang, H.; Liu, W.; O'Reilly, R. K., Rational design of substituted maleimide dyes with tunable fluorescence and solvafluorochromism. *Chem. Commun.* **2018,** *54*, 3339-3342.
7. Huang, Y.; Vezeridis, A. M.; Wang, J.; Wang, Z.; Thompson, M.; Mattrey, R. F.; Gianneschi, N. C., Polymer-Stabilized Perfluorobutane Nanodroplets for Ultrasound Imaging Agents. *J. Am. Chem. Soc.* **2017,** *139*, 15-18.

Additional Discussion on Characterization Data

As discussed in Section 4.2, investigations to develop a methodology that would allow for controlled aqueous ROMP at neutral pH carried out in our group after the publication of the articles included in Chapters 4 and 5 have revealed that Ru-based catalysts are susceptible to deactivation upon chloride ligand displacement by OH^- or H_2O species when in aqueous media (see https://pubs.acs.org/doi/abs/10.1021/jacs.0c05499 for further details). Importantly, both Cl^- concentration and pH value of the reaction medium have been shown to drastically affect final monomer conversion and polymerization control. In Figures S12 and S30 of Chapter 5, two distinct regimes are observed in the semi-logarithmic kinetic plots constructed upon monitoring of ROMPISA reactions in acidic aqueous media. In the first regime from 0 to ~ 0.5 min, ROMP occurs in solution with an apparent faster turnover being observed. However, **G3** deactivation is inevitably taking place to some extent even in acidified aqueous media by OH^-/H_2O resulting in a rate retardation in the second regime from 0.5 to 10 min. During this second regime, catalyst decomposition is markedly slower and the polymerization rate remains constant, suggesting the effective protection of the active chain ends from the solvent molecules by the developed nano-object hydrophobic cores.

In Figure S11, the quadruplet peak visible at approx. 6.5 ppm is attributed to EVE that was used for quenching the polymerization at different time points during kinetic monitoring of ROMPISA reactions. This peak is absent in the stacked spectra shown in Figure S29 due to EVE evaporation from the quenched kinetic samples prior to NMR analysis.

Chapter 6. Conclusions and Outlook

The overall aim of this thesis was to introduce simple, yet efficient, strategies for controlling the physical and chemical membrane properties of block copolymer vesicles (polymersomes) prepared *via* aqueous polymerization-induced self-assembly (PISA). In this Chapter, the key findings and emerging trends identified herein will be briefly highlighted, while important considerations and directions for potential future studies based on the original work discussed in this thesis will be also presented.

Over recent years, PISA has attracted tremendous research interest owing to its numerous advantages over traditional self-assembly procedures and has been successfully employed in various industrial and biomedical applications. Nevertheless, the projects discussed in this thesis have been amongst the pioneering studies in this rapidly expanding field focused on the development of polymersomes with tunable characteristics that could be further used as artificial biomembrane-mimicking models for the investigation of fundamental cellular and subcellular processes (e.g., compartmentalization, transport, diffusion, fusion, *etc*).

In particular, this thesis initially explored adaptable approaches to regulate the non-specific passive diffusion of small molecules across hydrophobic polymethacrylate-based membranes by either enhancing or reducing the permeability of polymersome nanoreactors prepared by aqueous RAFT-mediated photo-PISA. This was respectively achieved either *via* the surfactant-directed insertion of channel-forming protein OmpF within the membrane of PEG-*b*-PHPMA polymersomes during their formation *via* photo-PISA (Chapter 2), or by increasing the membrane thickness and hydrophobicity of PEG-*b*-P(HPMA-*co*-GlyMA) polymersomes through a post-PISA membrane functionalization approach based on epoxide ring-opening reactions using a series of primary amines (Chapter 3). In both cases, a model hydrophilic enzyme, HRP, was encapsulated within

the interior aqueous lumen of the polymersomes in order to provide a read-out of the nanoreactor catalytic activity and, as an extent, their membrane permeability upon monitoring the rate of an HRP-catalyzed reaction, in line with previous studies carried out by our group and others.

Furthermore, the one-pot methodology described in Chapter 2 presents an efficient alternative to existing processes that rely upon the energetically unfavored incorporation of membrane proteins into preformed bilayered formulations. This study could be also used as a general guide for the facile reconstitution of other functional membrane proteins or hydrophobic (macro)molecules within polymersome nanostructures in order to impart such bio-mimicking systems with higher complexity and selectivity and provide deeper insight into basic membrane trafficking and communication mechanisms. Inspired by the original membrane modification concept explored in Chapter 3, innovative strategies are expected to be developed in the next-generation PISA formulations that would allow for reversible manipulation over the polymersome membrane permeability based on the responsiveness of the core-forming block to various externally applied stimuli. This, in turn, will aid the occurrence of reactions or release of cargo on an “on-demand” fashion depending on the surrounding microenvironment of the nanostructures and promote the potential use of such advanced systems in targeted drug delivery and selective catalysis. However, it is expected to be rather difficult to follow similar permeability determination procedures entailing the encapsulation of hydrophilic enzymes into polymersome nanoreactors with stimuli-responsive membranes, since any microenvironment changes would simultaneously affect both the membrane diffusivity, as well as the enzymatic activity leading to misinterpretation of the apparent polymersome permeability. As such, new spectroscopic or chromatographic characterization methods should be also

established that would provide accurate measurement of the membrane diffusivity in these cases (ideally covering a wide range of small molecules and ions).

Building upon the knowledge acquired in Chapters 2 and 3 of this thesis and the evident relationships identified between the polymersome membrane hydration, porosity, thickness and observed permeability toward small molecules, an alternative mild PISA approach mediated by living ring-opening metathesis polymerization (ROMP) in acidic aqueous media was explored in Chapters 4 and 5 that allowed for preparation of a diverse set of polynorbornene-based polymersomes with conceivably more hydrophobic and, thus, less permeable membranes, which could be further employed in biocatalysis and nanomedicine applications.

In Chapter 4, a wide range of functional NB-based core-forming monomers for use in ROMPISA formulations were identified through computational oligomer hydrophobicity calculations that, in turn, were successfully utilized for the development of diblock copolymer nano-objects of controllable morphology and core domain composition. Interestingly, the majority of newly predicted monomers contained reactive pendant groups, such as alcohols, esters and ethers, that could potentially be utilized in subsequent post-PISA membrane modification reactions in a similar manner to the strategy followed in Chapter 3 to introduce specifically designed functionalities within their structure for certain bio-related applications. In Chapter 5, it was demonstrated that the uniquely small nanostructures obtained *via* aqueous ROMPISA were indeed "kinetically-frozen", exhibiting limited unimer rearrangement and exchange within or between particles due to the rapid polymerization kinetics achieved and the increased rigidity and T_g of constituent polymer chains. These intriguing characteristics of PNB-based nano-objects were further exploited for the *in situ* preparation of tubular polymersomes during ROMPISA, driven

by the inherent built-up of membrane tension exerted by the growing polymer chains and the occurrence of step-wise intervesicular fusion events as a way for the system to release its high membrane bending energy. Importantly, the presence or absence of positive charges within the particle coronae was shown to restrict or facilitate the polymerization-induced polymersome fusion, respectively. Moreover, initial findings discussed in Chapter 5 suggested that the membranes of these polymersomes were near impermeable toward hydrophilic small molecule encapsulates over prolonged periods of time, although a more thorough investigation on this preliminary results is deemed of particular significance for future studies using these nanostructures in biomimicry.

Considering the limited knowledge that currently exists in the literature on the interactions of PNB-based nanostructures with biological systems, future research is expected to be directed toward the assessment of the pharmacokinetics of these formulations that would provide valuable insight into the biodistribution, internalization profile, immune response and clearance pathways of assemblies with different characteristics (e.g., cationic *vs* neutral, spherical *vs* tubular). In addition, the universal character of the intriguing self-assembly behavior identified in Chapter 5 for direct access to tubesomes could be explored in other PISA systems that fulfill the requirements highlighted above (i.e., "glassy" and rigid block copolymers, fast polymerization and self-assembly procedures) and could provide deeper understanding of fundamental natural processes involving the fusion and fission of biological membranes for transport of cargo across cells (e.g., endo- and exocytosis mechanisms). Nonetheless, it should be mentioned that the main limitation of our aqueous ROMPISA methodology in its present state is the requirement of acidic additives to prevent rapid catalyst decomposition by OH^- species and achieve living polymerization processes, rendering the systems incompatible with the

majority of pH-sensitive proteins and enzymes. New synthetic protocols that would allow for controlled ROMP in neutral aqueous media without considerably affecting the polymerization kinetics and catalyst decomposition rate are currently being developed within our group and are expected to significantly broaden the application scope of such assemblies.

Ultimately, preparation of multi-compartmentalized vesicular nanoreactors has yet to be realized in PISA despite its well-documented procedural simplicity and versatility. Such synthetic "nanofactories" would more closely resemble the hierarchical organization found within a cell and its containing organelles and would better mimic interactions occurring in natural systems (i.e. enzymatic cascade reactions in confined environments). To this end, this thesis is expected to open new avenues toward the design of enzyme-loaded multivesicular polymersomes with high structural complexity *via* a PISA-in-PISA strategy upon exploiting the orthogonality between RAFT-mediated photo-PISA and ROMPISA, as well as the markedly different polymersome sizes typically obtained by the two techniques.